

Physicochemical Problems of Mineral Processing

Index No. 32213X

ISSN 1643-1049

Volume 51, Issue 1

January 1, 2015

Physicochemical Problems of Mineral Processing

Volume 51, Issue 1, January 1, 2015

www.minproc.pwr.wroc.pl/journal
www.dbc.wroc.pl/dlibra/publication/11251

Faculty of Geoengineering, Mining and Geology
Wroclaw University of Technology

Wydział Geoinżynierii, Górnictwa i Geologii
Politechniki Wrocławskiej
Wrocław 2015

Received March 11, 2014; reviewed; accepted April 14, 2014

EVALUATION OF FLOCCULATION BEHAVIOR OF MARBLE POWDER SUSPENSIONS

Selma DUZYOL

Department of Mining Engineering, Engineering Faculty, Selcuk University, Campus, Konya, 42075, Turkey
(selmad@selcuk.edu.tr)

Abstract: In this study, flocculation of marble powder suspensions was investigated depending on a polymer type and dosage. Polyacrylamide was used as a synthetic polymer, while starch was used as a natural polymer. The effect of polyacrylamide type was also examined using anionic, cationic and non-ionic polyacrylamides. Flocculation of suspensions was ascertained by turbidity measurements. It was found that anionic and especially non-ionic polymers flocculated the marble powder suspension more strongly than starch and cationic polymer. On the other hand, it was observed that the sequential addition of starch and polymer did not improve flocculation of suspension. On contrary, sequential addition of flocculants caused re-dispersion of the flocculated suspension. When a non-ionic polymer was used as the flocculant, the reached minimum turbidity of suspension was measured to be 38 NTU (nephelometric turbidity unit).

Keywords: *flocculation, marble powder, water soluble polymer, starch, turbidity*

Introduction

In marble cutting plants, production of ultra-fine powders is inevitable. A large amount of water is used during marble cutting and polishing, therefore, the necessity of water is the main problem of such plants. Another important problem is removal of ultra-fine powders from a recirculating plant water for the environmental apprehension. Flocculation enables both recycling of plant water without these impurities and fast settling of ultra-fine powder. There are some studies on the flocculation of marble powder suspensions in the literature (Bayraktar et al., 1996; Seyrankaya et al., 2000; Ersoy, 2005; Solak et al., 2009; Basaran and Tasdemir, 2014).

Aggregation of fine particles using polymolecules is called polymeric flocculation (Attia, 1992). Flocculation normally starts with mixing of particles and polymers in a solution. After realization of adsorption of polymer chains on a particle surface, re-conformation of adsorbed chains on the surface can be seen. Then, the aggregates are

formed and flocs are re-structured followed by the occurrences of flocs sedimentation (Gregory, 1988).

The polymeric flocculants consist of long-chain molecules with high molecular weights and they are characterized by their ionic nature (cationic, anionic and non-ionic). The molecular weight values of flocculants range from a few thousands up to tens of millions. They may be classified as natural, synthetic or modified flocculants. The interactions responsible for adsorption of the polymeric flocculants on the mineral surfaces can be either physical or chemical (Attia, 1992). Electrostatic and van der Waals forces are responsible for the physical adsorption which is usually weak and reversible (Parfitt and Rochester, 1983). Chemical adsorption is usually strong and irreversibly and occurs through covalent bonding between the adsorbate and surface species on the solid (Attia, 1992).

Starch is a polymer of glucose containing a mixture of linear sugar amylose and branched sugar amylopectin. Starch can be produced from many sources such as corn and wheat, and its molecular weight ranges from a few thousand to five or six millions (Klimpel, 1997). Starches consist mainly of the polysaccharides of monosaccharide with different degrees of molecular weight and chain formation. Some typical examples of starch derivatives are starches, anionic oxidized starches or amine-treated cationic starches and show the pre-gelatinized and water-soluble properties. Adsorption of starch and related polysaccharides on particles can be assumed to be more than one mechanism involved in the process. Starch can also illustrate a depressing action due to its strong adsorption mechanism on the mineral surface (Abdel-Khalek et al., 2012).

Utilisation of double flocculant systems seems to offer a promising route for enhanced solid-liquid separation of fine and ultrafine solid suspensions. Mixing-polymer addition can be detrimental as well as very beneficial for the flocculation and the use of combinations of oppositely charged polyelectrolytes under suitable conditions enhancing the flocculation. Different mixing-polymer addition conditions may result in varying flocs size and settling rates. Dual polymer flocculations have been investigated by some researchers (Yu and Somasundaran, 1993; 1996; Petzold and Lunkwitz, 1995; 1996; Fan et al., 2000; Abro et al., 2013).

For a successful flocculation, some variables such as pH, ionic strength, type of flocculants and its properties such as molecular weight, charge density, and molecular structure are counted as significant parameters (Werneke, 1979; Atesok, 1988; Hogg, 2000; Yazar, 2001; Karbassi et al., 2013). The floc size distribution is a key variable and influences settling rate as well as turbidity of suspensions (Runkana et al., 2005). The turbidity value of suspension represents suspended particulate matters in the suspension. Ideally, a well-flocculated suspension should settle leaving no suspended solids in the supernatant liquid and hence a very low turbidity. Therefore, the turbidity is the simple way to measure the performance of flocculation (Hogg, 2000).

The main objective of this paper is to reveal the flocculation behaviors of marble powder suspension by the use of individual and sequential addition of polymers.

Additionally, the aim of this study is to determine the effects of some operating parameters including the flocculant type and dosage, sequential addition of synthetic polymeric flocculant and starch as a natural flocculant.

Experimental

Materials and method

The marble powder sample known as Marmara White was obtained from the Ozaltintas marble cutting plant, Ordu/Turkey. The marble powder consisted of 92-95% dolomite ($\text{CaMg}(\text{CO}_3)_2$) and 5-8% calcite (CaCO_3). The density of sample was determined as 2.7 g/cm^3 . The particle size distribution of the sample was identified using an Andreasen pipette and the reached results are given in Fig. 1. By the use of the Andreasen pipette, the size distribution is found by letting a homogeneous suspension to have a settlement in a cylinder and by taking samples from the settled suspension at a fixed horizontal level with certain time intervals. The curves of the total size distribution of the particles dispersed and settled in the liquid are evaluated depending on the terminal settling velocity of the particles or on the diameter equivalent to the settling velocity (Allen, 1981). It can be seen from Fig. 1 that the marble powder sample has 80% passing through the sieve size of $30 \mu\text{m}$. The d_{50} value of the sample was determined to be $15.2 \mu\text{m}$.

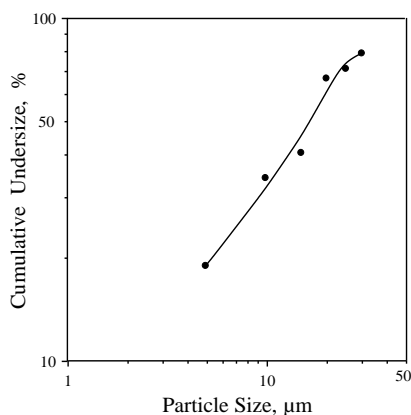


Fig. 1. Particle size distribution of marble powder

Three types of polymeric flocculants: anionic (A-150), cationic (C-521) and non-ionic (N-100) Superfloc flocculants obtained from the American Cyanamid Company (Cytec) were used during the experiments. The molecular weights of A-150 and N-100 polymers are in the range of $5-15 \cdot 10^6$ and C-521 is $2-6 \cdot 10^6$. The polymeric flocculants were prepared as 0.1% solutions using distilled water. Wheat starch was also used as a natural flocculant in a powder form without any modification. Sodium hydroxide and hydrochloric acid (Merck) were utilized for pH adjustment and pH

values of suspension were measured using a digital pH meter (Jenco 6230 model). All experiments were performed in distilled water.

Zeta potential measurements were carried out using a Zeta Plus zetameter produced by Brookhaven Company. The measurable zeta potential range is between -150 and $+150$ mV and a typical standard deviation of experimental measurements is in the order of 2 mV. The turbidity of the suspension was quantified by a Velp Scientifica turbidimeter.

The marble powder suspension was prepared with 5 g solid and 500 cm³ distilled water. The solid ratio of the suspension was selected as 1% (w/w), which is close to the medium value for the original plant water. At the beginning, the solution was mixed at 400 rpm for 2 min for good dispersion of solid. After addition of flocculant, the solution was mixed for another 3 min to obtain polymer adsorption onto the mineral surfaces. Then, the suspension was taken and poured into the graduated cylinder. The cylinder was sealed and inverted for ten times to obtain a good mixing and put on a flat place to track the flocculated sample. After 30 min of settling time, a small amount of solution was taken by using an automatic pipette at a certain height of suspension for a turbidity measurement. To determine the effect of sequential addition of flocculant on the flocculation behavior of marble suspension, the natural (starch) and synthetic flocculants were added in a sequence. A 3 min of conditioning time was allowed for each flocculant. The turbidity value of non-flocculated suspension could not be measured since it was above the upper limit (1000 NTU, nephelometric turbidity unit) of turbidimeter. The residual turbidity was measured as 307 NTU after sedimentation time of 30 min.

Results and discussion

Zeta Potential Measurements

The stability of colloidal suspensions can be controlled by the conduction of zeta potential. The greater value of zeta potential causes the stability of suspension. The zeta potential value depends on the pH value of the suspension. If the charge of particle surface is high enough, it results in significant mutual repulsion preventing the particles from coming closer to each other. Therefore, if the charge on these particles is reduced to zero, these repulsion forces can be eliminated. The value of pH for which zeta potential is zero, is called the point of zero charge (zpc). The zeta potential values versus the pH values of marble powder suspensions are presented in Fig. 2. As can be seen from Fig. 2, the zpc value was specified as 9.6. Under this value, the marble powder surfaces have a positive potential. The surface potential of marble powder was determined as $+2.5$ mV at pH = 9, which was natural pH of suspension. The marble powder mainly contains dolomite. The zeta potential value of dolomite varies between 0 mV and -20 mV (Chen and Tao, 2004; El-Midany, 2004; Gence and Ozbay, 2006; Marouf et al., 2009; Bastrzyk et al., 2011). Additionally, the measured zeta potential of natural stones can be positive, negative or variable depending on measurable

conditions, contribution of solubility products, hydrolyzing reactions and availability of other ions (Seyrankaya et al., 2000; Moulin and Roques, 2003; Ersoy, 2005; Zhang and Austa, 2006; Kurama and Karaguzel, 2013).

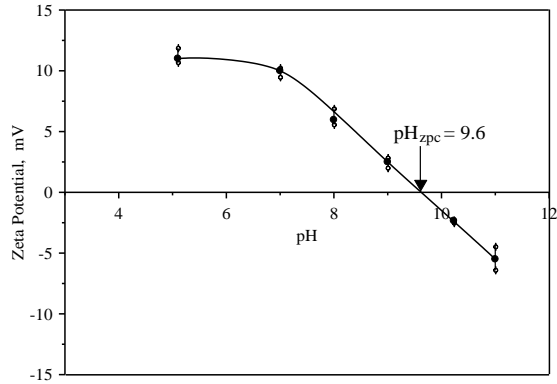


Fig. 2. Zeta potential of marble powder vs. pH

Turbidity

The turbidity is used to determine the presence of suspended particles in the suspension. The aim of flocculation process is to clarify the turbid water enabling the optimum conditions after sedimentation of the flocs. The supernatant turbidity of suspension is a function of settling time is given in Fig. 3. It can be seen that the settling of suspended particles takes a long time without usage of the flocculant. The turbidity of suspensions also shows the performance of the flocculant used. For this reason, the turbidity measurements were carried out on the supernatant sample following the flocculation experiments. A certain amount of supernatant was put into the cell of turbidimeter. The measurements were then realized and repeated for three times at least.

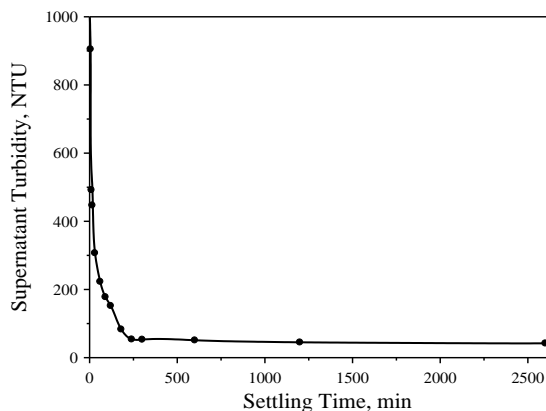


Fig. 3. Supernatant turbidity of marble powder vs. settling time

Flocculation with single flocculant

Klimpel (1997) showed that when the non-ionic polymers are not affected by the change of pH in the medium, the anionic polymers are effective at neutral and low alkali medium and the appropriate pH levels vary for the cationic polymers. Therefore, in this work the flocculation tests were performed at the pH = 9 which is the natural pH value of suspension and the obtained results are represented in Fig. 5. The polymeric flocculants A-150 and N-100 showed the best flocculation performance at low concentration level (0.02 g/dm^3). The adsorption mechanism is through the charge neutralisation resulted from the electrostatic interaction among the anionic flocculant and the positively charged mineral surfaces. It is assumed that adsorption of the non-ionic polymer onto the marble powder surfaces was realized via hydrogen bonding. The turbidity of suspension increased rapidly with increasing in A-150 concentration due to the steric forces, which are effective at high concentration of flocculant. The steric forces start to grow at higher concentration of flocculant causing the increase in the turbidity of suspension. The turbidity of suspension also increased with a rise in the N-100 concentration, however this increase was not compared to A-150. On the other hand, the cationic flocculant was effective only at high concentration levels. The molecular weight of C-521 is lower than that A-150 and N-100. Therefore, it can be said that this polymer could not be successful in marble powder suspension. The cationic flocculant could not be adsorbed onto the surfaces with the positive potential. It is very well known fact that, as the molecular weight of polymer increases, the flocs become larger and settle faster (Klimpel, 1997).

Additionally, it was observed that the starch showed better flocculation behavior than expected. The zeta potential of the starch was measured as -13.3 mV . When taking the marble surfaces having a positive potential into consideration, one can say that a charge neutralisation mechanism is responsible for adsorption of wheat starch

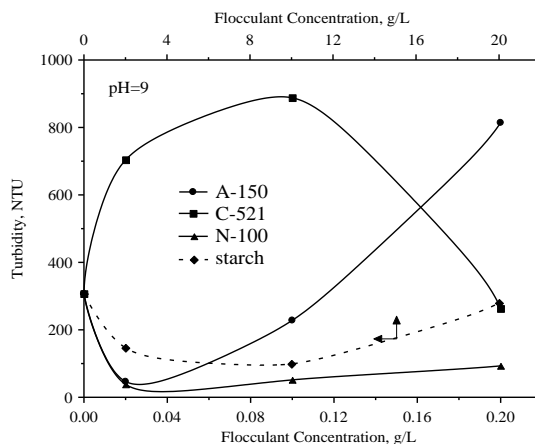


Fig. 4. Effect of polymer concentration (g/dm^3) on turbidity of marble powder

on the positively charged surfaces. When the upper axis is compared with the lower axis, it can be pointed out that the starch concentration is hundred times higher than the concentration of polymeric flocculant (Fig. 4). Whereas starch and other polysaccharides were widely used in flocculation of suspensions, the synthetic polymeric flocculants have many advantages over natural flocculants and are generally superior flocculation agents at low dosages (Tzoupanos and Zouboulis, 2008). When the required starch amount is over the polymer amount, the same turbidity value of suspension can be reached.

The sequential addition of flocculants

Figure 5 shows the effect of polymer addition on the turbidity of marble powder in the presence of the starch. The sequential addition of flocculants did not improve the flocculation of the suspension. On the contrary, the suspension turbidity increased with addition of A-150 and C-521. The sequential addition of N-100 did not change the turbidity of suspension. As it was mentioned before, adsorption of starch was carried out onto the positive charged marble powder surfaces via electrostatic attraction. The addition of anionic flocculant following immediate starch used can increase the ionic strength and causes the polymer to coil-up at the end weakening the bridging bonds. Inclusion of the cationic flocculant may also deteriorate the ionic situation between the starch and the mineral causing the increase in the turbidity of suspension. However, utilization of the non-ionic polymer is the effect described as neither favourable nor unfavourable.

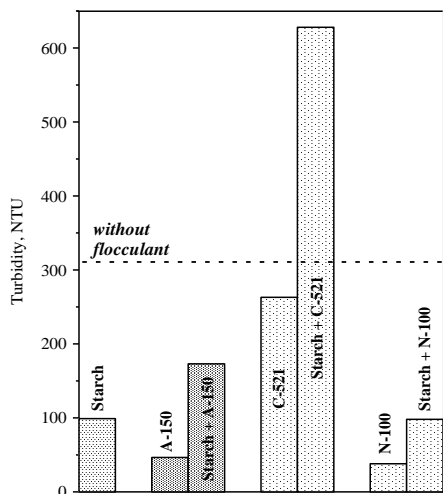


Fig. 5. Effect of polymer addition on turbidity of marble powder in the presence of starch (pH=9, polymer conc. (g/dm³); starch = 9, A-150 & C-521 = 0.02, N-100 = 0.2)

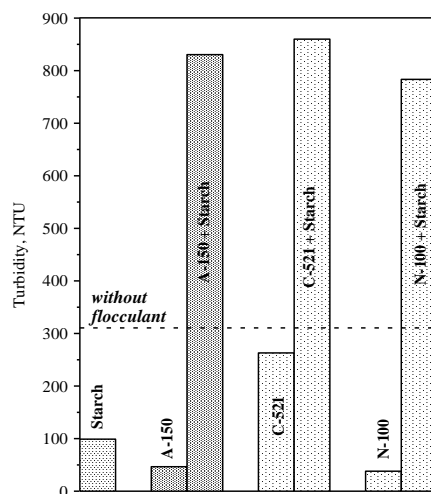


Fig. 6. Effect of starch addition on turbidity of marble powder in the presence of polymer (pH = 9, polymer conc. (g/dm³); starch = 9, A-150 & C-521 = 0.02, N-100 = 0.2)

Figure 6 shows the effect of the starch addition on the turbidity of marble powder in the presence of polymer. The sequential addition of the starch caused to re-stabilization of flocculated suspension. The measured turbidity value of suspension was 38 NTU in the presence of 0.02 g/dm³ N-100. After addition of 10 g/dm³ starch, the turbidity of suspension leaped up to 783.5 NTU. Therefore, the starch addition into the flocculated suspension with polymer showed the dispersion effect. This may be due to no more absorbable part being available on the polymer saturated marble powder surfaces. As a result, the steric stabilisation appears to cause re-dispersion of the particles in solution. Starch and its modified forms display both flocculant and dispersant properties (Nystrom et al., 2003; Poraj-Kozminski et al., 2007).

Conclusion

Suspension of the marble powder is flocculated by the use of natural starch polymer and three other types of synthetic polymers. The zeta potential of marble powder was measured to be +2.5 mV at the natural pH (= 9) value of suspension. The best flocculation behavior was obtained with A-150 and N-100 polymer at low concentration levels (0.02 g/dm³). The electrostatic interaction was defined to be responsible for flocculation between the anionic flocculant and positively charged mineral surfaces. The non-ionic polymer is adsorbed onto the mineral surfaces by the way of hydrogen bonding at pH 9. The charge neutralisation mechanism also postulated adsorption of the wheat starch on positively charged mineral surfaces. However, flocculation of the marble powder suspension can be reached at high concentrations of the starch such as 10 g/dm³. Besides, C-521 did not flocculate the positive charged marble powder. The sequential addition of polymers did not improve flocculation of marble suspension. Especially, the addition of the starch and C-521 strongly caused to the re-dispersion of flocculated suspension.

Acknowledgement

The financial support given by the Scientific Research Project Fund of Selcuk University is greatly acknowledged.

References

- ABDEL-KHALEK N.A., YASSIN K.E., SELIM K.A., RAO K.H., KANDEL A.H., 2012, *Effect of starch type on selectivity of cationic flotation of iron ore*, Mineral Processing and Extractive Metallurgy, 121, 98–102.
- ABRO M.I., PATHAN A.G., MEMON A.R., 2013, *Dual polymer flocculation approach to overcome activation of gangue minerals during beneficiation of complex iron ore*, Powder Technology, 245, 281–291.
- ALLEN T., 1981, *Particle Size Measurement*, 3rd edition, London: Chapman and Hall.
- ATESOK G., 1988, *Adsorption of polymers*, Bull. Tech. Univ. Istanbul, 41, 13–32.
- ATTIA Y.A., 1992, *Flocculation*, in: *Colloid Chemistry in Mineral Processing*, New York: Elsevier 277–308.

- BASARAN H., TASDEMIR T., 2014, *Determination of flocculation characteristics of natural stone powder suspensions in the presence of different polymers*, Physicochem. Probl. Miner. Process., 50, 1, 169–184.
- BASTRZYK A., POLOWCZYK I., SADOWSKI Z., SIKORA A., 2011, *Relationship between properties of oil/water emulsion and agglomeration of carbonate minerals*, Separation and Purification Technology, 77, 325–330.
- BAYRAKTAR I., ONER M., KARAPINAR N., SAKLAR S., 1996, *Wastewater treatment in marble industry*, in: *Changing Scopes in Mineral Processing*, Balkema, Rotterdam 673–677.
- CHEN G., TAO D., 2004, *Effect of solution chemistry on floatability of magnesite and dolomite*, Int. J. Miner. Process., 74, 343–357.
- EL-MIDANY A.A., 2004, *Separating dolomite from phosphate rock by reactive flotation: Fundamentals and application*, Ph.D. Thesis, University of Florida, p.129.
- ERSOY B., 2005, *Effect of pH and polymer charge density on settling rate and turbidity of natural stone suspensions*, Int. J. Miner. Process., 75, 207–216.
- FAN A., TURRO N.J., SOMASUNDARAN P., 2000, *A study of dual polymer flocculation*, Colloids and Surfaces A: Physicochem. Eng. Aspects, 162, 141–148.
- GENCE N., OZBAY N., 2006, *pH dependence of electrokinetic behavior of dolomite and magnesite in aqueous electrolyte solutions*, Applied Surface Science, 252, 8057–8061.
- GREGORY J., 1988, *Polymer adsorption and flocculation in sheared suspensions*, Colloids and Surfaces A: Physicochem. Eng. Aspects, 31, 231–253.
- HOGG R., 2000, *Flocculation and dewatering*, Int. J. Miner. Process., 58, 223–236.
- KARBASSI A.R., BASSAM S.S., ARDESTANI M., 2013, *Flocculation of Cu, Mn, Ni, Pb, and Zn during Estuarine Mixing (Caspian Sea)*, International Journal of Environmental Research, 7, 4, 917–924.
- KLIMPEL, R.R., 1997, *Introduction to chemicals used in particle systems*. ERC Particle Science & Technology, Florida.
- KURAMA H., KARAGUZEL C., 2013, *The effect of zeta potential on the sedimentation behavior of natural stone processing effluent*, Physicochem. Probl. Miner. Process. 49, 2, 575–586.
- MAROUF R., MAROUF-KHELIFA K., SCHOTT J., KHELIFA A., 2009, *Zeta potential study of thermally treated dolomite samples in electrolyte solutions*, Microporous and Mesoporous Materials, 122, 99–104.
- MOULIN P., ROQUES H., 2003, *Zeta potential measurement of calcium carbonate*, Journal of Colloid and Interface Science 261, 115–126.
- NYSTROM R., BACKFOLK K., ROSENHOLM J.B., NURMI K., 2003, *Flocculation of calcite dispersions induced by the adsorption of highly cationic starch*, Colloids and Surfaces A: Physicochem. Eng. Aspects, 219, 55–66.
- PARFITT G.D., ROCHESTER, C.H., 1983, *Adsorption of small molecules*, in: *Adsorption from Solution at the Solid/Liquid Interface*, Academic Press, New York 3–48.
- PETZOLD G., BUCHHAMMER H.M., LUNKWITZ K., 1996, *The use of oppositely charged polyelectrolytes as flocculants and retention aids*, Colloids Surf. A: Physicochem. Eng. Aspects, 119, 87–92.
- PETZOLD G., LUNKWITZ K., 1995, *The interaction between polyelectrolyte complexes made from poly (dimethyldiallylammonium chloride) (PDMDAAC) and poly (maleic acid-co- α -methylstyrene) (P(MS- α -MeSty)) and cellulosic materials*, Colloids Surf. A: Physicochem. Eng. Aspects, 98, 225–233.

- PORAJ-KOZMINSKI A., HILL R.J., THEO G.M. van de Ven., 2007, *Flocculation of starch-coated solidified emulsion droplets and calcium carbonate particles*, Journal of Colloid and Interface Science, 309, 99–105.
- RUNKANA V., SOMASUNDARAN P., KAPUR P.C., 2005, *A population balance model for flocculation of colloidal suspensions by polymer bridging*, Chemical Engineering Science, 61, 182–191.
- SEYRANKAYA A., MALAYOGLU U., AKAR A., 2000, *Flocculation conditions of marble from industrial wastewater and environmental consideration*, in: Proceedings of the 8th International Mineral Processing Symposium, 645–652, Rotterdam, NL: Balkema.
- SOLAK M., KILIC M., YAZICI H., SENCAN A., 2009, *Removal of suspended solids and turbidity from marble processing wastewaters by electrocoagulation: Comparison of electrode materials and electrode connection systems*, Journal of Hazardous Materials, 172, 345–352.
- TZOUPANOS N.D., ZOUBOULIS A.I., 2008, *Coagulation-flocculation processes in water/wastewater treatment: The application of new generation of chemical reagents*, 6th IASME/WSEAS International Conference on Heat Transfer, Thermal Engineering and Environment (HTE'08), Rhodes, Greece, 309–317.
- WERNEKE M.F., 1979, Application of synthetic polymers in coal preparation, Soc. Min. Eng. IME, 79–106.
- YARAR B., 2001, *Evaluation of flocculation and filtration procedures applied to WSRC Sludge*, Report no: WSRC-TR-2001- 00213. Colorado School of Mines, USA, 1–34.
- YU X., SOMASUNDARAN P., 1993, *Enhanced flocculation with double flocculation*, Colloids Surf. A: Physicochem. Eng. Aspects. 81, 17–23.
- YU X., SOMASUNDARAN P., 1996, *Role of polymer conformation in interparticle-bridging dominated flocculation*, J. Colloid Interface Sci., 177, 283–287.
- ZHANG P., AUSTA T., 2006, *Wettability and oil recovery from carbonates: Effects of temperature and potential determining ions*, Colloids and Surfaces A: Physicochem. Eng. Aspects, 279, 179–187..

Received January 29, 2014; reviewed; accepted May 18, 2014

A METHOD FOR DETERMINING SIEVE HOLES BLOCKING DEGREE

Katarzyna Ewa LAWINSKA, Piotr WODZINSKI, Remigiusz MODRZEWSKI

Lodz University of Technology, Department of Process Equipment, Division of Granular Material Classification, Lodz, Poland; k_lawinska@interia.pl

Abstract: The aim of this paper is to describe the process of sieve holes blocking. A series of tests and their results revealed a dependence describing the value of an average screen blocking coefficient as a function of two main factors affecting the process. These parameters are the toss indicator and the content of difficult-to-screen particles in the feed. The experiments presented in the paper showed that description in mathematical terms of the sieve holes blocking process is complex and difficult. A third degree polynomial function with two variables enables determination of the value of an average screen blocking coefficient in the processes of screening for specific arrangements: screen–particle–toss indicator–content of difficult-to-screen particles.

Keywords: *screen, sieving, screen blocking coefficient, granular materials*

Introduction

Screening of particulate materials is a process which has been performed in various branches of industry. There is a large number of publications describing this process and characteristics of screening machines (Akhmadiev and Gizzjatov, 2013, Beeckmans et al., 1985). The unfavourable process of sieve holes blocking and the screen blocking coefficient, however, are neither well-known nor widely discussed. As yet, this phenomenon has not been described quantitatively for minerals processing applications. During the screening of particulate materials under industrial conditions, sieve holes are often considerably clogged, which in turn significantly decreases screening performance. The mechanism of the sieve holes blocking process is largely random.

It was reported by Feller (1980) that both partial passage and clogging of the screen should be considered in order to evaluate screen performance. A screen rate function, defined as the sum of the passage and clogging rate factors versus relative particle size, was developed to characterize screen performance. It is independent of screening

duration, and is not limited to a particular size distribution of the material or one screening duration. The issue of sieve holes blocking is not the only problem of this kind encountered in engineering processes used in broadly defined minerals processing. In all processes of filtrating mixtures containing post-manufacturing contaminated water, originating from water and sludge circuits, there is also clogging of holes in the filtration mesh and the clogging of the filtration deposit pores (Piecuch et al., 2013).

The sieve clearance coefficient, A_0 , defined as the ratio of the holes surface area to the total screen surface area, provides information on the screening capacity of a particular screen (Sztaba, 1993). The probability of particles passing through the holes of the screen increases with the increase of this coefficient. The screen blocking coefficient f is applied for a quantitative description of screen blocking. It is defined as the ratio of the number of free holes to the total number of sieve holes. If coefficient f is combined with A_0 , one obtains an effective surface area F_{ef} of the screen, i.e. the surface area through which the stream of material is passing through the sieve as seen in Eq. 1 (Wodzinski, 1997)

$$F_{ef} = f \cdot F \cdot A_0 \quad (1)$$

where F is the screen surface area. Disregarding the screen blocking coefficient may lead to significant inaccuracies in design calculations that cause a major reduction in the screen active surface area. Particles which size is similar to the sieve holes clog those holes and considerably decrease the actual clearance coefficient p (Fraczak and Wodzinski, 1999), which is one of the most important characteristics of sieves (Eq. 2)

$$p = \frac{F_{ef}}{F} \quad (2)$$

A series of laboratory experiments was carried out to determine the factors which significantly affect the process of screening of fine-particulate materials ($d < 1.0$ mm) and very fine-particulate materials ($d < 0.1$ mm) (Lawinska and Wodzinski, 2012; Fraczak and Wodzinski, 1999). The tests also provided information on the parameters affecting the sieve holes blocking process. They proved that the toss indicator and the content of hard-to-screen particles have the greatest impact on the value and course in time of the blocking coefficient for various shapes of particulate materials. The toss indicator has a major effect on the screening efficiency and, consequently, on the value of the sieve holes blocking coefficient. It is defined as the ratio of the maximum inertial force to the maximum gravity force, i.e. the ratio of the maximum screen acceleration to the gravitational acceleration. Proper selection of this parameter is of great importance to the process of screening. The blocking process also occurs when there are particles in the feed which size is similar to the size of the sieve holes. Such particles are called hard-to-screen particles and they include particles that are slightly

smaller, equal to or slightly larger than the sieve holes. The particles are blocked between holes edges. The blocked particles, that partially protrude from the surface of the sieve, make it more difficult for the material to move around the sieve and accelerate its impairment. Furthermore, particles that remain in the upper fraction increase the thickness of the material layer on the screen, thus reducing the probability of the rest of the material passing through the holes.

Properties of particles may be divided into chemical, energy-related and physical ones. The latter, which include particle shape, particle surface toughness, abrasion susceptibility and hardness, are determining the sieve holes blocking probability (Baic, 2013). Three model shapes of particulate materials are known: round-like particles (spherical particles), particles with sharp edges (sharp-edged particles) and particles of an irregular shape (irregular particles). Particulate materials that are used in industry may be divided between the model groups according to their shape. The conducted tests prove that the shape of particles has a significant impact on the sieve holes blocking process. For this reason, this parameter is also considered in a further analysis.

Experimental

Materials

The screening process began with the preparation of mixtures of particulate materials of various particle-size compositions. The principal tests were preceded with the separation of the material into fractions (range of 0.1 mm to 2.5 mm). This enabled the determination of the content of particles in fractions, including the hard-to-screen particles. Particles of the dimensions of $0.8 \cdot l \leq \bar{d} \leq 1.2 \cdot l$ (\bar{d} – average particle size, l – sieve hole size) were assumed as the hard-to-screen particles. Weighing individual fractions and mixing them together led to the production of 10 mixtures, which content of the hard-to-screen particles amounted to $x = 10\%$, 20%, 30%, 40%, 50%, 60%, 70%, 80%, 90%, and 100%. This in turn enabled the determination of the impact of the hard-to-screen particles in the feed on the value of the blocking coefficient. Each mixture prepared in such a way weighed 1 kg. The material used for the tests was free of moisture and contamination. Because of the varying shapes of the particulate material, the tests were conducted separately for each group. Agalite particles (spherical particles), quartz sand (irregular particles) and marble aggregate (sharp-edged particles) were used for the experiments.

Methods

The mixtures were screened using a set of laboratory screens with square holes made of metal wire. The tests were conducted for five screens which hole sizes were 0.5, 0.63, 0.8, 1.0, 1.2 mm. The experiments involved a laboratory vibrator that is distinguished by linear vibrations and flexural vibrations. Regulated toss indicator provided for the assessment of the impact of this parameter on the sieve holes

blocking process. The toss indicator of the laboratory vibrator used in the experiment was calculated using Eq. 3:

$$K = \frac{A \cdot \omega^2 \cdot \sin(\alpha + \beta)}{g \cdot \cos \beta} \quad (3)$$

where A is the amplitude of the vibration, ω is the vibrations frequency, β is the angle of the sieve inclination to the horizontal line, α is the angle of vibrations inclination to the horizontal line, g is the gravitational acceleration. In the experiments angles α and $\beta = 0$. The series of experiments were conducted at the value of $K = 0.62, 1.98, 3.5$ and 4.9 . Such values of the toss indicator are applied when classifying materials which level of screening difficulty is “easy” or “medium”. Higher values of the toss indicator are only necessary in the case of hard-to-screen materials, i.e. moist materials and those easily adhering to an open grid plate.

A control screen with the mixture was placed in the vibrator. Prior to the start of the vibrator, the blocking coefficient f_0 (for time $t=0$) was calculated in relation to the given particulate material at the moment of being fed onto the screen. Next, the vibrator was started and the material was screened through the sieve in time t . After the mixture was screened, the number of clogged sieve holes in five areas of the screen was counted. For this purpose, a template with cut-out frames, each covering 100 sieve holes, was used (each screen had its own template). The blocking coefficient was calculated using the ratio of free holes to the total number of sieve holes. The values of coefficient f obtained from five different areas of the screen were averaged and treated as the blocking coefficient for the given screen in the given time. Blocked particles were removed from the holes and returned to the tested mixture. Screening continued until steady state t_∞ was reached (the number of clogged holes in the screen is constant, f_∞). Such a time span was selected to ensure that the measurement is as precise as possible and that the different stages of the vibrator start did not affect the test.

Results and discussions

The tests described above provided information on the value of the screen blocking coefficient and its fluctuation in time (for mixtures of different content of hard-to-screen particles and of different toss indicators). On the basis of the obtained data a series of diagrams $f = f(t)$ was prepared (Fig. 1). The course of this dependence is similar to the exponential function model known from literature (Blasinski and Wodzinski, 1973, 1976).

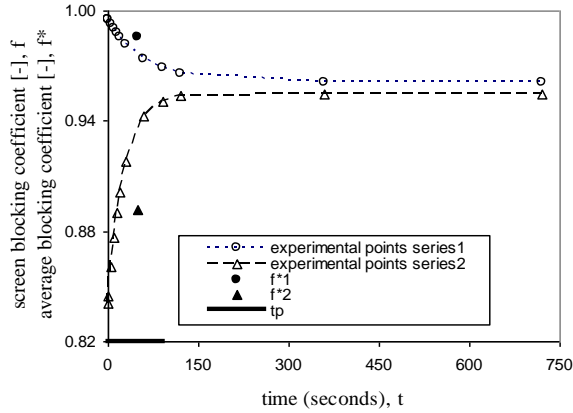


Fig. 1. Experimental screen blocking coefficient vs. time

A steady state was reached after the screening time of $t=720$ s. Considering the fact that the time of contact between the material and the screen is shorter in industrial processes, the obtained values of the screen blocking coefficient were averaged for each measurement series.

Time t_p is the process duration, i.e. residence time for an industrial sieve. The material residence time on an industrial sieve, in general, is from several to 90 s. The arithmetic mean from the range of $\langle f_0, f_{tp} \rangle$ was assumed to be (Eq. 4):

$$f^* = \frac{\sum_{t=0}^{t=t_p} f_t}{t} \tag{4}$$

An average value of the screen blocking coefficient f^* was obtained for each of the tested arrangements (f^*_1, f^*_2). The value of coefficient f^* , constant in time, enabled a comparison of the obtained results and drawing of diagrams $f^* = f(K, x)$ for three model shapes of particulate materials (Figs. 2-4).

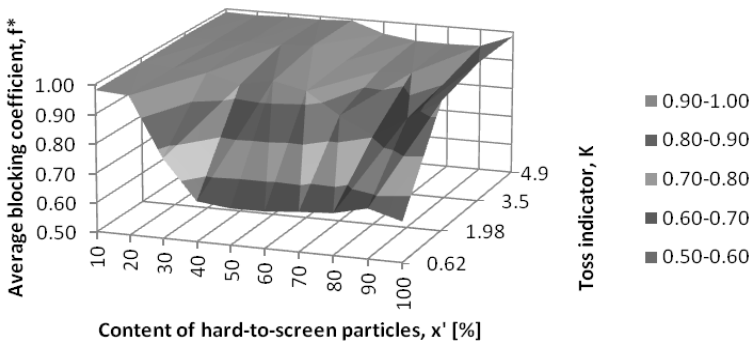


Fig. 2. Average screen blocking coefficient – spherical particles

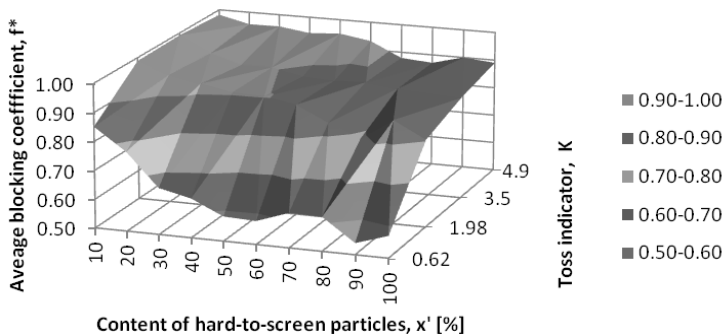


Fig. 3. Average screen blocking coefficient – irregular particles

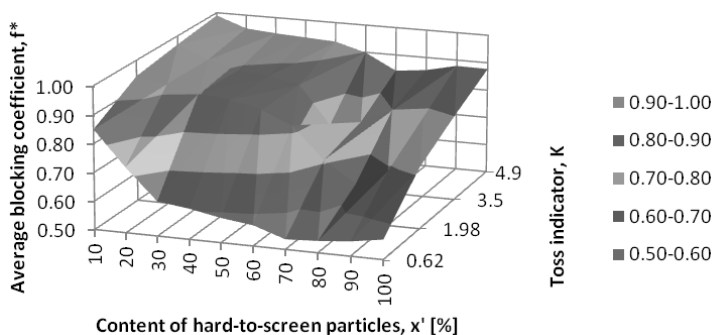


Fig. 4. Average screen blocking coefficient – sharp-edged particles

The diagrams (Figs. 2-4) confirm that the sieve holes blocking process is complex, random to a large degree and difficult to describe in mathematical terms. A significant impact of the toss indicator and the content of hard-to-screen particles on the value of the average blocking coefficient can be observed. A difference in the values of coefficient f^* for different model shapes of particles is also visible. For a sharp-edged material the value of coefficient f^* is the lowest, i.e. the greatest number of sieve holes are clogged. For this reason, the attempt to provide a quantitative description of the screen blocking process without dividing the material into various shapes is erroneous. The course of diagrams (Figs. 2-4) rules out a simple form of a typical dependence.

Mathcad13 software functions were used in order to determine dependence $f^* = f(K, x)$. Mathcad is equipped with a series of commands that make it possible to perform complicated operations in a simple manner, e.g. in order to define complex functions. A program in Mathcad is a special expression comprising a series of instructions generated using program operators (Gajewski, 2011). When defining the algorithm for determining the power matrix and the values of coefficients, a model of an n -degree polynomial of a function of two variables (K, x) was analysed. The determination coefficient R^2 was also calculated in order to verify the goodness of fit of the proposed model. Coefficients R^2 for a first- and second-degree polynomial

amounted to ≈ 0.7 and ≈ 0.8 respectively, which shows only a satisfactory fit. Much higher values of R^2 were obtained for a third-degree polynomial. The obtained forms of a third-degree polynomial and the values of coefficients R^2 with a division into shapes of the particulate material are listed in Table 1.

Table 1. A list of coefficients and powers of a third degree polynomial model of an average screen blocking coefficient as a function of the toss indicator and the content of hard-to-screen particles

| Shape of the material | Form of a third-degree polynomial $f^* = f(K, x)$ | R^2 |
|-----------------------|--|-------|
| spherical shape | $f^* = -0.211K^1x^2 + 0.58K^0x^3 - 0.033K^0x^3 - 1.04K^0x^1 + 0.439K^1x^1 - 0.025K^2x^1 + 0.945K^0x^0 + 0.192K^1xx^0 - 0.082K^2x^0 + 0.009K^3xx^0$ | 0.921 |
| irregular shape | $f^* = -0.1K^1x^2 - 0.284K^0x^3 + 0.972K^0x^2 + 1.087K^0 + 0.192K^1xx^1 - 0.00804K^2xx^1 + 0.709K^0x^0 + 0.415K^1x^0 - 0.144K^2x^0 + 0.015K^3x^0$ | 0.969 |
| sharp-edged shape | $f^* = -0.086K^1x^2 + 0.57K^0x^3 - 0.0373K^0x^2 - 0.438K^0x^1 + 0.031K^1x^1 + 0.018K^2x^1 + 0.633K^0x^0 + 0.4K^1x^0 - 0.13K^2x^0 + 0.013K^3x^0$ | 0.943 |

Table 1 provides a method for quantitative determination of an average screen blocking coefficient, considering two main factors affecting its value. The values of determination coefficient R^2 prove the goodness of fit of the discussed model. By reducing the equations given in Table 1, one can obtain three dependences for an average value of the screen blocking coefficient f^* for:

- mixtures with spherical particles

$$f^* = -0.211K^1x^2 + 0.58x^3 - 0.033x^2 - 1.04x^1 + 0.439K^1x^1 - 0.025K^2x^1 + 0.945 + 0.192K^1 - 0.082K^2 + 0.009K^3 \quad (5)$$

- mixtures with irregular particles

$$f^* = -0.1K^1x^2 - 0.284x^3 + 0.972x^2 - 1.087x^1 + 0.192K^1x^1 - 0.00804K^2x^1 + 0.709 + 0.415K^1 - 0.144K^2 + 0.015K^3 \quad (6)$$

- mixtures with sharp-edged particles

$$f^* = -0.086K^1x^2 + 0.57x^3 - 0.0373x^2 - 0.438x^1 + 0.031K^1x^1 + 0.018K^2x^1 + 0.633 + 0.4K^1 - 0.13K^2 + 0.013K^3 \quad (7)$$

On the basis of Eqs. 5–7, one can calculate the value of an average screen blocking coefficient and determine the active surface area of the screen, as well as the clearance coefficient, at the stage of planning the screening process and screening machine.

Conclusions

The screen blocking coefficient is an important parameter of each screen and the machine in which the screen is installed. The toss indicator and the content of hard-to-screen particles in the feed are the factors that have the greatest impact on the sieve holes blocking process.

Dependences given in this paper provide an evaluation of the extent of this negative phenomenon in the screening of fine-particulate materials. This information may be used for designing and optimizing industrial screening processes.

Acknowledgments

This study was performed as part of a chartered assignment W-10/1/2014 Dz.St.

References

- AKHMADIEV F.G., GIZZJATOV R.F., 2013, *Separation Processes of Granular Materials by Sizes at the Sieve Classifiers*, J. Chem. Chem. Eng., 7, 56-63.
- BAIC I., 2013, *Analysis of the chemical, physical and energetic parameters of coal sludge deposits inventoried in the Silesian Province*, Annual Set The Environment Protection, 15, 1525–1548.
- BEECKMANS J.M., HU E., GERMAIN R., MCINTYRE A., 1985, *Performance characteristics of a probability screening machine*, Powder Technology, 43(3), 249-256.
- BLASINSKI H., WODZINSKI P., 1973, *Sieve holes blocking*, Zeszyty Naukowe PŁ, Inż.Chem., Volume 2.
- BLASINSKI H., WODZINSKI P., 1976, *Research process of sieve holes blocking*, Zeszyty Naukowe PŁ, Inż.Chem., Volume 6.
- FELLER, R., 1980, *Screening analysis considering both passage and clogging*, Trans. ASAE, 23(4), 1054 - 1056.
- FRACZAK S., WODZINSKI P., 1999, *The effect of hard-to-screen grains content in the feed on sieve blocking*, Physicochemical Problems of Mineral Processing, XXXVI Symposium, 33-47.
- GAJEWSKI R.R., 2011, *MathCAD- engineering calculations and programming*, Oficyna Wydawnicza Politechniki Warszawskiej, 51-60.
- LAWINSKA K., WODZINSKI P., 2012, *Determination of the effective sieve blocking coefficient*, Physicochemical Problems of Mineral Processing 48(1), 247-252.
- PIECUCH T., PIEKARSKI J., MALATYŃSKA G., 2013, *The equation describing the filtration process with compressible sediment accumulation on a filter mesh*, Archives of Environmental Protection, 39(1), 93-104.
- SZTABA K., 1993, *Screening*, Śląskie Wydawnictwo Techniczne.
- WODZINSKI P., 1997, *Screening and screening machines*, Wydawnictwo Politechniki Łódzkiej, 20-36.

Received March 3, 2014; reviewed; accepted June 10, 2014

IMPROVEMENT OF MECHANICAL STRENGTH OF IRON ORE PELLETS USING RAW AND ACTIVATED BENTONITES AS BINDERS

**Alim GUL, Ayhan A. SIRKECI, Feridun BOYLU, Gunser GULDAN,
Firat BURAT**

Istanbul Technical University, Faculty of Mines, Mineral Processing Engineering Department, 34469, Maslak,
Istanbul-TURKEY, gulalim@itu.edu.tr

Abstract: In this study, sodium, calcium, and mixed bentonite samples were used as binders in the pelletizing fine iron ore concentrate obtained from the Divrigi Iron Ore Concentration Plant in Turkey. In the pelletizing tests, sodium bentonite sample was used as received and after upgrading process. Additionally, the calcium bentonite sample required activation by sodium bicarbonate while the mixed bentonites sample was used untreated and as well as activated. The pellets produced were tested for compressive strengths, drop number, and porosity in order to characterize the pellets. The results showed that untreated and upgraded sodium bentonite samples provided relatively stronger pellets compared to calcium and the mixed type bentonite samples needed activation with sodium bicarbonate to increase the strength of the pellets. Based on the results of the drop number, compressive strengths, and porosity, it is possible to make pellets which meet the standards by adequate addition of type and amount of bentonite.

Keywords: *bentonite, pelletizing, iron ore concentrate, binder, sodium bicarbonate*

Introduction

Major raw material in iron and steel industry is iron ore which can be classified as high grade and low grade in terms of its Fe content. High grade iron ores, which can directly be used in a blast furnace, are not abundant in earth's crust to supply the need of iron and steel industry. The exploitation of low grade iron ores is possible after enrichment. Low grade iron ores contain considerable amounts of impurities including compounds of silica, alumina, calcium, and magnesium. Hence the concentration process is required based on crushing, grinding for adequate liberation before the implementation of separation techniques. Liberation can mostly be achieved at considerable fine particle sizes. For this reason, the concentrate obtained is not suitable to be charged directly into the blast furnace or the direct reduction plant

without converting it into suitably sized agglomerates. The most commonly employed agglomeration technique is pelletizing by which a mixture of iron ore, water, and binder is rolled up in a mechanical disc or drum to produce agglomerates (green or wet pellets) (Sivrikaya and Arol, 2010).

A narrow size distribution in green pellets is an important criterion for the pellet quality because high permeability in the pellet bed is beneficial for reduction process in steelmaking. In practice, variations may occur in the incoming pellet feed properties (like moisture content, fineness and wettability) which result in variations in the green pellet growth rate and size distribution. Pellet size is controlled either mechanically, by adjusting the screen opening or “chemically” by slightly varying the moisture content or the binder dosage. Increasing the binder dosage is known to decrease the green pellet growth rate, making pellets smaller, while increasing the water content results in an opposite effect (Forsmo et al., 2006; Sastry and Fuerstenau, 1972). Eketorp (1962) found that the surface area of particles affects the moisture retaining capacity of pellets. Moisture content in green pellets is critical where the optimum amount is the case at which all open pores are filled by water. Insufficient moisture causes air inclusions which reduce the capillary effect. However, an excess amount forms a coherent film of water which neutralizes the capillary effect.

Green pellet strength and plasticity are important parameters for the productivity of an iron ore pelletizing plant. Green pellet strength is described by two test values, that is by drop number and compression strength. The drop number describes the green pellet strength during a fast impact such as the impact that occurs during unloading from a conveyor belt. The drop number must be high enough for the green pellets to survive the transportation from the balling circuits to the pelletizing machine. The drop number is, however, influenced by changes in both plasticity and elasticity, and it increases with increasing moisture content and bentonite dosage. The green pellet strength under static load, e.g., in the pellet bed in the drying zones, is described by the wet compression strength. It needs to be high enough to assure minimum deformation and breakage. Plastic deformation and green pellet breakage decrease the permeability of the pellet bed in the drying and oxidation zones of the pelletizing machine, resulting in negative consequences for both pelletizing capacity and pellet quality (Forsmo et al., 2008).

Bentonite is primarily used for improving dry compressive strength of iron concentrate pellets so that they go through the processes such as smelting without much damage. Ball et al. (1973) indicated that bentonite clay has the following effects.

- Bentonite absorbs moisture, allowing for higher moisture concentrate feeds to be pelletized. Moisture variations can be overcome by altering bentonite dosages.
- As bentonite is mixed into the iron ore concentrate it becomes wet so that clay layers expand and disperse by the hydration of exchangeable interlayer cations, transforming into a matrix that bonds the ore particles together.
- During tumbling, the pellets are formed by particles adhering to each other in layers, which are compacted by the weight of the other pellets into a spherical

shape. Bentonite is well dispersed and retains an even distribution of moisture throughout the wet pellet as it grows.

- During drying, bentonite increases the drying rate by providing a pathway for the moisture to be removed.

The binding of iron oxide grains by bentonite clay to form pellets is a complex process, with a large number of variables, many of which have never been adequately studied. Current practice for pelletizing iron ore concentrates was developed in 1950's during which bentonite clay was practiced as a binder and since then it has remained the most acceptable binder because of its effectiveness and relatively low cost. The minimum industrially acceptable dry pellet compressive strength is typically 22 N. A typical dosage of bentonite is 0.66% of the moist (typically 10% moisture) iron ore concentrate filter cake (Ripke and Kawatra, 2000). The dosage of sodium bentonite needs to be kept as low as possible because pellets containing more bentonite cost more to produce and contain higher silica content. This gives the industry an incentive to use bentonites in ways that produce adequate strengths at lower dosages. However, in the case of mixed or calcium bentonite usage as binder, the dosages can be higher because of their low binding properties. In pelletizing process, Na bentonite is generally used as a binding material which is more expensive than calcium and mixed types bentonites. Calcium bentonite and mixed type bentonite are cheaper, however, they must be activated with sodium bicarbonate or Na-CMC (sodium carboxyl methyl cellulose) before they can be used as binding materials (Ripke and Kawatra, 2003).

It is well known that sodium carbonate (soda ash) improves the capability of bentonite to bind iron ore into pellets and reduce the total amount of bentonite required for a given quantity of iron ore fines. Sodium in soda ash replaces some of the calcium and magnesium in the bentonite lattice and thereby improves the binding efficiency of Ca-bentonite. However, it was believed that bentonite would not combine with sodium carbonate except when sodium carbonate solution is employed to make the ion replacement (Erickson and Palusky, 1973). In this context, the aim of this study is to investigate the use of sodium, calcium, and mixed type of bentonite samples as a binder in the pelletizing of fine iron ore concentrate.

Experimental

Materials

Magnetite and bentonite samples

Magnetite concentrate (Fe_3O_4) used in the studies was obtained from the Divrigi Iron Ore Concentration & Pelletizing Plant (Turkey). The chemical analysis of magnetite sample is presented in Table 1 (Arslan et al., 2007). Three different bentonite samples were used for the experiments. Na- bentonite was brought from Resadiye district. Ca-bentonite and mixed bentonite were obtained from Somas and Canbensan Company, respectively. The chemical analyses of the bentonite samples are presented in Table 2.

Original bentonite samples were first dried at 60°C and then dry screened to determine the particle size distribution of the particles. In the case of wet screen analysis, bentonite samples were soaked overnight where the solids ratio was 6% by weight. The stainless steel screens were used for the dry and wet particle size analysis. The results of the particle size distributions of the samples are shown in Fig. 1.

Table 1. Chemical analysis of magnetite sample (Arslan et al., 2007)

| Compound | Fe | S | SiO ₂ | Al ₂ O ₃ | CaO | MgO | Na ₂ O | K ₂ O | Ni |
|-------------|------|------|------------------|--------------------------------|------|------|-------------------|------------------|------|
| Content (%) | 69.0 | 0.30 | 1.50 | 0.78 | 0.65 | 0.55 | 0.04 | 0.08 | 0.23 |

Table 2. Chemical analyses of bentonite samples

| Compound (%) | Resadiye | Somas | Canbensan |
|--------------------------------|----------|-------|-----------|
| SiO ₂ | 57.09 | 51.76 | 54.74 |
| Al ₂ O ₃ | 16.73 | 14.77 | 15.53 |
| Fe ₂ O ₃ | 3.24 | 5.48 | 5.06 |
| MgO | 2.03 | 3.31 | 3.11 |
| CaO | 3.18 | 3.56 | 2.51 |
| Na ₂ O | 2.51 | 0.47 | 1.70 |
| K ₂ O | 0.97 | 0.94 | 1.51 |
| TiO ₂ | 0.3 | 0.54 | 0.71 |
| P ₂ O ₅ | 0.15 | 0.16 | 0.09 |
| MnO | 0.08 | 0.11 | 0.04 |
| LOI | 13.4 | 18.7 | 14.8 |

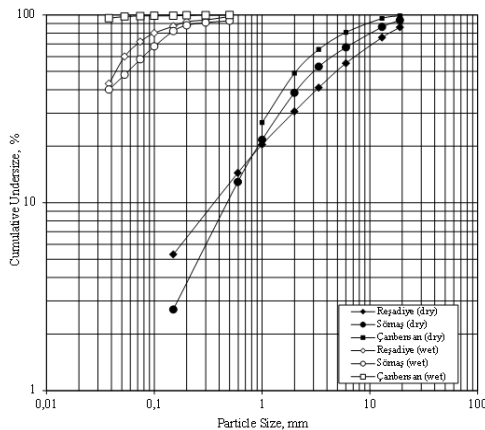


Fig. 1. Particle size distributions of bentonite samples

Methods

Upgrading bentonite sample

Upgrading of Na-bentonite sample was carried out employing a 50.8 mm (2 inch) lab scale Mozley hydrocyclone with apex diameters of 4.3 and 6.5 mm. Prior to concentration the run-of-mine bentonite sample was first crushed below 3–4 mm to avoid excessive size reduction of non clayey minerals, and then soaked for 24 hr after which agitated for 24 hr. This method was also explained in detail in a previous study (Boylu et al., 2010). Material balance on upgrading was not taken into consideration since the effect of upgrading on binding properties of bentonites was of primary interest.

Activation procedures of bentonites

Prior to the soda activation, the bentonite samples were initially water sprayed to adjust the desired moisture content of 35–40% as already done in industrial application. The effect of specific cations on the process was eliminated by using membrane filtered water with 30–35 ppm TDS (total dissolved solids) as the moisturizing agent. The homogenized bentonite samples with the desired moisture and soda powder were mixed to form bentonite dough as in industrial applications, and it was needed until all the soda was absorbed in the entire sample. The activated bentonite samples, approximately 3–4 mm in size, were then left to dry and/or to be cured in room temperature (23 ± 1 °C). Following the drying, the activated bentonite samples were ground below 150 μm using a mortar and pestle.

The cation exchange capacities (CEC) (based on the methylene blue test standard of ASTM 837 C) and swelling indexes (Boylu et al., 2010) of as received or upgraded bentonite samples were given in Table 3.

Table 3. CEC and swelling indexes of bentonite samples

| Bentonite Type | Activation | CEC (meq/100 g) | Swelling Index (cm^3) |
|-----------------------------|--------------------------|--------------------|-------------------------------------|
| Na-bentonite (as received) | – | 78.0 | 20.5 |
| Na-bentonite (upgraded) | – | 94.0 | 32.0 |
| Mixed bentonites | Activated with 0.5% soda | 64.5 | 14.0 |
| | Activated with 1.0% soda | | 16.0 |
| | Activated with 2.0% soda | | 20.0 |
| | Activated with 3.0% soda | | 22.0 |
| Ca-bentonites (as received) | Activated with 0.5% soda | 60.0 | 8.0 |
| | Activated with 1.0% soda | | 14.5 |
| | Activated with 3.0% soda | | 20.0 |
| Ca-bentonites (upgraded) | Activated with 0.5% soda | 78.5 | 11.0 |
| | Activated with 1.0% soda | | 14.0 |

Pelletizing tests

In the initial tests, different amounts of bentonite were added to the magnetite concentrate to determine the optimum binder ratio and moisture content and then pellets were prepared by rolling them carefully in hand. The compressive strength and drop tests were performed on green pellets. After determination of binder ratio and moisture content of the samples, further experiments were carried out at a laboratory-scale pelletizing disc under optimum test parameters and different types of green pellets were produced. The compressive strength, drop number, and porosity tests were applied to the pellets where following numbers were taken into consideration for the evaluation of the results (Meyer, 1980).

- Compressive strength: 1 kg/pellet for green, 1 kg/pellet for dried pellets and 200 kg/pellet for fired pellets,
- Drop number: 4 for green and dried pellets,
- Porosity: 25–32% for fired pellets.

A 60 cm diameter pelletizing disc was used in the experiments. The slope and rotation speed were 45° and 40 rpm, respectively. Previously mixed magnetite concentrate and bentonite (2 kg in dry basis) samples were fed to the disc. After the sample was introduced a little amount of water was added and nuclei generation started. The nuclei were moistened with water spray to retain moisture content while adding additional material to enlarge them into pellets. These products are called green pellets. The green pellets were immediately dried at 105 °C and held at this temperature for 20–24 hr to ensure that they were completely dried. The dry pellets were fired at 1200 °C for 30 min (Fig. 2). Finally, compressive strength, drop and porosity tests were applied on the respective samples.



Fig. 2. (a) Green, (b) dry, (c) fired pellets

Compressive strength tests

Compressive strength of dry pellets is a crucial factor. It is measured to find the required value for handling, drying, and firing processes. When pellets are fed to rotary furnaces they are exposed to high pressure. To prevent possible size reduction of pellets, they must be strong enough. Compressive strength of the pellets were

measured by compressing individual pellets between two plates where the speed of the moving plate was 10 mm/min. Tests were performed on 5 pellets, and the average compressive strength values were calculated.

Drop strength tests

The drop number describes the strength of green and dry pellets under impact. This test measures the ability of pellets to remain intact during handling. The type of bentonite, ore moisture, surface area, pelletizing conditions and mixing are the factors affecting the drop strength. In tests, green and dry pellets are allowed to fall from a height of 46 cm to a steel plate and the breakage is visually detected. The drop number gives the average number of drops before a fracture is observed. Tests were run for 5 pellets and the average value was calculated. Pellets are expected to remain unbroken after 4 drops.

Porosity tests

Porosity is a very important property of pellets. Lower porosity leads to a better particle-particle contact, but obstructs the diffusion of oxygen through the green pellet during oxidation. High porosity causes material loss. Therefore, it is very essential to test the porosity value of pellets. Porosity values were calculated using the following formula where D and d are actual and apparent specific gravities respectively:

$$\text{Porosity} = \frac{D-d}{D} \cdot 100. \quad (1)$$

Results and discussions

Results

Effect of sodium bentonite addition on specification of pellets

A series of pelletizing experiments were carried out to determine the effect of sodium bentonite addition on the formation of pellets. The binder ratio was chosen between 1% and 4% by weight of magnetite concentrate and the moisture content was adjusted as 8, 9, 10, and 12% for all binder ratios. When compared to industrial applications higher dosages of bentonite addition were tested in the case of bentonite samples other than enriched Na-bentonite. It is obvious that the dosages should be higher when mixed or calcium types were used because of their low binding properties. Regardless of the bentonite amount added, the increase in the dosage of water improves the strength of green pellets. This might be attributed to the colloidal nature of bentonite having high surface area. Hence, the plasticity of green pellets is increased (Dor et al., 1970). The results of drop number tests showed that the optimum binder ratio was 2.5% and the moisture content was 12% for both green pellets. Compressive strength tests were carried on dry and fired pellets obtained. Furthermore, the effect of

concentrated sodium bentonite was also investigated. The results of the tests are given Table 4.

Table 4 clearly shows that Na-bentonite addition leads to a substantial improvement in the pellet strength. The optimum test results were attained when 2.5% bentonite (as received) was added. An increase in bentonite addition causes an enhancement in drop number, compressive strength and porosity but compressive strength values tend to decrease with further addition of as received bentonite amount. In the case of upgraded bentonite addition, the compressive strength values increased with the increasing amount of bentonite. However, drop numbers of green and dry pellets were found to be low.

Table 4. Effect of sodium bentonite on crushing and drop strength of pellets

| Bentonite Type | As received Na-bentonite | | | Upgraded Na-bentonite | | |
|--|--------------------------|-----|-----|-----------------------|-----|-----|
| | 2 | 2.5 | 3 | 0.7 | 1 | 1.5 |
| Bentonite Amount (%) | 2 | 2.5 | 3 | 0.7 | 1 | 1.5 |
| Compressive Strength (kg/dry pellet) | 10 | 7 | 6 | 5 | 6 | 9 |
| Compressive Strength (kg/fired pellet) | 510 | 328 | 318 | 250 | 407 | 447 |
| Porosity (%) (fired pellet) | 24 | 28 | 30 | 25 | 29 | 32 |
| Drop Number (times/green pellet) | 5 | 7 | 10 | 2 | 2 | 7 |

Effect of calcium bentonite addition on specification of pellets

Sodium bentonites are more absorbent than calcium bentonites because the divalent calcium ions hold the clay platelets more strongly together than monovalent sodium ions, letting less water in between the platelets (Kawatra and Ripke, 2003). It is a fact that Turkey has more calcium bentonite reserves than sodium bentonite. On the other hand, the prices of sodium bentonites are more expensive compared to calcium bentonites. Therefore, Ca bentonite was used for the following tests.

Similar procedure was repeated with calcium bentonite. The binder ratio was adjusted between 1% and 4% by weight of magnetite concentrate and the moisture content was adjusted as 8, 9, 10 and 12% for all binder dosages. Preliminary test results showed that increasing the amount of bentonite results in an increase in the average drop number of green pellets. However, these values are still under the standard value which is 4.

In the initial tests, best results were obtained when sodium bicarbonate ratio was 0.5% of solids added. At this ratio drop number of both green and dry pellets had the standard drop number of 4. Secondary tests were accomplished using laboratory-scale pelletizing disc at 0.5, 1 and 3% soda addition and then crushing and drop strength tests were applied to the pellets produced. The results given in Table 4 show that increasing the dosage of sodium bicarbonate activated bentonite provided an increase in the compressive strength, drop number and porosity of pellets. The best results were

obtained when bentonite activated with 3% sodium bicarbonate was added at an amount of 4%.

The effects of sodium bicarbonate on the activation of upgraded calcium bentonite were tested individually. In the initial tests optimum binder ratio was found to be 4% for both raw and dry pellets. Further tests were carried out with pelletizing disc at 3% and 4% binder ratios. In the activation processes, sodium bicarbonate ratio was 0.5% and 1% by weight of solids (Table 5). The average drop number of pellets increases with the addition of 4% activated calcium bentonite binder. The same trend is reported for the compressive strength for raw and dry pellets. However, compressive strength of fired pellets is seen to be under standard values. Furthermore, the required porosity value could not be attained with the addition of either activator.

Effect of mixed type bentonite addition on specification of pellets

In these tests mixed type bentonite was added to magnetite concentrate at different dosages (1, 2, 3, and 4%). The moisture content was adjusted to 8, 9, 10, and 12% for all binder additions. The higher the binder addition the higher the average drop number for green pellets was noted.

In the case of sodium bicarbonate activation the ratios were 0.5, 1, and 3%. Best results with sodium bicarbonate activation were obtained when the binder ratio was 3%. Proceeding tests were accomplished using a laboratory-scale pelletizing disc at 0.5, 1, 2, and 3% sodium bicarbonate addition and then the pellets were tested for compressive and drop strengths. The results are given Table 5. As it is seen in Table 5, the addition of 1% sodium bicarbonate is enough to meet standard values. When activated bentonite ratio is increased the values of compressive strength, average drop number and porosity rise.

Discussion

It is well known that Na-bentonites are mostly preferred for pelleizing iron ore concentrates due to their high binding capacities. Binding capacities of Na-bentonites may possibly be related to the swelling index. It is obvious that possible replacement of alkaline activated mixed or Ca-bentonites as binding agents will be more economic since Na-bentonite reserves in the world are limited. The prices of Na-bentonites in pelleizing agent grade are also relatively high when compared to other bentonites. Therefore, the way to activate the mixed or Ca-bentonites into sodium form can be advantageous. In this study, the pelletizing characteristics of Na, mixed, and Ca-bentonites were investigated, and the results are summarized in Figs. 3–7.

As seen in Fig. 3, upgrading of Na-bentonites resulted in lower bentonite addition for standard dry pellets. Additionally, the required bentonite addition (minimum 2%) for original Na-bentonites (as received) was reduced to the levels of 0.7% after the upgrading process. Similar behavior was also obtained for the compressive strengths and porosity of fired pellets (Figs. 4 and 5). The higher swelling index or CEC, the better pellet properties are. When drop numbers of pellets are evaluated, it can be said

that bentonite addition in pellets increased the drop number of green pellets and the addition of bentonite can be reduced to lower levels with the soda activation of Ca or mixed bentonites and upgrading of Na-bentonites (Fig. 6). This can be attributed to increased binding characteristics of bentonite through soda activation or upgrading.

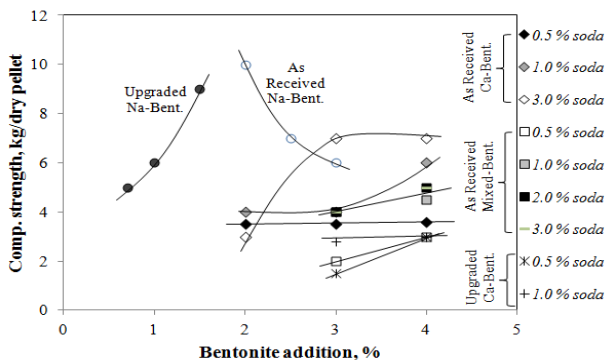


Fig. 3. Compressive strengths of dry pellets with different types of bentonites

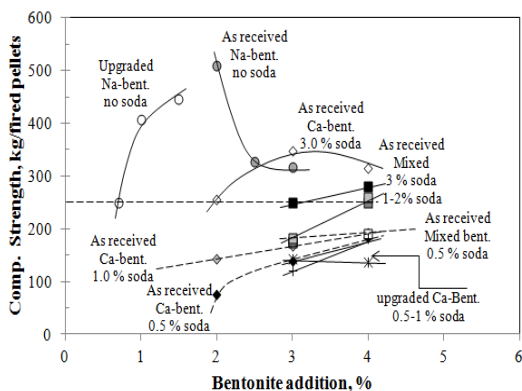


Fig. 4. Compressive strengths of fired pellets with different types of bentonites

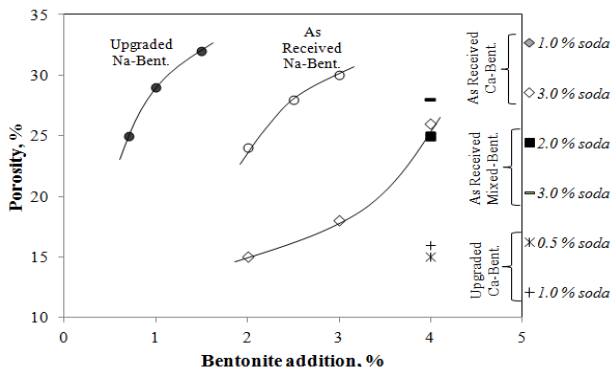


Fig. 5. Porosity of fired pellets with different types of bentonites

Table 5. Effect of activated Ca and mixed bentonite on compressive strength, porosity, and drop strength of pellets

| | Ca-bentonite (as received) | | | | | | Ca-bentonite (upgraded) | | | | | | Mixed-Bentonite (As received) | | | | | | | | |
|---|-------------------------------|-----|-----|-----|-----|-----|-------------------------------|-----|-----|-----|-----|-----|-------------------------------|-----|-----|-----|-----|-----|-----|-----|-----|
| | Sodium bicarbonate amount (%) | | | | | | Sodium bicarbonate amount (%) | | | | | | Sodium Bicarbonate Amount (%) | | | | | | | | |
| | 0.5 | | 1 | | 3 | | 0.5 | | 1 | | 0.5 | | 1 | | 2 | | 3 | | | | |
| Bentonite Amount (%) | 2 | 3 | 4 | 2 | 3 | 4 | 2 | 3 | 4 | 3 | 4 | 3 | 4 | 3 | 4 | 3 | 4 | 3 | 4 | | |
| Compressive Strength (kg/green pellet) | 1 | 1.2 | 1 | 1.5 | 1.5 | 2 | 1 | 2 | 2.2 | 0.8 | 1.1 | 0.9 | 1 | 1 | 1.5 | 1.3 | 2 | 1.5 | 1.5 | 1.6 | 2 |
| Compressive Strength (kg/dry pellet) | 3.5 | 3.5 | 3.6 | 4 | 4 | 6 | 3 | 7 | 7 | 1.5 | 3 | 2.8 | 3 | 2 | 3 | 4 | 4.5 | 4 | 5 | 4 | 5 |
| Compressive Strength (kg/fired pellet) | 75 | 140 | 184 | 144 | 167 | 192 | 255 | 348 | 314 | 143 | 137 | 120 | 183 | 173 | 190 | 176 | 250 | 182 | 260 | 250 | 280 |
| Porosity (%) (fired pellet) | - | - | - | - | - | - | 15 | 18 | 26 | - | 15 | - | 16 | - | - | - | 25 | - | 25 | - | 28 |
| Drop Number (times/green pellet) | 2 | 4 | 7 | 3 | 5 | 7 | 3 | 5 | 8 | 3 | 7 | 3 | 8 | 4 | 7 | 5 | 8 | 7 | 10 | 8 | 10 |

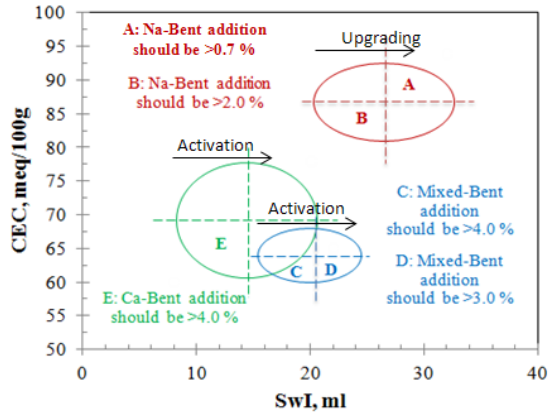


Fig. 7. Bentonite requirement in relation to swelling index and CEC

Conclusions

In pelletizing of fine magnetite concentrates, pellets with required mechanical strength could be produced when as received and upgraded Na-bentonites were used in the amounts of $>0.7\%$ and $>2\%$, respectively. On the other hand, in the case of calcium and mixed type bentonites much higher additions were needed, that is $>3\%$ and $>4\%$, respectively. When the activated bentonites were used to produce pellets with adequate mechanical strength, best results were obtained with calcium bentonite activated using 3% sodium bicarbonate and mixed type bentonite activated using 2% sodium bicarbonate. Finally, the overall results proved that the compressive strength, drop, and porosity values of pellets meet the specifications.

References

- ABOUZEID A.Z.M., KOTOB I.M., NEGM A.A., 1985, *Iron ore fluxed pellets and their physical properties*, Powder Technology, 42(3), 225–230.
- ARSLAN F., COŞAR Ş., GÜL A., PEREK K.T., ÖNAL G., AÇMA E., 2007, *Effect of Addition of Boron Minerals on Pelletizing of Iron Concentrate*, XII Balkan Mineral Processing Congress (XII BMPC 2007), Delphi, Greece, 10-14 June 2007, 305–310.
- ASTM C837 - 09 Standard Test Method for Methylene Blue Index of Clay.
- BALL D.F., DARTNELL J., DAVISON J., GRIEVE A., WILD R., 1973, *Agglomeration of iron ores*. Elsevier, London.
- BOYLU F., CINKU K., ESENLI F., CELIK M.S., 2010. The separation efficiency of Na-bentonite by hydrocyclone and characterization of hydrocyclone products, *International Journal of Mineral Processing*, 94 (3-4), 196–202 (Technical note).
- BOYLU F., 2010. Optimization of foundry sands characteristics of soda activated calcium bentonite, *Applied Clay Science*, 52, 104–108.
- BOYLU F., HODJIEV R., ERSEVER G., ULCAY Y., CELIK M.S., 2011. Production of ultrapure bentonite clays through centrifugation techniques, *Separation Science and Technology*, 47, 842–849.

- BOYLU F., 2013. Modelling and optimisation of ageing characteristics of soda activated Na⁺-bentonites, *Applied Clay Science* 83–84 (2013) 300–307.
- DOR A.A., ENGLISH A., FRANS F.D., WAKEMAN J.S., 1970, IX. International Mineral Processing Congress, Praha, Tschechoslowakei, I, 6VI, 173.
- EKETORP S., 1962, *Steel Making*, The Chapman Conference, Cambridge, Massachusetts, June, 180.
- ERICKSON D.V., PALUSKY E.L., *Bentonite Binder Composition*, United States Patent, No: 3, 779–782.
- FORSMO S.P.E, APELQVIST A.J.B., BJORKMAN M.T., SAMSKOG P.O., 2006, *Binding mechanisms in wet iron ore green pellets with a bentonite binder*, *Powder Technology*, 169, 147–158.
- FORSMO S.P.E, SAMSKOG P.O., BJORKMAN M.T., 2008, *A study on plasticity and compression strength in wet iron ore green pellets related to real process variations in raw material fineness*, *Powder Technology*, 181, 321–330.
- MEYER K., 1980. *Pelletizing of iron ores*, Berlin/Heidelberg/New York: Springer-Verlag und Dusseldorf: Verlag Stahleisen m. b. H.
- RIPKE S.J., KAWATRA S.K., 2000, *Can Fly-ash Extend Bentonite Binder for Iron Ore Agglomeration*. *Int. Journal of Min. Process.*, 60, 181–198.
- RIPKE S.J., KAWATRA S.K., 2003, *Laboratory studies for improving green ball strength in bentonite-bonded magnetite concentrate pellets*. *Int. J. Miner. Process.*, 72, 429–441.
- SASTRY K.V.S., FUERSTENAU D.W., 1972, *Ball ability index to quantify agglomerate growth by green pelletization*, *AIME Trans.*, 254–258.
- SIVRIKAYA O., AROL A. I., 2010, *Use of boron compounds as binders in iron ore pelletization*, *The Open Mineral Processing Journal*, 3, 25–35.

Received December 31, 2013; reviewed; accepted May 6, 2014

EXPERIMENTAL INVESTIGATION OF A HIGH TEMPERATURE RESISTANT AND LOW FRICTION FRACTURING FLUID

Bo XIAO*, Shicheng ZHANG*, Jian ZHANG**, Tengfei HOU*, Tiankui GUO***

* MOE Key Laboratory of Petroleum Engineering, China University of Petroleum, Beijing, China, 102249

** Huaneng Clean Energy Research Institute, Beijing 102209, China, victorxiao@163.com

*** China University of Petroleum (East China), Qingdao 266555, China

Abstract: The performance of a hydraulic fracturing fluid (HFF) system directly determines the efficiency of stimulation. Since the targeted formations of most oil fields in China are characterized by large depth (~5000 m), high temperature (160 to 180 °C) and tight lithology, newer and suitable HFFs have to be developed. Based on a newly synthesized organo-boron/-zirconium cross-linking agent (Gh-g), a composite temperature stabilizer (WJ-6) and other optimized additives via indoor evaluation, this study introduced a novel HFF, which is thermally stable at high temperature (HT) up to 180 °C and exerted low friction pressures. The performance of HFF was evaluated in the laboratory. The experimental results showed that the HFF system performed well at HTs. It maintained a viscosity of 100 mPa·s or more after 90 min of shearing (170 s^{-1}) at 180 °C. Furthermore, the system exhibited delayed cross-linking. It took 120 s for the cross-linking reaction to complete; therefore, the tube friction was reduced to a large extent. Another characteristic feature of the formulated HFF system was the low friction pressures, where the drag reduction percentage was in the range from 35% to 70%. Moreover, only minor damage was caused by the fluid to the formation core samples. The average core permeability damage was 19.6%. All these qualities ensure that this fluid system is in full compliance with the requirements of the fracturing treatment.

Keywords: *high temperature fracturing fluid, resistance to shearing, hydroxypropyl guar, low friction, delayed crosslinking*

Introduction

A critical factor in the successful stimulation of deep tight oil and gas reservoirs is the performance of HFF. Formulating a HFF system that maintains stable performance under ultra-HT and a prolonged shearing environment remains a challenge for engineers (Li et al., 2003; Zhang et al., 2005; Li et al., 2005; Han et al., 2006).

Each of the several additives in HFF has its specific function. However, not every component plays a decisive role in the performance of HFF at HT condition (Lagrone et al., 1983; Loveless, 2011). Critical factors affecting the performance of HT resistant HFF include components listed below.

Thickening agent, as a main component of the HFF, is to enhance the viscosity of the aqueous solution. Generally, the greater molecular weight of the thickening agent, the stronger is its thickening ability. Water solubility of viscosifier will be high and the residue after the gel breaks down will be less if the number of hydration groups on the molecular chain of the thickening agent is high (Yang et al., 2004).

Crosslinking agent like organic boron enhances the viscosity of HFF is a widespread practice. However, the organic boron cross-linker is unstable in deep and HT low-permeability reservoirs; cross-linking is gradually ruptured with increase in temperature. Domestic organic boron cross-linkers are not stable at temperatures $>140\text{ }^{\circ}\text{C}$. Reticular gel can be generated with an organozirconium cross-linker; covalent bonds result from the reaction between the transition metal ions and maleinoid form of hydroxyl groups on the galactose branched chain of the polymers. The cross-linking functional group is relatively stable and can endure temperatures up to $260\text{ }^{\circ}\text{C}$; however, the reforming ability of gel after high-speed shearing is extremely poor. A combination of boron- and zirconium-based cross-linking agents, which compensate for the shortcomings in each other, is a widely used cross-linking agent in HT ($>140\text{ }^{\circ}\text{C}$) HFF formulations (Chen et al., 2007; Wang et al., 2011; Lu et al., 1995).

Temperature stabilizer is a vital component in HT HFF. Modified guar is the preferred thickening agent in HT fracturing liquid. However, the main polysaccharide backbone of the plant guar begins to degrade at temperatures $>160\text{ }^{\circ}\text{C}$ and deteriorates rapidly at temperatures $>177\text{ }^{\circ}\text{C}$. A temperature stabilizer is usually added to improve the thermal resistance of the HFF (Zhang et al., 2012; Gupta et al., 2011).

pH adjusting agent is also adopted to regulate the acid-base property of the HFF for a better performance. Hydrolysis of guar gum and its derivatives occurs easily in a low pH environment and, more so, at HT environment. Therefore, the pH value of the HFF should be maintained within a suitable range (Abad et al., 2011; Terracina et al., 1999; Poleski et al., 2013).

Considering the factors in the formation of oil wells in China, a HFF system has been formulated in the laboratory and evaluated on the basis of the above key factors.

Materials and methods

Equipment and Materials

Viscosity of HFF systems was investigated by RS6000 rheometer (Germany Haake). Pincee capillary viscometer (HengTong Instrument Co., Ltd., Shanghai, China) was used to measure the viscosity of HFF after breaking. Leak-off coefficient of fluid was tested with HT dynamic fluid loss evaluating device HALS-1 (Huaan scientific

equipment corporation, Jiangsu, China). Friction of HFF was evaluated by large-scale friction tester YMC-1 (Huaan scientific equipment corporation, Jiangsu, China).

Samples studied include industrial products (hydroxypropyl guar (BG-1, SG-1, BXT-2), KCl, NaOH, Na₂CO₃, NaHCO₃), capsule gel breaking agent (XT-71), emulsion breaker (XH-2), cleanup additive (XT-5), temperature stabilizer (WJ-1, WJ-2, WJ-3) and bactericides (JA-1).

HT cross-linking agent Gh-g was prepared using the following protocol. Predetermined quantities of borax, sodium gluconate and water were mixed in a three-necked flask. The resulting mixture was agitated and refluxed for 1 h at 80 °C using an oil bath. Subsequently, zirconium oxychloride, lactic acid, triethanolamine, glycerin, citric acid and EDTA were added under an atmosphere of nitrogen. The faint yellow-colored fluid, i.e., the HT cross-linking agent Gh-g, was obtained after agitating and refluxing the mixture at the same temperature (80 °C) for 6 h.

Experimental methods

Formulation of HT resistant HFF

At the beginning, the main additives (thickening agent, cross-linking agent, temperature stabilizer and pH adjusting agent) and other additives were evaluated as the component candidate of HT HFF. Tests were conducted to ensure that the selected additives had no negative effects on the characteristics of the HFF. Subsequently, compatibility evaluation was carried out to see if any flocculates and deposits were observed. The HFFs were formulated with additives that had good compatibility with each other and no negative effects on HFF function. All experiments were implemented in accordance to Standards of Petroleum and Natural Gas Industry of China.

Evaluation of HT resistant HFF

The optimized base fluid was prepared and the components allowed to hydrate for 2 h to ensure complete polymer hydration. To minimize variations in the base fluid, its temperature and pH were measured before use. The viscosity of the base fluid was in the range of 170 s⁻¹. An aliquot of the base fluid was cross-linked. After cross-linking, the fluid was sheared at high speed for an additional minute before being placed in viscometer.

The cross-linked fluid was placed in the RS6000 viscometer and pressure was applied with the nitrogen gas. With a preheated oil bath at the predetermined test temperature, it took ~30 minutes for the sample to reach the designated temperature. The fluid was sheared at 10 s⁻¹ to 20 s⁻¹ during heating. The shear rate was increased to 170 s⁻¹ when the sample attained the test temperature and the shearing was continued for 90 minutes. After recording the initial rheogram, the evaluation was continued until the fluid viscosity dropped below 50 mPa·s.

The friction characteristics of the fluid system were evaluated by large-scale friction tester YMC-1. The inner diameter of coiled flow loop was 1.2 cm. Various

additives at the desired concentrations were added to the water and equilibrated for 5 minutes (to disperse, mix and hydrate) before the mixture was released into the flow loop. Pressure drops and flow rates were recorded after every 30 s to 60 s for several minutes while the fluid recirculated through the flow loop. Subsequently, pressure variation in the flow of additive-free water under the same conditions was recorded. The results from the two experiments were compared.

The formation damage potential of the HFF was assessed via regained permeability tests. Tests were performed in accordance to API RP39 recommended practices for measuring the viscous properties of a cross-linked water-based HFF.

Results and discussion

Formulation of HFF system

Thickening agent

Modified plant gum functions as a thickening agent owing to its high viscosity, resistance to HT, leaves less residue and is required in low quantities (GUO et al., 2011). The physical performance of the three widely used gums – imported guar gum BG-1 (1st grade), hydroxypropyl guar gum SG-1 (1st grade) and hydroxypropyl guar gum BXT-2 (1st grade) – under our experimental conditions is shown in Table 1.

Table1 The main properties of different thickening agents

| Type | Water-insoluble matter content [%] | Viscosity at 0.6% concentration [mPa·s] | Residue [mg·dm ⁻³] |
|-------|------------------------------------|---|--------------------------------|
| BG-1 | 4.39 | 123 | 229 |
| SG-1 | 4.58 | 108 | 249 |
| BXT-2 | 4.25 | 117 | 212 |

Each thickening agent was screened for its water-insoluble content, thickening ability and the quantity of residue remaining. The water-insoluble content and residues of thickening agents BG-1 and BXT-2 was less than that of SG-1 (Table 1), therefore, it is likely that the use of BG-1 and BXT-2 in the HFF will cause less damage to the formation. The relatively high viscosity observed with 0.6% solutions of BG-1 and BXT-2 indicated their strong thickening ability. The lower quantities of thickening agent would be, the stronger thickening ability and the lower damage could cause to the formation because of the lower quantities of residue left behind by the HFF. Although thickening ability of BXT-2 was slightly lower than that of BG-1, the water-insoluble content and the amount of residue was also relatively low. Permeability of block Hui 25 formation is quite low ($\sim 0.04 \times 10^{-3} \mu\text{m}^2$), therefore, a high residue in the HFF can cause serious damage to the conductivity of proppant and the matrix

permeability. Therefore, BXT-2 was selected as the thickening agent in the formulation of HT HFF system.

Cross-linking agent

Reasonable selection of cross-linking agent can greatly enhance the temperature resistance of a HFF. Widely used cross-linking agents for hydroxypropyl guar gum are organoboron compounds. However, these compounds lose the cross-linking ability due to chemical modifications when the temperature exceeds 140 °C. Organotitanium and organozirconium compounds, synthesized from titanium or zirconium ions, respectively, can maintain a relatively strong cross-linking ability at temperatures >140 °C, provided an appropriate pH value is maintained (AINLEY et al., 1993; WANG et al., 2004). Six different cross-linking agents, four of which were organoboron and organozirconium compounds, were evaluated. The remaining two cross-linking agents evaluated were organotitanium compounds.

As a based fluid for conducted experiments was a guar gum fluid containing compounds such as hydroxypropyl guar gum BXT-2 (0.6%), KCl (0.5%), cleanup additive XT-5 (0.5%), demulsifier XH-2 (0.5%), temperature stabilizer (1%), and bactericide JA-1 (0.1%). At room temperature (20 °C), different cross-linking agents (0.30 mL) were added separately to the fluid (100 g) and mixed. The cross-linking time was recorded and the thermal and shear resistance of each of the gel was evaluated. Similar tests were performed with increasing amounts of GH-g (0.40, 0.50, 0.55 and 0.60 mL) for the sake of comparison. The results showed that the cross-linking ability of GH-g was better. The cross-linking time and hang-up characteristics of the gel with various amounts of GH-g are shown in Table 2.

Table2. Characteristics of crosslinking and hang-up ability of HT crosslinker GH-g at different concentration

| Formula of basic fluid | Concentration of crosslinker Gh-g[%] | Thickening time[s] | Hang-up time [s] | Gel property |
|---|--------------------------------------|--------------------|------------------|----------------------------------|
| 0.6% hydroxypropyl guar BXT-2+0.5%KCl+0.5% cleanup additive+0.5% emulsion breaker +1% temperature stabilizer+0.1%JA-1 bactericide agent | 0.3 | 30 | 130 | easy to hang up |
| | 0.4 | 26 | 125 | easy to hang up |
| | 0.5 | 20 | 126 | easy to hang up |
| | 0.6 | 15 | 118 | can be hung up, slightly friable |

Rheological tests at 160 °C and a shear rate of 170 s⁻¹ were used for assessing the thermal and shear resistance of the HFFs containing different amounts of GH-g (Figure 1). The bimetallic organo-boron/-zirconium cross-linking agent GH-g showed

good performance when used at a concentration of 0.5%–0.6%. The initial viscosity of the fluid rose up to 1000 mPa·s and decreased after 1 h of shearing to 160 mPa·s.

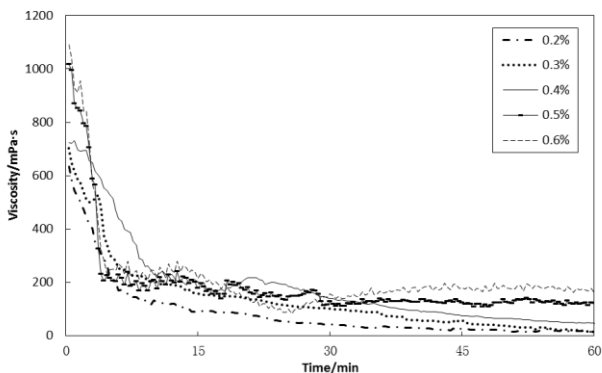


Fig.1. Rheological curve of HFF with different amount of GH-g at 160°C

Temperature stabilizer

Temperature resistance of cross-linked guar-based fluid degrades greatly when the temperature exceeds 120 °C. Therefore, a temperature stabilizer is typically added to enhance the temperature resistance and reduce the degradation rate of the cross-linked guar-based fluid at HT condition. Three temperature stabilizers, WJ-1, WJ-2 and WJ-3, were tested to identify which of them causes the greatest enhancement in temperature tolerance of cross-linked guar gum-based fluid. WJ-1 was a thiosulfate, WJ-2 was a ketoxime and WJ-3 was a hydrazine. The results showed that none of these temperature stabilizers can improve the thermal stability individually.

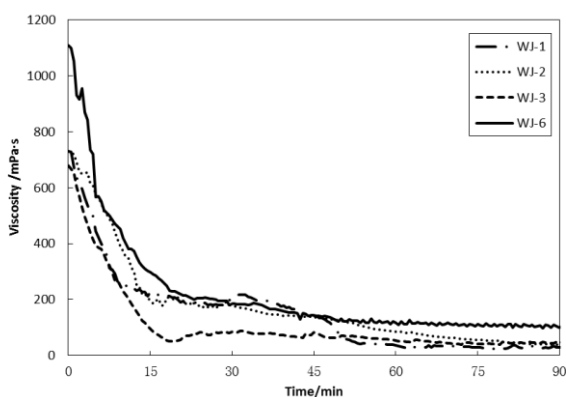


Fig. 2. Effect of different temperature stabilizer on the HT resistance at the concentration of 1%

Rheological curves of the three temperature stabilizers are shown in Figure 2. Thiosulfate had a good assistant effect in temperature tolerance at low temperature

conditions and the ketoxime, WJ-2, was relatively stable. Although hydrazine was expensive, its strong reducibility could improve the thermal stability of the HFF effectively. Therefore, various combinations of WJ-1, WJ-2 and WJ-3 were tested for their ability to enhance the temperature resistance of the fluid system. According to results from the rheological tests, the optimal enhancement in thermal stability was observed when the ratio of the three temperature stabilizers WJ-1:WJ-2:WJ-3 was 5:3:2. This combination of WJ-1, WJ-2 and WJ-3 was designated as WJ-6. On evaluation of its prolonged stability, no change in color or the emergence of flocculates and deposits were observed. As evident from Figure 2, when temperature and shearing rate were 160 °C and 170 s⁻¹, respectively, WJ-6 enhanced the temperature tolerance and shearing resistance significantly. Thus, WJ-6 was selected as the temperature stabilizer in the HT HFF system. WJ-6 provided thermal stability by two mechanisms. To begin with, the temperature stabilizer could take off the free oxygen in the fluid, thereby weakening the accelerating of thermal degradation and, consequently, enhancing the thermal stability of thickening agent. Additionally, the temperature stabilizer was able to react with the free radical of the polymer to improve the substantivity between cross-linker and polymer hydroxyl group, thus allowing the HFF to be stable at HT. These two mechanisms provide the thermal stability to the gel HFF system.

pH adjusting agent

The pH has a great effect on the characteristics of HT HFFs. Hydroxypropyl guar is hydrolyzed in solutions with low pH value and, more heavily, at HTs. Generally, polymers such as guar form cross-links only in an alkali environment. Rheology tests were performed on HFFs containing various amount of Na₂CO₃, NaHCO₃ and NaOH to analyze the temperature tolerance and shear resistance. Analysis of the rheological curve suggested that GH-g had the optimal cross-linking effectiveness with 0.15% NaOH.

Formulation of HT HFF system

After the identification and concentration optimization of thickening agent, cross-linker, temperature stabilizer and pH adjusting agent, the type and concentration of other additives were also determined. Compatibility tests showed that all the above listed additives have good compatibility with each other and present no flocculates or deposits. In addition, the other additives selected, i.e., cleanup additive, clay inhibitor, emulsion breaker and bactericide agent, had no negative effects on the properties of the HFF. As a result, the HT HFF system was a water-based fluid containing hydroxypropyl guar BXT-2 (0.6–0.65%), emulsion breaker XH-2 (0.5%), cleanup additive XT-5 (0.5%), clay inhibitor KCl (1%), bactericide agent JA-1 (0.1%), temperature stabilizer agent WJ-6 (1%), pH adjusting agent NaOH (0.10–0.15%), capsule gel breaker XT-71 (with “wedge” additional breaker technology, 0.0002%–0.2%) and cross-linker GH-g (0.5–0.6%).

Evaluation of HT HFF

The evaluation of the characteristics of the HT HFF was performed according to the requirements of Standards of Petroleum and Natural Gas Industry of China. The HFF was the water-based fluid containing hydroxypropyl guar BXT-2 (0.6%), bactericide agent JA-1 (0.1%), cleanup additive XT-5 (0.5%), pH adjusting agent NaOH (0.12%), clay inhibitor KCl (1%), emulsion breaker XH-2 (0.5%), temperature stabilizer agent WJ-6 (1%), cross-linker GH-g (0.5%) and capsule gel breaker XT-71 (0.1%).

Characteristics of base fluid and cross-linking fluid

Apparent viscosity and pH value are two important evaluation index for the base fluid of HFF. When the pH value was 12–13, at a temperature of 25 °C and a shearing rate of 170 s^{-1} , the apparent viscosity of HFF was 105 $\text{mPa}\cdot\text{s}$ to 115 $\text{mPa}\cdot\text{s}$. Since there was no alkali-sensitivity in Hui 25 block, this fluid system will be suitable for stimulation.

Vortex sealing method, which mainly measures the cross-linking time and the state after gel formation, was used to investigate the characteristics of cross-linking fluid. The HT HFF system started to form the gel after 20 s. At 120 s, the cross-linking was complete. All of this displayed a good delayed cross-linking characteristic. Furthermore, the surface of gel was smooth and showed no wall-hanging feature.

Resistance to temperature and shearing

Thermal and shear resistance of the fluid system was evaluated by simulating the treatment conditions (XIONG et al., 1996). Changes in apparent viscosity of HFF determines whether the rheological properties of HFF can meet the requirement of process design. Temperature and shearing resistance of the HFF system was measured at 180 °C and 170 s^{-1} , respectively, using a HAAKE RS6000 rheometer. As shown in Figure 3, after 90 min of shearing at the corresponding temperature, the results indicated that the viscosity of HT HFF remained at or above 100 $\text{mPa}\cdot\text{s}$, which was in full compliance with the requirements of the fracturing treatment.

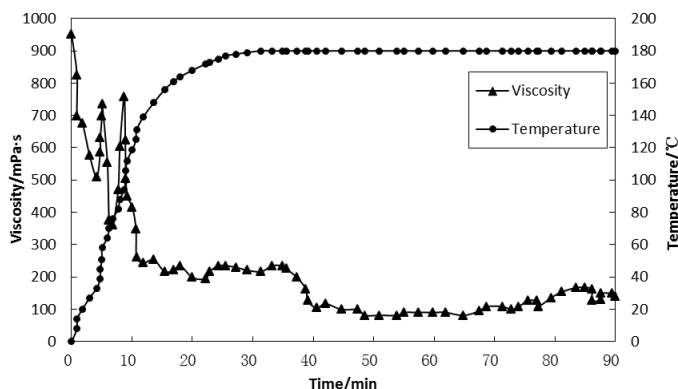


Fig. 3. Rheological curve of HT HFF at 180°C and 170 s^{-1}

Evaluation of friction characteristics

Both the choice of pumping equipment and the effectiveness of hydraulic power transmission are markedly affected by the friction produced as fluids flow through the pipes. More problems emerge in treatment when a HFF generates high friction. The targeted formation in well Hui 25 area lies ~5,000 m underground. The delayed cross-linking fluid will greatly reduce the friction by slowing down the process of cross-linking. Here, the friction resistance of HFF is marked by Drag Reduction Ratio – ratio of friction value difference between HFF friction and water to water friction. Results from the YMC-1 large-scale friction tester indicated that the developed HFF system can effectively reduce friction.

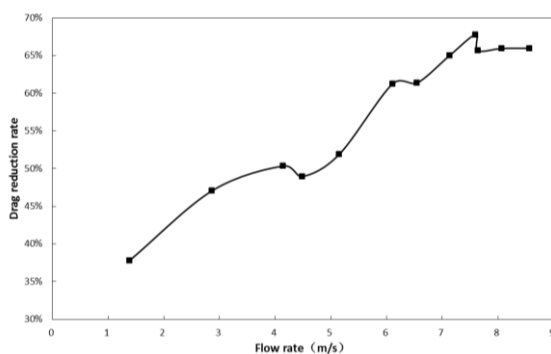


Fig. 4. Drag reduction of the HFF system at various flow rate

As evident from Figure 4, drag reduction ratio of the fluid varied between 35% and 70%, resulting from the different flow rates. Higher values of the ratio were observed for higher flow rates. However, when the average flow rate was $>8 \text{ m s}^{-1}$, the drag reduction ratio remained constant. Formation of whirlpools or transitions from a large whirlpool to a small one were hindered in pipe flow because of the swelling of HPG molecule in water, therefore, friction was reduced as a result of low energy loss. The reduction of friction was limited at higher flow rates, as the structural stability of HPG molecule was weakened by the increased shear force exerted on the fluid by walls of the tube.

Evaluation of gel breaking

The performance of flowback and the ultimate stimulation effect are largely influenced by the ability to break the gelled HFF. The compatibility of this HFF system with formation water was confirmed by experimentation, wherein the final solution was clear and contained no emulsion or sediments. The viscosity of fluid after breaking was only 4 mPa·s, which was in full compliance with industrial standard.

Evaluation of formation damage

Cores from the well at Hui 25 area in China were used as samples to evaluate the performance of HFF. The damage caused by the HFF to the formation should be limited, since the lithology in this area was so tight that the average determined core permeability was $0.04 \times 10^{-3} \mu\text{m}^2$. Six cores from the intended zone were evaluated for the damage to core permeability brought about by the filtrate of this fracture fluid. The extent of damage to the core permeability varied between 10.0% and 33.8%, while the mean damage percentage was only 19.6% (Table 3), which meets the requirements of industrial standards.

Table 3. Results of experiments for evaluating damage on cores of HT-tolerant HFF

| Core label | Original permeability [$10^{-3} \mu\text{m}^2$] | Permeability after experiment [$10^{-3} \mu\text{m}^2$] | Damage percentage [%] | Average damage percentage [%] |
|------------|--|---|-----------------------------|-------------------------------------|
| 1# | 0.043 | 0.037 | 14.5 | 19.6 |
| 2# | 0.045 | 0.039 | 12.7 | |
| 3# | 0.035 | 0.025 | 29.4 | |
| 4# | 0.056 | 0.050 | 10.0 | |
| 5# | 0.025 | 0.017 | 33.8 | |
| 6# | 0.041 | 0.034 | 17.2 | |

Conclusions

The variety and dosage of additives in HFF that can influence its properties were selected and optimized through in-lab experiments. The optimized formulation of a HT resistant HFF system was a water-based fluid containing hydroxypropyl guar gum BXT-2 (0.6%), emulsion breaker XH-2 (0.5%), clean up additive XT-5 (0.5%), clay inhibitor KCl (1%), bactericide JA-1 (0.1%), temperature stabilizer WJ-6 (1%), pH adjusting agent NaOH (0.10–0.15%), encapsulated gel breaker XT-71 (wedge-like adding advised, 0.0002–0.2%) and cross-linking agent GH-g (0.5–0.6%). The in-lab performance evaluation of the formulated HT resistant HFF indicated that this fluid system can meet the demands of stimulation. Evidence for the same is follows. The observed delayed cross-linking attribute was favorable to reduce friction and cross-linking of the molecular chains in guar gum started after 120 s. In addition, the HFF exhibited excellent temperature and shearing resistance and its viscosity was 100 mPa·s even after 90 min at a temperature of 180 °C and shearing rate of 170 s⁻¹. Moreover, the gel broke down completely and the viscosity of the solution after gel breaking was only 4 mPa·s. Furthermore, the formulated HFF exhibited low friction quality while tube friction just took up 35–70% of water friction. At last, the formulated HFF caused little damage to the formation of well of Hui 25 area and average damage percentage of core permeability was only 19.6%.

References

- HAN S., ZHANG H., ZHANG F.J., et al., 2006. *Development and application of HFFs at HTs for Daqing deep compacted gas reservoirs*, Journal of Daqing petroleum institute, 30, 34–39.
- ZHANG H., 2005. *HT fracture liquid flowed-denaturation influence factor analyse*. Journal of Daqing petroleum institute, 21, 98–100.
- LI D.P., 2003. *Decision-making Theory on Low-permeability Reservoir Development*. Beijing: Petroleum Industry Press, 160–153.
- YANG S.L., WEI J.Z., 2004. *Fundamentals of Petrophysics*. Beijing: Petroleum Industry Press: 159–170.
- LI Z.G., WU X.M., LI Z.F., 2005. *Premium N2 energized aqueous HFF for low-pressure and tight gas reservoir*. Drilling fluid&completion fluid, 22, 33–37.
- CHEN P.F., WANG X., YAN F., 2007. *Evaluation of a kind of modified guar gum*. Advances in fine petrochemicals. 12, 1–4.
- WANG W.T., ZHANG H., LIU H.S., et al., 2011. *Research and application of HT HFFs of low-damage and low-friction. Special oil and gas reservoirs*. 18, 100–104.
- LU Y.J., DU C.F., CHEN Y.D., 1995. *Application of organo-borate crosslinked HFFs in HT and deep wells*. Drilling fluid&Completion fluid, 12, 21–29.
- ZHANG H., ZHANG Y.G., WANG X.J., 2012. *Composite gelatinizer of super-HT HFF for deep buried and dense gas reservoir*. Journal of Daqing petroleum institute, 36, 59–65.
- SATYA GUPTA D.V., 2011. *HFF for extreme temperature conditions is just as easy as the rest*. SPE140176.
- ABAD C, MIRAKYAN A, PARRIS M, et al., 2009. *New HFF for HT reservoirs*. SPE121759.
- TERRACINA J.M., MCCABE M.A., SHUCHART.C.E., et al., 1999. *Novel oxidizing breaker for HT fracturing*. SPE56278.
- API RP39, *Recommended practices on measuring the properties of water-based HFF, third edition*. 1998. Washington, DC: API.
- LAGRONE C.C, BAUMGARTNER S.A, WOODROOF R.A., 1983. *Chemical evolution of a HT HFF*. SPE11794.
- LOVELESS D., HOLTSLOW J., SAINI R., et al. 2011. *HFF comprised of components sourced solely from the food industry provides superior proppant transport*. SPE147206.
- POLESKI M., ŁUCZAK J., ARANOWSKI R., JUNGnickel C., 2013. *Wetting of surfaces with ionic liquids*, Physicochem. Probl. Miner. Process. 49, 277–286.
- AINLEY B.R., NIMERICK K.H., CARD R.J., 1993. *HT, borate-crosslinked HFF: a comparison of delayed methodology*. SPE 25463.
- GUO J.C., WANG S.B., WU L., 2011. *Research and application of ultra-HT fracture fluid*, Oilfield Chemistry. 28, 49–52.
- WANG D., WANG J.Y., LIU H.S., et al., 2004. *Preparation of HT organic borate-zirconate crosslinker CZB-03 of delayed action for aqueous hydroHFFs*. Oilfield Chemistry. 2, 113–116.
- XIONG H.J., DAVIDSON B., SAUNDERS B., et al., 1996. *A comprehensive approach to select HFFs and additives for fracture treatments*. SPE 36603.

Received December 12, 2013; reviewed; accepted April 29, 2014

NOBLE METAL MODIFIED TiO₂ FOR PHOTOCATALYTIC AIR PURIFICATION

Marek KLEIN^{*}, Ewelina GRABOWSKA^{**}, Adriana ZALESKA^{*,**}

^{*} Department of Chemical Technology, Faculty of Chemistry, Gdansk University of Technology, Gdansk, Poland

^{**} Department of Environmental Technology, Faculty of Chemistry, University of Gdansk, 80-308 Gdansk, Poland, ewelina.grabowska@ug.edu.pl

Abstract: TiO₂ was surface modified with silver, gold, palladium and platinum ion clusters to improve its photocatalytic activity. The effect of metal content and kind of dopant used during preparation procedure on the photoactivity were investigated. in toluene removal which was used as a model volatile organic compound. Toluene, at the concentration of about 100 ppm, was irradiated over noble metal modified TiO₂ using light-emitting diodes (LEDs) in four subsequent cycles.

Keywords: photocatalysis, noble modified TiO₂, air treatment; toluene

Introduction

Volatile organic compounds (VOCs) are a group of air pollutants widely present in both indoor and outdoor environments. The main emission sources of VOCs are motor vehicle exhausts and solvent utilization (Zou et al., 2006). Toluene, as one of widespread volatile organic compounds, is found in polluted urban atmosphere. Due to its high toxicity, carcinogenicity, and long environmental persistence, it is regarded as a priority hazardous substance. Therefore, removal of toluene in the contaminated atmosphere has become an increasingly concerned issue in the field of environment protection (Zou et al., 2012).

The use of heterogeneous photocatalysis in the degradation of environment pollutants has aroused intensive attention during the past two decades (Minabe et al., 2000; Hoffmann et al., 1995). Among various semiconductor photocatalysts for environment purification, titania appears to be the most promising and important one due to its stable physical and chemical characteristics, unique electronic properties, strong oxidizing power, non-toxicity and low price. However, the wide band gap of TiO₂ (>3.2 eV) and the high recombination rate of the photoinduced electron-hole

pairs formed in photocatalytic processes limit the efficiency of the photocatalytic degradation of toxicants (Minabe et al., 2000).

Barraud et al. (2005) investigated the photocatalytic removal of toluene in the gas phase carried out over UV-illuminated sulfated titania materials in a cylinder-like continuous reactor. They have concluded that only CO₂ and H₂O were detected as gaseous reaction products whatever photocatalyst was used. The presence of the adsorbed reaction intermediates such as benzaldehyde and benzoic acid was identified by the FTIR spectra of the sulfated TiO₂ photocatalysts. Keller et al. (2007) compared the photocatalytic behavior of different TiO₂-based photocatalysts for the gas-phase toluene removal under both UV and visible light illumination. They reported that promotion by sulfates and the use of nanosized anatase TiO₂ prepared by sol-gel route did strongly increase the toluene removal efficiency under UV illumination. Sekiguchi et al. (2008) performed the photocatalytic degradation of toluene gas in a mist formed by ultrasonic atomization of slurried TiO₂. They revealed a new effective utilization of ultrasonic mist and TiO₂ photocatalyst over which gaseous toluene could be decomposed and mineralized. Nischk et al. (2013) prepared vertically ordered TiO₂ nanotube arrays and measured photocatalytic activity in the toluene removal. Toluene, at the concentration of about 100 ppm, was irradiated over TiO₂ nanotube arrays using xenon lamp and light-emitting diodes (LEDs) in four subsequent cycles. The results showed that toluene could be mostly removed from the air after 30 min of irradiation over TiO₂ nanotubes (NTs), even using LEDs (375 nm) as a irradiation source. Photoactivity increased with increasing of nanotubes lengths and decreasing of the crystallite size (Nischk et al., 2013).

In this work series of modified TiO₂-based photocatalysts were prepared by the photodeposition of noble metals at the surface of P25 (TiO₂ loaded with Pt, Pd, Ag, Au nanoparticles). Photocatalytic activity of prepared TiO₂ photocatalysts was determined in the process of cleaning air from volatile organic compounds (VOC). Toluene was used as a model air contaminant.

Materials and methods

P25 (70:30% anatase-to-rutile mixture with a BET surface area of 55 ± 15 m²/g and crystallite sizes of 30 nm in 0.1 μm diameter aggregates) was obtained from Evonik Industries, Germany (Ohno et al., 2001, Ohtani et al., 2010). 98% KAuCl₄, 99% H₂PtCl₆, PdCl₂ (anhydrous, 60% Pd basis) were purchased from Sigma-Aldrich. 99,9% AgNO₃ was purchased from POCh S.A. (Poland).

Toluene (99.5%, p.a., POCh S.A., Poland) was used as a model air contaminant. All reagents were used without further purification.

All the photocatalysts were obtained by radiolysis reduction of noble metals in the TiO₂ suspension. 70 cm³ of solution containing TiO₂ P25 (3 g), metal precursor (0.1 or 1 % m/m Au, Pt, Pd and Ag respectively), water (68 cm³) and isopropanol (2 cm³) was degassed with nitrogen in dark for 40 min. Then the suspension was illuminated by

1000 W Xe lamp used as an irradiation source for 2 h. Obtained samples were rinsed with deionized water, dried in air (80°C for 24 h) and grinded in the agate mortar.

Light-absorption properties of TiO₂ nanotubes were characterized by recording diffuse reflectance (DR) spectra and converting the data in order to obtain absorption spectra. The measurements were performed on UV-Vis spectrophotometer (Evolution 220, Thermo Scientific) equipped with an integrating sphere. The baseline was determined using barium sulfate as a reference

Total metal content of the samples was determined by X-ray fluorescence spectrometry (XRF). Pressed pellet (diameter 8mm) were analyzed using WD-XRF (Bruker S8 Tiger 1KW). The instrument is equipped with a rhodium tube and a proportional and scintillation detector. Linear intensity range was more than 10 million cps. All analyses were conducted at maximum 50 keV and 50 mA. Standardless analysis was used to determine the concentrations of the measured elements.

The modified TiO₂ samples were examined by transmission electron microscopy (STEM-EDX, FEI Europe, model Tecnai F20 X-Twin). To obtain a suitable sample for TEM characterization metal modified TiO₂ powder was dispersed in ethanol in an ultrasound bath for a few minutes. Some drops of suspension were deposited on carbon covered microgrid.

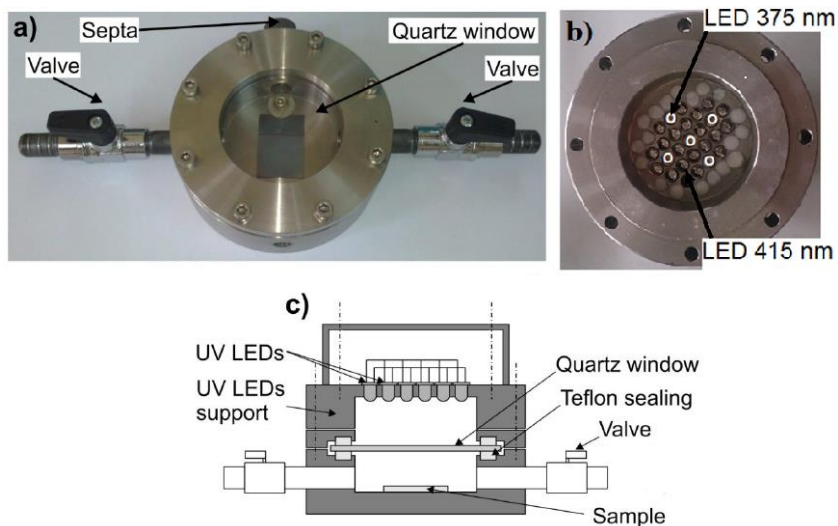


Fig. 1. Photocatalytic set-up for gas phase reaction: (a) image of gas phase photoreactor; (b) image of UV-Vis LEDs array; (c) scheme of photoreactor equipped with UV-Vis LEDs as an irradiation source

Photocatalytic activity of prepared TiO₂ photocatalysts was determined in the process of cleaning air from volatile organic compounds (VOC). Toluene was used as a model air contaminant. The photocatalysts activity tests were carried out in a flat stainless steel reactor with the working volume of about 30 cm³ (see details in Fig. 1)

equipped with a quartz window, two valves and a septa (Fig. 1a). An array of 20 UV LEDs ($\lambda_{\max} = 375$ nm, 63 mW per diode) and 5 VIS LEDs ($\lambda_{\max} = 415$ nm) was used as an irradiation source. Glass plate covered by noble metal modified TiO_2 was placed at the bottom side of the reactor followed by closing the reactor with a quartz window. Subsequently, the gaseous mixture was passed through the reaction chamber for 2 min. After closing the valves, the reactor was kept in dark for 10 min in order to achieve equilibrium. A reference sample was taken just before starting irradiation. The analysis of toluene concentration in the gas phase was performed using gas chromatograph (Clarus 500, PerkinElmer) equipped with flame ionization detector (FID) and Elite-5 capillary column (30 m \times 0,25 mm, 0,25 μm). Details of GC analysis are reported by Nischk et al., 2013.

Result and discussion

Sample labeling and coloration of the samples after metal modification are given in Table 1.

Table. 1 Preparation method and coloration of the samples after metal photodeposition

| Sample label | Metal precursor | Concentration of metal precursor used during photodeposition % (m/m) | Metal amount based on XRF analysis % (m/m) | Sample color |
|--------------|----------------------------------|--|--|--------------|
| P25_Au(0.1) | KAuCl ₄ | 0.1 | 0.1 | violet |
| P25_Au(1) | | 1 | 0.8 | |
| P25_Ag(0.1) | AgNO ₃ | 0.1 | 0.1 | light pink |
| P25_Ag(1) | | 1 | 0.71 | |
| P25_Pt(0.1) | H ₂ PtCl ₆ | 0.1 | 0.1 | light grey |
| P25_Pt(1) | | 1 | 0.9 | |
| P25_Pd(0.1) | PdCl ₂ | 0.1 | 0.1 | grey |
| P25_Pd(1) | | 1 | 0.65 | |
| P25 | – | – | – | white |

Microstructures of the selected samples and their surface morphologies were examined by TEM equipped with EDS. TEM images and EDS mapping of gold, platinum and palladium nanoparticles deposited at the surface of P25_TiO₂ are given in Fig. 2. TEM observations show small metal nanoparticles homogeneous in size. Metal nanoparticles with mean sizes 20, 4 and 1.5 nm were obtained for the P25 samples loaded with gold, platinum and palladium, respectively. As it can be observed from Fig. 2B and C, photodeposited Pt and Pd particles are always found to be spherical in shape. It can be also observed that the photodeposited gold and platinum show poor homogeneity and dispersion of deposits with some areas of the TiO₂ surface having a high density of Au or Pt particles and others being relatively empty.

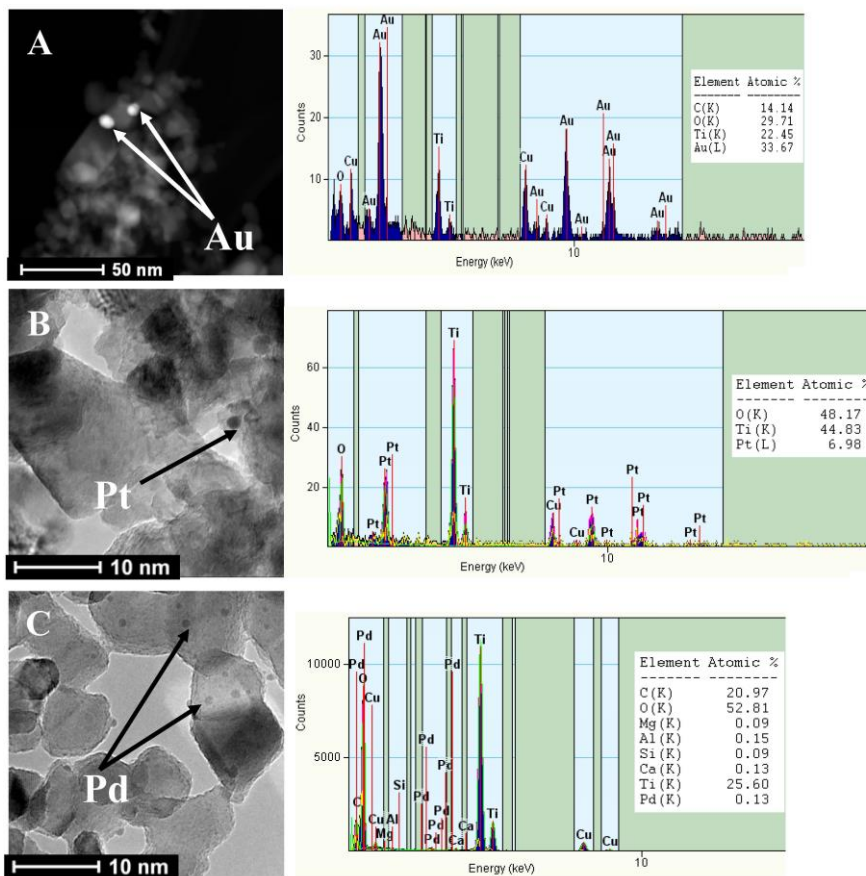


Fig. 2. EDS mappings of 1 % (m/m) (A) gold- (B) platinum (C) palladium-modified TiO₂

This results are in correlation with literature data. Zielinska et al. (2011) obtained Au-TiO₂ nanoparticles using a water-in-oil microemulsion system of water/AOT/cyclohexane and water/Triton X-100/cyclohexane. They obtained gold nanoparticles on the surface of TiO₂ in the range of 10-69 nm. Silva et al. (2010) obtained Pt nanoparticles on Ce-Ti-O support by photochemical deposition. They identified Pt particles ranging in size from 2.5 to 4 nm. A comparative study of the photodeposition of Pt, Au and Pd under the same experimental conditions onto pre-sulfated and non-sulfated TiO₂ was performed by Maicu et al. (2011). They observed that for the nonsulphated TiO₂ most of the Pt deposits have diameters ranging from 3 to 6 nm, while for the pre-sulphated material the average particle size is smaller, having more than 50% of the platinum particles an average diameter in the range of 2–4 nm. In case of Au particles deposited via this method are irregularly sized, varying from around 10nm to more than 100 nm in diameter. The estimation of Pd average particle size shows that Pd particles deposited on non-sulfated TiO₂ have diameters

ranging from approximately 3 to 7 nm while on the pre-sulfated sample the average size is higher with particles ranging from 4 to 10 nm (Maicu et al., 2011).

The optical properties have been studied in details by Diffuse Reflectance Spectroscopy (DRS). Figure 3 shows the absorption spectra of pure and metal modified TiO₂-based photocatalysts. The measurement of the samples was made at the wavelength of light in the range from 300 to 750 nm. The absorbance in the visible region is always higher for the modified than for pure TiO₂. It should be pointed out that the DRS of the modified samples shows a shift in the band-gap transition to longer wavelengths for all kinds of surface-modified photocatalysts.

The DR spectra of gold-modified titanium dioxide nanoparticles are shown in Fig. 3A. In the visible region the absorption spectrum for Au-TiO₂ nanoparticles is characterized by a pronounced plasmon band, whose maximum location depends on the gold nanoparticles size.

The P25_Au- TiO₂ nanoparticles show plasmon absorption bands at about 560 nm. Au doping has a significant effect on the absorption properties of TiO₂ and that the absorption of light by TiO₂ in the visible region increases when particles size decreases.

In the case of Ag-modified samples (Fig. 3B), a wide absorption is observed with a maximum at 450 nm. Silver nanoparticles are known to exhibit a plasmon band with a maximum at around 400 nm in water. This plasmon band is sensitive to the environment and can be shifted depending on the stabilizer or on the substrate.

The spectra of the Pt and Pd-loaded samples show a slight shift in the band gap transition to longer wavelengths (Fig. 3C and D). The red shift in the band gap transition revealed by diffuse reflectance spectra can be explained by the introduction of energy levels of the metal ions into the band gap of TiO₂. The absorbance in the visible region for the metallised systems shows that lower-energy transitions are possible. This is because the metal clusters give rise to localised energy levels in the bandgap of TiO₂ into which valence band electrons of TiO₂ are excited at wavelength longer than 400 nm (Sakthivel et al., 2004).

The effect of kind and amount of metal precursor on the photocatalytic activity of modified TiO₂ as well as their stability in four measurements cycles under UV-Vis LEDs irradiation were presented in Fig. 4. In the case of pure TiO₂ P25 (Fig. 4a) all toluene was removed from gas phase after 20 min irradiation in three subsequences cycles. Only in the last cycle toluene removal efficiency reached about 86% after 30-min process.

Definitely, the highest photocatalytic activity was observed in the case of P25_Pd(1) and P25_Pt(0.1) sample. In both cases all toluene was removed after 20 min irradiation in three subsequences cycles. Only in the last cycle toluene removal efficiency reached about 100% (the final toluene concentration was below detection limit) after 25-min process.

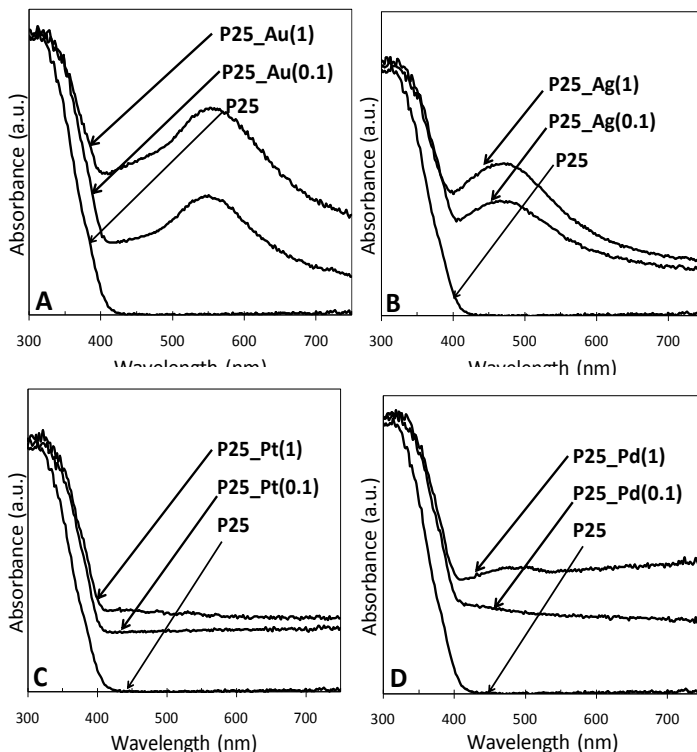


Fig. 3. Diffuse reflectance spectra of pure and: (A) gold- (B) silver (C) platinum (D) palladium-modified TiO₂

In the case of all samples the photocatalysts' activity decreased in subsequent measurement cycles which suggests that active sites of TiO₂ may have been blocked by toluene partial decomposition products. The lowest photoactivity was observed for samples modified with silver. Even in the first cycle of toluene degradation in the presence of P25_Ag(1) sample toluene removal efficiency reached only 67% after 30-min process and decreased to about 34% in the last cycle.

Conclusions

In summary, photocatalytic activity of noble metal modified TiO₂ in the gas phase reaction depends on the kind of metal and noble metal precursor concentration used during synthesis.

Generally, TiO₂-P25 surface modified with silver, gold, palladium and platinum clusters exhibits high efficiency in toluene removal. 30-min of irradiation by twenty five UV-LEDs ($\lambda_{\max} = 375$ nm, 63 mW per diode) was enough to complete removal of toluene ($C_0 = 100$ ppm) from the gas phase in four subsequent cycles in the presence

of almost all samples (except P25_Pt(1), P25_Ag(1) and P25-Pd(0.1)). The same photoactivity was observed in four subsequent cycles for P25_Au(0.1) and P25_Pd(1) samples.

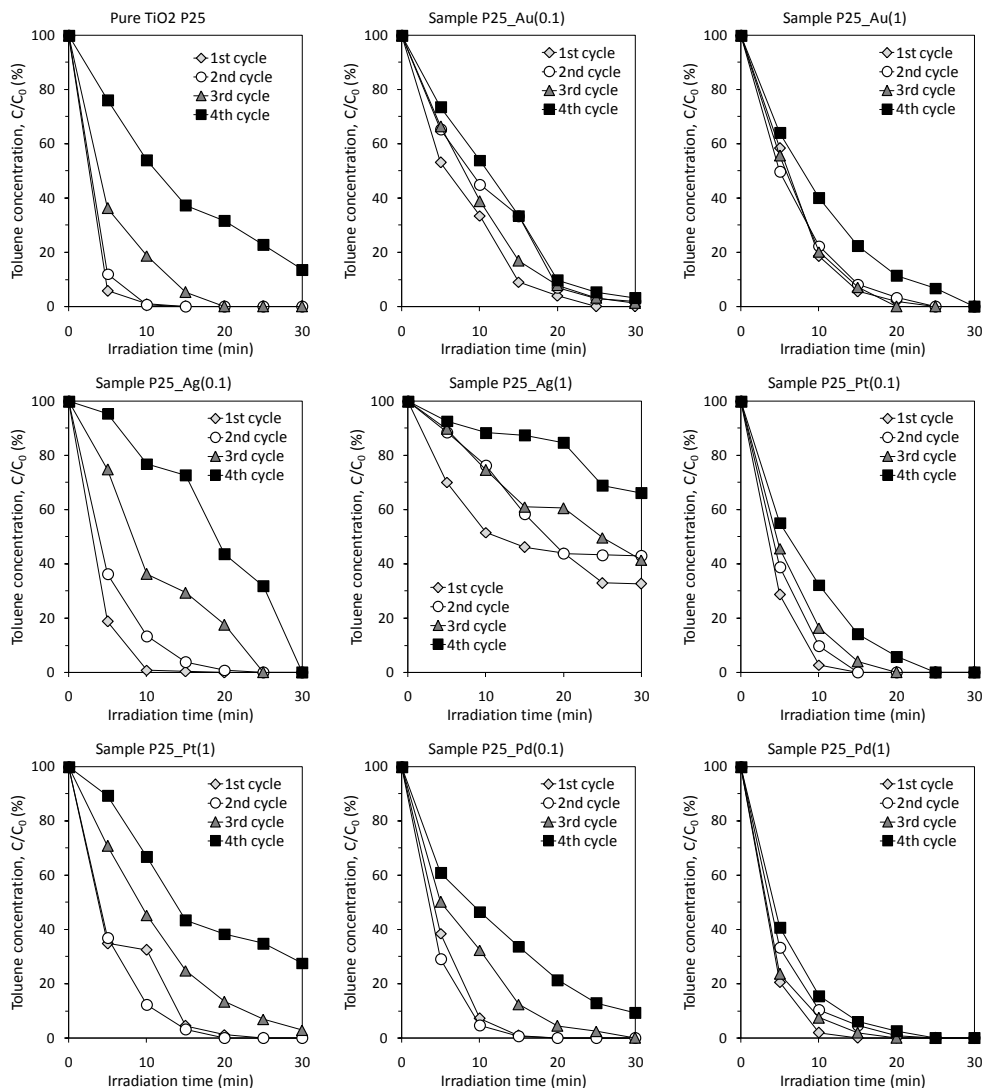


Fig. 4. Toluene photodegradation efficiency as the function of irradiation time. The influence of kind and amount of metal precursor on the initial photocatalytic activity of TiO₂ nanotubes and their stability in four measurement cycles under UV-Vis LEDs irradiation

Acknowledgments

This work was supported by the Polish National Science Centre (contract No.: 2011/03/B/ST5/03243)

References

- BARRAUD E., BOSCH F., EDWARDS D., KELLER N., KELLER V., 2005, *Gas phase photocatalytic removal of toluene effluents on sulfated titania*, J. Catal., 235, 318-326.
- HOFFMANN M. R., MARTIN S. T., CHOI W., BAHNEMANN D. W., 1995, *Environmental Applications of Semiconductor Photocatalysis*, Chem. Rev., 95, 69-96.
- KELLER N., BARRAUD E., BOSCH F., EDWARDS D., KELLER V., 2007, *On the modification of photocatalysts for improving visible light and UV degradation of gas-phase toluene over TiO₂*, Appl. Catal. B, 70, 423-430.
- MAICU M., HIDALGO M. C., COLON G., NAVIO J. A., 2011, *Comparative study of the photodeposition of Pt, Au and Pd on pre-sulphated TiO₂ for the photocatalytic decomposition of phenol*, J Photochem. Photobiol. A, 217, 275-283.
- MINABE T., TRYK D. A., SAWUNYAMA P., KIKUCHI Y., HASHIMOTO K., FUJISHIMA A., 2000, *TiO₂-mediated photodegradation of liquid and solid organic compounds*, J Photochem. Photobiol. A, 137, 53-62.
- NISCHK M., MAZIERSKI P., GAZDA M., ZALESKA A., 2014, *Ordered TiO₂ nanotubes: The effect of preparation parameters on the photocatalytic activity in air purification process*, Appl. Catal. B-Environ, 144, 674-685.
- OHNO T., SARUKAWA K., TOKIEDA K., MATSUMARA M., 2001, *Morphology of a TiO₂ Photocatalyst (Degussa, P-25) Consisting of Anatase and Rutile Crystalline Phases*, J Catal., 203 (1), 82-86.
- OHTANI B., PRIETO-MAHANEY O. O., LI R. ABE R., 2010, *What is Degussa (Evonik) P25? Crystalline composition analysis, reconstruction from isolated pure particles and photocatalytic activity test*, J. Photochem Photobiol A, 216, 179-182.
- SEKIGUCHI K., YAMAMOTO K., SAKAMOTO K., 2008, *Photocatalytic degradation of gaseous toluene in an ultrasonic mist containing TiO₂ particles*, Catal. Commun., 9, 281-285.
- SILVA A. M., MACHADO B. F., GOMES H. T., FIGUEIREDO J. L., DRAZIC G., FARIA J. L., 2010, *Pt nanoparticles supported over Ce-Ti-O: the solvothermal and photochemical approaches for the preparation of catalytic materials*, J. Nanopart. Res. 12, 121-133.
- ZIELINSKA-JUREK A., KOWALSKA E., SOBCZAK J. W., LISOWSKI W., OHTANI B., ZALESKA A., 2011, *Preparation and characterization of monometallic (Au) and bimetallic (Ag/Au) modified-titania photocatalysts activated by visible light*, Appl. Catal. B, 101, 504-514.
- ZOU L., LUO Y.G., HOOPER M., HU E., 2006. *Removal of VOCs by photocatalysis process using adsorption enhanced TiO₂-SiO₂ catalyst*, Chem. Eng. Process. 45, 959-964.
- ZOU L., XINYONG L., QIDONG Z., SHAOMIN L. 2012, *Synthesis of LaVO₄/TiO₂ heterojunction nanotubes by sol-gel coupled with hydrothermal method for photocatalytic air purification*, J. Colloid Interface Sci., 383, 13-18.

Received November 30, 2013; reviewed; accepted March 18, 2014

GOLD LEACHING FROM A SAUDI ORE BY THE NONPOLLUTING THIOSULFATE PROCESS

Mohamed H.H. MAHMOUD^{*,}, Hesham M. AWAD^{*,***},
Osman A. ELHABIB^{****,*****}**

^{*} College of Science, Taif University, P. N. 888, Taif, Saudi Arabia

^{**} Central Metallurgical R & D Institute, P.O. Box 87, Helwan, Cairo, Egypt

^{***} Ceramic Department, Natural Resources Division, National Research Center, Cairo, Egypt

^{****} Faculty of Engineering, Taif University, P. N. 888, Taif, Saudi Arabia

^{*****} Faculty of Engineering, Al-Neelain University, Khartoum, Sudan

e-mail address: mheshamm@gmail.com

Abstract: In all working Saudi gold mines, ores are treated using the hazardous cyanidation process. Some Saudi gold ores, such as Al-Amar, is known to be refractory to cyanidation. In this work, we have examined the extraction of gold from Al-Amar gold ore by the much environmentally safer and efficient thiosulfate process. The run of mine (ROM) and carbon-in-leach (CIL) feed, that is obtained after separation of copper concentrate from ROM, samples were found to contain 6.5 and 3.6 ppm gold, respectively. The mineralogical microscopic investigations of ROM samples confirmed that fine gold specks were scattered and encapsulated inside sulfide or quartz base minerals. This could explain the expected reason of the difficult leaching of gold by cyanidation. The X-ray diffraction analysis showed that the CIL feed contained quartz, pyrite, sphalerite and chlorite minerals. After detailed leaching studies of CIL feed, almost 70% of gold could be extracted at 0.2 M ammonium thiosulfate and 0.3 M ammonium hydroxide after 24 h. Addition of copper(II) as <0.2 mM only slightly enhanced the gold leaching in the ammoniacal thiosulfate solution. Gold leaching drastically decreased as the concentration of copper(II) increased 0.2 mM due to the degradation of $S_2O_3^{2-}$.

Keywords: *gold, extraction, leaching, thiosulfate, Saudi ore*

Introduction

Gold dissolution in an alkaline cyanide solution was first reported by Elsner in 1846. About 92% of all gold metal in the world is produced using the hazardous cyanidation process [McNulty, 2001]. The major problems of the cyanidation process are: (i) the use of cyanide, an extreme toxic chemical, that has been banned in many countries (Rainforest Information Centre, 2005), (ii) its reduced efficiency, i.e. high reagent

consumption and/or low gold leaching, during the treatment of refractory and complex ores (La Brooy et al., 1994). Due to environmental concerns, mining companies are now applying the stringent regulations and codes on the transportation, handling, usage and disposal of cyanide containing materials. A list of recent cyanide spillage disasters suggested that the only ultimate solution for this problem is to replace cyanide with a lixiviant that is significant environmentally friendly (Rosenhek, 2007). It is believed that the use of cyanidation process will be increasingly restricted in the near future.

Several alternative lixiviants were investigated to provide a solution for the treatment of refractory ores and to develop an environmentally friendly gold leaching process. Au(I) forms strong complexes with different non-cyanide reagents such as thiourea, halogens, thiocyanate and thiosulfate (Wan et al., 1993). Some of processes based on these reagents have a higher overall production cost and/or difficult to control. For instance, thiourea is requiring an acidic leaching conditions; where high reagent consumption, gold passivation problems, and high capital costs have hindered further developments (Tremblay et al., 1996). Furthermore, thiourea is considered to be a potential carcinogen.

On the other hand, Au(I) forms strong complex with thiosulfate, which is more stable than the thiourea and the thiocyanate complexes. Compared to thiourea, thiosulfate has demonstrated greater potentials in both leaching performance and environmental considerations. One significant advantage of thiosulfate leaching is its ability to treat preg-robbing ores containing carbonaceous materials (Wan, 1993; West-Sell and Hackl, 2005). It is also thought that thiosulfate leaching might provide an alternative option for the leach of copper-bearing ores, which are not economical in cyanidation. Compared to cyanide, thiosulfate is a much more safer chemical. Thiosulfate salts, including ammonium thiosulfate, ATS, are regarded as nonhazardous by Worksafe Australia (NOHSC, 1999). They are also classified as "General Recognized as Safe" in the US and not considered as dangerous substances by European standards (Bean, 1997, EEC/FDA, 2001). Another fact that has to be considered is that ATS (US\$0.1-0.15/kg) is about 10 times cheaper than sodium cyanide (US\$1.8-2.0/kg) in bulk chemical market. Moreover, thiosulfate leaching has similar or faster kinetics compared to cyanidation (Jeffrey, 2001). Therefore, thiosulfate has become the most promising noncyanide lixiviant and is receiving extensive attentions from both academic and industrial points of view. However, there are numerous obstacles those hinder the industrial application of thiosulfate process such as high consumption of chemicals in treating copper bearing sulfidic ores, and gold recovery problems by the popular CIP/CIL (carbon-in-pulp/carbon-in-leach) technologies (Aylmore, 2001). However, solvent extraction, ion exchange, zinc and copper cementation were found to be effective recovery techniques (Navarro, 2004, Liu, 2004, Zhang and Dreisinger, 2004). The interferences of associated minerals may in some cases increase the complexity of the reaction chemistry and the instability of thiosulfate. Developing has been made to find alternative leaching catalysts in

thiosulfate media other than copper and ammonia (Zhang et al., 2005; Chandra et al., 2005). Carbonaceous sulfide ores after oxidative pre-treatment are typically very easy to leach with thiosulfate, while complex metal sulfide ores are much more difficult to treat. The presence of various amount of pyrite, pyrrhotite, chalcopyrite, arsenopyrite, chalcocite, bornite, and some lead species, has significant detrimental effects on thiosulfate leaching of gold (Chen, 2008). This shows how much a mineralogical investigation is important to be performed before leaching study of any gold ore by the thiosulfate process.

Several gold localities are scattered in the Arabian Shield of the kingdom of Saudi Arabia which has about 20 million tons of recoverable gold ores. In working gold mines, ores are treated using the hazardous cyanidation process through the CIL or heap leaching. Although several Saudi gold mines are in operation since 1980s, very few published studies were found in the literature dealing with Saudi gold ores (Madani et al., 2012, Khandaker et al., 1997, Salpeteur et al., 1989, Huckerby et al., 1982, Hakim 1982, Al-Hobaib et al., 2010). All these studies are of geological, mineralogical or environmental nature. Tailings (mining wastes) are stored in the dumping area as a dam that contains residual cyanide. Moreover, no published work was found concerning with leaching of gold from Saudi ores with the thiosulfate process. Thus, a comprehensive detailed studies are needed to investigate the suitability of Saudi gold ores to the thiosulfate leaching and to develop a leaching strategy for gold leaching. The study should include the several factors affecting the efficiency of gold leaching.

The aim of this research is to investigate the mineralogical nature and study the optimum leaching conditions of a selected Saudi gold ore using the thiosulfate process. Leaching time and concentrations of main reagents were studied to reach the optimum concentrations.

Experimental

Samples collection and preparation

Three types of samples were collected from Al-Amar gold mine and processing plant those are located West Riyadh city, Saudi Arabia. Rough block samples from run of mine, ROM, were selected for the microscopic petrography investigation, and thin section and polished samples were prepared and the nature of the minerals and gold inclusion have been identified. Another rock samples from ROM were collected in the form of midsize boulders and crushed to the size of approximately 1 x 1 cm using Jaw crusher and then a 20 kg were taken and divided two times to obtain a well representative sample which was ground to the size of 100% - 100 mesh and kept in plastic bags. These samples were used for chemical and X-ray diffraction analyses. Another wet sample was collected from CIL feed, that is obtained after separation of copper concentrate by flotation of ROM in the plant. The sample was filtered off and washed with fresh water. The wet cake was dried at about 50 °C for 72 h, broken

down, ground and packed in plastic bags. These samples were used for chemical and mineralogical analyses and also for the leaching experiments.

X-ray diffraction and chemical analysis

X-ray diffraction (XRD) analysis was performed on ROM and CIL feed samples using an automated diffractometer (Philips type: PW1840), at a step size of 0.02° , scanning rate of 2° in $2\theta/\text{min}$, and a 2θ scale range from 4° to 80° .

Chemical analysis was performed on ROM and CIL feed after opening of 2 g finely ground representative samples in *aqua regia* and dilution to 250 cm^3 with de-ionized water. Inductively Coupled Plasma-Atomic Emission Spectrometer, ICP-AES (Type: Perkin Elmer Optical Emission Spectrometer 2100 DV) was used for elemental analysis in solutions. SiO_2 contents were performed gravimetrically, and referred as Si.

Mineralogical studies

Both thin and polished sections of the studied ROM rocks were used for petrographic studies. Also, the environmental scanning electron microscopy (ESEM) technique was used to identify some opaque minerals in the studied samples to support the microscopic identification. Polished sections of selected samples of the studied rocks were examined with a Philips XL30 environmental scanning electron microscope (ESEM), operating at 25 kV and equipped with EDAX energy dispersive analytical X-ray sensitivity.

Leaching

Leaching experiments were carried out in a sealed 100 cm^3 conical flask glass reactor at room temperature ($\sim 25^\circ\text{C}$). A 10 g ore sample and a 20 cm^3 solution containing all reagents (e.g. ammonium thiosulfate, ammonium hydroxide, copper sulfate, etc.) was added into the flask and the mixture was horizontally shaken at 480 rpm using an electric shaker. After the required time, the slurry was filtered off and the filtrate was chemically analyzed to determine the Au content.

Results and discussion

Gold dissolution in ammoniacal thiosulfate can be described as shown in Fig. 1.

Leaching of gold in thiosulfate solutions is a metal oxidation process as described in Eq. 1 (Chen, 2008)



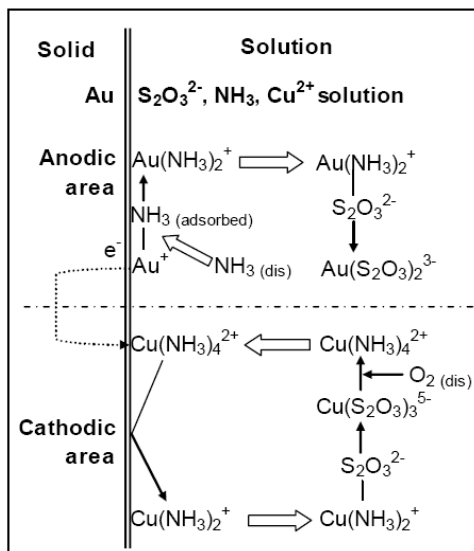


Fig. 1. Gold dissolution sketch by the ammoniacal thiosulfate process

The reaction chemistry using cupric amine as an oxidant can be explained by the intermediate reactions as shown in Eqs. 2 and 3:



According to this theory, the dissolution of gold is a “corrosion” process. The ultimate oxidant is oxygen or any other oxidative chemicals that are capable of oxidizing Cu(I) amine to Cu(II) amine. Unlike cyanidation, thiosulfate leaching of gold does not require a diffusion of oxygen onto the solid-liquid interface of gold, which can be very slow under atmospheric conditions. The direct oxidant of gold is Cu(II) amine after it is adsorbed on to the surface of gold in the cathodic area. After accepting one electron, Cu(II) amine is reduced to Cu(I) amine, which is desorbed and diffused into the bulk solution phase. In the anodic area of gold surface, a gold atom loses one electron and produces an aurous ion. It is then complexed with ammonia. The aurous ammonia complex diffuses to the bulk solution phase where ammonia is substituted and aurous ion is stabilized as a more stable complex, $Au(S_2O_3)_2^{3-}$. There are four diffusion steps: the diffusions of ammonia and Cu(II) amine to the gold solid-liquid interface and the diffusions of Cu(I) amine and Au(I) amine complex to the bulk solution phase. In all these diffusion steps, ammonia plays important roles. This partially explains the slow dissolution rates in the absence of sufficient ammonia ligand. First of all, ammonia works as ligand of copper, which stabilizes copper and forms the oxidation catalyst in the anodic area. Also, free ammonia must be present, so it can be adsorbed on the surface of gold and form an aurous complex.

Mineralogical studies

Environmental Scanning Electron Microscopy (ESEM) showed noticeable concentrations of opaque minerals, especially in the sheared or contact samples as well as silica-rich samples. The opaque minerals in the studied rocks are represented as Fe-Ti oxides and sulfides together with gold specks as well as small amounts of goethite (FeO(OH)) and malachite. Sulfides are represented by pyrite (FeS₂), chalcopyrite (CuFeS₂) and galena (PbS). Figures 2a and b show the microscopic images of pyrite-gold association and its ESMS. Magnetite (Fe₃O₄) occurs as eu-hedral homogeneous crystals. Ilmenite (FeTiO₃) is found as homogeneous sub-hedral crystals or form composite texture with magnetite. Pyrite occurs as cubic crystals or as aggregates of subhedral crystals altered to goethite which shows colliform texture. Chalcopyrite (CuFeS₂) is less abundant than the pyrite.

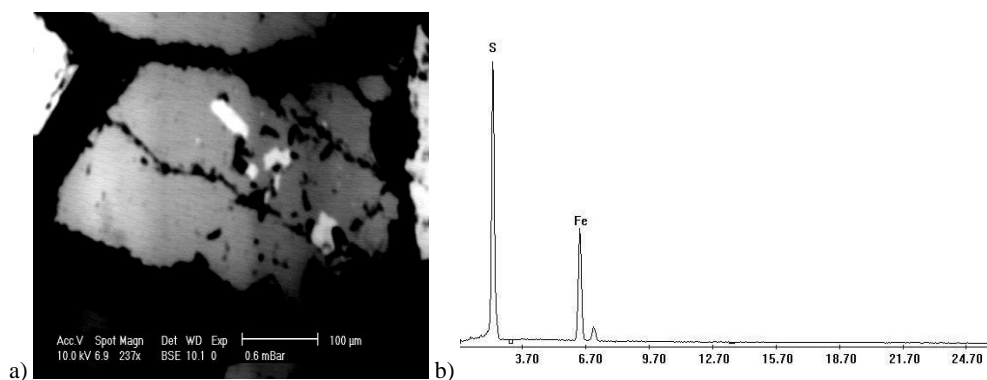


Fig. 2. (a) Pyrite-gold association, and (b) ESEM of pyrite

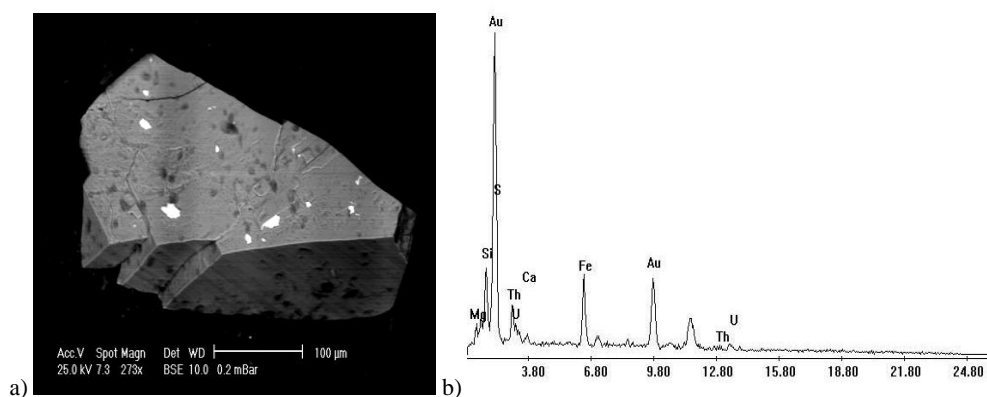


Fig. 3. (a) Gold specks in sulfides and (b) ESEM of gold

Gold occurs as inclusions in the sulfides or as small irregular specks along the fractures. There are noticeable amounts of gold, especially in the samples which are rich in quartz. Figures 3 and 4 show the microscopic images and the ESMS of gold in sulfide and quartz minerals.

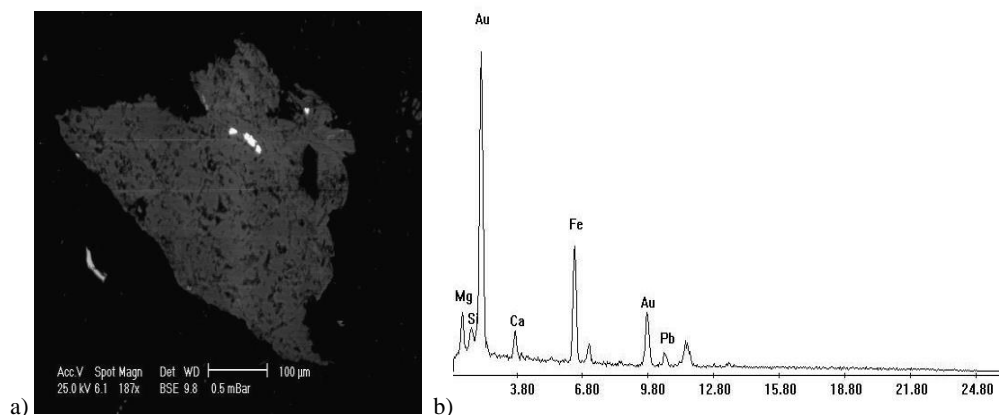


Fig.4. (a) Gold specks in quartz and (b) ESEM of gold

X-ray diffraction analysis and chemical analysis

Figure 5 shows the X-ray diffraction patterns of ROM and CIL feed samples. The main peaks in ROM are referring to quartz, sphalerite, pyrite and chalcocopyrite. The CIL feed sample shows the absence of chalcocopyrite peaks and a new peak of chlorite. Table 2 shows the detected minerals with their chemical composition and card number. Table 3 shows the chemical analysis of representative samples of ROM and CIL feed. These samples contain SiO_2 as a major constituent (about 30% as Si). The ROM sample contains about 6.5 ppm Au which is considered as a low grade gold ore, while the CIL feed contains only 3.6 ppm Au. On the other hand, the ROM and CIL contain small amounts of silver of 11.7 ppm and 6 ppm, respectively.

Table 2. Detected minerals in X-ray diffraction analysis of ROM and CIL feed samples

| Detected mineral name | Chemical composition | Card number |
|-----------------------|---|---------------|
| Quartz | SiO_2 | [99-101-1988] |
| Sphalerite | ZnS | [99-200-5214] |
| Pyrite | FeS_2 | [99-201-6098] |
| Chalcocopyrite | CuFeS_2 | [99-100-8979] |
| Chlorite | $\text{Mg}_{2.29}\text{Fe}_{0.255}\text{Al}_{0.865}\text{Si}_{1.588}\text{O}_9\text{H}_4$ | [99-100-4282] |

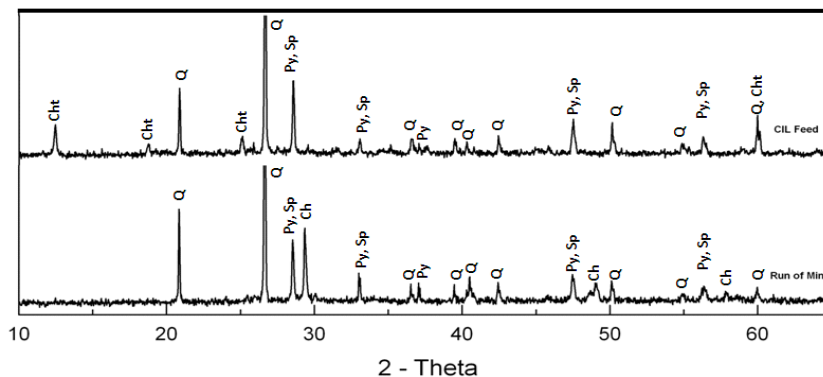


Fig. 5. X-ray diffraction patterns of ROM and CIL feed. Q: quartz, Ch: chalcopyrite, Py: pyrite, Sp: sphalerite, Chl: chlorite

Table 3. Chemical analysis of ROM and CIL feed samples

| Element | Percentage | |
|---------|------------|----------|
| | ROM | CIL |
| Au | 6.47 ppm | 3.64 ppm |
| Ag | 11.7 ppm | 5.97 ppm |
| Si | 28.0 | 30.6 |
| Zn | 13.1 | 12.96 |
| Fe | 12.8 | 6.51 |
| Cu | 5.09 | 0.16 |
| Pb | 0.96 | 0.05 |
| Cd | 0.02 | 0.02 |
| V | 0.56 | 0.45 |
| Cr | 0.01 | 0.01 |
| Mn | 0.05 | 0.44 |

Appreciable amounts of iron is present in both samples, 12.8 and 6.5% in ROM and CIL feed, respectively. ROM contains 5.1% copper which is separated by flotation in the following steps. That is why the CIL feed contains neglected amount of copper (0.16%). Zinc is a major constituent; about 13%, in all samples.

Gold leaching

Effect of $(\text{NH}_4)_2\text{S}_2\text{O}_3$ concentration

As discussed above, extraction of gold is usually performed by leaching with a solution containing an oxidizing and a complexing agents. The thiosulfate concentration in the leaching slurry is an important factor affecting the leaching process from the effectiveness and economical points of view. A series of experiments was conducted to study the effect of ammonium thiosulfate (ATS) concentration (from

0.05 M to 0.8 M) on the leaching of gold from Al-Amar CIL feed in absence of an additional oxidizing agent. The equilibrium pH was about 3. The results under the condition of 0.3 M ammonium hydroxide (AH), for 24 h are shown in Fig. 6. At 0.05M ATS, the gold leaching was as low as 24%. The leaching of gold was greatly improved with increasing the ATS concentration and reached its maximum at 0.2 M where about 66% gold was extracted. In the range of 0.2 M and 0.6 M ATS, the gold leaching stayed at a plateau of 66%. Thus, ATS concentration of 0.2 M is considered to be a minimum concentration to maximize the gold leaching performance under the above mentioned conditions. A sharp drop in leaching was observed at higher thiosulfate concentration than 0.6 M. This behavior is probably due to the possible degradation of thiosulfate at this high concentration forming elemental sulfur and other degradation products which cause passivation of gold and minerals surfaces.

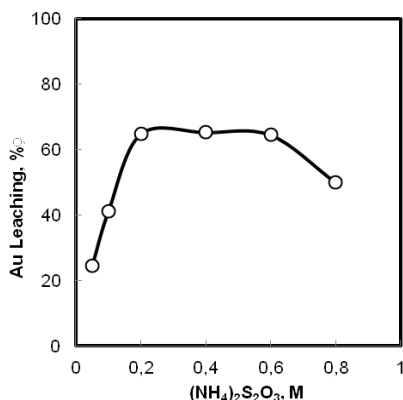


Fig. 6. Effect of ATS concentration on gold leaching. 0.3 M AH, pH = 9.3, 24 h

Effect of NH₄OH concentration

It is known that ATS is stable in alkaline medium and quickly dissociates in acidic medium where fine elemental sulfur is formed. Thus, an alkaline condition is important to keep the ATS un-dissociated during gold leaching. The effect of AH concentration (from 0.05 M to 1 M) on gold leaching from Al-Amar mine CIL feed was studied and the results under the conditions of 0.2 M ATS, 24 h, are represented in Fig. 7. The equilibrium pH was also measured at the end of each experiment and shown in the same figure. It is clear that gold leaching was gradually improved with increasing AH concentration mostly. At 0.05 M AH about 45% of the Au was extracted at which the equilibrium pH was 9, where about 66% of Au was extracted at 0.3 M AH where the pH was 9.3, but the leaching leveled off at higher concentrations. It appears that the improvement of leaching with increasing AH concentration is due to the increasing stability of the thiosulfate $S_2O_3^{2-}$ ions where the accompanied pH increased to 9.3 at 0.3 M AH. The result supports that 0.3 M of AH is the optimum concentration with the combination of the mentioned conditions.

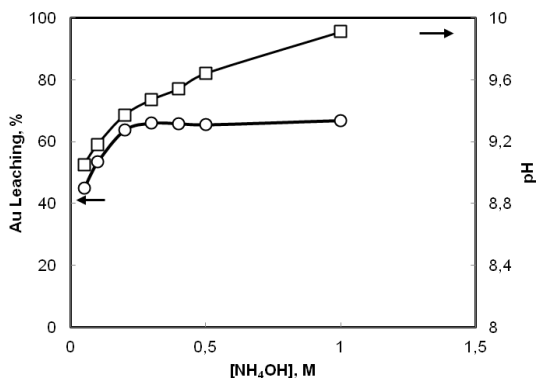


Fig. 7. Effect of AH concentration on gold leaching. 0.2 M ATS, 24 h

Effect of shaking time

Figure 8 shows the effect of shaking time on the leaching of gold from Al-Amar CIL feed at 0.2 M ATS and 0.3 M AH. It can be seen that more than 40% of gold was extracted after only 2 hours. At longer times, the gold leaching slightly increased. About 70% of gold was extracted after 20 hours and almost stayed at this level at longer times.

Effect of CuSO₄ concentration

Oxidation of gold with the naturally dissolved oxygen in thiosulfate solution is not favorable due to the very slow reaction kinetics. Therefore, an oxidizing agent such as copper(II) may enhance the rate of gold leaching. Cupric ion has been previously used as an effective oxidizing agent during ammoniacal thiosulfate leaching of gold.

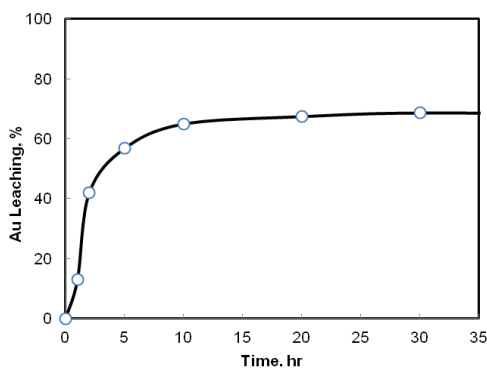
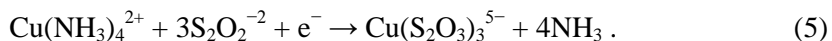
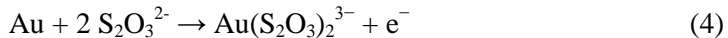


Fig. 8. Effect of shaking time on gold leaching. 0.3 M AH, 0.2 M ATS, pH 9.3

The leaching of gold in thiosulphate solutions is an electrochemical reaction, with the constituent half reactions being the oxidation of gold to gold thiosulphate, and the

reduction of Cu(II) amine to Cu(I) thiosulfate, i.e. Cu(II) oxidizes Au(0) to Au(I) in presence of $S_2O_3^{2-}$ as a complexing agent. The formed Cu(I) is re-oxidized to Cu(II) by the dissolved O_2 . These half-cell reactions are shown in Eqs. 4 and 5, respectively (Breuer and Jeffrey, 2000).



However, the thiosulphate leaching system is complicated by the side reaction of reduction of Cu(II) by the thiosulfate ions in solution as shown in Eq. 6 (Breuer and Jeffrey, 2003):



We have examined the effect of $CuSO_4$ on leaching of gold from pure gold wires. Figure 9 shows the dissolution rate of pure gold wires (0.1 g) at different time intervals in presence and absence of $CuSO_4$ (0.1 mM) in 0.3 M AH, 0.2 M ATS. It can be seen that the gold dissolution was very slow at the first 10 hours and then more faster increased at longer times. It is also noticed that the dissolution percentage of gold in presence of Cu(II) ions was usually higher than that in its absence. This is in good agreement with the expected catalyzation of gold oxidation in presence of Cu(II) as explained above.

Figure 10 shows the leaching of gold from Al-Amar CIL feed at different time intervals in presence and absence of Cu(II) (as 0.2 mM $CuSO_4$) at 0.3 M AH and 0.2 M ATS. It can be seen that Cu(II) could only slightly enhance the leaching kinetics of gold. This little improving effect of Cu(II) on leaching of gold may be explained by the existence of small residual amount of chalcopyrite in the CIL feed (0.16% as Cu). This may dissolve as Cu(II) ions in leaching medium and cause the catalyzing effect on oxidation of gold. Thus, the effect of additional Cu(II) would be limited. It is worth mentioning that at prolonged time such as 24 h (not seen in the figure) the leaching percentages of gold is almost similar in presence and absence of Cu(II) reaching near to 70%. Figure 11 shows the effect of Cu(II) concentration on leaching of gold. It is clear from this figure that addition of Cu(II) very slightly enhanced gold leaching at low concentration and the leaching gradually decreased as the concentration of Cu(II) increased. The maximum leaching of gold was near to 70% at 0.2 mM Cu(II) where excessive amounts of Cu(II) blocks the gold leaching; that is no gold practically extracted at Cu(II) concentration as high as 0.1 M. This deteriorative effect of Cu(II) can be explained by the oxidative degradation of $S_2O_3^{2-}$ with increasing Cu(II) concentration as explained in Eq. 6.

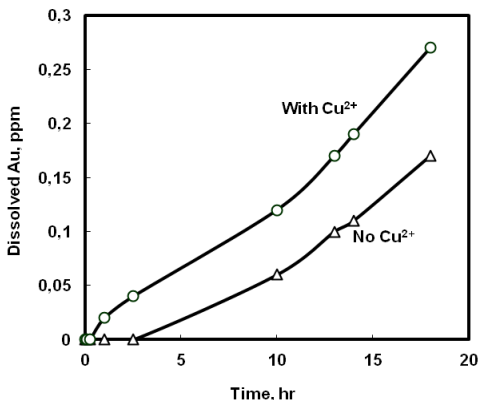


Fig. 9. Dissolution of pure gold wires (0.1 g) in presence and absence of CuSO_4 at different time periods. Leaching solution: 200 cm^3 containing 0.1 mM CuSO_4 , 0.3 M AH, 0.2 M ATS. Shaking speed: 480 rpm at ambient temperature and sealed vessel

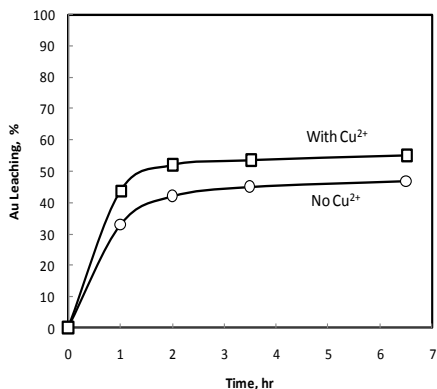


Fig. 10. Leaching of gold in presence and absence of Cu(II). 0.3 M AH, 0.2 M ATS, pH 9.3

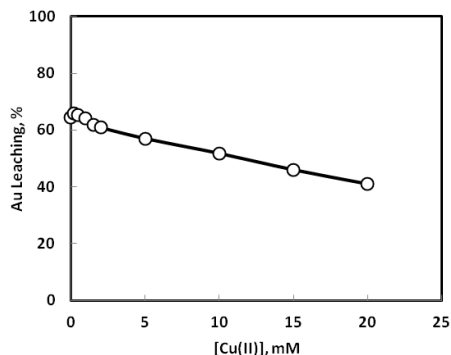


Fig. 11. Effect of Cu(II) concentration on gold leaching. 0.3 M AH, 0.2 M ATS, 24 h, pH 9.3

Conclusion

The microscopic examinations of rocks from Al-Amar mine proved the presence of fine gold specks and granules inclusions within sulfide and quartz base minerals which may be the reason of the expected difficulty of leaching of gold. About 70% of the gold could be extracted under the following condition: 0.3M NH_4OH , 0.2M $(\text{NH}_4)_2\text{S}_2\text{O}_3$, 24 h, 480 rpm, Liquid : Solid = 1:2.

Acknowledgement

The authors would like to thank Ma'aden company in KSA for allowing them to visit their Al-Amar mine and processing plant and for providing the rock samples.

References

- AL-HOBAIB A. S., AL-JASEEM K. Q., BAI OUMY H. M., AHMED H. A. 2010. *Environmental impact assessment inside and around Mahd Adh Dhahab gold mine*, Saudi Arabia, Arab. J. Geosci. DOI 10.1007/s12517-010-0259-2. AYLMORE, M.G., 2001. *Treatment of a refractory gold-copper sulfide concentrate by copper ammoniacal thiosulfate leaching*, Minerals Eng., 14, 6, 615-637.
- BEAN, S.L., 1997, *Thiosulfates*. In: Kroschwitz, J.I. (Ed.), Kirk-Othmer Encyclopaedia of Chemical Technology. John Wiley & Sons Inc. New York, 51-58.
- BREUER, P.L. JEFFREY, M.I., 2003. *The reduction of copper(II) and the oxidation of thiosulfate and oxy-sulfur anions in gold leaching solution*, Hydrometallurgy 70, 163-173.
- CHANDRA, I., JEFFREY, M., 2005. A fundamental study of ferric oxalate for dissolving gold in thiosulfate solutions, Hydrometallurgy, 77, 191-201.
- CHEN, X., 2008, *Associated Sulfide Minerals in Thiosulfate Leaching of Gold: Problems and Solutions*. A thesis submitted to the Department of Mining Engineering in Conformity with the requirements for the degree of Doctor of Philosophy Queen's University Kingston, Ontario, Canada.
- EEC/FDA, 2001. (i) European MSDS: Directive 67/548/EEC. (ii) American MSDS: 29 CFR 1910-1200 (US FDA).
- HAKIM, H.D., 1982. *A new contribution to the study of gold-silver mineralization at Mahd Ad Dahab*, Saudi Arabia, Precambrian Research, 16, 4, A22.
- HUCKERBY, J.A., MOORE J.M.C.M., DAVID G.R.D., 1982. *Mineralization and structure at the Mahd Adh Dahab gold mine*, Saudi Arabia, Precambrian Research, 16, 4, A24.
- JEFFREY, M.I., BREUER, P.L., CHOO, W.L., 2001. *A kinetic study that compares the leaching of gold in the cyanide, thiosulfate, and chloride systems*, Metallurgical Mater. Transaction B, 32 B, 979.
- KHANDAKER, N.I., AHMED, M., HARIRI, M.M., AL-OHALI, M.M., GARWAN, M.A., KHAN, K.R., 1997. *Microanalytical investigation of gold-bearing rocks from the an Najadi Region in Saudi Arabia*, Nuclear Instruments and Methods in Physics Research Section B: Beam Interactions with Materials and Atoms, 130, 654-659.
- LA BROOY, S.R., LINGE, H.G., WALKER, G.S., 1994. *Review of gold extraction from ores*, Minerals Eng., 7, 1213-1241.
- LIU, K.J., YEN, W.T., SHIBAYAMA, A., MIYAZAKI, T., FUJITA, T., 2004. *Gold extraction from thiosulfate solution using trioctylmethylammonium chloride*, Hydrometallurgy 73, 41-53.
- MADANI A., HARBI H., 2012. Spectroscopy of the Mineralized Tonalite-diorite Intrusions, Bulghah Gold Mine Area, Saudi Arabia: Effect of Opaques and Alteration Products on Fieldspec Data. Ore Geology Reviews, 44. McNulty, T., 2001. Cyanide substitutes. Mining Magazine, 184, 256-261.
- NAVARRO, P., ALVAREZ, R., VARGAS, C., AND ALGUACIL, F.J., 2004, *On the use of zinc for gold cementation from ammoniacal-thiosulfate solutions*. Minerals Eng., 17, 825-831.
- NAVARRO, P., VARGAS, C., VILLARROEL, A., ALGUACIL, F.J., 2002. *On the use of ammoniacal/ammonium thiosulfate for gold extraction from a concentrate*. Hydrometallurgy, 65, 37-42.
- NOHSC, 1999. Approved Criteria for Classifying Hazardous Substances, National Occupational Health and Safety Commission, Sydney, Australia.
- Rainforest Information Centre, Cyanide ban worldwide. Last updated: July 24, 2005. <http://www.rainforestinfo.org.au/gold/Bans.html>
- ROSENHEK, R., Reported incidences of cyanide spills from May 2002 to August 2004 , http://www.mpi.org.au/campaigns/cyanide/cyanide_spills.

- SALPETEUR I., SABIR H., 1989. Orientation Studies for Gold in the Central Pediplain of Saudi Arabian Shield. *Journal of Geochemical Exploration*, 34, 189-215.
- TREMBLAY, L., DESCHENES, G., GHALI, E., MACMULLEN, J., LANOQUETTE, M., 1996. *Gold recovery from a sulfide bearing gold ore by percolation leaching with thiourea*, *Intl. J. Min. Proc.*, 48, 225-244.
- Wan, R.Y., Le Vier, M., Milles J.D., 1993. *Research and development activities for the recovery of gold from non-cyanide solutions*. *Hydrometallurgy, Fundamentals, Technology and Innovatives*, Chapter 27.
- WEST-SELLS, P.G., HACKL, R.P., 2005. A novel thiosulfate leach process for the treatment of carbonaceous gold ores. *Treatment of Gold Ores, CIM, Alberta*, 209-223.
- ZHANG H., DREISINGER D.B., 2004. *The recovery of gold from ammoniacal thiosulfate solutions containing copper using ion exchange resin columns*. *Hydrometallurgy* 72,225-234.
- ZHANG, H., NICOL, M.J., STAUNTON, W.P., 2005. *An electrochemical study of an alternative process for the leaching of gold in thiosulfate solutions*. *Treatment of Gold Ore, 44th Annual Conference of Metallurgists, Met. Soc, CIM*, 243-257.

Received April 16, 2014; reviewed; accepted May 29, 2014

RECOVERY OF COPPER FROM COPPER SLAG AND COPPER SLAG FLOTATION TAILINGS BY OXIDATIVE LEACHING

Daniela M. UROSEVIC^{*}, Mile D. DIMITRIJEVIC^{**}, Zoran D. JANKOVIC^{***},
Dejan V. ANTIC^{**}

^{*} Mining and Metallurgical Institute, Zelene Bulevar 35, 19210 Bor, Serbia

^{**} University of Belgrade, Technical Faculty at Bor, P.O. Box 50, 19210 Bor, Serbia: mdimitrijevic@tf.bor.ac.rs

^{***} University of Toronto, CFIE, 33 St. George Street, Toronto, Ontario, Canada M5S 2E3

Abstract: Copper smelter slag and copper smelter slag flotation tailings were leached using sulphuric acid solutions, without or with the addition of either ferric sulphate or hydrogen peroxide. Copper extraction from the slag was typically found to be twice as high as that from the slag flotation tailings. Hydrogen peroxide was determined to be the best lixiviant. Thus, copper and iron extractions were 63.4% and 48.6%, respectively, when leaching the slag with 3 M H₂O₂, after 120 minutes of reaction at room temperature. Copper dissolution was generally found to be the dominant process within the first 60 minutes of reaction, whereas iron dissolution dominated afterwards.

Keywords: copper slag, copper slag flotation tailings, leaching, sulphuric acid, ferric sulphate, hydrogen peroxide

Introduction

The pyrometallurgical processing of copper concentrates generates large amounts of copper-containing slag. Management options for this slag include recycling, recovery of metal values, production of value added products and disposal (Gorai and Jana, 2003). However, there are no universal methods to recover copper from copper-bearing slags as the chemical and phase composition of a slag depend on factors such as the type of ore mined and the type of pyrometallurgical process utilized (Shen and Forsberg, 2003).

The reverberatory furnace slag that has been dumped in the vicinity of the Bor Copper Smelter, Serbia, is currently processed by flotation using an existing production line at the nearby Bor Copper Concentrator. However, the copper recovery

obtained has been rather low (about 40%). Previous research indicated that such a low recovery was due to the presence of copper oxides in the slag, as well as to the fact that copper sulphides were predominantly found in particle size fractions below 38 μm . Accordingly, the objective of the present work was to investigate whether implementation of the hydrometallurgical processing of the slag or the slag flotation tailings could result in an increase in copper recovery.

A number of studies have been conducted on the hydrometallurgical recovery of base metals from various copper-containing slags. Thus, the lixivants investigated include sulphuric acid (Banza et al., 2002), ferric chloride (Anand et al., 1980), chlorine (Herreros et al., 1998), aqueous sulphur dioxide (Gbor et al., 2000), hydrogen peroxide (Banza et al., 2002), mixed nitric-sulphuric acid (Xie et al., 2005), potassium dichromate (Altundogan et al., 2004) and sodium chlorate (Yang et al., 2010). In addition, research has been done into pressure leaching (Anand et al., 1983, Papangelakis and Perederiy, 2009), bioleaching (Carranza et al., 2009, Kaksonen et al., 2011) and the effect of ultrasound on acid leaching (Bese, 2007). In the present paper, the results obtained for the leaching experiments with the copper smelter slag and the slag flotation tailings in sulphuric acid solutions, in the absence as well as in the presence of either ferric sulphate or hydrogen peroxide, will be presented.

Materials and experimental methods

The experiments were performed using either reverberatory furnace slag or reverberatory furnace slag flotation tailings from the Bor Copper Concentrator. The slag was sampled from the crushing line before entering the milling section of the concentrator, whereas the slag flotation tailings were sampled from the tailings disposal line. The slag sample was ground to pass through a 75 μm sieve. The tailings sample was used as received because its particle size was finer than 75 μm . Quantitative determination of elements in the samples was performed by gravimetric and volumetric analysis and atomic absorption spectrophotometry (FAAS/GFAAS). The chemical compositions of the two samples are given in Table 1.

The samples of the copper slag and leach residue were characterized by using X-ray diffraction (XRD). Figure 1 shows XRD data for the slag sample. The XRD peaks indicate the presence of magnetite, olivines (among which fayalite was found to be the most abundant), pyroxene and granate.

The leaching experiments were conducted in a 250 cm^3 glass reactor at atmospheric pressure. Five grams of the sample was leached with 150 cm^3 of the lixiviant. Most of the experiments performed at room temperature at a stirring speed of 350 min^{-1} by using a magnetic stirrer. The experiments performed at set temperatures were conducted in a three-necked glass reactor fitted with a glass stirrer, condenser and thermometer, which was immersed in a thermostated water bath. The reaction

Table 1. Chemical compositions of the copper smelter slag and the slag flotation tailings

| Constituent | Content (wt.%) | |
|--------------------------------|----------------|-------------------------|
| | Copper Slag | Slag Flotation Tailings |
| Cu – total | 0.97 | 0.59 |
| Cu – oxides | 0.15 | 0.06 |
| Cu – sulphides | 0.82 | 0.53 |
| SiO ₂ | 33.75 | 34.62 |
| Al ₂ O ₃ | 3.78 | 3.93 |
| Fe ₂ O ₃ | 8.05 | 1.10 |
| FeO | 33.80 | 34.44 |
| Fe ₃ O ₄ | 9.39 | 10.60 |
| Fe – total | 39.09 | 35.19 |
| CaO | 6.00 | 4.79 |

time was either 120 minutes or 180 minutes. Sampling was performed at regular time intervals by taking 1 cm³ of the leach liquor with a pipette. The leach liquor sample was filtered and the filtrate was transferred to a 50 cm³ volumetric flask. The flask was filled with distilled water to the mark. The diluted solution was analyzed by atomic absorption spectrophotometry. All the experiments were performed in duplicate and some were repeated several times to establish the reproducibility of the results.

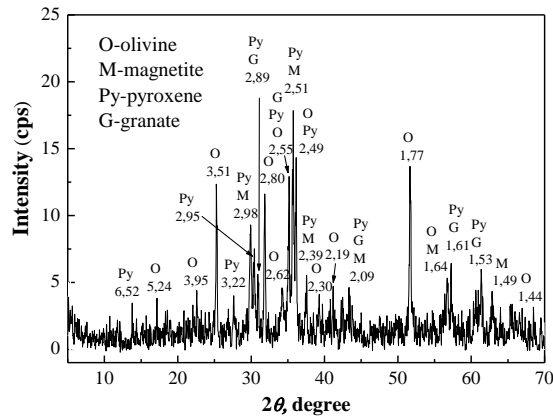


Fig. 1. XRD pattern for the copper slag sample

Results and discussion

Leaching with sulphuric acid

The effect of sulphuric acid concentration on metal dissolution from the slag and the slag flotation tailings was investigated at initial sulphuric acid concentrations ranging from 0.5 M to 3.0 M. The results are illustrated in Figure 2 and 3.

A common feature of the slag and the slag flotation tailings is higher iron dissolution compared to that of copper. Further, as seen in Figure 2 and 3, higher copper dissolution is accompanied with higher iron dissolution. That is, higher copper and iron extractions were observed with the slag rather than slag flotation tailings. Thus, the maximum copper and iron extractions achieved with the slag were 26.0% and 62.5%, respectively, as opposed to the slag flotation tailings where the maximum copper and iron extractions were 13.5% and 48.0%, respectively. Carranza et al. (2009) found that most of the copper-bearing species in slag flotation tailings were occluded in the slag phase and thus unable to interact with the collector. Therefore, the slag flotation tailings are inferior in terms of leaching when compared to the slag because most of the liberated copper phases have been removed by flotation.

Based on the chemical compositions of the slag and the slag flotation tailings (Table 1), it can be concluded that the copper dissolved from the slag flotation tailings mainly originates from the copper oxide phases (about 10 wt.%), which are not amenable to flotation. Low copper extractions both from the slag and the slag flotation tailings indicate that sulphuric acid is not a suitable reagent for leaching these materials, at room temperature. This conclusion is in line with the study by Banza et al. (2002) where the leaching of copper smelter slag with sulphuric acid (500 kg/Mg slag) resulted in copper and iron extractions of 20% and 52%, respectively, at 20°C, whereas the maximum copper and iron extractions were 60% and 90%, respectively, at 90°C. Also, based on the results depicted in Figure 2 and 3, it can be concluded that the iron minerals are dissolved more easily in sulphuric acid than the copper minerals, both from the slag and the slag flotation tailings, which is in accord with Banza et al. (2002).

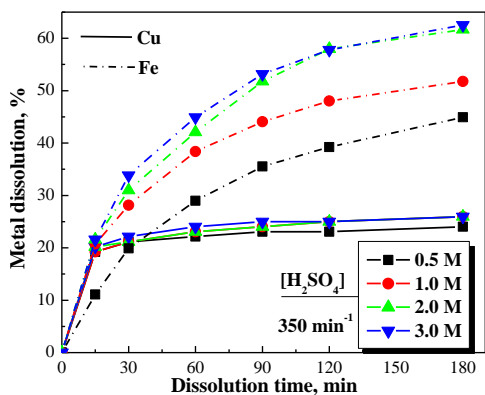


Fig. 2. Copper and iron extractions from the slag as a function of time at different initial sulphuric acid concentrations

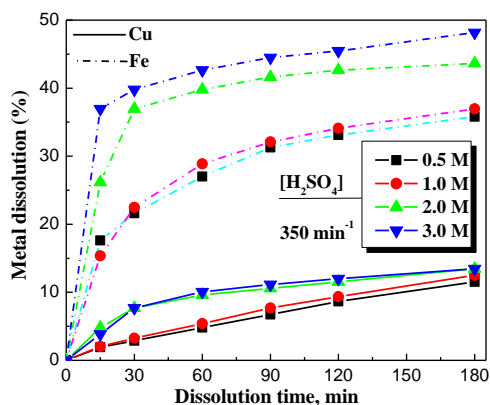


Fig. 3. Copper and iron extractions from the slag flotation tailings as a function of time at different initial sulphuric acid concentrations

Leaching with ferric sulphate

The slag and the slag flotation tailings were leached with ferric sulphate in 1 M sulphuric acid. The ferric iron concentration was varied in the range from 5 g/dm³ to 40 g/dm³ and from 5 g/dm³ to 20 g/dm³ for the slag and the slag flotation tailings, respectively. The results are shown in Figure 4. It can be seen that copper extractions from the slag were low and similar for all the ferric iron concentrations studied, that is, between 26% and 29% after 180 minutes of reaction. Most of the copper was dissolved in the first 30 minutes of reaction. In addition, copper extractions from the slag flotation tailings were slightly lower than those from the slag (between 22% and 24%). Finally, the dissolution curves obtained with both materials have a similar shape.

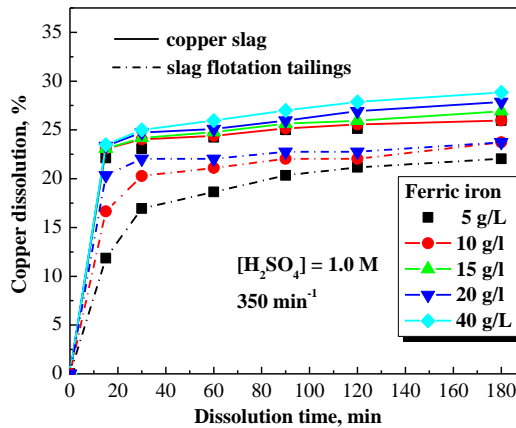


Fig. 4. Copper extractions from the copper smelter slag and the copper smelter slag flotation tailings as a function of time at different initial ferric iron concentrations

By comparing Figure 2 and 4, it can be seen that both the copper extractions and the copper dissolution curves were similar in sulphuric acid alone and in the presence of ferric iron. This observation suggests that these two lixivants have a similar, low potential for leaching copper from the slag and the slag flotation tailings at room temperature.

Leaching with hydrogen peroxide

Effect of hydrogen peroxide concentration

As copper extractions in the leaching experiments performed with sulphuric acid and ferric sulphate were low, a series of leaching experiments was conducted with hydrogen peroxide which is a strong oxidant. To this end, the slag and the slag flotation tailings were leached in 1 M sulphuric acid with the addition of different initial concentrations of hydrogen peroxide (0.5–3 M). The results are shown in Figures 5 and 6.

As seen in Figure 5, copper dissolution from the slag increases with increasing hydrogen peroxide concentration. The final copper extractions attained were 57.7% and 63.4% at initial hydrogen peroxide concentrations of 2 M and 3 M, respectively. These extractions are twice as high as those obtained in the leaching experiments with sulphuric acid and ferric iron. Copper extractions from the slag flotation tailings leached with hydrogen peroxide (Fig. 6) were approximately half as high as those achieved when the slag was leached with hydrogen peroxide. Thus, a copper extraction of 32.7% was obtained for the highest hydrogen peroxide concentration. However, this value is still about twice as large as those reported when the slag was leached with sulphuric acid and ferric iron.

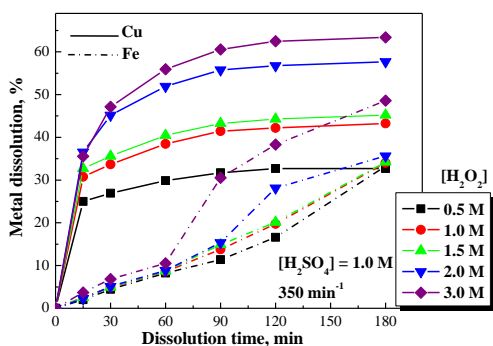


Fig. 5. Copper and iron extractions from the slag as a function of time at different initial hydrogen peroxide concentrations

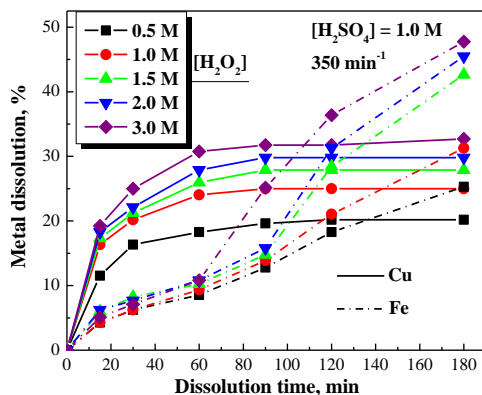
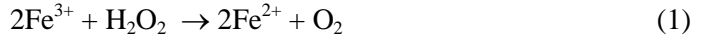


Fig. 6. Copper and iron extractions from the slag flotation tailings as a function of time at different initial hydrogen peroxide concentrations

With regard to iron dissolution, it is significantly lower than that of copper for both the slag and the slag flotation tailings in the first 60-90 minutes of leaching. Following that, iron dissolution increases, in particular in the case of the slag flotation tailings, but also in the case of the slag at the highest hydrogen peroxide concentration. Thus, after 60 minutes of reaction, iron extractions from the slag and the slag flotation tailings are 10.5% and 10.8%, respectively, whereas the corresponding values are 48.6% and 47.8%, respectively, after 180 minutes of leaching (at 3 M H_2O_2). A possible explanation for this phenomenon could be that hydrogen peroxide has a greater affinity towards copper than towards iron, that is, the copper may be present as a phase that is more amenable to oxidation with hydrogen peroxide than the form in which the iron exists. Once most of the available copper from the slag (or from the slag flotation tailings) has been dissolved (i.e., after about 60 min), hydrogen peroxide is consumed primarily for iron oxidation. The more iron there is in solution, the faster the dissolution. This acceleration is due to the catalytic decomposition of hydrogen peroxide to oxygen and water through a redox process caused by the $\text{Fe}^{3+}/\text{Fe}^{2+}$ redox couple (Eqs. 1, 2 and 3).



The higher the decomposition of hydrogen peroxide, the higher the dissolution of iron (Dimitrijevic et al., 1999). As copper dissolution from the slag flotation tailings is much lower than that from the slag, the sharp increase in iron dissolution is significantly higher in the case of the former.

It can be seen that even the application of a strong oxidant such as hydrogen peroxide ($E^\circ = 1.776 \text{ V}$) does not result in complete copper dissolution, with the attained copper extractions being 60% and 30% from the slag and the slag flotation tailings, respectively. This observation indicates that much of the copper that is locked within the slag matrix was not liberated prior to leaching. As shown in Table 2, the finest fraction (-38+0 μm) of the slag comprises in excess of 60% of the sample and contains almost 1.1% copper. However, further particle size reduction would probably be economically unjustified.

Table 2. Particle size distribution for the copper smelter slag sample and the copper content of the various size fractions

| Size fraction (μm) | Weight (%) | Cu content (wt. %) |
|---------------------------------|------------|--------------------|
| -75+53 | 13.60 | 0.75 |
| -53+38 | 17.80 | 0.81 |
| -38+0 | 68.60 | 1.07 |

XRD analysis of the leach residue showed the same mineral phases as those found in the slag, but with more pronounced peaks. The crystallinity of the residue was higher than that of the slag, but nevertheless low.

In contrast to the results of this study, where iron dissolution from the slag and, in particular, from the slag flotation tailings sharply increases after 60 min of leaching, Banza et al. (2002) found, when leaching slag with hydrogen peroxide ($\text{H}_2\text{O}_2 + \text{H}_2\text{SO}_4$, pH 2.5, 70 °C), that iron extraction drops from about 95% to 5%, with copper extraction being 85%, at hydrogen peroxide concentrations in excess of 62 dm^3/Mg slag.

Effect of stirring

It is well known that the decomposition of hydrogen peroxide is catalysed by a number of elements and their ions, as well as by stirring, shaking and similar operations (Dimitrijevic et al., 1999). For this reason, the effect of stirring on copper and iron extractions was studied. Two experiments were performed, namely one without stirring the slag slurry and the other one at a stirring speed of 350 min^{-1} . The results are shown in Figure 7.

It can be seen that stirring has a beneficial effect on copper and iron extractions. This effect may be due to a better contact between the peroxide and the slag which has a high density (i.e., 3600 kg m^{-3}).

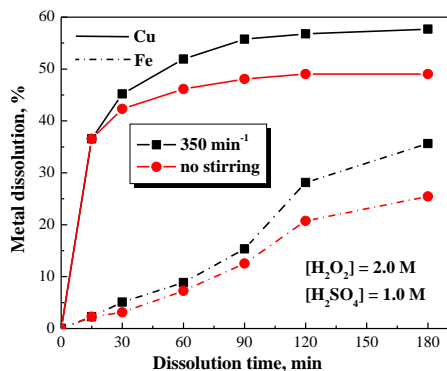


Fig. 7. Copper and iron extractions from the slag with and without stirring

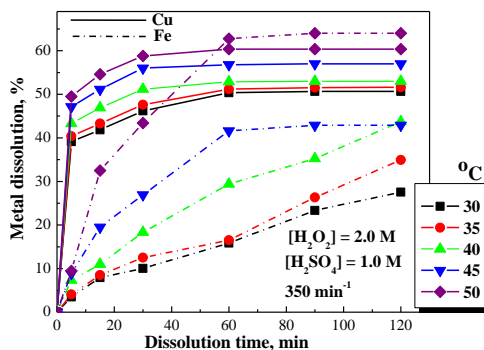


Fig. 8. Copper and iron extractions from the slag as a function of temperature

Effect of temperature

The effect of temperature was investigated in a narrow temperature range from $30 \text{ }^{\circ}\text{C}$ to $50 \text{ }^{\circ}\text{C}$ as hydrogen peroxide is unstable at temperatures above $40 \text{ }^{\circ}\text{C}$. The temperatures were kept constant in a thermostated water bath. The reaction time was reduced to 120 minutes because shapes of the dissolution curves suggested that copper dissolution ceases after that time. The results are shown in Figure 8.

From Figure 8, it can be concluded that temperature has no significant effect on copper dissolution from the slag in an acidic solution of hydrogen peroxide. However, the effect of temperature is greater in the case of iron. Thus, at $50 \text{ }^{\circ}\text{C}$, iron extraction becomes greater than that of copper, that is, 64%. The copper extractions were in the 50-60% range between $30 \text{ }^{\circ}\text{C}$ and $50 \text{ }^{\circ}\text{C}$, whereas 57.7% of Cu was dissolved at room temperature. As this value was close to that found at $45 \text{ }^{\circ}\text{C}$ (i.e., 57%), a possible reason was sought why this was the case. To this end, a series of experiments was conducted where changes in the slurry temperature were recorded at different hydrogen peroxide concentrations. The results are given in Table 3.

It was observed that the leaching reaction was more vigorous and accompanied with loud hissing sound due to hydrogen peroxide decomposition and oxygen effervescence at hydrogen peroxide concentrations equal to or in excess of 2 M. In addition, the temperature was measured to be the highest after 90-120 minutes of reaction, which is the time when iron dissolution was found to increase sharply. This means that increasing $\text{Fe}^{3+}/\text{Fe}^{2+}$ concentration results in an increase in the catalytic decomposition of hydrogen peroxide. As hydrogen peroxide decomposition is exothermic, there is an increase in temperature, which in turn accelerates hydrogen peroxide decomposition.

The effect of temperature on the leaching of slag flotation tailings was not studied as copper extractions from the slag flotation tailings were rather low.

Table 3. Change in slurry temperature with time as a function of hydrogen peroxide concentration ($[\text{H}_2\text{SO}_4] = 1.0 \text{ M}$, 350 min^{-1}).

| H ₂ O ₂ Concentration | 0.5 M | 1.0 M | 2.0 M | 3.0 M | 4.0 M |
|---|-----------------|-------|-------|-------|-------|
| Time, min | Temperature, °C | | | | |
| 0 | 24 | 24 | 24 | 23 | 23 |
| 15 | 25 | 25 | 25 | 25 | 25 |
| 30 | 28 | 27 | 27 | 27 | 27 |
| 60 | 30 | 31 | 31 | 36 | 42 |
| 90 | 32 | 35 | 37 | 51 | 71 |
| 120 | 34 | 38 | 44 | 42 | 42 |
| 150 | 32 | 34 | 36 | 34 | 34 |
| 180 | 32 | 32 | 33 | 31 | 30 |

Conclusions

Copper smelter slag and copper smelter slag flotation tailings were leached using sulphuric acid solutions, without or with the addition of either ferric sulphate or hydrogen peroxide. The highest copper extraction was attained with hydrogen peroxide at room temperature. Copper extraction from the slag was much higher than that from the slag flotation tailings. However, the maximum copper extraction achieved was only 63.4% when using 3 M H₂O₂, with the iron extraction being rather high at 48.6%. The lixivants studied were not selective and consequently iron extraction was relatively high, which is unfavourable in terms of further treatment of the leach liquors. In the majority of experiments, most of the copper was dissolved in the first 30-60 minutes of reaction, whereas iron dissolution was comparatively low in the first 60 minutes (around 10% with H₂O₂) but sharply increased afterwards.

Acknowledgements

The authors acknowledge financial support from the Ministry of Science and Technological Development of Serbia (Project no. BR172031 and TD33023).

References

- ALTUNDOGAN H. S., BOYRAZLI M., TUMEN F., 2004. *A study on the sulphuric acid leaching of copper converter slag in the presence of dichromate*. Minerals Engineering 17, 465–467.
- ANAND S., KANTA RAO P., JENA P.K., 1980, *Recovery of metal values from copper converter and smelter slags by ferric chloride leaching*. Hydrometallurgy 5, 355–365.

- ANAND S., SARVESWARA RAO K., JENA P.K., 1983. *Pressure leaching of copper converter slag using dilute sulphuric acid for the extraction of cobalt, nickel and copper values*. Hydrometallurgy 10, 305–312.
- BANZA A.N., GOCK E., KONGOLO K., 2002. *Base metals recovery from copper smelter slag by oxidizing leaching and solvent extraction*. Hydrometallurgy 67, 63–69.
- BESE A.V., 2007. *Effect of ultrasound on the dissolution of copper from copper converter slag by acid leaching*. Ultrasonics Sonochemistry 14, 790–796.
- CARRANZA F., ROMERO R., MAZUELOS A., IGLESIAS N., FORCAT O., 2009. *Biorecovery of copper from converter slags: Slags characterization and exploratory ferric leaching tests*. Hydrometallurgy 97, 39–45.
- DIMITRIJEVIC M., ANTONIJEVIC M., DIMITRIJEVIC V., 1999. *Kinetics of pyrite oxidation by hydrogen peroxide in phosphoric acid solutions*, J. Serb. Chem. Soc. 753–764.
- GBOR P.K., HOQUE S., JIA C.Q., 2006. *Dissolution behavior of Fe, Co, and Ni from non-ferrous smelter slag in aqueous sulphur dioxide*. Hydrometallurgy 81, 130–141.
- GORAI B., JANA R.K., PREMCHAND, 2003. *Characteristics and utilisation of copper slag – a review*. Resources, Conservation and Recycling 39, 299–313.
- HERREROS O., QUIROZ R., MANZANO E., BOU C., VINALS J., 1998. *Copper extraction from reverberatory and flash furnace slags by chlorine leaching*. Hydrometallurgy 49, 87–101.
- KAKSONEN A.H., LAVONEN L., KUUSENAHO M., KOLLI A., NARHI H., VESTOLA E., PUHAKKA J.A., TUOVINEN O.H., 2011. *Biorecovery and recovery of metals from final slag waste of the copper smelting industry*. Minerals Engineering 24, 1113–1121.
- LI Y., PAPANGELAKIS V.G., PEREDERIY I., 2009. *High pressure oxidative acid leaching of nickel smelter slag characterisation of feed and residue*. Hydrometallurgy 97, 185–193.
- SHEN H.T., FORSSBERG E., 2003. *An overview of recovery of metals from slags*. Waste Management 23, 933–949.
- XIE Y., XU Y., YAN L., YANG R., 2005. *Recovery of nickel, copper and cobalt from low-grade Ni-Cu sulfide tailings*. Hydrometallurgy 80, 54–58.
- YANG Z., RUI-LIN M., WANG-DONG N., HUI W., 2010. *Selective leaching of base metals from copper smelter slag*. Hydrometallurgy 103, 25–29.

Received December 6, 2013; reviewed; accepted February 18, 2014

EFFECTS OF ACID LEACHING ON HALLOYSITE

Saruhan SAKLAR*, Abdulkerim YORUKOGLU**

* General Directorate of Mineral Research and Exploration (MTA), Turkey, saklar@mta.gov.tr

** Department of Technology, Mineral Processing Division, Ankara, Turkey

Abstract: A characteristic iron-containing halloysite sample from Turkey was subjected to acid leaching using organic and inorganic acids for removing iron impurities. The aim of this study was to compare the raw hydrated and dehydrated halloysites with the leached products. Hydrochloric acid and oxalic acid were chosen as leaching agents for the removal of iron impurities at 80 °C for 2.5 h. The physicochemical properties of the acid-treated halloysite were analyzed by XRF, XRD, FTIR, TGA, DTA, SEM, and TEM. The XRF results showed that the acid treatment caused the dissolution of minor amounts of Al³⁺ ions from the clay layer. The XRD results indicated that the crystalline structure was unchanged after the leaching. However, it was observed that the hydrated (1 nm) halloysite readily lost its interlayer water and was transformed to the dehydrated (0.7 nm) form. In addition, no visible effects of the acid treatment on the tubular structure of halloysite were detected in the SEM and TEM images. Typical pores of varying dimensions were observed in all of the samples regardless of their form or treatment. Furthermore, the TG-DTA and FTIR analysis results were similar for both the raw and the acid-treated samples.

Keywords: halloysite, kaolin, leaching, dehydration, characterization

Introduction

Halloysite is a monoclinic clay mineral formed by surface weathering or hydrothermal alteration of alumina silicate minerals. It occurs in nature in two forms. The first form is called as hydrated halloysite, and its composition is Al₂Si₂O₅(OH)₄·2H₂O which can be easily identified by XRD (Murray, 2007). Hydrated halloysite readily and irreversibly loses its interlayer water even at ambient temperature and humidity (Churchman et al., 1984) to generate dehydrated halloysite (Al₂Si₂O₅(OH)₄). Attempts to differentiate this material from kaolin continue often by the application of intercalation methods (Joussein et al., 2007). A distinguishing property of halloysite is the inclusion of prismatic structures, mostly in the shape of cylindrical tubules, of sizes down to a few nanometers. Other shapes such as spheres and ellipsoids have also been reported depending on the geology of the deposit (Levis and Deasy, 2002). Hence, SEM is another important method for detecting the distinct prismatic halloysite

structures and differentiating dehydrated halloysite from kaolin, which is composed of plate-like structures.

As in kaolin ores, iron and titanium oxides and micas are the main discoloring impurities in halloysites. If the impurity content in clay concentrates is above the acceptable limits, product quality with respect to firing color, plasticity, and shrinkage declines. It is known from the literature that low quantities of fine iron oxides or hydroxides may cause strong pigmentation in kaolin (Pruett and Pickering, 2006). Therefore, it is typically necessary to remove or decrease the content of these impurities to the accepted *lowest standard level*, particularly if the material is to be used in ceramics. Although the beneficiation of halloysite is not a common issue, detailed studies have been carried out for kaolin (Ambikadevi and Lalithambika, 2000; Mandal and Banerjee, 2004; Arslan and Bayat, 2009). The leaching of iron oxides and the effect of their removal on the surface properties of kaolins have also been extensively studied (Mako et al., 2006; Panda et al., 2010).

Commercial halloysite deposits are located in northwestern Turkey, particularly in the Canakkale and Balikesir regions where mineralization occurred as a result of hydrothermal alterations (Ece and Schroeder, 2007). A large percentage of the deposits suffer from coloring due to the presence of fine iron oxide/hydroxide minerals such as hematite and goethite as well as minor quantities of muscovite, manganese, anatase, alunite, and even pyrite. The dark brownish-reddish-colored halloysites must be blended with white material or subjected to beneficiation by leaching in order to obtain saleable product.

In this study, a characteristic iron-containing halloysite sample from Turkey was subjected to acid leaching using organic and inorganic acids for removing the iron impurities. The raw hydrated and dehydrated halloysites were then compared with the leached products, and the variations in the physicochemical properties were analyzed by instrumental techniques such as SEM, XRF, XRD, FTIR, TG-DTA, and TEM.

Materials and methods

Iron-containing halloysite clay (2.50 g/cm^3) from one of the largest active mining zones (Balikesir-Gonen) in northwestern Turkey was selected for experimental studies. Raw massive hydrated (RMH) halloysite samples were collected for characterization. Raw powder hydrated (RPH) samples were then prepared stepwise using cone and roll crushers and a cup mill. Next, a representative amount of RPH (~500 g) was wet sieved at 90 μm , 30 μm , and 10 μm to determine the size distribution (Table 1).

Based on this analysis, it was determined that clay was dispersed, and that most of the particles were less than 10 μm in size. To provide homogeneity and simplicity, the fraction with the largest size (>90 μm) was neglected, and particles with sizes less

Table 1. Size distribution of the raw hydrated halloysite ore

| Fraction (μm) | %Wt. |
|----------------------------|-------|
| +90 | 3.03 |
| -90 + 30 | 2.39 |
| -30 + 10 | 3.17 |
| -10 | 91.41 |

than 90 μm were chosen for the leaching tests by wet screening using a Russell screen (ϕ 52 cm). Before the wet screening, the clay sample was dispersed using a Denver 12 laboratory flotation machine without added dispersant at an agitation speed of 1500 rpm. The sieved slurry was then filtered, dried in a furnace above 70 $^{\circ}\text{C}$, and powdered using a hand roller to provide the raw powder dehydrated sample (RPD).

XRD patterns were obtained with an X-ray diffractometer at 40 kV and 40 mA using Cu-K α radiation and a step width of 0.08 (Bruker D8 Advance). SEM analyses (FEI Quanta 400 MK2) were performed on Au/Pd-plated samples, and for powder samples, a field emission gun (FEG) was used. The chemical compositions of the samples were determined using an XRF spectrometer (Philips Axios, *Almelo*). FTIR spectra were recorded on a Thermo Scientific Nicolet 6700 (Madison, USA) spectrophotometer using KBr pellets. Thermogravimetric analyses were carried out using a Perkin Elmer *SII Exstar 6000* (TG-DTA 6300) instrument. The sample was heated in a platinum crucible at a constant heating rate of 10 $^{\circ}\text{C}/\text{min}$ under a stream of dry air with a flow rate of 2 dm^3/min from 25 $^{\circ}\text{C}$ to 1000 $^{\circ}\text{C}$. The tube morphologies were observed by transmission electron microscopy (TEM) analyses (FEI Tecnai G² F30). The samples were ultrasonically dispersed in ethanol, and then evaporated on a specimen holder before the TEM analysis.

Two types of leaching agents were chosen: oxalic acid ((COOH)₂) as the organic agent and hydrochloric acid (HCl) as the inorganic agent. The halloysite sample (15 g) was mixed with a 0.2–1.3 M solution of the acid (150 cm^3 at 80 $^{\circ}\text{C}$ for 2.5 h. To determine the effect of time on the leaching experiments, kinetic data were collected for 1.3 M HCl and 0.9 M (COOH)₂ solutions with a solid/liquid ratio of 10 at 80 $^{\circ}\text{C}$ from 15 to 150 min. Subsequently, the slurry was filtered, and the residue was washed with hot distilled water, dried, and analyzed by XRF.

Results and discussions

Leaching experiments

The results of the leaching experiments indicated that the dissolution of iron increased up to the acid concentrations of 0.25 M (COOH)₂ and 0.75 M HCl (Fig. 1a). Above

these concentrations, iron dissolution remained nearly constant, while at low acid concentrations, greater than 90% of Fe_2O_3 was removed.

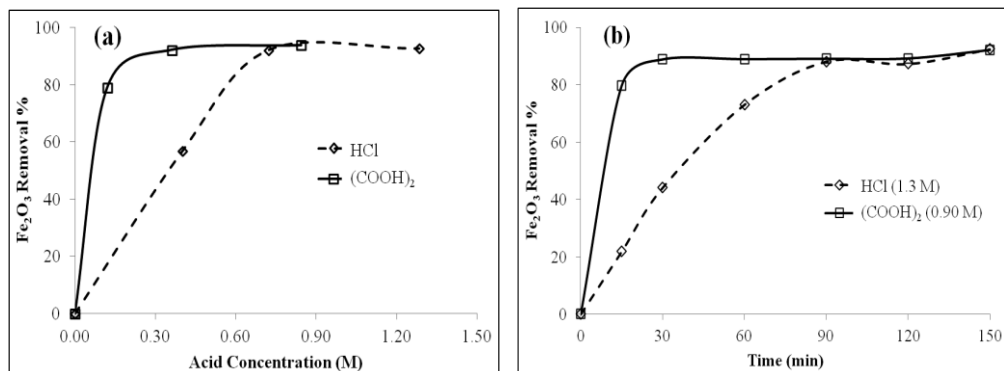


Fig. 1. Effect of acid concentration on (a) Fe_2O_3 removal and (b) reaction kinetics of raw halloysite

To compare the physicochemical properties of the raw and the acid-treated samples, the reactions with 1.30 M HCl and 0.90 M $(\text{COOH})_2$ were investigated, and the products were evaluated. The highest concentration was selected for these studies to best observe the potential effects of the different acid treatments on the crystalline and tubular structures of halloysite.

The dissolution of Fe_2O_3 was observed to increase for up to 30 min and 90 min of the leaching time for the $(\text{COOH})_2$ and HCl treatments, respectively (Fig. 1b) but then remained unchanged with a further increase in the leaching time. $(\text{COOH})_2$ is a relatively fast leaching agent compared with HCl; even at a lower concentration, 90 % of iron was removed in 30 min using $(\text{COOH})_2$, while this level was achieved only after 90 min of leaching with HCl at a higher concentration. The leaching potential of oxalic acid has already reported in several studies (Veglio et al., 1998; Ambikadevi and Lalithambika, 2000; Luevanos et al., 2011).

XRD characterization

First, the effect of the acid leaching on the structure of clay was investigated using XRD analysis (Fig. 2). The typical characteristic basal reflections (1 nm) of hydrated halloysite can be observed for the RMH and RPH samples. However, for the RPD, HCl, and $(\text{COOH})_2$ samples, the broad 1nm peaks were displaced with 0.7 nm reflections, which are the equivalent basal reflections for dehydrated halloysite. The dehydration of the hydrated halloysite occurs because of the loss of the interlayer water, and consequently, the distance between the clay layers decreases from 1 nm to 0.7 nm (Churchman and Carr 1975).

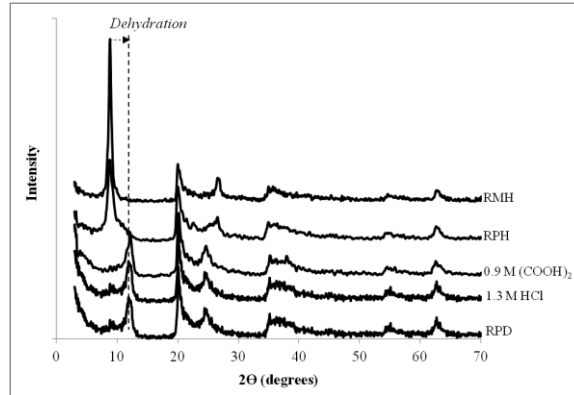


Fig. 2. XRD patterns of the raw and acid-treated halloysites

The XRD patterns of the acid-treated samples and raw halloysites were nearly the same except for the shift of the broad 1 nm peak of RMH. It has been reported that the reflection intensity of raw clay decreases and ultimately disappears (amorphous phase) as the acid treatment strength increases (Mako et al. 2006; Panda et al. 2010; Zhang et al. 2012). The current results (Fig. 1), however, suggest that the acid treatment under the conditions employed in this study did not affect the crystalline structure of halloysite. This lack of structural change must be attributed to the use of relatively low acid concentrations for leaching compared to those reported in the literature.

XRF characterization

The chemical analysis of the halloysite samples (Table 2) confirmed that the elemental composition of the raw samples was similar to the theoretical values for halloysite (Anthony et al., 1995) whether in the hydrated or dehydrated form. The difference between hydration and dehydration could not be observed by XRF due to the loss on ignition (LOI) that occurs during XRF analyses. The differences between the theoretical and measured values that were detected were due to the presence of the iron oxides/hydroxides such as goethite and hematite, and minor amounts of feldspar, anatase, alunite, muscovite, and/or illite (Saklar et al., 2012).

Table 2. Chemical analysis of the halloysite samples

| Sample | SiO ₂ | Na ₂ O | MgO | Al ₂ O ₃ | P ₂ O ₅ | K ₂ O | CaO | TiO ₂ | Fe ₂ O ₃ | SO ₃ | LOI |
|------------------------|------------------|-------------------|------|--------------------------------|-------------------------------|------------------|------|------------------|--------------------------------|-----------------|-------|
| Theoretical | 46.54 | - | - | 39.50 | - | - | - | - | - | - | 13.96 |
| RMH | 44.10 | <0.01 | 0.19 | 37.26 | 0.13 | 0.20 | 0.03 | 0.12 | 1.95 | 0.06 | 15.78 |
| RPH | 44.14 | 0.08 | 0.21 | 37.66 | 0.15 | 0.21 | 0.02 | 0.09 | 2.05 | 0.12 | 15.10 |
| RPD | 44.53 | 0.07 | 0.21 | 37.53 | 0.16 | 0.22 | 0.05 | 0.12 | 2.10 | 0.14 | 14.65 |
| 0.9M COOH ₂ | 55.51 | <0.01 | 0.19 | 29.22 | 0.02 | 0.24 | 0.03 | 0.14 | 0.16 | 0.03 | 14.35 |
| 1.3M HCl | 48.63 | <0.01 | 0.19 | 35.59 | 0.03 | 0.22 | 0.02 | 0.12 | 0.17 | 0.03 | 14.88 |

Furthermore, based on the XRF analyses, it was concluded that leaching of the halloysite sample with either acid led to an increase in the SiO_2 content and a decrease in the Al_2O_3 content. Thus, the Si/Al ratio also increased. A similar example of this behavior in halloysite treated with high acid concentrations was shown by Zhang et al. (2012), and it is thought to be due to the leaching of Al^{3+} ions from the clay layer via hydrolysis under acidic conditions. In addition, the content of K_2O , MgO , and TiO_2 remained practically unchanged, even at high acid concentrations. Therefore, the source of these compounds was attributed to muscovite and/or anatase, which cannot be directly removed by acid treatment alone (Yoon and Shi, 1986; Veglio et al., 1998; Oelkers et al., 2008).

TG/DTA analyses

Two weight-loss regions of nearly the same magnitude were detected in the TG/DTA analysis of the raw and acid-treated samples (Fig. 3). The DTA results verified that the TG curves resulted from water removal from the clay structure, which is a well-known phenomenon (Singer et al., 2004; Horvath et al., 2011). The first weight-loss region was below 90°C and due to the loss of physisorbed or interlayer water. In parallel with the TG curves, the first endothermic peaks in the DTA analyses occurred at 40°C for RMH and 5°C for RPH, both of which were hydrated samples, and indicated the loss of interlayer water at slightly lower temperatures. The dehydrated samples RPD, HCl, and COOH_2 exhibited initial endotherms between 60°C and 70°C due to the need for higher energy to achieve full dehydration (Joussein et al., 2006). The second distinctive weight loss occurred between 400°C and 550°C and resulted from the dehydroxylation of the clay sheet or the loss of structural water. This loss can be seen in the DTA curves as secondary broad endotherms between 485°C and 495°C that have very similar values. The successive exothermic peaks (between 990 and 995°C) indicate the formation of the mullite phase in each sample (Sonuparlak et al., 1987).

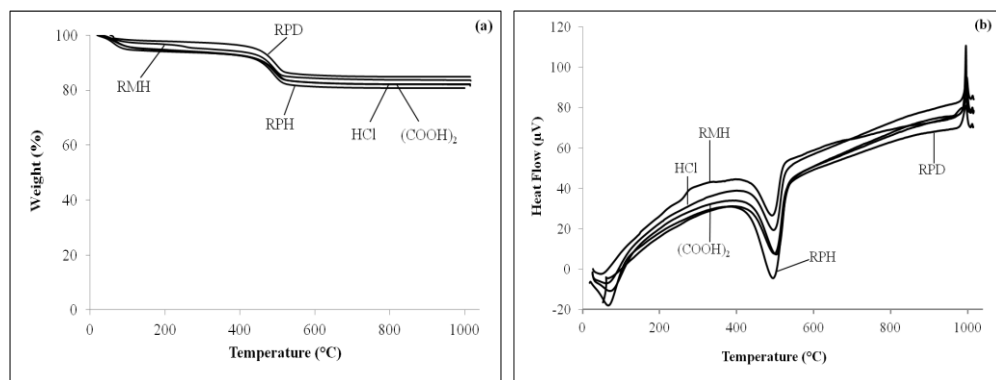


Fig. 3. a) TGA and b) DTA curves of the raw and acid-treated halloysites

The TG/DTA behavior of the raw halloysite samples was practically unchanged following the acid treatment under the conditions employed in this study. The small variations that can be noted are due to the conversion from the hydrated to the dehydrated form.

FTIR results

The IR spectrum of halloysite is characterized by an intense band at 459 cm^{-1} due to Si–O bending vibrations. The bands attributed to the Al–OH vibrations of the surface hydroxyl groups are observed at 744.5 and 792.7 cm^{-1} (Frost, 1995) or 746 and 796 cm^{-1} (Mellouk et al., 2009). The OH⁻ bending vibrations of the hydroxyl groups are observed at 910 cm^{-1} while the Si–O stretching region bands are observed at 1030 cm^{-1} , and the H–O–H (adsorbed water) deformation band appears at 1635 cm^{-1} . Finally, the characteristic OH⁻ stretching bands of halloysite can be observed at 3620 , 3629 , and 3696 cm^{-1} (Bobos et al., 2001; Frost et al., 2000).

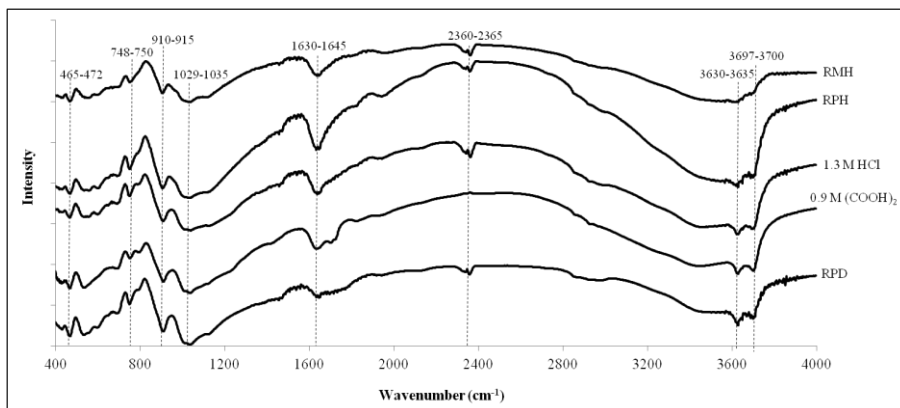


Fig. 4. FTIR spectra of the raw and acid-treated halloysites

In the FTIR spectra of the raw and the acid-treated samples (Fig. 4), the bands nearly match with only slight deviations. The bending bands for the Si–O ($465\text{--}472\text{ cm}^{-1}$), Al–OH ($748\text{--}750\text{ cm}^{-1}$), OH⁻ ($910\text{--}915\text{ cm}^{-1}$), and adsorbed water ($1630\text{--}1645\text{ cm}^{-1}$), and the stretching bands for Si–O ($1029\text{--}1035\text{ cm}^{-1}$) and OH⁻ ($3630\text{--}3635\text{ cm}^{-1}$ and $3697\text{--}3700\text{ cm}^{-1}$) are shifted to smaller values. The CO₂ bands ($2360\text{--}2365\text{ cm}^{-1}$) are also similar for each sample. This similarity of the FTIR spectra of the hydrated and the dehydrated raw samples may be ascribed to the relatively high degree of crystallinity. The similarity of the spectra for the raw and the acid-treated samples, nevertheless, proved that the acid concentrations used in this study were not sufficiently high to change the FTIR profiles.

SEM and TEM analyses

The SEM results (Fig. 5) for the halloysite sample indicated tubular particle morphology with most of the tubules having lengths of up to a few micrometers. No differences were observed in the morphology of the raw and the acid-treated samples, although the acid-treated samples were agglomerated (as if stacked together) when compared to the raw samples. This result may be attributed to the leaching, washing, and drying processes. It should be noted that SEM is a practical method for the analysis of bulk samples, but it is inappropriate for samples in powder form due to the difficulty of coating such samples. Not surprisingly, the micrographs of the bulk sample were therefore cleaner than those of the powders.

The TEM results (Fig. 6) give further information about the appearance and morphology of the particles in the halloysite samples. Typical hollow tubes with inner diameters as low as 10 nm were detected (Fig. 6). Again, no differences were observed for the raw and the acid-treated, or the hydrated and the dehydrated samples, respectively. Damage of the tubular structure has only been reported when the acid treatment was carried out at much higher concentrations (3 M H_2SO_4 at 90 °C for 8 hr (Zhang et al., 2012) and 5 N HCl at 70 °C for 4 hr (Belkassa et al., 2013).

Both smooth and porous surfaces were detected in the tubules, and the pores varied in size and shape independent of whether the samples were the raw or the acid-treated. Such pores in halloysites have been previously reported as a characteristic feature, and they have been shown to lead to particle size distribution and/or dehydration processes (Churchman et al., 1995). They may be generated during the analysis due to the transmission of electrons through the sample, which may cause the partial heating of the transmission zone.

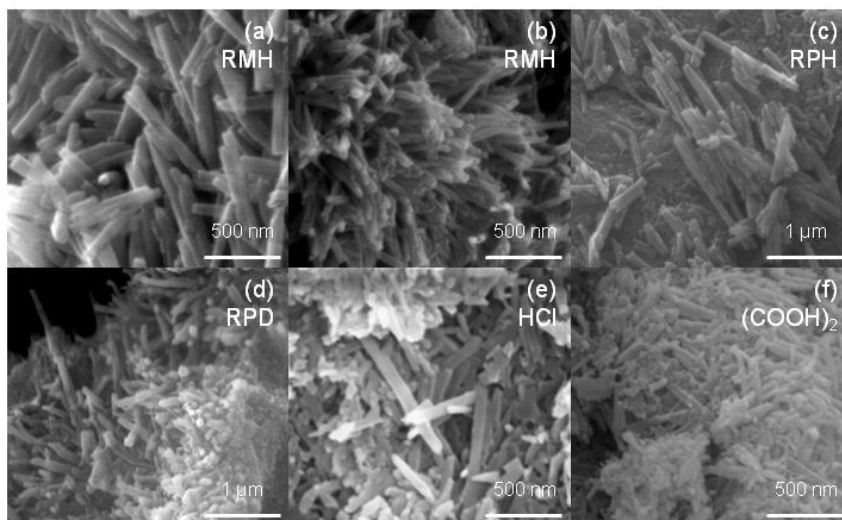


Fig. 5. SEM micrographs of the raw and acid-treated halloysites (a) and (b) raw massive hydrated (RMH) (c) raw powder hydrated (RPH) (d) raw powder dehydrated (e) HCl (f) COOH_2

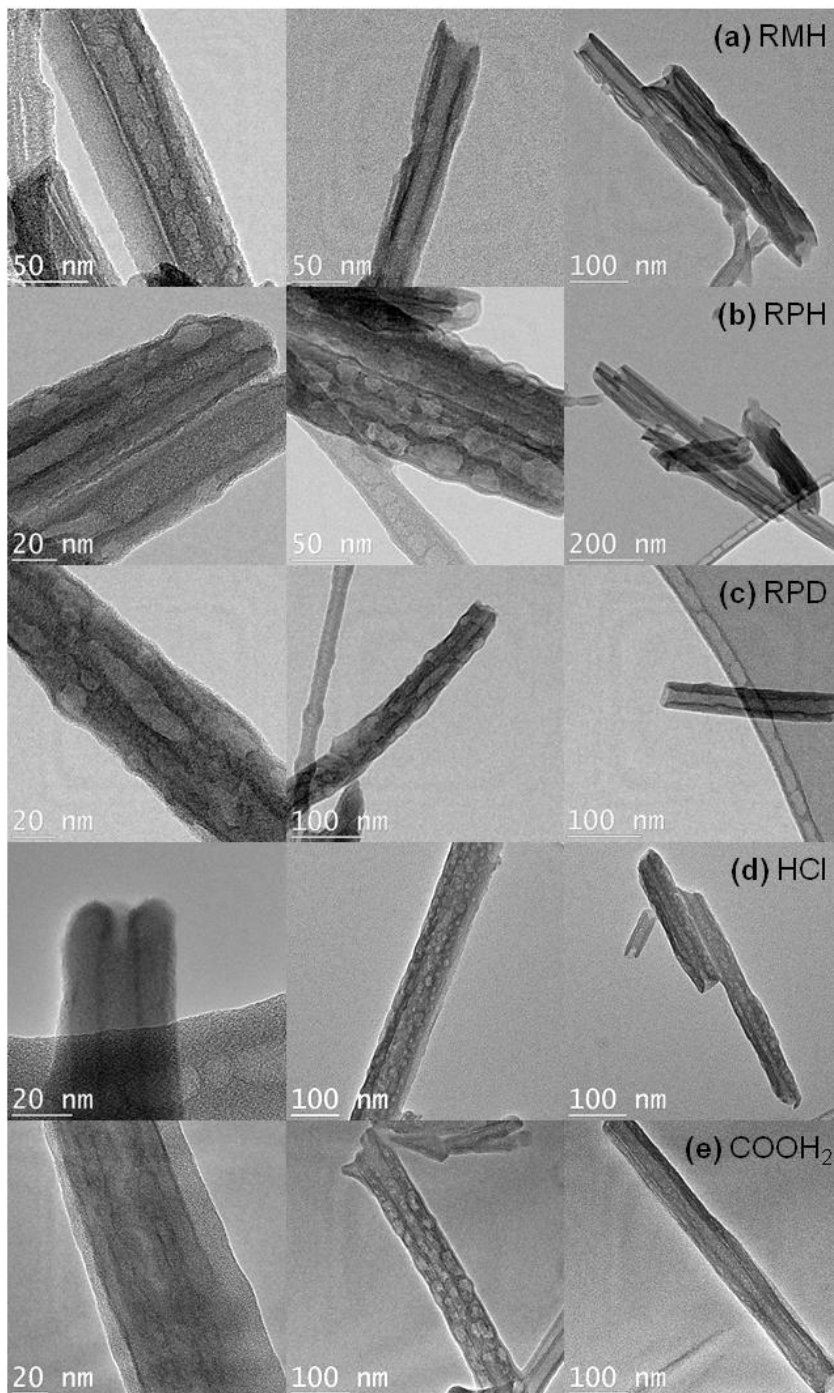


Fig. 6. TEM micrographs of the raw and acid-treated halloysites (a) raw massive hydrated (RMH) (b) raw powder hydrated (RPH) (c) raw powder dehydrated (d) HCl (e) COOH₂

Conclusions

Based on the results of this study, it was determined that iron can be removed from halloysite samples by chemical leaching without the deformation of the crystalline structure or changes in the particle morphology. Most of the iron (~90 %) in the samples tested was dissolved upon stirring with 0.25 M (COOH)₂ or 0.75 M HCl 10/1 liquid/solid ratio) for 2.5 hr at 80 °C.

The XRF results indicated that the SiO₂ content slightly increased while the Al₂O₃ content decreased with the acid treatment due to leaching of the Al³⁺ ions from the clay layer, which resulted in an increase in the Si/Al ratio. The XRD studies confirmed that hydrated (1 nm) halloysite readily lost interlayer water, and thus transformed into the dehydrated (0.7 nm) form, but without the deformation of the crystalline structure. Furthermore, no visible effect of the acid treatment on the particle morphology of halloysite was observed by the SEM and the TEM. From the SEM and TEM images, it was also determined that the halloysite particles are typically tubular in shape with diameters as low as 10 nm and lengths up to a few micrometers. Pores on the tubes were also detected in all of the samples independent of the acid treatment and the hydrated/dehydrated form. Finally, the TG-DTA and FTIR analysis results were also very similar for the raw and the acid-treated samples.

References

- AMBIKADEVI V.R., LALITHAMBIKA M., 2000, *Effect of organic acids on ferric iron removal from iron-stained kaolinite*, Applied Clay Science, 16, 133-14.
- ANTHONY J.W., BIDEAUX R.A., BLADH K.W., NICHOLS M.C., 1995, *Handbook of Mineralogy, Vol. II. Silica, Silicates, Mineral Data Publishing*, Tucson, Arizona.
- ARSLAN V., BAYAT O., 2009, *Removal of Fe from kaolin by chemical leaching and bioleaching*, Clays and Clay Minerals, 57(6), 787-794.
- BELKASSA K., BESSAHA F., MAROUF K., BATONNEAU I., COMPAROT J., KHELIFA A., 2013, *Physicochemical and adsorptive properties of a heat-treated and acid-leached Algerian halloysite, Colloids and Surfaces A: Physicochemical and Engineering Aspects*, 421, 26-33.
- BOBOS I., DUPLAY J., ROCHA J., GOMES C., 2001, *Kaolinite to halloysite-7 A transformation in the kaolin deposit of Sao Vicente De Pereira-Portugal*, Clays and Clay Minerals, 49(6), 596-607.
- CHURCHMAN G.J., CARR R.M., 1975, *The definition and nomenclature of halloysites*, Clays and Clay Minerals, 23, 382-388.
- CHURCHMAN G.J., DAVY T.J., AYLMOORE L.A.G., GILKES R.J., SELF P.G., 1995, *Characteristics of fine pores in some halloysites*, Clay Minerals, 30, 89-98.
- CHURCHMAN G.J., WHITTON J.S., CLARIDGE G.G.C., THENG B.K.G., 1984, *Intercalation method using formamide for differentiating halloysite from kaolinite*. Clays and Clay Minerals, 32, 241-248.
- ECE Ö.İ., SCHROEDER P.A., 2007, *Clay mineralogy and chemistry of halloysite and alunite deposits in the Turplu area-Balikesir-Turkey*, Clays and Clay Minerals, 55(1), 18-35.
- FROST R.L., 1995, *Fourier transform raman spectroscopy of kaolinite, dickite and halloysite*, Clays and Clay Minerals, 43(2), 191-195.

- FROST R.L., KRISTOF J., HORVATH E., KLOPROGGE J.T., 2000, *Rehydration and phase changes of potassium acetate-intercalated halloysite at 298 K*, *Journal of Colloid and Interface Science*, 226, 318-327.
- HORVATH E., KRISTOF J., KURDI R., MAKO E., KHUNOVA V., 2011, *Study of urea intercalation into halloysite by thermoanalytical and spectroscopic techniques*, *Journal of Thermal Analysis and Calorimetry*, 105, 53-59.
- JOUSSEIN E., PETIT S., DELVAUX B., 2007, *Behavior of halloysite clay under formamide treatment*, *Applied Clay Science*, 35, 17-24.
- JOUSSEIN E., PETIT S., FIALIPS C., VIEILLARD P., RIGHI D., 2006, *Differences in the dehydration-rehydration behavior of halloysites: new evidence and interpretations*, *Clays and Clay Minerals*, 54 (4), 473-484.
- LEVIS S.R., DEASY P.B., 2002, *Characterization of halloysite for use as a microtubular drug delivery system*, *International Journal of Pharmaceutics*, 243, 125-134.
- LUEVANOS A.M., DELGADO M.G.R., SALAS A.U., PEDROZA F.R.C., ALARCON J.G.O., 2011, *Leaching kinetics of iron from low grade kaolin by oxalic acid solutions*, *Applied Clay Science*, 51, 473-477.
- MAKO E., SENKAR Z., KRISTOF J., VAGVÖLGYI V., 2006, *Surface modification of mechano-chemically activated kaolinites by selective leaching*, *Journal of Colloid and Interface Science*, 294, 362-370.
- MANDAL S.K., BANERJEE P.C., 2004, *Iron leaching from China clay with oxalic acid: effect of different physico-chemical parameters*, *International Journal of Mineral Processing*, 74, 263-270.
- MELLOUK S., CHERIFI S., SASSI M., MAROUF-KHELIFA K., BENGUEDDACH A., SCHOTT J., KHELIFA, A., 2009, *Intercalation of halloysite from Djebel Debagh (Algeria) and adsorption of copper ions*, *Applied Clay Science*, 44, 230-236.
- MURRAY H.H., 2007, *Applied Clay Mineralogy: Developments in Clay Science 2*, Elsevier, Amsterdam.
- OELKERS E.H., SCHOTT J., GAUTHIER J.M., HERRERO-RONCAL T., 2008, *An experimental study of the dissolution mechanism and rates of muscovite*, *Geochimica et Cosmochimica Acta*, 72, 4948-4961.
- PANDA A.K., MISHRAA B.G., MISHRAC D.K., SINGHA R.K., 2010, *Effect of sulphuric acid treatment on the physico-chemical characteristics of kaolin clay*, *Colloids and Surfaces A: Physicochemical and Engineering Aspects*, 363, 98-104.
- PRUETT R.J., PICKERING S.M., 2006, *Kaolin*, Pp. 383-399 in: *Industrial minerals and rocks: commodities, markets and uses* (J.E. Kogel, N.C. Trivedi, J.M. Barker and S.T. Krukowski, editors) 7th edn. SME. Colorado,
- SAKLAR S., AGRILI H., ZIMITOGLU O., BAŞARA B., KAAAN U., 2012, *The characterization studies of the Northwest Anatolian halloysites/kaolinites*, *Bulletin of the Mineral Research and Exploration*, 145, 48-61.
- SINGER A., ZAREI M., LANGE F.M., STAHR K., 2004, *Halloysite characteristics and formation in the northern Golan Heights*, *Geoderma*, 123, 279-295.
- SONUPARLAK B., SARIKAYA M., AKSAY I.A., 1987, *Spinel phase formation during the 980°C exothermic reaction in the kaolinite-to-mullite reaction series*, *Journal of the American Ceramic Society*, 70 (11), 837-842.
- VEGLIO F., PASSARIELLO B., BARBARO M., PLESCIA P., MARABINI A.M., 1998, *Drum leaching tests in iron removal from quartz using oxalic and sulphuric acids*, *International Journal of Mineral Processing*, 54, 183-200.

- YOON R.H., SHI J., 1986, *Processing of kaolin clay*, Pp 366-379 in: *Advances in Mineral Processing* (P. Somasundran, Editor). AIME, New York.
- ZHANG A., PAN L., ZHANG H., LIU S., YE Y., XIA M., CHEN X., 2012, *Effects of acid treatment on the physico-chemical and pore characteristics of halloysite*, *Colloids and Surfaces A: Physico-chemical and Engineering Aspects*, 396, 182–188.

Received April 24, 2014, reviewed; accepted June 5, 2014

IMPROVING SEPARATION EFFICIENCY OF 6-1 MM COAL BY INTRODUCING VIBRATION ENERGY TO DENSE MEDIUM GAS-SOLID FLUIDIZED BED

Jingfeng HE, Yuemin ZHAO, Zhenfu LUO, Jie ZHAO,
Chenlong DUAN, Yaqun HE

School of Chemical Engineering and Technology, China University of Mining and Technology, Xuzhou 221116, China; jfhe@cumt.edu.cn

Abstract: Effects of the vibration energy on the fluidization quality and separation performance of dense medium gas-solid fluidized bed were investigated experimentally. The magnetite powder with a wide size range of 0.3-0.074 mm was utilized as the basic medium solids. 6-1 mm fine coal sample from Yongcheng (China) was used to perform the separation experiments. The results indicate that the vibration amplitude A and superficial gas velocity U are greatly significant to the fluidization stability and the density distribution uniformity. Comparing with the bed without vibration, the optimal S_p and S_p values of 0.034 kPa and 0.018 g/cm³ are acquired in vibration bed with the operating factors of $A = 1$ mm, $U = 1.8U_{mf}$, $f = 15$ Hz and $H_s = 150$ mm. The coal ash content was reduced from 27.84% to 9.50% at a separating density of 1.68 g/cm³ with a probable error E value of 0.505. The separation efficiency of 6-1mm fine coal is effectively improved by introducing vibration energy to dense medium gas-solid fluidized bed. The technology provides a novel approach to achieve high-efficiency separation of 6-1 mm fine coal in the arid and water-shortage areas.

Keywords: vibration energy, dense medium gas-solid fluidized bed, fluidization quality, density uniformity, separation efficiency

Introduction

The high-efficiency coal beneficiation has been recognized as the most efficient approach to achieve the coal resource saving and environment protection. Water-based wet separation technology is the traditional coal beneficiation process, which has been widely popularized around the world, including the wet dense medium cyclone separation, hydraulic jigging separation, flotation etc. (Brozek and Mlynarczykowska, 2013; Nakhaei and Irannajad, 2013; Svoboda et al., 1998; Sampaio et al., 2008; Zou et al., 2013). However, these technologies are not suitable for the coal separation in arid

and water-shortage areas and countries. Especially, as the gradually decreasing of coal resource, the exploitation and utilization of low-rank coal has become the focused concern. Brown coal is a type of the common low-rank coal, which shows the special physical property of an easy degradation in water. Thus, it is unfavorable to separate brown coal by wet processing technology as well. Therefore, it is significantly important to develop a dry coal beneficiation technology in current energy utilization field.

Recently, a number of scientists and engineers in many countries have contributed to the dry coal beneficiation technology based on the dense medium gas-solid fluidized bed (DMGFB). With the fine glass beads of 2500 kg/m^3 as basic separating medium, Takana and Sato (1996) utilized a $0.2 \text{ m} \times 0.1 \text{ m}$ rectangular fluidized bed separator to separate the mixed coal sample with the densities of 1300 and 1700 kg/m^3 . The coal ash content was reduced from 8.50% to 3.50%. Sahu et al. (2011) investigated the stability of an air dense medium fluidized bed separator (ADMFBS) by different expressions. Indian high ash noncoking coal at particular size (-25+6 mm) was separated with the pilot-scale ADMFBS. The probable error E and imperfection value were found to be 0.12 and 0.071, respectively. Macpherson et al. (2010) designed a Reflux Classifier with an air-sand dense-medium and vibration to achieve an effective separation of 1–8 mm fine coal. Xu et al. (2010) studied the separation performance of bituminous coal by a laboratory continuous Air Dense Medium Fluidized Bed separator. The coal ash content was reduced from 26% to 10% with a recovery rate of 80% for the cleaning coal. Technology University of Aachen developed a new type of vibrating fluidized bed separator without utilizing the separating medium. Raw coal sample with an ash content of 47.5% was effectively separated, and the cleaning coal and tailings with ash contents of 9.6% and 40.0% were finally obtained (Weitkamper et al., 2010). China University of Mining and Technology have been contributing to the fundamental theoretical research and practical application of DMGFB for dry coal beneficiation since 1980s, acquiring lots of achievements in the past few years (Chen and Yang, 2003; Zhao et al., 2004, 2012; He et al., 2012, 2013a-c, 2014). The technology could form stable dense medium fluidized bed by utilizing the fluidizing gas and medium solids within a specified size range. According to Archimedes theorem, the feedstock stratifies according to the bed density with the lighter particles (cleaning coal) floating and the denser particles (tailings) sinking. At present, the 40-60 Mg/h pilot dry coal beneficiation system based on DMGFB has been established and developed, which could achieve a highly efficient separation of 50–6 mm raw coal. However, as the development of the large-scale mechanized coal mining, the cumulative production of <6 mm fine coal increase rapidly year by year. Thus, it is of great significance to develop a novel fine coal beneficiation technology. Normally, the magnetite powder with a wide particle size distribution of 0.3–0.074 mm is utilized as the basic separating medium solids for different sized raw coal. Comparing with the beneficiation of 50–6 mm coarser coal, it needs finer separating medium solids to achieve the effective separation of <6 mm

fine coal. The increasing of the specific surface area of fine magnetite powder leads to the increase of viscosity between medium solids and the decrease of their kinetic activities. The fluidization quality of the bed becomes worsen with unstable bubble dynamical behaviors and circulating back-mixing of fine coal and medium solids, resulting in a bad and unsteady separation performance of <6mm fine coal by density differences. Hence, the vibration and magnetic energy were introduced to fluidized bed in order to improve the separation efficiency (Luo and Chen, 2001; Luo et al., 2002, 2008; Luo and Zhao, 2002). The vibration energy cross the bed could suppress the generation of large bubbles and strengthen the contacting of gas-solid phases and solid-solid phases. The fluidization quality could be significantly improved.

In this work, the fluidization characteristics and separation performance of the DMGFB with and without the vibration were investigated and compared. The significance of the critical operating factors acting on the fluidization quality was analyzed. The separation experiments of 6-1 mm fine coal sample were carried out by applying the fluidized bed separator with and without the vibration, respectively. The improvement of separation efficiency by introducing the vibration energy to DMGFB was studied.

Material and Methods

Materials

Separating medium solids

Preparation of fine magnetite powder needs more energy consumption in the sieving and grinding process. Additionally, it also brings great difficulty for the recycling and reutilization of fine magnetite powder. Thus, it is not suitable for industrial application to use the fine magnetite powder as the separating medium. Therefore, the magnetite powder with a wide particle size distribution of 0.3–0.074 mm was utilized along in the study. The physical properties of different sized magnetite powder are shown in Table 1. The size fractions of the magnetite powder are divided into nine grades. The test results show that the dominant size fractions are 0.3–0.2, 0.2–0.15, 0.15–0.125, 0.125–0.1 and 0.1–0.074 mm, which accounts for 92.55% of the whole. The real density is 4.2 g/cm³. The bulk density decreases gradually from 2.88 to 2.42 g/cm³ with the decrease in fraction size. It is because that the interspaces between the magnetite powders increase gradually with the size decrease. The magnetic material content and magnetization are all larger than 99.30% and 76.0 A²/kg, respectively. The overall physical properties of the magnetite powders indicate a uniform composition of size fraction, a stable density distribution and a higher magnetic material content. Thus, it is greatly favorable to form the steady fluidization environment and uniform density distribution for coal beneficiation by density.

Table 1. The physical properties of magnetite powder

| Size fraction (mm) | Yield (%) | Real density (g/m ³) | Bulk density (g/cm ³) | Magnetic material content (%) | Magnetization (A ² /kg) |
|--------------------|-----------|----------------------------------|-----------------------------------|-------------------------------|------------------------------------|
| >0.300 | 1.10 | 4.2 | 2.88 | 99.36 | 76.01 |
| 0.300-0.200 | 20.91 | 4.2 | 2.85 | 99.53 | 76.21 |
| 0.200-0.150 | 28.39 | 4.2 | 2.71 | 99.61 | 77.33 |
| 0.150-0.125 | 20.33 | 4.2 | 2.66 | 99.59 | 77.52 |
| 0.125-0.100 | 17.46 | 4.2 | 2.62 | 99.72 | 77.98 |
| 0.100-0.074 | 5.36 | 4.2 | 2.59 | 99.68 | 78.11 |
| 0.074-0.060 | 2.51 | 4.2 | 2.55 | 99.43 | 78.16 |
| 0.060-0.050 | 3.02 | 4.2 | 2.52 | 99.52 | 78.21 |
| <0.050 | 0.82 | 4.2 | 2.42 | 99.79 | 78.76 |

Raw coal sample

The basic properties of 6-1mm fine coal sample from Yongcheng (China) were analyzed. The sample has a low moisture content of 2.68%, an ash content of 27.84%, a volatile component of 9.22%, a low sulphur content of 0.37%, and a high heat productivity of 30.51 MJ/kg.

The washability of fine coal sample was analyzed by the float-sink tests, as shown in Table 2 and Fig. 1. The dominant density distribution are <1.3, 1.3-1.4, 1.4-1.5 g/cm³ with a mean ash content of 8.66% and >2.0 g/cm³ with an ash content of 86.41%, accounting for 90.22% of the total products. It indicates that a sufficient dissociation of low-density and high-density products is achieved in fine coal sample, which is beneficial to achieve effective separation.

Table 2. The float-sink results of 6-1mm fine coal sample

| Density (g/cm ³) | Yield (%) | Ash content (%) | Accumulation | | | | Separating density $\delta \pm 0.1$ | |
|------------------------------|-----------|-----------------|--------------|-----------------|-----------|-----------------|-------------------------------------|--------------|
| | | | Floats | | Sinks | | Density (g/cm ³) | Recovery (%) |
| | | | Yield (%) | Ash content (%) | Yield (%) | Ash content (%) | | |
| <1.3 | 9.62 | 4.68 | 9.62 | 4.68 | 100.00 | 27.72 | 1.30 | 55.22 |
| 1.3-1.4 | 45.60 | 7.67 | 55.22 | 7.15 | 90.38 | 30.17 | 1.40 | 59.34 |
| 1.4-1.5 | 13.74 | 14.72 | 68.96 | 8.66 | 44.78 | 53.08 | 1.50 | 18.07 |
| 1.5-1.6 | 4.33 | 24.66 | 73.29 | 9.60 | 31.04 | 70.06 | 1.60 | 6.27 |
| 1.6-1.8 | 3.87 | 36.89 | 77.16 | 10.97 | 26.71 | 77.41 | 1.70 | 3.87 |
| 1.8-2.0 | 1.58 | 55.63 | 78.74 | 11.87 | 22.84 | 84.28 | 1.90 | 1.58 |
| >2.0 | 21.26 | 86.41 | 100.00 | 27.72 | 21.26 | 86.41 | | |
| Total | 100 | 27.72 | | | | | | |
| Coal slurry | 7.78 | 29.26 | | | | | | |
| Total | 100 | 27.84 | | | | | | |

The washability curves are mainly composed of an elementary ash curve, an accumulative floats curve, an accumulative sinks curve, a density curve, and a near-density curve. It could be assumed that the theoretical yield of the cleaning coal could achieve more than 75% with an ash content of 10.0% at a separating density of 1.71 g/cm³. The fine coal sample belongs to the moderate difficulty for separation. Additionally, as the quality of cleaning coal increases, the recovery of cleaning coal decreases and the washability of fine coal sample drops.

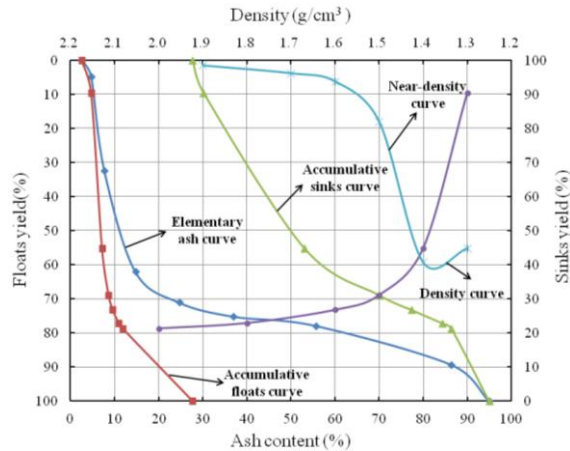


Fig. 1. Washability curves of 6-1mm fine coal sample

Experimental apparatus

Figure 1 illustrates the experimental apparatus of the vibration fluidized bed. It mainly consists of an air supply and control system, vibration fluidized bed separator, measurement devices of bed pressure drop and density, control and adjusting system of vibration parameters. A cylindrical fluidized bed with a diameter of 160 mm and height of 500 mm was designed and installed on the vibration platform. The compressed air generated by a fan blower is pushed into an air buffer, and then transported into the fluidized bed uniformly through a gas distributor located at bed bottom. The gas distributor is composed of double layer filtration fabric and single layer steel wire gauze. The air flowrate is controlled by an air valve, and a rotermeter is used to adjust the gas velocity within a suitable variation range. The pressure drops at different bed heights are measured by the pressure transducer. The bed densities at different bed positions are measured by a group of portable densitometer. The vibration amplitude and frequency of fluidized bed are adjusted by the computer controlling system. The magnetite powder with a wide size range was fed into the fluidized bed initially. The bed expansion height and pressure drops are measured after achieving stable fluidization status. 6-1mm fine coal was a sample fed into bed to carry out the separating experiments. The fine coal sample stratifies by density differences after a certain separating period. Finally, the fine coal samples at different

layers of bed interspaces are taken and tested to compare and verify the separation efficiency.

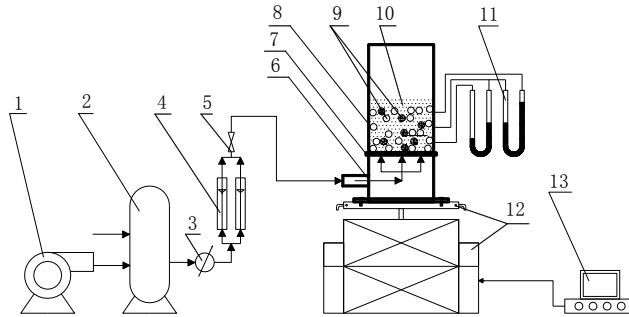


Fig. 2. Experimental apparatus of vibration fluidized bed

1. Fan blower, 2. Air buffer, 3. Air valve, 4. Rotameter, 5. Butterfly valve, 6. Air chamber, 7. Gas distributor, 8. Fluidized bed separator, 9. Fine coal sample, 10. Separating medium solids, 11. Pressure transducer, 12. Vibration platform, 13. Vibration control and adjusting system

Evaluation approach

Bed pressure drop and density distribution are major indicators to evaluate the fluidization quality in DMGFB. Therefore, the standard deviations of pressure drops and densities at different bed positions are proposed to characterize the fluidization stability and density uniformity in the interspaces of bed.

The mean bed pressure is $\bar{P} = \frac{1}{n} \sum_{i=1}^n P_i$, standard deviation of bed pressure drops

$$S_p = \sqrt{\frac{1}{n} \sum_{i=1}^n (P_i - \bar{P})^2}, \text{ mean bed density } \bar{\rho} = \frac{1}{n} \sum_{i=1}^n \rho_i, \text{ standard deviation of bed densities}$$

$$S_\rho = \sqrt{\frac{1}{n} \sum_{i=1}^n (\rho_i - \bar{\rho})^2} \text{ where, } P_i \text{ and } \rho_i \text{ refer to the instantaneous values in position } i, \bar{P}$$

and $\bar{\rho}$ refer to the mean values, n refers to the sample numbers of different positions in bed.

Results and Discussion

Fluidization stability and density distribution uniformity in the bed without vibration

The major factors influencing the fluidization quality of the bed without vibration are the static bed height and superficial gas velocity. The static bed height H_s of 60, 90, 120, 150, 180, 210 and 240 mm were selected, respectively. The minimum fluidization velocity U_{mf} of the bed is 7.2 cm/s at $H_s = 150$ mm. The research achievements indicate that the superficial gas velocity U , should be adjusted in the

range of $U = 1.6\text{--}2.0U_{mf}$ in order to maintain a stable fluidization (He, 2012). Firstly, the effects of the static bed heights on the fluidization quality and density uniformity were investigated at $U = 1.8U_{mf}$ and $1.9U_{mf}$, respectively, as shown in Fig. 3(a) and Fig.3(b). When $U = 1.8U_{mf}$, the standard deviation of bed pressure drops S_p decreases sharply from 0.125 to 0.062Kpa with increasing static bed height H_s from 60 to 150mm. Then, S_p increases sharply from 0.068 to 0.129 kPa with increasing H_s from 180 to 240 mm. It indicates that the bed maintains stable fluctuations of pressure drop with a static bed height H_s of 150-180 mm. Similarly, the standard deviation of bed densities S_ρ varies from 0.043 to 0.045g/cm³ with H_s increasing from 150 to 180 mm, which also indicates a uniform density distribution. The similar conclusion is obtained by analyzing the results at $U = 1.9 U_{mf}$, as shown in Fig. 3(b). Thus, the static bed height should be adjusted in the range of 150-180 mm in this study.

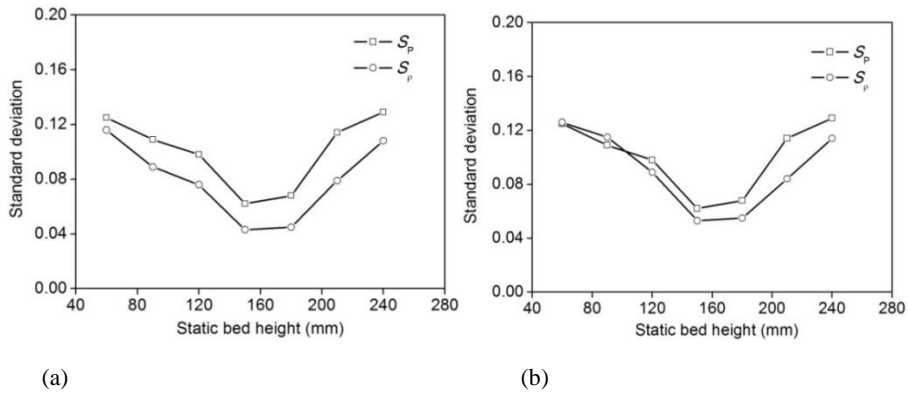


Fig. 3. Effect of the static bed height on the fluidization quality and density uniformity

Figure 4 illustrates the standard deviations of bed pressure drop S_p and bed density S_ρ with different static bed heights H_s of 150, 160, 170, 180 mm at $U = 1.7\text{--}2.0 U_{mf}$, respectively. Overall, the values of S_p and S_ρ increase slightly with the H_s increasing from 150 to 180mm. It means that the fluctuations of bed pressure drops and densities increase slightly. The reason is that the distance of the rising bubbles passing through the bed increases with the increasing of H_s . It leads to an intense bubble kinetic behavior and the back-mixing of fine medium solids. Thus, the stability of the whole bed decreases slightly. However, as H_s vary in a suitable extent, the value of S_p maintains stable variation of 0.06–0.08 kPa, and the value of S_ρ also shows steady variation of 0.04–0.07 g/cm³. Especially, when $U = 1.8U_{mf}$ (12.96 cm/s), the optimal S_p and S_ρ values of 0.062 Kpa and 0.043 g/cm³ are acquired at $H_s = 150$ mm. The results indicate that the favorable fluidization stability and uniform density distribution could be achieved by setting a suitable static bed height and selecting a reasonable superficial gas velocity.

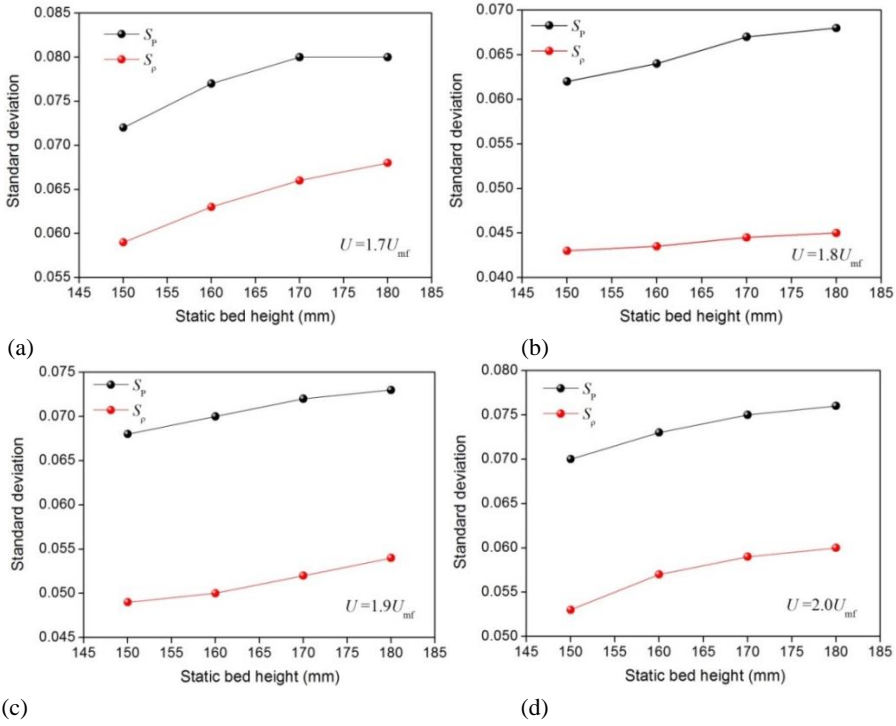


Fig. 4. The standard deviations of bed pressure drop S_p and bed density S_ρ at different gas velocity

Fluidization stability and density distribution uniformity in vibration bed

Based on the traditional DMGFB, the vibration energy is introduced to improve the fluidization quality and separation efficiency. The major factors influencing the fluidization quality include the vibration amplitude, vibration frequency, static bed height and superficial gas velocity. In order to examine the effects of above factors on the fluidization quality, a group of orthogonal experiment was designed to verify the S_p and S_ρ values under different operating conditions. Table 3 shows the levels of the factors used in the experiment. Four levels were selected for each factor. The designed experimental program and analyzed results of orthogonal experiment are listed in Table 4. 16 interactive experiments were designed and conducted under different operating conditions, and the values of S_p and S_ρ were obtained in each experiment. The analyzed results show that the value of S_p mainly distributes in the range of 0.034–0.072 kPa, and S_ρ value of 0.018–0.056 g/cm³. The analysis of a variance approach is applied to verify the significance of four factors. The analyzed results are shown in Table 5, among which, F value represents the significance of different factor. Normally, the larger the F value is, the more significance of the factor is emphasized. Hence, it could be obtained that the significance of four factors appears vibration amplitude $A >$ superficial gas velocity $U >$ vibration frequency $f >$ static bed height H_s . The most significant factors influencing the fluidization quality are

vibration amplitude A and superficial gas velocity U with the F values of 4.42 and 4.11, respectively. The static bed height H_s shows the least influence. Therefore, factors of A and U should be considered as the most important operating condition in vibration bed. In the orthogonal experiment, the optimal S_p and S_ρ values of 0.034 kPa and 0.018 g/cm³ are acquired with the operating factors of $A = 1$ mm, $U = 1.8U_{mf}$, $f = 15$ Hz and $H_s = 150$ mm, respectively.

Table 3. The levels of different factors used in the experiment

| No. | Factors | | | |
|-----|---------------------------------|---------------------------------|---------------------------------|--|
| | Vibration amplitude A (mm) | Vibration frequency f (Hz) | Static bed height H_s (mm) | Superficial gas velocity U (cm/s) |
| 1 | 1 | 10 | 120 | $1.7 U_{mf}$ |
| 2 | 2 | 15 | 150 | $1.8 U_{mf}$ |
| 3 | 3 | 20 | 180 | $1.9 U_{mf}$ |
| 4 | 4 | 25 | 210 | $2.0 U_{mf}$ |

Table 4. The designed program and results of orthogonal experiment

| No. | Factors | | | Evaluation indexes | | |
|-----|---------------------------------|---------------------------------|---------------------------------|--|----------------|----------------------------------|
| | Vibration amplitude A (mm) | Vibration frequency f (Hz) | Static bed height H_s (mm) | Superficial gas velocity U (cm/s) | S_p (Kpa) | S_ρ (g/cm ³) |
| 1 | 1 | 10 | 120 | $1.7 U_{mf}$ | 0.037 | 0.023 |
| 2 | 1 | 15 | 150 | $1.8 U_{mf}$ | 0.034 | 0.018 |
| 3 | 1 | 20 | 180 | $1.9 U_{mf}$ | 0.041 | 0.029 |
| 4 | 1 | 25 | 210 | $2.0 U_{mf}$ | 0.052 | 0.046 |
| 5 | 2 | 10 | 150 | $1.9 U_{mf}$ | 0.039 | 0.024 |
| 6 | 2 | 15 | 120 | $2.0 U_{mf}$ | 0.050 | 0.043 |
| 7 | 2 | 20 | 210 | $1.7 U_{mf}$ | 0.037 | 0.022 |
| 8 | 2 | 25 | 180 | $1.8 U_{mf}$ | 0.039 | 0.025 |
| 9 | 3 | 10 | 180 | $2.0 U_{mf}$ | 0.043 | 0.030 |
| 10 | 3 | 15 | 210 | $1.9 U_{mf}$ | 0.048 | 0.035 |
| 11 | 3 | 20 | 120 | $1.8 U_{mf}$ | 0.067 | 0.053 |
| 12 | 3 | 25 | 150 | $1.7 U_{mf}$ | 0.055 | 0.045 |
| 13 | 4 | 10 | 210 | $1.8 U_{mf}$ | 0.063 | 0.048 |
| 14 | 4 | 15 | 180 | $1.7 U_{mf}$ | 0.051 | 0.039 |
| 15 | 4 | 20 | 150 | $2.0 U_{mf}$ | 0.072 | 0.056 |
| 16 | 4 | 25 | 120 | $1.9 U_{mf}$ | 0.054 | 0.041 |

Table 5. Analysis of variance for the orthogonal experiment

| Variance source | Sum of squares | Degrees of freedom | Mean square | <i>F</i> value | Confidence interval of <i>F</i> value | Significance |
|----------------------|----------------|--------------------|--------------|----------------|---------------------------------------|--------------|
| <i>A</i> | $2.4e^{-3}$ | 3 | $8.14e^{-4}$ | 4.42 | [3.86,6.99] | Significant |
| <i>f</i> | $6.38e^{-4}$ | 3 | $2.13e^{-4}$ | 1.15 | [3.86,6.99] | -- |
| <i>H_s</i> | $3.21e^{-4}$ | 3 | $1.07e^{-4}$ | 0.58 | [3.86,6.99] | -- |
| <i>U</i> | $2.3e^{-3}$ | 3 | $7.57e^{-4}$ | 4.11 | [3.86,6.99] | Significant |
| Error | $1.7e^{-3}$ | 9 | $1.84e^{-4}$ | | | |
| Sum | $6.4e^{-3}$ | 15 | | | | |

Comparison of bed stability and density uniformity in the bed with and without vibration

Bed stability and density uniformity in the bed with and without vibration were compared to investigate the effect of the vibration energy. Under the optimal operating conditions, the pressure drop fluctuation of the whole bed was compared with and without vibration, as presented in Fig. 5. In general, the pressure drop of the bed without vibration is approximate 6.6 kPa after achieving a stable fluidization. It is a little larger than the bed pressure drop of 5.6 kPa in vibration bed. The minimal fluidization velocity U_{mf} of the bed without vibration is 7.2 cm/s, which is also larger than U_{mf} of 4.9 cm/s in vibration bed. Comparing with the bed without vibration, introducing the vibration energy obviously lowers bed pressure drop and decreases the minimum of the fluidized velocity of the bed. It is because that the effect of vibration energy enhances the collision and friction between the fine medium solids, which leads to a great loose effect on the static packed bed. It provides a favorable condition for the gas to overcome the bed resistance and pass through the interspace of the packed fine powders. As the enhancement of the interaction between the vibration energy and gas, the whole bed changes to a complete fluidization state gradually. At the moment, fine medium solids in the bed were held up with the effects of gas and effective excitation force. Then, the movement behaviors of fine particles change to the free-moving states with the effects of their own natural vibration. Therefore, the bed not only shows favorable stability across its whole space, but also owns sufficient activity. It is greatly conducive to the effective separation of 6-1 mm fine coal.

Additionally, it has an obvious turning point of bed pressure drop before achieving a stable fluidization of the bed without fluidization. The fluctuation of bed pressure drop is a little intense at $U < 1.7U_{mf}$ (12.24 cm/s). However, it shows a smooth transition when achieving stable fluidization in vibration bed. The bed pressure drop maintains a steady variation with less fluctuation for the increase of gas velocity after achieving U_{mf} (4.9 cm/s). It also indicates that the vibration energy is helpful to form good fluidization quality at a smaller gas velocity in a short period. If increasing the vibration amplitude and superficial gas velocity further, the collision and friction between the fine powders will become more intense, resulting in the exacerbation of back-mixing of medium solids. Besides, as the increasing of gas velocity, the bubble

quantity and sizes will increase rapidly and the bubble kinetic behaviors will become more complex and confused. These performances of fine medium solids and rising bubbles worsen the fluidization quality and density uniformity in bed. Thus, the significant factors of vibration amplitude A and superficial gas velocity U should be adjusted in a suitable variation range so as to maintain the bed stability and density uniformity in vibration bed.

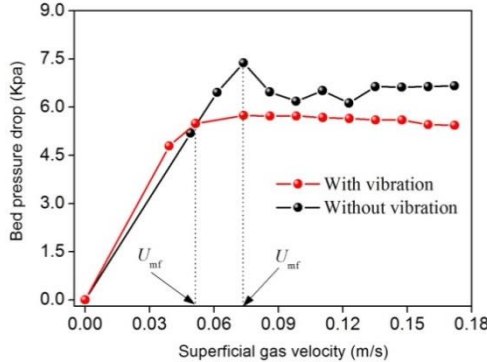


Fig. 5. Pressure drop fluctuation of the bed with and without vibration

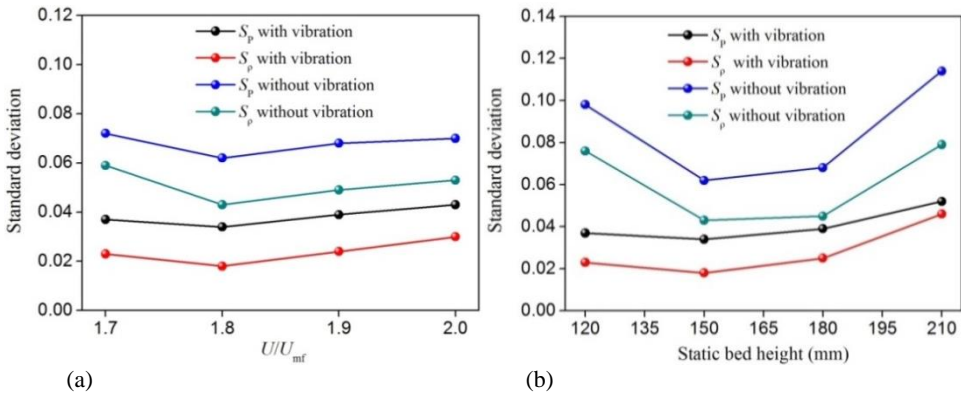


Fig. 6. Comparison results of S_p and S_ρ values in the bed with and without vibration

The comparison of the standard deviations of bed pressure drop S_p and bed density S_ρ are presented in Fig. 6. The values of S_p and S_ρ in the bed with and without vibration were compared at $U = 1.7, 1.8, 1.9$ and $2.0U_{mf}$, respectively, as shown in Fig. 6(a). The S_p and S_ρ values in the vibration bed are obviously smaller than the values without vibration. The optimal S_p and S_ρ values of 0.034 kPa and 0.018 g/cm³ with vibration are much smaller than the optimal values of 0.062 kPa and 0.043 g/cm³ without the vibration at $U = 1.8U_{mf}$. Comparing with the bed without vibration, S_p and S_ρ values reduce sharply by 45.2% and 58.1%. This indicates a more stable fluidization quality and uniform density distribution in vibration bed. The values of S_p and S_ρ in the bed with and without vibration were also compared at different static bed

height H_s of 120, 150, 180 and 210 mm, respectively, as shown in Fig. 6(b). Similarly, the comparison of the results shows that the S_p and S_ρ values are obviously smaller in vibration bed. The optimal S_p and S_ρ values reduce sharply by 45.2% and 58.1% as well at $H_s = 150$ mm. Thus, the vibration energy with a suitable vibration amplitude and frequency should be introduced to DMGFB for better fluidization quality and separation efficiency.

Comparison of separation performance of 6-1mm fine coal in the bed with and without vibration

The separation performance of 6-1 mm fine coal sample from Yongcheng (China) applying the fluidized bed with and without vibration were compared and analyzed with the optimal operating conditions. The detailed operating parameters in the separation experiments are listed in Table 6.

Table 6. Detailed operating parameters in separation experiments

| Operating parameter | Without vibration | With vibration |
|-------------------------------------|-------------------|----------------|
| Vibration amplitude A (mm) | 0 | 1 |
| Superficial gas velocity U (cm/s) | 12.96 | 8.82 |
| Vibration frequency f (Hz) | 0 | 10 |
| Static bed height H_s (mm) | 150 | 150 |
| Separating time T (s) | 60 | 60 |

After achieving stable fluidization, a certain amount of 6-1mm fine coal sample was fed into the fluidized bed separator with and without the vibration, respectively. After the separating time of 60 seconds, the feedstock stratifies by the density differences. Then, the products distributing in different layers of the bed were removed from the bed to carry out the float-sink experiments. The partition curves of the separation experiments are shown in Fig. 7.

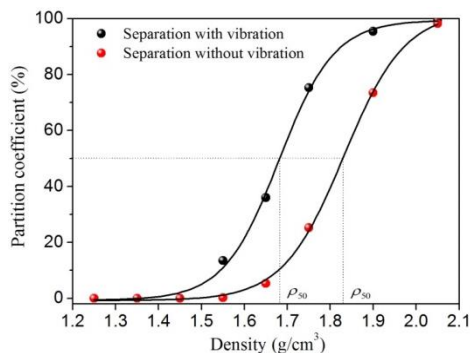


Fig. 7. Partition curves of the separation experiments with and without vibration

The partition coefficient represents the mass fraction of coal particles reporting to the tailing. The coal particles with densities of ρ_{25} , ρ_{50} and ρ_{75} have the mass fractions

of 25%, 50% and 75%, respectively. ρ_{50} represents the separating density in the experiment. The value of probable error E could be calculated as $(\rho_{75} - \rho_{25})/2$. The lower E value indicates the better separation performance. The ash content of 6–1mm fine coal was reduced from 27.84% to 9.50% at a separating density of 1.68 g/cm³ in the separation experiments with vibration. The probable error E shows 0.505, which is much lower than the E value of 0.9 in the separation experiments without vibration. It demonstrates that the vibration fluidized bed performs favorable separation efficiency of 6-1mm fine coal.

Conclusions

The vibration amplitude A and superficial gas velocity U are the most significant factors influencing the fluidization stability and density distribution uniformity. The optimal operating factors are $A = 1$ mm, $U = 1.8 U_{mf}$, $f = 15$ Hz and $H_s = 150$ mm with S_p and S_ρ values of 0.034 kPa and 0.018 g/cm³, respectively.

Comparing with the bed without vibration, the minimum fluidization velocity U_{mf} was lowered from 7.2 to 4.9 cm/s, and the optimal values of S_p and S_ρ reduced sharply by 45.2% and 58.1% at $H_s = 150$ mm. It indicates that introducing a vibration energy to the bed could effectively improve the fluidization quality and separation density environment.

The ash content of 6-1mm fine coal from Yongcheng (China) was reduced from 27.84% to 9.50% at a separating density of 1.68 g/cm³ in the separation experiments with vibration. A probable error E value of 0.505 was achieved, indicating a favorable separation performance in vibration bed. This technology provides a novel approach to deal with the 6-1 mm fine coal in arid and water-shortage areas.

Acknowledgements

We gratefully acknowledge the financial supported by the Fundamental Research Funds for the Central Universities (2014QNA28) and The National Natural Science Foundation of China (No.51221462).

References

- BROZEK M., MLYNARCZYKOWSKA A., 2013. *An analysis of effect of particle size on batch floatation of coal*. Physicochemical Problems of Mineral Processing, 49(1), 341–356.
- CHEN Q.R., YANG Y., 2003. *Development of dry beneficiation of coal in China*. Coal Preparation, 23(1-2), 3-12.
- HE J.F., 2012. *Numerical simulation of multiphase fluid dynamic in air dense medium fluidized bed based on Euler-Euler model*. PhD Thesis: China University of Mining and Technology, Xuzhou, China. (In Chinese)
- HE J.F., HE Y.Q., ZHAO Y.M., DUAN C.L., YE C.L., 2012. *Numerical simulation of the pulsing air separation field based on CFD*. International Journal of Mining Science and Technology, 22(2), 201-207.
- HE J.F., ZHAO Y.M., HE Y.Q., LUO Z.F., DUAN C.L., 2013b. *Fluidization characteristics of the dense Gas-solid fluidized bed separator based on the Mixed-medium solids of magnetite and paigeite powder*. International Journal of Coal Preparation and Utilization, 33 (5), 225-241.

- HE J.F., ZHAO Y.M., HE Y.Q., LUO Z.F., DUAN C.L., 2013c. *Separation performance of raw coal from South Africa using the dense gas-solid fluidized bed beneficiation technique*. Journal of The Southern African Institute of Mining and Metallurgy, 113 (7), 575-582.
- HE J.F., ZHAO Y.M., HE Y.Q., LUO Z.F., DUAN C.L., 2014. *Force characteristic of the large coal particle moving in a dense medium gas-solid fluidized bed*. Powder Technology, 254, 548-555.
- HE J.F., ZHAO Y.M., HE Y.Q., WALZEL P., SCHALDACH G., DUAN C.L., 2013a. *Force measurement and calculation of the large immersed particle in dense gas-solid fluidized bed*. Powder Technology, 241, 204-210.
- HE J.F., ZHAO Y.M., LUO Z.F., HE Y.Q., DUAN C.L., 2013d. *Numerical simulation and experimental verification of bubble size distribution in an air dense medium fluidized bed*. International Journal of Mining Science and Technology, 23 (3) ,387-393.
- LUO Z.F., ZHAO Y.M., 2002. *Beneficiation Theory of Fluidization*. China University of Mining and Technology Press, Xuzhou, China. (In Chinese)
- LUO Z.F., ZHAO Y.M., CHEN Q.R., FAN M.M., TAO X.X., 2002. *Separation characteristics for fine coal of the magnetically fluidized bed*. Fuel Processing and Technology, 79(1), 63-69.
- LUO Z.F., CHEN Q.R., 2001. *Dry beneficiation technology of coal with an air dense medium fluidized bed*. International Journal of Mineral Processing, 63, 167-175.
- LUO Z.F., CHEN Q.R., 2001. *Effect of fine coal accumulation on dense phase fluidized bed performance*. International Journal of Mineral Processing, 63(2), 217-224.
- LUO Z.F., FAN M.M., ZHAO Y.M., TAO X.X., CHEN Q.R., CHEN Z.Q., 2008. *Density-dependent separation of dry fine coal in a vibrated fluidized bed*. Powder Technology, 187 (2) , 119-123.
- MACPHERSON S.A., IVESON S.M., GALVIN K.P., 2010. *Density based separations in the Reflux Classifier with an air-sand dense-medium and vibration*. Minerals Engineering, 23, 74-82.
- NAKHAEI F., IRANNAJAD M., 2013. *Prediction of on-line froth depth measurement errors in industrial flotation columns: a promising tool for automatic control*. Physicochemical Problems of Mineral Processing, 49(2), 757-768.
- PRASHANT D., XU Z., SZYMANSKI J., GUPTA R., BODDEZ J., 2010. *Dry cleaning of coal by a laboratory continuous Air Dense Medium Fluidized Bed separator*. 2010 International Coal Preparation Congress, Lexington, America.
- SAHU A.K., TRIPATHY A., BISWAL S.K., PARIDA A., 2011. *Stability study of an air dense medium fluidized bed separator for beneficiation of high-ash Indian coal*. International Journal of Coal Preparation and Utilization, 31 (3-4), 127-148.
- SAMPAIO C.H., ALIAGA W., PACHECO E.T., PETTER E., WOTRUBA H., 2008. *Coal beneficiation of Candiota mine by dry jigging*. Fuel Processing Technology, 89(2), 198-202.
- SVOBODA J., COETZEE C., CAMPBELL Q.P., 1998. *Experimental investigation into the application of a magnetic cyclone for dense medium separation*. Minerals Engineering, 11(6), 501-509.
- TAKANA Z., SATO H., KAWAI M., OKADA K., TAKAHASHI T., 1996. *Dry Coal Cleaning Process for High-quality Coal*. Journal of chemical engineering of Japan, 29(2), 257-263.
- WEITKAMPER L., WOTRUBA H., SAMPAIO C.H., 2010. *Effective dry density beneficiation of fine coal using a new developed fluidized bed separator*. 2010 International Coal Preparation Congress, Lexington, America.
- ZHAO Y.M., LUO Z.F., CHEN Q.R., 2004. *Fundamental and practical developments of dry coal cleaning in China: a Review*. Coal Preparation Society of America Journal, 3 (3), 14-18.
- ZHAO Y.M., TANG L.G., LUO Z.F., LIANG C.C., XING H.B., DUAN C.L., SONG S.L., 2012. *Fluidization characteristics of a fine magnetite powder fluidized bed for density-based dry separation of coal*. Separation Science and Technology , 47 (16), 2256-2261.
- ZOU W.J., CAO Y.J., ZHANG Z.J., LIU J.T., 2013. *Coal petrology characteristics of middlings from Qianjiaying fat coal mine*. International Journal of Mining Science and Technology, 23 (5) ,777-782.

Received November 29, 2013; reviewed; accepted July 22, 2014

APPLICATION OF LEACHING KINETICS MODELLING TO A GOLD CYANIDE LEACH PLANT BY USING REAL PLANT DATA

Baris SAYINER

Independent researcher, Izmir, Turkey; bsayiner@outlook.com

Abstract: Gold cyanide leach kinetics modeling was applied to the Bergama Ovacik gold cyanide leach plant in Turkey by processing the real plant data without need of any laboratory work. For this aim, solid ore samples were taken from each leaching tanks and analysed for gold contents as Au ppm while plant variables such as solid % concentrations in each tank, feed rate of plant as megagrams per hour (Mg/h), slurry flow rate as m³/h and the slurry residence times in each tank calculated and noted for modelling study. Five sampling work performed at plant at different times. Each sampling data were modelled separately by the Anglo-American Research Laboratories (AARL) leach kinetics model to obtain five separate model parameters and regression coefficient (R^2) values. Then, total five sampling data were all together modelled to obtain just one model equation and R^2 value to represent the plant generally. All R^2 values were above 0.90 indicating that the AARL gold leaching kinetics model fits well on real plant leaching conditions. By using the model parameters, the residual gold contents in each tank were predicted for different possible ore feed rate tonnages such as 80, 90, 100, 110 and 120 megagrams per hour. Thus, leaching recoveries for any ore feed rate would be estimated for possible tonnage increases in the future.

Keywords: gold, cyanide, leach, kinetics, model

Introduction

Gold is produced from its ores by cyanide leaching. The cyanide leaching process is applied by, first, grinding the ore below 75 micrometers and dissolving gold as $\text{Au}(\text{CN})_2^-$ by mixing the ground ore with dilute cyanide solution to obtain slurry above pH 10 and by providing oxygen to the leaching tanks. Dissolution of gold-cyanide completes in about 24 hours. The hydrometallurgical reaction for extracting gold from its ores can be shown as:



Following dissolution of gold in leaching tanks, the slurry passes through the carbon adsorption tanks. In those tanks, granulated activated coconut carbon is mixed with the slurry and the dissolved gold is adsorbed by carbon. Thus, gold loaded carbon is separated from the barren slurry and gold is stripped from the carbon. (Cerovic et al., 2005; Davidson and Sole, 2007; Pleysier, et al. 2008).

The slurry passes from the leaching tanks to the first adsorption tank through the last tank, while the activated carbon follows the reverse direction from the last tank to the first one. By this counter current flow of the slurry and carbon. The $\text{Au}(\text{CN})_2^-$ complex is loaded onto the carbon. At the first adsorption tank the most Au loaded final activated carbon is obtained and the loaded gold is gained by stripping it from carbon by the column elution method. To prevent the granulated carbon to move the slurry, there are special sieves at the tanks discharge openings, so carbon is driven in a reverse direction by special carbon pumps.

The research study was performed by using plant data of the gold cyanide leaching plant in Ovacik Gold Mine in Turkey. The Ovacik gold cyanide leach plant includes initial two leaching tanks and following eight adsorption tanks. In both leaching and adsorption tanks, gold dissolution from the ore continues. Leaching time of the ore depends on the feed tonnage rate, solid concentration and the amount of the leach and adsorption tanks. Thus, the gold contents of the solid residue samples from each tank provides an opportunity to model the leach kinetics of the plant. By modeling the plant, the residual gold contents in each tank, thus the final gold % recovery was predicted for any planned ore feed rates and for any gold contents of the feed ore.

In the literature, several gold ore cyanide leach kinetics modelling laboratory investigations were conducted (Bellec et al., 2009; de Andrade Lima, 2007; Guo et al., 2004; Jeffrey, et al., 2001; Rubisova et al., 1996; Srithammavut et al., 2011; Woollacott et al., 1990). There, the plant data were used for the modelling of the cyanide leach kinetics of gold.

Gold cyanide leach kinetics model

Modelling study was performed by using AARL (Anglo American Research Laboratories) gold cyanide leach kinetics model (Woollacott, L.C. et. al., 1990). The model is described by Eqs. 2 and 3:

$$R = -\frac{dS(t)}{dt} \quad (2)$$

$$R = a \frac{S_0}{(a + bt)^2} \quad (3)$$

Thus, integration of Eqs. 2 and 3 gives Eq. 4:

$$S(t) = S_0 \left(1 - \frac{t}{a + bt} \right). \tag{4}$$

In the equations, R is decreasing of the ore gold content, depending on leaching time, t . Parameter S_0 is the initial gold content of the ore (ppm), $S(t)$ is the ore content at time t , while a and b are parameters that are determined by a non linear regression analysis. Once the a and b parameters are determined modelling of the plant can be performed for any ore feed rate, solid concentration and tank volume.

Materials and methods

Plant data were used for the gold leach kinetics modelling. The Ovacik plant has two leaching tanks and eight adsorption tanks. At five different times, the residual solid from each tank were taken and analysed for gold while the ore feed rate and solid concentration values, occurred at the time of sampling, were noted. For a feed rate (Mg per hour), solid concentration (%) and tank volumes (m³), residence time (h) and flow rate (m³/h), of the slurry in each tank were calculated. The plant data for the five separated sampling conditions were shown in Tables 1 and 2.

Table 1. Plant data for the five different samplings

| | Leaching time (slurry residence time in tank) t , hours | | | | | |
|-------------------------------------|---|--------|--------|--------|--------|--------|
| | Tank volume m ³ | A | B | C | D | E |
| Leach tank 1 | 749 | 4.42 | 5.14 | 5.58 | 5.19 | 4.44 |
| Leach tank 2 | 743 | 8.80 | 10.23 | 11.11 | 10.35 | 8.84 |
| Ads. tank 1 | 256 | 10.31 | 11.99 | 13.02 | 12.12 | 10.36 |
| Ads. tank 2 | 252 | 11.79 | 13.71 | 14.90 | 13.87 | 11.85 |
| Ads. tank 3 | 249 | 13.26 | 15.42 | 16.75 | 15.60 | 13.33 |
| Ads. tank 4 | 246 | 14.71 | 17.11 | 18.59 | 17.30 | 14.79 |
| Ads. tank 5 | 242 | 16.14 | 18.77 | 20.39 | 18.98 | 16.22 |
| Ads. tank 6 | 239 | 17.55 | 20.41 | 22.17 | 20.64 | 17.64 |
| Ads. tank 7 | 236 | 18.94 | 22.02 | 23.93 | 22.28 | 19.04 |
| Ads. tank 8 | 232 | 20.30 | 23.61 | 25.65 | 23.89 | 20.41 |
| slurry flow rate, m ³ /h | | 169.62 | 145.85 | 134.24 | 144.19 | 168.72 |
| feed tonnage, Mg/h | | 90 | 88 | 81 | 87 | 105 |
| solid concentration, % | | 40 | 44 | 44 | 44 | 45 |

Gold contents in each solid residue in the tanks are given in Table 2. By using plant data noted in Tables 1 and 2, modelling was performed by considering the five plant conditions both separately (A, B, C, D, E) and together to determine one a and b parameter which would be applicable for all plant sampling conditions.

Table 2. Gold contents of the residue in each tanks for the five sampling periods

| | Au content in residue solid, ppm | | | | |
|--------------|----------------------------------|------|------|------|------|
| | A | B | C | D | E |
| Leach tank 1 | 1.70 | 4.55 | 1.25 | 1.37 | 1.28 |
| Leach tank 2 | 1.44 | 3.49 | 0.81 | 0.97 | 1.01 |
| Ads. tank 1 | 0.98 | 2.16 | 0.52 | 0.51 | 0.59 |
| Ads. tank 2 | 0.68 | 1.56 | 0.40 | 0.43 | 0.33 |
| Ads. tank 3 | 0.63 | 1.36 | 0.29 | 0.41 | 0.32 |
| Ads. tank 4 | 0.54 | 1.07 | 0.23 | 0.38 | 0.27 |
| Ads. tank 5 | 0.47 | 0.86 | 0.22 | 0.33 | 0.24 |
| Ads. tank 6 | 0.44 | 0.77 | 0.20 | 0.31 | 0.20 |
| Ads. tank 7 | 0.32 | 0.69 | 0.17 | 0.28 | 0.18 |
| Ads. tank 8 | 0.25 | 0.61 | 0.16 | 0.26 | 0.16 |

Results and discussion

First, by using the AARL (Anglo-American Research Laboratories) model equation (4), the five conditions were modelled to find a , b and S_0 model parameters by non linear regression analysis. Besides, regression coefficients (R^2) were found for the five conditions. The modelling results for five conditions are shown in Table 3.

Table 3. Model parameters determined for five plant periods

| | A | B | C | D | E |
|-------|--------|--------|--------|--------|--------|
| a | 10.67 | 7.84 | 4.69 | 3.19 | 5.72 |
| b | 0.56 | 0.72 | 0.85 | 0.92 | 0.76 |
| S_0 | 2.65 | 8.46 | 3.10 | 3.97 | 2.59 |
| R^2 | 0.9406 | 0.9470 | 0.9675 | 0.9333 | 0.9122 |

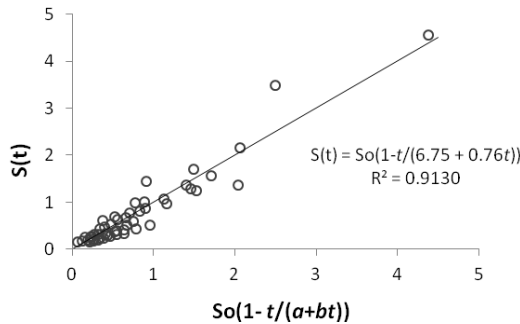


Fig. 1. The plants characteristic leach kinetics model graph

Thus, for the first modelling study model parameters a , b and S_0 were calculated for the five conditions separately. As shown in Table 3, all R^2 values are above 0.90

indicating the AARL model is appropriate for the plant gold leaching modelling. Secondly, all five plant data were modelled together to obtain one a and b parameters. The model graph is shown in Fig. 1. In Figure 1, the model graph and equation indicating the general leach kinetics characteristic of the plant are shown. The R^2 value is 0.9130 indicating that the model fits well to the plant leaching kinetics. The a and b values are determined as 6.75 and 0.76, respectively. Besides, S_0 is determined as 4.15 ppm, which is the average ore feed gold content of the plant.

Consequently, the plant was modelled according to the model parameters a and b , 6.75 and 0.76 respectively for different feed rates as 80, 90, 100, 110 and 120 Mg/h. For those feed rates, the final gold recovery and residual gold contents in each tank were predicted. The prediction results are shown in Table 4.

Table 4. The predicted values of residual gold contents and final gold recoveries for different feed rates

| | Predicted Au content in residue, ppm | | | | |
|-----------------------|--------------------------------------|-------|-------|-------|-------|
| | | | | | |
| Leach tank 1 | 2.03 | 2.18 | 2.31 | 2.42 | 2.52 |
| Leach tank 2 | 1.10 | 1.26 | 1.40 | 1.53 | 1.65 |
| Ads. tank 1 | 0.89 | 1.04 | 1.19 | 1.32 | 1.43 |
| Ads. tank 2 | 0.71 | 0.87 | 1.00 | 1.13 | 1.25 |
| Ads. tank 3 | 0.57 | 0.71 | 0.85 | 0.98 | 1.09 |
| Ads. tank 4 | 0.44 | 0.58 | 0.72 | 0.84 | 0.95 |
| Ads. tank 5 | 0.33 | 0.47 | 0.60 | 0.72 | 0.83 |
| Ads. tank 6 | 0.24 | 0.37 | 0.50 | 0.61 | 0.72 |
| Ads. tank 7 | 0.15 | 0.28 | 0.41 | 0.52 | 0.63 |
| Ads. tank 8 | 0.08 | 0.21 | 0.32 | 0.44 | 0.54 |
| Total leach time, h | 25.98 | 23.09 | 20.78 | 18.89 | 17.32 |
| feed tonnage, Mg/h | 80 | 90 | 100 | 110 | 120 |
| Solid concentration % | 44 | 44 | 44 | 44 | 44 |
| Feed Au content g/Mg | 4.15 | 4.15 | 4.15 | 4.15 | 4.15 |
| Final Au recovery, % | 98.05 | 95.03 | 92.18 | 89.50 | 86.97 |

According to Table 4, the final gold recoveries and residual gold contents in each tank were predicted for 80, 90, 100, 110 and 120 Mg/h. The final gold recovery is decreased down to 86.97% in case of 120 Mg/h. Thus, as the planned tonnage increases, additional leaching and adsorption tanks may be considered to maintain the higher gold recoveries. The amount of additional tanks may be determined by this modelling work as well.

Conclusions

Gold cyanide leaching kinetics modelling of the Ovacik Plant were performed by using plant data, first by five different plant periods, secondly by all five periods together to determine the characteristic leach kinetics model parameters of the plant. Consequently, according to the model parameters a , and b , the expected gold

recoveries and expected residual gold contents in each tank were predicted for feed rates of 80, 90, 100, 110 and 120 megagrams per hour.

The AARL model was used to model the leach kinetics of the plant. All modelling regression coefficients (R^2) values were above 0.90, indicating that the AARL model fits well to the Ovacik plant and the predictions performed depending on this model were reasonable.

References

- BELLEÇ, S., HODOUIN, D., BAZIN, C., KHALESİ, M. R. AND DUCHESNE C. 2009. *Modelling and simulation of gold ore leaching*. World Gold Conference 2009, The Southern African Institute of Mining and Metallurgy, 51–60.
- CEROVIC, K., HUTCHISON, H., SANDENBERGH, R.F., 2005. *Kinetics of gold and a gold – 10% silver alloy dissolution in aqueous cyanide in the presence of lead*, Minerals Engineering 18, 585–590.
- DAVIDSON, R.J. AND SOLE, M.J. 2007. *The major role played by calcium in gold plant circuits*. The Journal of The Southern African Institute of Mining and Metallurgy, Volume 107 refereed paper July 463–468.
- DE ANDRADE LIMA, L.R.P., 2007. *Dynamic Simulation of the Carbon in Pulp and Carbon in Leach Processes* Brazilian Journal of Chemical Engineering Vol. 24, No. 04, 623–635.
- GUO, H., DESCHÊNES, G., PRATT A., FULTON M., LASTRA R. 2004. *Leaching Kinetics and Mechanisms of Surface Reactions During Cyanidation of Gold in the Presence of Pyrite or Stibnite* SME Annual Meeting Denver, Colorado 1–8.
- JEFFREY, M. I., BREUER, P. L., CHOO W. L. 2001. *A kinetic study that compares the leaching of gold in the cyanide, thiosulfate, and chloride systems* Metallurgical and Materials Transactions B, Volume 32, Issue 6, 979–986.
- PLEYSIER, R., DAI, X., WINGATE, C.J., JEFFREY, M.I. 2008. *Microtomography based identification of gold adsorption mechanisms, the measurement of activated carbon activity, and the effect of frothers on gold adsorption* Minerals Engineering, Volume 21, Issue 6, May, 453–462
- RUBISOVA, D.H., PAPANGELAKISA, V.G., KONDOSA, P.D. 1996. *Fundamental kinetic models for gold ore cyanide leaching* Canadian Metallurgical Quarterly Volume 35, Issue 4, 353–361.
- SRITHAMMAVUT, W., LUUKKANEN, S., LAARI, A., KANKAANPÄÄ, T., TURUN I. 2011. *Kinetic Modelling of Gold Leaching and Cyanide Consumption in Intensive Cyanidation of Refractory Gold Concentrate*, Journal of the University of Chemical Technology and Metallurgy, Volume 46, 2, 181–190.
- WOOLLACOTT, L.C., STANGE, W. AND KING, R.P. 1990. *Towards more effective simulation of CIP and CIL processes. 1. The modelling of adsorption and leaching* J. S. Afr. Inst. Min. Metal., vol. 90, no. 10., 275–282.

Received July 21, 2014; reviewed; accepted August 1, 2014

THE USE OF CONTINUOUS CENTRIFUGAL GRAVITY CONCENTRATION IN GRINDING CIRCUIT. MODIFIED APPROACH FOR IMPROVED METALLURGICAL PERFORMANCE AND REDUCED GRINDING REQUIREMENTS

N. Emre ALTUN*, **Givemore SAKUHUNI****, **Bern KLEIN****

* Middle East Technical University, Mining Engineering Department, Ankara, Turkey; ealtun@metu.edu.tr

** University of British Columbia, NBK Institute of Mining Eng., Vancouver, BC, Canada

Abstract: The use of centrifugal gravity concentration in the closed-grinding circuit of a gold-containing massive sulphide ore was tested on classifier underflow and overflow. A continuous Knelson CVD6 was retrofitted to the hydrocyclone underflow for recovery of Au and Pb at a coarser feed size. The objective of treatment of overflow was recovering unliberated Au prior to flotation. The tests were performed in actual operating conditions at Nyrstar's Myra Falls Mine. The results of the tests on the cyclone underflow revealed that both liberated and unliberated Au and Pb were recovered by the Centrifugal Variable Discharge (CVD) concentrator. Concentrate grades <60g/Mg Au were attainable at a more than 20% recovery. This application also allowed early and increased Pb recovery before it became gravity unrecoverable by over-grinding. Other benefits included capturing middlings for regrinding as well as potential coarser grinding and increase in mill throughput. A coarse grind also corresponds to a reduction in deformation of Au-particles, and is beneficial for increased Au recovery in downstream processing. Treatment of cyclone overflow by the CVD also provided favourable results. The outcomes included capturing unliberated gold prior to flotation and potentially reducing pumping requirements and reagent consumption. A comparison of the metallurgical performances showed that CVD application on classifier underflow was more effective. The CVD was capable of recovering unliberated gold in sulphides and performed better at a coarser particle size. Therefore, when used with the grinding circuit, a coarser grind can be applied and the CVD could be used to reject gangue at a coarser size.

Keywords: *centrifugal gravity concentrator, grinding, classification, liberation*

Introduction

By the introduction of centrifugal gravity concentrators, the conventional gravity concentration in mineral processing has moved one step further. The centrifugal type concentrators, particularly the continuous types have the distinction of recovering

targeted values from the undesired fractions at relatively low specific gravity difference conditions on accounts of the sophisticated separation mechanism depending on centrifugal, gravitational effects as well as effective utilization of air and water. In addition, compared to conventional gravity concentration, separation at finer sizes is possible with these concentrators due to high centrifugal acceleration that the particles are subject to in these units. As a result, continuous centrifugal concentrators produced by leading manufacturers such as Knelson, Falcon, Kelsey, Mozley have found increasing application in mineral processing industry, particularly in the processing of precious metals in the last three decades. In addition to the effective use and growing reputation of these units in typical processing flowsheets, such as in the processing of gold, various applications were reported to be effective. These include talc rejection from iron oxides, separation of siliceous gangue from metallic minerals, concentration of base metals and even coal preparation (Lambert et al., 1999; Byron and Roberts, 2004; McLeavy et al., 2001; Honaker et al., 1996). All these results point to a significant opportunity about the use of these units and increased effort should be dedicated to explore potential areas and new ways for the utilization of these devices. Recent research by Klein et al. (2010) on hybrid flotation-gravity circuits tested potential application of the centrifugal gravity concentration using a Knelson CVD unit, to scavenge unliberated gold in sulphides from final tailings. The basis for this application is reduced flotation performance for sizes generally below 10 micrometer and above 100 micrometers. The Centrifugal Variable Discharge (CVD) concentrator was capable of recovering coarse middlings that were normally non-recoverable or poorly recoverable by flotation. The hybrid use of CVD and flotation enabled a coarser grind size providing a preferred size distribution for flotation and thereby increasing the mill throughput.

In this study, the use of continuous centrifugal gravity concentration was assessed for the treatment of the underflow and overflow streams of a classifier operating in the closed-grinding circuit of Nyrstar's Myra Falls concentrator that processes a polymetallic massive sulphide ore with significant gold content mainly by flotation. The objectives of this novel installation on the existing flowsheet were exploring the opportunity of reducing metal losses, seeking the possibility of a coarser grind size, increasing the effectiveness of gold recovery and overcoming some critical mineralogical and morphological obstacles imposed due to the grinding conditions in the mill.

Materials and methods

Figure 1 illustrates the simplified flowsheet of Nyrstar's Myra Falls Operation at Vancouver Island, BC, Canada. A full scale continuous Knelson CVD6 (Centrifugal Variable Discharge) concentrator was retrofitted during normal operation of the concentrator for the treatment of underflow and overflow streams of the cyclone

classifier working in conjunction with the ball mill. These configurations are shown in Fig. 2.

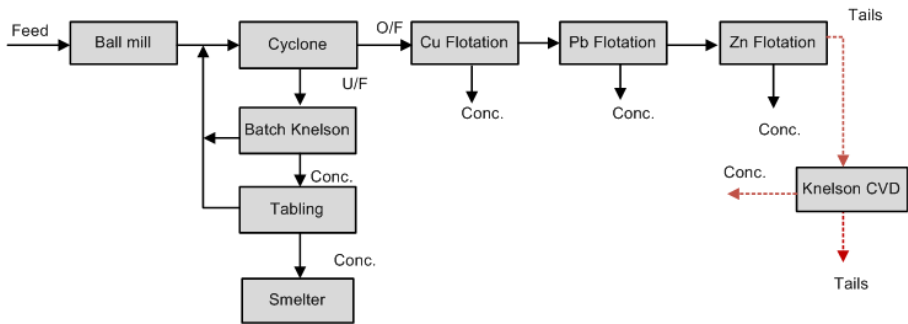


Fig. 1. Simplified flowsheet of Myra Falls concentrator

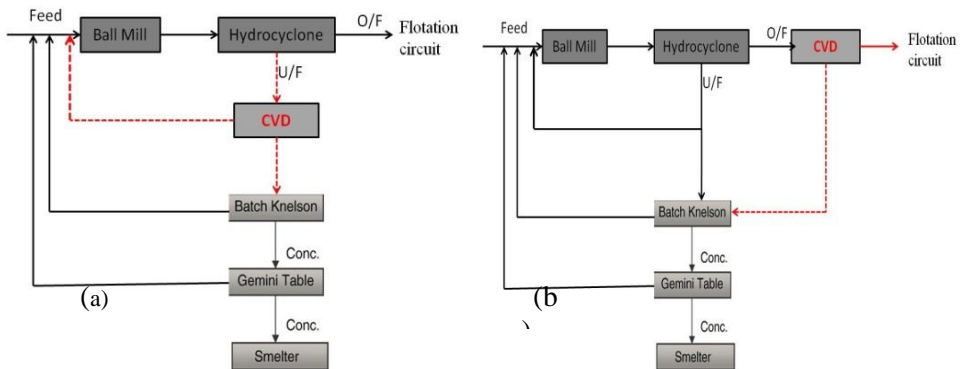


Fig. 2. Treatment of (a) classifier underflow (b) classifier overflow streams, by the CVD

Table 1. CVD machine parameters for tests on classifier underflow and overflow

| Test No | Tests on Classifier Underflow | | | Tests on Classifier Overflow | | |
|---------|-------------------------------|---------|---------|------------------------------|---------|---------|
| | PVO (s) | PVC (s) | G Force | PVO (s) | PVC (s) | G Force |
| 1 | 0.2 | 5 | 30 | 0.18 | 5 | 30 |
| 2 | 0.2 | 30 | 30 | 0.18 | 20 | 30 |
| 3 | 0.3 | 5 | 30 | 0.32 | 5 | 30 |
| 4 | 0.3 | 30 | 30 | 0.32 | 20 | 30 |
| 5 | 0.25 | 15 | 60 | 0.32 | 20 | 30 |
| 6 | 0.2 | 5 | 90 | 0.18 | 5 | 90 |
| 7 | 0.3 | 5 | 90 | 0.18 | 20 | 90 |
| 8 | 0.3 | 30 | 90 | 0.32 | 5 | 90 |
| 9 | 0.25 | 15 | 60 | 0.32 | 20 | 90 |
| 10 | 0.2 | 30 | 60 | 0.25 | 10 | 60 |
| 11 | 0.25 | 30 | 60 | 0.2 | 12 | 60 |

The two configurations were assessed by varying main operating parameters, i.e. the pinch valve open time (PVO, seconds), pinch valve closed time (PVC, seconds) and G force of CVD, as presented in Table 1, and collecting cross cut samples from the feed and CVD concentrates. To evaluate the effect of operating variables on the metallurgical outcomes, the non-machine variables, i.e. feed pulp density, feed rate and ore specific variables were kept constant. Fluidisation flow rate and feed rate were maintained at 30.3 dm³/min and at 1 Mg per hour, respectively and continuously monitored. The samples were collected, weighed, filtered and dried. Representative sub-samples were obtained by riffing for chemical analysis and size-assays. Size-assays were obtained by ICP at Myra Falls' facilities.

Results and discussion

Mineralogical studies

The feed to the mill comes from three sources which are mainly polymetallic massive sulphides: the Lynx-Myra-Price system averaging 15% pyrite, the HW system with 75% pyrite; and the Battle- Gap system, a massive sulphide with comparatively higher sphalerite, tennantite/bornite and variable amounts of pyrite. In the ore, the principal gold carrier is electrum with 22 to 30% silver and with a grain size of 2–50 μm . The finer fractions of electrum are enclosed in tetrahedrite and tennantite which are associated with sphalerite and pyrite. Gold was also observed associated with bornite and as intergrown with galena and chalcocite. In order to identify the gangue minerals the flotation tails was analysed using XRD analysis with Rietveld. Main accessory minerals were quartz, pyrite and muscovite (Table 2).

Figure 3 is a typical optical view of gravity gold concentrate. It shows flattened, tarnished gold particles and composite particles which could be the source of gold losses from the batch Knelson and flotation circuit. The presence of flattened gold was attributed to the deformation during grinding and regrinding where coating of gold particles with iron fines is also likely to occur. The difficulty of recovering flattened and/or coated gold particles in flotation circuits even at high collector dosages was explained by Bulatovic (1997). In addition, rod-shaped and rolled gold entities were observed. This is also an evidence of high residence time in the grinding circuit. The tarnished particle surfaces was attributed to the high silver content of the ore since electrum is known to tarnish in the presence of sulphide ions where a 1–2 μm thick silver sulphide layer is formed. The effective density of the electrum particles is less than that of native gold and when further deformed due to prolonged grinding, the electrum particles become less susceptible to gravitational recovery. When tarnished electrum particles also become less hydrophilic, making their recovery during flotation difficult.

Table 2. XRD results of flotation tails

| Mineral | % |
|-------------|------|
| Quartz | 41.5 |
| Pyrite | 23.5 |
| Muscovite | 22.7 |
| Clinochlore | 2.5 |
| Carbonates | 2.5 |
| Barite | 2.3 |
| Others | 5.0 |

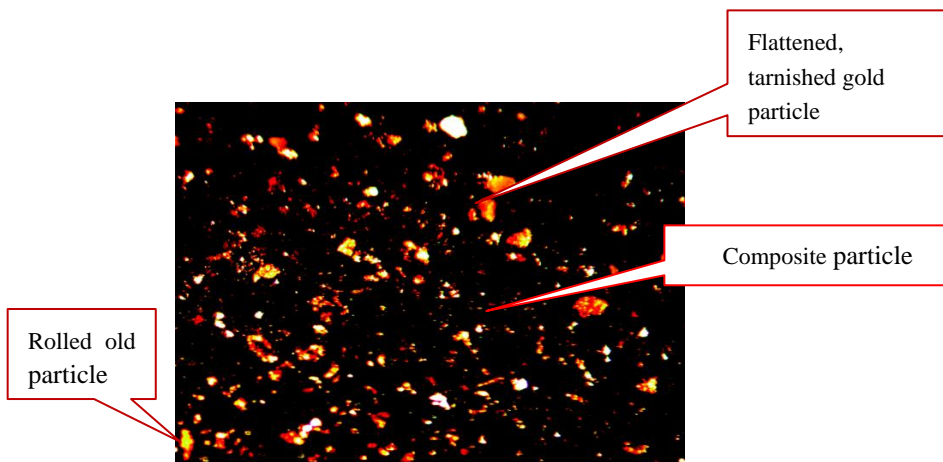


Fig. 3. Typical forms of Au particles and Au bearing entities in the gravity concentrate

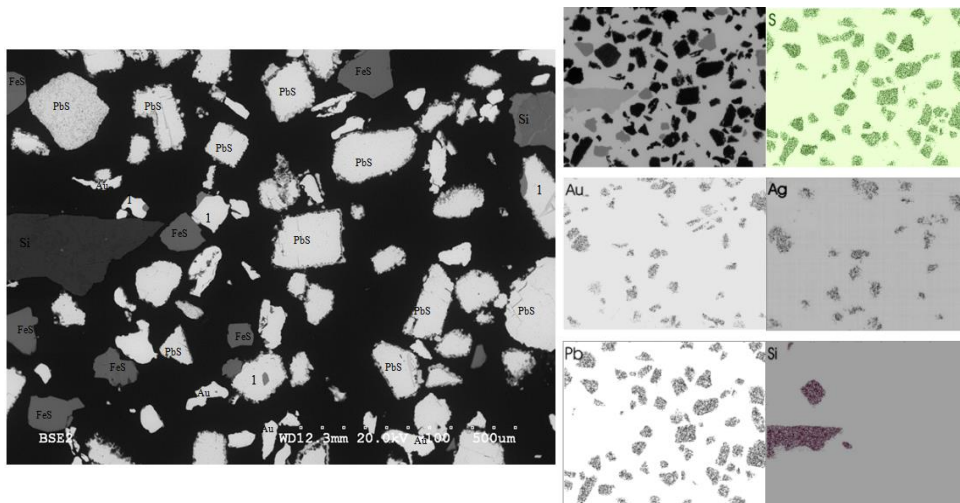


Fig. 4. SEM micrograph and EDX mapping of gravity concentrate: electrum (labeled as Au), galena, pyrite, gangue grains (labeled as Si) and electrum and sulphide composites

The SEM work showed that gold existed mainly in two forms, as liberated electrum grains and as unliberated associations with base metal sulphides. This could be seen in the EDX mapping, particularly by an examination of the prints of Au, Ag and Pb and S (Fig. 4). Au particles or Au bearing composites in elongated (rod like) form were again observed probably due to overgrinding and could be the source of Au losses in flotation, as mentioned. It should also be noted that galena is the main constituent in the gravity concentrate from the classifier underflow as galena particles were still coarse enough to be recoverable by gravity.

CVD installation on classifier underflow stream

The main objective of installing a Knelson CVD on the classifier underflow was to investigate the possibility of treating a coarser feed. In other words, by this application, the recovery of free gold, gold bearing entities and galena at a coarser feed size was targeted. To evaluate this opportunity, the metal content of the underflow stream were assessed in terms of weight and grade distributions of Au and Pb with respect to size fractions (Fig. 5). Fig. 5a illustrates that almost half of the feed is coarser than 150 μm . This coarser fraction in the classifier underflow included a significant amount of metal values, approximately 29% of Pb and 35% Au in the feed. The +150 μm fraction along with -150+75 μm fraction corresponds to around 80% of the total feed weight, 60 % of Pb and more than 55% of Au. The -75+38 μm fraction is distinguished with high Au and Pb grades as compared to other fractions (Fig. 5b). The high Pb and Au grade in the -38 μm fraction should also be noted. The association of Au and Pb with other metals were also investigated and used to assess the liberation mode and componential form of minerals in the classifier underflow as shown in Fig. 6. The close association between gold and silver was verified (Fig. 6a) implying the presence of Au in electrum form. The correlations of Au, Ag and Pb grades in Figs. 6b and 6c demonstrate the strong association of Pb, Au and Ag. In accordance with the mineralogical analysis, significant association of electrum with galena could be suggested. Almost no association between Au, Cu and Zn was observed. Some part of the electrum and galena could be associated with pyrite, as implied by Fig. 6d.

In view of the mineralogical data and these results, it was understood that electrum remains mostly unliberated after grinding. Also, being associated and/or intergrown with galena, a potential existed for the recovery of the unliberated electrum by the CVD. This would provide an opportunity for recycling back these values to grinding for further liberation prior to final upgrading by the batch Knelson concentrator. The CVD was retrofitted to the original flowsheet as shown in the configuration in Fig. 2a to treat the cyclone underflow. By this application it was expected that only the fully liberated gold and galena entities report to the batch Knelson unit. The tailings of the CVD, batch Knelson and Gemini Table were fed back to the grinding circuit to ascertain further liberation of metal values.

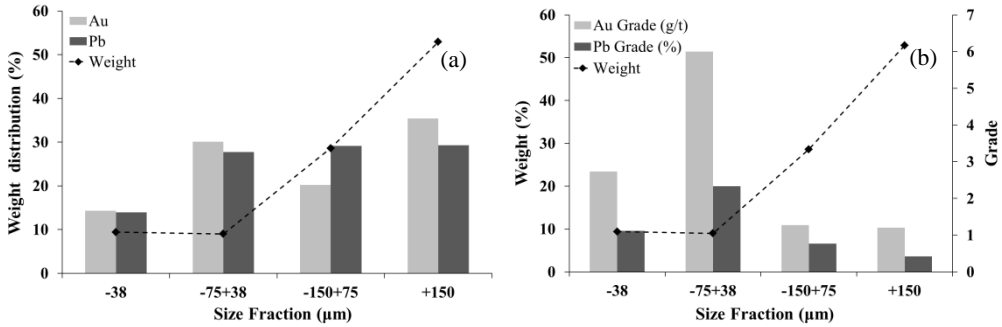


Fig. 5. Distribution of (a) Au and Pb weight, (b) Au and Pb grade, vs particle size in the cyclone underflow

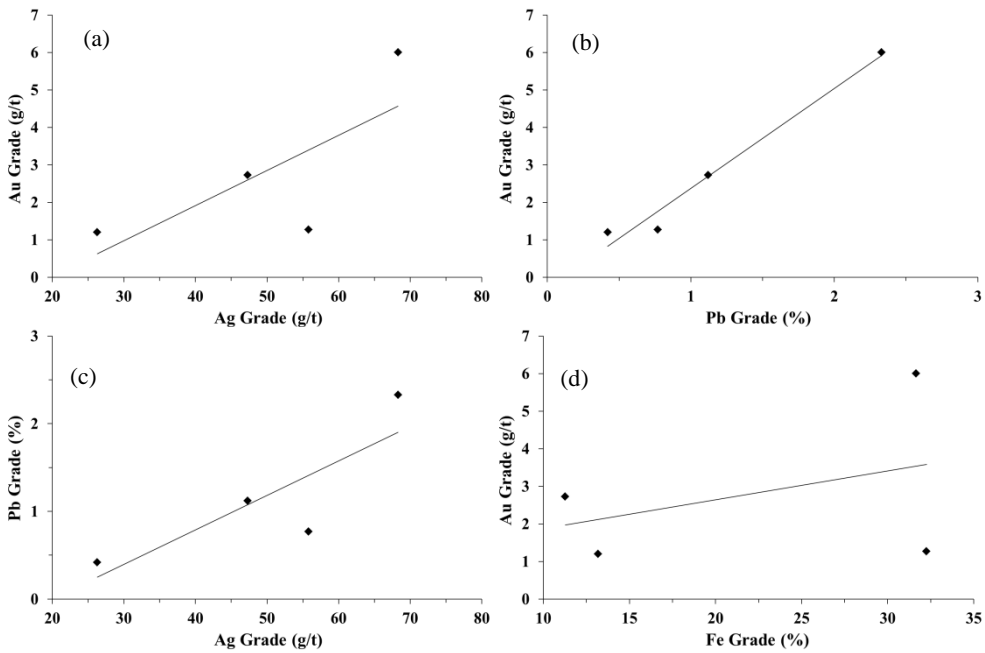


Fig. 6. (a) Au vs. Ag, (b) Au vs. Pb, (c) Pb vs. Ag, (d) Au vs. Fe grades in the underflow

The anticipated benefits from such an application included increase in galena recovery before it was rendered gravity unrecoverable due to over-grinding and setting a coarser grind size from the ball mill to achieve a more favourable size distribution for flotation as described by Klein et al. (2010) and thereby increasing the mill throughput and reducing grinding energy requirements. An increase in recovery, due to a decrease in overgrinding and fines generation as well as capture of middlings, was also expected. The benefit of a coarser grind on gold recovery both by gravity concentration and flotation also includes a reduction in the deformation of gold particles (Bulatovic, 1997). Retrofitting the CVD this way will enable treatment of the whole stream. It has been proved using modelling by Grewal and Fullam (2004) that

there is no recovery benefit for gravity treatment of more than 30% of circulating load using the batch unit. Thus, the benefit of capturing liberated and partly liberated gold early by an additional CVD unit becomes obvious. The results are shown in Table 3.

Table 3. Summary of results of treatment of cyclone underflow by the CVD unit

| Test | Mass Pull % | Grade | | | | | Recovery, % | | | | |
|------|-------------|---------|---------|------|------|------|-------------|------|------|------|------|
| | | Au g/Mg | Ag g/Mg | Cu % | Pb % | Zn % | Au | Ag | Cu | Pb | Zn |
| 1 | 12.6 | 54.1 | 287.2 | 1.6 | 6.6 | 10.2 | 41.7 | 22.0 | 16.2 | 34.8 | 12.7 |
| 2 | 2.5 | 77.0 | 315.4 | 1.6 | 9.1 | 9.9 | 11.4 | 5.1 | 3.1 | 12.7 | 2.8 |
| 3 | 38.9 | 30.7 | 222.7 | 1.6 | 4.3 | 10.5 | 75.5 | 53.6 | 47.4 | 65.9 | 42.5 |
| 4 | 6.7 | 64.9 | 306.5 | 1.4 | 8.4 | 9.4 | 25.3 | 12.8 | 6.5 | 22.8 | 5.8 |
| 5 | 16.4 | 49.2 | 260.7 | 1.5 | 5.4 | 10.3 | 45.9 | 28.0 | 18.1 | 40.2 | 17.7 |
| 6 | 48.9 | 24.3 | 210.3 | 1.6 | 4.1 | 10.3 | 76.2 | 62.0 | 54.7 | 79.3 | 52.3 |
| 7 | 60.1 | 24.3 | 202.6 | 1.4 | 3.3 | 10.7 | 85.8 | 73.0 | 66.4 | 81.2 | 67.4 |
| 8 | 11.6 | 59.9 | 245.4 | 1.4 | 5.2 | 10.7 | 22.1 | 16.7 | 11.9 | 22.1 | 12.3 |
| 9 | 18.7 | 44.1 | 250.5 | 1.5 | 6.4 | 9.8 | 46.4 | 28.2 | 20.9 | 43.9 | 17.8 |
| 10 | 3.7 | 60.2 | 237.2 | 1.4 | 5.4 | 10.1 | 14.2 | 5.9 | 3.7 | 13.4 | 3.7 |
| 11 | 8.6 | 61.2 | 263.5 | 1.3 | 5.9 | 10.8 | 45.1 | 16.6 | 7.9 | 29.4 | 9.3 |

The typical grade of Au in the cyclone underflow is 16 g/Mg. By the treatment of this stream, concentrates with Au grades above 60 g/Mg at recoveries above 25% were achieved (Table 3). Obtaining a product with 77 g/Mg Au at 11.4% recovery at a very low mass pull of 2.5% was possible. At this test, Pb and Ag grades were also high, but their recoveries remained relatively limited due to a mass pull of 2.5%. An Au grade of 61.2 g/Mg at 45.1% recovery and 8.6% mass pull obtained at Test 11 was distinctive. At this test acceptable Pb grade and recovery values were also attained. Tests that yielded higher mass pulls generally provided better Au, Pb and Ag recoveries at acceptable metal grades, as seen in Tests 3, 6 and 7.

Figure 7 summarizes the metallurgical performance of the application for Au and Pb. The curves show good metallurgical response for both electrum and galena. Overall, it could be deduced that capturing liberated gold, silver and lead by using a batch machine to treat the CVD product will result in significant reductions in grinding energy requirements, increased recovery of gold due to reduced over grinding, particle deformation and tarnishing during grinding. This application provides the flexibility to target a high mass yield-high metal recovery or a low mass yield-high metal grade operation. The balance between metal price and grinding costs will be the basis for choosing between early gangue rejection or high upgrading options with the CVD where a coarser grind will be viable for both options.

CVD installation on classifier overflow stream

The motivation of installing a CVD concentrator on the cyclone overflow was the recovery of unliberated gold in the flotation feed since such entities are difficult to be

effectively recovered by flotation, causing reduced metallurgical performance. This application was preferred over scavenging flotation tailings because it would also decrease the consumption of flotation reagents, pumping requirements and costs. For preliminary assessment of this potential, the classifier overflow was characterized and the results are shown in Fig.8. More than 50% of the feed was finer than 38 μm . This fine fraction was highly loaded with metal values with around 65% of Au and more than 70% of Pb by weight. Generally, the metal content increased with decrease in particle size (Fig. 8a) in contrast with the classifier underflow where Au and Pb were more evenly distributed (Fig. 5a). Also, Au and Pb grades apparently increased with increasing fineness, particularly in the -75+38 μm and -38 μm fractions (Fig.8b). Considering higher Au and Pb grades in the fines of both classifier overflow (Fig. 8b) and underflow (Fig. 5b), it is evident that the batch Knelson unit in the original flowsheet recovered coarse gold or gold bearing entities, leaving the gold bearing fine entities to flotation. Hence it was necessary to verify if the gold was sufficiently liberated to ascertain why it escapes the batch Knelson and account as losses. Fig. 9 shows typical metal associations in the overflow to assess the degree of liberation.

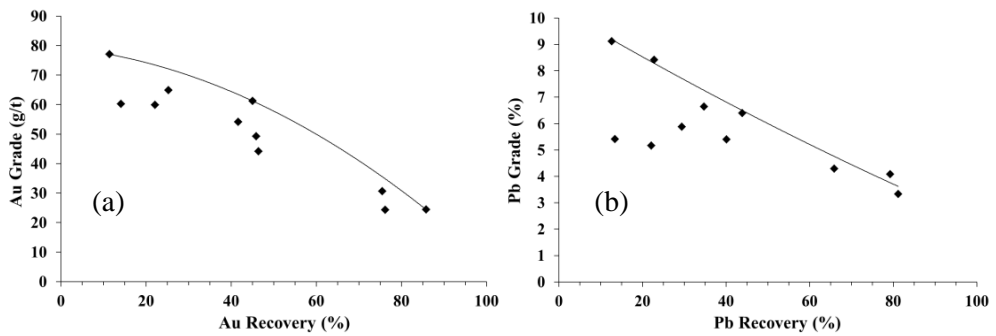


Fig. 7. Recovery vs grade for (a) Au, and (b) Pb for CVD application on classifier underflow

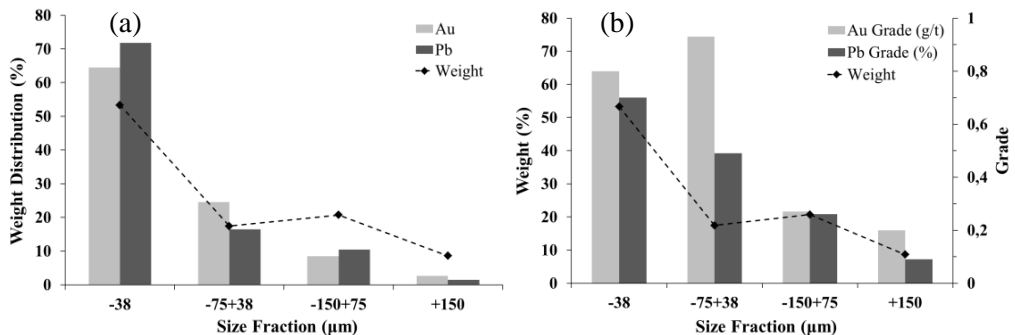


Fig. 8. Distribution of (a) Au and Pb weight (b) Au and Pb grade, vs. particle size in the cyclone overflow

In the overflow, Au and Ag are closely associated and gold mainly occurs as electrum (Fig. 9a). The strong correlations between Au and Pb (Fig. 9b) as well as Au

and Fe (Fig. 9d) show that gold in the form of electrum occurred in association with galena and pyrite. The Au-Zn correlation should also be noted (Fig. 9d). This implies that besides being associated with galena and pyrite, electrum was found attached to sphalarite in the classifier overflow. This is a mineralogical distinction of classifier overflow as compared to the underflow stream. The grade correlations suggested that despite P_{80} of 75 μm for classifier overflow in the plant, most of the electrum remained unliberated. In this application the concentrate from the CVD unit is fed to the batch Knelson (Fig. 2b) so that unliberated gold is captured before reporting to flotation. This would provide a reduction in Au losses during flotation and improvement in plant performance as described by Klein et al. (2010) as well as the benefit of reduced pumping requirements and reagent consumption. The results of the test set are presented in Table 4. The results showed that for this application acceptable metallurgical performance for Au and Pb were obtained at relatively high mass pulls. For instance, in Test 8 around 1/3 of Au was recovered at a mass pull of 28.2 %. For all tests Pb grades hardly exceeded 2% at generally low recoveries. Fig. 10 summarizes the metallurgical performance for Au and Pb. Au curve showed a degree of inhibition at higher mass yields. This was attributed to presence of fine unliberated gold in this stream. Pb curve did not show inhibition probably due to better liberation.

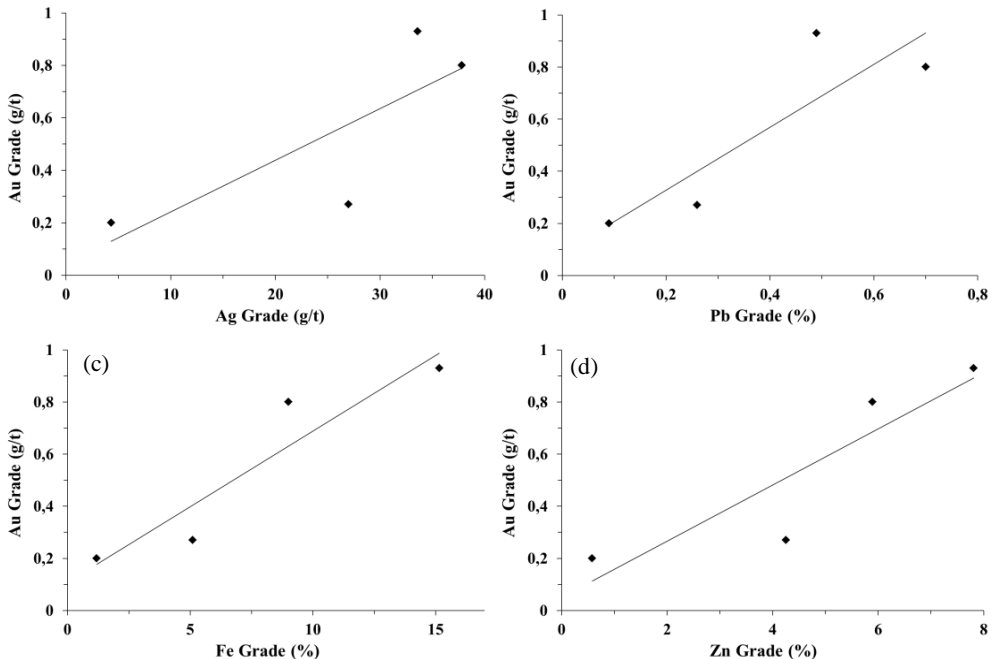


Fig. 9. (a) Au vs Ag, (b) Au vs Pb, (c) Au vs Fe and (d) Au vs Zn grades in the overflow

Table 4. Summary of results of treatment of cyclone overflow by the CVD unit

| Test | Mass Pull % | Grade | | | | | Recovery, % | | | | |
|------|-------------|--------|--------|------|------|------|-------------|------|------|------|------|
| | | Au g/t | Ag g/t | Cu % | Pb % | Zn % | Au | Ag | Cu | Pb | Zn |
| 1 | 0.8 | 10.9 | 42.6 | 1.3 | 0.8 | 12.2 | 4.0 | 1.7 | 1.0 | 1.3 | 0.9 |
| 2 | 0.2 | 14.9 | 46.3 | 1.1 | 2.1 | 8.1 | 1.2 | 0.4 | 0.2 | 0.8 | 0.1 |
| 3 | 20.8 | 2.9 | 18.2 | 1.1 | 0.6 | 10.8 | 24.9 | 18.4 | 20.6 | 22.9 | 19.8 |
| 4 | 7.3 | 3.7 | 22.8 | 1.3 | 0.8 | 12.0 | 12.6 | 7.4 | 7.9 | 11.8 | 7.5 |
| 5 | 5.6 | 5.2 | 28.6 | 1.4 | 0.9 | 12.7 | 14.2 | 8.1 | 6.7 | 10.1 | 6.3 |
| 6 | 3.0 | 3.1 | 21.5 | 1.4 | 1.7 | 11.7 | 4.3 | 3.4 | 3.6 | 9.6 | 3.0 |
| 7 | 0.9 | 9.2 | 33.2 | 1.3 | 2.2 | 10.6 | 4.0 | 1.4 | 1.0 | 4.1 | 0.8 |
| 8 | 28.2 | 3.1 | 21.6 | 1.2 | 0.6 | 11.0 | 37.3 | 31.0 | 29.6 | 33.7 | 27.2 |
| 9 | 13.1 | 7.7 | 33.8 | 1.3 | 1.0 | 11.2 | 32.6 | 21.3 | 14.7 | 22.0 | 12.4 |
| 10 | 7.6 | 5.3 | 29.3 | 1.3 | 0.8 | 12.6 | 18.8 | 10.6 | 9.1 | 14.7 | 10.3 |
| 11 | 1.4 | 10.5 | 36.6 | 1.5 | 1.3 | 12.3 | 6.2 | 2.3 | 1.7 | 3.7 | 1.7 |

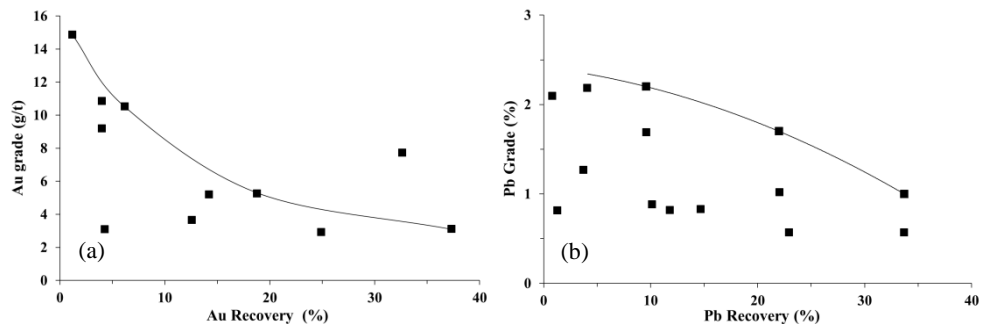


Fig. 10. Recovery vs grade for (a) Au and (b) Pb for CVD application on overflow

Conclusions

CVD application on the classifier underflow provided better performance as compared to the application on the classifier overflow. This implies that CVD6 was capable of recovering unliberated gold associated to metal sulphides and performed better at a coarser particle size. This provides the opportunity for the implication of a coarser grind size and early rejection of barren gangue. Associated outcomes include the reduction of grinding costs, grinding energy consumption, increase in the capacity and performance of downstream processes, achieving better liberation or targeted entities and reduction of metal losses.

Acknowledgement

The authors gratefully acknowledge the support of FLSmidth, Knelson and Nyrstar, Myra Falls to this work.

References

- BULATOVIC, S.M., 1997. *Flotation behaviour of gold during processing of porphyry copper-gold ores and refractory gold-bearing sulphides*, Minerals Engineering, 10, pp. 895-908.
- BYRON, R., ROBERTS, K., 2004. *Flotation improvements in the Luzenac Pehhorwood talc concentrator*, Proceedings 36th Annual Meeting of the Canadian Mineral Processors, Ottawa, Canada, pp. 177-188
- GREWAL, I., FULLAM, M., 2004. *Gravity Circuit Optimisation via Mathematical Modelling by Particle Size Classes*, Technical Notes, Knelson Gravity Solutions.
- HONAKER, R.Q., WNAG, D., HO, K., 1996. *Application of the Falcon Concentrator for Fine Coal Cleaning*, Minerals Engineering, 11 (12), pp. 1191-1199
- KLEIN, B., ALTUN, N.E., GHAFARI, H., MCLEAVY, M., 2010. *A hybrid flotation-gravity circuit for improved metal recovery*, International Journal of Mineral Processing, 3-4, pp. 159-165.
- LAMBERT, M., KLEIN, B., GREWAL, I., MCLEAVY, M., 1999. *Preliminary Studies with a New Continuous Centrifugal Concentrator*, Presentation at BC and Yukon CMP Annual Meeting.
- MCLEAVY, M., KLEIN, B., GREWAL, I., 2001. *Knelson continuous variable discharge concentrator: Analysis of Operating Variables*, International Heavy Minerals Conferences, Fremantle, Australia, pp. 119-125.

Received December 10, 2013; reviewed; accepted June 27, 2014

SWELLING PRESSURE OF NATURAL AND MODIFIED SMECTITE-BEARING CLAY RAW MATERIALS

Wojciech PANNA^{*}, Piotr WYSZOMIRSKI^{*,**}, Magdalena SZUMERA^{*}

^{*} AGH University of Science and Technology, 30-059 Kraków, Mickiewicza 30, Poland, wojpan@agh.edu.pl

^{**} State Higher Vocational School in Tarnow, 33-100 Tarnów, Mickiewicza 8, Poland

Abstract: Smectite clays, due to their barrier properties and swelling ability, are often applied for waterproofing purposes. A proper value of swelling pressure is one of the parameters, which must be met by the fillers used in hybrid waterproofing materials. The authors determined the swelling pressure of selected clay raw materials in their natural state and after chemical modification. This parameter was measured by the Komine method, as this procedure is more accurate than the standard edometric method. The authors introduced some changes in the method. The samples represent Krakowiec clays (Miocene) and a Triassic clay, collected in active pits of building clays, which are widely exploited in south Poland. The content of the smectite group minerals, determined from the sorption of methylene blue and copper(II) triethylenetetramine, ranges between 15 and 35%. Further characteristics of the clays were obtained with X-ray diffraction, chemical analyses (calcium carbonate content including) and pH measurements. It has been found that the activation of smectite clays with sodium lowers their swelling pressure as water penetrates easier the interlayer spaces of the smectites modified. This is important from the viewpoint of assessing the quality of bentonite fillers.

Keywords: *clay raw materials, swelling pressure, sodium activated smectites, waterproofing materials, Krakowiec clays, Triassic clay*

Introduction

Smectite-rich clays have been used in engineering since the second half of the 20th century. Initially, they were applied as a sealing additive in constructing river dams and other water plants. In 1970s it was established that the use of bentonites prevents penetration of various contaminants into the soil system. Two special examples of the effective use of the smectite-rich clays include their sorption abilities of heavy metals and radioactive elements in environmental engineering of dyes applied in the paint and textile industries (see, among others, Komine 2003; Gulgonul 2012; Janotka et al. 1996; Klapyta and Zabinski 2008). Based on such properties, clay rocks were utilized

in Germany in the early 1980s in constructing barriers protecting disposal sites of hazardous waste (Koch 2002).

Currently, smectite-bearing materials are more often applied in civil engineering for waterproofing purposes. Besides pure bentonite granulates, a range of the products used in protecting buildings from water includes bentonite-containing mats, panels, tubes, putties and swelling tapes. The major feature made use of in such applications, is the capability of bentonite to adsorb polar compounds, water included, within smectite interlayers (Murray 2007). As a result, the distance between the smectite layers increases, the volume of an intergranular space of smectite-bearing clay gradually decreases, and the system becomes eventually sealed (Szarugiewicz 2007). Favorable properties of waterproofing clays depend mainly upon their content and type of the smectite group minerals (Panna et al. 2012). The most desirable are bentonite clays rich in montmorillonite. This mineral is common, but usually occurs in nature as the calcium-rich variety, whose sorption properties are inferior in comparison with those of the sodium-rich variety. However, the capability of exchanging interlayer ions, a typical feature of the montmorillonite group minerals, can be used to manufacture bentonites with better sorption properties by treating them with Na-bearing modifiers (Komadel 2003; Klapyta and Zabinski 2008). The modified smectite, which Ca^{2+} and Mg^{2+} ions has been replaced by Na^+ ions, strongly swells if exposed to water as its aggregates disintegrate into single unit layers.

The capability of adsorbing water into the interlayer spaces of smectites results from many factors, which can be divided into two main categories: of the physico-chemical nature and of the mechanical nature. The first of them are associated with the structure of clay minerals. Due to the presence of not compensated total layer charges of these minerals, their interlayer spaces may be entered by exchangeable cations. The molecules of water that hydrate the exchangeable cations expand the layers to various distances. In addition, the concentration of cations in the immediate vicinity of clay particles becomes much higher than in pure water. A difference of the cation concentrations contributes to building up the osmotic pressure. As a result, water molecules move from the areas of a lower cation concentration to those where the cation concentration is higher until of the concentrations are equilibrated. The mechanical factors of the clay swelling process include, first of all, its time, load history, an effect of sample size, volume changes, temperature, surface pressure (Kulesza-Wiewiora 1982).

The authors assessed an impact of a soda (sodium carbonate) addition to smectite-bearing clays on their swelling pressure. The test materials represented clays from south Poland, containing smectite in the range from 15 to 35% and characterized by marked fineness.

Methods of investigations

Swelling parameters were determined in clays sampled *in situ* in the Ligota Dolna (Poland) deposit or in depositories of clay commodities used by three brickyards: Harasiuki, Przeclaw and Wola Rzedzinska (Poland). General characteristics of the clay materials were obtained using the following methods: analyses of the mineral and chemical compositions, measurements of cation exchange capacity, determinations of smectite and calcium carbonate contents.

The natural clays were modified into their sodium varieties by treating them with sodium carbonate in the amount from 0.5 to 2.5% (in increments 0.5%) relative to dry mass of the clay, followed by chemical activation, 30-day homogenization, and final drying and grinding of the modified clay samples. This procedure produced so-called swelling smectite powders. Their swelling pressure was determined using the method proposed by Komine (2004), but changed in details by the present authors. The changes involved preparing for pressure tests samples in the form of pellets and then measuring the pressure of the swelling pellets exerted on the piezometric sensor of a materials test frame device.

The pellets for the swelling pressure tests were prepared from 15 g of the smectite powders, pressed monoaxially at a pressure of 20 MPa in a steel cylinder with the diameter 60 mm. Then the pellets with the apparent density 1.60-1.65 g/cm³ were placed into a die (Fig. 1) and positioned under a piston of the test frame. Next, distilled water was continuously supplied into the pellet trough steel, perforated rollers to initiate its swelling. The pressure inserted by the swelling sample (i.e. the pellet) onto the piezometric sensor of the test frame was finally measured. The test frame software records the pressure as a the function of time, due to which the maximum pressure value can be determined. From this value the swelling pressure of the sample is calculated.

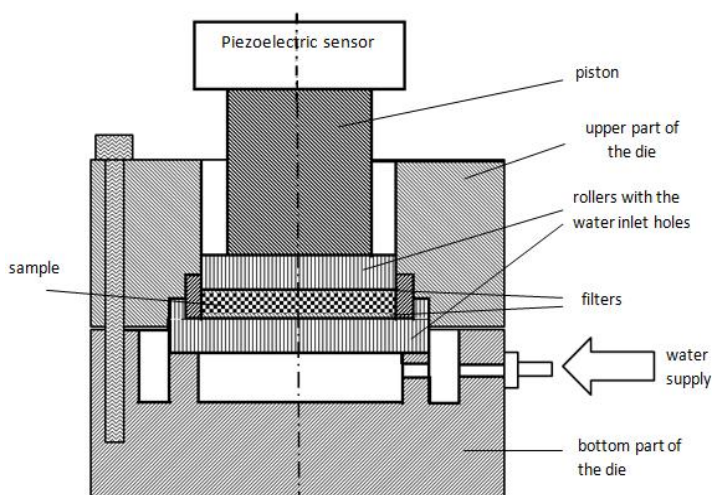


Fig. 1. Device for measuring the swelling pressure using a materials test frame

Characteristics of clay

The investigations were carried out on four samples representing the Miocene Krakowiec clays from the Carpathian Foredeep (Harasiuki, Przeclaw, Wola Rzedzinska) and the Triassic red clays (Ligota Dolna). The first of them are the essential raw materials of the building ceramics in south-east Poland, the other used in some brickyards located within the area of the Silesian-Cracow Monocline, i.e. between Kepno and Tarnowskie Gory (Wyszomirski and Galos 2005). These clay commodities, particularly the Krakowiec clays, are more and more often considered as starting materials in constructing the protection barriers that prevent various contaminants from penetration into soils (Branski 2007). The Krakowiec clays, occurring as grey, bluish-grey and dark grey varieties, in the engineering geology classification represent most often clays and silty clays. In places they contain more sandy inserts and admixtures of dispersed calcium carbonate (Pajak and Dobak 2008). The mineral and chemical characteristics of the clays considered are presented in Table 1.

Table 1. Some parameters of the clays under study

| Sample | Deposit | Montmorillonite content [%] determined by sorption of: | | Calcium carbonate content [%] | pH | CEC [mval/100g] |
|--------|------------------|---|---|-------------------------------------|-----|--------------------|
| | | methylene blue according to BN- 77/4024-16 | copper(II) triethylenetetramine according to Meier and Kahr (1999) | | | |
| 640 | Ligota Dolna | 29 | 35 | 11.2 | 8.7 | 34 |
| 835 | Harasiuki | 17 | 23 | 9.2 | 7.9 | 20 |
| 839 | Przeclaw Wola | 16 | 22 | 15.3 | 8.6 | 18 |
| 1187 | Rzedzinska | 17 | 20 | 17.9 | 9.5 | 16 |

The highest content of montmorillonite, in the range of 35%, has been established in the Triassic clays from the Ligota Dolna deposit (Silesian-Cracow Monocline). The remaining three samples, representing the Krakowiec clays, contain about 20% smectite. These figures were obtained from the sorption of copper(II) triethylenetetramine. This method is more reliable than the method based on the sorption of methylene blue, as the latter gives correct determinations only in the case of samples, which smectite contents exceed 40% (Kosciowko and Wyrwicki 1996). All the samples reveal basic reaction, which results from the presence of fine-crystalline calcite and Ca,Mg-smectite. Isomorphic replacement of Al^{3+} ions, for instance by Mg^{2+} and/or Fe^{3+} , in the structure of smectites significantly affects their overall unit layer charge and, in turn, results in diversified CEC (cation exchange capacity) properties in clay samples with comparable smectite contents (Bobrowska and Szaniewska 2011).

Chemical analysis of major elements (Table 2) revealed an insignificant variability of the SiO_2 and Al_2O_3 contents in the Krakowiec clays, which is explained by small differences in their contents of main components, i.e., quartz and clay minerals. All the clay commodities studied are characterized by elevated amounts of magnesium and calcium, the elements being present as exchangeable cations in the structure of Ca,Mg-smectite, whereas in the case of calcium also in calcite. High contents of iron result from the presence of Fe^{3+} ions in the structure of montmorillonite, i.e. the most common smectite, and from the presence of hematite in the Triassic red clay from Ligota Dolna.

Table 2. The chemical composition of tested samples

| Component | Content [%wt] | | | |
|-------------------------|---------------------|-----------------|----------------|------------------------|
| | Ligota Dolna (640)* | Harasiuki (835) | Przeclaw (839) | Wola Rzedzinska (1187) |
| SiO_2 | 50.81 | 58.43 | 51.47 | 51.61 |
| Al_2O_3 | 12.66 | 12.77 | 14.37 | 12.5 |
| Fe_2O_3 | 5.39 | 5.22 | 5.58 | 4.86 |
| TiO_2 | 0.76 | 0.69 | 0.71 | 0.64 |
| MnO | 0.15 | 0.09 | 0.14 | 0.14 |
| MgO | 2.82 | 2.41 | 2.97 | 3.34 |
| CaO | 9.53 | 5.22 | 7.05 | 7.96 |
| Na_2O | 0.35 | 1.01 | 0.77 | 1.00 |
| K_2O | 1.34 | 2.51 | 2.88 | 2.59 |
| P_2O_5 | 0.11 | 0.17 | 0.13 | 0.13 |
| LOI | 16.35 | 11.9 | 14.01 | 13,99 |

* sample symbols are given in parenthesis

X-ray diffraction analyses (Fig. 2) showed that the clay from Ligota Dolna has the highest amounts of smectite as indicated by the intensity of the first, low-angle, distinctly broaden reflection with the d_{001} value ≈ 1.5 nm. Also in case of the remaining clays, the fields under their broad 001 reflections point to elevated amounts of smectite, whereas the diffusion of these reflections results from a typical, high fineness of smectite (Wyszomirski et al. 2005). The list of the X-ray identified clay minerals is supplemented by illite and kaolinite. The Miocene Krakowiec clays show also a considerable presence of chlorite, which is another clay mineral. The clay minerals listed above occur most probably as mixed-layer structures: chlorite/smectite, illite/smectite and chlorite/illite. Quartz and calcite are present in all the clays studied, and are accompanied in the Krakowiec clays by K-feldspars, plagioclases and dolomite.

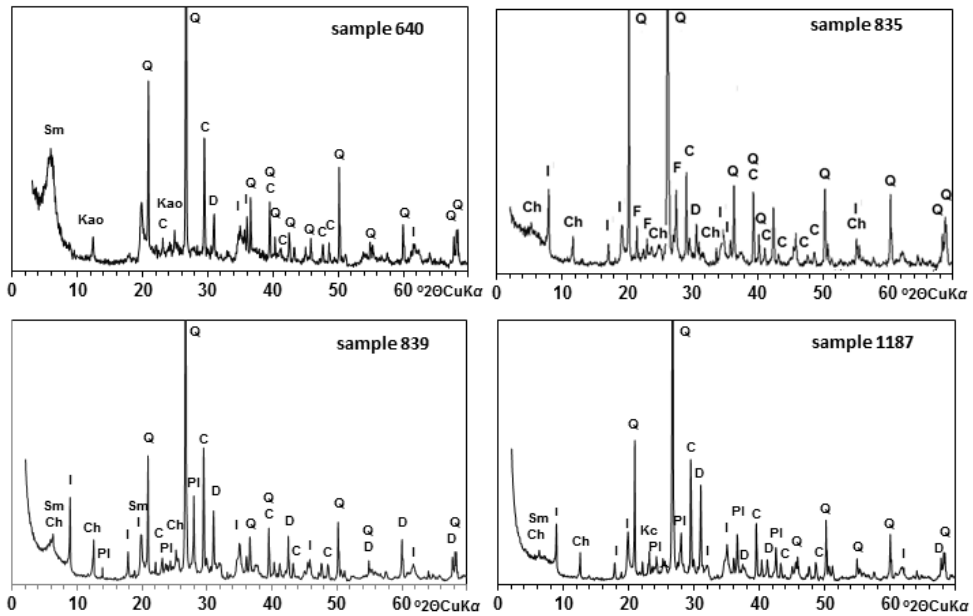


Fig. 2. X-ray patterns of studied clays from Ligota Dolna (sample 640), Harasiuki (835), Przeclaw (839) and Wola Rzedzinska (1187). Symbols: Sm – smectite, I – illite, Kao – kaolinite, Q – quartz, C – calcite, D – dolomite, Ch – chlorite, F – K-feldspar, PI – plagioclase

Results of pressure experiments and discussion

The results of pressure experiments indicate that swelling pressure decreases with an increase of the sodium carbonate addition into the smectite-bearing clays. It is a result of different values of the Cartledge ionic potential of calcium and sodium ions, entering the interlayer spaces of smectites. X-ray analyses of the clay from Ligota Dolna (Fig. 3) indicate a gradual transition of Ca,Mg-smectite into Na-smectite in the clay activated. This process can be deduced from the shift the first, low-angle reflection of smectite from about 1.5 nm towards 1.25 nm which is accompanied by diffusion of this reflection and lowering its intensity. Such an X-ray pattern results from a considerable development of the specific surface of Na-smectite that took place due to disintegration of aggregates of this mineral into single unit layers after activation with soda.

Among not activated clays, the highest value of the swelling pressure shows the Triassic clay from Ligota Dolna (Fig. 4). This parameter reaches a value of above 600 kPa after water interaction lasting 1500 s. It is a result of the clay composition, i.e., a significant content of Ca,Mg-smectite that is prone to intercrystalline swelling. As the Krakowiec clays contain less smectite, their swelling pressure values are lower. In addition, a high value of the swelling pressure of the not activated clay from Wola Rzedzinska (sample 1187) may indicate a relatively low, negative resultant charge of

its smectite unit layers. Laird (2006) showed that the intercrystalline swelling decreases when the layer charge increases.

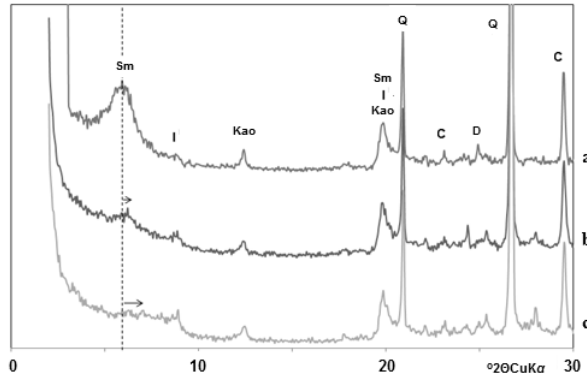


Fig. 3. X-ray patterns of the clay from Ligota Dolna (sample 640): a – air-dry state, b – after activation with 0.5% Na_2CO_3 , c – after activation with 2.5% Na_2CO_3 . Symbols: Sm – smectite, I – illite, Kao – kaolinite, Q – quartz, C – calcite, D – dolomite

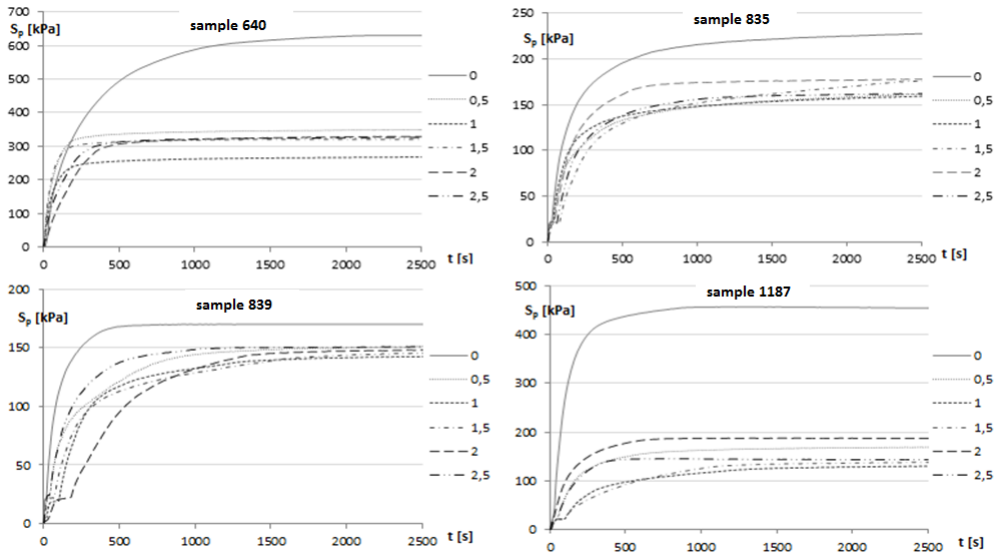


Fig. 4. Swelling pressure S_p of natural and activated smectite clays depending on the time of their water exposure. Samples: Ligota Dolna (640), Harasiuki (835), Przeclaw (839), Wola Rzedzinska (1187). Explanation: 0; 0.5; 1; 1.5; 2; 2.5 – the percentage content of Na_2CO_3 relative to the dry weight of samples

Sodium modification decreases the swelling pressure of the smectite-bearing clays, which is associated with the Cartledge ionic potential being almost twice as high for interlayer Ca^{2+} cations in comparison with Na^+ cations. So, the swelling pressure S_p of

the samples activated with the highest content of soda (2,5%) varied in the range 150-300 kPa. In the case of Ca^{2+} cations, the interaction among smectite layers is much stronger due to this potential. Therefore, the smectite varieties containing calcium cations tend to form aggregates, which presence affects considerably intergranular swelling (Kulesza-Wiewiora 1982). The intercrystalline swelling results from the formation of an electric double layer between the interacting layers. The water entering the structure of smectites causes a considerable difference in concentration of the solutions separated by smectite layers. The interlayer solutions being in contact tend to equilibrate their concentrations, and the process results in a build-up of the osmotic pressure. This pressure takes higher values in the smectites, whose interlayer spaces are filled with cations with a high ion potential. An increase of the pressure is associated with strong interlayer reactions that hinder diffusion of migrating water molecules into consecutive interlayer spaces. In contrary, replacing Ca^{2+} by Na^+ cations decreases the interaction forces within the electric double layer (Laird 2006). Making the structure of clay layers less compact results in easier diffusion of water molecules, which favors equilibrating cation concentrations and, finally, considerably lowers the swelling pressure of the modified smectite-bearing clay raw materials. Such lowering of the swelling pressure has been just established by the authors.

Summary

The authors have presented the method of measuring the swelling pressure of clay raw materials that extend their volume when being in contact with water. The investigations were carried on Polish clays with considerable smectite contents on the natural samples and after their chemical modification with Na_2CO_3 . Laboratory tests have revealed lowering the swelling pressure of the clays as a result of such a modification procedure. The swelling pressure decreases despite the fact that the modification with soda enhances water adsorption among the smectite layers. It can be explained by diversified migration of water molecules in the interlayer spaces of smectite, which builds up the osmotic pressure. In the clays rich in smectite which contains in interlayer spaces cations with low ion potential (e.g. Na^+), equilibration of the concentrations of hydrating ions within the whole rock volume takes place under a much lower osmotic pressure than in case of the smectite varieties with bivalent cations (Ca^{2+} and Mg^{2+}). It was manifested in the tests by lower values of the swelling pressure of the clay samples modified with soda. This finding may be important when assessing the quality of bentonite fillers used in manufacturing of hybrid waterproofing materials.

Acknowledgement

This study was carried out within the AGH University of Science and Technology (Krakow), grant number 11.11.160.603.

References

- BOBROWSKA M., SZANIAWSKA D., 2011. *Badania modyfikacji bentonitów do zastosowań w ochronie środowiska*. Inżynieria i Aparatura Chemiczna, 50, 5, 20-21.
- BRANSKI P., 2007. *Ocena możliwości wykorzystania wybranych przedkenozoicznych kopalin ilastych z obszaru Polski do celów ochrony środowiska*. Przegląd Geologiczny, 55: 467-474.
- GULGONUL 2012. *Evaluation of Turkish bentonite for removal of dyes from textile wastewaters*. Physicochemical Problems of Mineral Processing 48 (2), 369-380.
- JANOTKA I., FRANKOVSKA J., BASLIK R., STRESKO V., 1996. *Bentonite-based materials for environmental protection*. Geologica Carpathica – Series Clays, 5, 1 – 2, 43-48.
- KLAPYTA Z., ZABIŃSKI W. [EDS.], 2008. *Sorbenty mineralne Polski*. ISBN 978-83-7464-107-4. Wyd. UWND AGH Kraków.
- KOCH D., 2002. *Bentonites as a basic material for technical base liners and site encapsulation cut-off walls*. Applied Clay Science 21, 1–11.
- KOMADEL P. 2003. *Chemically modified smectites*. Clay Minerals 38, 127-138.
- KOMINE H., 2003. *Simplified evaluation for swelling characteristics of bentonites*. Engineering Geology 71, 265–279.
- KOMINE H., 2004. *Simplified evaluation on hydraulic conductivities of sand-bentonite mixture backfill*. Applied Clay Science 26, 13–19.
- KOŚCIÓWKO H., WYRZYCKI R. [EDS] 1996. *Metodyka badań kopalni ilastych*. Państwowy Instytut Geologiczny, Warszawa – Wrocław 1996.
- KULESZA-WIEWIORA K., 1982. *Piecznienie wewnątrzkrystaliczne mineralów ilastych*. Biuletyn Geologiczny 27, 5–62.
- LAIRD D. A., 2006. *Influence of layer charge on swelling of smectites*. Applied Clay Science 34, 74-87.
- MEIER L.P., KAHR G., 1999. *Determination of the cation exchange capacity (CEC) of clay minerals using the complexes of copper (II) ion with triethylenetetraamine*. Clays and Clay Minerals 47, No. 3, pp. 386-388.
- MURRAY, H.H., 2007. *Occurrences, processing and application of kaolins, bentonites, palygorskite-sepiolite, and common clays*. In: Applied Clay Mineralogy. Elsevier, Amsterdam.
- PAJAK R., DOBAK P., 2008. *Określenie parametrów filtracyjnych ilów krakowieckich z badań w konsolidometrze Rowe'a*. Geologia, nr 34, Zeszyt 4, 677-689.
- PANNA W., WYSZOMIRSKI P., MOTYKA J., 2012. *Możliwości wykorzystania wybranych surowców smektytowych jako materiałów dla celów hydroizolacyjnych*. Zeszyty Naukowe IGSMiE PAN, nr 83, 131-145.
- SZARUGIEWICZ C., 2007. *Zastosowania bentonitowych materiałów hydroizolacyjnych Cetco Poland Sp. z o.o. w budownictwie ziemnym*. Zeszyty Naukowe. Inżynieria Środowiska / Uniwersytet Zielonogorski nr 133(13), 399–410.
- WYSZOMIRSKI P., GALOS K., 2005. *Czerwone iły triasowe rejonu Tarnowskie Góry-Kepno w aspekcie przydatności dla polskiego przemysłu ceramicznego*. Gospodarka Surowcami Mineralnymi 21, Zeszyt Specjalny 1, 149-166.
- WYSZOMIRSKI P., GALOS K., LEWICKA E., 2005. *Charakterystyka łu poznańskiego z KWB Konin w aspekcie możliwości pozyskiwania surowca smektytowego*. Ceramika/Ceramics vol. 91(2), 1331-1338.

Received April 29, 2014; reviewed; accepted July 26, 2014

FINITE ELEMENT METHOD BASED SIMULATION OF ELECTRICAL BREAKAGE OF IRON-PHOSPHATE ORE

Seyed Mohammad RAZAVIAN, Bahram REZAI*, Mehdi IRANNAJAD

* Department of Mining and Metallurgical Engineering, Amirkabir University of Technology, Tehran, Iran, rezai@aut.ac.ir; b_rezai@hotmail.com

Abstract: In this study, the effect of minerals composition, particle size and shape as well as electrodes distance from iron-phosphate ore samples, was investigated by using a commercial software. Comparison between high voltage pulses and conventional crushing showed that minerals of interest in the electrical comminution product are better liberated than in the conventional comminution. In order to elucidate and confirm the experimental results, numerical simulation of electrical field distributions/intensity were performed. The software uses the finite element method, a numerical technique for calculating approximate solutions of partial differential equations with known boundary conditions. Magnetite, apatite and quartz were the basic minerals of iron-phosphate ore components, and the main material property used in the simulations was electrical permittivity. The results showed that the induced electrical field was strongly dependent on the electrical properties of minerals, the feed particle size and the location of the magnetite mineral (due to higher permittivity) in the ore. The angle of particle contact surface with high voltage electrode was an important factor in the intensity of electrical field. Smaller contact angle resulted in higher intensity of the electrical field. Electrical discharge within the material was converted to electrohydraulic discharge within the surrounding water environment by increasing the distance between the high voltage electrode and the material contact surface.

Keywords: *finite element method, numerical simulation, electrical breakage, iron-phosphate ore, COMSOL Multiphysics*

Introduction

The term high voltage usually means electrical energy at voltages high enough to inflict harm or death upon living organisms. Equipment and conductors that carry high voltage warrant particular safety requirements and procedures. In certain industries, high voltage means voltage above a particular threshold. One of the high voltage terms is pulse (or impulse) voltage. High-voltage pulses are used to test electrical equipment and to simulate system-generated over voltages and lightning surges in power distribution systems and lightning-protection equipment. In experimental physics,

high-voltage pulses are used to generate strong pulsed electrical fields to study processes of electrical breakdown, to produce short bursts of X radiation (10^{-7} to 10^{-6} s), to generate pulsed electron and ion beams, and to provide power supply for spark chambers, image converters, Kerr cells, and charged-particle accelerators (Kuffel et al. 2000). In recent years, usage of high voltage electrical pulses in mineral processing field has been developed. A more efficient technique for rock breaking by high voltage pulses is called electrical disintegration, in which the energy of high voltage pulses is transferred to the rock by electrodes directly contacting the surface of the rock immersed in water. This differs from electrohydraulic disintegration, in which the energy is transferred through the surrounding water in the form of a shock wave impact (Andres 1995). History of research in this field is mainly related to the works done by Andres (1989, 1995, 1996, 2010) and Andres et al. (1999, 2001). His first systematic comparative liberation tests were performed on a sample of apatite–nepheline ore from Kola Peninsula at the Institute of Rare Elements of the Russian Academy of Science in Moscow in 1971. The experimental results indicated higher percentage of the liberated minerals and lower fine particles in electrical comminution in comparison with mechanical comminution (Andres 2010). While some reports demonstrated the effectiveness of mineral liberation by high voltage pulses (Anon 1986; Lastra et al. 2003; Ito et al. 2009; Dal Martello et al. 2012; Dodbiba et al. 2012), some of them demonstrated better mineral recovery or higher concentrate grade as a result of the better mineral liberation. It is expected that if the recovery/grade performance improves the cost of energy, the technology would be economical. However, the application of the high voltage pulse technology to the mineral industry is rather slow because the benefits are not demonstrated sufficiently to justify the perceived risks. One major concern has been the amount of energy consumption used in the electrical breakage process itself. Andres et al. (2001) reported that the consumption of energy per unit volume of the tested ores used for mineral liberation was on average 2–3 times higher than in conventional mechanical comminution. Usov and Tsukerman (2006) pointed out that there is a possibility to use the electrical pulse method of destruction for reduction of energy consumption but this possibility is limited. Combined application of electrical pulse destruction, electrical discharge weakening and traditional mechanical methods of destruction may give an option of reducing energy consumption for mineral processing. The most comprehensive investigation was performed on electrical comminution in the past five years with the aim of energy consumption optimization at the Julius Kruttschnitt Mineral Research Center (JKMRC) (Wang et al. 2011, 2012a, 2012b, 2012c). The research at the JKMRC was conducted in two major areas using high voltage pulses, that is particle pre-weakening and mineral liberation, both focused on improving energy efficiency. The studies showed that the ores treated by high voltage electrical pulses with low specific energy input (a few kWh/Mg) developed cracks and microcracks in the rock, and became weaker than untreated particles. Comparison of Bond work indices showed that the electrical treatment can reduce the energy consumption in downstream

grinding processes by up to 24%. Moreover, the research conducted at the JKMRC showed that higher mineral liberation can be achieved using the electrical comminution (Wang et al. 2011).

Numerical simulation is a new approach that can help predict the behavior of systems related to their performance. After simulating the system, its performance is considered in response to changes in different parameters. The importance of simulation becomes evident when changing the parameters is difficult or impossible in virtual or laboratory conditions. Wang et al. (2012a, 2012b) performed numerical simulation of electrical field distribution using a commercial software package, COULOMB 3D, for various six ore-related properties to assist in identifying the major factors affecting electrical comminution performance and elucidating the reasons for the observed trends in the experimental results. They showed that the electrical comminution depends strongly on ore properties. Particles having coarse grained minerals of interest, large feed particle size, conductive minerals embedded within gangues and angular particle shape may enhance the electrical comminution performance. High electrical field intensity is found to occur along the boundaries of two mineral phases with large difference in their permittivity and conductivity. The existence of conductive minerals on the particle surface distorts the field distribution of the entire particle, changing the breakdown path and pattern, in turn, impacting the breakage and liberation results (Wang et al. 2012c).

In this paper, a high voltage electrical pulses crusher (HVEPC) was simulated by a commercial software, COMSOL Multiphysics®. Electricity principles suggest that the locations of breakdown or the paths of streamer are strongly related to the location of high intensity field (Andres 1995; Wang et al. 2012a). The simulated electrical field intensity was therefore used as an indicator of preferential breakdown because the higher value indicated the easier breakdown and inferring better liberation. The effect of such parameters as mineralogical composition, feed particle size and shape, and distance of the HV electrode from ore surface on electrical field distribution/intensity were investigated in detail.

Materials and methods

Materials

The sample used in this study was obtained from the Esfordi iron-phosphate mining complex located in Bafgh, Iran. The particle size distribution of this sample showed that 80% of particles were smaller than 15.5 mm, 17.6% finer than 150 μm , and 8.5% finer than 37 μm . The X-ray diffraction (XRD) and electron probe micro-analyzer (EPMA) analyses results showed that the sample mainly consisted of magnetite, apatite, and quartz with the grade of 30.5%, 15.74%, and 14.27%, respectively.

High voltage electrical pulse crusher (HVEPC)

The electrical treatment of the ores was conducted with HVEPC (high voltage electrical pulse crusher) based on a single stage impulse generator that has been developed at the Iran Mineral Processing Research Center (IMPRC). The 3D schematic diagram of circuits for single-stage impulse generators is shown in Fig.1. The capacitor C is slowly charged from a DC source (HV transformer and diodes) until the spark gap breaks down. This spark gap acts as a voltage-limiting and voltage-sensitive switch, which ignition time (time to voltage breakdown) is very short. The control table of the system was equipped with a periodic shutdown system. Thus, by adjusting the frequency of pulse discharge, the required period of time could be easily determined, and then the number of pulses could be obtained.

The crushing chamber consisted of a rod-shaped electrode made of copper. The voltage between the generator and ground electrode made of an iron plate was measured by a probe connected to an oscilloscope. The ground electrode consisted of circular apertures to pass the crushed particles and prevent over-crushing (control sieve). The sample was immersed into water in the chamber between the two electrodes and then a high-voltage pulse was directly discharged to disintegrate the sample.

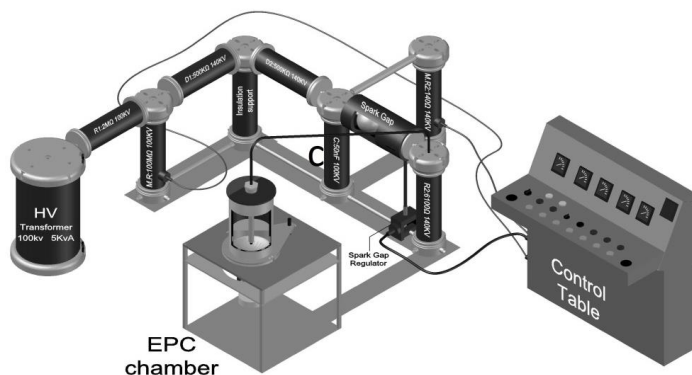


Fig. 1. 3D schematic diagram of high voltage electrical pulses crusher (HVEPC); C: capacitor

Experimental tests

One of the most critical design criteria for mineral processing plants is the choice of the particle size to which the comminution step must reduce the host rock (grind size) to ensure an economic level of liberation. The classical method of measuring the composition of rocks or broken particles is by manual mineral identification, fractionation, and counting under a binocular microscope. In order to investigate of degree of liberated minerals, representative samples of the HVEPC, laboratory jaw crusher and cone crusher products were taken for quantitative mineralogical analysis using the ZEISS Axioplan 2 polarizing optical microscope (reflected and transmitted light). In both methods, thin-smooth and smooth sections were prepared from

fractionated samples in sizes of +1-2 mm, +0.7-1 mm, +0.5-0.7 mm, +0.3-0.5 mm, +0.15-0.3 mm, and +0.075-0.15 mm. In each fraction the particles composed of liberated mineral and locked minerals were counted and the ratio of liberated particles and the total number of particles was presented as percentage. Based on the valuable minerals present in the Esfordi iron-phosphate ore, the studies were conducted on apatite and magnetite. Graphical results of these studies are shown in Figs 2 and 3.

As clearly seen from Figs 2 and 3, the ratio of liberated particles to total particles was higher for electrical breakage than for mechanical one for both apatite and magnetite in all fractions. The differences of these results are related to the mechanism of the breakage methods. Furthermore, numerical simulations of electrical field distributions were applied in order to elucidate and confirm the experimental results.

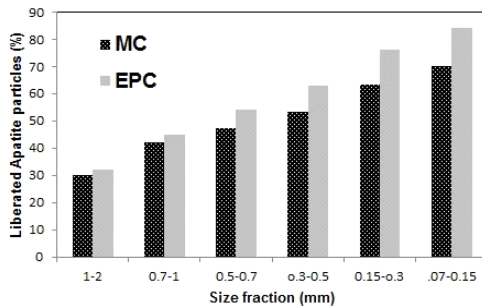


Fig. 2. Comparison of liberated particles of apatite comminuted by mechanical crushing (MC) and electrical pulses crushing (EPC)

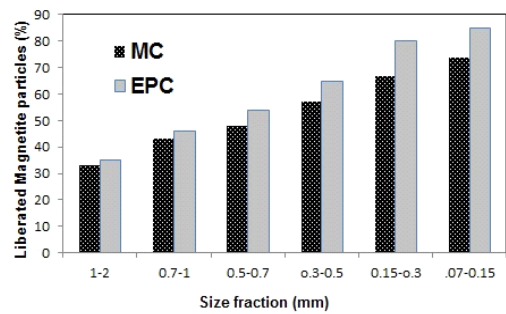


Fig. 3. Comparison of liberated particles of magnetite comminuted by mechanical crushing (MC) and electrical pulses crushing (EPC)

Finite element method simulation

In order to elucidate and confirm the experimental results, numerical simulation of electrical field distributions were performed. The COMSOL Multiphysics® software (its early version is called FEMLAB) was used for this aim. COMSOL Multiphysics® is a simulation software package for various physics and engineering applications, and consists of several add-on products among which the AC/DC Module add-ons were used in this paper. This software is based on the finite element method (FEM), a numerical technique in mathematics for calculating approximate solutions of partial differential equations (PDEs) with known boundary conditions (Reddy 2005). In this paper, major PDEs that define electromagnetic phenomena are Maxwell's equations which could be numerically solved relatively, quickly, and accurately using the software.

The complete set of Maxwell's equations is (Huray 2010):

$$\nabla \times H = J + \frac{\partial D}{\partial t} \quad (1)$$

$$\nabla \cdot B = 0 \quad (2)$$

$$\nabla \times E = -\frac{\partial B}{\partial t} \quad (3)$$

$$\nabla \cdot D = \rho \quad (4)$$

where H is the magnetic field intensity, J current density, D electrical flux density, B magnetic flux density, t time, E electrical field intensity, and ρ is the electrical charge density. There is interdependency between all variables in the equations and therefore, a unique solution. For stationary or quasi-stationary electromagnetic field distribution cases, the displacement current density term, $\frac{\partial D}{\partial t}$, is neglected, which gives the equations as below (Huray 2010):

$$\nabla \times H = J \quad (5)$$

Since the divergence of the curl of any vector field in three dimensions is equal to zero, the following equation is obtained:

$$\nabla \cdot J = \nabla \cdot (\nabla \times H) = 0 \quad (6)$$

The macroscopic material properties are defined by the constitutive relations:

$$D = \varepsilon E \quad (7)$$

$$B = \mu H = \mu_r \mu_o H \quad (8)$$

$$J = \sigma E \quad (9)$$

where ε is the permittivity, μ is the magnetic permeability, μ_r is the relative permeability, μ_o is the permeability in free space, and σ is the electrical conductivity.

FEM divides the geometry under study into many small tetrahedral parts, named finite elements, and solves the approximated PDEs for all of these simpler sub-domains. Such subdividing simplifies the inclusion of properties for dissimilar materials and facilitates the modeling of complex geometries. The main steps in setting up the simulations are mentioned below.

Building the geometry

The simulation model consists of four main objects: iron-phosphate ore, high-voltage electrode, zero-voltage electrode, and a spherical domain filled with water. In order to investigate the effects of several parameters that might affect the results, the ore morphology and size as well as the material and the electrodes distance should be flexible. The basic shape of the iron-phosphate ore was assumed to be elliptical (due to

initial particle shapes before HV treatment, see Fig. 4) and other shapes obtained by subtraction of cubic shapes from this one as shown in Fig. 5.



Fig. 4. Initial iron-phosphate ore particles shape

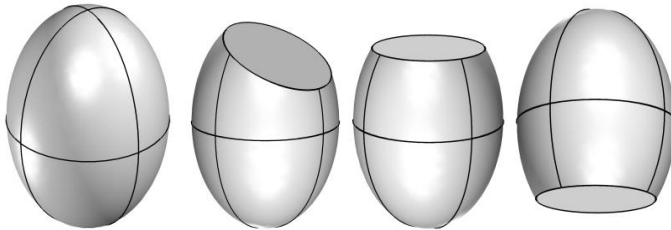


Fig. 5. Four shapes of iron-phosphate ore used in simulation models

Four diameters: 3.35 mm, 6.35 mm, 12.5 mm and 19 mm were used for basic elliptical ores to define four different sizes. In order to verify the effects of material, three different configurations and four compositions were defined. As shown in Fig. 6(a), the ore consisted of two equal parts. Therefore, these three compositions were conceivable: 50% magnetite-50% apatite, 50% magnetite-50% quartz, 50% apatite-50% quartz.

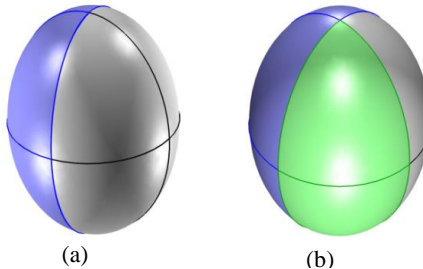


Fig. 6. Composition of minerals forming iron-phosphate ore (a) when ore consists of two equal parts (b) when ore consists of three parts (final composition)

The ore was made up of 50% magnetite, 25% quartz, 25% apatite (this composition was assumed to be the final composition due to Esfordi iron-phosphate ore mineralogy) as shown in Fig. 6(b).

Four electrodes distances: to match ore diameters, with a gap equals half of the elliptical radius between high-voltage electrode and ore, with a gap equals the radius, and with a gap equals the diameter, were used. Figure 7 shows a typical model of simulation geometry where iron-phosphate ore consists of 50% magnetite-25% quartz-25% apatite and electrode distance matches the diameter of elliptic.

Assigning materials

The main material property used in the simulations was the electrical permittivity. COMSOL Multiphysics® has a noticeable material database with required properties and users can assign materials to each object, instead of directly assigning the physical properties. However, it is possible to define and change the properties of materials or requirements that might not be provided in the library. Table 1 presents material properties used in simulations.

Table 1. Electrical permittivity of compounds used in simulations (Telford et al. 1990)

| Material | Electrical permittivity |
|-----------|-------------------------|
| Water | 80.36 |
| Quartz | 4.20 |
| Magnetite | 81.00 |
| Apatite | 7.40 |

Defining boundary conditions

The voltages of electrodes are the boundary values entered in the software. In the simulations the peak value of voltage pulses were assumed to be 100 kV.

Meshing the geometry

Solving with FEM requires meshing the geometry. By using free tetrahedral option in Mesh entity of defined models, an appropriate mesh will be fitted to the geometry. Figure 8 shows the typical geometry defined in pervious parts with an appropriate mesh.

Solving the model

By using default options of the COMSOL solver, simulation was run, and the results were computed. The arrow colors and sizes as well as surface colors represent the electrical field intensity. The flux always flew from high potential toward low potential. The magnitude of the flux was presented on a color scale from red (high intensity) to blue (low intensity). The distance between the flux represented the

concentration of charges such that shorter the distance is, the higher the concentration of charges is.

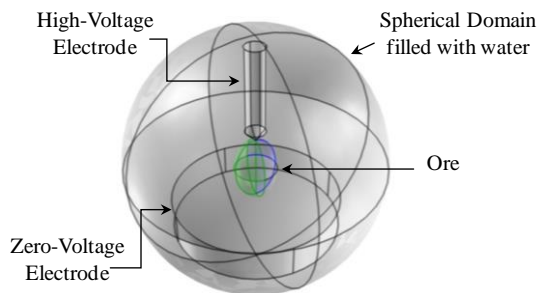


Fig. 7. Typical model of simulation geometry with iron-phosphate ore consists of three parts

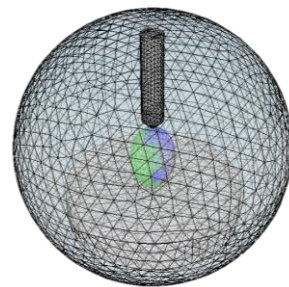


Fig. 8. Meshed typical geometry defined in section (a)

Results and discussion

Effect of minerals composition

The numerical simulation results for particles with different mineralogical compositions are shown in Fig. 9.

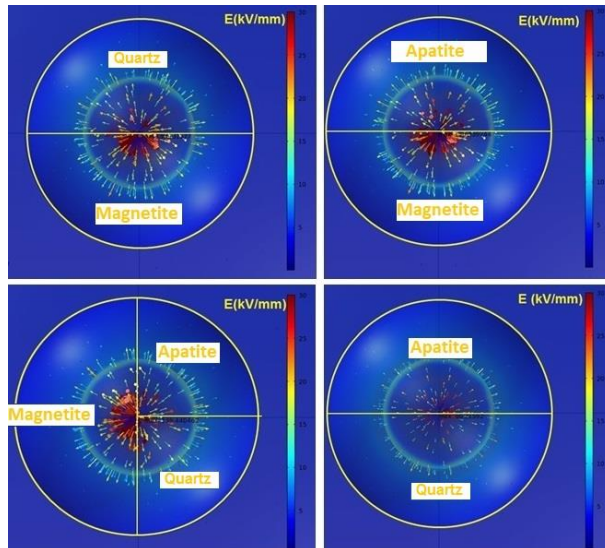


Fig. 9. Numerical simulation of the effect of mineral composition on electrical field intensity and distribution (top view)

In Fig. 9 the particle size is considered to be constant and equal to 12.5 mm. Three particles are considered to have dual composition and the final particle ternary composition. In the binary compound, one fraction contains magnetite, towards which

the field intensity is steadily inclined which is due to higher permittivity of magnetite in comparison to the other two compounds. It is also noticeable in the case of the ternary compound. In the binary compounds of apatite and quartz, no clear difference is seen in the field intensity distribution due to proximity of the permittivity values of the two compounds. Another important point visible in all four cases of Fig. 9 is that the focus of field intensity shifted to the boundary of components. This confirms the prominent feature of crushing by electrical pulses in which crushing occurs at the contact surface of minerals. In other words, the electrical crushing is selective and not accidental, unlike the mechanical crushing.

Effect of particle shape

As already mentioned before, four general forms were considered according to the particles shape of Esfordi iron-phosphate ore. The numerical simulation results of these four particle shapes are shown in Fig. 10 (front view). For better comparison, the distance between the HV and zero electrodes in all cases was assumed to be 12.5 mm.

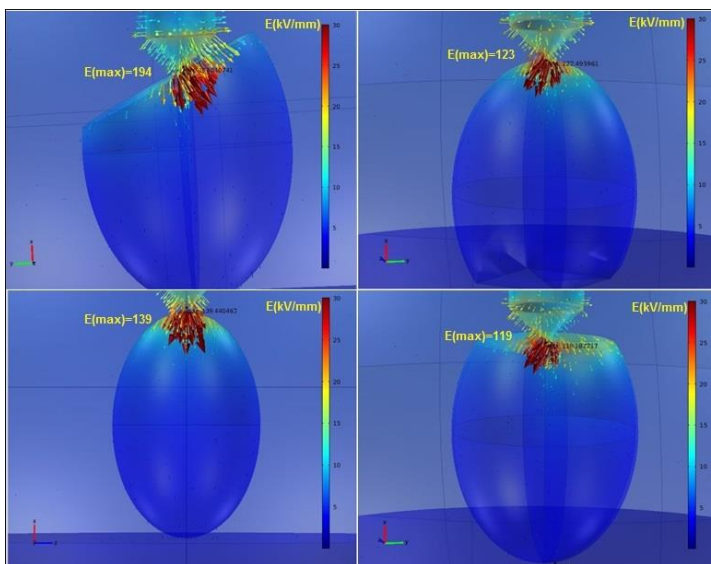


Fig. 10. Numerical simulation of the effect of particle shape on electrical field intensity and distribution (front view)

The results showed that the intensity of the electrical field decreased from full elliptical, incomplete elliptical (diagonal), partial elliptical (from bottom), and truncated elliptical (from above) forms, respectively. This is due to the angle between the HV electrode and contact surface of the material. Wang et al. (2012a) showed that sharpness of the material contact surface increases the intensity of the electrical field. Thus, for incomplete elliptical form (diagonal), contact with surface of the material and mineral is sharper than for other forms, and thus the intensity of the electrical field

is maximum. The higher field intensity for the complete ellipse relative to truncated elliptical form (from below) is due to the scale up of the former. The scale up caused the elliptic surface to be smoother for the partial elliptical form (from bottom), relative to complete elliptical one, and thus the field intensity decreased. Minimum field intensity is seen for truncated elliptical form (from above), which has a completely smooth surface.

Effect of feed size

To observe the effect of particle size, four particle sizes of 19, 12.5, 6.35, and 3.35 mm were considered. The numerical simulation results of these four particle sizes are shown in Fig. 11 (front view). As can be seen from Fig. 11, the smaller the particle size the greater intensity of the electrical field. The reason for this behavior is related to the distance between two electrodes. The field intensity increases with the decreasing distance between the electrodes. In fact, particle size is one of the most important parameters in the electrical breakage as mentioned by Wang et al. (2012a). The maximum values of field intensity versus particle size (distance between two electrodes) are shown in Fig. 12. The maximum electrical field intensity decreases with particle size almost exponentially and the equation shown in Fig. 12 can be adequately used to define the relationship between maximum intensity and particle size.

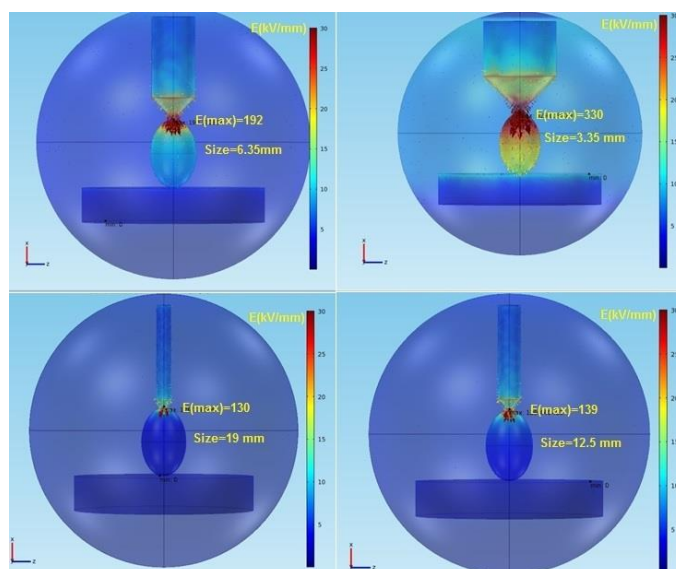


Fig. 11. Numerical simulation of the effect of feed size on electrical field intensity and distribution (front view)

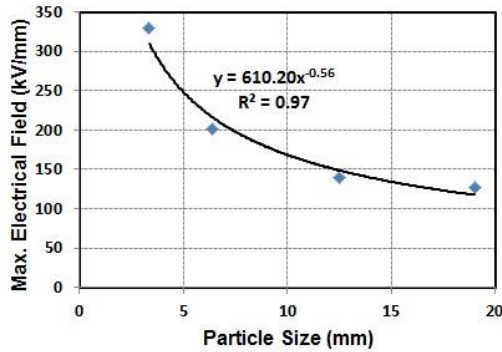


Fig. 12. Relationship between particle size (mm) and maximum electrical field intensity (kV/mm) in HVEPC

Effect of HV electrode distance

The effect of distance between the HV electrode and particle surface is shown (top view) in Fig. 13. In this case the particle size is 12.5 mm and mineralogical compositions are considered constant. Four cases: a quarter of diameter ($0.25 \cdot D$), half of diameter ($0.5 \cdot D$), and the whole diameter are considered for the distance between the HV electrode and particle. Comparison of the results shows that increasing of the distance of HV electrode from the particle surface resulted in a decreased effect of mineralogical composition on electrical field distribution. In other words, the increased distance decreases the length, color, and distribution of field intensity vectors, and for a higher distance, the intensity distribution becomes equal in all directions. Increasing the HV electrode distance from the surface of ore particles causes the effect of water around the electrode to be higher than the effect of minerals

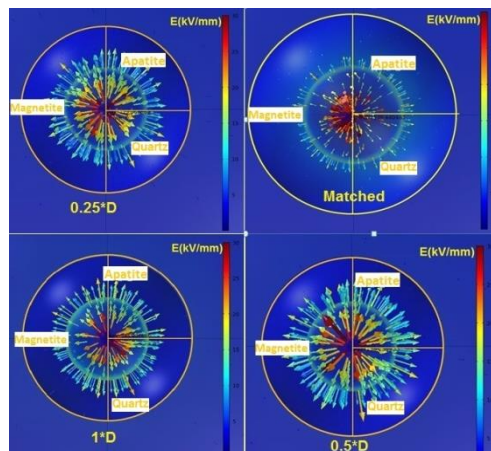


Fig. 13. Numerical simulation of the effect of HV electrode distance from particle surface on electrical field intensity and distribution (top view) (D: largest diameter of elliptical)

which means that the electrical discharge occurs in water instead of the particle. According to previous studies (Andres 1995, Andres et al. 2001), when the electrical discharge occurs in water, it is known as electrohydraulic disintegration. Thus, the increasing the distance of HV electrode from the particle surface increases the probability of electrohydraulic disintegration to occur instead of electrical disintegration.

Conclusions

Numerical simulation results involving iron-phosphate ore showed that the electrical field intensity distribution was highly dependent on electrical properties of the constituent minerals. For the iron-phosphate ore, magnetite, apatite, and quartz were considered in the experiments as the major minerals. Due to the higher permittivity of magnetite, the field intensity was higher for this mineral than for others. In addition, concentration of field intensity in the ternary compound showed that the intensity focus was on the boundary of mineral, which was also an indication of the selectivity feature of electrical crushing.

Electrical field intensity was proportional to the distance between the electrodes. Increasing the electrode distance, while the other factors were constant, would decrease the intensity of electrical field.

The angle of material contact surface with HV electrode was an important factor in the intensity of electrical field. Sharper contact angle induced higher intensity of the electrical field.

Increasing the distance between the HV electrode and material contact surface caused the intensity of the electrical field to decrease and change its distribution. In other words, the electrical disintegration in the material was converted to electrohydraulic disintegration by using the surrounding water environment.

Acknowledgments

The authors would like to acknowledge both Iran Mineral Processing Research Center (IMPRC) and Esfordi iron-phosphate complex for their effective cooperation and substantial input into the research essential for this paper.

References

- ANDRES U., 1989, *Parameters of disintegration of rock by electrical pulses*, Powder Technology, 58, 265-269.
- ANDRES U., 1995, *Electrical disintegration of rock*, Mineral Processing and Extractive Metallurgy Review, 14, 87-110.
- ANDRES U., 1996, *Dielectric separation of minerals*, Journal of Electrostatics, 37, 227-248.
- ANDRES U., 2010, *Development and prospects of mineral liberation by electrical pulses*, International Journal of Mineral Processing, 97, 31-38.
- ANDRES U., JIRESTIG J., TIMOSHKIN I., 1999, *Liberation of minerals by high voltage electrical pulses*, Powder Technology, 104, 37-49.

- ANDRES U., TIMOSHKIN I., SOLOVIEV M., 2001. *Liberation of valuable inclusions in ores and slags by electrical pulses*, Powder Technology, 114, 40-50.
- ANON 1986. *New ideas in minerals processing*, World Mining Equipment, 10, 4-19.
- CABRI L.J., 2008. *New technology for process mineralogy: Electric Pulse Disaggregation (EPD)*, CNT Mineral Consulting Inc. Ottawa, Canada, <http://www.cnt-mc.com>.
- CABRI L.J., RUDASHEVSKY N.S., RUDASHEVSKY V.N. AND GORKOVETZV.YA., 2008. *Study of native gold from the Luopensulo deposit (Kostomuksha area, Karelia, Russia) using a combination of Electric Pulse Disaggregation (EPD) and Hydroseparation (HS)*, Minerals Engineering, 21, 463-470.
- DAL MARTELLO E., BERNARDIS S., LARSEN R.B., TRANELL G., DI SABATINO M., ARNBERG L., 2012. *Electrical fragmentation as a novel rout for the refinement of quartz raw materials for trace mineral impurities*, Powder Technology, 224, 209-216.
- DODBIBA G., NAGAI H., WANG L. P., OKAYA K., FUJITA T., 2012. *Leaching of indium from obsolete liquid crystal displays: comparing grinding with electrical disintegration in context of LCA*, Waste Management, 32(10), 1937-1944.
- HURAY P. G., 2010. *Maxwell's Equations*, John Wiley & Sons, Inc., Hoboken, New Jersey.
- ITOM., OWADA S., NISHIMURA T., OTA T., 2009. *Experimental study of coal liberation: electrical disintegration versus roll- crusher comminution*, International Journal of Mineral Processing, 92, 7-14.
- KUFFEL E., ZAENGL W.S., KUFFEL J., 2000. *High Voltage Engineering Fundamentals*, Second edition published by Butterworth-Heinemann, 539.
- LASTRA R., CABRI L., WEIBLEN P., 2003. *Comparative Liberation study by image analysis of Merensky Reef samples comminuted by electric- pulse disaggregation and by conventional crusher*, Proceeding of XXII International Mineral Processing Congress, Cape Town, South Africa,1, 251-260.
- REDDY J.N., *An Introduction to the Finite Element Method*, 2005. Third Edition, McGraw-Hill Science/Engineering/Math.
- TELFORD W.M., GELDART L.P., SHERIFF R.E., 1990. *Applied Geophysics*, second edition, Cambridge University Press, 291.
- USOV A.F., TSUKERMAN V.A., 2006. *Electric pulse processes for processing of mineral raw materials: Energy aspect*. In: Proceedings of the XXIII International Mineral Processing Congress, Istanbul, Turkey, 2084-2088.
- WANG E., SHI F., MANLAPIG E., 2011. *Pre-weakening of mineral ores by high voltage pulses*, Minerals Engineering, 24, 455-462.
- WANG E., SHI F., MANLAPIG E., 2012A. *Factors affecting electrical comminution performance*, Minerals Engineering, 34, 48-54.
- WANG E., SHI F., MANLAPIG E., 2012B. *Experimental and numerical studies of selective fragmentation of mineral ores in electrical comminution*, International Journal of Mineral Processing, 112-113, 30-36.
- WANG E., SHI F., MANLAPIG E., 2012C. *Mineral liberation by high voltage pulses and conventional comminution with same specific energy levels*, Minerals Engineering, 27-28, 28-36.

Received July 21, 2014; reviewed; accepted August 1, 2014

MECHANICAL COMPACTION OF COKING COALS FOR CARBONIZATION IN STAMP-CHARGING COKE OVEN BATTERIES

Michał REJDAK, Ryszard WASIELEWSKI

Institute for Chemical Processing of Coal, Zamkowa 1, 41803 Zabrze, Poland, rejdak@ichpw.zabrze.pl

Abstract: The density of the coal charge plays an important role in the coke quality. The increase of the bulk density usually improves the coke strength due to increased coal particle contact and increased coke density. There are a few possibilities to increase the coal charge bulk density: adjusting the grain size distribution or moisture content (drying), oil addition and mechanical treatment (e.g., partial briquetting or stamping). A renewed interest in stamp charging cokemaking technology has been observed in recent years, especially in Asia, but also in Europe (Poland, Germany and Ukraine). The paper presents the results of studies on the effects of selected factors on the coal cake density and mechanical strength i.e. stamping energy, coal type, water content and crushing fineness. There is possibility to influence these parameters in industrial conditions. The investigations were carried out with use of mechanical stamping apparatus and strength testing machine specially designed for this purpose.

Keywords: *coke making, stamp charging, compaction, mechanical strength, bulk density, coal stamping*

Introduction

Density of coal charge influences the quality of the received coke and production capacity of the coking chambers (Karcz, 1991; Vander et al., 1996; Karcz and Strugala, 2008). There are a few possibilities to increase the coal charge bulk density (Karcz and Strugala, 2008; Czaplicki and Janusz, 2012): adjusting the grain size distribution, moisture content (drying), oil addition and mechanical treatment (e.g. partial briquetting or stamping). A renewed interest in stamp charging cokemaking technology has been observed in recent years, especially in Asia, but also in Europe, e.g. in Poland, Germany and the Ukraine (Gural et al., 2008; Kurunov et al., 2010; Loddo et al., 2011). This situation results from the decreasing supply and increasing price of prime coking coals. A stamp charging system enables the enhancement of the bulk density of the coal charge. Consequently, it has a positive influence on the mechanical strength of the coke, particularly on abrasion index - Micum 10 (Loison et

al., 1989; Chatterjee et al., 2001) The coke produced from blends with higher densities is less porous which is beneficial for mechanical strength (Loison et al., 1989; Herman, 2002; Strugala, 2002). What is important, it also allows using a higher amount of weaker coals in the coking blend (Chatterjee et al., 2001; Krishnan et al., 2004; Kuyumcu and Sander, 2014). The stamp charged coke ovens (Fig.1) differ little from the conventional top charged ovens, but the battery equipment is clearly different. The coking blend is compacted in a metal box with dimensions that are slightly smaller than the coke oven (20 to 30 mm). The stamping process is accomplished by a row of mechanical stampers that produce a durable coal cake. The prepared coal cake is charged into the chamber through the oven door after the compaction process. This method allows obtaining coal charge bulk density of 1100 kg/m^3 (wet basis) and higher, whereas for top charged coke ovens this value is on the order of 800 kg/m^3 .

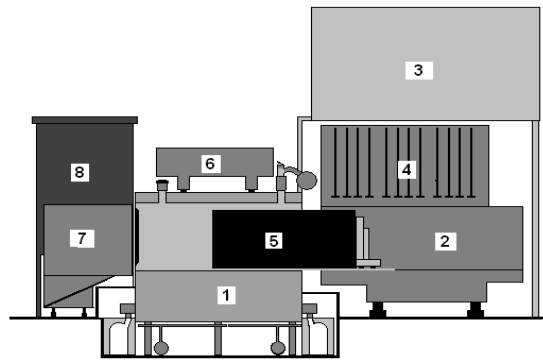


Fig. 1. Stamp – charged coke oven battery: 1 – battery refractory brickwork, 2 – SCP (Stamping-Charging-Pushing) machine, 3 – coal tower, 4 – stamping units, 5 – coal cake, 6 – CGT (Charging Gas Transfer) car, 7 – coke guide car, quenching car, 8 – quenching tower

In industrial practice the stamped cakes are characterized by the following dimensions: c.a. 3.5–6 m height, 12–16 m length and 0.4–0.5 m width. The goal is to prepare the coal cake with a certain density which provide its proper mechanical strength necessary to trouble-free oven charging and enable to achieve adequate productivity of ovens and coke quality (Kuyumcu and Sander, 2014). In aspect of productivity, process should be realized in a short time. Failure of the cake during charging causes operational and environmental problems (fugitive emission). Factors that directly affects both the cake density and mechanical strength are cumulative stamping energy (stamping time) and physicochemical properties of coal. The uniform distribution of density and coal charge properties (i.a. moisture content, crushing fineness) of the whole volume of the cake is essential.

The paper presents the results of studies on the effects of selected factors on the coal cake density and mechanical strength i.e. stamping energy, coal type, water content and crushing fineness. There is possibility to influence these parameters in industrial condition.

Materials and methods

For the investigation purposes, five coking coals and one coking blend were selected. The coals used for the preparation of the blends originate from the mines of the Upper Silesian Coal Basin (USCB). These coals are used as the basic components of the coking blends used in Polish coke plants for the production of metallurgical coke. The properties of selected coals are presented in Table 1.

Table.1 Properties of investigated coals

| Parameters | A | B | C | D | E |
|--|-------|-------|-------|-------|-------|
| Moisture content, M^a , % | 0.6 | 0.7 | 0.9 | 1 | 1,1 |
| Ash content, A^d , % | 4.8 | 10.5 | 7.9 | 4.6 | 5.6 |
| Volatile matter, VM^{daf} , % | 22.32 | 27.87 | 24.82 | 35.92 | 34.06 |
| Carbon content, C^{daf} , % | 90.2 | 88.4 | 89.3 | 85.4 | 86.3 |
| Nitrogen content, N^{daf} , % | 1.3 | 1.5 | 1.4 | 1.5 | 1.5 |
| Hydrogen content, H^{daf} , % | 4.7 | 5.0 | 4.8 | 5.3 | 5.24 |
| Sulfur content, S_t^{daf} , % | 0.12 | 0.52 | 0.47 | 0.49 | 0.3 |
| Oxygen content, O^{daf} , % | 3.8 | 4.5 | 4.0 | 6.4 | 6.6 |
| Roga index, RI | 64 | 74 | 71 | 77 | 62 |
| Free swelling index, FSI | 7.5 | 8 | 8 | 7.5 | 7 |
| True density, ρ^t , g/cm ³ | 1.373 | 1.401 | 1.389 | 1.344 | 1.341 |
| Crushing fineness, %<3,15mm | | | 93 | | |

The analyses of single coals were performed following the Polish Standard procedures for moisture M (PN-G-4512:1980), ash content A^d (PN-ISO 1171:2002), and volatile matter content VM^{daf} (PN-G-04156:1998). Carbon, hydrogen and nitrogen contents were determined according to procedure PN-G-04571:1998 and sulfur content according to PN-G-04584:2011. Oxygen content was calculated from the difference of mass balance. Polish Standard procedures were also followed to determine the Roga Index, RI, PN-G-04518:1981, the Free Swelling Index, FSI, PN-ISO 501:2007. True density was determined with use of helium pycnometer AccuPyc II 1340 which works on the basis of gas-displacement method, made of Micromeritics, USA. During the measurement of absolute density the temperature were remained constant at value of 25 °C by means of refrigerating/heating circulator.

Stamping test were performed with use of mechanical stamping apparatus (Fig.2). The installation was equipped with a digital shift sensor that enabled the control of the charge height. Weighted portion of coal is charged into cylindrical mold (with diameter of 95 mm and 150 mm nominal height) and then compacted by means of series of stamper dropping (11 kg) from the same height (0.64 m). Cumulative stamping energy is calculated from the potential energy of the stamper. Volume of the obtained coal cake is determined based on its diameter and height. Bulk density of the coal charge is determined from the quotient of mass and the volume of compacted coal.

The mechanical strength tests were conducted with use of strength testing machine equipped with bidirectional load cell with maximum load of 5 kN (Fig. 4). Prepared sample was placed between compression plates and then pressed with speed of 2 mm/min. Value of the measured force increases until the destruction of sample takes place and later decreases (Fig.5). The measurement is conducted until the value drops below 80% of its maximum. Value of compressive strength was determined from the quotient of maximum force recorded and surface of stamped coal sample. In case of shear test, the coal sample is placed in a mold where it is divided into two symmetrical parts. For one of them, a force is exerted, which is perpendicular to the cross-sectional area of sample. Value of shear strength was determined from the quotient of maximum exerted force and sheared section area.

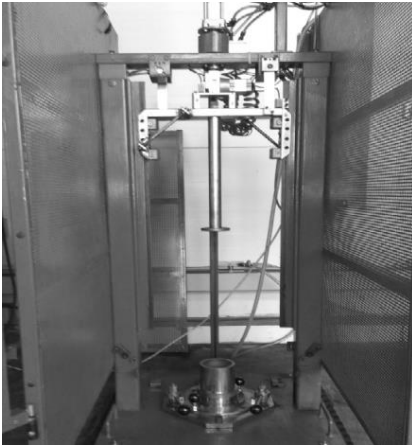


Fig. 2. Mechanical stamping apparatus

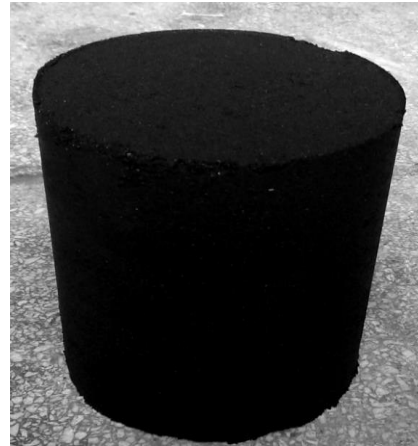


Fig. 3. Prepared coal cake

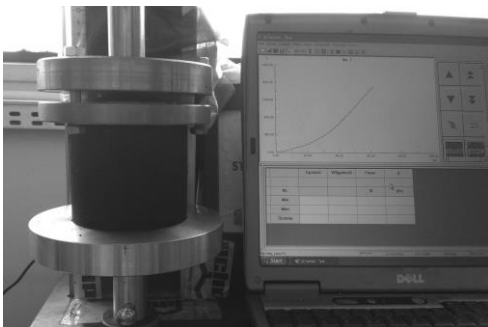


Fig. 4. Strength test device

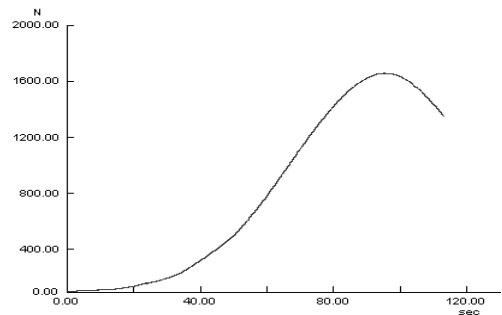


Fig. 5. Screenshot of compressive strength test

Results and discussion

Influence of stamping energy on coal cake density and its compressive strength

The influence of cumulative stamping energy on coal cake density is presented in Fig. 6. Investigation was carried out for coal blend with composition similar to the one used in one of the Polish coking plants. The crushing fineness was 93% below 3.15 mm ($d'_{RRSB} = 1.31$ mm) and water content was 10%. Fifteen stamping steps were performed which corresponds to stamping energy of approximately 1780 J/kg coal. It can be clearly observed that density increases together with the increase of stamping steps. Relationship between stamping energy and cake density is logarithmic. Coal particles under the influence of impact energy move between themselves, small particles consecutively fill voids between particles and create dense agglomerate. Movement of particles is facilitated by surface moisture which reduces the friction forces. At the beginning of the process, the density rapidly increases, but further, the increase is noticeably lower. With increase in charge density, porosity decreases which causes growth of water saturation index (Fig. 7). Stamping of coal enables obtaining bulk density at the level of approximately 75–80% true density of coal (ρ^d/ρ^t). Increase in charge bulk density positively influence the mechanical strength of coal cake due to enhanced particle-particle contact area and increased capillary forces caused by pore saturation growth (Fig. 8). Increase in charge bulk density from approximately 990 to 1063 kg/m³ caused significant enhancement of coal cake compressive strength. The values of strength increased from approximately 151 to 462 kPa i.e. for each 10 kg/m³ rise of bulk density, the increase of compressive strength was 43.8 kPa. At industrial scale the stamping energy of 450-800 J/kg coal charge is applied and the stamping process takes about 4.5 to 8 minutes. The obtained coal cake density is around 1000 kg/m³ (db – dry basis). The density of coal cakes obtained at laboratory scale is similar.

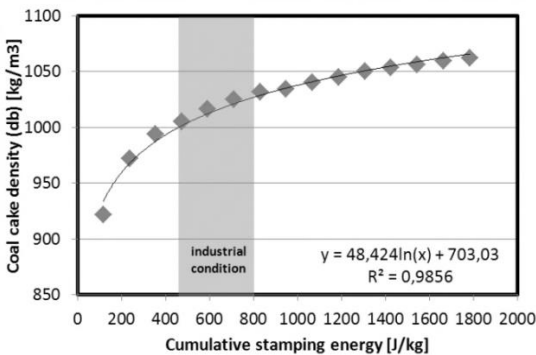


Fig. 6. Coal cake density vs. cumulative stamping energy (coal blend)

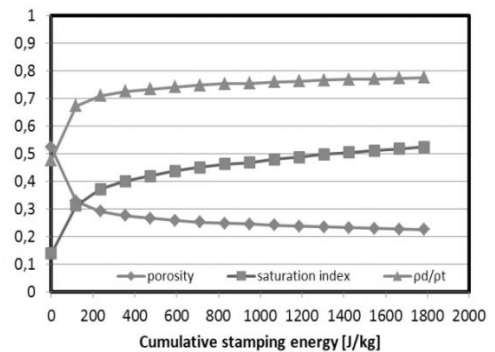


Fig. 7. Changes of porosity, saturation index and ratio of cake density/coal true density (coal blend)

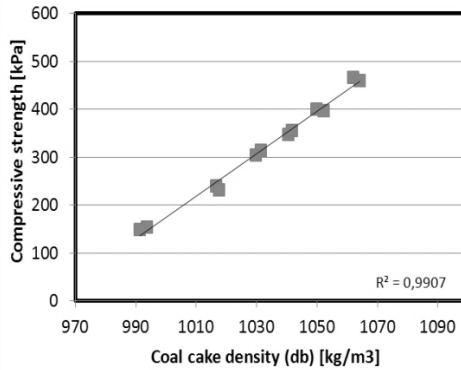


Fig. 8. Compressive strength vs. coal cake density (coal blend)

Influence of coal type and moisture content on coal cake density and its mechanical strength

The tests were carried out for 5 single coals mentioned in Table 1. The range of moisture content was 7-13%. For each test 5 stamping steps were carried out, i.e. the cumulative stamping energy was constant. The water in coal charge acts as a lubricant which reduces the forces between coal particles, facilitating their rearrangement and acts as a binder that provides proper mechanical strength of compacted coal (Kuyumcu and Sander, 2014). This is due to the presence of capillary forces (liquid bridges, capillary pressure) between coal particles. From the other hand, water is unfavorable in aspect of both thermal (higher energy demand to evaporate water) and ecological balance (greater quantity of wastewater) of carbonization process. Additionally, water can negatively affects the ceramic lining of the coke ovens.

In Figures 9 and 10 the influence of coal type and moisture content on coal cake has been presented. As can be seen, the moisture has a large effect on wet bulk density of coal, but a slight effect on bulk density calculated on dry state (dry coal charge - important for the productivity of coke ovens). The higher level of bulk density for coal B was achieved. Increase in moisture content from 7 to 13% caused growth of wet bulk density from 1096 to 1200 kg/m³ (9.5%) while dry bulk density increased from 1020 to 1044 kg/m³ (only 2.4%). In case of coal C, wet bulk density increased by 8.2% (from 1088 to 1177 kg/m³) while dry density only by 1.7% (from 1009 to 1026 kg/m³). For coal A similar relationships was noticed. Wet bulk density increased by 9.3% (from 1068 to 1167 kg/m³) whereas dry bulk density increased by 2.4% (from 991 to 1015 kg/m³). In the case of coal D and E a slightly different relationship was noted. While wet bulk density increased by 7.1% and 6.9% respectively (for D from 1008 to 1088 kg/m³ and E from 1012 to 1082 kg/m³), the level of dry density remained largely unchanged. The dry bulk density is approximately 940 kg/m³ for both coals.

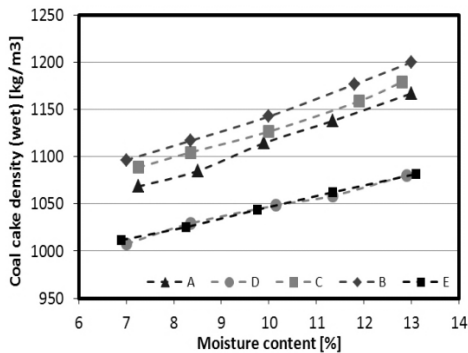


Fig. 9. Influence of coal type and moisture content on coal cake density (wet basis)

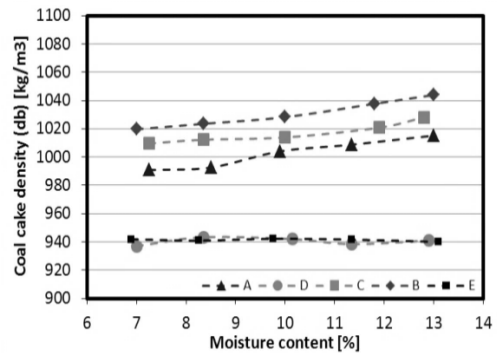


Fig. 10. Influence of coal type and moisture content on coal cake density (dry basis)

As can be seen from Figs. 9 and 10, the coals have different level of density obtained for constant stamping energy (5 stamping steps). A varied level of coal cake density (depending of coal type) can result from several causes. Firstly, due to different true density of coals resulting from various degree of coalification and ash (mineral matter) content. Generally, the higher the degree of coalification and the ash content, the higher is the true density of coal. The second reason may be varied mechanical (grindability, hardness of coal structure) and surface (wettability) properties of selected coals. The wettability of coals depends on various factors i.a. coalification degree, ash content and maceral composition (Orumwense, 1998; Laskowski, 2001; Gosiewska et al., 2002). Less coalified coals contains more oxygene and hydrophilic functional groups than more coalified coals (Fuerstenau et al., 1983; Gutierrez-Rodriguez and Aplan, 1984). The coal A is the most coalified from the selected coals ($VM^{daf} = 22.32\%$, $O^{daf} = 3.8\%$) while coal D is the lowest coalified ($VM^{daf} = 35.92$, $O^{daf} = 6.4\%$). Higher wettability of surface of coal grains is associated with higher works of adhesion (reversible work to separate the interfaces of two coal grains) which can adversely affect rearranging of coal particles and prevent creating of dense coal cake. For the coals D and E (potentially characterized by the lowest wettability) increase in moisture content did not improve the dry density which can be related to the described effect. In the case of different mechanical properties, higher density can be obtained due to spalling of coal particles. For coking coals, the grindability which reflects coal structure hardness, decrease with increase of volatile matter content. During the stamping process plastic-elastic deformation takes place. Locally the mechanical strength of the particles may be exceeded thus some parts of coal grains can be crushed and fill particle-particle voids. For the low rank coals with lower grindability this phenomena might be limited. From the other hand, excessive particles breakage during stamping can negatively affect bulk density of coal cake.

As was aforementioned, the moisture play important role in preparation of stamped coal cakes. From the practical point of view, proper amount of water is essential to

provide required strength of industrial coal cake. For all samples, the increase in water content from 7% to 8.5-10% improves the mechanical strength (both compressive and shear strength) of the stamped cake (Figs.11 and 12). Increase in strength is caused by increased density and surface forces between coal particles (i.a. increasing the number of particle-particle contacts points with capillary bridges). With further increase in moisture content, the strength decreases despite of higher cake density. This may be due to that excessive moisture inside the pore and between coal particles can prevent the formation of surface forces (Dash et al., 2005). Therefore, it can be concluded that there is an optimal level of moisture content which provides suitable strength of coal cake. In the case of compressive strength the higher values was obtained for 10% of moisture content and for D, C, and A coals respectively. For coals B and E, the optimum moisture content was 8.5%. Similar relationships was noticed for shear strength measurement, with the exception of coal B for which the maximum values of shear strength was obtained for 8.5% of moisture.

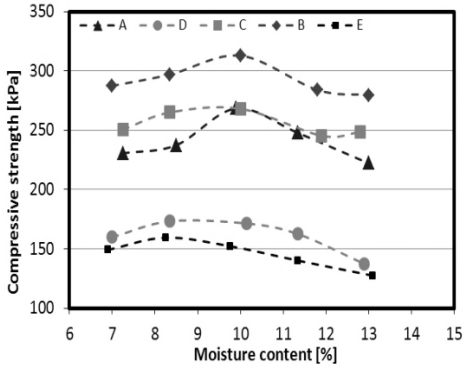


Fig. 11. Influence of coal type and moisture content on coal cake compressive strength

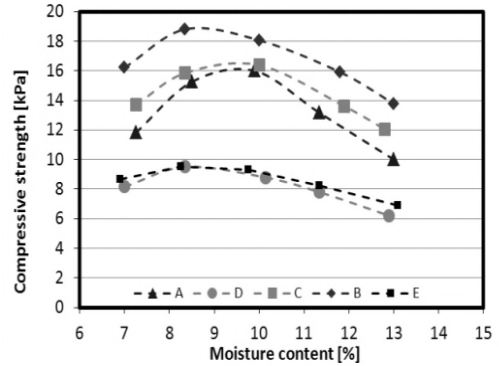


Fig. 12. Influence of coal type and moisture content on coal cake shear strength

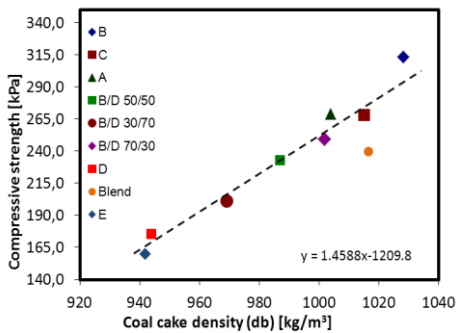


Fig. 13. Influence of coal type on coal cake compressive strength (constant stamping energy)

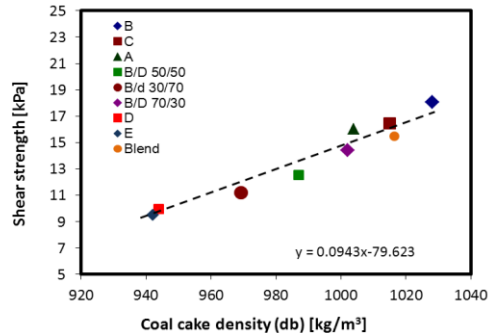


Fig. 14. Influence of coal type on coal cake shear strength

In Figures 13 and 14 the influence of coal type on bulk density and compressive and shear strength has been presented. Additionally, three binary blends with various proportion of coals B and D were prepared (50/50, 30/70 and 70/30). As is apparent from Figs. 13 and 14, the relationship between coal cake density and compressive and shear strength is linear. The determination coefficients are $R^2=0.898$ and $R^2=0.947$ respectively. As was previously mentioned it is due to enhanced particle-particle contact points resulting greater cohesion of coal cake.

Influence of crushing fineness on coal cake density and its mechanical strength

Apart from coal type and moisture content, bulk density of stamped cake can be influenced by crushing fineness. In industrial scale coals which are used for stamp charging batteries are crushed with use of hammer mills to the level of 90-96% below 3.15 mm. For classic top-charged batteries, the crushing fineness of 75-85% below 3.15 mm is used. Higher crushing fineness enables to obtain proper mechanical strength of coal cake, but it can affect the bulk density. As is presented on Fig. 15, increase in crushing fineness of coal charge from 87 to 99% below 3.15 mm causes reduction of bulk density from 1036 to 991 kg/m³. The main advantage of a greater degree of crushing is undoubtedly higher strength of stamped coal cake (Fig. 16). With increase in crushing fineness from 87 to 99%, the compressive strength linearly increases from 231 to 253 kPa (for constant stamping energy) despite of lower density. The improvement is much higher for constant cake density (Fig. 17). In that case, the compressive strength of stamped cake increased from 231 to 359 kPa. The strength growth mechanism is similar to that obtained for density increase. Greater crushing fineness is related to higher number of particle-particle contact points (higher surface of contact between particles, stronger total bonding forces) which positively influences cake strength. Additionally, crushing fineness has an impact of quality of produced coke also, which should be taken into consideration while choosing its level.

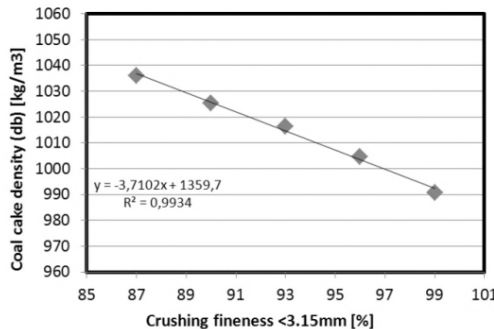


Fig. 15. Influence of crushing fineness on coal cake density (constant stamping energy)

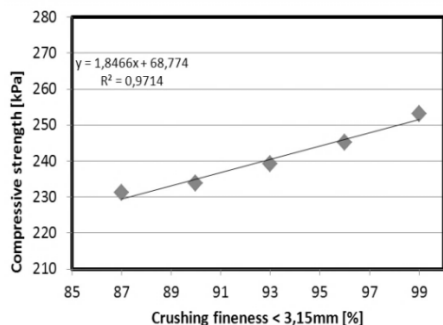


Fig. 16. Influence of crushing fineness on coal cake compressive strength (constant stamping energy)

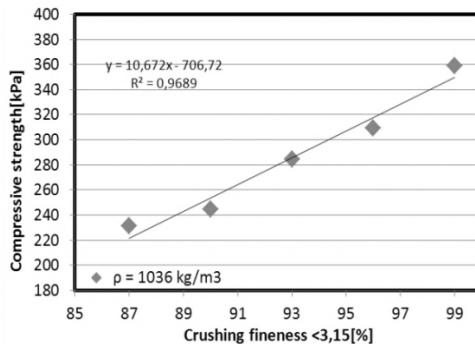


Fig. 17. Influence of crushing fineness on coal cake compressive strength (constant cake density)

Conclusions

The aim of the investigation was to evaluate the influence of selected parameters (i.e. stamping energy, coal type, moisture content and crushing fineness) on coal cake density and mechanical strength. The results are summarized as follows.

- Increase of stamping energy causes increase of density of coal cake.
- Increase in moisture content positively influences both wet and dry bulk density of coal cake. Changes of wet bulk density was from 6.9 to 9.5% (depending on the coal type). In the case of dry bulk density the differences were lower (from 1.7 to 2.4%) except for two coals D and E for which there was no significant differences.
- Coal type has an impact on density of stamped cake. For constant stamping energy, the density of stamped cake is greater for higher rank coals.
- The density of coal cake influences mechanical strength of stamped coal cake. The higher the density, the higher the strength of coal cake.
- There is an optimum level of moisture content in coal charge which provide maximum strength of cake. For the investigated samples, this level was 8.5-10%.
- Increase in crushing fineness reduces the coal cake density while mechanical strength is improved.

Acknowledgements

This study was carried out within the framework of “Smart coking plant meeting the requirements of the Best Available Techniques”, contract no. 01.01.02-24-017/08 financed by the Innovative Economy Operational Program funding of the European Regional Development Fund.

References

- CHATTERJEE A., SINGH B.K., BAUER G., VEIT G., 2001. *The changeover of the coke production at Tata Steel from top charging to stamp charging technology*, Cokemak. Int., 13, 75.
- CZAPLICKI A., JANUSZ M., 2012. *Preparation of Coal Batch for Top Loading: Experimental Research*, Coke and Chem. 55, 366-371.

- DASH P.S., KRISHNAN S.H., SHARMA R., BANERJEE P.K., HALDAR S.K., 2005. *Laboratory scale investigation to improve the productivity of stamp charge coke oven trough optimization of bulk density of coal cake*, ISIJ Int., 45, 1577-1586.
- FUERSTENAU D.W., ROSENBAUM J.M., LASKOWSKI J.S., 1983. *Effect of surface functional groups in the floatability of coal*, Colloids and Surfaces, 8, 153-174.
- GOSIEWSKA A., DRELICH J., LASKOWSKI J.S., PAWLIK M., 2002. *Mineral matter distribution on coal surface and its effect on coal wettability*, J. of Colloid and Interface Science, 247, 107-116.
- GURAL V.V., KRIVONOS V.V., RUDYKA V.I., TARUTA A.A., 2008. *Metallurgical-Coke Production on the Basis of Rammed Batch and Dry Slaking: An Efficient, Ecologically Sound and Energy-Saving Technology*, Coke and Chem., 51, 309.
- GUTIERREZ-RODRIGUEZ J.A., APLAN F.F., 1984. *The effect of oxygen on the hydrophobicity and floatability of coal*, Colloids and Surfaces, 12, 27-51.
- HERMANN W (2002). *Coke Reactivity and Coke Strength, Part 1: Coke Reactivity – Summary and Outlook*, Cokemak. International, 14, 18.
- KARCZ A., 1991. *Koksownictwo*, AGH, Kraków.
- KARCZ A., STRUGAŁA A., 2008. *Increasing chances of utilizing the domestic coking coal resources through technological operations in coal blend preparation*, Miner. Resour. Manag., 24, 5-18.
- KRISHNAN S.H., DASH P.S., GUHA M., KUMAR D., DESHPANDE D.P., 2004. *Application of Binder in Stamp Charge Coke Making*, ISIJ Int., 44, 1150.
- KURUNOV I., LIZOGUB P., GOLUBEV O., 2010. *Coal Preparation, Coking, and Slaking in China and Japan*, Coke and Chem., 9, 22.
- KUYUMCU H.Z., SANDER S., 2014. *Stamped and pressed coal cakes for carbonization in by-product and heat-recovery coke ovens*, Fuel, 121, 48-56.
- LASKOWSKI J., 2001. *Coal Flotation and Fine Coal Utilization*. Elsevier.
- LODDO R., ESPOSITI A., PIVOT S., 2011. *A modern design approach in the new stamp charging coke oven batteries in Dillingen*, The 6th European Coke and Ironmaking Congress, session 19, Dusseldorf.
- LOISON R., FOCH P., BOYER A., 1989. *Coke: Quality and Production*, Butterworths, London, 353.
- ORUMWENSE F.O., 1998. *Estimation of the wettability of coal from contact angles using coagulants and flocculants*, Fuel, 77, 1107-1111.
- STRUGAŁA A., 2002. *Change in porosity during carbonization of bituminous coals: effect due to pores with radii less than 2500nm*, Fuel, 81, 1119.
- VANDER T., ALVAREZ R., FERRARO M., FOHL J., HOFNERR K., HUART J.M., MATILLA E., PROPSON, WILLMERS R., VD VELDEN B., 1996. *Coke Quality Improvement Possibilities and Limitations*, 3-rd International Cokemak. Congr. Proc., Gent, 28 -37.

Received April 20, 2013; reviewed; accepted March 22, 2014

ESTIMATION OF COPPER CONCENTRATE GRADE BASED ON COLOR FEATURES AND LEAST-SQUARES SUPPORT VECTOR REGRESSION

Chuancheng REN^{*}, Jianguo YANG^{**}, Chuan LIANG^{**}

^{*} College of Information Management, Dezhou University, Dezhou, 250323, China, renchuancheng@163.com

^{**} National Engineering Research Center of Coal Preparation and Purification, China University of Mining and Technology, Xuzhou, 221116, China

Abstract: In this paper, a new method based on color features of microscopic image and least-squares support vector regression model (LS-SVR) is proposed for indirect measurement of copper concentrate grade. Red, green and blue (RGB), hue and color vector angle were extracted from color microscopic images of a copper concentrate sample and selected for the comparison. Three different estimation models based on LS-SVR were developed using RGB, hue, and color vector angle, respectively. A comparison of three models was carried out through a validation test. The best model was obtained for the hue giving a running time of 30.243 ms, root mean square error of 0.8644 and correlation coefficient value of 0.9997. The results indicated that the copper concentrate grade could be estimated by the LS-SVR model using the hue as input parameter with a satisfactory accuracy.

Keywords: concentrate grade, copper concentrate, LS-SVR, color features, microscopic image

Introduction

In copper industry, the content of useful component (grade) is one of primary quality parameters in the final concentrate and a key control parameter in a flotation circuit. The grade determines selling price, so industry increases the grade of final product for the greatest interest (Kaartinen et al., 2006; Malewski and Krzeminska, 2012). The copper grade is the percentage of copper mineral captured into the final flotation concentrate. Usually, the copper grade could be determined by direct and indirect measurements. The direct measurements mainly involves an X-ray fluorescence measurement and chemical assay methods. The X-ray fluorescence measurement is performed in a few copper mineral industries due to high cost (Haavisto et al., 2008). However, the chemical assay method is a time consuming process. Therefore, a faster

and cheaper indirect measurement is desirable to achieve the estimation of copper grade.

A machine vision system has potential applications for the concentrate grade evaluation, which is highly dependent on the features of froth and concentrate particle appearance. This is due to the fact that flotation operators always roughly evaluate the concentrate grade through the characteristics of froth surface or concentrate particle in order to monitor and improve flotation processes (Tasdemir and Kowalczyk, 2014). Currently, the concentrate grade measurement can be improved by means of machine vision in mineral industry. The final concentrate image features can be used to estimate various parameters, i.e. grade, recovery and other process variables. In particular, if the concentrate grade is measured by an inexpensive machine vision, the flotation performance could be improved through a feedback control. Consequently, a sufficiently accurate image analysis method can interpret the correlation between the characteristic of concentrate particle and grade.

In the past, several methods have already been utilized in order to determine the relationship between the concentrate grade and image analysis. Oestreich et al. (1995) applied a color video camera to characterize the color of dry material, slurry, and flotation froth mixtures of chalcopyrite and molybdenite. In addition, they built a strong correlation between the color vector angle and mineral composition. The color vector angle is used to characterize the color of mineral mixtures. Although the estimated expression was mentioned, there was a little indication of data to validate it directly. A regression method is one of the most prevalent methods for estimating the concentrate grade. Bonifazi et al. (2000) adopted a multiple regression method for evaluating Pb, Zn, Cu and MgO froth grades, which used fractal parameters derived from froth, along with froth color parameters (i.e. RGB, HSI and HSV spectra statistical parameters) as input variables. Additionally, Bonifazi et al. (2002) adopted a simple second-order polynomial approach with the parameters extracted from a 3D model of froth surface and image analysis (color and morphological features) to forecast the mineral grade. When input parameters were mutually independent, Morar et al. (2005) applied a multivariate linear regression model to predict the concentrate grade based on color, velocity and stability information of the froth. In this method, the best prediction model was obtained with a combination of color and stability information. Forbes (2007) gave a description of relationships among froth velocity, bubble size, froth class and concentrate grade by using both linear and non-linear regression model respectively. When the input parameters were highly dependent on each other, Haavisto et al. (2006) applied a partial least squares (PLS) method to suit well the problem. It formed a mapping from input to output variables using a lower dimensional latent basis, and built a set of latent variables that interpreted input and output variables. The PLS method using the measured froth spectrum as input variables, was calculated to estimate the grade of zinc flotation circuit concentrate.

Recently, an artificial neural networks (ANN) method has been increasingly applied in grade estimation. Based on the ANN method, Marais (2010) set up a

nonlinear model to estimate the platinum froth grade and recovery. In this nonlinear model, the input variables was extracted from froth images based on the laboratory and industrial data. Based on the ANN and multivariate non-linear regression (MNL) models, Nakhaei et al. (2012) also developed two simulation models to estimate the grade and recovery of a pilot plant flotation column with the input variables, such as the values of chemical reagents dosage, froth height, air and wash water flow rates, etc. They found that the model based on the ANN approach had a better prediction performance than the MNL method. Furthermore, Nakhaei et al. (2013) adopted a genetic algorithm to optimize the input variables within the ANN, and applied the GANN approach to predict the metallurgical performance (grade and recovery) of the pilot flotation column with the variables, i.e. chemical reagents dosage, froth height, air, wash water flow rates etc. Yong et al. (2012) proposed a concentrate grade prediction model based on the RBF neural network using the froth image characteristics, in which the input variables were optimized the by immune evolution method to improve predictable accuracy.

All of above mentioned methods are applied to a large amount of samples. In addition, the existing methods also include the preprocessing of input variables and demand a large training set. To offset disadvantage, this paper introduces the LS-SVR method (Suykens and Vandewalle, 1999) into the model of concentrate grade estimation. The LS-SVR method, combining the properties of regression method and the advantages of support vector machine, attracted great interests and become a popular tool for model estimation. It shows a surprising effectiveness in estimating the concentrate grade with a small amount of concentrate samples.

In this study, the concentrate grade of copper flotation process was predicted. Firstly, the colors of microscopic images of copper concentrate were obtained, and the usefulness color features were extracted from these images. Secondly, the estimated model for copper concentrate grade was developed by the least-squares support vector regression model (LS-SVR) method using the training set from the color features and chemical assay.

Materials and methods

Characteristics of copper concentrate

In flotation experiments, copper ore taken from Pulang Copper Mine in China is a typical ore of copper-sulfide minerals. The ore contains mainly chalcopyrite, subordinately bornite, and rarely covellite. The associated minerals are pyrrhotite, molybdenite, magnetite, quartz. The series of copper concentrate were obtained through a laboratory flotation cell. The flotation concentrates were dewatered, dried, and sampled for a chemical assay. The results showed that the sample ranged from 8 to 20% of Cu. The sample was characterized with a complex mineral composition and fine dissemination size, which was a mixture of particle size mainly less than 74 μm . Thus, the macroscopic visualization of sample was extremely difficult to obtain.

The minerals of the copper concentrate sample varied in color. The minerals influencing the overall sample color included: chalcopyrite (brassy yellow), bornite (brown to black with a reddish bronze color on freshly broken surfaces or a typical purplish-bluish tarnish), covellite (a deep metallic indigo blue with iridescent yellow and flashing red), pyrrhotite (bronze), magnetite (black iron), quartz (clear quartz/white/ pink/brown to black). The above-named minerals displayed a range of colors in the concentrate samples, thus the samples had not a homogeneously distributed colors.

Microscopic image acquisition

In image processing, one of the critical steps is the appropriate acquisition of images. A schematic diagram of acquisition system for color microscopic images of copper concentrate is given in Fig. 1. It consists of a digital monocular microscope, ring of LED light source and computer (PC). The digital monocular microscope with a special design for a CCD camera, was an instrument to help viewing very small particles under a magnification. The camera (3.0 MP camera) had a CCD sensor with a resolution of 2048×1536 pixels. The ring of a LED light source, which mounting around the objective could be adjusted to obtain the best illumination intensity. A concentrate sample image was displayed on a PC screen through a USB cable. The magnification of this image acquisition system ranged from 50 to 300.

Random samplings were performed in each copper concentrate sample to obtain a smaller subsample (around 0.6 g). An 1×3 cm subsample with a flat surface was used for the microscopic image acquisition system. Ten microscopic images were captured from different parts of each subsample (Fig. 2).

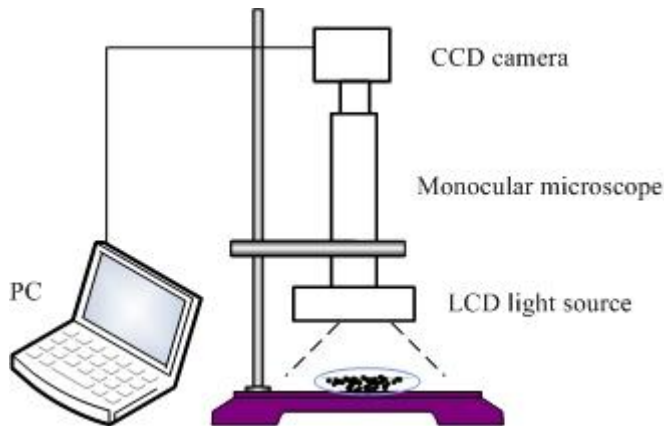


Fig. 1. Schematic diagram of image-acquisition experimental setup

Color features

The image analysis involved extraction of red, green and blue components from microscopic images in the RGB color space, from which the mean values of red, green

and blue components were calculated. Other parameters such as the color vector angle and mean value of hue component in the HSV color space were also obtained. These parameters were used to estimate the copper concentrate grade.

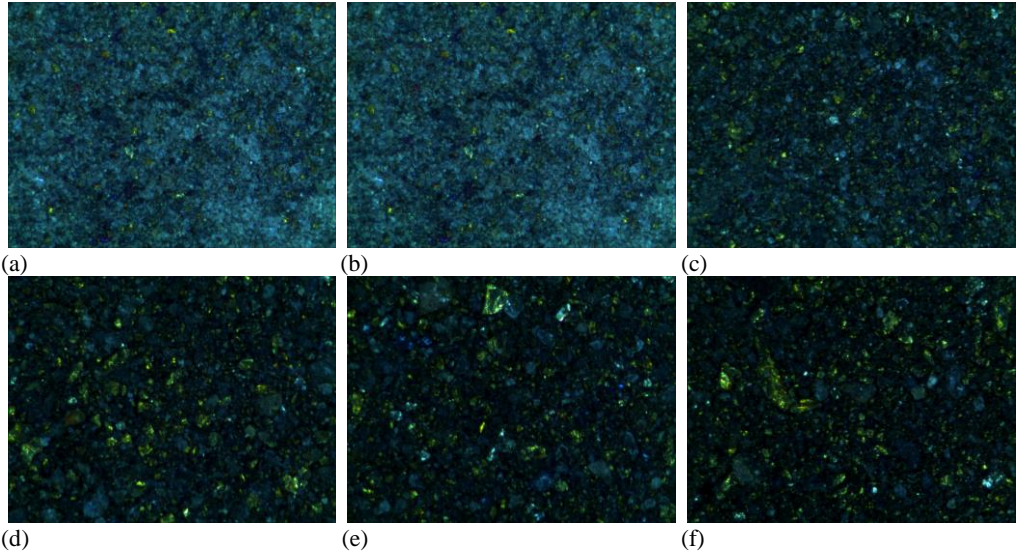


Fig. 2. Example microscopic images from different concentrate grade samples used in study (original magnification $\times 260$): (a) Cu 10.89%, (b) Cu 13.65%, (c) Cu 15.66%, (d) Cu 16.86%, (e) Cu 18.32%, (f) Cu 19.22%

The mean values of red, green and blue components for a concentrate sample are expressed as follows:

$$\begin{cases} R_i = \frac{1}{10} \sum_{k=1}^{10} \left(\frac{1}{M \times N} \left(\sum_{m=1}^M \sum_{n=1}^N R_{m,n} \right) \right) \\ G_i = \frac{1}{10} \sum_{k=1}^{10} \left(\frac{1}{M \times N} \left(\sum_{m=1}^M \sum_{n=1}^N G_{m,n} \right) \right) \\ B_i = \frac{1}{10} \sum_{k=1}^{10} \left(\frac{1}{M \times N} \left(\sum_{m=1}^M \sum_{n=1}^N B_{m,n} \right) \right) \end{cases} \quad (1)$$

where i is an index of all the concentrate samples, and k is a serial number of i -th sample image. $R_{m,n}$, $G_{m,n}$ and $B_{m,n}$ denote a pixel of $M \times N$ matrix of red, green and blue components from a color microscopic image, respectively.

The HSV color space is closer to human perception and better color conversion accuracy (Ren and Yang, 2012). The hue component is particularly important, since it refers the spectral composition of color, of which the range is from 0 to 360 degree. The mean value of hue component for i -th sample image can be obtained:

$$H_i = \frac{1}{10} \left(\sum_{k=1}^{10} \frac{1}{M \times N} \left(\sum_{m=1}^M \sum_{n=1}^N H_{m,n} \right) \right) \quad (2)$$

where $H_{m,n}$ is a value of $M \times N$ matrix of hue component in the HSV color space.

The color vector angle (CVA) is insensitive to variations in an illumination component, but sensitive to differences in the hue and saturation, since the luminance (Y) and chromatic components (I , Q) are independently denoted in YIQ color space (Ford and Roberts, 1998). The CVA is defined with (Tkalcic and Tasic, 2003)

$$\begin{cases} I_i = 0.596R_i - 0.274G_i - 0.322B_i \\ Q_i = 0.211R_i - 0.523G_i - 0.312B_i \\ \theta_i = \tan^{-1}(Q_i / I_i) \end{cases} \quad (3)$$

where I_i and Q_i are the mean values of the chromatic components for i -th sample image, respectively. θ_i is the CVA value of i -th sample image.

LS-SVR method

The least-squares support vector regression model (LS-SVR) (Suykens and Vandewalle, 1999; Suykens, 2001) is a nonparametric regression, which is an extension of support vector machines with taking equality instead of inequality constraints and using a squared loss function. The LS-SVR method for function estimation is done in the Kernel-induced feature space, as follows:

$$y = w^T \varphi(x) + b \quad (4)$$

where $x \in \mathbb{R}^n$, $y \in \mathbb{R}$, w is an unknown coefficient vector, $\varphi(x)$ is a nonlinear map function which maps the input data into a high dimensional feature space, and b is a bias constant. For a given training set $\{(x_i, y_i)\}$, where $i \in \mathbb{N}$, and N denotes the number of training data, $x_i \in \mathbb{R}^n$ and $y_i \in \mathbb{R}$ are i -th input and output data, respectively, the optimization problem with a regularized cost function can be defined as:

$$\begin{cases} \min_{w, e_i} & \frac{1}{2} w^T w + \frac{1}{2} \gamma \sum_{i=1}^N e_i^2 \\ \text{s.t.} & y_i = w^T \varphi(x_i) + b + e_i \end{cases} \quad (5)$$

where $\gamma > 0$ is a regularization constant which controls the bias-variance trade-off, and e_i is an error term for i -th training data.

The optimization problem (Eq. 5) can be solved using the Lagrangian multipliers, and the resulting LS-SVR method is given by

$$y = \sum_{i=1}^N a_i K(x, x_i) + b \tag{6}$$

where $a_i \in \mathbb{R}$ are Lagrange multipliers, x and y are input and output parameters respectively, $K(x, x_i)$ is a certain positive-definite kernel function.

Grade estimation model

The color features of concentrate microscopic images are the key parameters in order to estimate the concentrate grade. Hence, an inherent relationship between the color features and concentrate grade was built by using the LS-SVR method. For grade estimation, 23 groups of sample data were acquired. The 85% groups of dataset were randomly selected as the training and remaining sets. The number of sample such as 3, 6 and 21 were used as the validation tests. The color features and copper concentrate grades measured by the chemical assay are presented in Table 1.

Table 1. Color features and chemical assay for copper concentrate

| Samples | The mean values | | | | CVA | Actual Cu% |
|---------|-----------------|---------|---------|--------|--------|------------|
| | Red | Green | Blue | Hue | | |
| 1 | 24.0195 | 71.8487 | 90.5993 | 1.6467 | 1.102 | 8.870 |
| 2 | 19.6249 | 58.8243 | 69.4159 | 1.5432 | 1.1633 | 10.89 |
| 3 | 15.3936 | 49.9594 | 61.9018 | 1.558 | 1.1251 | 11.31 |
| 4 | 15.3363 | 48.6774 | 58.834 | 1.5345 | 1.1457 | 11.88 |
| 5 | 15.3134 | 49.1808 | 59.1731 | 1.5376 | 1.1506 | 12.31 |
| 6 | 13.6008 | 45.0216 | 54.8837 | 1.5391 | 1.1412 | 13.06 |
| 7 | 10.9599 | 37.8641 | 44.5042 | 1.508 | 1.1764 | 13.65 |
| 8 | 11.4011 | 38.7724 | 44.7765 | 1.4944 | 1.1913 | 14.28 |
| 9 | 15.1702 | 48.3923 | 56.635 | 1.5241 | 1.175 | 14.53 |
| 10 | 11.7008 | 38.825 | 42.4789 | 1.4728 | 1.2388 | 15.66 |
| 11 | 9.1404 | 31.6074 | 33.2607 | 1.4554 | 1.2756 | 16.12 |
| 12 | 9.9737 | 32.6556 | 32.0527 | 1.4259 | 1.3384 | 16.68 |
| 13 | 7.4984 | 27.5487 | 29.0742 | 1.4587 | 1.2738 | 16.75 |
| 14 | 7.7483 | 27.446 | 27.8441 | 1.4505 | 1.3081 | 16.86 |
| 15 | 6.2625 | 24.1291 | 25.1321 | 1.4596 | 1.286 | 17.06 |
| 16 | 7.270 | 26.8296 | 27.7515 | 1.4637 | 1.2919 | 17.50 |
| 17 | 8.3434 | 29.6707 | 31.2064 | 1.4638 | 1.2763 | 17.84 |
| 18 | 9.3754 | 31.0781 | 29.7923 | 1.4202 | 1.3598 | 17.97 |
| 19 | 7.0299 | 25.782 | 25.4689 | 1.4522 | 1.3316 | 18.32 |
| 20 | 6.7748 | 25.2065 | 25.6412 | 1.467 | 1.3063 | 18.41 |
| 21 | 6.5704 | 23.9987 | 23.7016 | 1.4485 | 1.328 | 18.62 |
| 22 | 7.1414 | 25.6158 | 24.8186 | 1.4439 | 1.3488 | 18.69 |
| 23 | 6.5176 | 23.8093 | 22.0975 | 1.4248 | 1.3863 | 19.22 |

Suppose training set are $\{(R_i, G_i, B_i, y_i)\}$, $\{(H_i, y_i)\}$ and $\{(\theta_i, y_i)\}$, where i is a sample index. With the estimation model from Eq. (6), three models are expressed in the following forms:

$$\begin{cases} y_{RGB} = \sum_{i=1}^{20} \alpha_i K((R, G, B)_{new}, ((R_i, G_i, B_i), y_i)) + b \\ y_{Hue} = \sum_{i=1}^{20} \alpha_i K(H_{new}, (H_i, y_i)) + b \\ y_{CVA} = \sum_{i=1}^{20} \alpha_i K(\theta_{new}, (\theta_i, y_i)) + b \end{cases} \quad (7)$$

where $(R, G, B)_{new}$, H_{new} and θ_{new} are the input parameters, y_{RGB} , y_{Hue} and y_{CVA} are the predicted grades of copper concentrate, respectively.

Results and discussion

In this paper, all proposed estimation grade models were performed using a MATLAB R2010b software. For each prediction model, the radial basis function (Hamers et al., 2002) was selected as the Kernel function, which is defined by $K(x, x_i) = \exp(-\|x - x_i\|_2^2 / \sigma^2)$, where σ means the bandwidth parameter. Parameters σ and γ in Eq. (5) were obtained by an intensive grid search process with the cross-validation approach (An et al., 2007) in order to give high prediction accuracy and stability. The final predicted and actual grade values are presented in Table 2.

In order to evaluate the performances of estimation models based on the LS-SVR, running time, root mean square error (RMSE) and correlation coefficient (R^2) were computed. The statistical results are given in Table 3. The color features for grade estimation are presented in the first column. The running time using only the same validation test is quoted in the next column. The RMSE shows the error between the predicted grades and actual values. The R^2 is reported in the last column.

Table 2. Predicted grade and actual grade measured by chemical assay

| Sample | Predicted Cu% | | | Actual Cu% |
|--------|-------------------|-----------|----------------|------------|
| | $(R, G, B)_{new}$ | H_{new} | θ_{new} | |
| 3 | 9.68 | 10.91 | 10.63 | 11.31 |
| 6 | 11.90 | 12.07 | 11.51 | 13.06 |
| 21 | 18.11 | 17.57 | 17.99 | 18.62 |

From Table 3 it can be seen that the running times are almost the same for the hue and color vector angle models and longer for the mean values of red, green and blue model. By comparing the RMSE values from Table 3, it can be found that the copper

concentrate grades are predicted well with low error ($< 2\%$) by using three types of color features as the inputs. Furthermore, the estimated model using the hue parameter has more accuracy as its RMSE value is the smallest. It can be also seen that there is a strong correlation between the predicted and actual copper concentrate grades since the values of correlation coefficient R^2 are very high.

Table 3. Statistical analysis of predicted copper concentrate grade based on LS-SVR models

| Models | Performances of LS-SVR models | | |
|--------------------|-------------------------------|---------|--------|
| | Running time (ms) | RMSE, % | R^2 |
| Red, green, blue | 56.455 | 1.1907 | 0.9977 |
| Hue | 30.243 | 0.8644 | 0.9997 |
| Color vector angle | 30.362 | 1.0391 | 0.9926 |

Conclusions

This paper proposes a new method, based on the least-squares support vector regression model (LS-SVR), to estimate the copper concentrate grade. This method uses color features as inputs with a small amount of samples. The color features, RGB, hue, and color vector angle were extracted from the color microscopic images of copper concentrate sample. Three models of grade estimation based on these color features were created. A comparison of the three models was made by validation test. The results pointed out that there was a strong correlation between the concentrate grade and color feature. It was also found that the model using the hue as the input parameter had more satisfactory performance than the models using the RGB and color vector angle. The model using the hue parameter provided a maximum R^2 value and the least error on the same validation test. In addition, this model required much less running time to estimate the grade than other two models.

References

- AN S., LIU W., VENKATESH S., 2007, *Fast cross-validation algorithms for least squares support vector machine and kernel ridge regression*, Pattern Recognition, 40(8), 2154-2162.
- BONIFAZI G., MASSACCI P., MELONI A., 2000, *Prediction of complex sulfide flotation performances by a combined 3D fractal and colour analysis of the froths*, Minerals Engineering, 13(7), 737-746.
- BONIFAZI, G., MASSACCI P., MELONI A., 2002, *A 3D froth surface rendering and analysis technique to characterize flotation processes*, International Journal of Mineral Processing, 64(2), 153-61.
- FORBES, G., 2007, *Texture and bubble size measurements for modelling concentrate grade in flotation froth systems*, PhD Thesis, University of Cape Town.
- FORD A., ROBERTS A, 1998, *Colour space conversions*, <http://www.poynton.com/PDFs/coloureq.pdf>.
- HAAVISTO O., KAARTINEN J., HYOTYNIEMI H., 2006, *Optical spectrum based estimation of grades in mineral flotation*, ICIT 2006, Industrial Technology, 2529-2534.

- HAAVISTO O., KAARTINEN J., HYOTYNIEMI H., 2008, *Optical spectrum based measurement of flotation slurry contents*, International Journal of Mineral Processing, 88(3), 80-88.
- HAMERS B., SUYKENS J.A.K., de MOOR B., 2002. *Compactly supported RBF kernels for sparsifying the gram matrix in LS-SVM regression models*, Artificial Neural Networks—ICANN 2002, Springer, 720-726.
- KAARTINEN J., HÄTÖNEN J., HYOTYNIEMI H., MIETTUNEN J., 2006, *Machine-vision-based control of zinc flotation—a case study*, Control Engineering Practice, 14(12), 1455-66.
- MALEWSKI J., KRZEMINSKA M., 2012, *Dependence of mine revenue on the grade of copper concentrate*, Physicochemical Problems of Mineral Processing, 48(2), 545-554.
- MARAIS C., 2010, Estimation of concentrate grade in platinum flotation based on froth image analysis, PhD Thesis, University of Stellenbosch.
- MORAR S.H., FORBES G., HEINRICH G.S., BRADSHAW D.J., 2005, *The use of a colour parameter in a machine vision system, Smart-Froth, to evaluate copper flotation performance at Rio Tinto's Kennecott Utah Copper Concentrator*, Centenary of Flotation Symposium, 147-151.
- NAKHAEI F., MOSAVI M.R., SAM A., VAGHEI Y., 2012, *Recovery and grade accurate prediction of pilot plant flotation column concentrate: Neural network and statistical techniques*, International Journal of Mineral Processing, Vol. 110, 140-154.
- NAKHAEI F., MOSAVI M.R., SAM A., 2013, *Recovery and grade prediction of pilot plant flotation column concentrate by a hybrid neural genetic algorithm*, International Journal of Mining Science and Technology, 23, 69-77.
- OESTREICH, J. M., TOLLEY W.K., RICE D.A., 1995, *The development of a color sensor system to measure mineral compositions*, Minerals Engineering, 8(1), 31-9.
- REN CH., YANG J., 2012, *A novel color microscope image enhancement method based on HSV color space and curvelet transform*, International Journal of Computer Science Issues, 9(6), 272-277.
- SUYKENS J.A.K, VANDEWALLE J., 1999, *Least squares support vector machine classifiers*, Neural processing letters, 9(3), 293-300.
- SUYKENS J.A.K., 2001, *Nonlinear modelling and support vector machines*, Instrumentation and Measurement Technology Conference, 1, 287-294.
- TASDEMIR A., KOWALCZUK P.B., 2014, *Application of statistical process control for proper processing of the Fore-Sudetic Monocline copper ore*. Physicochemical Problems of Mineral Processing, 50(1), 249–264.
- TKALCIC M., TASIC J.F., 2003, *Colour spaces: perceptual, historical and applicational background*, IEEE, 1, 304-308.
- YONG Z., KEJUN J., YUKUN W., 2012, *Flotation concentrate grade prediction model based on RBF neural network & immune evolution algorithm*, Proceedings of the 31st Chinese Control Conference, 3319-3323.

Received February 2, 2013; reviewed; accepted November 22, 2013

EVALUATION OF ELECTROMAGNETIC FILTRATION EFFICIENCY USING LEAST SQUARES SUPPORT VECTOR MODEL

Mehmet YUCEER^{*}, Zehra YILDIZ^{**}, Teymuraz ABBASOV^{***}

^{*} Department of Chemical Engineering, Faculty of Engineering, Inonu University, Turkey

^{**} Department of Bioengineering, Engineering and Natural Science Faculty,
Adana Science and Technology University, Turkey, zyildiz@adanabtu.edu.tr

^{***} Department of Electrical and Electronical Engineering, Faculty of Engineering, Inonu University, Turkey

Abstract. The present study aims to apply a least squares support vector model (LS–SVM) for predicting cleaning efficiency of an electromagnetic filtration process, also called quality factor, in order to remove corrosion particles (rust) of low concentrations from water media. For this purpose, three statistical parameters: correlation coefficient, root mean squared error and mean absolute percentage error were calculated for evaluating the performance of the LS–SVM model. It was found that the developed LS–SVM can be used to predict the effectiveness of electromagnetic filtration process.

Keywords: *electromagnetic filtration, disperse systems, support vector machine*

Introduction

Water is an important process fluid used for industrial applications. Re-use of disposed water by cleaning a dispersed particle contaminant, thus improving the water quality, has become an important topic in many applications. Natural water may contain a wide range of impurities, mostly arising from weathering of rocks and soils. The most fundamental issue concerning the impurities in an aquatic environment is distinction between dissolved and particulate forms. Substances that are relatively insoluble in water may exist as small particles, which remain suspended in water for long periods. Such impurities in water are undesirable and must be removed, as in water and effluent treatments, or they may be valuable materials that need to be recovered, as in mineral processing or biotechnology. Essentially, particulates can be removed from water by various separation methods such as sedimentation, flotation, membrane filtration, coagulation, adsorption, oxidation, ion exchange, and

precipitation depending on the characteristics of the solids in a medium (Abbasov, 2002; Gregory, 2006). In order to remove ferrous particles from water, many methods such as membrane filtration, coagulation, adsorption, oxidation, ion exchange, and precipitation can be used. Using the classical methods for separating these particles typically provides low cleaning efficiencies, but some method can be accepted because of low cost and productivity, and lack of broad areas of use. The most common particle impurities in water are the iron(II) and iron(III) compounds such as Fe_3O_4 , $\gamma\text{-Fe}_2\text{O}_3$ and Fe_2O_3 . Since oxides of iron (Fe^{+2}) can be easily removed magnetically, electromagnetic filtration process (EMF) is frequently used to separate these compounds from water. On the other hand, the performance of the EMF methods strongly depends on the percentage of magnetite or other kind of magnetic species. The EMF involves passing a suspension through filter matrices elements such as steel balls, steel wools, metal wires, and rods. Such filter matrices are composed of magnetic packed beds that can be magnetized easily by an external magnetic field. Local high gradient fields are formed around these packing elements through the effect of the low external magnetic field (such as 0.05 T). Purification of liquid or gas is then achieved by passing either suspension or the colloidal systems and holding from the micron to nano sized magnetic impurities in these areas. The most important characteristic of the magnetic filters that makes them more useful compared to conventional filters was separation of micron/submicron particles from the carrier medium with a very high efficiency.

The electromagnetic filtration process (EMF) is preferred than the others as it does not require any reagents or extreme conditions such as high temperature or pressure. Also, these filters can be easily cleaned and the process is more economical. For this reason, the EMF is competently used for separation of heavy metal ions, phosphates, corrosion products, such as the rusts in mining, glass, ceramic, oil, power and nuclear power generation industries (Oberteuffer, 1974; Sandulyak, 1988; Abbasov, 2002; Yildiz et al., 2010; 2011).

The separation efficiency and performance of the electromagnetic filters depend on several factors such magnetic, hydrodynamic and geometrical parameters of the system. The geometric parameters are the diameter of ball, filter length, size of the captured particles, hydrodynamic parameters are the filtration and suspension viscosities and the magnetic parameters are the magnetic permeability, and diameter of the ball and external magnetic field strength. It is obvious that the separation efficiency of the electromagnetic filter depends on these parameters. For this reason, a modelling study was performed to quantify how these parameters can affect the separation performance of electromagnetic filters for water contaminated with the rust particles. In this study, a least squares support vector model (LS-SVM) was used for prediction of the EMF quality factor using five input variables, namely: filtration velocity, external magnetic field strength, diameter of the filter elements, filter length and suspension viscosity. The results of the developed LS-SVM model are compared with the results obtained from a previous study by Yildiz et al. (2011). In the previous

study, the artificial neural network (ANN), multivariable least square regression (MLSR), and mechanistic modelling approaches were applied and compared for prediction of the cleaning efficiency for the electromagnetic filtration process. The results clearly showed that the use of ANN leads to more accurate results than the mechanistic filtration and MLSR models. In this work, the proposed model can be used to predict the quality factor within a smaller value (2.9%) of the mean absolute percentage error.

Experimental method

The filter used in these experimental studies was consisted of a non-magnetic filter body and stainless steel balls as filter elements. An electromagnet was used as an external magnetizing medium. The experimental studies were carried out by placing the filter into this equipment, which is about 0.05 m in diameter. The magnetic field intensity was within the range of 0-0.50 T. A scanning electron microscope (SEM) analysis was necessarily made in order to determine the mean particle sizes of rust particles that form the suspension. From the measurements taken from eleven different points of sample, the mean particle size for the dry rust samples were verified. As a result of the SEM analysis (Fig. 1), the particle sizes vary between 0.2-2 μm . In this work, the mean particle size was taken as 1 μm .

The X-ray analysis was necessarily made in order to determine the magnetic properties of the rust particles that form the suspension. The X-ray diffraction of particles (Fig. 2) revealed that a corroded material is a composition of ferromagnetic (CoMn_2O_4 , $\text{Co}_2\text{Mn}_3\text{O}_8$, CoCrO_4), ferrimagnetic (Fe_3O_4 , $\gamma\text{-Fe}_2\text{O}_3$), and paramagnetic (FeO , $\alpha\text{-Fe}_2\text{O}_3$, Cr_2O_5) compounds. This composition of rust particles used in this study is similar to that of corrosion particles occurring during various industrial processes.

The experiments were carried out under various conditions for different filtration (range 0.10-0.95 m/s) and suspension (range 0.8-10.96 cP) viscosities, external magnetic field strength (range 175-279 kA/m), diameter of the balls (range 4-11 mm), and filter length (range 0.01-0.10 m).

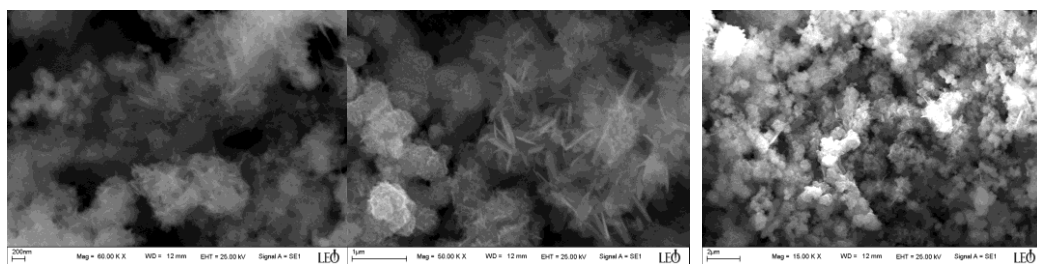


Fig. 1. SEM photos of rust particles

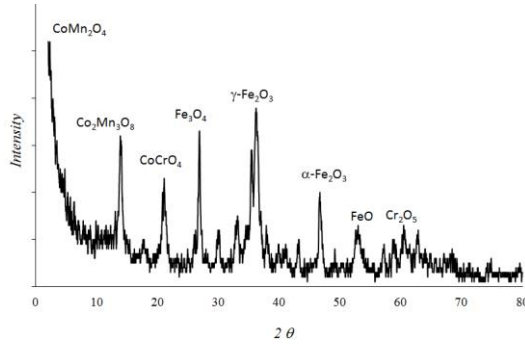


Fig. 2. X-ray diffraction of rust particles

The suspension to be filtered was prepared by the mixing tap water and rust particles. The amount of Fe was determined using an atomic absorption spectrometer (AAS). The magnetic filtration efficiency (Ψ) was determined according to the following formula:

$$\Psi = \frac{C_i - C_0}{C_i} \lambda \quad (1)$$

where λ is a magnetic fraction of a mixture, C_i and C_0 are the total amount of Fe (ppm) at the inlet and outlet, respectively. The total amount of Fe at the inlet was held constant. A 10 g sample of the rust particles was spread over a permanent magnet and a fraction of particles having ferromagnetic properties was weighed. It was found that 85% of the corrosion products exhibited good magnetic properties ($\lambda = 0.85$). The solid/liquid ratio of the suspension used in the experiments was kept as 0.050 g/dm^3 . The experiments were carried out at room temperature ($23 \pm 1 \text{ }^\circ\text{C}$). In order to prevent agglomeration of rust particles, a continuous mixing was applied. Statistical parameters of the experimental setups are given in Table 1, where H is the external magnetic field strength, L filter length, d diameter of the filter elements, V_f filtration velocity and μ viscosity of suspension.

Table 1. Parameters of the data considered for the present study

| Parameters | Min. | Max. | Average | Standard deviation σ |
|--|---------|---------|---------|-----------------------------|
| H (kA/m) | 175.070 | 278.521 | 224.500 | 40.618 |
| L (m) | 0.0100 | 0.1000 | 0.0908 | 0.0236 |
| d (m) | 0.00475 | 0.014 | 0.0077 | 0.0027 |
| V_f (m/s) | 0.1000 | 0.9500 | 0.1862 | 0.1398 |
| μ $\left(\frac{\text{kg}}{\text{m}\cdot\text{s}} \right)$ | 0.00008 | 0.01096 | 0.00123 | 0.00197 |
| Ψ | 0.1800 | 0.8300 | 0.6733 | 0.1247 |

In this work the modeling procedure was provided by the support vector model (SVM). The SVM is a machine learning technique which is based on the statistical learning theory and structural risk minimization principle. The SVM was introduced by Vapnik (1998) and is an efficient technique for the problems characterized by small samples, nonlinearity, high dimension, or local minima (Suykens and Vandewalle, 1999). The SVM uses a based quadratic programming (QP) optimization to identify model parameters, while avoiding local minima, and have an advantage over other regression methods (Li et al., 2007). SVM shows the outstanding performance since it can lead to global models that are often unique by embodying structural risk of minimization principle as developed by Vapnik (1998). Furthermore, sparse solutions can be found. However, building the SVM model is computationally difficult because it involves a solution of a nonlinear optimization problem. A modified version of SVM, called the least square support vector model (LS-SVM) was proposed by Suykens and Vandewalle (1999). This model results in a set of linear equations instead of quadratic optimization problem as in original SVM. Further details of the LS-SVM algorithm can be found in the literature (Suykens and Vandewalle, 1999; Suykens et al., 2002). The schematic diagram of the LS-SVM model is shown in Fig. 3, where x_1, x_2, \dots, x_n and y are input and output variables, respectively.

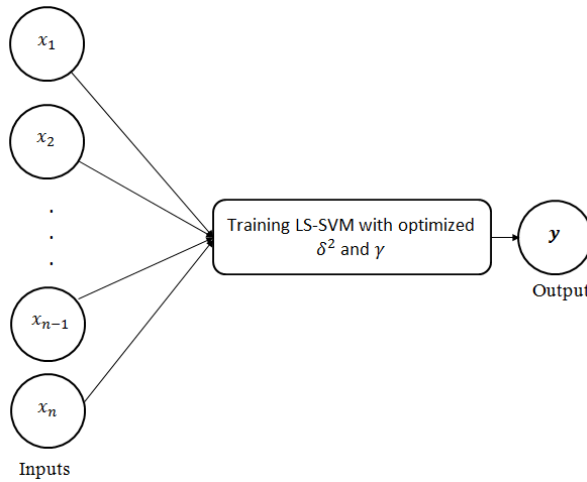


Fig. 3. Schematic diagram of LS-SVM model

In this work, the original 53 data points was divided into training and test sets. The 38 patterns were used for the training set and the remaining 15 for the test set. All data were normalized to be between 0.1–0.9 using Eq. (2) in order to increase the model accuracy and prevent any parameter from dominating the output values (Pyle ,1999):

$$x_{scaled} = 0.8 \left(\frac{X - X_{min}}{X_{max} - X_{min}} \right) + 0.1. \quad (2)$$

The model performance was then assessed by evaluating the scatter between the experimental and predicted results via statistical parameters, that is correlation coefficient (R), mean absolute percentage error (MAPE %), and root mean square error (RMSE). The statistical values were determined as follows:

$$R = \frac{\sum_{i=1}^N (x_i - \bar{x}) \cdot (y_i - \bar{y})}{\sqrt{\sum_{i=1}^N (x_i - \bar{x})^2} \sqrt{\sum_{i=1}^N (y_i - \bar{y})^2}} \quad (3)$$

$$MAPE = \frac{1}{N} \sum_{i=1}^N \left[\frac{|y_i - x_i|}{x_i} \right] \cdot 100 \quad (4)$$

$$RMSE = \sqrt{\frac{\sum_{i=1}^N (y_i - x_i)^2}{N}} \quad (5)$$

where, x_i is an observed value, y_i is a simulated value, N is the number of data points, \bar{x} is the mean value of observations, and \bar{y} is the mean value of simulations.

A higher value of the correlation coefficient and smaller values of MAPE and RMSE would indicate a better performance of the model. All scripts were written in MATLAB using the LS-SVM toolbox (LS-SVMLab1.8, 2013).

Results and discussion

The cleaning efficiency of the electromagnetic filtration process was modeled using the least square support vector machine method. The LS-SVM which was developed using experimental observations as the input, in order to identify the effects of operating parameters on the quality factor. In this study, the optimal output y and standard deviation σ values were found to be 165.43 and 0.0059, respectively. The results of the LS-SVM model for the test data are shown in Fig. 4. As can be seen from Fig. 4, the LS-SVM model captures the general trend in the output, and the test results showed that the developed model can accurately predict the quality factor of the electromagnetic filtration EMF process.

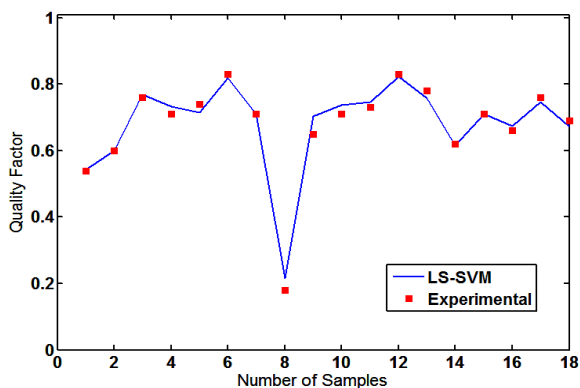


Fig. 4. Experimental values and LS-SVM predictions of quality factor for data

In this work we compared the obtained results with different EMF modeling approaches that were used in our previous work for the same set of compounds (Yildiz et. al., 2011). Table 2 shows the performance evaluation parameters for the LS-SVM model and our previous study. For the a least squares support vector model (LS-SVM), correlation coefficient (R), mean absolute percentage error ($MAPE$), and root mean square error ($RMSE$) values were found to be 0.99, 2.98 % and 0.019, respectively.

Table 2. Comparison of different models to predict the cleaning efficiency for EMF process

| Test Data | | | |
|-----------------------------|------|------------|--------|
| Model | R | $MAPE$, % | $RMSE$ |
| ANN (Yildiz et. al., 2011) | 0.94 | 5.8 | 0.050 |
| MLSR (Yildiz et. al., 2011) | 0.92 | 12.9 | 0.077 |
| Abbasov (2002) | 0.86 | 15.3 | 0.126 |
| LS-SVM | 0.99 | 2.98 | 0.019 |

From Table 2 it can be seen that the correlation coefficient given by the LS-SVM model was higher than for other models, and the LS-SVM model gave the lowest MAPE and RMSE values. It means that described in this work model gives the most satisfactory results compared with the results obtained from our previous work. Consequently, the LS-SVM approach currently constitutes a more accurate method for prediction the cleaning efficiency of the EMF process.

Conclusion

In this work, a model based on the least squares support vector model (LS-SVM) was developed for predicting cleaning efficiency of the electromagnetic filtration process. The results based on statistical parameters of experimental data, clearly showed that the LS-SVM had better performance when compared to other approaches and can be used for predicting the cleaning efficiency of the electromagnetic filtration EMF process. The LS-SVM proved to be a powerful and useful tool for predicting cleaning efficiency of electromagnetic filtration process. It means that LS-SVM as a very powerful and useful tool can be used in applications to the quality factor of the EMF process in different settings.

References

- ABBASOV, T., 2002. *Electromagnetic Filtration Processes*; Seckin Publishers: Ankara
- GREGORY, J., 2006. *Particles in water*; IWA publishing: Taylor & Francis Group
- LI, J. Z., LIU, H. X., YAO X. J., LIU, M. C., HU, Z. D., FAN, B. T., 2007, *Identification of the Hammerstein model of a PEMFC stack based on least squares support vector machines*, Anal. Chim. Acta. 581: 333–342
- OBERTEUFFER, J. A., 1974, *Magnetic Separation: A Review of Principles, Devices, and Applications*, IEEE Transactions on Magnetics, 10:2, 223–238
- PYLE, D., 1999, *Data preparation for data mining*; San Francisco CA: Morgan Kaufmann
- SANDULYAK, A.V., 1988, *Magnetic filtration of liquids and gases*; Moscow: Ximiya
- SUYKENS, J. A. K., VANDEWALLE, J., 1999, *Least squares support vector machines classifiers*, Neural Processing Letters, 9:3, 293–300
- SUYKENS, J. A. K., GESTEL, T. V., BRABANTER, J. D., MOOR, B. D., VANDEWALLE, J., 2002, *Least squares support vector machines*, Singapore: World Scientific.
- VAPNIK, V., 1998, *Statistical Learning Theory*; New York: John Wiley
- YILDIZ, Z., ABBASOV, T., SARIMEŞELI, A., 2010, *Effect of Some Process Parameters on the Separation of the Dispersed Ferrous Impurities Using Cycled Electromagnetic Filter*, Journal of Dispersion Science Technology, 31:8, 1072-1076
- YILDIZ, Z., YUCEER, M., ABBASOV, T., 2011, *Comparison of modeling approaches for prediction of cleaning efficiency of the electromagnetic filtration process*, Applied Computational Electromagnetics Society Journal, 26:11, 899–906
- LS-SVMLab1.8, 2013, www.esat.kuleuven.ac.be/sista/lssvmlab

Received May 29, 2014; reviewed; accepted June 3, 2014

KINETICS OF HYDROPHOBIC AGGLOMERATION OF MOLYBDENITE FINES IN AQUEOUS SUSPENSIONS

Bingqiao YANG*, Shaoxian SONG**, Alejandro LOPEZ-VALDIVIESO*

* Instituto de Metalurgia, Universidad Autonoma de San Luis Potosi, Av. Sierra Leona 550, San Luis Potosi, C.P. 78210, Mexico

** School of Resources and Environmental Engineering, Wuhan University of Technology, 122 Luoshi Road, Wuhan, 430070, China, shaoxian@uaslp.mx

Abstract: The kinetics of hydrophobic agglomeration of molybdenite fines in aqueous suspensions has been studied in this work. This study was performed on minus 5 μm molybdenite particles through turbidity measurements and imaging. The results have showed that stirring strength and kerosene addition greatly affected the agglomeration rate of molybdenite fines in aqueous suspensions. The higher was the stirring strength, the larger the agglomeration rate was. Kerosene addition enhanced not only the agglomeration rate, but also the agglomerates structure. It was recommended to use radial impeller for the formation of hydrophobic agglomeration, because it produced a stronger shear field in impeller zone.

Keywords: *Agglomeration rate; molybdenite fines; hydrophobic agglomeration.*

Introduction

Molybdenite (MoS_2) is the primary natural source for the extraction of molybdenum. It consists of hexagonal layer of molybdenum atoms between two layers of sulfur atoms, in which strong covalent bonds act within S-Mo-S layers and weak van der Waal forces exist between adjacent S-S sheets. This strong anisotropy causes preferential cleavage of molybdenite along the adjacent S-S sheet, producing platelet shape fragment (Lince et al., 2001). Therefore, ground molybdenite particles show two kinds of surfaces, namely face and edge. The face is hydrophobic because of the weak unsaturated band, while the edge is hydrophilic due to the strong band. Molybdenite is generally considered as a naturally hydrophobic mineral and is generally concentrated by froth flotation. However, as the reduction of particle size, the face/edge ratio decreased and thus the hydrophobicity of the molybdenite surfaces decreased (Castro et al., 1994; Yang et al., 2014), leading to sharp declining of flotation efficiency (Chander et al., 1994; Ornela-Tabares et al., 2006). On the other hand, it is generally accepted that

froth flotation is not effective to respond fine particles, because of the lower collision and adhesion probability between particles and air bubbles (Zeng et al., 2004; Liu et al., 2006). Thus, conventional flotation fails in beneficiating molybdenite fines from ores.

Increasing particle size through the formation of hydrophobic agglomerates is an effective method to improve the poor flotation response of mineral fines (Song et al., 2012). This process is termed as floc-flotation, and has been commercially used for the flotation of fine scheelite (Coleman et al., 1995) and anatase (Greene et al., 1962). Hydrophobic agglomeration arises as a result of hydrophobic interaction between particles in aqueous suspensions, and is realized by means of mechanical agitation (Cebe-ci, 2003; Duzyola et al., 2010; Lu et al., 1991; Spicer et al., 1998). In the agitation, the formation and disruption of agglomerates occurred simultaneously (Lu et al., 1998). The stronger is the agitation, the stronger the disruption effect is. A lumped population balance model was used for studying agglomerate coalescence and breakage in the hydrophobic agglomeration of scheelite particles, showing that the breakage rate was approximately proportional to the 0.70 power of the agglomerates volume (Patil et al., 2001).

Although numerous researches have been performed on the fundamental aspects of hydrophobic agglomeration of mineral fines in aqueous suspensions, few reports have concerned the kinetics of hydrophobic agglomeration, especially for molybdenite fines. In this work, an attempt has been made to study the kinetics of hydrophobic agglomeration of molybdenite fines in aqueous suspensions. The objective is to obtain the understandings of the agglomeration rate of molybdenite fines in aqueous suspensions as affected by several parameters, such as stirring speed, kerosene and impeller type.

Experimental

Material

The molybdenite sample used in this work was natural molybdenite powder ($<5\mu\text{m}$) from Yiji chemical agent Co. Ltd., Shanghai, China. The purity was 96.41% MoS_2 . It was first washed by CS_2 to remove kerosene and other organics on the surfaces, followed by thermal drying in a vacuum oven at $40\text{ }^\circ\text{C}$. The X-ray diffraction (XRD) pattern of the samples is shown in Fig. 1. All of the peaks belonged to molybdenite, indicating that there was no impurity over 5% in the sample. scanning electron microscope (SEM) image as shown in Fig. 2 reveals that the particle size was less than $5\mu\text{m}$, and the shape was plate-like. SEM-EDX analysis showed that the impurities in the sample were silica and pyrite.

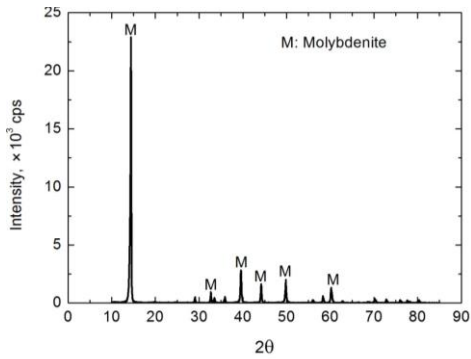


Fig. 1. XRD pattern of the molybdenite sample

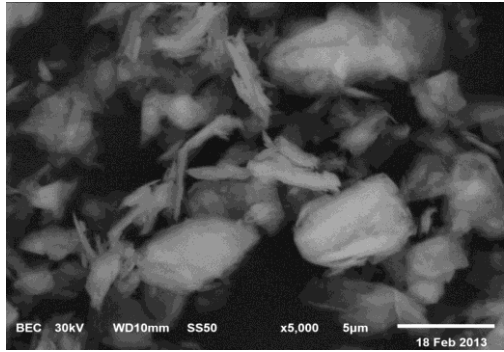


Fig. 2. SEM image of the molybdenite sample

Kerosene (50 mg/cm^3 hexane) from the Fisher Scientific without further purification was used. It was added into molybdenite suspensions in the form of oil emulsion. Prior to contact with molybdenite suspension, the mixture of kerosene and water (1.23% w/w) was first prepared by mechanically conditioning at 14000 rev/min for 10 min with a high speed mixer and then by ultrasonic treating for 15 minutes. The emulsified kerosene was imaged by Leica DMLP optical microscope, as shown in Fig. 3.

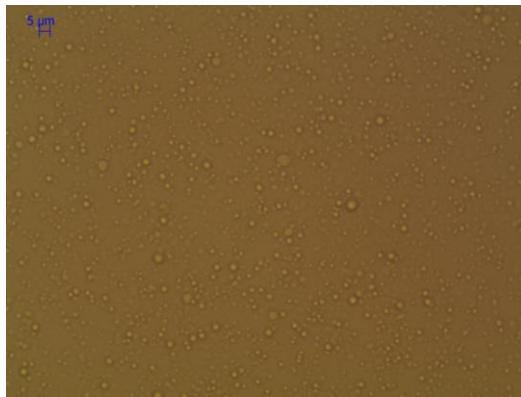


Fig. 3. Emulsified kerosene imaged with an optical microscopy

Potassium butyl xanthate that was originally from the Industria Quimica de Mexico and purified in our laboratory with the method described elsewhere (Song et al., 2001). The analytical grade hydrochloric acid and sodium hydroxide were used to adjust the pH of aqueous suspensions. The water used was distilled first, and then treated by passing through resin beds and a 0.2 mm filter.

Determination of agglomeration rate

The hydrophobic agglomeration of molybdenite fines in aqueous suspensions was realized in a standard four-baffle stirred tank with 9.5 cm of height and diameter. The baffle is 8.2×0.95 in length and width. A Servodyne mixing head with a digital Servodyne mixer controller was used for slurry stirring.

Molybdenite sample with amount of 1.12 g with 620 cm³ water was first conditioned with magnetic stirrer for 5 min. During the conditioning, hydrochloric acid or sodium hydroxide solution was added to adjust pH. Then, the suspension was dispersed by a Branson 2510 ultrasonic cleaner for 15 min. After that, the molybdenite suspensions were transferred into the stirred tank to be stirred at a given speed for a given time, while a given dosage of emulsified kerosene was added. During the stirring, 3 cm³ of suspension was carefully sampled from the tank at given time intervals using a 5 mm diameter of Eppendorf research plus pipette. The samples were diluted by adding 60 ml distilled water. Finally, the diluted sample was determined for the turbidity by using a MicroTOL turbidimeter. It was reported that the pipette didn't modify the agglomerate size if the pipette openings were more than 2 mm (Gibbs and Konwar, 1982). In addition, hydrophobic agglomerates are very strong against rupture. Therefore, it is reasonable to presume that the sampling would not cause a significant disruption of the agglomerates.

The dispersion and agglomeration of the molybdenite fines is evaluated by agglomeration degree (E), given by:

$$E = \frac{\tau_o - \tau_E}{\tau_o} \quad (1)$$

where τ_o and τ_E are the turbidities of the well-dispersed suspensions and of agglomerated suspensions at a given time of stirring. The agglomeration rate (dE/dt) was obtained by differentiating E over t at the stirring time of 20 seconds:

$$K = \left. \frac{dE}{dt} \right|_{t \rightarrow 20s} \quad (2)$$

Observation of hydrophobic agglomerates

A Leica DMLP optical microscope equipped with digital camera was used to observe hydrophobic agglomerates in aqueous suspensions. The samples were prepared by dropping molybdenite suspensions on a glass plate, followed by putting a thin glass slide on the drop to fix the suspensions. Some of agglomerates were photographed.

Results and discussions

Effect of stirring strength on agglomeration rate

The strength of the shear field closely correlated with stirring speed in a mechanical agitation. Figure 4 illustrates the effect of stirring speed on the agglomeration rate of molybdenite fines in aqueous suspensions. As it is shown, the agglomeration rate increased with the increase of stirring speed. The increase was sharp in the low speeds, and became mild at the critical speed, 1900 rev/min. The results indicated that the hydrophobic agglomerates of molybdenite could withstand great floc-rupture forces and keep growing at high stirring strengths. This observation might be due to the strong coalescence between the hydrophobic particles in aqueous solutions, because the agglomerate disruption process was dominated mainly by the fragmentation mechanism (Lu et al., 1998).

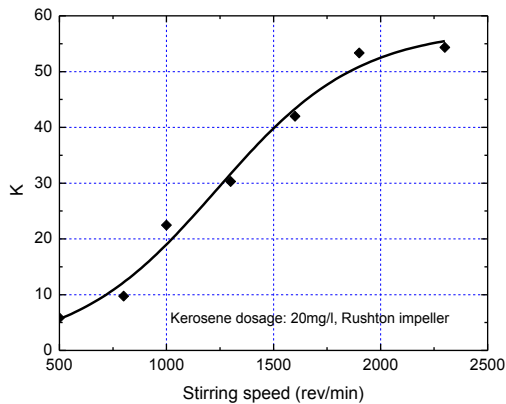


Fig. 4. Agglomeration rate of molybdenite fines in aqueous suspensions as a function of stirring speed

Influence of kerosene dosage on agglomeration rate

The agglomeration rate of molybdenite fines in aqueous suspensions as a function of kerosene dosage is shown in Fig. 5. As the kerosene dosage increases, the agglomeration rate increases substantially and then flattens out, indicating that non-polar oil enhances the hydrophobic agglomeration of molybdenite fines. The enhancement was due to the increase of surface hydrophobicity and agglomerate strength through spreading oil droplets on molybdenite faces and forming oil bridges between the agglomerated particles, resulting in a high ability against rupture force from turbulence flows (Song et al., 1999). At the kerosene dosage above 60 mg/dm^3 , the agglomeration rate reached a plateau.

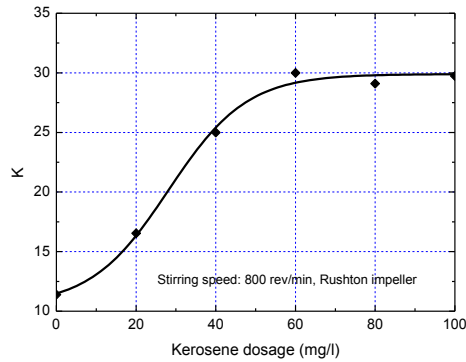


Fig. 5. Agglomeration rate of molybdenite fines in aqueous suspensions at 20 s as a function of kerosene dosage

Figure 6 shows the microscopy images of the hydrophobic agglomerates of molybdenite fines at the kerosene addition of 20 mg/dm^3 and 60 mg/dm^3 . It can be observed that at the 20 mg/dm^3 kerosene, the agglomerates consisted of small compact agglomerates with big space between them, indicating a loose structure. At the 60 mg/dm^3 kerosene, the agglomerates became more compact and there were no obvious spaces. The results suggested that kerosene could intensify hydrophobic agglomeration of molybdenite fines through compacting the agglomerate structure.

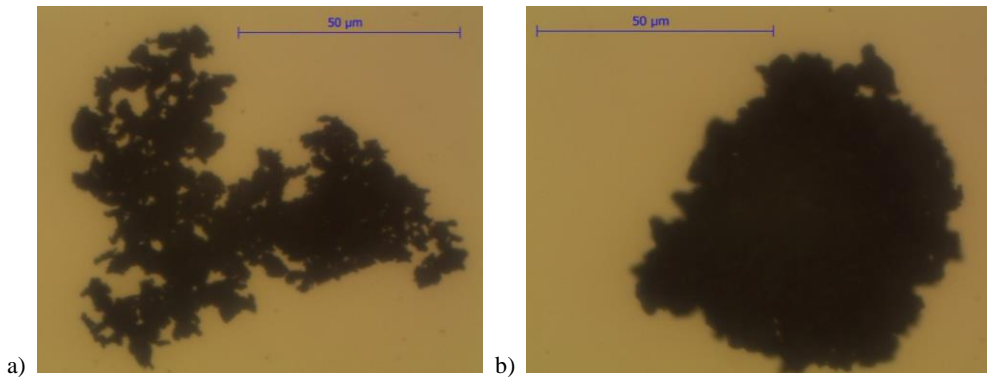


Fig. 6. Optical microscopy images of hydrophobic agglomerates of molybdenite fines at kerosene dosage 20 mg/dm^3 (a) and 60 mg/dm^3 (b)

Effect of butyl xanthate on agglomeration rate

The effect of butyl xanthate on the agglomeration kinetics of molybdenite fines is shown in Fig. 7. The agglomeration degree greatly increased in the presence of butyl xanthate at the same time, suggesting that the xanthate could enhance the hydrophobic agglomeration. The enhancement might be attributed to the increase of hydrophobicity

of the edges of molybdenite upon the adsorption of xanthate. Moreover, at the same butyl xanthate dosage, the agglomeration was enhanced with the addition of 20 mg/dm³ kerosene.

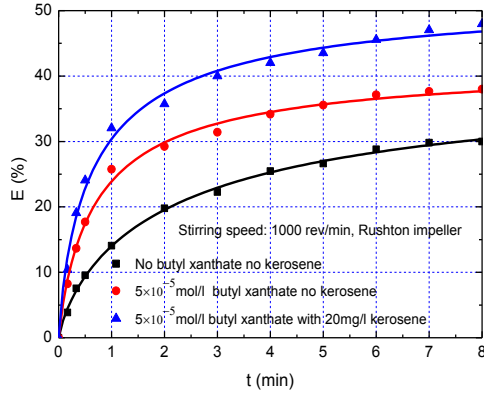


Fig. 7. Agglomeration degree of molybdenite fines in aqueous suspensions as a function of stirring time in the absence and presence of butyl xanthate

Effect of impeller type on agglomeration rate

The flow characteristic (circulation time and strength) in the stirred tank is very important in hydrophobic agglomeration, which is closely related to the impeller type. Figure 8 shows the top view of three different impellers in this work. The impeller 1 and 2 produce an axial flow and radial flow, respectively, while impeller 3 produces a combined axial and radial flow. Impeller 1 produces flows toward the bottom of the tank followed by circulation to the top and a relatively rapid return to the impeller zone. Impeller 2 radiates fluid flow outward from the impeller and back to the impeller zone. Impeller 3 produces the flow downward at a certain angle from the vertical axis (Spicer et al., 1996).



Impeller 1



Impeller 2 (Rushton)



Impeller 3

Fig. 8. Top views of different impellers

The effect of impeller type on the agglomeration kinetics of molybdenite fines is illustrated in Fig. 9. Impeller 2 produced the best agglomeration, followed by impeller 3 and impeller 1. The results indicated that the radial flow achieved by impeller 2 was better for the formation of hydrophobic agglomerates than the axial flow. It might be attributed to that a greater shear field might exist in a radial flow than in an axial flow, because it produced flow perpendicular to the original direction of the approaching agglomerates (Spicer et al., 1996).

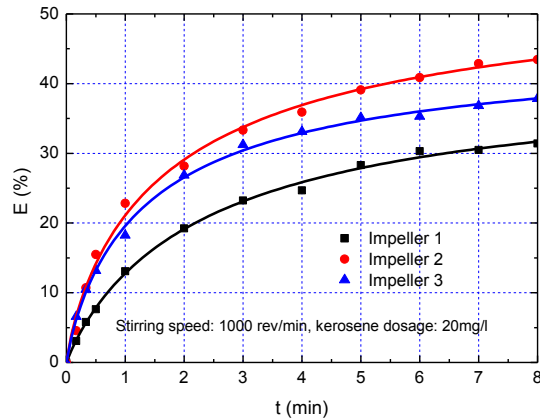


Fig. 9. Agglomeration degree of molybdenite fines in aqueous suspensions as a function of stirring time by different impellers

Conclusions

The agglomeration rate of molybdenite fine in aqueous suspensions was closely correlated with the stirring strength in agitation. The higher was the stirring strength, the larger the agglomeration rate was. Kerosene played an important role in the hydrophobic agglomeration of molybdenite fines. It not only increased the agglomeration rate, but also enhanced the agglomerate structure. It was better to use radial impeller to generate hydrophobic agglomeration, because it produced a stronger shear field in impeller zone.

Acknowledgments

The financial supports for this work from the Consejo Nacional de Ciencia y Tecnología (CONACyT) of Mexico under the Grant Nos. 123487 and 155148 are gratefully acknowledged. Also, B. Yang would like to thank the CONACyT of Mexico for offering him the scholarship under the grant No 416789 during his Ph.D. studying.

References

- CASTRO, S. H., MAYTA, E., 1994, *A kinetics approach to the effect of particle size on the flotation of molybdenite*, 4th Meeting of the Southern of the Hemisphere on Mineral Technology and 3rd Latin American Congress on Froth Flotation, Concepcion, Chile

- CEBECI, Y., 2003, *Investigation of kinetics of agglomerate growth in oil agglomeration process*, Fuel 82, 1645-1651.
- CHANDER, S., FUERSTENAU, D.W., 1972, *On the natural floatability of molybdenite*, Trans. AIME. 252, 62-69.
- COLEMAN, R.D., SPARKS, B.D., MAJID, A., TOLL, F.N., 1995, *Agglomeration-flotation: recovery of hydrophobic components from oil sands fine tailings*, Fuel 74, 1156-1161.
- DUZYOLA, S. OZKAN, A., 2011, *Correlation of flocculation and agglomeration of dolomite with its wettability*, Sep. Sci. Technol. 46, 876-881.
- GIBBS, R.J., KONWAR, L.N., 1982, *Effect of pipetting on mineral flocs*, Environ. Sci. Technol. 16, 119-121.
- GREENE, E.W., DUKE, J.B., 1962, *Selective Froth Flotation of Ultrafine Minerals or Slimes*, Trans. AIME. 223, 389-395.
- LINCE, J. R., FRANTZ, P., 2001, *Anisotropic oxidation of mos2 crystallites studied by angle-resolved x-ray photoelectron spectroscopy*, Tribol. Lett. 9, 211-218.
- LIU, Q., WANNAS, D., PENG, Y., 2006, *Exploiting the dual functions of polymer depressants in fine particle flotation*, Int. J. Miner. Process. 80, 244-254.
- LU, S., DING, Y., GUO, J., 1998, *Kinetics of fine particle aggregation in turbulence*, Adv. Colloid Interface Sci. 78, 197-235.
- LU, S., SONG, S., 1991, *Hydrophobic interaction in flocculation and flotation I. hydrophobic flocculation of fine mineral particles in aqueous solution*, Colloids Surf. A 57, 49-60.
- ORNELAS-TABARES, J., MADRID-ORTEGA, I., REYES-BAHENA, J. L., SANCHEZ-LOPEZ, A. A., VALDEZ-PEREZ, D., LOPEZ-VALDIVIESO, A., 2006, *Surface properties and floatability of molybdenite*, Proceedings of 2006 China-Mexico Workshop on Minerals Particle Technology, San Luis Potosi, Mexico.
- PATIL, D. P., ANDREWS, J. R. G., UHLHERR, P. H. T., 2001, *Shear flocculation—kinetics of floc coalescence and breakage*, Int. J. Miner. Process. 61, 171-188.
- SONG, S., LOPEZ-VALDIVIESO, A., DING, Y., 1999, *Effects of nonpolar oil on hydrophobic flocculation of hematite and rhodochrosite fines*, Powder Technol. 101, 73-80.
- SONG, S., LOPEZ-VALDIVIESO, A., REYES-BAHENA, J. L., BERMEJO-PEREZ, H. I., 2001, *Hydrophobic flocculation of sphalerite fines in aqueous solution induced by ethyl and amyl xanthates*, Colloids Surf. A, 181, 159-169
- SONG, S., ZHANG, X., YANG, B., LOPEZ-MENDOZA, A., 2012, *Flotation of molybdenite fines as hydrophobic agglomerates*, Sep. Purif. Technol. 98, 451-455.
- SPICER, P. T., KELLER, W., PRATSINIS, S. E., 1996, *The effect of impeller type on floc size and structure during shear-induced flocculation*, J. Colloid Interface Sci. 184, 112-122.
- SPICER, P. T., PRATSINIS, S. E., RAPER, J., AMAL, R. BUSHELL, G., MEESTERS, G., 1998, *Effect of shear schedule on particle size, density, and structure during flocculation in stirred tanks*, Power Technol. 97, 26-34.
- YANG, B., SONG, S., LOPEZ-VALDIVIESO, A., 2014, *Effect of particle size on the contact angle of molybdenite powders*, Miner. Proces. Extract. Metal. Rev. 35, 208-215.
- ZENG, L., LI, X., LIU, J., 2004, *Adsorptive removal of phosphate from aqueous solutions using iron oxide tailings*, Water Res. 38, 1318-1326.

Received May 28, 2014; reviewed; accepted June 26, 2014

RECOVERY OF COBALT AND NICKEL BY ATMOSPHERIC LEACHING OF FLOTATION SULFIDE CONCENTRATE FROM LUBIN CONCENTRATOR

**Krzysztof GIBAS, Kamil BOROWSKI, Tomasz CHMIELEWSKI,
Katarzyna WEJMAN**

Wrocław University of Technology, Faculty of Chemistry, Division of Chemical Metallurgy
Wybrzeże Wyspiańskiego 27, 50-370 Wrocław, Poland (krzysztof.gibas@pwr.edu.pl)

Abstract. An experimental study on leaching of cobalt and nickel from a Lubin (Poland) sulfide flotation copper concentrate with oxygenated sulphuric acid solution in the presence of iron(III) sulfate is presented. The effect of temperature, iron(III) concentration, initial sulphuric acid concentration, oxygen flow rate and chloride ions addition on cobalt and nickel leaching were examined. The obtained results show, that enhancing investigated leaching parameters increases both the rate and leaching recovery of nickel and cobalt. The effect of iron(III) ions concentration is particularly significant. Additionally, a significant correlation between copper and nickel/cobalt leaching recovery was observed. Due to the fine dissemination of nickel and cobalt, they were leached remarkably faster when copper leaching recovery exceeded 90%.

Keywords: *atmospheric leaching, cobalt, nickel, sulphuric acid, Lubin copper concentrate.*

Introduction

The traditional treatment of copper flotation sulphide concentrates by smelting, converting and electrorefining is becoming dominant in the world copper industry for technical and economic reasons. Research and development of hydrometallurgical alternatives to traditional pyrometallurgical processes has remarkably been intensified in the recent years. A wide range of chemical and biological processes for copper recovery from concentrates have been developed (Gupta and Mukherjee, 1990; Habashi, 1999; 2005; 2007; Jansen and Taylor, 2000; Peacey et al., 2003; Dreisinger, 2006; Marsden and Wilmot, 2007; Ramahadran et al., 2007). These processes are all successful in leaching of copper from polymineral and chalcopyrite concentrates, purifying pregnant leach solutions (PLS) using modern separation processes, mainly solvent extraction, and recovering a high value and purity copper metal product.

A complex and unique mineralogical structure as well as polymetallic chemical composition of Polish Kupferschiefer copper ores mined from sedimentary deposits is the principal reason for copper, silver and other metals losses to flotation tailings (Luszczkiewicz, 2000). The presence of clay-carbonate shale and increasing content of organic carbon in ores and concentrates creates additional technical and ecological issues, particularly in flash smelting. Therefore, it can be concluded that the existing beneficiation technologies combined with smelting and refining have already reached the limit of their technological efficiency for processing of Polish copper ores (Chmielewski and Charewicz, 2006; Chmielewski et al., 2007).

The quality of the Polish copper ores, which exhibit a decreasing copper content and growing amount of shale fraction as well as increasing concentration of impurities (Pb, As) have been deteriorating for many years (Chmielewski and Charewicz, 1984; Bachowski et al., 2003; Grotowski, 2007; Konieczny et al., 2009; Chmielewski, 2012). It essentially affects the decreasing copper content and recovery in the flotation concentrates (KGHM data, Konieczny et al., 2009) and is the main reason of high costs of copper production. An analysis of flotation indices at all KGHM Polska Miedz S.A. concentrators reveals a descending trend for both recovery and concentrate grade. It is particularly apparent at Lubin Concentrator (ZWR Lubin), where copper recovery is currently below 87% and the metal content in concentrate is about 14% (Fig. 1).

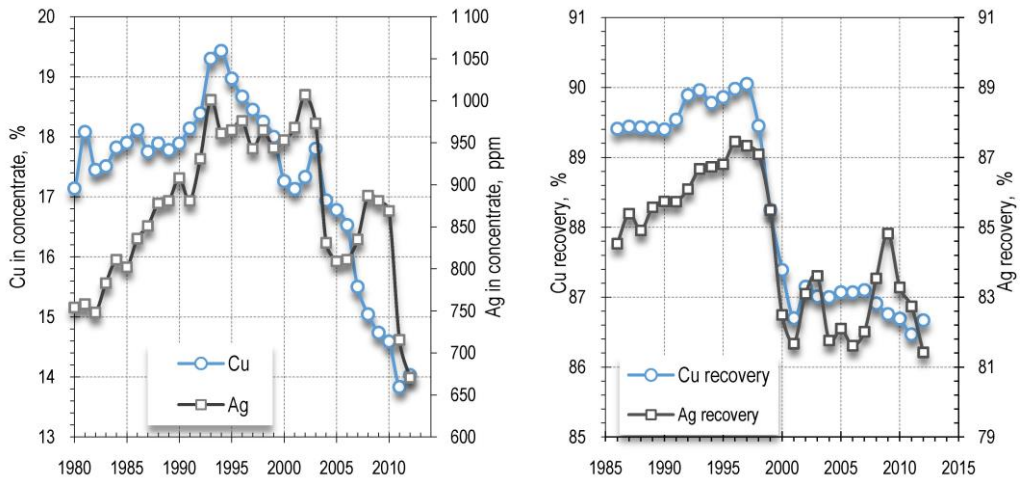


Fig. 1. Lubin flotation copper concentrate quality and Cu and Ag recovery within the period from 1980 to 2012 (based on Kukuc and Bazan, 2013)

A similar unfavorable trend is also observed for silver. Moreover, even when the content of other accompanying metals is relatively high (Pb, Zn, Ni, Co, Mo, V) some of them are either recovered only partially or not at all. Currently used technologies at

ZWR Lubin have already reached limit of their efficiency and they are the major reason of increasing metals losses and production costs.

In this paper the results of recovering of nickel and cobalt observed during atmospheric leaching of the Lubin concentrate in oxygenated sulphuric acid and in the presence of Fe(III) are presented. The paper discusses the effect of major parameters on leaching rate and metals recovery during the investigated process.

Experimental

Material and experimental procedure

The subject of the study is a commercial flotation sulfide concentrate produced at Lubin Concentrator (KGHM Polska Miedz S.A.). The concentrate consists of copper and other metals, such as Zn, Co, Ni, Ag, V, Mo, that significantly increase the value of this material. The decreasing concentrate copper grade, high content of organic carbon, presence of lead and arsenic, make the concentrate a potential and suitable feed for a hydrometallurgical treatment (Chmielewski, 2012).

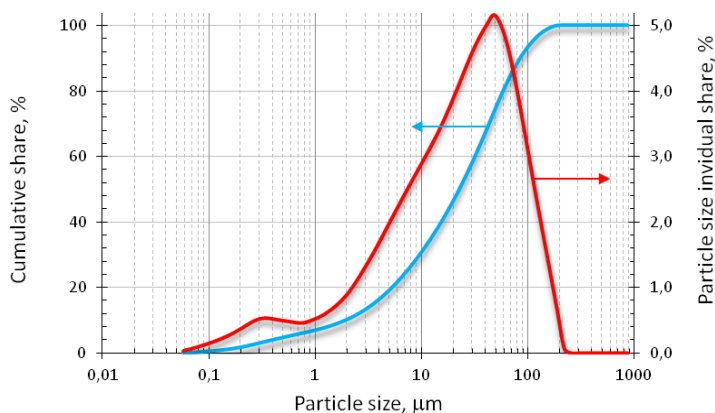


Fig. 2. Granulometric analysis of copper concentrates from Lubin Concentrator

The Lubin concentrate is a polymetallic and polymineral material. The valuable metals are present in the sulfide form, while the majority of barren contents are magnesium and calcium carbonates. A chemical composition of the concentrate is presented in Table 1. The possibility of cobalt and nickel recovery by hydrometallurgical methods becomes more attractive when considered is the stable content of nickel and increasing concentration of cobalt, which currently is totally lost, and the efficiency of nickel extraction is rather low (Chmielewski, 2012).

The content of carbonates and particle size distribution of the concentrate were determined during concentrate characterization. The carbonates content is described by the $Z_{H_2SO_4}^{\max}$ parameter, which is the mass of sulfuric acid consumed during total chemical decomposition of carbonates contained in 1 kg of dry concentrate. For the studied material the $Z_{H_2SO_4}^{\max}$ values were between 200 and 250 g of sulphuric acid per 1 kg of concentrate. The particle size distribution is given in Fig. 2.

Three commercial flotation copper concentrate samples were examined (KLA, KLB and KLC). Table 1 shows that the samples have similar chemical composition.

Table 1. The chemical composition of "Lubin" flotation concentrate

| Concentrate symbol, | $Z_{H_2SO_4}^{\max}$ g/kg | Cu, % | Zn, % | Ni, g/Mg | Co, g/Mg | Fe, % | Pb, % | Ag, g/Mg | As, % | V, g/Mg | Mo, g/Mg | S, % | C_{org} , % |
|---------------------|---------------------------|-------|-------|----------|----------|-------|-------|----------|-------|---------|----------|-------|---------------|
| KLA | 228 | 15.85 | 0.95 | 415 | 1040 | 7.05 | 3.63 | 881 | 0.29 | 762 | 344 | 12.41 | 8.10 |
| KLB | 255 | 15.26 | 0.93 | 488 | 1206 | 6.71 | 3.95 | 938 | 0.34 | 569 | 265 | 12.40 | 8.10 |
| KLC | 248 | 14.56 | 0.57 | 483 | 1250 | 7.55 | 3.91 | 755 | 0.26 | 672 | 221 | 13.54 | 7.23 |

Leaching procedure

A series of atmospheric leaching experiments were conducted. The effect of following process parameters on the cobalt and nickel leaching efficiency was examined: temperature, iron(III) concentration, sulfuric acid concentration, solid/liquid ratio (s/l), oxygen flow rate and chloride ions addition. The leaching experiments were conducted in a stirred glass reactor immersed in a water bath. The agitation rate of 500 min^{-1} was kept the same for all experiments. A leaching slurry was continuously oxygenated using a glass tube. The oxygen flow rate was controlled by a rotameter. The leaching reactor was equipped with a condenser, to avoid rapid vaporization of the leaching solution at higher process temperatures. The density of the leaching slurry was described as a solid to liquid phase ratio (g/cm^3).

During each leaching experiment, the slurry samples were taken from the reactor and filtered for analysis of metals concentration, using an atomic absorption spectroscopy technique (AAS). The redox potential of the leaching slurry was also measured using a Pt-Ag/AgCl combined electrode and a mV/pH-meter. Because of carbonates presence in the concentrate, each leaching experiment was preceded by the controlled, selective carbonates decomposition process with sulfuric acid under non-oxidative conditions (in the absence of oxygen iron(III) ions). After non-oxidative carbonates decomposition, the leaching slurry was heated and when it reached a given temperature, oxygen and iron(III) ions were introduced into the reactor. The leaching efficiencies were evaluated by determining metals leaching recoveries, according to equation:

$$R_{\%} = \frac{cV}{m\alpha} \cdot 100\% \quad (1)$$

where:

- $R_{\%}$ metal leaching recovery, %
 c metal concentration in the solution, g/dm^3 (mg/dm^3)
 V leaching solution volume, dm^3
 m mass of the concentrate, g
 α metal content in the concentrate, % (g/Mg).

Results and discussion

Correlation between Co, Ni and Cu leaching recoveries

The analysis of metals leaching exhibited a very strong relationship between nickel, cobalt and copper recovery. It was found, that both the Ni and Co leaching rate and leaching recovery depend on copper leaching recovery value. Cobalt and nickel start to leach very rapidly when about 90 – 95% of copper is leached out. This suggests, that Co and Ni sulfides are disseminated in the matrix of copper minerals and leaching solution has a very limited access to them at the beginning of the process. It is expected, that enhancing the copper leaching rate will have a positive effect on the leaching recoveries of cobalt and nickel as the Co and Ni bearing minerals will be faster exposed to the leaching solution. Figure 3 presents the relationship between Co and Ni recovery vs. Cu recovery for one of the leaching processes, as an example. A similar dependency was observed in all experiments.

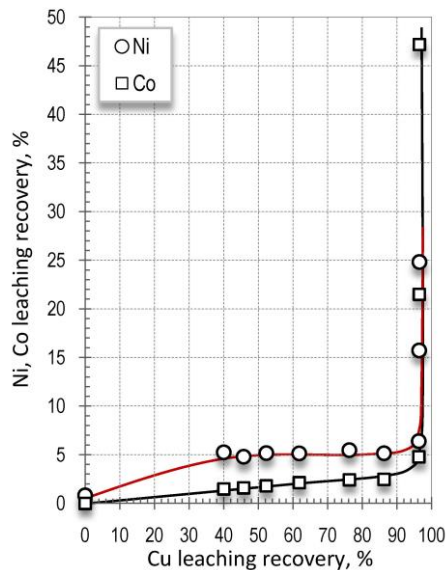


Fig. 3. Ni and Co recovery vs. Cu recovery in atmospheric leaching; $s/l = 1:6$, initial H_2SO_4 concentration 100 g/dm^3 , temperature $90 \text{ }^\circ\text{C}$, O_2 flow rate $60 \text{ dm}^3/\text{h}$, iron(III) ions concentration 30 g/dm^3

Effect of temperature

A series of atmospheric leaching experiments were conducted using a KLA sample of the Lubin concentrate (Table 1). Three different temperatures were examined (50, 70 and 90 °C). Other process parameters were constant ($s/l = 1:8$, initial H_2SO_4 concentration = 50 g/dm^3 , no iron(III) ions addition, oxygen flow rate = 30 dm^3/h , leaching time = 5 h).

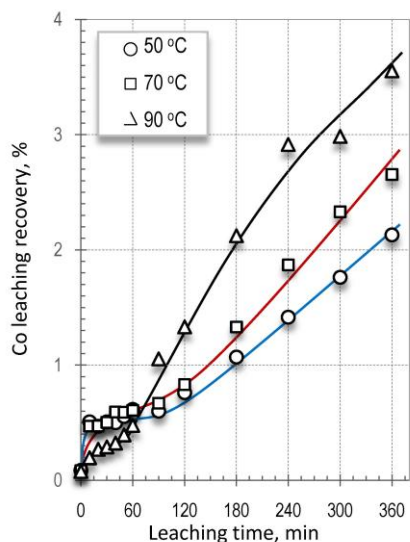


Fig. 4. Effect of temperature on Co leaching recovery; $s/l = 1:8$, initial H_2SO_4 concentration 50 g/dm^3 , O_2 flow rate 30 dm^3/h

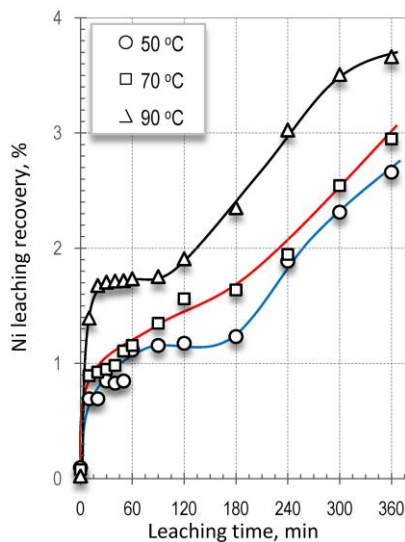


Fig. 5. Effect of temperature on Ni leaching recovery; $s/l = 1:8$, initial H_2SO_4 concentration 50 g/dm^3 , O_2 flow rate 30 dm^3/h

The leaching results (Figs. 4 and 5) showed that temperature has a significant effect on the Co and Ni leaching rate and efficiency. However, in the examined range of parameters the leaching recovery of these metals was relatively low even at the highest tested temperature (90 °C). It was a result of using only oxygen as an oxidizing agent (iron(III) ions were not added). For the further leaching experiments the temperature of 90 °C was chosen.

Effect of iron(III) ions concentration

To investigate the iron(III) ions effect on Co and Ni leaching, a KLA concentrate sample was used. The initial concentration of iron(III) ions varied from 10 to 30 g/dm^3 . Other leaching parameters were as follows: temperature = 90°C, $s/l = 1:8$, initial H_2SO_4 concentration = 50 g/dm^3 , oxygen flow rate = 30 dm^3/h , leaching time = 5 h. The sample “zero” was taken after carbonates decomposition. It was found that

even the lowest iron(III) ions addition would have a significant effect on the Co and Ni leaching rate and efficiency (Figs. 6 and 7).

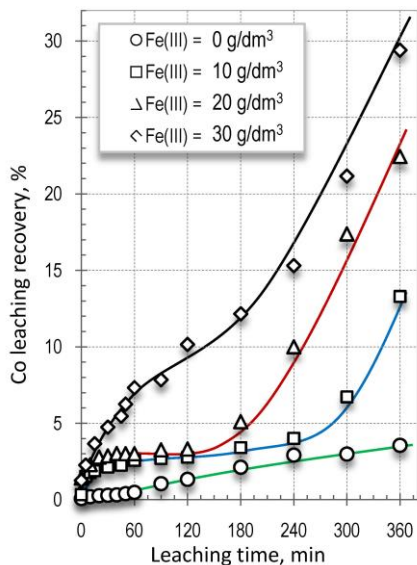


Fig. 6. Effect of iron(III) ions concentration on Co leaching recovery; $s/l = 1:8$, initial H_2SO_4 concentration 50 g/dm^3 , temperature $90 \text{ }^\circ\text{C}$, O_2 flow rate $30 \text{ dm}^3/\text{h}$

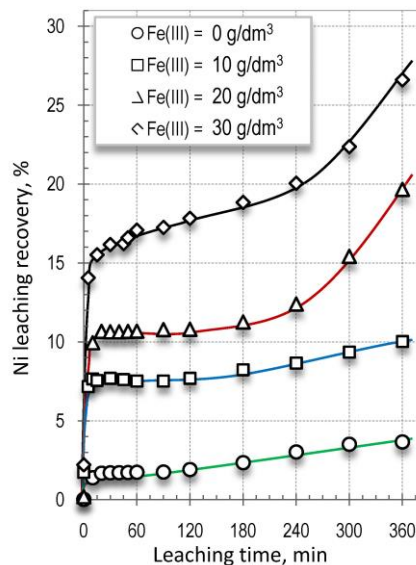


Fig. 7. Effect of iron(III) ions concentration on Ni leaching recovery; $s/l = 1:8$, initial H_2SO_4 concentration 50 g/dm^3 , temperature $90 \text{ }^\circ\text{C}$, O_2 flow rate $30 \text{ dm}^3/\text{h}$

With increasing iron(III) ions addition, the cobalt and nickel leaching recovery increase remarkably, compared to the process without iron(III) ions (Figs. 6 and 7). Although the standard reduction potential of oxygen ($+1.23 \text{ V}$) is much higher than the one for Fe^{3+}/Fe^{2+} ($+0.77 \text{ V}$), leaching of Co and Ni with oxygen as the only oxidant is ineffective. This can be explained by low oxygen dissolution in the leaching solution and low reduction rate on the sulphides surface.

Effect of initial sulfuric acid concentration

A sample of KLB Lubin concentrate was used as the feed for investigation of initial H_2SO_4 concentration effect on Co and Ni leaching. Two initial acid concentrations were compared: 50 and 100 g/dm^3 . Other leaching parameters were as follows: temperature $90 \text{ }^\circ\text{C}$, s/l $1:6$, iron(III) ions concentration 30 g/dm^3 , oxygen flow rate $60 \text{ dm}^3/\text{h}$, leaching time 10 h . Results are given in Figs. 8 and 9.

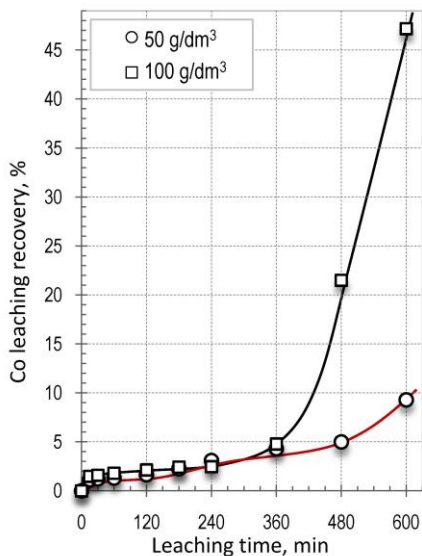


Fig. 8. Effect of initial sulphuric acid concentration on Co leaching recovery; s/l 1:6, iron(III) ions concentration 30 g/dm³, temperature 90 °C, O₂ flow rate 60 dm³/h

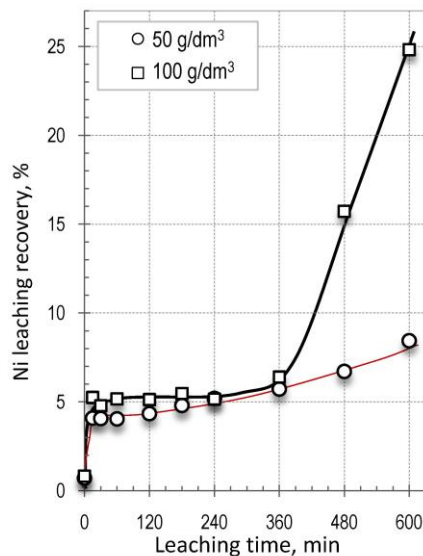


Fig. 9. Effect of initial sulphuric acid concentration on Ni leaching recovery; s/l 1:6, iron(III) ions concentration 30 g/dm³, temperature 90 °C, O₂ flow rate 60 dm³/h

The cobalt and nickel leaching recovery was much higher in experiments with higher initial acid concentration. After 10 hours of leaching for 100 g/dm³ of initial acid concentration the recovery of cobalt and nickel was found as 48 and 25%, respectively (compared to 10 and 8% for 50 g/dm³ of acid). It can be seen that the cobalt and nickel recovery curves are almost flat from the beginning of leaching and tend to raise in later leaching stages. The time needed for Co and Ni to begin their effective leaching is much shorter and the leaching rate of these metals is much higher in the experiments with higher initial acid concentration. This fact can be explained by a strong correlation between recoveries of Co, Ni and Cu (Fig. 3).

Effect of oxygen flow rate

A sample of KLA Lubin concentrate was used for evaluation of the oxygen flow rate on Co and Ni leaching. Three O₂ flow rates were compared: 30, 60 and 90 dm³/h. Other process parameters remained constant for all experiments (temperature 90 °C, s/l 1:8, initial H₂SO₄ concentration 50 g/dm³, iron(III) ions concentration 30 g/dm³, leaching time 5 h).

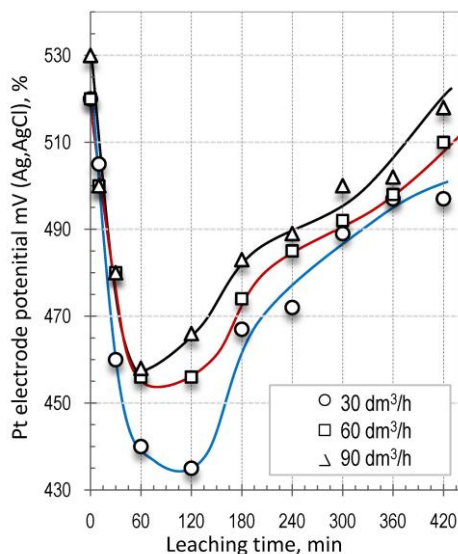


Fig. 10. Effect of oxygen flow rate. Potential of Pt electrode – leaching time during atmospheric leaching: initial H_2SO_4 concentration 50 g/dm^3 , s/l 1:8, iron(III) ions concentration 30 g/dm^3 , temperature 90°C

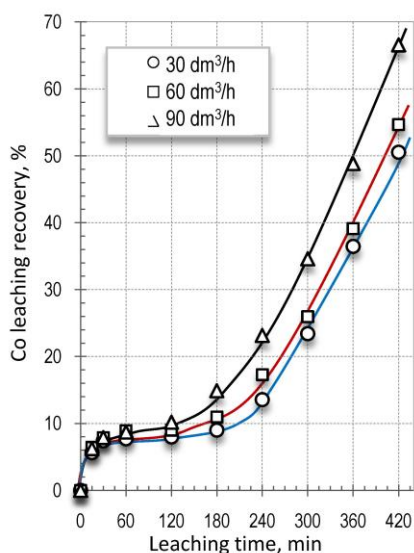


Fig. 11. Effect of oxygen flow rate on Co leaching recovery: initial H_2SO_4 concentration 50 g/dm^3 , s/l 1:8, iron(III) ions concentration 30 g/dm^3 , temperature 90°C

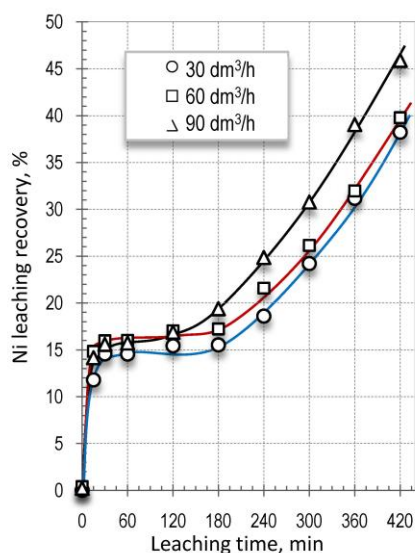


Fig. 12. Effect of oxygen flow rate on Ni leaching recovery: initial H_2SO_4 concentration 50 g/dm^3 , s/l 1:8, iron(III) ions concentration 30 g/dm^3 , temperature 90°C

The oxygen flow rates had an expected effect on the redox potential of the slurry (Fig. 12). The main role of oxygen in the presence of iron(III) ions is to regenerate them by oxidizing Fe^{2+} to Fe^{3+} . With increasing O_2 flow rate, the redox potential values were slightly higher, as the iron(III) ions regeneration reaction was more efficient. This had also an effect on Co and Ni leaching recoveries (Figs. 10 and 11).

In the atmospheric leaching processes there are two simultaneous reactions: anodic dissolution of sulfide minerals, where sulfur is oxidized from its sulfide to elemental form by iron(III) ions, which are reduced to iron(II) and reaction of iron(II) to iron(III) ions regeneration with oxygen. For all leaching experiments the initial redox potential was about 530 mV (Ag, AgCl). In the first phase of atmospheric leaching a rapid decrease in the potential is observed. This is due to the dissolution rate of easy-to-leach copper minerals (bornite and chalcocite), which is much higher than the rate of iron(III) ions regeneration reaction. It shows, that the atmospheric leaching process needs to be optimized in terms of oxygen distribution and hydrodynamic conditions (more efficient way of introducing oxygen, use of baffles, etc.) in order to enhance the copper leaching rate in the first phase of the process by limiting the redox potential drop. The highest decrease of redox potential was observed in the experiment with 30 dm^3/h of O_2 flow rate (Fig. 12). Higher oxygen flow rates cause a higher potential of the slurry. Furthermore, with higher oxygen flow rates it takes less time for iron(III) ions regeneration rate to dominate over the sulfide minerals leaching rate.

Effect of chloride ions addition

Mining plants at KGHM Polska Miedz S.A. (Lubin, Polkowice-Sieroszowice and Rudna) generate together 75 000 m^3 of mine water per day (KGHM data, 2013). The 95% of the mine water contains 3–5 g/dm^3 of chloride ions. In the case of application of the hydrometallurgical technology for concentrates, mine water would be used for the atmospheric leaching process. Therefore, it is necessary to evaluate the effect of chloride ions on the leaching rate and efficiency.

In this experiment the commercial flotation concentrate KLC sample was selected. Two atmospheric leaching experiments were conducted: the first one without chloride ions addition, and the second one with 3 g/dm^3 addition of chlorides. The experiments showed (Figs. 13 and 14) that even a small addition of chloride ions causes significant increase in the leaching recovery. The Co recovery after 7 hours of leaching with chlorides addition was 28%, whereas the Ni recovery was 23%. The chloride ions concentration of 3 g/dm^3 is low enough to prevent silver and lead leaching into the solution (less than 0.1% of lead and silver was leached out). Only leaching process at elevated concentration of chloride ions gives the possibility for effective recovery of Pb and Ag. Therefore, the presented research confirms possible application of mine water in the atmospheric leaching processes.

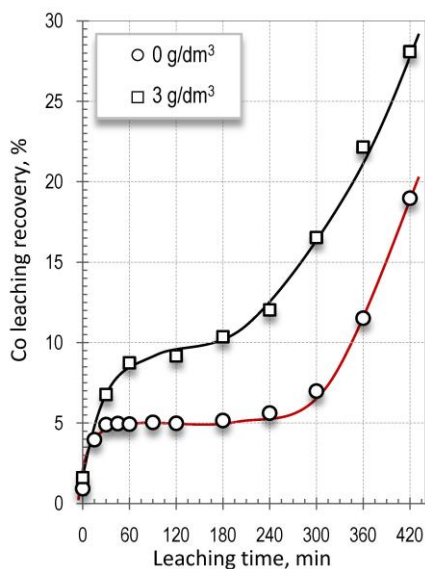


Fig. 13. Effect of chloride ions addition on the Co leaching: initial H_2SO_4 concentration 50 g/dm^3 , s/l 1:6, iron(III) ions concentration 30 g/dm^3 , temperature $90 \text{ }^\circ\text{C}$, O_2 flow rate $60 \text{ dm}^3/\text{h}$

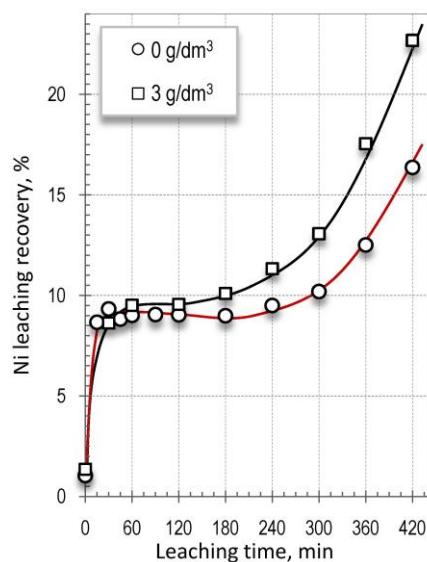


Fig. 14. Effect of chloride ions addition on the Ni leaching: initial H_2SO_4 concentration 50 g/dm^3 , s/l 1:6, iron(III) ions concentration 30 g/dm^3 , temperature $90 \text{ }^\circ\text{C}$, O_2 flow rate $60 \text{ dm}^3/\text{h}$

Conclusions

In this paper atmospheric leaching of cobalt and nickel from the Lubin copper concentrate is presented. The effect of following parameters on the leaching efficiency was investigated: temperature, iron(III) ions, sulfuric acid and chloride ions concentration and oxygen flow rate. It was found that enhancing all the investigated parameters resulted in the higher rate of cobalt and nickel leaching. The most significant effect was observed for increased both, iron(III) ions and initial sulfuric acid concentrations. It was also observed, that cobalt and nickel leaching rates dramatically increased when the copper recovery was higher than 90%.

Acknowledgements

The research presented in this paper was co-financed by the European Union as part of the European Social Fund. The work was also co-financed by statutory activity subsidy from the Polish Ministry of Science and Higher Education for the Faculty of Chemistry of Wrocław University of Technology.

References

BACHOWSKI C., STASZAK J., BYSZYNSKI L., BOCZAR W., TEODORSKI D., 2003, *Search for alternative methods of processing of copper ores in KGHM „Polska Miedz” S.A.* –

- hydrometallurgical technologies*, VIII Seminar „Hydrometallurgy of Sulphide Copper Resources”, Lubin, June 26. 2003: 125, (In Polish).
- CHMIELEWSKI T., 2012. *Hydrometallurgy in KGHM Polska Miedz SA – Circumstances, Needs and Perspectives of Application*, Separation Science and Technology 47, 9, 1264-1277.
- CHMIELEWSKI T., CHAREWICZ W., 1984. *Pressure leaching of sulphide copper concentrate with simultaneous regeneration of the leaching agent*, Hydrometallurgy 13, 63-72.
- CHMIELEWSKI T., CHAREWICZ W., 2006, *Hydrometallurgical processing of shale by-products from beneficiation circuits of Lubin Concentrator*, In: *Perspectives for applying bioleaching Technology to process shale-bearing copper ores*, BIOPROCOP'06, Lubin 2006, KGHM Cuprum, Wroclaw 2006, 125-145.
- CHMIELEWSKI T., LUSZCZKIEWICZ A., KONOPACKA Z., *Acidic pretreatment of hard-to-treat copper ore flotation middlings to facilitate flotation efficiency*. Proceedings of XXIV International Mineral Processing Congress, Beijing 24-28 Sept. 2008, Vol. 3, Wang D.D., Sun C.Y., Wang F.L., Zhang L.C., Han L. (Eds), Science Press, 1189-1200
- DREISINGER D., 2006. *Copper leaching from primary sulfides: Options for biological and chemical extraction of copper*, Hydrometallurgy 83, 10 – 20.
- GROTOWSKI A. 2007. *Possibilities and perspectives for implementation of hydrometallurgical methods in KGHM Polska Miedz S.A.*, Proc. VIII International Conference on Non-ferrous Ore Processing, Wojcieszycze (Poland), May 21–23, KGHM Cuprum Wroclaw 2007.
- GUPTA C.K., MUKHERJEE T.K., 1990. *Hydrometallurgy in Extraction Processes*, Vol. I and II; CRC Press: Boca Raton, FL.
- HABASHI F., 1999, *Textbook of hydrometallurgy*, Metall. Extract. Quebec.
- HABASHI F., 2005, *Recent Advances in the Hydrometallurgy of Copper*, Proc. Int. Copper Hydrometallurgy Workshop “Hydrocopper 2005” (Menacho J.M., Casas de Prada J.M., Eds.), Santiago, Chile, pp. 43-55.
- HABASHI F., 2007, *Abandoned but not forgotten – the recent history of copper hydrometallurgy*, The John Dunitz Symposium on Copper Hydrometallurgy, Proceedings 6th International Copper-Cobre International Conference, August 3-20, 2007, Toronto, Canada, vol. IV, Met. Soc.
- JANSEN M., TAYLOR A., 2000, *Key elements in the selection of sulphide leach processes for copper concentrate leaching*, Alta Cu 2000, August 2000, Int. Proj. Dev. Serv. Pty Ltd.,
- KONIECZNY A., KASIŃSKA-PILUT E., PILUT R., 2009. *Technological and technical problems in mineral processing of Polish copper ores at Division of Concentrators KGHM “Polska Miedz” SA*, Proc. IX International Conference on Non-Ferrous Ore Processing, ICNOP Ladek Zdroj (in Polish), 18–20 May 2009: 11, in Polish.
- KUKUC R., BAZAN B., *Improvement of technology indices of DoC Lubin Plant within the context of decreasing copper content in ore*, Proceedings of the Mineral Engineering Conference MEC2013, Kowalczyk P.B. (ed.), Swieradow-Zdroj, Poland, 16-19 September 2013, pp. 95-108
- LUSZCZKIEWICZ A., 2000, *Utilisation of black copper shale ores from Lubin-Glogow region. in: Recent problems on copper ores processing in Poland*, November 16, 2000., Conference Proceedings, Mining Committee of Polish Academy of Sciences and KGHM “Polish Copper”, 137-156 (in Polish).
- LUSZCZKIEWICZ A., 2009, *Physicochemical Problems of Minerals Processing Seminar*, Niepolomice, Poland, 16-18 Sept, 2009, plenary lecture.
- MARSDEN J.O., WILMOT J.C., 2007a, *Medium-temperature pressure leaching of copper concentrates – Part I: Chemistry and initial process development*, Min. Metall. Processing, 24(4) 193-204.
- MARSDEN J.O., WILMOT J.C., 2007b, *Medium-temperature pressure leaching of copper concentrates – Part II: Development of direct electrowinning and acid-autogenous process*, Min. Metall. Processing, 24(4) 205-217.

- MARSDEN J.O., WILMOT J.C., 2007c, *Medium-temperature pressure leaching of copper concentrates* – Part III: Commercial demonstration at Bagdad, Arizona, *Min. Metall. Processing*, 24(4) 218-225.
- MARSDEN J.O., WILMOT J.C., 2007d, *Medium-temperature pressure leaching of copper concentrates* – Part IV: Application at Morenci, Arizona, *Min. Metall. Processing*, 24(4) 226-236.
- MARSDEN J.O., 2007e, *Sulphate-based flowsheet options for hydrometallurgical treatment of copper sulphide concentrates*, The John Durtizac Symposium on Copper Hydrometallurgy, *Proceedings 6th International Copper-Cobre Conference*, August 25-30, 2007, Toronto, Canada, vol. IV, *Met. Soc.*, pp.77-100.
- PEACEY J.I., GUO X.J., ROBLES E., 2003, *Copper Hydrometallurgy – Current Status, Preliminary economics, Future Direction and Positioning versus Smelting*, *Copper 2003 - Cobre 2003*, vol.VI, (Book 1) Santiago – Chile (Riveros P.A., Dixon D., Dreisinger D., Eds.), pp. 205-222.
- RAMACHADRAN V., LAKSMANAN V.I., KONDOS P.D., 2007, *Hydrometallurgy of copper sulphide concentrate*, The John Durtizac Symposium on Copper Hydrometallurgy, *Proceedings 6th International Copper-Cobre Conference*, August 25-30, 2007, Toronto, Canada, vol. IV, *Met. Soc.*, pp.101-128.

Received April 19, 2014; reviewed; accepted July 18, 2014

COMPARISON OF SURFACE PROPERTIES OF ANTHRACITE COALS BEFORE AND AFTER HIGH TEMPERATURE HEATING PROCESS

Wencheng XIA, Guangyuan XIE

School of Chemical Engineering and Technology, China University of Mining and Technology, Xuzhou 221116, Jiangsu, China. E-mail: w.xia.cumt@gmail.com, xiawencheng@cumt.edu.cn.

Abstract: Surface property plays a very important role on coal hydrophobicity which determines flotation behavior of fine coals. However, coal spontaneous combustion makes coal suffer both oxidation and high temperature heating processes. Coals from the outside of coal piles primarily suffer oxidation (or combustion process) while coals from the inside of coal piles primarily suffer high temperature heating process. It is necessary to investigate the changes in surface properties of coal before and after high temperature heating process. In this investigation, X-ray photoelectron spectroscopy (XPS), scanning electron microscope (SEM), surface area (BET) and contact angle measurements were used to indicate the changes in surface properties of anthracite coal before and after high temperature heating process. Throughout this study, surface properties of coal changed significantly after high temperature heating process. Meanwhile, coal hydrophobicity can be also reduced after high temperature heating.

Keywords: heating, coal hydrophobicity, XPS, SEM, BET, contact angle

Introduction

Coal has both inorganic and organic materials. Inorganic materials consist of silicate, pyrites and other clays. Organic materials consist of carbon, hydrogen, oxygen, nitrogen, organic sulfur and other elements. Surface properties of coals are determined by the ratio of inorganic materials to organic materials. Therefore, coal hydrophobicity is related to the surface properties of coal as well as the ratio of inorganic materials to organic materials on coal surface. In a way, organic materials usually make coal surface more hydrophobic while inorganic materials make coal surface more hydrophilic. Bituminous and anthracite coal usually have good natural hydrophobicity. Based on this natural hydrophobicity, bituminous and anthracite coal can be easy to float with only a little oily collector. However, coal oxidation processes can reduce this natural hydrophobicity and make fine coals difficult to float with the common oily

collectors (Wu et al., 1988; Bolat et al., 1998; Fuerstenau and Diao, 1992; Jia et al., 2000; Tao et al., 2002; Hao et al., 2013).

The types of coal oxidation processes generally include low temperature oxidation (weathering) and high temperature oxidation (combustion). Low temperature oxidation (weathering) process is considered as mild oxidation reaction and the surface properties of coal can be changed by this mild oxidation process (Kozłowski et al., 2002; Pilawa et al., 2002; Grzybek et al., 2002, 2006; Pietrzak and Wachowska, 2003; Pietrzak et al., 2004, 2007). In contrast, high temperature oxidation process is a fast oxidation process. During high temperature oxidation process of coal, coals from the outside of coal piles primarily suffer oxidation process (or combustion process) while coals from the inside of coal piles primarily suffer high temperature heating process. The phenomenon of coal spontaneous combustion can be seen in many coal mines or coal piles around the world. Coal spontaneous combustion makes coal suffer high temperature oxidation. However, the inner part of coal piles or coal mines may primarily suffer high temperature heating process during coal spontaneous combustion because there is only a little oxygen in the inner part of coal piles or coal mines. In contrast, the outer part of coal piles should primarily suffer combustion process because it is in contact with the atmosphere easily.

Taixi oxidized coal is primarily formed by high temperature heating process during coal spontaneous combustion. Meanwhile, Taixi oxidized coal is difficult to float using the common oily collectors (Xia et al., 2012; 2013; Xia and Yang, 2013). It is necessary to investigate the changes in both surface properties and hydrophobicity of coal before and after high temperature heating process. However, there are little literatures about the effects of high temperature heating process on the changes in both surface properties and hydrophobicity of coal. The aim of this paper is to reveal the changes in both surface properties and hydrophobicity of Taixi coal before and after high temperature heating process. Furthermore, this paper used a sample of anthracite coal with very low ash content to conduct this study. The low ash content anthracite coal may be more suitable for reveal accurate changes in both surface properties and hydrophobicity of coal before and after high temperature heating process.

Experimental section

Coal samples

In this investigation, a sample of fresh anthracite coal with very low ash content was selected prior by hand preparation and density separation. The density fraction of low ash content coal sample was 1.350~1.375 g/cm³. These coal bulks were crushed and screened. The size fraction of 0.125-0.074 mm was selected to be used in this study. The proximate analysis of fresh coal samples is given in Table 1. Where Mad is the moisture matter content, Vad the volatile content, FCad the fixed carbon content, Aad is the ash content. The contents of elements (C, H, O, N and S) based on dry ash free are also shown in Table 1.

Table 1. Proximate analysis of fresh anthracite coal

| Mad (%) | Vad (%) | FCad (%) | Aad (%) | Cdaf (%) | Hdaf (%) | Odaf (%) | Ndaf (%) | St,daf (%) |
|---------|---------|----------|---------|----------|----------|----------|----------|------------|
| 4.20 | 7.40 | 86.85 | 1.55 | 94.43 | 3.73 | 0.91 | 0.79 | 0.13 |

High temperature heating process

High temperature heating process was conducted in a quartz crucible and a muffle furnace. High temperature heating temperature was fixed at 800 °C. High temperature heating time was 120 minutes. After high temperature heating process, coal samples were cooled in a vacuum drying chamber and then stored in air for 48 hours.

XPS measurement

For the indication of surface properties of coals before and after high temperature heating process, coal samples were pressed into pellets firstly. The XPS experiments were carried out at room temperature in an ultra high vacuum (UHV) system with the surface analysis system (ESCALAB 250 Xi, America). The data processing (peak fitting) was performed with XPS Peak fit software, using a Smart type background subtraction and Gaussian/Lorentzian peak shapes. The binding energies were corrected by setting the C1s hydrocarbon ($-\text{CH}_2-\text{CH}_2$ -bonds) peak at 284.6 eV.

SEM measurement

The FEI Quanta 250 SEM was used to analyze the surface morphology of coals before and after high temperature heating process. The coal samples were prepared by surface cleaning using absolute ethyl alcohol. After surface cleaning, the coal samples were dried in air. Before SEM, the coal samples were sputter-coated with a layer of gold.

BET measurement

Specific surface area measurements of coals before and after high temperature heating process were made by the Brunauer, Emmett and Teller (BET, BELSORP-max) method of adsorption of nitrogen gas. Surface area (m^2/g) was obtained from experimental data.

Contact angle measurement

Coal samples before and after high temperature heating process were pressed to form plates. The plates of coal samples were measured using water contact angle analyzer (JC2000D), such as a water droplet on the surface of coal plate in air. The contact angles were obtained while the water droplet contacts with the coal plate at the exact moment.

Results and discussion

XPS analysis

C1s peaks at binding energies of 284.6 eV, 285.6 eV, 286.6 eV and 289.1 eV correspond to the following groups: C-C or C-H, C-O (alcohol, phenol or ether), C=O (carbonyl or quinone) or O-C-O (in low rank coals) and COOH (carboxyl) (Desimoni et al., 1992; Fiedler and Bendler, 1992; Xia and Xie, 2014; Xia et al., 2014). C-C and C-H groups are the primary hydrophobic functional groups while C-O, C=O and COOH groups are the primary hydrophilic functional groups on coal surface (Cinar, 2009). The contents of C-C or C-H, C-O, C=O and COOH groups can be calculated (Table 2) by the analysis of C1s peaks shown in Figs. 1 and 2.

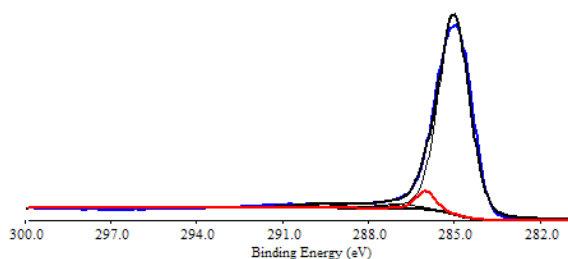


Fig. 1. C1s peak for anthracite coal before high temperature heating process

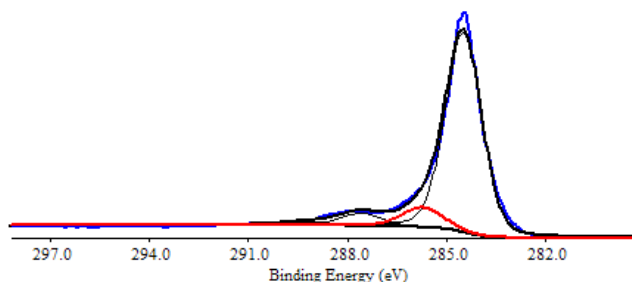


Fig. 2. C1s peak for anthracite coal after high temperature heating process

Table 2. Fraction of C on the surface of anthracite coal before and after high temperature heating process (relative % of C1s)

| Coal types | C-C, C-H (%) | C-O (%) | C=O (%) | COOH |
|------------------------|--------------|---------|---------|------|
| Before heating process | 88.78 | 5.35 | 3.17 | 2.71 |
| After heating process | 82.49 | 9.25 | 6.11 | 2.15 |

The content of C-C/C-H groups is 88.78% in fresh anthracite coal. After high temperature heating process, the content of C-C/C-H groups is reduced to 82.49%. In contrast, the content of C-O group increases from 5.35% to 9.25% and the content of

C=O group increases from 3.17% to 6.11%. C-C and C-H groups can be cracked during high temperature heating process and can release gas (i.e. CO, CO₂ and CH₄) and coal tar. Therefore, the relative content of C-H and C-C groups on coal surface is reduced after high temperature heating process and the contents of C-O and C=O groups are increased. However, the content of COOH group decreases from 2.71% to 2.15% (Table 2). It seems that COOH group can also be cracked during high temperature heating process. COOH group can be cracked and can release CO, H₂O and CO₂ during the high temperature heating process. The thermal stability of COOH group is lower than C=O group as well as the thermal stability of C=O group is lower than C-O group. During high temperature heating process, COOH group will be cracked first and quickly (Schafer, 1979; Zhou et al., 2007). C-C and C-H groups are the primary hydrophobic functional groups while C-O, C=O and COOH groups are the primary hydrophilic functional groups on coal surface (Cinar, 2009). After high temperature heating process, the content of hydrophilic functional groups is increased while the content of hydrophobic functional groups is reduced, and hence the hydrophobicity of coal surface may be also reduced.

SEM analysis

Figures 3 and 4 are the SEM pictures for anthracite coal before and after high temperature heating process. It is obvious that heated coal surface is much rougher than the fresh coal surface. Meanwhile, some new cracks are produced by high temperature heating process. It indicates that anthracite coal may be expanded during high temperature heating process and constricted after high temperature heating process while it is cooled at room temperature. Furthermore, there are nearly no holes on the fresh coal surface while there are many holes on heated coal surface. The depth of these holes is very small. It seems that these holes have a bubble structure. The

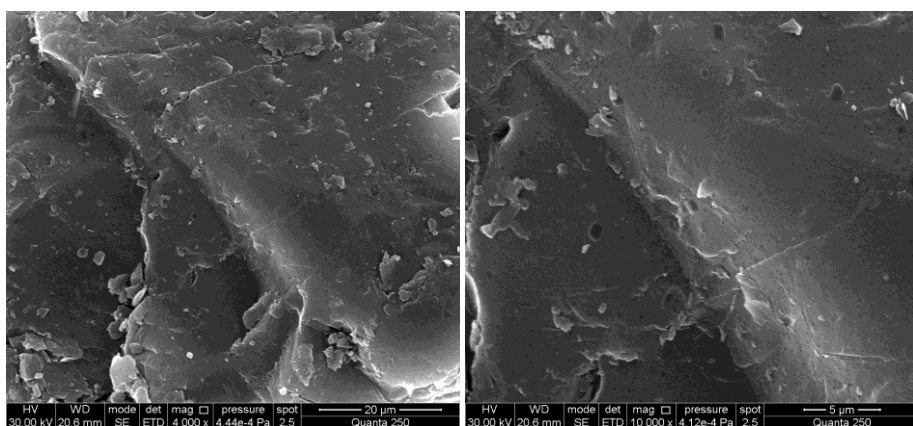


Fig. 3. SEM pictures for anthracite coal before high temperature heating process

surface topography of heated anthracite coal surface looks like the surface topography of unburned carbon particles in the fly ash from the literatures (Niewiadomski et al., 1999; Kutchko and Kim, 2006). It is well known that unburned carbon particles in fly ash are difficult to float with the common oily collectors due to its low hydrophobicity. Therefore, heated coal may be much more hydrophilic than fresh coal.

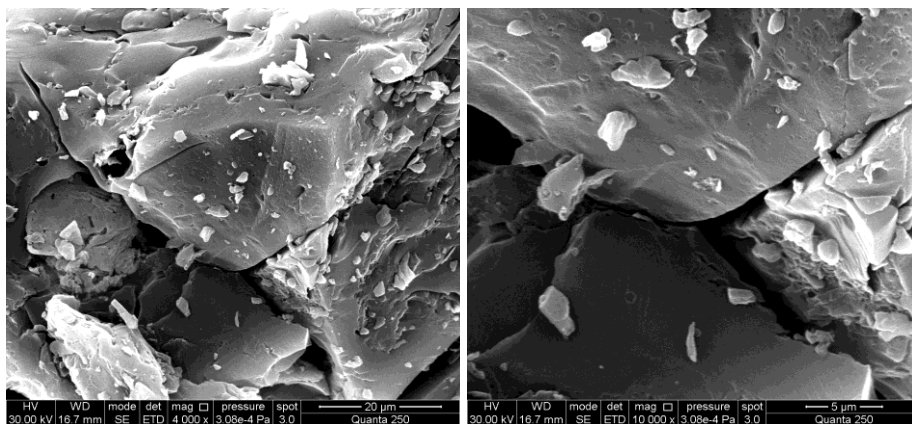


Fig. 4. SEM pictures for anthracite coal after high temperature heating process

BET analysis

Table 3 shows surface area (m^2/g) of anthracite coal before and after high temperature heating process. Surface area of fresh anthracite coal is much lower than that of heated anthracite coal. Figure 3 shows that there are nearly no cracks and holes on fresh coal surface. As shown in Fig. 4, there are many cracks and holes on heated coal surface. Therefore, the BET results match the SEM results very well.

Table 3. BET results for anthracite coal before and after high temperature heating process

| Coal types | Surface area (m^2/g) |
|------------------------|--|
| Before heating process | 0.24 |
| After heating process | 44.78 |

Contact angle analysis

Figure 5 and 6 are the pictures of contact angles of anthracite coal before and after high temperature heating process. The contact angle of fresh coal is about 112° while that of heated coal is only about 45° . After high temperature heating process, anthracite coal surface becomes more hydrophilic. From the above-mentioned results, heated anthracite coal surface has much more holes, cracks and hydrophilic functional groups. Hydrophilic functional groups make coal surface easy to be wetted. Meanwhile, the infiltration of water into the cracks and holes is also occurred during the measurements of contact angles. Therefore, the contact angle of heated anthracite

coal is much lower than that of fresh anthracite coal. The hydrophilicity of anthracite coal surface is increased by high temperature heating process.

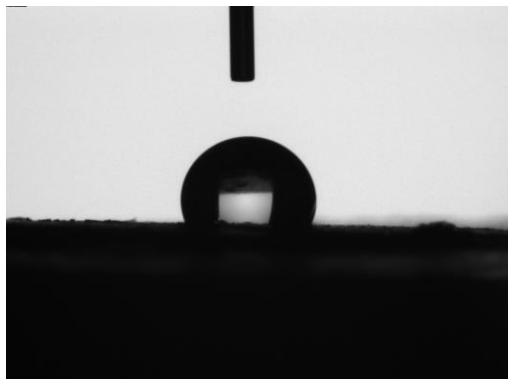


Fig. 5. Contact angle of anthracite coal before high temperature heating process

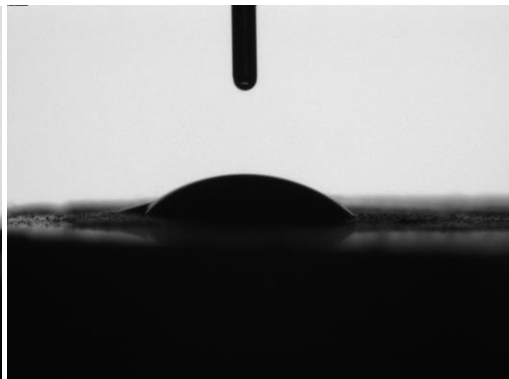


Fig. 6. Contact angle of anthracite coal after high temperature heating process

Conclusions

- The results of XPS, SEM, BET and contact angle measurements indicate that high temperature heating process not only changes the surface properties of anthracite coal but also reduces the hydrophobicity of coal surface.
- Compared with fresh anthracite coal surface, there are more holes, cracks and hydrophilic functional groups on heated anthracite coal surface.
- Both surface area and pore volume of fresh anthracite coal are much lower than those of heated anthracite coal.
- The contact angle of heated anthracite coal is much lower than that of fresh anthracite coal, and hence anthracite coal becomes much easier to be wetted after high temperature heating process than fresh anthracite coal.

Acknowledgment

This work was supported by A Project Funded by the Priority Academic Program Development of Jiangsu Higher Education Institutions.

References

- BOLAT E., SAGLAM S., PISKIN S., 1998. *The effect of oxidation on the flotation properties of a Turkish bituminous coal*. Fuel Processing Technology, 55(2), 101-105.
- CINAR M., 2009. *Floatability and desulfurization of a low-rank (Turkish) coal by low-temperature heat treatment*. Fuel Processing Technology, 90(10), 1300-1304.
- DESIMONI E., CASELLA G. I., SALVI A. M., 1992. *XPS/XAES study of carbon fibres during thermal annealing under UHV conditions*. Carbon, 30(4), 521-526.

- FUERSTENAU D. W., DIAO J., 1992. *Characterization of coal oxidation and coal wetting behavior by film flotation*. *Coal Preparation*, 10(1-4), 1-17.
- FIEDLER R., BENDLER D., 1992. *ESCA investigations on Schleenhain lignite lithotypes and the hydrogenation residues*. *Fuel*, 71(4), 381-388.
- GRZYBEK T., PIETRZAK R., WACHOWSKA H., 2006. *The influence of oxidation with air in comparison to oxygen in sodium carbonate solution on the surface composition of coals of different ranks*. *Fuel*, 85(7): 1016-1023.
- GRZYBEK T., PIETRZAK R., WACHOWSKA H., 2002. *X-ray photoelectron spectroscopy study of oxidized coals with different sulphur content*. *Fuel Processing Technology*, 77: 1-7.
- HAO S., WEN J., YU X., CHU W., 2013. *Effect of the surface oxygen groups on methane adsorption on coals*, *Applied Surface Science*, 264, 433-442.
- JIA R., HARRIS G. H., FUERSTENAU D. W., 2000. *An improved class of universal collectors for the flotation of oxidized and/or low-rank coal*. *International Journal of Mineral Processing*, 58(1), 99-118.
- KUTCHKO B. G., KIM A. G., 2006. *Fly ash characterization by SEM-EDS*. *Fuel*, 85(17), 2537-2544.
- KOZŁOWSKI M., PIETRZAK R., WACHOWSKA H., YPERMAN J., 2002. *AP-TPR study of sulphur in coals subjected to mild oxidation. Part I. Demineralised coals*. *Fuel*, 81(18): 2397-2405.
- NIEMIADOMSKI M., HUPKA J., BOKOTKO R., MILLER J. D., 1999. *Recovery of coke fines from fly ash by air sparged hydrocyclone flotation*. *Fuel*, 78(2), 161-168.
- PIETRZAK R., WACHOWSKA H., 2004. *Thermal analysis of oxidised coals*. *Thermochimica Acta*, 419(1): 247-251.
- PIETRZAK R., GRZYBEK T., WACHOWSKA H., 2007. *XPS study of pyrite-free coals subjected to different oxidizing agents*. *Fuel*, 86(16): 2616-2624.
- PIETRZAK R., WACHOWSKA H., 2003. *Low temperature oxidation of coals of different rank and different sulphur content*. *Fuel*, 82(6): 705-713.
- PILAWA B., WIĘCKOWSKI A. B., PIETRZAK R., WACHOWSKA H., 2002. *Oxidation of demineralized coal and coal free of pyrite examined by EPR spectroscopy*. *Fuel*, 81(15): 1925-1931.
- SCHAFER H. N. S., 1979. *Pyrolysis of brown coals. I. Decomposition of acid groups in coals containing carboxyl groups in the acid and cation forms*. *Fuel*, 58(9), 667-672.
- TAO D., JOHNSON S., PAREKH B. K., 2002. *A flotation study of refuse pond coal slurry*. *Fuel Processing Technology*, 76(3), 201-210.
- WU M. M., ROBBINS G. A., WINSCHEL R. A., BURKE F. P., 1988. *Low-temperature coal weathering: its chemical nature and effects on coal properties*. *Energy & Fuels*, 2(2), 150-157.
- XIA W., YANG J., ZHAO Y., ZHU B., WANG Y., 2012. *Improving floatability of Taixi anthracite coal of mild oxidation by grinding*. *Physicochemical Problem of Mineral Processing*, 48 (2), 393-401.
- XIA W., YANG J., LIANG C., 2013. *A short review of improvement in flotation of low rank/oxidized coals by pretreatments*. *Powder Technology*, 237, 1-8.
- XIA W., YANG J., 2013. *Reverse flotation of Taixi oxidized coal*. *Energy & Fuels*, 27(12), 7324-7329.
- XIA W., XIE G., 2014. *Changes in the hydrophobicity of anthracite coals before and after high temperature heating process*. *Powder Technology*, 264, 31-35.
- XIA W., XIE G., PAN D., YANG J., 2014. *Effects of cooling conditions on surface properties of heated coals*. *Industrial & Engineering Chemistry Research*, 53 (26), 10810-10813.
- ZHOU J. H., SUI Z. J., ZHU J., LI P., CHEN D., DAI Y. C., YUAN W. K., 2007. *Characterization of surface oxygen complexes on carbon nanofibers by TPD, XPS and FT-IR*. *Carbon*, 45(4), 785-796.

Received March 3, 2014; reviewed; accepted June 30, 2014

PRE-CONCENTRATION AND FLOTATION OF ALUNITIC KAOLIN AND ITS POSSIBLE USE IN CERAMIC TILE INDUSTRY

Nezahat EDIZ*, Ilknur TATAR**, Ahmet AYDIN*

* Dumlupinar University, Department of Mining Engineering, Kutahya, TURKEY, nezahatediz@hotmail.com

** Ilksem Ar&Ge, Eskisehir Osmangazi University Technopark, Eskisehir, TURKEY

Abstract: The aim of this research was to remove sulphur and alunitic parts by the flotation method from alunitic kaolin obtained from the Balikesir-Sindirgi region of Turkey, which is not currently used by the ceramic industry because of its high sulphur content. In the process, mineral alunite was floated while kaolinite was depressed. The effect of pre-concentration on the flotation process was also investigated. Pre-concentration included several processes such as wetting, mechanical scrubbing, and screening for removal of fine alunite particles and colouring oxides from kaolin as well as screening after consecutive milling for the separation of hard minerals such as quartz from kaolin. After the pre-concentration and flotation processes, kaolin concentrate having a SO₃ content of 0.48% was obtained with a sulphur removal efficiency of 88.55%, and this kaolin was coded as F4. Afterwards, the use of F4 kaolin in the ceramic industry was investigated. For this purpose, the F4 kaolin was used in angobe preparation, and the angobes prepared were used for the production of floor and wall tiles. The properties of the angobes were also compared to those of commercial floor and wall tile angobes from a ceramic factory. These tests indicated that the floor and wall tile angobes prepared by using F4 kaolin could be used as an alternative for the angobes currently used by the factory.

Keywords: *alunitic kaolin, kaolin flotation, angobe, ceramic tiles*

Introduction

Kaolin has a wide range of industrial applications since it is a white coloured, fine grained, non-abrasive, and relatively cheap clay mineral with good coating and forming ability, low electrical conductivity, and easily dissolving nature in water (Bergaya et al., 2006; Murray, 2007; Castellano et al., 2010). Kaolin extracted from the commercial deposits contains kaolinite as a major component along with accessory minerals such as quartz, muscovite, limonite, anatase, hematite, illite, and organic matters. For industrial applications, kaolin must be extensively processed and highly

refined in order to be used as pigment, filler, coater, extender, and ceramic raw material. Coarser impurities (generally quartz) are easily separated by screening or classification while micrometer size impurities require special treatments. The partial or complete removal of these impurities by economical and practical methods has been the subject of many studies (Newns and Pascoe, 2002; Raghavan et al., 2004; Calderon et al., 2005; He et al., 2011).

Apart from the generally occurring impurities given above, there are more than 12 kaolin deposits in Turkey where sulphur is the major impurity. Sulphur in these deposits is generally associated with pyrite and/or alunite. The physical and chemical characteristics (except sulphur content) of the kaolin extracted from these deposits are generally suitable for ceramic production. Since sulphur causes cracks and pores during firing at elevated temperatures, it is impossible to use such ores in ceramic production directly. Therefore, SO_3 content of such raw materials must be reduced to lower than 0.5% (Ekmekci et al., 2001). Unfortunately, the sulphur content of the kaolin deposit within the Balikesir-Sindirgi region of Turkey is also very high hindering its use in the ceramic industry.

Typical methods used for the separation of alunite from kaolin are thermo-chemical, physico-chemical, and physical methods (Koca, 1992). From literature reviewed on the sulphur content of Balikesir kaolins at fractional base, it was realized that sulphur accumulated at finer fractions ($\sim 38 \mu\text{m}$). In other words, alunite particles existed together with mineral kaolinite (Girgin et al., 1993; Yapa, 1994). As seen from Table 1, it is rather difficult to remove alunite from kaolin at such fine fractions by using physical methods. The sulphur content of alunitic kaolins can be reduced by employing thermo-chemical methods (Table 2). In such methods, however, it is necessary to keep the roasting temperature of the thermal process well below the decomposition temperature of kaolinite to avoid any undesired physical and chemical changes in the properties. As explained from the related studies, the chemical structure of the kaolinite starts to change after 600°C , and it is converted to metakaolin (Ekmekci et al., 2001). With this change to metakaolin, kaolin loses its plastic property which is one of the most crucial parameters in ceramic production.

Table 1. Beneficiation of alunitic kaolin by physical methods

| Reference | Process applied | SO_3 in the feed (%) | SO_3 in kaolin concentrate (%) | SO_3 removal efficiency (%) |
|---------------|---|-------------------------------|---|--------------------------------------|
| Sumer, 1991 | Comminution and classification | 13.87 | 13.62 | – |
| Acar, 1995 | Mechanical scrubbing and classification | 4.73 | 4.23 | – |
| Ekmekci, 2001 | Mechanical scrubbing and classification | 1.09 | Not beneficiated | – |

Table 2. Beneficiation of alunitic kaolin by thermal methods

| Reference | Roasting temperature (°C) | SO ₃ in the feed (%) | SO ₃ in kaolin concentrate (%) | SO ₃ removal efficiency (%) |
|---------------|--|---------------------------------|---|--|
| Sumer, 1991 | 900 | 12.73 | 2.14 | - |
| | 1100 | 13.37 | 0.43 | - |
| Girgin, 1993 | 600 (with 5% Na ₂ CO ₃ addition) | 7.15 | 0.48 | - |
| Genc, 1994 | 900 | 10.10 | 1-1.5 | - |
| | 700 (with KCl, NaCl addition) | 10.10 | 1-3 | (91.5-92.1) |
| Ekmekci, 2001 | 1000 | 1.09 | 0.48 | - |

Therefore, physico-chemical methods are regarded to be the most effective methods to reduce the sulphur content of alunitic kaolin to a desired level (<0.5%) for its use in the ceramic industry without altering its chemical and physical properties. From the very limited studies carried out to remove alunite from kaolin at fine particle sizes, it was observed that the efficiencies of such processes were rather low (Table 3). The reason for low efficiencies was explained by the fact that liberation could be obtained at particle sizes finer than 10 µm, which in turn, caused a slime coating problem during the process (Koca, 1992; Miller and Acherman, 1980).

Table 3. Beneficiation of alunitic kaolin by flotation

| Reference | Flotation stage | SO ₃ in the feed (%) | SO ₃ in kaolin concentrate (%) | SO ₃ removal efficiency (%) |
|---------------|-----------------|---------------------------------|---|--|
| Sumer, 1991 | One stage | 10.07 | 8.36 | - |
| Koca, 1992 | One stage | 17.85 | Not beneficiated | - |
| Yapa, 1994 | Two stages | 1.94 | 0.22 | 39.60 |
| Ekmekci, 2001 | Two stages | 1.09 | 1.06 | 18.24 |

In the ceramic industry, angobe production is one of the most common utilization areas for kaolins, if its physical and chemical properties are suitable. As is well known, red firing clays and some industrial waste materials are commonly used as starting materials in ceramic tile production whose final products are not white in colour. Therefore, angobe application is required in floor and wall tile production to improve aesthetic and/or functional properties before glazing. The use of frit glazing increases the cost of tile production; however, greyish appearances and dark shadows may occur when raw glazes are used. These types of glazing problems can also be solved by angobe application in ceramic tile production.

Angobe is a semi-liquid, viscous, and finely grained ceramic product which tends to give a dry-matt surface on its own and is generally used under a clear glaze. After

application, angobe slurry covers ceramic bodies at a desired density and colour, eliminates any thermal expansion disconformity between the glaze and the body and reduces the water absorption properties of the product. Moreover, production cost and glaze consumption is reduced; adhesion of fast firing glazes to the body can be maintained by angobe application (Ryan and Radford, 1987; Stefanov and Batschwarov, 1985).

In general, the floor and wall tile angobe compositions include such raw materials as clay, kaolin, quartz, feldspar, frit-type of semi-raw materials, oxides such as zirconium oxide, zinc oxide, aluminium oxide, and ceramic paints. The ratio of such ingredients in angobe composition may vary according to parameters such as body composition, firing temperature, firing duration, and glaze composition. However, a typical commercial floor and wall tile angobe recipe composition is comprised of 30-40% clay, 10-15% feldspar, 5-15% quartz, 5-10% zircon, and 10-20% frit. These ingredients are used in angobe recipes after removing the impurities and being comminuted to micron sizes (Kingery et al., 1973). Production stages of an angobe are summarized in Fig. 1.

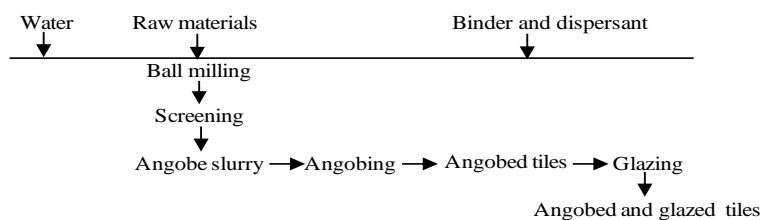


Fig. 1. Production stages for angobes

In this study, flotation method was employed to reduce sulphur content of alunitic kaolins obtained from the Balıkesir-Sındırgı region of Turkey, which is the largest kaolin deposit in the country, following mechanical scrubbing, classification, and grinding stages. Moreover, possible use of the kaolin concentrates whose sulphur content were reduced without heat treatment were investigated for angobe production which is a common practice in the ceramic tile industry.

Materials and methods

Materials

The alunitic kaolin used in the experiments was collected from the Balıkesir-Sındırgı region of Turkey, and the flotation method was applied to remove SO_3 from the kaolin. Preparation of the kaolins to be used in flotation tests were made by two different methods. In the first method, only the particle size of the kaolin was reduced, and then they were used in the flotation tests. The particle size of the kaolin was reduced to -2 mm by using jaw and roller type of crushers and then ground to -38 μm

using a ceramic ball mill of 2 L capacity. During grinding operations 3 different sized alubite balls were used as grinding media. Milling was carried out as wet at 50% solid concentration. In order to determine the optimum milling time, some milling tests were conducted at 60, 90, 120, 150, 180, 240 and 360 min. After milling, kaolin samples were dried and particle size analysis was made. After the tests, the optimum milling time for the kaolin was found to be 120 min. Consequently, raw kaolin samples were ground in the ball mill for 120 min and then passed through a 38 μm screen. The kaolin was then dewatered and dried at 100 °C before they were stockpiled for flotation tests. The kaolin samples prepared by this method were coded as NS.

In the second method, kaolin was subjected to mechanical scrubbing and screening operations (pre-concentration) and then used in the flotation tests. Before pre-concentration, the particle size of the kaolin was reduced to -2 mm using jaw and roller types of crushers. Afterwards, 500 g from this kaolin was taken to prepare a suspension at a solid/liquid ratio of 50% and then kept in water for 1 h. This was later mixed in a mechanical mixer at 1000 rpm for 30 min and screened through a 125 μm sieve. Under sieve was dewatered and dried then coded as S1. The over sieve was ground in a ball mill for 20 min and screened using a 125 μm sieve. The second under sieve was also dewatered and dried then coded as S2. The over sieve was ground in a ball mill for 20 min and screened using a 125 μm sieve again. The third under sieve was also dewatered and dried then coded as S3 (Fig. 2). The over sieve was removed as waste owing to the milling difficulties created by high quartz content. The S1, S2, and S3 kaolin samples obtained were used in the flotation tests.

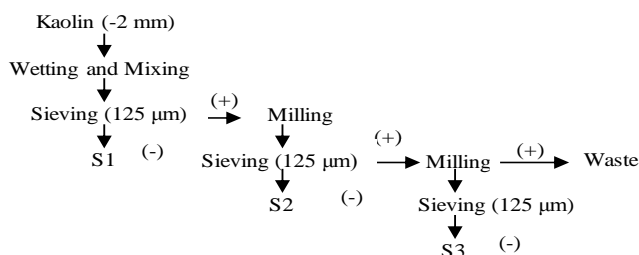


Fig. 2. Flow scheme for S1, S2 and S3 kaolin preparation

Chemical analysis of NS, S1, S2, and S3 kaolin samples was made using an XRF instrument (Rigaku-ZSX Primus II). Mineralogical analysis of the samples was made using an XRD instrument (Rigaku Miniflex ZD13113 series) using CuK α X-rays ($\lambda = 1.54056 \text{ \AA}$) in the range of 5-70° and at a rate of 2°/min. The variations in the colour of NS, S1, S2, and S3 kaolin samples were investigated using a Minolta colour measuring device. The micro structure of NS kaolin was investigated using a scanning electron microscope (ZEISS brand SUPRA 50 V model).

Methods

Preliminary tests were conducted to determine optimum flotation parameters such as the types and dosages of collector, frother and depressant, flotation time, pulp density, agitating rate, and pH. NS kaolin was used for these tests. The kaolin concentrates after these tests were coded as F1. S1, S2 and S3 kaolins were then floated at the optimum conditions, and the concentrates obtained were coded as F2, F3 and F4. DENVER type flotation cell of 1 L capacity was used for the flotation tests. In these tests, alunite was floated while kaolin was depressed using a depressant.

Angobe preparation

F4 kaolin whose SO_3 content was reduced after pre-concentration and flotation was used for angobe preparation. The properties of the angobes prepared by using F4 kaolin were compared to those of the angobes used by a ceramic factory in floor and wall tile production. The angobe recipes of the ceramic factory were taken as the reference and F4 kaolin was used in replace of quartz, kaolin, and aluminium oxides in the reference recipes. The composition of the angobe recipes prepared is summarized in Table 4, and the codes used in these tests were F, F1, W, and W1 for the reference floor tile angobe recipe, experimental floor tile angobe recipe, reference wall tile angobe recipe, and experimental wall tile angobe recipe, respectively.

Table 4. Floor and wall tile angobe compositions

| Raw materials | Amount (%) | | | |
|-------------------------|------------|------|------|------|
| | F | F1 | W | W1 |
| Kaolin | 23.0 | – | 12.0 | – |
| Quartz | 12.0 | – | 21.0 | 5.8 |
| Al_2O_3 | 4.0 | 0.8 | – | – |
| Others | 61.0 | 61.0 | 67.0 | 67.0 |
| F4 | – | 38.2 | – | 27.2 |

The raw materials used for the preparation of the angobes were first weighed according to the ratios given in Table 4, and then ground in a jet mill for 32 min. The milling process was carried out as wet at a solid ratio of 72%. The material was then passed through a 100 μm sieve before being applied onto the surface of wall (WM) and floor (FM) tiles of the factory by pouring method. The amount of angobe for each tile was determined as 20 g. The angobed tiles were dried at 105 °C for 2 h. The dried tiles were fired at 1195 °C for 33 min (floor tiles) and 1130 °C for 33 min (wall tiles) in a roller type of industrial kiln of the factory. The reference angobed floor tile was coded as FA, the experimental angobed floor tile was coded as FA1, reference angobed wall tile was coded as WA, and the experimental angobed wall tile was coded as WA1.

An industrial glazing process was also applied to the angobed wall and floor tiles produced. The firing process of the angobed+glazed tiles was kept similar to that of angobed tiles. The material used in glazing was similar to those normally used for the glazing of floor and wall tiles in the factory. The reference angobed+glazed floor tile was coded as FG, the experimental angobed+glazed floor tile was coded as FG1, reference angobed+glazed wall tile was coded as WA, and finally experimental angobed+glazed wall tile was coded as WG1.

In order to find out whether the expansion characteristics of the floor and wall tile angobes prepared would be suitable when applied to the floor and wall tiles bodies of the factory, the thermal expansion coefficients of the angobes and the bodies were also determined. Moreover, the thermal expansion coefficients of the glazes used were determined to find out the suitability to the angobes and the bodies. Thermal expansion analysis of the angobes, bodies, and glazes were made using a dilatometer (NETZSCH DIL 402 PC).

In order to determine the colour differences between the surfaces of angobed and angobed+glazed tiles, colour measurements were made using a Minolta brand colour measuring device. The micro-structure of the angobed and angobed+glazed surfaces was analysed using a JEOL JSM-5600 V brand scanning electron microscope (SEM).

Finally, permeability and Harcourt tests were conducted on the angobed+glazed tiles. While the factory's standard method was used for the permeability tests, the Turkish National Standard procedure, coded as TS EN ISO 10545-9 (1997), was used as a method of determining thermal shock resistance of the tiles (Harcourt tests).

Results and discussions

Chemical analysis of kaolin

Chemical analysis of NS and pre-concentrated S1, S2, S3 kaolin is given in Table 5. As seen from Table 5, the amount of SiO₂ increases from S1 to S3. In other words, some of the quartz within the ore was removed from the over sieve at each stage of sieving after the mechanical scrubbing operation (Fig. 2). This result was caused by the low grindability of the free quartz within the kaolin composition. As shown in Table 5, the amounts of SO₃ and K₂O coming from alunite and other oxides were reduced from S1 to S3. This result can be explained by the fact that most of the fine

Table 5. Chemical composition of the kaolins (w/w %)

| Samples | SiO ₂ | Al ₂ O ₃ | Fe ₂ O ₃ | TiO ₂ | SO ₃ | K ₂ O | L.O.I. |
|---------|------------------|--------------------------------|--------------------------------|------------------|-----------------|------------------|--------|
| NS | 55.24 | 25.58 | 1.08 | 0.38 | 4.05 | 1.08 | 11.88 |
| S1 | 43.44 | 31.37 | 2.58 | 0.52 | 6.08 | 1.72 | 16.50 |
| S2 | 56.19 | 25.87 | 0.65 | 0.35 | 4.34 | 1.10 | 12.21 |
| S3 | 59.73 | 23.00 | 0.38 | 0.33 | 2.44 | 0.86 | 8.37 |

grained kaolinite, alunite minerals, and the colouring oxides within the ore are obtained from the under sieve. This result was also supported by the semi-quantitative chemical analysis given in Table 6.

Table 6. Semi quantitative analysis of NS, S1, S2, S3 kaolins

| Samples | Kaolinite | Alunite | Quartz |
|---------|-----------|---------|--------|
| NS | 54.93 | 10.49 | 29.70 |
| S1 | 64.66 | 15.75 | 13.37 |
| S2 | 54.96 | 11.24 | 30.61 |
| S3 | 52.31 | 6.32 | 35.39 |

Mineralogy of kaolin samples

Mineralogical analysis of the kaolin samples (NS, S1, S2 and S3) is given in Fig. 3. When the XRD pattern of NS kaolin is examined (Fig. 3), it is seen that SO_3 and K_2O in the chemical composition originated from alunite mineral ($\text{KAl}_3(\text{SO}_4)_2(\text{OH})_6$). Alunite peak in S3 kaolin is much lower than those of NS, S1 and S2. This result proved that alunite was removed from the NS body by mechanical scrubbing-milling-sieving operations.

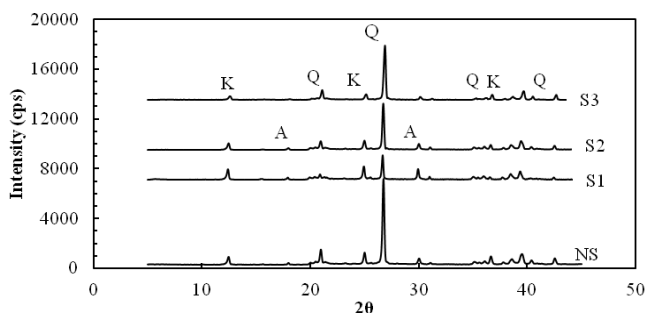


Fig. 3. XRD patterns of NS, S1, S2, S3 kaolins (K: kaolinite, A: alunite, Q: quartz)

Colour measurements of kaolin samples

Colour values (Lab) of the kaolin samples (NS, S1, S2 and S3) are presented in Table 7. As seen from Table 7, whiteness of the kaolin samples (L value) was increased from S1 to S3. This indicated that most of the colouring oxides (TiO_2 and Fe_2O_3) were

Table 7. Colour values of NS, S1, S2 and S3 kaolins

| Samples | L | a | b |
|---------|-------|------|-------|
| NS | 74.87 | 9.23 | 19.15 |
| S1 | 72.35 | 8.22 | 18.70 |
| S2 | 82.74 | 4.92 | 11.13 |
| S3 | 91.09 | 2.40 | 3.55 |

removed at each stage of milling and sieving during pre-concentration. This result was also supported by the decrease in positive “a” and “b” values (meaning a decrease in yellowish-reddish colours) from S1 to S3. This result is also in good correlation with the results given in Tables 5 and 6.

Lab colour plane (Fig. 4) was used for the interpretation of the colour values. L is a scale for brightness/darkness and it ranges from “100” for a perfect white to “0” for an absolute black. Red/green is designated by “a” and higher positive values of “a” denotes more red colouring. The higher negative value of “a”, means that there is greener colour in the environment. Yellow/blue is designated by “b”, positive values of “b” refer yellowish colour whereas negative “b” values define bluishness (Chandrasekhar and Ramaswamy, 2006).

Additionally, the micro structure of NS kaolin is given in Fig. 5. Rhombusal alunite minerals (5-10 μm in particle size) are seen in kaolinite and quartz minerals (Fig. 5).

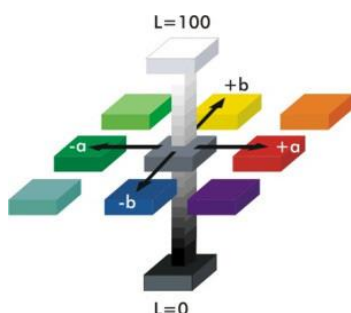


Fig. 4. CIE Lab colour plane (Ozcan, 2008)

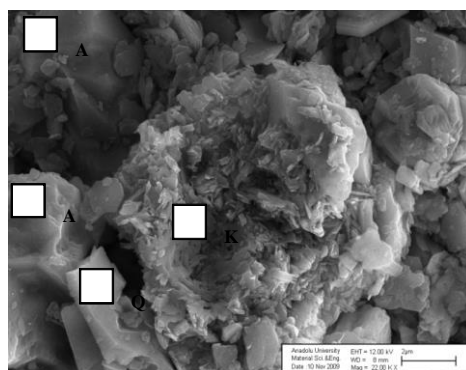


Fig. 5. SEM picture of the NS kaolin (K: kaolinite; A: alunite; Q: quartz)

Results

Flotation tests

The parameters used to determine optimum conditions for NS kaolin flotation are summarized in Table 8. The first experiment was carried out to determine the type and amount of collector and successive tests were performed using the previous optimum result.

Effect of dosage and type of collector

Four different types of anionic collectors were tested in order to determine the suitable collector type for the flotation of alunite which was sodium oleate, AERO 825, AERO 801 and AERO 845. The dose of 3000 g/Mg for each collector type were used in the

Table 8. Flotation test parameters

| Parameters | Values | Parameters | Values |
|--------------------|-------------------------------|------------------------------------|--------------|
| Particle size | -38 μm | Flotation time | 1-6 min |
| Type of collector | Na Oleate, AERO-825, 801, 845 | Conditioning time (for depressant) | 1 min |
| Collector dosage | 0.5-3.5 kg/Mg | Conditioning time (for collector) | 5 min |
| Type of frother | MIBC, pine oil | Pulp density (solid rate) | 5%-15% |
| Frother dosage | 0-120 g/Mg | Agitation rate | 900-1400 rpm |
| Type of depressant | Sodium silicate | pH | 4.5-9.5 |
| Depressant dosage | 0-700 g/Mg | | |

experiments and SO_3 grades in kaolin concentrates were measured. SO_3 grades were measured as 2.94%, 2.47%, 2.97%, and 2.10% when sodium oleate, AERO 825, AERO 801 and AERO 845 were used, respectively. Since the lowest SO_3 grade was obtained with AERO 845, it was chosen as the optimum collector type for NS kaolin flotation.

For the determination of optimum dosage, the flotation tests were carried out using 500, 1000, 1500, 2000, 2500, 3000, and 3500 g/Mg of AERO 845. The obtained SO_3 grades in the kaolin concentrates and the sulphur removal efficiencies were summarized in Fig. 6a. As the collector dosage increased, the sulphur removal efficiencies increased while the SO_3 grades in the kaolin concentrates were reduced up to a point (Fig. 6a). When the collector dosage exceeded 3000 g/Mg, the effect of collector quantity to the efficiency was reversed. In flotation, if an excessive amount of collector is used, particle surfaces may be covered by collectors as a multi-layer rather than a mono-layer. This phenomenon may reduce the hydrophobicity of the particles since the non-polar parts of the collector molecule cannot orient into the solution. Moreover, excessive collector usage increases the possibility of bubble collision in the froth and may cause the particles attached to the air bubbles to return to the pulp. Therefore, collectors must be used at optimum quantity and it is typically considered that excessive use of collectors reduces the efficiency of the flotation (Saklara et al., 1998).

As seen from Fig. 6a, the increase of SO_3 grades in the kaolin when more than 3000 g/Mg of collector was used was thought to be caused by the return of particles attached to the air bubbles to the pulp. As a matter of fact the size of the air bubbles was noticed to be considerably enlarged when more than 3000 g/Mg of collector was used. After the weighing of the concentrates and wastes of each experiments, it was also realized that this opinion was supported by the increase in the amount of kaolin (sunken part) when more than 3000 g/Mg of collector was used (Tatar, 2012). Therefore, 3 kg/Mg of collector was chosen as the optimum value since it provided the minimum sulphur grade in the kaolin concentrate and the highest sulphur removal

efficiency. At first glance, the amount of collector chosen can be considered to be rather high, however, this result was inevitable considering the very high specific surface area of the fine grained materials used (Mathur, 2002; Cilek, 2006).

Effect of dosage and type of frother

In order to determine the optimum frothing agent, the most common types of frothers such as pine oil and MIBC (methyl isobutyl carbinol) were used for the experiments. These frothers were used as 60 g/ton and the SO₃ grades in the kaolin concentrates were measured. After these tests, the SO₃ grades in the kaolin concentrates were determined as 2.77% and 1.77% when pine oil and MIBC were used, respectively. The bubbles were noticed to be fewer, smaller, and easily broken down when pine oil was used whereas the bubbles were larger and more durable when MIBC was chosen. Therefore, MIBC was selected as the frother owing to its better froth formation and the lower SO₃ grades in the kaolin concentrates obtained.

The flotation experiments were carried out using 0, 20, 40, 60, 80, 100, and 120 g/Mg of MIBC in order to find out the optimum dosage of the frothing agent. The obtained SO₃ grades in the kaolin concentrates and the sulphur removal efficiencies were summarized in Fig. 6b. As seen from Fig. 6b, the SO₃ grades in the kaolin concentrates were reduced as the frother dosage increased, that is to say, more alunite mineral were removed together with the froth occurred. This result is in good correlation with the literature. As a matter of fact, frothing agents create a homogeneous bubble size distribution and durable froth layer in a flotation system. These functions work better and a more durable and homogeneous froth occurs with the increase in the amount of frothing agent up to an optimum point. Hence, particle transfer from the pulp to froth phase becomes easier and the possibility of particle returning from the froth phase to the pulp decreases. In lower frother usage, the froth layer is easily broken down, obtaining mineral particles from the froth becomes more difficult and particles may tend to return to the pulp (Saklara et al., 1998). The grade and efficiency values did not change considerably when the amount of frothing agent used was more than 100 g/Mg. Therefore, it was selected as the optimum amount of frothing agent since it produced the lowest sulphur grade and the highest sulphur removal efficiency.

Effect of dosage and type of depressant

Sodium silicate is known as a good dispersant together with its depressant effect. It increases surface charge between the particles in the solution. Hence, the fine grained slam layer is easily dispersed and a clear mineral surface to react with collector is obtained (Wills and Napier, 2006). For these reasons, sodium silicate was chosen as a depressant in the tests. In order to find out the optimum depressant dosage, the experiments were carried out using 0, 100, 300, 500, and 700 g/Mg of sodium silicate. After the tests, the obtained SO₃ grades in the kaolin concentrates and the sulphur removal efficiencies were summarized in Fig. 6c. As seen from Fig. 6c, the SO₃ grades in the kaolin concentrates were decreased as the depressant dosage increased

up to 300 g/Mg. The effect was, however, reversed as the depressant dosage increased to more than 300 g/Mg. This can be explained by the fact that mineral particles to be floated are depressed as the amount of depressant used is increased above an optimum value. This result was proven in the tests in which more than 300 g/Mg of depressant were used by the increase in the weight of sunken part (kaolin) and by the decrease in the weight of floated part (alunite) (Tatar, 2012). As a result, 300 g/Mg was selected as the optimum depressant dosage to be used since it provided the minimum SO₃ grade in the kaolin concentrate and the highest sulphur removal efficiency in the waste.

Effect of flotation time

In order to determine optimum flotation time, several flotation tests were carried out for 1, 2, 3, 4, 5, and 6 min. The SO₃ grades in the kaolin concentrates were reduced as the flotation time was increased which is expected in a flotation process. Therefore, 5 min was chosen as the optimum flotation time since no further improvement was obtained at longer periods.

Effect of pulp density

Various pulp densities such as 5%, 10% and 15% were prepared to determine the optimum value. After the tests, the obtained SO₃ grades in the kaolin concentrates and the sulphur removal efficiencies were summarized in Fig. 6d. As seen from Fig. 6d, SO₃ grades in the kaolin concentrates were only slightly increased as the pulp density was increased. This result can be considered to be normal since the distribution of the air flow in the cell owing to the changes in the pulp density is changed and free bubble surfaces are decreased. Therefore in general, efficiency of the separation decreases with the increase in the pulp density (Saklara et al., 1998).

Consequently, 5% was chosen as the optimum pulp density for the flotation tests since the SO₃ grade in the kaolin concentrate was the minimum although there was no noticeable change in the sulphur removal efficiency. A pulp density of 5% should not be considered as too low in a flotation process of finely grained minerals (Mathur, 2002).

Effect of agitation rate

To determine the optimum agitation rate for the flotation tests, 900, 1000, 1100, 1200, 1300, and 1400 rpm were tested. After the tests on the prepared pulps, the obtained SO₃ grades in the kaolin concentrates and the sulphur removal efficiencies were summarized in Fig. 6e. As seen from Fig. 6e, the SO₃ grades in the kaolin concentrates were decreased as the agitation rate increased up to 1200 rpm. This result is considered to be normal since increasing the agitation rate up to an optimum point increases the efficiency of the separation by increasing particle-bubble contact and the probability of collision within the flotation cell. Increasing the agitation rate also promotes the dispersing effects onto the fine grains. Hence, interaction between the

clean particle surfaces and the chemical reagents is increased and removal of the particles by air bubbles can be performed easily (Cilek, 2006).

Again from Fig. 6f, the SO_3 grades in the kaolin concentrates were seen to be increased after agitation rates of over 1200 rpm. This was thought to have occurred by the break off the aggregates (particles attaching the air bubbles) from the bubbles as a result of turbulence caused by the high agitation rates. Consequently, 1200 rpm was selected as the optimum agitation rate since the SO_3 grade in the kaolin concentrate was the minimum and the sulphur removal efficiency was the maximum.

Effect of pH

The tests were carried out in order to determine the optimum pH values for the flotation tests using pulp pH values of 4.5, 5.5, 6.5, 7.5, 8.5 and 9.5. After the tests with these pH values, the obtained SO_3 grades in the kaolin concentrates and the sulphur removal efficiencies were summarized in Fig. 6f which reveals that the SO_3 grades in the kaolin concentrates increased together with the increase in pH values.

As is well known, mineral behaviours such as dispersion, aggregation and flotation depend on surface charges. From the studies in which the surface charges of the minerals (kaolinite, alunite and quartz) within the kaolin ore used with respect to pH were investigated and it was found that the zero point of charge (zpc) for alunite were determined at pH 7.2 (Koca, 1992; Dixit, 1980) and pH 10.3 (Kosmulski, 2009). However, Ustaer (1975) could not determine the zpc value for alunite in his research. According to Ustaer's findings, the surface charge of alunite remains positive at all pH values. On the other hand, the zpc for kaolinite were mostly determined at between pH 2 and pH 4.5 (Kosmulski, 2009; Dikmen et al., 2011). From the findings of these studies, it was understood that the zpc for kaolinite became negative after these pH values. Quartz was also reported to have similar surface charges with kaolinite (Kosmulski, 2009). As a summary, while there was not much difference in the zpc values of quartz and kaolinite, it was found to be considerably diverse for alunite which was thought to be caused by the differences in their origins. Moreover, the adsorption of anionic collectors onto the alunite surfaces was negatively increased depending on the collector concentration and pH (Koca 1992). As a matter of fact, the highest alunite flotation recovery was obtained at slightly acidic-alkali pH values (pH 5-9) from the pH based flotation experiments (Miller and Misra, 1985; Miller and Acherman, 1980; Dixit 1980).

In this research, sulphur removal efficiencies obtained according to pH variation did not exhibit considerable differences and reasonably high efficiency values were achieved (Fig. 6f). The SO_3 grades within the kaolin were slightly increased. The reason for that can be explained by the fact that alunite approached its zero point of charge and hence the adsorption of anionic reactive (AERO 845) was decreased on the surfaces of alunite. Therefore, it was decided to use pH 8.5 (natural pH value) as the optimum pH value in the flotation tests. Consequently, the corrosion within the

flotation cell and the pipes was kept to a minimum and acid use was not needed to arrange pH, by choosing an alkali media at pH 8.5 (Pearse, 2005).

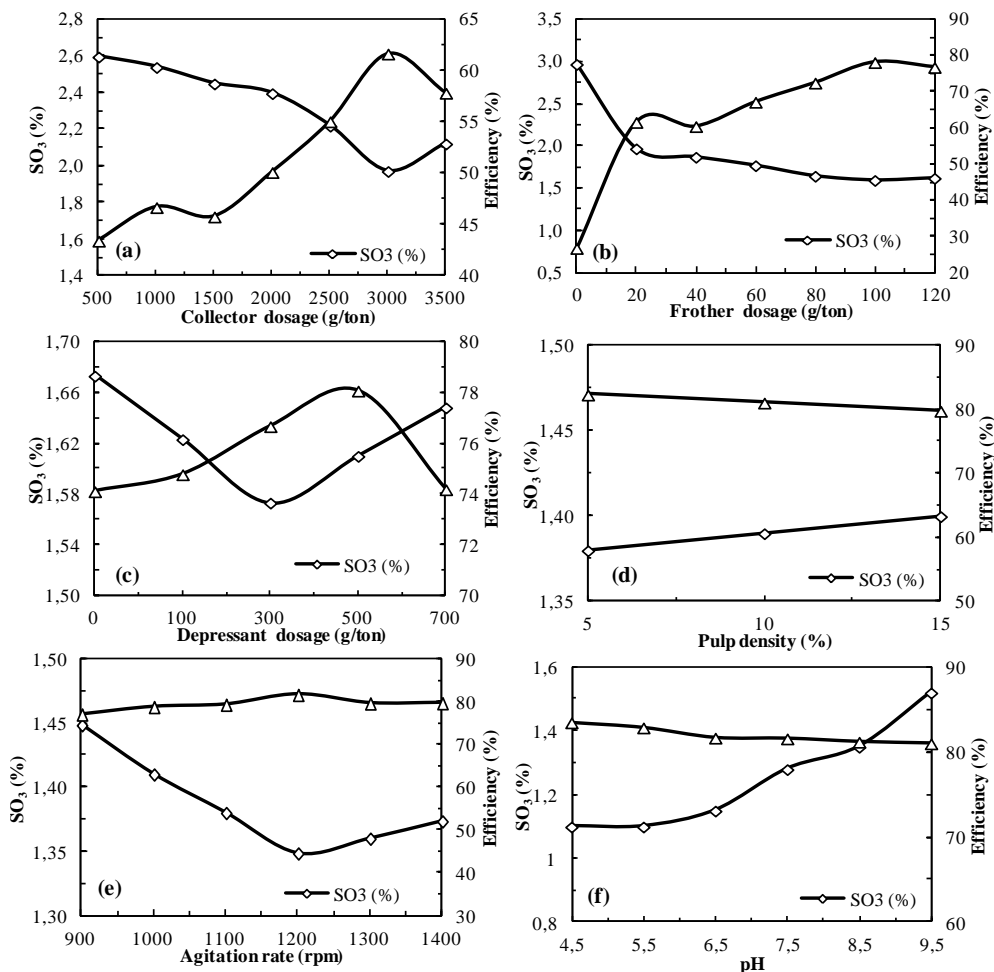


Fig. 6. Effect of (a) collector dosage (b) frother dosage (c) depressant dosage (d) pulp density (e) agitation rate (f) pH on flotation

Summary of the flotation test results

The optimum parameters selected for the flotation of alunitic kaolin (NS) are given in Table 9. In order to determine the effect of pre-concentration to the flotation of alunitic kaolin (NS), flotation tests were applied to the pre-concentrated kaolins (S1, S2, S3) under the same conditions. The obtained SO₃ grades in the kaolin concentrates and the sulphur removal efficiencies are summarized in Table 10.

Table 9. Optimum flotation parameters for NS kaolin

| Parameters | Values |
|-------------------|--------------------------|
| Collector dosage | 3000 g/Mg AERO 845 |
| Frother dosage | 100 g/Mg MIBC |
| Depressant dosage | 300 g/Mg sodium silicate |
| Flotation time | 5 min |
| Pulp density | 5% |
| Agitation rate | 1200 rpm |
| pH | 8.5 |

Table 10. Flotation test results for NS, S1, S2, S3 kaolins

| Kaolin samples | SO ₃ in the feed | SO ₃ in the kaolin concentrate | SO ₃ removal efficiency |
|----------------|-----------------------------|---|------------------------------------|
| | (%) | (%) | (%) |
| NS | 4.05 | 1.35 (F1) | 81.22 |
| S1 | 6.08 | 2.33 (F2) | 79.09 |
| S2 | 4.34 | 1.33 (F3) | 80.28 |
| S3 | 2.44 | 0.48 (F4) | 88.55 |

As seen from Table 10, the SO₃ grade in the concentrate of S3 kaolin after flotation was found to be as low as 0.48%. Since this kaolin concentrate (F4) could be used in ceramic industry, the following tests were done to prove its use in wall and floor tile angobe production.

Angobe production

Thermal expansion

One of the most important task of the angobes is to eliminate the thermal expansion disconformity between the glaze and the body. Otherwise, flaws grow within the glaze and chipping could occur. Thermal coefficients of the angobes prepared by F4 kaolin (F1, W1), tile bodies of the factory (FM, WM), the angobes of the factory (F, W), and the glazes of the factory (GF, GW) at 400 °C were measured. The results are given in Table 11.

Table 11. Thermal expansion coefficient of the angobes, bodies and the glazes

| Thermal expansion coefficient ($\alpha(1/K).10^{-6}$) | FM | F | F1 | GF | WM | W | W1 | GW |
|---|------|------|------|------|------|------|------|------|
| | 6.80 | 5.64 | 6.30 | 6.40 | 6.90 | 6.92 | 7.16 | 5.90 |

As a general rule, thermal expansion coefficient of a glaze must be concordant to that of a body. As seen from Table 11, the thermal expansion coefficient of the floor tile angobe of the factory (F) was much lower than that of the body (FM). On the other hand, the thermal expansion coefficient of the floor tile angobe (F1) prepared by using F4 kaolin was higher than that of the angobe called F. Therefore, thermal expansions

of the angobe, glaze, and the body will be in more harmony if F1 angobe is used. Again it is seen from Table 11 that the thermal expansion coefficient of the wall tile angobe (W) of the factory is almost similar to that of the body (WM). The thermal expansion coefficient of the wall tile angobe (W1) prepared by using F4 kaolin is slightly higher than that of the W angobe. In order to find out the conformity between the body, glaze and the angobe, Harcourt and Autoclave tests were carried out on the angobed+glazed wall tiles. The Harcourt and Autoclave tests were applied to both floor and wall tiles, and there were no chipping observed on the surface of the tiles tested. Permeability tests were also conducted on these tiles, and they proved to be impervious to water. In other words, the tiles tested did not emit the water absorbed by the body to the surface. This ensures that the decorative finish will remain stable during the use of the tiles.

Colour

Another important feature of angobes is to cover the surface colour and roughness at the desired colour and density. Generally, the surfaces of the wall and floor tiles are desired to be as white as possible. Therefore, L values of the angobed and angobed+glazed tiles were measured in order to determine the effect of the angobes prepared by F4 kaolin onto the surface whiteness of the bodies. The results are summarized in Table 12.

Table 12. Whiteness of the angobed and angobed+glazed wall and floor tile surfaces

| L | FA | FA1 | FG | FG1 | WA | WA1 | WG | WG1 |
|-------|-------|-------|-------|-------|-------|-------|-------|-------|
| Value | 82.94 | 82.01 | 86.54 | 87.97 | 91.75 | 91.25 | 90.10 | 89.71 |

As seen from Table 12, the whiteness value of the FA1 surface is slightly lower than that of the FA surface. It means that the coating ability of the F1 angobe is slightly lower than that of the F angobe. This situation can easily be seen from Figs. 7 (a) and (b) where the FA1 surface has a more porous texture than the FA surface. On the other hand, the whiteness value of the FG1 surface is higher than those of both FA and FG which indicates that the coating ability of the F1 angobe increased after glazing. This is corrected by the similar SEM pictures of FG and FG1 surfaces given in Figs. 7 (c) and (d). Consequently, it is clearly seen from these results that the F1 angobe could be used as an alternative for the F angobe of the factory for floor tiles.

For wall tiles, the whiteness of the WA1 surface is almost similar to that of the WA surface (Table 12). The micro-structure of the tiles in Figs. 8 (a) and (b) are seem to be similar as well. Similarly, the micro-structure and the whiteness of the glazed surface of these tiles (WG and WG1) are quite identical as seen in Figs. 8 (c) and (d). Therefore, the W1 wall tile angobe can easily be used as an alternative for the W angobe of the factory.

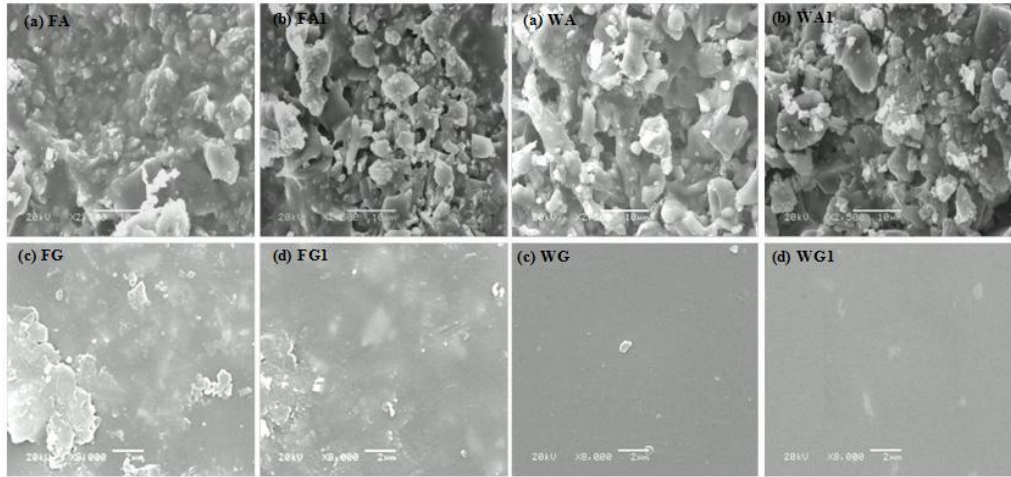


Fig. 7. SEM pictures for the angobed and the angobed+glazed floor tiles

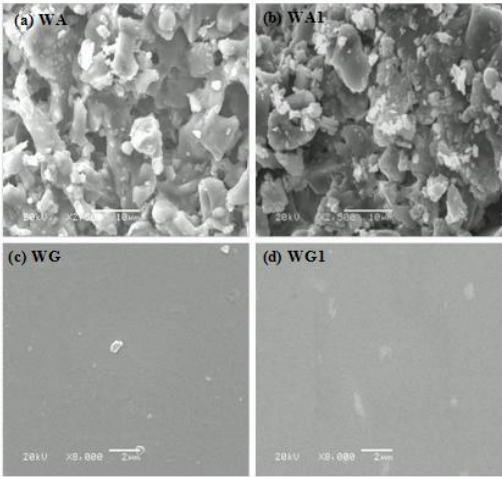


Fig. 8. SEM pictures for the angobed and the angobed+glazed wall tiles

Conclusions

In this research, the prepared floor tile angobe (F1) and wall tile angobe (W1) were used as alternatives for floor and wall tile angobes of a ceramic factory, respectively. These angobes were prepared by using F4 kaolin which was obtained by the flotation of pre-concentrated kaolin samples. The main results of the research are as follows.

- It was found that the Balıkesir-Sındırgı kaolins contained 4.05% SO_3 within the composition and were comprised of mineral kaolinite, alunite, and quartz.
- Most of the alunite and colouring impurities within the composition of the Balıkesir-Sındırgı kaolins were removed by using pre-concentration techniques such as wetting and mechanical scrubbing. After the pre-concentration process, the whiteness of the kaolin was considerably increased.
- After flotation of kaolin with 4.05% SO_3 content, the kaolin concentrate (F1) was obtained with a SO_3 grade of 1.35% and a sulphur removal efficiency of 81.22%.
- The kaolin concentrate (F4) was obtained with a SO_3 grade of 0.48% and a sulphur removal efficiency of 88.55% from the tests carried out to determine the effect of pre-concentration onto the flotation of Balıkesir-Sındırgı kaolin.
- From the tests conducted to determine possible use of F4 kaolin concentrate in ceramic industry, it was understood that the floor and wall tile angobes prepared by F4 kaolin could be used as alternatives for floor and wall tile angobes of a ceramic factory.
- Finally, the SO_3 content of the Balıkesir-Sındırgı kaolins were reduced to an acceptable level ($<0.5\%$) without using heat treatment which was the main obstacle for them to use in ceramic industry. This will make this material

extremely attractive for ceramic factories using angobes in their floor and wall tile productions.

References

- BERGAYA, F., THENG, B.K.G. and LAGALY, G. (Eds.), 2006, *Handbook of Clay Science*, Elsevier, Amsterdam.
- CALDERON, G.D.T., RODRIGUEZ, J.I., ORTIZ-MENDEZ, U. and TORRES-MARTINEZ, L.M., 2005, *Iron Leaching of a Mexican Clay of Industrial Interest by Oxalic Acid*, Journal of Materials Online, 1, 1-8.
- CASTELLANO, M., TURTURRO, A., RIANI, P., MONTANARI, T., FINOCCHIO, E., RAMIS, G. and BUSCA, G., 2010, *Bulk and Surface Properties of Commercial Kaolins*, Applied Clay Science, 48, 446-454.
- CHANDRASEKHAR, S. and RAMASWAMY, S., 2006, *Iron Minerals and Their Influence on the Optical Properties of two Indian Kaolins*, Applied Clay Science, 33, 269-277.
- CILEK, E.C., 2006, *Mineral Flotation*, Publication of Suleyman Demirel University, No: 59, Isparta-Turkey. (In Turkish)
- DIKMEN, S., ERSOY, B., AKPINAR, S., BIRCAN, H. and ORHUN, O., 2011, *Electrokinetic Properties of the Kaolins Belonging to Eskisehir-Mihallicik*, Afyon Kocatepe University, Journal of Science, Vol. 11, 9-18. (In Turkish)
- DIXIT, S.G., 1980, *Flotation Chemistry of Alunite/Oleate System*, Society of Mining Engineers of AIME, No: 80-111, 30.
- EKMEKCI, Z., GULSOY, O., ERSAYIN, S. and BAYRAKTAR, I., 2001, *Desulphurisation of Ivrandi Alunitic Kaolin*, Bulletin of Earth Sciences Application and Research Centre of Hacettepe University, 23, 53-60.
- GENC, S., 1994, *Removal of Sulphate and Production of Ceramic Raw Materials from Alunitic Kaolins*, Ph.D. Thesis, Eskisehir Osmangazi University. (In Turkish).
- GIRGIN, I., EKMEKCI, Z. and ERKAL, F., 1993, *Beneficiation of Sindirgi alunitic kaolins*, in : *Turkish XVth Mining Congress*, 549-560. (In Turkish)
- HE, Q., HUANG, X. and CHEN, Z., 2011, *Influence of Organic Acids, Complexing Agents and Heavy Metals on the Bioleaching of Iron from Kaolin Using Fe (III) - Reducing Bacteria*, Applied Clay Science, 51, 478-483.
- KINGERY, W.D., BOWEN, H.K. and UHLMANN D.R., 1973, *Introduction to Ceramics*, Journal of Materials Science, 793.
- KOCA, S., 1992, *The Effect of Reactive Adsorption Mechanism of Kaolin and Alunite to the Determination of Flotation Reagents*, Ph.D. Thesis, Anadolu University. (In Turkish).
- KOSMULSKI, M., 2009, *Surface Charging and Points of Zero Charge*, Surfactant Science, Taylor and Francis Group, 145, 1064.
- MATHUR, S., 2002, *Kaolin Flotation*, Journal of Colloid and Interface Science, 256, 153-158.
- MILLER, J.D. and ACHERMAN, J.B., 1980, *Bench scale flotation of alunite ore with oleic acid*, in : *Processing of the International Symposium on Fine Particles Processing*, Las Vegas, Nevada, February 24-28 Volume 1.
- MILLER, J.D. and MISRA, M., 1985, "The hydrophobic character of semi-soluble salt minerals with oleate as collector," in : *Proceedings of the Recent Advances in Mineral Science and Technology*, MINTEK 50.
- MURRAY, H.H., 2007, *Applied Clay Mineralogy, Occurrences, Processing and Application of Kaolins, Bentonites, Palygorskite-Sepiolite, and Common Clays*, 33-39, 85-108.

- NEWNS, A. and PASCOE, R.D., 2002, *Influence of Path length and Slurry Velocity on the Removal of Iron from Kaolin Using a High Gradient Magnetic Separator*, Minerals Engineering, 15, 465-467.
- OZCAN, A., 2008, *The Effect of Paper Surface Roughness to the L^*a^*b Values*, Journal of Engineering and Science, Istanbul Ticaret University, Year: 7, No:14, 53-61. (In Turkish).
- PEARSE, M.J., 2005, *An Overview of the Use of Chemical Reagents in Mineral Processing*, Minerals Engineering, 139-149.
- RAGHAVAN, P., CHANDRASEKHAR, S., VOGT, V. and GOCK E., 2004, *Separation of Titaniferrous Impurities from Kaolin by High Shear Pre-treatment and Froth Flotation*, Applied Clay Science, 25, 111-120.
- RAVISHANKAR, S.A., PRADIP and KHOSLA, N.K., 1995, *Selective Flocculation of Iron Oxide from its Synthetic Mixtures with Clays: A Comparison of Polyacrylic Acid and Starch Polymers*, Int. J. Miner. Processing, 43, 235-247.
- RYAN, W., and RADFORD, C., 1987, *White-ware Production, Testing and Quality Control, Including Materials, Body Formulations and Manufacturing Processes*, Pergamon Press, U.S.A., 298.
- SAKLARA, S., ERSAYIN, S., BAYRAKTAR, I., 1998, *Flotation Models*, Journal of Mining, Society of Mining Engineers in Turkey, Vol. 37, No: 2. (In Turkish).
- STEFANOV, S. and BATSCHWAROV, S., 1985, *Ceramic Glazes*, Germany.
- SUMER, G., 1991, *Beneficiation of alunitic kaolins*, in : Vth National Clay Symposium, Eskisehir-Turkey, 349-362. (In Turkish).
- TATAR, I., 2012, *Determination of Usage Areas of the Products Obtained from Alunitic Kaolins by Means of Different Enrichment Approaches*, Ph.D. Thesis, Dumlupinar University. (In Turkish).
- TS EN ISO 10545-9, December 1997, *Ceramic Tiles-Determination of Thermal Shock Resistance*, Turkish National Standard Institute. (In Turkish).
- USTAER, C. and GURGEY, I., 1975, *The Separation of Alunite in Alunitic Kaolin*, Clays and Clay Minerals, Pergamon Press, Vol. 23, 468-472.
- WILLS, B.A. and NAPIER MUM, T.J., 2006, *Froth Flotation: Wills' Mineral Processing Technology*, ISBN 978 0 7506 4450-1, Elsevier, USA..
- YAPA, N. and ATAK, S., 1994, *Beneficiation of north-west Anatolian alunitic kaolins by flotation*, in : 2nd National Ceramic Congress of Turkey, Vol. 1, 108-115. (in Turkish).

Received June 4, 2014; reviewed; accepted August 4, 2014

MAGNESIUM HYDROXIDE RECOVERY FROM MAGNESIA WASTE BY CALCINATIONS AND HYDRATION PROCESSES

Haldun KURAMA*, H. Levent HOSGUN**

* Eskisehir Osmangazi University, Mining Engineering Department, Eskisehir-Turkey, (hkurama@ogu.edu.tr)

** Bursa Technical University, Chemical Engineering Department, Bursa-Turkey

Abstract: In this study, hydration behavior of the magnesia waste, supplied from the electrostatic bag house of the sintering unit of MAS Company, Eskisehir-Turkey was studied to find out re-usability of the material as a source of magnesium hydroxide ($Mg(OH)_2$) production. According to chemical and crystalline phase analyses, MgO content of the sample was determined as 49.9 wt% and consists of mainly raw magnesite ($MgCO_3$), sintered magnesia-periclase (MgO) and small amount of serpentine (lizardite) phases. In hydration process, the reactivity of magnesium oxide determines the rate and extent of hydration of the sample. Therefore, the waste samples both calcined and uncalcined forms were hydrated in water and the efficiencies were compared according to sample source. The hydration experiments were carried out at temperatures ranging from 30 °C and 80 °C to evaluate the influence of temperature on particle morphology and surface areas of the products. The efficiency of the hydration was evaluated by using thermogravimetric (TG) and scanning electron microscopy (SEM) analyses. The test results suggest that the magnesia waste could be used as a source material for production of magnesium hydroxide.

Key words: *magnesium hydroxide, hydration, magnesia waste, characterization*

Introduction

Magnesium hydroxide is an important compound that finds application in various industries such as additives in pulp-paper production, pharmaceutical products and flame retardant in polymeric materials (Rothon, 2000; Dong et al., 2010). The use of catalyst, catalysts support, sorbent for chemical and destructive adsorption of various pollutants, adsorbent or pH regulator for wastewater treatment (Gulkova et al., 2004; Climent et al., 2007; Gao et al., 2008) and a source material for the production of magnesium oxide, metal or chemicals are also common application areas (Shand et al., 2006; Aphane et al., 2007). In recent years, the advances in imaging, engineering and

manipulating system at the nanometer scale have led to numerous research studies dealing with synthesis of $\text{Mg}(\text{OH})_2$ nanoparticles or nanosurfaces. For example, the utilization of superfine $\text{Mg}(\text{OH})_2$ as a smoking and toxic-free flame retardant filler in plastic, rubber, and other halogen-free polymeric materials has attracted much attention due to the improved properties such as a good thermal stability, good fire retardant and low toxicity (Li et al., 2014). Recent studies performed by Dong et al. (2010 and 2011) showed that nano-sized $\text{Mg}(\text{OH})_2$ can be an antibacterial agent. Pan et al. (2013) also reported that the nano-sized $\text{Mg}(\text{OH})_2$ is adsorbed on bacterial surface by charge attraction first, and then destroys the integrity of cell walls resulting in death of bacteria.

In literature, many methods were proposed to produce nano-sized $\text{Mg}(\text{OH})_2$. However, the wet precipitation was proved to be the most simple and a low-cost way to synthesize $\text{Mg}(\text{OH})_2$ crystals (Fernandez et al., 2014). $\text{Mg}(\text{OH})_2$ with different morphologies such as rods, tubes, needles, and lamina have been synthesized by hydrothermal reaction using different magnesium sources such as magnesium powder, MgSO_4 , and $\text{Mg}(\text{NO}_3)_2 \cdot 6\text{H}_2\text{O}$. In the study performed by Beall et al. (2013), magnesium chloride, magnesium acetate and metallic magnesium have been used as the magnesium source. The synthesis results showed that production of pure hydromagnesite, utilizing hydrothermal methods, is much simpler and faster. The effect of type and concentration of modifiers on the physicochemical and functional properties of magnesium hydroxide obtained by precipitation, and its calcinate magnesium oxide, was studied by Pilarska et al. (2013). In this study, magnesium hydroxide obtained from magnesium sulfate and sodium hydroxide was subjected to thermal decomposition at 450 °C. The modifiers were non-ionic compounds representing poly(ethylene glycols) including PEG 200, 8000, and 20000. It was found that the modifier introduced into the reaction system had a direct influence on the morphological and dispersive properties of the products as well as their surface character and high surface area. Qiang et al. (2014) also reported that hexagonal $\text{Mg}(\text{OH})_2$ nanoflakes were successfully synthesized in the presence of polyethylene glycol 20,000 (PEG-20,000) surfactant. Recently Fernandez et al. (2014) released a paper in which $\text{Mg}(\text{OH})_2$ nano-flakes, with different morphologies, were synthesized via the hydrothermal method. It was found that synthesis temperature and reaction time have a strong influence on the product morphology, particle size, agglomeration level and crystallographic structures. It was also suggested that the prolongation of reaction time improves the crystalline degree of magnesium hydroxide particles. Besides than the particle morphology, the agglomeration behavior of the nano-sized particles within the polymer matrix was also defined as an important parameter that determines the usability of the synthesized product. An exemplary modification applied to reduce water absorption of magnesium hydroxide precipitate with addition of octadecyl dihydrogen phosphate as a surface modifier was proposed by Dongmin et al. (2009). Song et al. (2010) reported that hydrophobic magnesium hydroxide nanoparticles can be synthesized by the simultaneously addition of reactant solutions

into an organic phase instead of an aqueous phase. Later, Pilarska et al. (2011) proposed that the PEGs can be used to modify the surface properties of $\text{Mg}(\text{OH})_2$.

The natural form of magnesium hydroxide (brucite) deposits are scarce and often contaminated by fibrous minerals. Therefore, it is mainly produced by the hydration of magnesia (MgO) obtained either from a heat treatment of mineral magnesite, precipitation from seawater or magnesium containing brines. The use of seawater as starting material is more costly because of the huge amount of water required and has some difficulties in the crystallization stages. Therefore, it preferentially produce by calcinations of MgCO_3 for decomposition to MgO , and than, it is subsequently hydrated in water to convert MgO to $\text{Mg}(\text{OH})_2$ (Thorp and Gilpin, 1949). Due to a wide spectrum of application areas as discussed above, the hydration mechanism of $\text{Mg}(\text{OH})_2$ obtained from magnesia has been received an interest by several researchers in literature. In general, it was found that calcination temperature and treatment time prior the hydration, surface area, particle size of starting material, slurry density, hydration temperature and the hydration time were the main parameters that can influence the hydration performance and product properties. The term of hydration can be referred as a formation of a hydrated compound from the reaction of water with a solid compound. Therefore, most of studies were carried out with water. The earlier study performed by Maryska and Blaha (1997) showed that the hydration rate of MgO , obtained from the calcination of magnesium hydroxide carbonate, is strongly affected by both calcination and hydration temperatures. The effect of calcination temperature on the surface area, activity of MgO and response of these parameters to MgO hydration was studied by Birchal et al. (2000). It was reported that calcination temperature is the main variable affecting the surface area and reactivity of MgO , where both parameters increase with increasing temperature up to 900 °C. Later, Rocha et al. (2004) reported that the hydration performance of high purity magnesia increases with increasing of hydration temperature. Strydom et al. (2005), also studied the effect of calcining temperature on the hydration of industrially obtained MgO . It was found that degree of hydration is influenced significantly by temperature and contact time. Recently, Pilarska et al. (2014) showed that the higher reactivity and better hydration performance of the calcined sample could be caused by microstructural changes.

Although much attention has paid to produce low cost material for large scale applications, current synthetic version of magnesium hydroxide still tent to be costly. Furthermore, the waste material produced from metallurgical and mining activities has been taken into consideration not only by the governments related with the stringent environmental legislations but also by the producers to maintain the sustainable and cost efficient production. The recent studies performed by Fernandez et al. (2009) and Formosa et al. (2011) showed that low-grade magnesium hydroxide, an industrial by-product obtained in the calcination of magnesia, can be used as cheap filler in polymeric materials. Turkey has about 160 teragrams of the world reserve of 3 600 teragrams. Raw, calcined, dead burned and fused form of magnesite are the main

products of Turkey. In 2012, Turkey ranked second in magnesite exports in the world with a share rate of 32%. MAS magnesite company (located in Eskisehir) one of the biggest sintered magnesia producers of Turkey. The company processes yearly 150 gigagrams of sintered product. With a help of recently installed rotary furnace, the company is planning to increase the processing capacity near 250 gigagrams in 2014. The sintered magnesia produced by crushing, screening, drying, classification, magnetic separation and sintering at horizontal rotary furnace. By this route, every year, approx. 20 Gg of waste material is collected in the furnace electrofilters and the amount of waste stock has been progressively increased year by year due to the lower recycling rate of it. Therefore, the objective of the study is to determine the recyclability of magnesia waste as a cost effective relatively pure magnesium hydroxide for filler applications.

Methodology

Material

The waste sample (EFD) used in the experiments was supplied from the electrostatic bag house of MAS Company, Eskisehir-Turkey. The chemical composition of representative sample (determined by XRF analyses) indicated that SiO_2 and CaO are the main impurities together with little amount of Fe_2O_3 and Al_2O_3 . The magnesium oxide content of the sample was determined as 49.70 wt%. However, MgO to MgCO_3 ratio (0.185), determined by the carbon content of the sample (LECO furnace analysis), showed that unreacted MgCO_3 still is the main mineral component.

Table 1. Chemical analysis results of magnesite dust sample

| Oxide % | EFD | Oxide % | EFD |
|-------------------------|------|--------------|-------|
| SiO_2 | 4.45 | CaO | 2.79 |
| Fe_2O_3 | 1.04 | MgO | 49.70 |
| Al_2O_3 | 0.06 | LOI* | 41.94 |

*LOI, loss of ignition

The detected by XRD analyses mineral phases are given in Fig. 1. These results confirmed that the chemical analyses date and it was found that the sample mainly consisted of raw (MgCO_3) and sintered magnesite (periclase) and small amounts of serpentine (lizardite) phases. Particle sizes distribution of the sample was determined by wet screening. It was found that the D_{80} value's of sample was about 0.130 μm .

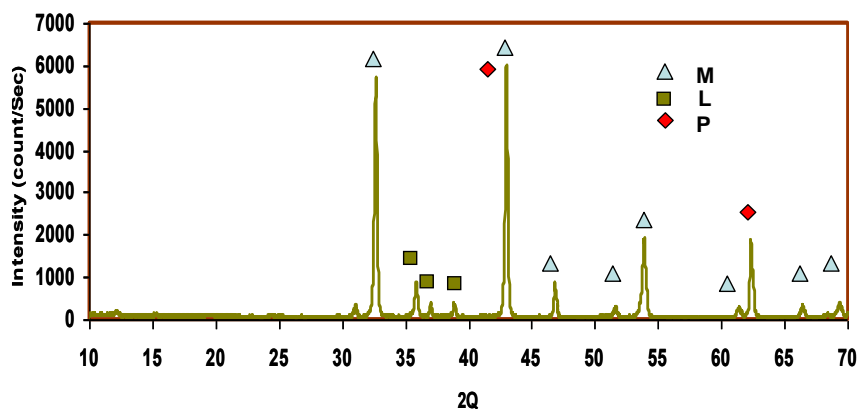


Fig. 1. XRD diffraction pattern of EFD; M: magnesite, L: lizardite, P: periclase

Methods

The hydration experiments were performed in a closed 250 cm³ glass beaker. In order to determine the effect temperature variation on hydration reaction, the beaker was immersed in water containing another glass beaker placed on a temperature-controlled magnetic stirrer. In each test 10 g of sample as calcined or received form, was added in to the 250 cm³ glass beaker containing 100 cm³ of aqueous solution.

The temperature of the aqueous solution was previously adjusted to predetermined value (40 °C, 60 °C and 80 °C) and kept constant during the hydration. The hydration temperatures selected in this study were determined based on the previous studies (Van der Merwe, 2006; Fillippou, 1999; Aphane, 2007; Pilarska, 2012). In hydration tests, the slurry was continuously stirred at a constant rate of 250 rpm for two hours and pH variations of the solution was recorded according to time intervals. The products were then filtered under vacuum, dried in an oven at 100 °C for two hours and weighted. The concentration of dissolved Ca and Mg ions in solution after hydration were analyzed by the complexometric method. The TG analyses of the samples were carried out with a NETZSCH STA 409 PC/PC instrument. A heating rate of 10 K min⁻¹ in a nitrogen atmosphere from 30 to 1000 °C was applied. The percentage of Mg(OH)₂ in the products was obtained from the curves of mass loss as described earlier by (Aphane, 2007). A NOVA 1000e surface analyzer with nitrogen gas as an adsorbent was used to determine the BET surface areas of the products. The samples were degassing at 240 °C during 16 hours. Scanning electron microscope (SEM) analysis of samples was investigated by using a high vacuum electron microscope ZEISS SUPRA VP 50. In order to prevent the charging, samples were firstly coated with sputter coater using Au-Pd target. The e-beam used for analysis was 20 keV and working distance was 12.7 mm. At these working conditions 5000- and 30000-fold magnified images were taken at the secondary electron image mode (SEI).

Table 2. The test design employed for studying the effect of individual parameters on the hydration processes

| Sample code | Temperature (°C) | |
|-------------|------------------|----------------------------|
| N1-40R | 40 | Received form |
| N2-60R | 60 | Received form |
| N3-80R | 80 | Received form |
| N4-40C | 40 | Calcined at 900 °C for 2 h |
| N5-60C | 60 | Calcined at 900 °C for 2 h |
| N6-80C | 80 | Calcined at 900 °C for 2 h |

Results and discussion

pH variation of hydration solution and product weight

The variations of solution pHs during hydration processes are given in Fig. 2. Although relatively higher values were measured for calcined samples, in general, a similar trend was observed for all samples subjected to hydration processes. The pH's of the solutions slightly decreases with increasing treatment time up to two hours, and then, remains almost constant for further progressing contact times. It was also observed that the increase of the solution temperature leads to a decrease of the solution pH's for both calcined and un-calcined samples.

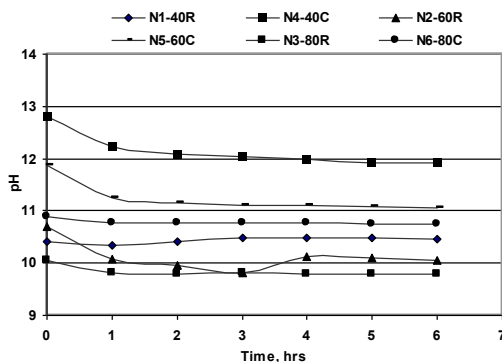
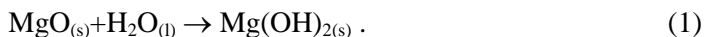


Fig. 2. pH variation of solution during the hydration process

The hydration reaction of MgO to Mg(OH)₂ can be given as following chemical equation:



According to the stoichiometric calculation, it can be expected that weight of the product should be higher than that of the starting material proportionally to the

hydration efficiency. The higher weights measured for the calcined samples and given in Fig. 3 clearly indicated the importance of calcinations step prior the hydration process. The material used in this study is a by-product of the sintering processing of MgCO_3 and may expected to react with water for hydration. However, the results showed that effective conversion of to $\text{Mg}(\text{OH})_2$ requires calcination steps prior to hydration in water. As discussed earlier, the received sample consists of mainly raw magnesite, little amounts of sintered magnesia and impurities. The lower weights measured for the un-calcined samples indicated limited reactivity of the starting material for hydration in water. For hydration of the calcined sample, it was observed, that the weight of the products increases with increasing solution temperatures. However, these are limited and can be concluded that increase in solution temperature has a slight affect on hydration processes within the studied temperature range.

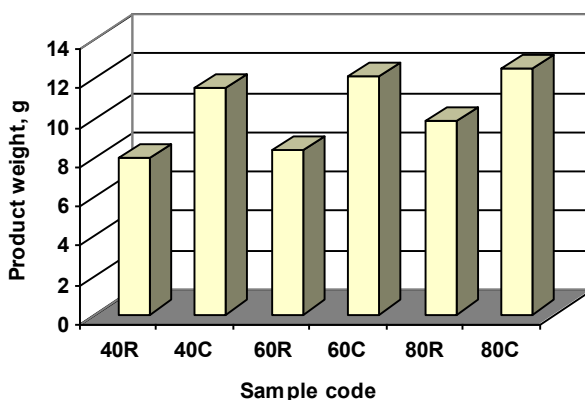


Fig. 3. Effect of sample source and hydration temperature on product weight

Thermogravimetric analyses

The TG curves of the hydrated samples both received and calcined forms according to employed hydration temperatures are given in Fig. 4a and 4b, respectively. For uncalcined samples (Figure 4a), a number of weight loss steps up to a temperature of 600 °C was observed. These steps can be ascribed to moisture loss (between 50 and 200 °C), $\text{Mg}(\text{OH})_2$ decomposition (after 200 °C to 450 °C) and MgCO_3 decomposition (450 °C to 600 °C). The TG curves of calcined samples completely match the characteristic $\text{MgO} - \text{Mg}(\text{OH})_2$ transformation mass loss-temperature curve between 200 °C and 450 °C. Although the mass losses are lower than the theoretical value obtained for pure MgO (30.9%), they are confirmed by the formation of $\text{Mg}(\text{OH})_2$ after hydration processes as previously reported by several researchers (Aphane, 2007).

The similarity of the decomposition curves and slight increase of mass losses with increasing solution temperatures showed that hydration reactions were affected by the solution temperature. It was found that the mass losses increase from 19.05 to 19.78%

with increasing solution temperature from 40 °C to 80 °C. However, the relatively lower mass losses analyses of the calcined sample and the effect of temperature contribution to the hydration reactions compared with the previous reports, can be attributed the lower particle size of the waste material, presence of some impurities in the starting material and lower solubility tendency of water as hydrating agent. Van der Merwe and Strydom, (2006) studied the effect of hydration temperature on the percentage of $\text{Mg}(\text{OH})_2$ by using different hydrating agents and reported that the increase on hydration temperature enhances the performance of the process for all hydrating agent. However, the hydration performed in water was the least temperature dependent. Hydration performed in magnesium acetate was found more intensive than any of the other hydrating agents. Although the product obtained from the hydration of MgO in magnesium acetate solutions contains also some unreacted magnesium acetate, Aphane (2007) also released a similar report later, and proposed that the magnesium acetate was a better hydrating agent than water. These reports concluded that the solubility of the various compounds plays an important role in the mechanism of the process, and that the rate of hydration is controlled by the rate of the chemical reactions taking place at the MgO particle surface.

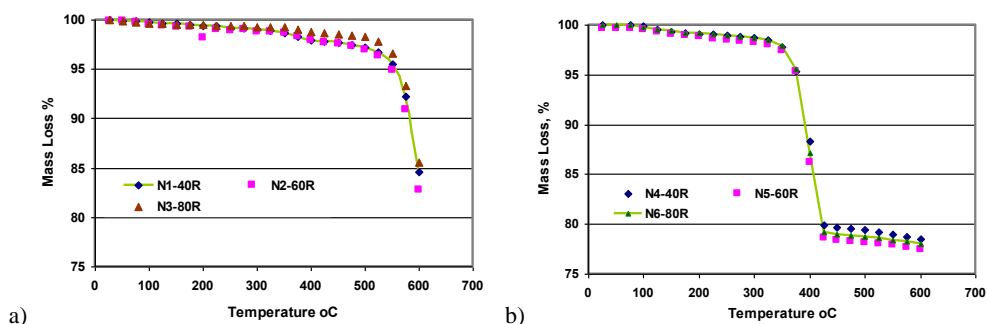


Fig. 4. TG results of samples: uncalcined (a) and calcined (b)

Due to relatively complexity of the hydration of MgO in water, the rate of the hydration process is receiving more interest and concern as a key parameter for the hydration reaction occurring on the solid surface and also its important effect on the final product morphology. In an early study, Kitamura et al. (1969) proposed that a modified version of the chemical shrinking core model could be used for describing the reaction kinetic. This model has been found adequate to fit kinetic data at high temperatures (between 135 °C and 200 °C), but could not fit kinetic data for hydration in water at lower temperatures. Birchall et al. (2001) developed an alternative, semi-empirical model, that also assumes chemical control of the reaction with no diffusive contribution. This model assumes an increasing resistance to the hydration process caused by the filling of the porosity inside and between the MgO particles with the $\text{Mg}(\text{OH})_2$ product. Later Rocha et al. (2004) reported that two distinct hydration

processes may occur depending on the temperature. At high temperatures, the hydration of magnesia seems to be initially governed by the oxide dissolution (chemical control). As the reaction progresses, both surface and pores of magnesia particles are covered progressively by the hydroxide produced, changing the porosity of the solid. As a result, the diffusion of water is hindered inside particles, thus reducing the overall reaction rate (diffusive control). At low temperatures, the hydration is purely chemical-controlled. These studies clearly indicated beneficial effect of temperature contribution to the chemical reaction. In a recent study, Thomas et al. (2014) suggested an interesting approach and reported that variation with temperature more than one mechanism is controlling the hydration rate in the temperature range. They applied an alternative model known as the boundary nucleation and growth (BNG) model that has previously been applied to the hydration of Portland cement and tricalcium silicate. Although, the analyses results showed that the hydration kinetics of both light and hard-burned MgO can be fit using a BNG model, the experiment performed with using light-burned MgO was found to be an almost ideal BNG system within the temperature range from 20 °C to 50 °C. The calorimetric analyses results for the light-burned MgO between 20 °C to 50 °C showed that the hydration reaction is affected by temperature variation. The values of G (the linear rate of growth of a product region in any direction) at 30 °C and 50 °C are not too different for these two powders. This indicates that it is primarily the higher surface area of the light-burned powder that leads to the much faster hydration at a given temperature. Greater surface area results in more nucleation, and thus more regions of hydration product growing at the same time. Beside the calcinations affect, the particle size of the solid material that is subjected to hydration also determines the reaction rate. The smaller particle size supports the dissolution of material and subsequent nucleation of Mg(OH)₂ on MgO. Higher surface resulting from lower particles size would lead to a faster reaction.

Surface area

Figure 5 shows the variation of the surface area of Mg(OH)₂ formed by hydration of the samples, both in received and calcined forms, at elevated solution temperatures. It was found that variation of BET values follows a similar trend with thermogravimetric analysis results, as discussed above. According to the applied hydration temperature, the surface areas of the hydrated products increased from 5.04 m²/g to 6.34 m²/g for uncalcined samples. On the other hand, for calcined samples, considerably higher values were determined. The surface areas of the products increase from 18.32 m²/g to 19.20 m²/g by increasing temperature from 40 °C to 80 °C, respectively. The higher surfaces areas measured for calcined samples can be attributed to higher conversion rates compared to un-calcined samples due to lower surface area. The surface areas of the samples were determined as 3.36 m²/g and 39.15 m²/g for un-calcined and calcined samples, respectively. As discuses previously (Birchal et al., 2000; Rocha et al., 2004; Strýdom et al., 2005; Aphone, 2007), calcination temperature is the main variable that

affects the surface area and reactivity of MgO during hydration process. The results show that by hydrating MgO calcined material between 650 and 1000 °C, about the same percentage of Mg(OH)₂ was obtained, whereas at higher calcination temperatures (1200 °C or more) the percentage of magnesium hydroxide decreases considerably. In the first stage of the hydration the oxide dissolution occurs within particles, changing porosity within this stage leads to creation of supersaturation, nucleation and growth of Mg(OH)₂ at the surface or internal boundaries of MgO particles.

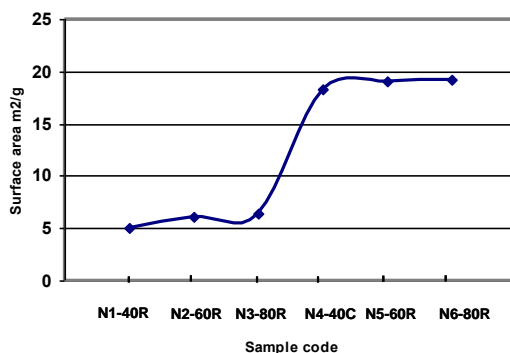


Fig. 5. Surface area variation of samples according to sample source (calcined and un-calcined) and hydration temperature

Product morphology

In general, the crystalline Mg(OH)₂ belongs to the hexagonal system and is characterized by platelet-like crystals arrangement. However, it may also adopt several morphologies and sizes which offer to them advantageous for industrial applications. The morphologies of selected samples, analyzed by SEM, are given in Fig. 6.

The observed cryptocrystalline form of magnesite crystals for the sample N1-40R, suggested that the sample still conserves the previous form. This indicates that the inefficiency of the hydration processes on the waste sample as received form (Fig. 6a and b). On the other hand, the calcined samples have a spherical morphology and consist of aggregated irregular and tiny crystals, which reflect the characteristic crystallographic structure of brucite. The morphology of these aggregates results from rapid rates of precipitation rate under high supersaturating conditions. As previously reported by Rocha et al. (2004), during hydration of MgO in water, the supersaturation is reached rapidly in a few minutes. If the hydration is performed at low temperatures, the higher initial supersaturation level leads to formation of a significant amount of fine magnesium hydroxide particles with the high nucleation rate. Water

diffuses rapidly into MgO particles and Mg(OH)₂ precipitates inside the whole magnesia particle, so higher conversion levels are obtained at short periods of time. In contrast, with increasing hydration temperatures the morphology of the product is changed and result in a slightly more compact particles as observed in Fig. 6e.

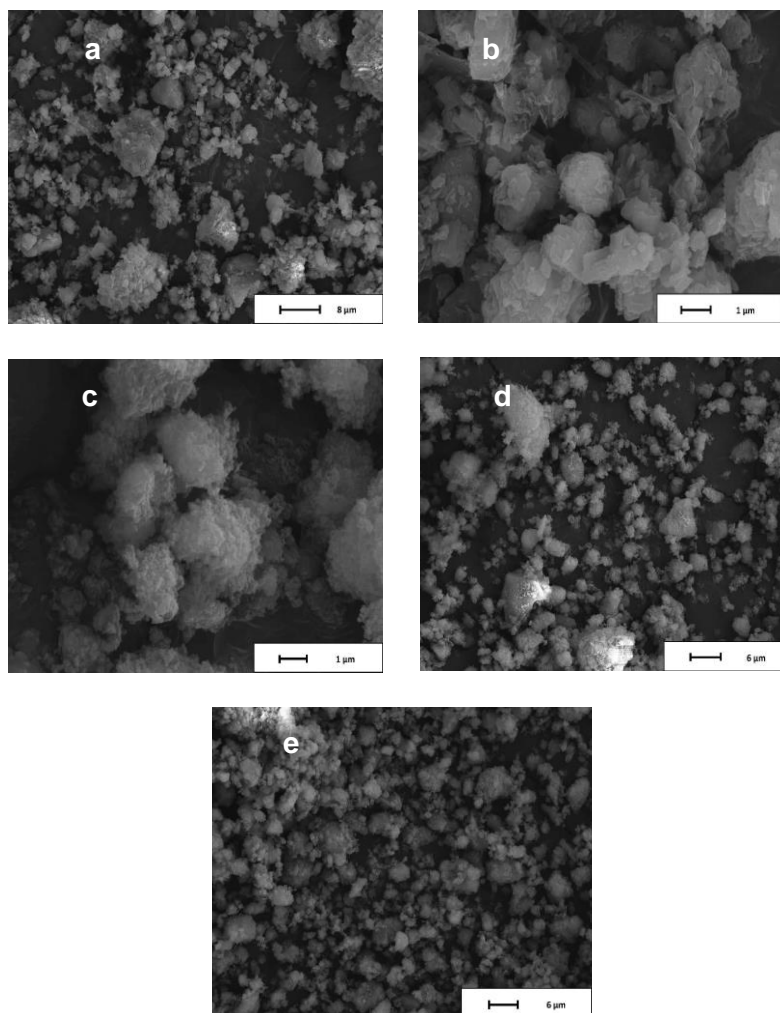


Fig. 6. SEM images of hydrated N1-40R, N5-60C and N6-80C

Conclusion

In this study, the recyclability of magnesia waste as a relatively pure magnesium hydroxide was investigated. According to hydration tests result it can be concluded

that effective conversion of them to $\text{Mg}(\text{OH})_2$ requires calcination steps prior the hydration in water. The increase of hydration temperature has a positive effect on the hydration efficiency and grain texture. However, it was found that this effect was not significant. The mass losses increase from 19.05 to 19.78% with increasing solution temperatures from 40 °C to 80 °C, respectively. This can be attributed a higher activity of the calcined samples. Higher surface area of the powder leads to much faster hydration at lower temperatures. On the other hand, as observed from SEM images, the increase of hydration temperature caused a slightly more dense coverage of the surface and internal boundaries with the nuclei of hydrated products. The results suggested that the hydrated product could be considered as filler material for plastic industry. However, the polarity and stability of the additives in plastic mixtures are important parameters, therefore, further studies should also be performed on the electrokinetic properties of the hydrated product.

References

- APHANE M.E., 2007, *The hydration of magnesium oxide with different reactivities by water and magnesium acetate*. M.Sc. Thesis, University of South Africa
- BEALL G.W., DURAIA M.E., TANTAWY F., AL-HAZMI, F., AL-GHAMDI A.A., 2013, *Rapid fabrication of nanostructured magnesium hydroxide and hydromagnesite via microwave assisted technique*, Powder Technol., 234, 26-31.
- BIRCHAL V.S., ROCHA S.D.F., CIMINELLI, V.S.T., 2000, *The effect of magnesite calcination conditions on magnesia hydration*, Minerals Engineering, 13, 1629-1633
- BIRCHAL V.S., ROCHA S.D.F., MANSUR M.B., CIMINELLI V.S.T., 2001, *A simplified mechanistic analysis of magnesia hydration*, Can. J. Chem. Eng., 79, 507-511.
- CLIMENT W.J., CORMA A., IBORRA S., MIFSUD M., 2007, *MgO nanoparticle-based multifunctional catalysts in the cascade reaction allows the green synthesis of anti-inflammatory agents*, J. Catal., 247, 223-230.
- DONG C., CAIRNEY J., SUN Q., MADDAN O.L., HE G., DENG Y., 2010, *Investigation of $\text{Mg}(\text{OH})_2$ nanoparticles as an antibacterial agent*, J. Nanopart. Res., 12, 2101-2109.
- DONG C.X., SONG D., CAIRNEY J., MADDAN O.L., HE G., DENG Y., 2011, *Antibacterial study of $\text{Mg}(\text{OH})_2$ nanoplatelets*, Mater. Res. Bull., 46, 576-582.
- FERNÁNDEZ A.I., HAURIE, L., FORMOSA, J., CHIMENOS, J.M., ANTUNES, M., VELASCO, J.I., 2009, *Characterization of poly(ethylene-co-vinyl acetate) (EVA) filled with low grade magnesium hydroxide*, Polym. Degrad. Stabil., 94, 57-60.
- FERNANDEZ A. S., GOMEZ-VÍLLALBA, L.S., MILOSEVIĆ O., FORTA R., RABANAL M.E., 2014, *Synthesis and morpho-structural characterization of nanostructured magnesium hydroxide obtained by a hydrothermal method*, Ceramics International, 40, 12285-12292.
- FILIPPOU D., KATIFORIS, N., PAPASSIOPI, N., ADAM, K., 1999, *On the of magnesia hydration in magnesium acetate solutions*, J. Chem. Technol. Biotechnol., 74, 322-328.
- FORMOSA J., CHIMENOS J.M., LACASTA A.M., HAURIE L., 2011, *Thermal study of low-grade magnesium hydroxide used as fire retardant and in passive fire protection*, Thermochimica Acta, 515, 43-50.
- GAO C., ZHANG W., LI H., LANG L., AND XU Z., 2008, *Controllable Fabrication of Mesoporous MgO with Various Morphologies and Their Absorption Performance for Toxic Pollutants in Water*, Crystal Growth Design, 8, 3785-3790.

- GULKOVA D., SOLCOVA O., ZDRAZIL M., 2004, *Preparation of MgO catalytic support in shaped mesoporous high surface area form*, Microp. Mesop. Mater., 76, 137-149.
- HENRIST C., MATHIEU J.-P., VOGELS C., RULMONT A., CLOOTS R., 2003, *Morphological study of magnesium hydroxide nanoparticles precipitated in dilute aqueous solution*, Journal of Crystal Growth, 249, 321-330.
- KĪTAMURA A., ONĪZUKA O., AND TANAKA K., 1969, *Hydration characteristics of magnesia*, Taikabutsu Overseas, 16, 3-11.
- LI X., SHI T., CHANG P., HU H., XIE J., LIU Y., 2014, *Preparation of magnesium hydroxide flame retardant from light calcined powder by ammonia circulation method*, Powder Technol., 260, 98-104.
- MARYŠKA M. & BLÁHA, J., 1997, *Hydration kinetics of magnesium oxide, part 3 - hydration rate of MgO in terms of temperature and time of its firing*, Ceramics -Silikaty, 41, 121-123.
- PAN X., WANG Y., CHEN Z., PAN D., CHENG Y., LIU Z., LIN Z., GUAN X., 2013, *Investigation of antibacterial activity and related mechanism of a series of nano-Mg(OH)₂*, ACS Appl. Mater. Interfaces, 5, 1137-1142.
- PILARSKA A. WYSOKOWSKI M., MARKIEWICZ E., JESIONOWSKI T., 2013, *Synthesis of magnesium hydroxide and its calcinates by a precipitation method with the use of magnesium sulfate and poly(ethylene glycols)*, Powder Technology, 235, 148-157.
- PILARSKA A., LINDA I., WYSOKOWSKI M., PAUKSZTA D., JESIONOWSKI T., 2012, *Synthesis of Mg(OH)₂ from magnesium salts and NH₄OH by direct functionalisation with poly(ethylene glycols)*, Physicochem. Probl. Miner. Process. 48(2), 631-643.
- QIANG W., CHUNHONG L., MĪNG G., LĪNGNA S., CHANGWEN H., 2014, *Hydrothermal synthesis of hexagonal magnesium hydroxide nanoflakes*, Mater. Res. Bull., 51, 35-39.
- ROCHA S. DF, MANSUR M. B. AND CIMINELLI V. ST., 2004, *Kinetics and mechanistic analysis of caustic magnesia hydration*, J. Chem. Technol. Biot., 79, 816-821
- SHAND M.A., 2006, *The chemistry and technology of magnesia*, A John Wiley & Sons, Inc. Publication, New Jersey US.
- STRYDOM C. A. VAN DER MERWE E.M & APHANE, M. E., 2005, *The effect of calcining conditions on the rehydration of dead burnt magnesium oxide using magnesium acetate as a hydrating agent*, J. Therm. Anal. Cal., 80, (3), 659-662.
- THOMAS J. J., MUSSO S., PRESTĪNĪ I., 2014, *Kinetics and activation energy of magnesium oxide hydration*, J. Am. Ceram. Soc., 97, 275-282.
- THORP H.W., GILPIN, WC., 1949, *Chemical engineering problems in the sea water magnesia process*, Proceedings of the society of chemical industry, Society of Chemical Industry, London , UK, 31, 46-48.
- VAN DER MERWE E. M. & STRYDOM C. A., 2006, *Hydration of medium reactive magnesium oxide using hydration agents*, Journal of Thermal Analysis and Calorimetry, 84, 467-471.
- YU J. C., XU, A., ZHANG, L., SONG R., WU, L., 2004, *Synthesis and Characterization of Porous Magnesium Hydroxide and Oxide Nanoplates*, J. Phys. Chem. B, 108, 64-74.

Received June 13, 2014; reviewed; accepted August 18, 2014

COPPER DEPOSITION ON STAINLESS STEEL SHEETS IN COPPER NITRATE SOLUTION

Antti KEKKI, Jari AROMAA, Olof FORSEN

Aalto University, School of Chemical Technology, Department of Materials Science and Technology, P.O. Box 16200, FI-00076 Aalto, Espoo Finland, antti.kekki@aalto.fi

Abstract: The aim of this study was to examine factors that influence copper nitrate based electrorefining of copper and to search the best process parameters for high-purity copper deposition on AISI 316L steel blanks. Considering impurities, the most important goal was to minimize sulfur content in a copper cathode. The effect of Cu^{2+} concentration, current density, temperature and pH were studied. The best parameters for the best copper purity were sorted out. The most important factors for quality copper deposition are sufficiently low Cu^{2+} concentration, low current density, right zone and careful control of pH. Active nitrate ion reduction reactions catalyzed by copper ions are suggested to affect detrimentally both copper deposition current efficiency and purity. Furthermore, nitrate ion reactions seem to elevate an electrolyte pH so that the deposition appears to be dark brown copper oxide. The 6N purity for copper was not reached with this cell construction and it fell behind about 7 ppm (99.9993% Cu). Both, sulfur and silver concentration were slightly above 1 - 2 ppm. To minimize the impurities, electrolyte circulation and filtration are needed. Also, either a separate silver cementation cell or cementation membrane is needed.

Keywords: *copper nitrate, electrorefining, high purity copper, hydrometallurgy*

Introduction

Development of copper based applications in the 21st century requires demanding properties from copper, especially in electronics, semiconductor and superconductor industries (Kim et al., 2007; Moreau et al., 2007; Ojebuoboh and Michels, 2004). For example, it is suggested that control of a copper microstructure in interconnects is an important issue for better conductivity performance of devices (Carreau et al., 2007). Furthermore, the purer the copper, the lower the resistivity and the lower annealing temperature can be used for copper (Kato, 1991; Kato, 1995). Pure copper also has less impurities that precipitate in the grain boundaries from which electrons readily scatter and cause an increase in resistivity (Carreau et al., 2007; Feng et al., 2008). Low resistivity also means better energy performance in traditional conductivity

applications. In electrorefining of copper, this requires new techniques and new means to reduce the impurity level in the cathode. Traditionally, in copper sulfate electrolyte, sulfur is one of the main impurity element in cathode, so that over 5.5N-6N purity (over 99.9995 % Cu) cannot be reached. The normal composition of cathode copper from sulfuric acid electrolyte is better than 4N, ~99.998 % Cu. A copper nitrate bath has no sulfur in the electrolyte and nitrogen has lower affinity towards copper than sulfur (Bruning et al., 1985). To minimize sulfur and silver content, the copper nitrate bath has been studied in the past 25 years. Copper nitrate electrolyte has been tested from the copper nitrate solutions regenerated from etching (Kim and Choi, 2003) and has been described in different patents with different cell constructions and circulation, cementation and filtration processes (Masaki and Masaharu, 2005; Ogata et al., 1989; Shindo and Takemoto, 2005). Additionally, a refining and float-zone melting method has been tried out (Bruning et al., 1985). Target purity for copper in these studies is usually set to 6N but measurement and definition of allowed impurity and non-impurity elements and amounts in copper vary with different authors (Kato, 1995; Takahashi and Kano, 2002; Ojebuoboh and Michels, 2004). In some of the studies silver, for example, is not included as the impurity.

In this paper we investigate the best parameters for copper deposition on 316L steel blanks from the copper nitrate bath to obtain high purity copper of 5.5N - 6N quality. We study the effect of Cu^{2+} concentration, current density, temperature and pH on copper purity.

Materials and methods

A copper nitrate electrolyte solution was made out of >98% copper nitrate pentahemihydrate salt $\text{Cu}(\text{NO}_3)_2 \cdot 2.5 \text{H}_2\text{O}$ (Sigma – Aldrich, 12837), distilled water and nitric acid (Jt – Baker 65 %). A large 140 mm x 100 mm x 5 mm copper anode was made out of copper that had already been refined once in traditional copper sulfate electrorefining. The purity of this anode was 99.998 wt. % Cu (Boliden Harjavalta Oy). Cathode steel blanks were made out of AISI 316L steel and set into a teflon mask, where only one side of the steel plate with area of 62 mm x 49 mm was in contact with the electrolyte. Both, the anode and cathode were polished with 1200 grade sandpaper and rinsed with distilled water before experiments.

The experimental setup

A 3 dm³ electrorefining cell was made out of inert glass and cleaned with nitric acid and distilled water before the experiments. Cathode to anode distance was 50 mm in all tests. This glass cell was immersed in the water bath with temperature control system. For the cell, a cover lid was made with holes for anode, cathode, pH electrode and thermometer (Fig. 1). A regulated power supply Lab 522 Finn Metric Oy and current meter Hewlett Packard 34401A were used in the experiments. The pH-electrode was manufactured by Mettler Toledo (SevenEasy pH). Cathodic polarization

experiments for copper nitrate electrolyte were done in a standard three-electrode cell with the Luggin capillary connected to a saturated Ag/AgCl reference electrode.



Fig. 1. Left: stainless steel blank in teflon mask. Right: cell cover lid attached with two steel blank cathodes

Electrorefining and cathode analysis

After mixing the copper nitrate salt with distilled water and concentrated nitric acid was added (3 cm^3) in 3 dm^3 of electrolyte to adjust the pH level to 1.3 – 1.6 (Mockrin and Hobin, 1977; Bruning et al., 1985; Kim and Choi, 2003). Just before the experiments the anode and cathode were activated with 1200 sandpaper and cleaned with distilled water and dried. Both, the anode and cathode were immediately connected to the power supply and the experiment was started and lasted for 96 hours. The constant current mode was used. During electrorefining pH alteration, the cell voltage and temperature were measured. After the experiment the copper plate was detached from the steel blank under running distilled water to avoid oxidation, and cleaned in an ultrasonic bath. The cathode elements were analyzed with an ICP mass spectrometry. Copper purity was calculated as 100 % minus the impurities analyzed.

Copper and nitrate reactions

Nitrate ion (NO_3^-) reduction reactions have higher standard electrode potential than the copper reduction reaction (Bruning et al., 1985; Shriver and Atkins, 1999). This makes it possible that nitrate ions reduce at the same time with copper(II) ion. This indicates that the current efficiency for copper deposition might suffer. The equilibrium potential is defined by the Nernst equation:

$$E = E^0 - \frac{RT}{zF} \ln(k). \quad (1)$$

Nitrate ion reduction to weak nitrous acid can be written as



For this reaction we obtain a new equilibrium potential E^0 . If NO_3^- activity is one and temperature 25 °C, then

$$\begin{aligned} E^0 &= 0.94 - \frac{RT}{zF} \ln \left(\frac{[\text{HNO}_2]}{[\text{H}^+]^3 [\text{NO}_3^-]} \right) = 0.94 - \frac{0.059}{2} (\log(1) - 3\log[\text{H}^+]) \\ &= (0.94 - 0.09\text{pH})V \end{aligned} \quad (3)$$

Equation 3 shows that if pH is low, the potential for the nitrate ion reduction reaction is higher. Consequently, if the activity coefficient and concentration of nitrate ion is high, the potential is also higher. This suggests that nitrate ion reduction reactions occur before or at the same time with the copper reduction reaction at the cathode:



If the electrolyte pH value increases too high due to the reaction (2) (hydrogen consumption), copper will deposit as porous copper oxide CuO or Cu_2O on the cathode (Fig. 2) Additionally, copper ions are known to have a catalytic effect on nitrate ion reduction reactions, which is again detrimental for the copper refining process (Ohmori et al., 1998; Bouzek et al., 1999; Epron et al., 2003; Filimonov and Shcherbakov, 2004; Kyriacou and Polatides, 2005; Polatides et al., 2005; Vazquez-Arenas et al., 2007). According to Filimonov and Shcherbakov (2004), nitrate ions can also be reduced chemically:



The exact kinetics of the nitrate reduction reactions are still less known and studied but some suggestions for the mechanism have been presented in different acid media (Vazquez-Arenas et al., 2007).

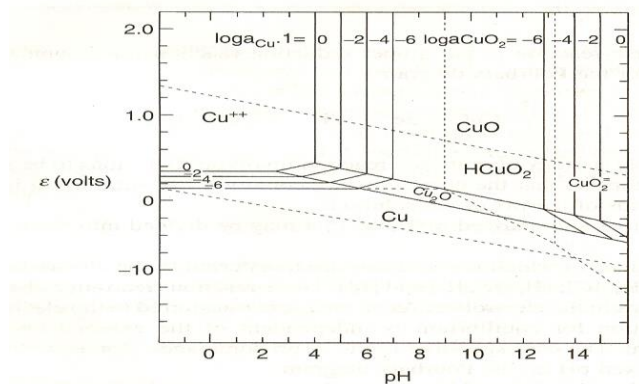


Fig. 2. Pourbaix diagram for copper in water solution at 25°C

Results and discussion

Cathodic polarization experiments

Cathodic polarization experiments were made for copper nitrate electrolyte of 40 and 100 g/dm³ Cu at room temperature. The results are shown in Fig. 3.

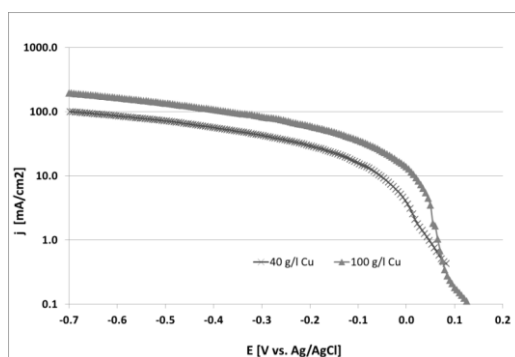


Fig. 3. Cathodic polarization experiment with 40 and 100 g/dm³ Cu concentrations

In the 100 g/dm³ Cu experiment, the polarization effect is smaller than in the 40 g/dm³ Cu test. The limiting current density due to diffusion is higher for the 100 g/dm³ test than for the lower concentration, which correlates with the limiting current theory. With the knowledge of polarization tests, we decided to test three different current densities of 100 A/m² (10 mA/cm²), 200 A/m² and 300 A/m², so that the cell voltage would not increase too high and the process efficiency would still be moderate.

Effect of Cu^{2+} concentration and current density

Three different copper concentrations (40, 100 and 150 g/dm^3) were used in the experiments. Only with the lowest concentration (40 g/dm^3 Cu) we managed to produce pure 99.9993 % (5N) copper and a cathode plate, which was bright copper color and solid (Table 1). In all other experiments, with two highest copper concentrations, the purity remained under 5N and the current efficiency (CE) was poor. In these tests the cathode color was dark, which indicates copper oxide deposition (Figs. 4 - 5). The dark copper oxide cathode plate was very fragile, soft and porous.

Table 1. Results of cathode copper purity analysis

| Cu [g/dm^3] | j [A/m^2] | T [$^{\circ}\text{C}$] | E [V] | | pH | | CE [%] | Cu cal.% | quality / color |
|------------------------|----------------------|--------------------------|-------|-------|-------|-------|--------|----------|-----------------|
| | | | start | final | start | final | | | |
| 40 | 100 | 22 | 0.35 | 0.21 | 1.7 | 2.2 | ~90 | 99.99827 | good |
| 40 | 100 | 35 | 0.29 | 0.20 | 1.4 | 2.1 | 80 | 99.99934 | good |
| *40 | 100 | 35 | 0.34 | 0.20 | 1.5 | 1.9 | ~ 90 | 99.99929 | good |
| 40 | 200 | 22 | 0.66 | 0.29 | 1.3 | 2.1 | ~ 90 | 99.99904 | good |
| 100 | 300 | 22 | 0.60 | 0.27 | 1.4 | 2.2 | 35 | 99.99888 | bad |

*repetition test

It is known that very low and very high concentrations of salts in electrolytes have higher ion activities and mean activity coefficients than the mid-range concentration of salts of 0.1–1 M (Lobo, 1989; Grenthe et al., 2000). Competing nitrate ion reduction reactions with copper ions are harmful for the quality of copper deposition, because they increase the electrolyte pH to the porous copper oxide deposition level, which is seen in the 100 and 150 g/dm^3 Cu concentration experiments (1.57 and 2.36 M) (Figs. 4 - 5). In addition, it is suggested that the copper ions work as catalyzers for the nitrate ion reduction reactions. Good quality deposition of copper was achieved with 40 g/dm^3 Cu if the pH did not increase much above 2 (Fig. 4). It is suggested that the harmful nitrate ion reduction reactions occur slower at the low concentrations and activity levels than at higher concentrations of 100 and 150 g/dm^3 Cu. However, the concentration of 40 g/dm^3 Cu seems to be high enough for copper deposition at the decent current density but low enough for slow copper nitrate reactions or copper reducing reactions to be preferable at the cathode.

The 100 A/m^2 cathodic current density was low enough for a good copper deposit without diffusion problems. The cell voltage remained just at +0.2 – 0.35 V. With 200 A/m^2 current density the cell voltage rose to +0.6 V at the beginning but dropped during copper growth to under 0.3 V (Table 1). Dendrite growth was considerably

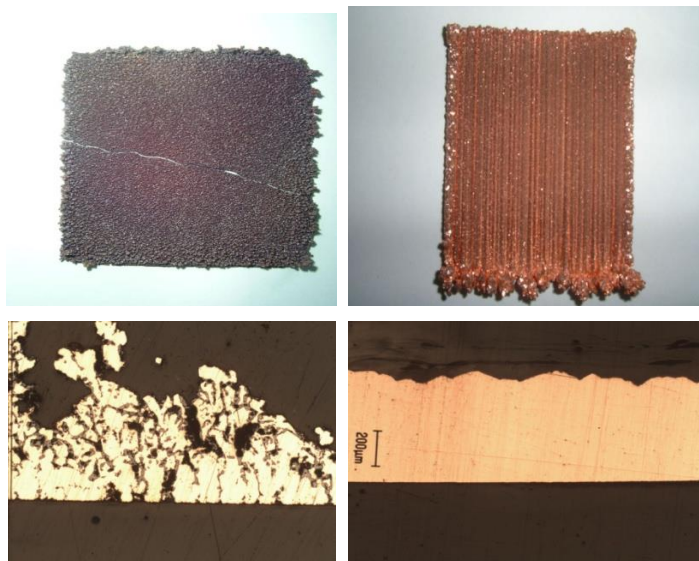


Fig. 4. Left: copper cathode plate ($\text{Cu } 40 \text{ g/dm}^3$) with cross section image.
Right: copper oxide cathode plate ($\text{Cu } 100 \text{ g/dm}^3$) with porous structure

higher with the higher current density. The purity of cathode copper was over 5N with both 100 and 200 A/m^2 experiments. With higher concentrations of copper the higher current density can be used, which is good for the productivity. However the detrimental effect of nitrate ion reduction reactions becomes too high with high concentrations of 100 and $150 \text{ g/dm}^3 \text{ Cu}$ (Fig. 5). A low enough amount of copper in the electrolyte and high current density for higher productivity is a compromise.

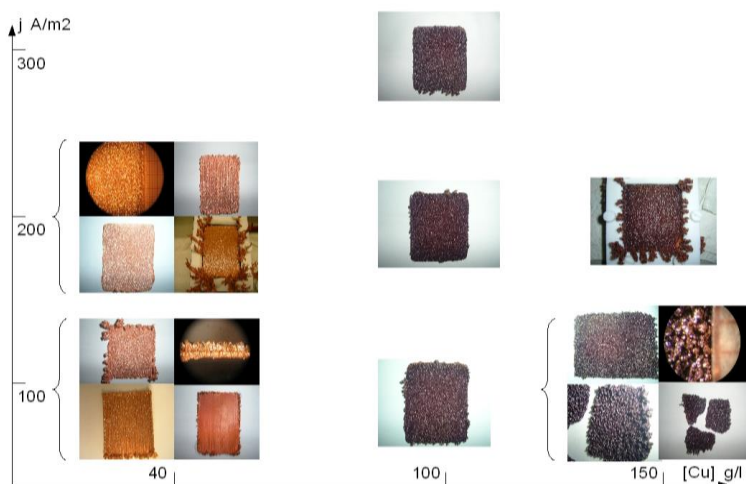


Fig. 5. Current density and copper concentration effect on cathode appearance and quality

Effect of temperature

According to previous studies it seems that copper nitrate based electrorefining works better at relatively low temperatures (Mockrin and Hobin, 1977; Kim and Choi, 2003). At lower temperatures detrimental nitrate reduction reactions might be inhibited significantly. We tested two different temperatures (22 and 35 °C) but no significant differences in the copper quality or purity were noticed (Table 1). At $T = 35$ °C the conductivity of the electrolyte was slightly higher than at 22 °C (74 mS/cm vs. 101 mS/cm) for 40 g/dm³ Cu electrolyte. For 100 g/dm³ Cu electrolyte, the conductivities at the same temperatures were 116 and 132 mS/cm, respectively. In theory, raising temperature to 35 °C should lower the cell voltage slightly but we did not see the major difference in the cell voltage either (Table 1).

Effect of pH

Electrolyte pH is a critical value for the success of refining. The pH tends to increase due to hydrogen ion consumption in nitrate ion reduction reactions or due to hydrogen ion activity drop in reactions with copper and nitrate ions. With high concentrations of copper nitrate salt 100 and 150 g/dm³ Cu, the cathode was covered with dark copper oxide even though pH stayed below 2. This indicates that copper and nitrate ion activities are too high and copper oxide deposits also at lower pH values as can be seen from Table 1. If pH is adjusted too low with nitric acid at the beginning, the nitrate ion reduction potential becomes higher (Eq. 3) and could accelerate the nitrate ion reduction reaction and end with a fast pH increase. Electrolyte pH monitoring and adjustment is needed during a long refining period for better copper deposit. One problem with nitric acid addition is that it increases the NO₃⁻ activity in the solution.

Cathode purity

Over 5.5 N copper purity is not reached with this cell construction. In the cathode, sulfur concentration remained from 0.25 to 1.7 ppm (4 ppm in anode) and silver 1–3 ppm (10 ppm in anode). Iron and nickel remained between 0.2–1 ppm, which is approximately the same amount than in the anode. Silver in the electrolyte varied between 0.02–0.11 mg/dm³. Concentration of 40 g/dm³ Cu, current density 100 A/m², and temperature 35 °C were found to be the best parameters for dense and hard copper deposit (99.9993 %). Although at $T = 22$ °C and $j = 200$ A/m² the result was also 5N (99.9990 %) copper, but with more dendritic growth.

Conclusions

In this work copper nitrate based electrorefining of copper was studied. Monitoring and controlling of pH makes copper electrorefining in copper nitrate electrolyte especially challenging. The pH tends to increase due to the nitrate ion reduction reactions and the pH increase occurs without a clear rate. The pH range of 1.4 - 1.7

should be maintained if possible. In this range, the nitrate reduction reactions are suggested to be inhibited and dense quality copper is able to deposit on the steel plate. To achieve 6N copper with copper nitrate electrolyte more sophisticated cell structure with anode sludge filtration, acid addition and silver cementation processes are needed. For measuring the final purity of copper and how the purity affects properties of copper, it might be reasonable to measure the final product performance i.e. conductivity with the calculated copper purity percent in the future. Lower temperatures (5–15 °C) might be worthwhile to inhibit the nitrate reduction reactions.

References

- BOUZEK, K., PAIDAR, M., ROUSAR, I., 1999. *Electrochemical removal of nitrate ions in waste solutions after regeneration of ion exchange columns*. Journal of Applied Electrochemistry(29): 611-617.
- BRÜNING, H., HERICY, J.L., LÜCKE, K., 1985. *Production of Ultra High Purity Copper by Nitrate Electrolysis and Floating Zone Melting I - II*. Ann. Chim. Fr., 10: 121-133 & 521-533.
- CARREAU, V., MAITREJEAN, S., VERDIER, M., BRÉCHET, Y., 2007. *Evolution of Cu microstructure and resistivity during thermal treatment of damascene line: influence of line width and temperature*. Microelectronic Engineering, 84(11): 2723-2728.
- EPRON, F., GAUTHARD, F., BARBIER, J., 2003. *Palladium and platinum-based catalysts in the catalytic reduction of nitrate in water: effect of copper, silver, or gold addition*. Journal of Catalysis, 220: 182-191.
- FENG, H.P., LIN, J.Y., CHENG, M.Y., WANG, Y.Y., WAN, C.C., 2008. *Behaviour of Copper Removal by CMP and Its Correlation to Deposit Structure and Impurity Content*. Journal of The Electrochemical Society, 155(1): H21-H25.
- FILIMONOV, E.V., SHCHERBAKOV, A.I., 2004. *Catalytic Effect of Copper Ions on Nitrate Reduction*. Protection of Metals, 40(3): 304-309.
- GRENTHE, I., WANNER, H., ÖSTHOLS, E., 2000. *Guidelines for the Extrapolation to Zero Ionic Strength*, TDB-2. OECD Nuclear Energy Agency.
- KATO, M., 1991. *High conductivity copper alloys with excellent workability and heat resistance*. Nippon Mining Co. Ltd. Tokio, Japan.
- KATO, M., 1995. *The Production of Ultrahigh-Purity Copper for Advanced Applications*. JOM Journal of the Minerals, Metals and Materials Society, 47(12): 44-46.
- KIM, D.S., CHOI, J.Y., 2003. *Production of ultrahigh purity copper using waste copper nitrate solution*. Journal of Hazardous Materials(B 99): 147-158.
- KIM, N.-H., KIM, S.-Y., LEE, W.-S., CHANG, E.-G., 2007. *Electromigration characteristics in dual-damascene copper interconnects by difference of via structures*. Microelectronic Engineering, 84(11): 2663-2668.
- KYRIACOU, G., POLATIDES, C., 2005. *Electrochemical reduction of nitrate ion on various cathodes - reaction kinetics on bronze cathode*. Journal of Applied Electrochemistry(35): 421-427.
- LOBO, V.M.M., 1989. *Handbook of electrolyte solutions; Part A*. Elsevier Science, Amsterdam-Oxford-New York-Tokyo, 1168 pp.
- MASAKI, M., MASAHARU, I., 2005. *High-purity electrolytic copper and its production method*. Mitsubishi Materials Corp., Japan.
- MOCKRIN, I., HOBIN, M.A., 1977. *Recovery of copper from waste nitrate liquors by electrolysis*. Kawecki Beryco Industries, Inc., U.S.

- MOREAU, S., MAITREJEAN, S., PASSEMARD, G., 2007. *Fatigue of damascene copper lines under cyclic electrical loading*. *Microelectronic Engineering*, 84(11): 2658-2662.
- OGATA, T., KATO, M., KAWASUMI, Y., TOMINAGA, C., TANAKA, K., 1989. *Method for producing high purity electrolytic copper*. Nippon Mining Co. Ltd. Tokio, U.S.
- OHMORI, T., EL-DEAB, M.S., OSAWA, M., 1998. *Electroreduction of nitrate ion to nitrite and ammonia on a gold electrode in acidic and basic sodium and cesium nitrate solutions*. *Journal of Electroanalytical Chemistry*, 470: 46-52.
- OJEBUOBOH, F., MICHELS, H.T., 2004. *High-Purity copper for semiconductor applications*, Copper 2003 - Cobre 2003; Fifth International Conference Canadian Institute of Mining, Metallurgy and Petroleum, Santiago, Chile, pp. 517-530.
- POLATIDES, C., DORTSIU, M., KYRIACOU, G., 2005. *Electrochemical removal of nitrate ion from aqueous solution by pulsing potential electrolysis*. *Electrochimica Acta*(50): 5237-5241.
- SHINDO, Y. , TAKEMOTO, K., 2005. *Ultrahigh-purity copper and process for producing the same*. Nippon mining & metals Co., Ltd. Tokyo, Japan.
- SHRIVER, D.F., ATKINS, P.W., 1999. *Inorganic Chemistry 3rd edition*. Oxford University Press, Oxford, 763 pp.
- TAKAHASHI, K., KANO, O., 2002. *High-purity copper sputtering targets and thin films*. Japan Energy Corporation, U.S.
- VAZQUEZ-ARENAS, J., VAZQUEZ, G., MELENDEZ, A.M., GONZÁLES, I., 2007. *The Effect of the Cu^{2+}/Cu^{+} Step on Copper Electrocrystallization in Acid Noncomplexing Electrolytes*. *Journal of The Electrochemical Society*, 154(9): D473-D481.

Received April 6, 2014; reviewed; accepted June 6, 2014

EFFECT OF ELECTROLYTE ADDITION ON FLOTATION RESPONSE OF COAL

Haijun ZHANG

National Engineering Research Center for Coal Processing and Purification, China University of Mining and Technology, Xuzhou 221116, China, zhjcumt@163.com

Abstract: In this study, the flotation of naturally hydrophobic coal particles in salt solutions with different cations (Na^+ , Ca^{2+} , and Al^{3+}) was investigated to clarify the flotation enhancement mechanism. The surface chemistry aspects were examined using the zeta potential measurements and bubble-particle attachment time experiments. The results of the flotation experiments showed that the presence of electrolytes in the flotation system clearly enhanced the flotation performance in a manner dependent on the type and concentration of the electrolytes. In the experiments, the AlCl_3 and NaCl solutions showed the highest and the lowest flotation performance improvements, respectively. The zeta potential measurements showed that AlCl_3 had a stronger influence on the surface charge of coal particles than CaCl_2 or NaCl did. The induction time measurements indicated that the attachment decreased with increasing salt concentration and ionic valency state. In addition, abundant fine bubbles were generated in higher concentration salt solutions, particularly for the AlCl_3 solutions, which prevented from the bubble coalescence and increased froth stability. It is concluded that the addition of salt solutions to a flotation system enhances the coal flotation performance, particularly for high-valence electrolyte solutions, which is attributed to the abundance of finer bubbles in the froth phase, depending on the type and concentration of the electrolyte.

Keywords: coal flotation, salt solutions, zeta potential, induction time, froth stability

Introduction

Flotation, undoubtedly the most important and versatile mineral processing technique, is a physico-chemical separation process that utilises the difference in surface properties of particles of various minerals (Arnold and Aplan, 1989; Nguyen et al., 1998; Subrahmanyam and Forssberg, 1988). Since researchers first discovered that the electrolyte ions could enhance the flotation of naturally hydrophobic particles, there has been an intense interest in the study of mineral flotation in the seawater and electrolyte solutions (Hampton and Nguyen, 2009; Kurniawan et al., 2011; Wellham et al., 1992; Yoon, 1982). Several theories have been proposed to explain the

enhancement of coal flotation in salt solutions, which can be divided into three categories: i) the inorganic electrolytes destabilise the hydrated layers surrounding the mineral particles and reduce the surface hydration of particles, which in turn increases the attachment efficiency of the valuable mineral particles to air bubbles (Dishon et al., 2009), ii) the inorganic electrolytes compress the electrical double-layer between and reduce the zeta potential of bubbles and particles, which corresponds to the reduction of the electrostatic force between bubbles and particles (Paulson and Pugh, 1996; Yoon and Sabey, 1989), and iii) the inorganic electrolytes decrease the coalescence of bubbles, which produces an abundance of fine bubbles and increases froth stability (Bournival et al., 2012; Craig et al., 1993; Marrucci and Nicodemo, 1967).

However, these theories only partially explain the mechanism of coal flotation in salt solutions, which is very complex. There is undoubtedly a correlation among the flotation recovery, flotation kinetics, bubble size distribution, and froth stability profile with the addition of salt solutions (Marrucci and Nicodemo, 1967; Harvey et al., 2002; Marcelja, 2006; Pugh et al., 1997; Weissenborn and Pugh, 1996). Paulson and Pugh (1996) proposed that the improved flotation of hydrophobic graphite in electrolytes was related to the dissolved gas concentration gradient in the electrolyte solutions. Ozdemir et al. (2009) investigated the surface chemistry aspects of coal flotation. The results indicated that the enhancement of coal flotation in hypersaline water was not entirely due to surface chemistry aspects, as previously proposed. Recently, a study performed by Kurniawan et al. (2011), showed that the addition of salt solutions to a flotation system produced smaller bubbles in the froth phase and that the bubble size decreased with increasing salt concentration, improving the coal flotation performance. Bournival et al. (2012), also investigated the coalescence behaviour of bubbles with NaCl using high-speed video imaging compared with a similar system using 4-methyl-2-pentanol. The results showed that NaCl had no surface-restoring effect, even at high concentration, whereas MIBC prevented the bubble surface from the deformation during coalescence at relatively high concentrations. Ozdemir (2013), investigated the flotation of bituminous coal in the presence of NaCl, KCl, CaCl₂ and MgCl₂ without use of any flotation chemicals. The results clearly indicated that the Na⁺, K⁺, Ca²⁺, Mg²⁺ ions had a strong ion specific effect on the flotation of bituminous coal, and there was an optimum salt concentration to produce a clean coal in these salt solutions.

A review of the literature shows that the previous studies mainly focused on the enhancement of a coal flotation performance in salt solutions. Therefore, to further understand the role of electrolytes in coal flotation, three salt solutions with different cations (Na⁺, Ca²⁺, and Al³⁺) were compared in terms of the coal flotation enhancement using the micro-flotation experiments, zeta potential measurements, and bubble-particle attachment time experiments.

Materials and Methods

Materials

The pure coal sample used in this study was obtained from Alberta, Canada, and was naturally hydrophobic. The volatile matter content for the coal was less than 10%. The $-250+212$ μm particle size fraction was selected for all tests. Analytical grade (>99%) electrolytes (NaCl, CaCl₂, and AlCl₃) were used in the experiments. The electrolyte concentrations used in the tests were 0.01 M, 0.05 M, 0.1 M, 0.15 M, and 0.2 M. Analytical grade hydrochloric acid (HCl) and sodium hydroxide (NaOH) were used to adjust the pH level. For all experiments, the pH value was kept at ~ 6.4 .

Methods

Micro-flotation experiments

The coal samples taken from the $-250+212$ μm fraction were used for the micro-flotation, which was performed in a Hallimond tube equipped with an air flowmeter and magnetic stirrer. In each test, 1 g of the coal sample was mixed with 150 ml of a given salt solution, and the mixture was placed in a 250 ml beaker agitated for 5 min. The slurry was then transferred to the tube followed by a stream of N₂ at a flow rate at 45 ml/min. A constant stirrer speed of 250 rpm and a constant water level were maintained within the tube during each experiment. All tests were performed at room temperature. The flotation time was 3 min for each test. Finally, the flotation products were filtered, dried, and weighed.

Zeta potential measurements

The zeta potential measurements were performed using Brookhaven ZetaPALS. The coal samples taken from the $-250+212$ μm fraction were further ground to a -45 μm particle size for zeta potential measurements. For each experiment, 0.05–0.1 wt.% suspensions of the ground coal particles were prepared using the desired salt solutions. The suspensions were allowed to stand for 12 h prior to the measurement. The pH value was adjusted using either acid (HCl) or alkali (NaOH). The zeta potential was measured 6 times during each experiment, and the average value was reported. The measurements were performed at 22 °C.

Induction time measurements

Induction time measurements between coal particles and air bubbles were performed with a homemade induction time device (Gu et al., 2003), as shown in Fig. 1. The coal samples taken from the $-250+212$ μm fraction were used to measure the bubble-particle attachment time. For each measurement, 1 g of coal was conditioned in a given salt solution for 5 min. Next, the conditioned particles together with the solution were transferred to the measurement vessel under the bubble holder. The bubble generated from a glass capillary was brought into contact with the particle bed at a set contact time.

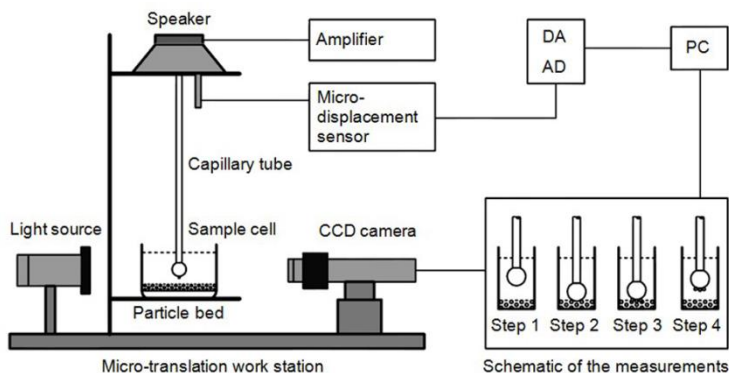


Fig. 1. Schematic of the bubble-particle attachment time measurement device (Gu et al., 2003)

Each experiment was repeated 20 times at different locations in the particle bed. The induction time was characterised as the contact time, at which the pickup probability was 50%. The approach and attachment processes were recorded by a CCD camera. The initial distance between the bubble pole and particle bed (0.40 mm), the amplitude of the bubble motion (5 volt), the approach and retraction velocities of bubbles (40 ms), the bubble size (1.2 mm), were all kept constant during the measurements. The measurements were carried out at room temperature.

Results and discussion

Micro-flotation experiments

Coal flotation was carried out in three salt solutions without a frother or collector. The coal recovery as a function of salt concentration is plotted in Fig. 2. The results show that the coal recovery increased with an increasing salt concentration under the

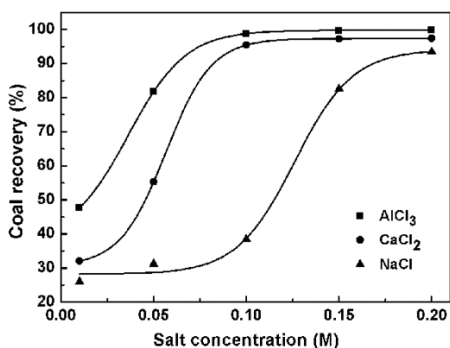


Fig. 2. Effect of salt concentration on coal recovery

test conditions. The coal recovery plateaued when the salt's concentration exceeded 0.1 M for AlCl_3 and CaCl_2 and 0.2 M for NaCl . The results indicated that AlCl_3 produced the highest coal recovery, followed by CaCl_2 and NaCl . These results were in agreement with the findings of Li and Somasundaran, 1993, who investigated the flotation of bituminous coal in the NaCl solutions using a modified Hallimond tube and concluded that the flotation of coal increased significantly upon the addition of inorganic electrolytes. Ozdemir et al., 2009, also indicated that coal particles could float in bore water, which contained mostly Na^+ and Mg^{2+} , without using any frother or collector, obtaining a coal concentrate recovery of 85%.

Zeta potentials

The zeta potential of the coal particles as a function of a salt type and concentration were measured. The results for the measurements are given in Fig. 3. As seen in this figure, similarly to the flotation recovery response, the mean value for the zeta

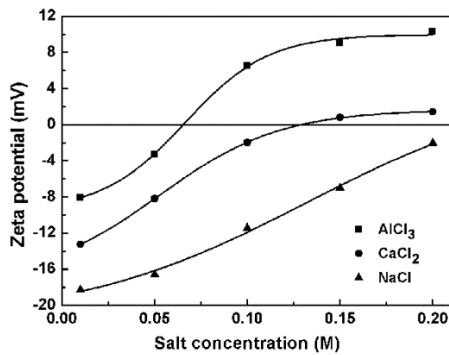


Fig. 3. Effect of salt concentration on zeta potential

potentials were becoming less negative with an increasing salt concentration at constant pH. The AlCl_3 and NaCl solutions showed both the lowest and the highest salt concentration for the point of zero charge of the coal particles, respectively. The results indicated that AlCl_3 had the strongest influence on the zeta potential at a given salt concentration, followed by CaCl_2 and NaCl . The changes in the zeta potential can be linked with the difference in charge and radius among Al^{3+} , Ca^{2+} , and Na^+ . Li and Somasundaran (1993), studied the reversal of bubble charge in multivalent inorganic salt solutions and also concluded that the charge of gas bubbles can even be reversed in the electrolyte solutions of multivalent metal ions. In addition, a study performed by Li et al. (1993), showed that trivalent metal cations had the strongest effect on the surface charge of particles, followed by divalent and monovalent metal cations.

Bubble-particle attachment time measurements

Minerals are separated by their attachment to rising air bubbles in the flotation system. The floatability of the coal particles can be measured using the bubble-particle attachment time (Ye et al., 1989). The bubble-particle attachment time experiments were carried out to measure the flotation of the coal particles as a function of the salt's type and concentration. The results for attachment time are shown in Fig. 4. As seen from Fig. 4, an increase in the salt concentration led to a decrease in the bubble-particle attachment time over the entire tested salt concentration range, which was consistent with the results of the micro-flotation experiments. The shortest induction time was obtained for AlCl_3 , followed by CaCl_2 and NaCl . In the case of NaCl , the result was consistent with the findings of Yoon and Sabey (1989), who concluded that the attachment time was reduced in the NaCl solutions. However, this effect is not yet conclusive. For example, according to the bubble-particle attachment time results from Ozdemir et al. (2009), the bubble-particle attachment in bore water was significantly longer than that in the distilled water. Thus, the coal particles would be more floatable in distilled water than in bore water, which contained mostly Na^+ and Mg^{2+} . The flotation tests showed the opposite results, indicating that the induction time experiments could not be precisely correlated with the flotation behaviour of the coal particles in bore water.

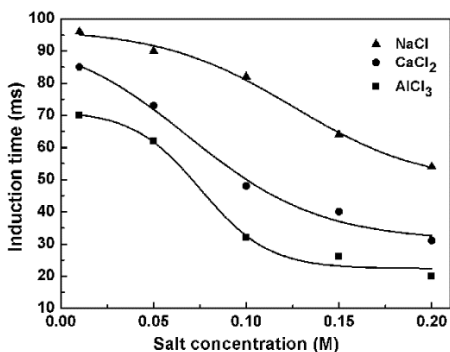


Fig. 4. Effect of salt concentration on bubble-particle attachment time

Discussion

It has been reported that the flotation of naturally hydrophobic coal can be increased significantly by the addition of the inorganic electrolytes (Hampton and Nguyen, 2009; Kurniawan et al., 2011; Wellham et al., 1992; Yoon, 1982; Li and Somasundaran, 1993). The overall results of this study showed that the effect of the

salt on the coal recovery depends on the salt type and concentration. Under the test conditions used in this study, the coal can be recovered from salt solutions without using flotation reagents. AlCl_3 showed the best flotation recovery response, followed by CaCl_2 and NaCl . This result was consistent with other researchers' earlier findings that the flotation of naturally hydrophobic materials increased significantly upon the addition of inorganic electrolytes (Kurniawan et al., 2011; Yoon, 1982; Yoon and Sabey, 1989; Li and Somasundaran, 1993; Laskowski, 1965).

The zeta potential measurements indicated that the salt solutions had a strong influence on the reduction of the zeta potential due to the compression of the electrical double layers (Paulson and Pugh, 1996; Yoon and Sabey, 1989). Therefore, the electrostatic repulsion between bubbles and particles decreased. Some previous studies on the coal particles and bubbles indicated that the soluble cations significantly reduced the magnitude of the zeta potential of particles and bubbles (Paulson and Pugh, 1996; Li and Somasundaran, 1993). The results of our study contradict those of Paulson and Pugh, 1996, who demonstrated that the flotation recovery was the highest for the lowest zeta potential, which can be attributed to the fact that the surface charge of the coal particles would change from negative to positive in the salt solutions under some certain conditions, whereas the bubbles would remain negatively charged. For this reason, the electrostatic attraction would most likely dominate the bubble-particle attachment, which further corresponds to an improvement in the flotation response.

It has been previously indicated that the inorganic electrolytes can destabilise the hydrated layers surrounding particles and reduce the surface hydration of particles, which corresponds to a reduction of the induction time between bubbles and particles (Dishon et al., 2009; Yoon and Sabey, 1989). According to the bubble-particle attachment measurements, it is evident that the induction time of coal particles in the NaCl solutions was longer comparing to those in the CaCl_2 and AlCl_3 solutions. As for the bubble-particle attachment time results, the coal particles would be more floatable in the AlCl_3 solutions. Therefore, the decrease in bubble-particle attachment time for coal particles in the AlCl_3 solutions could have a significant effect on the coal flotation in the AlCl_3 solutions, which was further supported by the results of micro-flotation tests. These results clearly indicated that the induction time results could be precisely correlated with the micro-flotation behaviour of the coal particles in the salt solutions.

In addition, the flotation efficiency also depends on the bubble size distribution and on the degree of the bubble coalescence because fine bubbles are generally more effective at capturing the particles (Li and Somasundaran, 1991). Figure 5 shows the snapshots of the bubbles in the salt solutions in a 1 dm^3 Denver cell. An abundance of smaller bubbles was produced with the electrolyte addition, particularly at the higher salt concentrations, which agrees with the literature. It is known that the bubble size is reduced, the bubble coalescence was decreased, and the froth stability increased with the increase of the electrolyte concentration (Ozdemir, 2013; Marrucci and Nicodemo, 1967). It should be noted that the electrolytes used in this study were not purified, which would affect size of the bubbles formed because of surface active contaminants

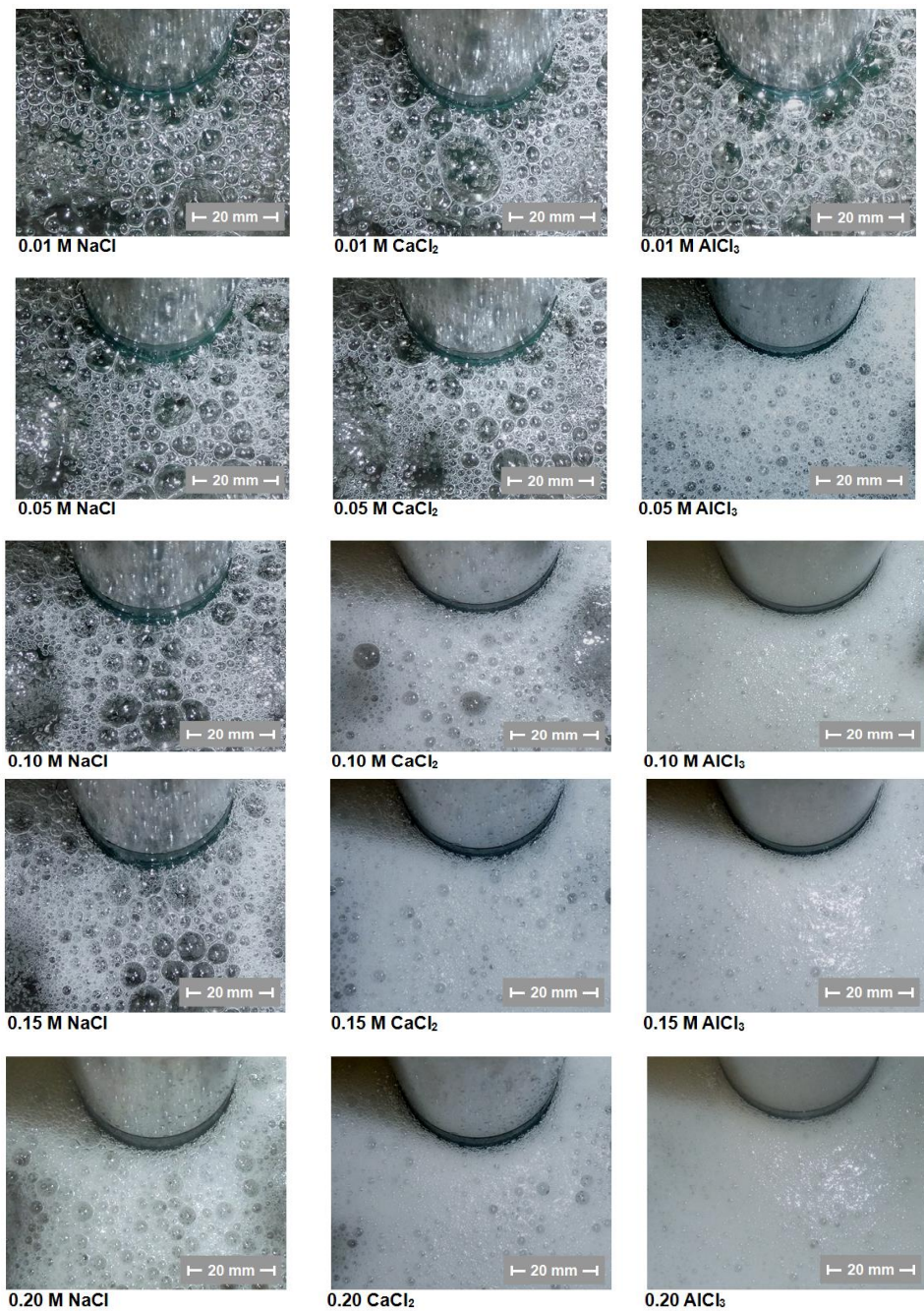


Fig. 5. Snapshots of the bubbles in salt solutions (1 dm^3 Denver cell, impeller speed 1500 rpm, air flow rate $1.25 \text{ dm}^3/\text{min}$)

at higher electrolyte concentration. But it is undeniable that the addition of salt would increase the froth stability of the system. Accordingly, the coal recovery was significantly improved in the presence of an abundance of fine bubbles. The results indicated that the type and the concentration of the salt solutions significantly affected the froth properties. This phenomenon was consistent with the previous findings (Kurniawan, 2011; Craig et al., 1993). Kurniawan et al. (2011), suggested that there was a correlation between the coal recovery and the stability profile of the froth and concluded that the coal recovery and the bubble size distribution of the froth phase were directly correlated. Recently, Bournival et al. (2012), also concluded that NaCl, albeit at a higher concentration, could be as effective as MIBC in preventing bubble coalescence in a dynamic environment and that the bubbles became more stable with an increasing salt concentration. The reduction of bubble coalescence decreases bubble size and increases froth stability, which is affected by the type and the concentration of the salt (Bournival et al., 2012; Craig et al., 1993; Marrucci and Nicodemo, 1967).

Conclusions

The results of the naturally hydrophobic coal flotation experiments in the presence of salt solutions with different cations (Na^+ , Ca^{2+} , and Al^{3+}) showed that the inorganic electrolytes enhanced the flotation performance, depending on the type and the concentration of the salt. AlCl_3 showed the highest flotation recovery response with increasing salt concentrations, whereas CaCl_2 showed a moderate increase, and NaCl showed the lowest increase. The zeta potential and bubble-particle attachment time were affected by the type and the concentration of the salt. Similar to the flotation recovery response, AlCl_3 produced the highest zeta potential at a given salt concentration, followed by CaCl_2 and NaCl. The results indicated that trivalent metal cations had the strongest effect on the surface charge of the particles. The induction time measurements indicated that the attachment decreased with increasing salt concentration and ionic valency state. In addition, abundant fine bubbles were generated in higher-concentration salt solutions, particularly for the AlCl_3 solutions, which prevented bubble coalescence and increased froth stability. It is concluded that the addition of salt solutions to a flotation system enhances the coal flotation performance, particularly for high-valence electrolyte solutions, which is due to the abundance of smaller bubbles at the froth phase, depending on the type and concentration of the electrolyte.

Acknowledgements

The author would like to thank the financial support of the Fundamental Research Funds for the Central Universities (2014QNB09).

References

- ARNOLD B.J., APLAN F.F., 1989, *The hydrophobicity of coal macerals*. Fuel, 68, 651–658.
- BOURNIVAL G., PUGH R.J., ATA S., 2012, *Examination of NaCl and MIBC as bubble coalescence inhibitor in relation to froth flotation*. Minerals Engineering, 25, 47–53.
- CRAIG V.S.J., NINHAM B.W., PASHLEY R. M., 1993, *Effect of electrolytes on bubble coalescence*. Nature, 364, 317–319.
- DISHON M., ZOHAR O., SIVAN U., 2009, *From repulsion to attraction and back to repulsion: the effect of NaCl, KCl, and CsCl on the force between silica surfaces in aqueous solution*. Langmuir, 25, 2831–2836.
- GU G.X., XU Z.H., NANDAKUMAR K., MASLIYAH J., 2003, *Effects of physical environment on induction time of air-bitumen attachment*. International Journal of Mineral Processing, 69, 235–250.
- HAMPTON M.A., NGUYEN A.V., 2009, *Accumulation of dissolved gases at hydrophobic surfaces in water and sodium chloride solutions: Implications for coal flotation*. Minerals Engineering, 22, 786–792.
- HARVEY P.A., NGUYEN A.V., EVANS G.M., 2002, *Influence of electrical double-layer interaction on coal flotation*. Journal of Colloid and Interface Science, 250, 337–343.
- KURNIAWAN A.U., OZDEMIR O., NGUYEN A.V., OFORI P., FIRTH B., 2011, *Flotation of coal particles in MgCl₂, NaCl, and NaClO₃ solutions in the absence and presence of Dowfroth 250*. International Journal of Mineral Processing, 98, 137–144.
- LASKOWSKI J., 1965, *Coal flotation in solutions with raised concentration of inorganic salts*. Colliery Guardian, 361–365.
- LI C., SOMASUNDARAN P., 1991, *Reversal of bubble charge in multivalent inorganic salt solutions—effect of magnesium*. Journal of Colloid and Interface Science, 146, 215–218.
- LI C., SOMASUNDARAN P., 1993, *Reversal of bubble charge in multivalent inorganic salt solutions—effect of lanthanum*. Colloids and Surfaces A: Physicochemical and Engineering Aspects, 81, 13–15.
- LI C., SOMASUNDARAN P., 1993, *Role of electrical double layer forces and hydrophobicity in coal flotation in sodium chloride solutions*. Energy Fuels, 7, 244–248.
- LI C., SOMASUNDARAN P., HARRIS C.C., 1993, *A levitation technique for determining particle hydrophobicity*. Colloids and Surfaces A: Physicochemical and Engineering Aspects, 70, 229–232.
- MARRUCCI G., NICODEMO L., 1967, *Coalescence of gas bubbles in aqueous solutions of inorganic electrolytes*. Chemical Engineering Science, 22, 1257–1265.
- MARCELLJA S., 2006, *Selective coalescence of bubbles in simple electrolytes*. The Journal of Physical Chemistry, 110, 13062–13067.
- NGUYEN A.V., RALSTON J., SCHULZE H.J., 1998, *On modelling of bubble–particle attachment probability in flotation*. International Journal of Mineral Processing, 53, 225–249.
- OZDEMIR, O., TARAN, *Surface chemistry aspects of coal flotation in bore water*. International Journal of Mineral Processing, 92, 177–183.
- OZDEMIR, O., 2013, *Specific ion effect of chloride salts on collectorless flotation of coal*. Physicochemical Problems of Mineral Processing, 49(2), 511–524.
- PAULSON O., PUGH R.J., 1996, *Flotation of inherently hydrophobic particles in aqueous solutions of inorganic electrolytes*. Langmuir, 12, 4808–4813.
- PUGH R.J., WEISSENBORN P., PAULSON O., 1997, *Flotation in inorganic electrolytes: the relationship between recovery of hydrophobic particles, surface tension, bubble coalescence and gas solubility*. International Journal of Mineral Processing, 51, 125–138.

- SUBRAHMANYAM T.V., FORSSBERG E., 1988, *Froth stability, particle entrainment and drainage in flotation—A review*. International Journal of Mineral Processing, 23, 33–53 .
- WEISSENBORN P.K., PUGH R.J., 1996, *Surface tension of aqueous solutions of electrolytes: relationship with ion hydration, oxygen solubility, and bubble coalescence*. Journal of Colloid and Interface Science, 184, 550–563.
- WELLHAM E.J., ELBER L., YAN D.S., 1992, *The role of carboxy methyl cellulose in the flotation of a nickel sulfide transition ore*. Minerals Engineering, 5, 381–395.
- YE Y., KHANDRIKA S.M., MILLER J.D., 1989, *Induction-time measurements at a particle bed*. International Journal of Mineral Processing, 25, 221–240.
- YOON R.H., 1982, *Flotation of coal using micro-bubbles and inorganic salts*. Mining Congress Journal, 68, 76–80.
- YOON R.H., SABEY J.B., 1989, *Coal flotation in inorganic salt solution*. In: Botsaris, G.D., Glazman, Y.M. (Eds.). Interfacial phenomena in coal technology, New York: Marcel Dekker, 87–114.

Received June 12, 2014; reviewed; accepted July 20, 2014

DISSOLUTION OF GOLD WITH CYANIDE REPLACING REAGENTS

Jari AROMAA, Lotta RINTALA, Mikko KAHARI, Olof FORSEN

Aalto University, Department of Materials Science and Engineering, PO Box 16200, 00076 Aalto, Helsinki, Finland, jari.aromaa@aalto.fi

Abstract: Cyanide is used in the leaching phase of hydrometallurgical recovery of gold. The toxicity and environmental risks have created a need for safer alternatives. There is a vast amount of information about gold extraction and a selection has been collected and formalized to be used in a decision support tool. The tool Auric Advisor uses case-based reasoning (CBR) to provide process alternatives for the user queries. The aim of this paper is to study leaching of gold with cyanide replacing alternatives such as ammonium thiosulfate, chloride-hypochlorite, thiourea and thiocyanate to provide new cases for the tool. The behaviour of gold was examined with electrochemical tests and weight loss measurements using quartz crystal microbalance (QCM) were used to determine the dissolution rate. Based on literature, the dissolution rate determined for cyanide solution was $2.5 \text{ mg}\cdot\text{cm}^{-2}\cdot\text{h}^{-1}$. Based on polarisation experiments and potential measurements, the ammonium thiosulfate system with cupric ion as oxidant was estimated to dissolve gold slower than cyanide. In the QCM tests the chloride-hypochlorite alternative showed highest dissolution rate of $8.6 \text{ mg}\cdot\text{cm}^{-2}\cdot\text{h}^{-1}$ at the redox potential of 900 mV vs. SHE. The thiocyanate system with ferric ion dissolved gold at a rate of $3.4 \text{ mg}\cdot\text{cm}^{-2}\cdot\text{h}^{-1}$ at the redox potential of 620 mV vs. SHE. Thiourea system with ferric ion showed the dissolution rate of $1.65 \text{ mg cm}^{-2} \text{ h}^{-1}$ at the redox potential of 450 mV vs. SHE. The results of the rapid tests were comparable with literature and were included in the case base of the Auric Advisor decision-support tool.

Keywords: *gold leaching, ammonium thiosulfate, chloride, thiourea, thiocyanate*

Introduction

The most common hydrometallurgical methods of primary raw material utilization in the production of gold are based on the use of cyanide (Hilson, 2006). In this method a weak sodium cyanide solution (NaCN) of 100-500 ppm is used. Since the Baia Mare disaster in Romania in January 2000, the use of cyanide has been resisted. Germany passed a decree in 2002 prohibiting mines from using cyanide in leaching processes. The Czech Senate and Czech Parliament made decisions 2000-2002 to forbid cyanide leaching in the Czech Republic. Hungarian Parliament voted against the use of cyanide at mine sites in 2009 (Laitos, 2012, Eurostat, 2010). In 2010, the European

Union rejected a proposal to ban all cyanide use, but set stringent cyanide limits for tailings ponds in Directive 2006/21/EC. In the U.S. several states have restricted use of cyanide. Many provinces in Argentina have banned the use of cyanide in mining operations. Costa Rica banned cyanide in 2010 (Laitos, 2012).

The gold producers have been looking for alternative solutions to cyanide. Some of the alternative methods are thiourea, thiocyanate, thiosulphate, agglomerates of oil and coal, and halides (Hilson, 2006). Operating windows for cyanide leaching and alternative chemistries are shown in Fig. 1. The most actively studied chemistries are thiosulfate, thiourea, halides and α -hydroxynitriles (Aylmore, 2005, Hilson, 2006, Syed, 2012).

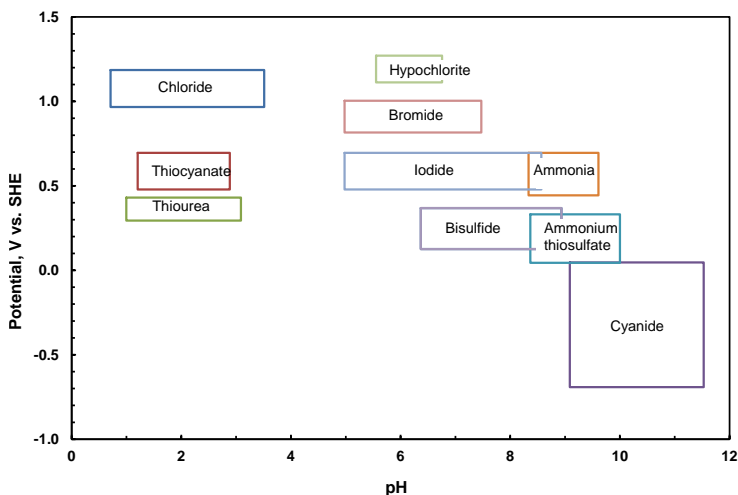


Fig. 1. Potential-pH diagram showing typical operating windows for gold lixiviants (after Aylmore, 2005)

In leaching of gold a complexing ligand and oxidant are needed. Dissolution of gold in cyanide solution is shown in Eq. 1. At low cyanide concentrations, the dissolution rate is a function of cyanide concentration. At high cyanide concentrations the dissolution rate of reaction



is a function of oxygen concentration (Deschenes, 2005). Dissolution of gold in alkaline thiosulfate solution is shown in Eq. 2. Reaction 2 is slow unless Cu^{2+} , that works as an oxidant, catalyses it (Eq. 3) (Feng, 2011). Ammonia is also needed to stabilize the solution

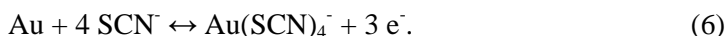
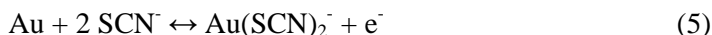


Dissolution in thiourea is shown as:



The reaction is sensitive to pH and redox potential. Thiourea is intrinsically unstable and decomposes rapidly to substances that are unable to leach gold (Murthy, 1996; Aylmore, 2005)

Thiocyanate can dissolve gold as either Au(I) (Eq. 5) or Au(III) (Eq. 6) complexes:



The ferric ion can be used as the oxidant and it can also oxidize thiocyanate to thiocyanogen and/or trithiocyanate (Li, 2012a). Dissolution of gold in a chloride system is:

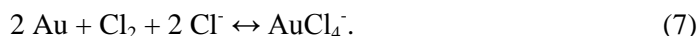


Table 1. Dissolution rates of gold in selected cyanide and alternative lixiviant solutions

| Cyanide-based system | Rate / $\text{mg}\cdot\text{cm}^{-2}\cdot\text{h}^{-1}$ | Rate / $\text{mol}\cdot\text{m}^{-2}\cdot\text{s}^{-1}$ | Reference |
|---|---|---|-------------------|
| 0.26 mM O_2 , 5 mM CN^- | 0.07 | $0.1 \cdot 10^{-5}$ | Senanayake (2004) |
| O_2 , 77 mM CN^- , pH 10.5 | 0.85 | $1.2 \cdot 10^{-5}$ | Senanayake (2004) |
| Aerated cyanide, 41 mM NaCN | 2.5 | $3.5 \cdot 10^{-5}$ | Nam (2008) |
| Thiosulfate-based system | | | |
| 0.7 mM Cu^{2+} , 0.1 M $(\text{NH}_4)_2\text{S}_2\text{O}_3$, 0.5 M NH_3 | 0.09 | $0.13 \cdot 10^{-5}$ | Feng (2011) |
| 10 mM Cu^{2+} , 100 mM $\text{S}_2\text{O}_3^{2-}$, 0.4 M NH_3 | 2.7 | $3.8 \cdot 10^{-5}$ | Senanayake (2004) |
| Thiourea-based system | | | |
| Sat. O_2 , 5 mM $\text{SC}(\text{NH}_2)_2$, 200 mM $\text{Na}_2\text{S}_2\text{O}_3$ | 0.03 | $0.04 \cdot 10^{-5}$ | Senanayake (2004) |
| 5 mM Fe^{3+} , 26.3 mM $\text{SC}(\text{NH}_2)_2$, 0.1 M H_2SO_4 | 1.7 | $2.4 \cdot 10^{-5}$ | Senanayake (2004) |
| Thiocyanate-based system | | | |
| 50 mM SCN^- , pH = 2 | 0.73-2.2 | $1.0 \cdot 10^{-5}$ - $3.1 \cdot 10^{-5}$ | Li (2012b) |
| Halide-based system | | | |
| 27 mM NaOCl, 85 mM NaCl, pH 6 | 0.5 | $0.7 \cdot 10^{-5}$ | Senanayake (2004) |
| 0.8 mM HOCl, 1700 mM NaCl, pH 3.5 | 1.0 | $1.4 \cdot 10^{-5}$ | Senanayake (2004) |
| 135 mM NaOCl, 850 mM NaCl, pH 6 | 10 | $14 \cdot 10^{-5}$ | Senanayake (2004) |
| 190 mM OCl $^-$, 1.7 M NaCl, pH 6 | 13 | $18.3 \cdot 10^{-5}$ | Nam (2008) |

A gold complex AuCl_2^- forms first and it is rapidly oxidized to AuCl_4^- (Aylmore, 2005; Nam, 2008). A residual amount of oxidant is required to maintain a high solution potential to avoid precipitation of metallic gold from the solution (Aylmore, 2005). Some reported dissolution rates of gold in the cyanide solution and in alternative lixiviants are listed in Table 1. Using the same basic lixiviant, the reported dissolution rates can vary up to two orders of magnitude depending on the concentrations of complex forming ligand and oxidant.

In this work we have studied alternative chemistries to cyanide in leaching of gold. The target was to develop a rapid test method for determination of dissolution rates for primary and secondary raw materials that do not require pre-treatment, such as a free-milling ore. The verified experimental test results can then be included in the case base of decision support tool Auric Advisor for process development (Sauer, 2013). The Auric Advisor tool takes a query from the user using selected attributes related to process chemistry, reaction rate etc., and retrieves the most similar cases as a result.

Materials and methods

The experiments included measurement of polarization curves for gold in different media, determination of the redox potential to achieve wanted dissolution rates and measurement of gold dissolution rate with a quartz crystal microbalance (QCM) (Jeffrey, 2005; Zelinsky, 2012). The electrochemical measurements were conducted using a rotating disc electrode (RDE) type PARC RDE0005 at 300 rpm and an ACM Instruments Gill AC potentiostat. The electrochemical measurements were conducted in a three-electrode cell, where a Luggin capillary and KCl bridge connected the cell to the reference electrode. The reference electrode used in the experiments was saturated Ag/AgCl electrode, type Radiometer REF 201. The counter electrode used in the experiments was platinum wire. Polarization curves were measured using 100 mV/min sweep rate. The tests to determine oxidant concentration to achieve wanted redox potential were done by addition of the oxidant and measuring redox potential with a Mettler Toledo combination redox electrode ($E_h = 0.207$ V) using the potentiostat as data logger. All the potential values are reported versus saturated Ag/AgCl ($E_h = 0.197$ V). The dissolution rate tests were done using the SRS 200 quartz crystal microbalance and measuring continuously the weight loss of the gold plated the QCM crystal in a solution with controlled redox potential. The weight loss tests were done in one litre reactor with continuous laminar flow $300 \text{ cm}^3/\text{min}$ to the QCM surface (Von Bonsdorff, 2007).

The test solutions were based on ammonia - thiosulfate, chloride - hypochlorite, thiourea and thiocyanate. The test solutions are shown in Table 2. The pH of the thiosulfate solution was adjusted by ammonia, pH of thiourea and thiocyanate solutions with sulphuric acid and pH of chloride solution with hydrochloric acid. The test solutions were purged with air.

Table 2. Compositions of the test solutions

| Solution | Ligand and stabilisator, M | Oxidant | Temperature, °C | pH |
|-----------------------|--|------------------|-----------------|-------|
| Ammonia – thiosulfate | 0.1-1, Na ₂ S ₂ O ₃ 1-4, NH ₃ | Cu ²⁺ | 25-40 | 10-11 |
| Thiourea | 0.13, SC(NH ₂) ₂ 36·10 ⁻³ , Na ₂ SO ₃ | Fe ³⁺ | 25-40 | 1-2 |
| Thiocyanate | 0.05-0.2, NaSCN 5·10 ⁻³ , SC(NH ₂) ₂ | Fe ³⁺ | 25-40 | 1-2 |
| Sodium chloride | 3, NaCl | NaClO | 25-40 | 1-3 |

Results and discussion

Polarization curves

Potentiodynamic polarization curves were measured to determine the overall dissolution behavior of gold in the test solutions. The measurements were done in air-purged solutions without other oxidants. The dissolution rate of gold at different potentials was estimated by using the Faradays law. Figure 2 shows polarization curves in an ammonia – thiosulfate solution. The open circuit potential varied between -200 and 0 mV and dissolution current densities at open circuit potential were in the order of 0.1-6 $\mu\text{A}\cdot\text{cm}^{-2}$. The polarization curves showed passivation at potentials above 200 mV. Figure 3 shows the polarization curves in the thiourea solution. The open circuit potential varied between -100 and 0 mV and the current densities at the open the circuit potential were in the order of 0.7-6 $\mu\text{A}\cdot\text{cm}^{-2}$. The current density increased continuously when the potential was increased and approached limiting

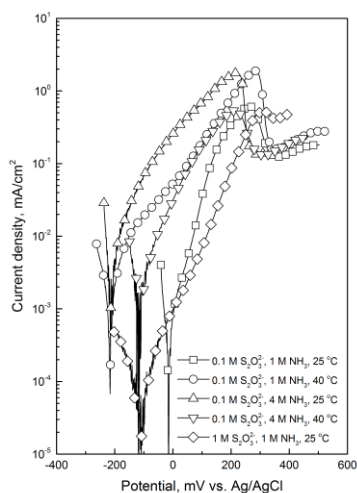


Fig. 2. Polarization curves of gold in ammonia – thiosulfate solution with NH₃ concentration 1 and 4 M and 25 and 40 °C

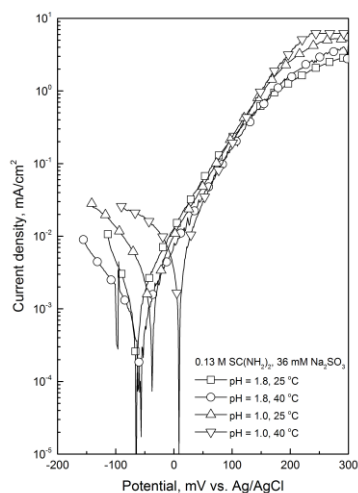


Fig. 3. Polarization curves of gold in thiourea solution with pH = 1.0 and 1.8 and temperatures 25 and 40 °C

current density $2\text{--}6\text{ mA}\cdot\text{cm}^{-2}$ at the potentials above 200 mV. Figure 4 shows polarization curves in the thiocyanate solution. The open circuit potential was 50–100 mV and the current densities at the open circuit potential were $0.1\text{--}0.4\text{ }\mu\text{A}\cdot\text{cm}^{-2}$. The current density increased continuously when the potential was increased and approached limiting current density in the order of $1\text{ mA}\cdot\text{cm}^{-2}$ at the potentials above 500 mV. Figure 5 shows the polarization curves in the chloride solution. The open circuit potential varied strongly with pH being 100–200 mV at pH = 3, 350–450 mV at pH = 2 and 500–600 mV at pH = 1. The current densities at the open circuit potential were $0.2\text{--}3\text{ }\mu\text{A}\cdot\text{cm}^{-2}$. Rapid dissolution started at the potentials above 600–700 mV and the current density increased more rapidly at low pH values.

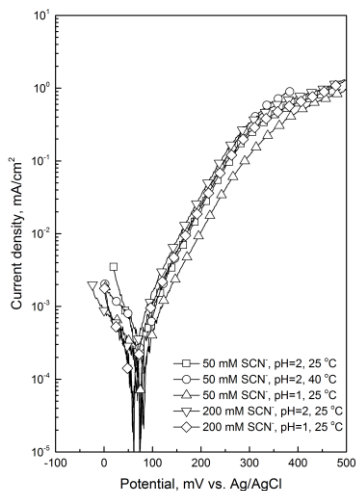


Fig. 4. Polarization curves of gold in 50 and 200 mM thiocyanate solution at pH = 1 and 2 and temperatures 25 and 40 °C

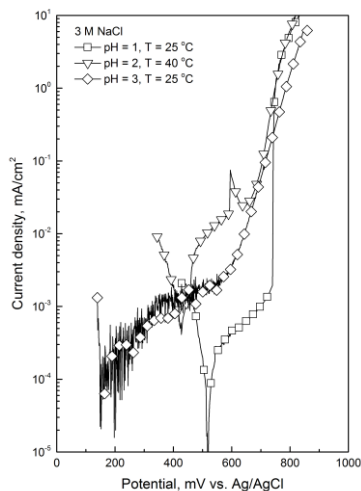


Fig. 5. Polarization curves of gold in 200 g/dm³ sodium chloride solution

Redox potential measurements

The maximum dissolution rate of gold in cyanide solutions equal to $2.5\text{ mg}\cdot\text{cm}^{-2}\cdot\text{h}^{-1}$ corresponds to the current density $1\text{ mA}\cdot\text{cm}^{-2}$. This was used to determine conditions for QCM reaction rate measurements. The tests at different oxidant concentrations were done to determine the redox potential that exceeds the gold dissolution rate $1\text{ mA}\cdot\text{cm}^{-2}$. Based on the polarization curves, the potential was 150–250 mV in the ammonia–thiosulfate solution, 60–100 mV in the thiourea solution, 400–500 mV in the thiocyanate solution, and 750–800 mV in the chloride solution. In the ammonia–thiosulfate solution passivation was noticed at the potentials over 200 mV and this may prevent reaching the wanted dissolution rate.

The control of redox potential was easy when using ferric sulfate in the thiourea and thiocyanate solutions and when using sodium hypochlorite in the sodium chloride solution. The redox potential increased with increasing oxidant concentration

(Table 3) and they remained constant for several minutes. The effect of cupric ions on the redox potential in the ammonia–thiosulfate solution was fluctuating and not easy to control (Fig. 6).

Table 3. Redox potentials in thiourea, thiocyanate and sodium chloride solutions

| Oxidant | E_{redox} , mV in 0.13 M $\text{SC}(\text{NH}_2)_2$, 36 mM $\text{Na}_2\text{S}_2\text{O}_3$, pH = 1.0, T = 25 °C | E_{redox} , mV in 0.2 M NaSCN , 5 mM $\text{SC}(\text{NH}_2)_2$, pH = 2.0, T = 25 °C | E_{redox} , mV in 3 M NaCl T = 25 °C |
|--|---|--|--|
| 10 g dm^{-3} Fe^{3+} | 555±5 | | |
| 2.5 g dm^{-3} Fe^{3+} | 545±5 | | |
| 1.3 g dm^{-3} Fe^{3+} | 505±5 | | |
| 1.0 g dm^{-3} Fe^{3+} | | 650±5 | |
| 0.5 g dm^{-3} Fe^{3+} | | 610±5 | |
| 0.25 g dm^{-3} Fe^{3+} | | 570±5 | |
| 25 g dm^{-3} OCl^- , pH = 2 | | | 1320±10 |
| 3.5 g dm^{-3} OCl^- , pH = 2 | | | 1220±10 |
| 3.5 g dm^{-3} OCl^- , pH = 3 | | | 1170±10 |

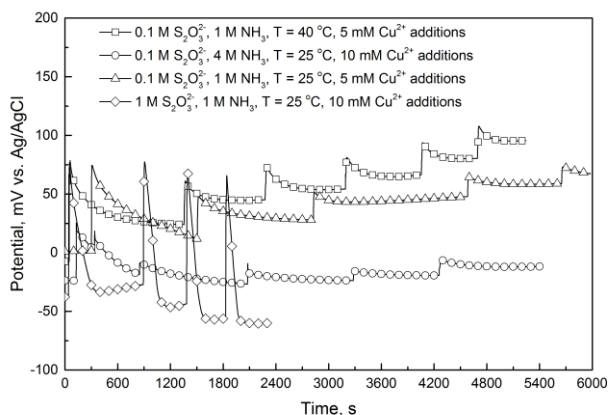


Fig. 6. Effect of Cu(I) ion on redox potential in ammonia – thiosulfate solution

Weight loss tests

Weight loss tests with gold plated QCM crystal were done in three solutions:

- 0.13 M $\text{SC}(\text{NH}_2)_2$, 36 mM $\text{Na}_2\text{S}_2\text{O}_3$, 2.2 g· dm^{-3} Fe^{3+} , pH = 1.0, T = 25 °C
- 0.2 M NaSCN , 5 mM $\text{SC}(\text{NH}_2)_2$, 0.4 g· dm^{-3} Fe^{3+} , pH = 2.0, T = 25 °C
- 3 M NaCl , 3.5 g· dm^{-3} OCl^- , pH = 3.0, T = 25 °C.

The redox potential was 250±15 mV in the thiourea solution, 420±10 mV in the thiocyanate solution, and 700±100 mV in the chloride solution. The ammonia–thiosulfate solution was excluded from this test series because of difficulties in controlling the redox potential.

Figure 7 shows the weight losses during the QCM measurements. The quartz crystal lost weight as gold was dissolved and the weight change stopped when only the chromium layer was in contact with the solution. The dissolution rate was determined from the decreasing slope. Dissolution rate was $1.66 \pm 0.08 \text{ mg} \cdot \text{cm}^{-2} \cdot \text{h}^{-1}$ in the thiourea solution, $3.40 \pm 0.04 \text{ mg} \cdot \text{cm}^{-2} \cdot \text{h}^{-1}$ in the thiocyanate solution, and $8.60 \pm 0.23 \text{ mg} \cdot \text{cm}^{-2} \cdot \text{h}^{-1}$ in the chloride solution. The dissolution rates are in the high end of the rates shown in Table 1.

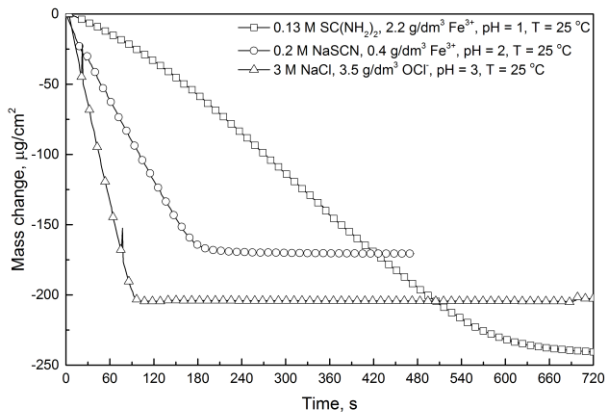


Fig. 7. Weight loss in QCM tests

Decision-support tool

A decision-support tool for development of gold extraction processes was developed using case-based reasoning (Sauer, 2013). The case-based reasoning is similar to human problem solving based on an experience. It operates by taking a problem (query) and searching for similar problems and their solutions (cases) from the case base. The tool called Auric Advisor operates on two levels. The first level searches for cases that describe existing processes most similar to the currently studied raw material. The process development follows the idea that similar raw materials can be treated using similar processes. The second level searches for cases that describe single unit processes or modifications of the unit processes. Literature and laboratory experiments are the sources for the cases (Rintala, 2012). The tests reported in this work provided new cases for the second level case base of the Auric Advisor tool.

Knowledge formalisation is the process of encoding knowledge in a case-based reasoning system. The target is to find balance between necessary grade of detail of knowledge and a lean and minimalistic knowledge model for efficient calculations. Knowledge formalisation begins with identification of the relevant entities in a domain, as well as their relationship with each other. Then, characteristics and important attributes are established for each entity and the form of case representation

is determined. The important attributes in leaching are presented in Table 4. These attributes and their values form in the case base. The most important outcomes of leaching are the dissolution rate, gold recovery and leaching time. The attribute values in Table 4 are taken from Table 1, and the results presented in this paper are included. The lixiviant chemistry has high weight, as basic chemistries cannot be mixed. The ligand concentration is known to affect the dissolution rate, but ligand, stabilisator and oxidant concentrations have to be matched. The oxidant and its concentration can also be coded as the redox potential. Temperature and pH will have a certain variation range, where their effect can be assumed to be monotonous. The missing information, like in Table 4, can be modeled using the regression analysis of similar cases.

Table 4. Case base consists of these attributes and their values for different systems (CN cyanide, TS thiosulfate, TU thiourea, TCN thiocyanate, CL chloride. New results in bold)

| System | Ligand and concentration, mM | | Stabilisator and concentration, mM | | Oxidant and concentration, mM | | T, °C | pH | Rate, mg cm ⁻² h ⁻¹ |
|--------|---|------|---|-----|-------------------------------|------|-------|------|---|
| CN | CN ⁻ | 5 | | | O ₂ | 0.26 | 20 | | 0.07 |
| CN | CN ⁻ | 77 | | | O ₂ | | 25 | 10.5 | 0.85 |
| CN | NaCN | 41 | | | Aerated | | | | 2.5 |
| TS | (NH ₄) ₂ S ₂ O ₃ | 100 | NH ₃ | 500 | Cu ²⁺ | 0.7 | 25 | | 0.09 |
| TS | S ₂ O ₃ ²⁻ | 100 | NH ₃ | 400 | Cu ²⁺ | 10 | 20 | | 2.7 |
| TU | SC(NH ₂) ₂ | 5 | Na ₂ S ₂ O ₃ | 200 | Sat. O ₂ | | 30 | | 0.03 |
| TU | SC(NH ₂) ₂ | 26.3 | H ₂ SO ₄ | 100 | Fe ³⁺ | 5 | 25 | | 1.7 |
| TU | SC(NH ₂) ₂ | 130 | Na ₂ S ₂ O ₃ | 36 | Fe ³⁺ | 40 | 25 | 1.0 | 1.66 |
| TCN | SCN ⁻ | 50 | | | | | amb. | 2 | 0.73-2.2 |
| TCN | NaSCN | 200 | SC(NH ₂) ₂ | 5 | Fe ³⁺ | 7 | 25 | 2 | 3.4 |
| CL | NaCl | 85 | | | NaOCl | 27 | 20 | 6 | 0.5 |
| CL | NaCl | 1700 | | | HOCl | 0.8 | 20 | 3.5 | 1.0 |
| CL | NaCl | 850 | | | NaOCl | 135 | 20 | 6 | 10 |
| CL | NaCl | 1700 | | | OCl ⁻ | 190 | 20 | 6 | 13 |
| CL | NaCl | 3000 | | | OCl ⁻ | 70 | 25 | 3 | 8.6 |

Information in the case base such as Table 4 is used by following way. The wanted outcome of the process step is defined. A vector containing the outcome attributes and their values is formed. The Auric Advisor tool will then select from the case base process alternatives that have similar outcome vectors as the wanted target. When the suitable cases are not found, the decision support tool can use models to indicate possible changes in attribute values to provide an outcome vector that is closer to the target.

Conclusions

The most studied alternative lixiviants for cyanide in gold extraction are the thiosulfate, thiourea, thiocyanate and halide solutions. The dissolution rates in these systems can vary up to two orders of magnitude depending on the lixiviant and oxidant concentrations. For selection of suitable leaching chemistry a decision-support tool has been developed.

In this work dissolution rates of gold have been measured in thiosulfate, thiourea, thiocyanate and halide solutions using the rotating disc electrode (RDE) and quartz crystal microbalance (QCM) methods. The dissolution rates at the open circuit potential in air saturated solutions without other oxidants were in the order of 0.1 to 6 $\mu\text{A}\cdot\text{cm}^{-2}$, and several orders of magnitude lower than what is needed in realistic processes. Oxidant levels to reach the current density equal to 1 $\text{mA}\cdot\text{cm}^{-2}$ were determined. The QCM tests in the determined solutions showed the rate of $1.66\pm 0.08 \text{ mg}\cdot\text{cm}^{-2}\cdot\text{h}^{-1}$ in the thiourea solution, $3.40\pm 0.04 \text{ mg}\cdot\text{cm}^{-2}\cdot\text{h}^{-1}$ in the thiocyanate solution, and $8.60\pm 0.23 \text{ mg}\cdot\text{cm}^{-2}\cdot\text{h}^{-1}$ in the chloride solution.

Acknowledgements

This research was carried out as part of the Finnish Metals and Engineering Competence Cluster (FIMECC)'s ELEMET program. One of the authors (M.K.) is thankful to the K.H. Renlund's Foundation for financial support.

References

- AYLMORE M.G., 2005, *Alternative lixiviants to cyanide for leaching gold ores*. Developments in Mineral Processing, Vol. 15. Mike D. Adams (Ed.), Elsevier, Amsterdam, pp. 501-539.
- DESCHENES G., 2005, *Advances in the cyanidation of gold*. *Developments in Mineral Processing*, Vol. 15. Mike D. Adams (Ed.), Elsevier, Amsterdam, pp. 479-500.
- EUROSTAT (European Commission), 2010, Impacts of Gold Extraction in the EU. Information Hub Enquiry 2010-001, online: http://ec.europa.eu/environment/waste/mining/pdf/IH_2010-001.pdf.
- FENG D., VAN DEVENTER J.S.J., 2011, *Thiosulphate leaching of gold in the presence of orthophosphate and polyphosphate*. Hydrometallurgy 106(1-2), 38-45.
- HILSON G, MONHEMIUS A.J., 2006, Review article: *Alternatives to cyanide in the gold mining industry: what prospects for the future?* Journal of Cleaner Production 14(12-13), 1158-1167.
- JEFFREY M.I., CHOO W.L., BREUER P.L., 2005, *A comparison of electrochemical methods and the rotating electrochemical quartz crystal microbalance for measuring hydrometallurgical reaction kinetics*. Hydrometallurgy 79(1-2), 69-79.
- LAITOS J.G., 2012, *The Current Status of Cyanide Regulations*. Engineering & Mining Journal, online: <http://www.e-mj.com/features/1656-the-current-status-of-cyanide-regulations.html>.
- LI J., SAFARZADEH M.S., MOATS M.S., MILLER J.D., LEVIER K.M., DIETRICH M., WAN R.Y., 2012a, *Thiocyanate hydrometallurgy for the recovery of gold. Part I: Chemical and thermodynamic considerations*. Hydrometallurgy 113-114(1), 1-9.
- LI J., SAFARZADEH M.S., MOATS M.S., MILLER J.D., LEVIER K.M., DIETRICH M., WAN R.Y., 2012b, *Thiocyanate hydrometallurgy for the recovery of gold. Part II: The leaching kinetics*. Hydrometallurgy 113-114(1), 10-18.

- MURTHY D.S.R, PRASAD P.M., 1996, *Leaching of gold and silver from Miller Process dross through non-cyanide leachants*. Hydrometallurgy 42(1), 27-33.
- NAM K.S., JUNG B.H., AN J.W., HA T.J., TRAN T., KIM M.J., 2008, *Use of chloride-hypochlorite leachants to recover gold from tailing*. International Journal of Mineral Processing 86(1-4), 131-140.
- RINTALA L., AROMAA J., FORSEN O., 2012, *Use of published data in the development of hydrometallurgical flow sheet for gold using decision-support tools*. XXVI International Mineral Processing Congress 2012, New Delhi, India, 24-28.9.2012. p. 4485.
- SAUER C.S., RINTALA L., ROTH-BERGHOFER T., 2013, *Knowledge formalisation for hydrometallurgical gold ore processing*. Research and Development in Intelligent Systems XXX, M. Bramer, M. Petridis (eds.) Springer, pp. 291-304.
- SENANAYAKE G., 2004, *Gold leaching in non-cyanide lixiviant systems: critical issues on fundamentals and applications*. Minerals Engineering 17(6), 785-801.
- SYED S. 2012. *Recovery of gold from secondary sources - A review*. Hydrometallurgy 115-116(1), 30-51.
- VON BONSDORFF R., AROMAA J., FORSEN O., BARKER M., 2007, *Rate of gold dissolution in concentrated cupric chloride solutions*. Cu2007 Volume IV: The John Dutilleul International Symposium on Copper. Toronto, Canada, 25-30.8.2007, pp. 121-131.
- ZELINSKY A.G., NOVGORODTSEVA O.N., 2013, *E_{QCM} study of the dissolution of gold in thiosulfate solutions*. Hydrometallurgy 138(1), 79-83.

Received May 2, 2014; reviewed; accepted July 25, 2014

HIGHLY EFFICIENT FACILITATED MEMBRANE TRANSPORT OF PALLADIUM(II) IONS FROM HYDROCHLORIC ACID SOLUTIONS THROUGH PLASTICIZER MEMBRANES WITH CYANEX 471X

Beata POSPIECH

Department of Chemistry, Czestochowa University of Technology, Armii Krajowej 19, 42-200 Czestochowa, Poland, b.pospiech@wip.pcz.pl

Abstract: In this work the efficient recovery of palladium(II) ions from hydrochloric acid solutions by transport through polymer inclusion membranes (PIMs) was studied. The membrane consisted of cellulose triacetate (CTA) as the polymeric support, o-nitrophenyl octyl ether (ONPOE) as the plasticizer and Cyanex 471X (triisobutylphosphine sulphide) as the ion carrier. The effect of various parameters on the transport kinetics and the recovery factor of palladium(II) was studied, including concentration of Cyanex 471X in the membrane, hydrochloric acid concentration in the source phase and potassium thiocyanate (KSCN) concentration in the receiving phase.

Keywords: *palladium, platinum group metals (PGMs), Cyanex 471X, polymer inclusion membrane (PIM)*

Introduction

Recently, we can observe growing interest in application of membrane processes for metal ions separation. Transport processes across liquid membranes, especially polymer inclusion membranes (PIMs) are a good alternative to classical separation methods, such as solvent extraction, ion exchange, precipitation etc. (De San Miguel et al., 2011). Liquid membrane processes have been suggested as a clean technology due to their characteristic of high specificity, high intensity and productivity as well as low energy requirements (O'Rourke et al., 2011). Moreover, in liquid membranes the extraction and stripping processes occur simultaneously, in a single stage. High selectivity, operational simplicity, use of small amount of solvents/extractants, as well as low cost of process belong to the most important advantages of transport through liquid membranes (De Agreda et al., 2011).

Polymer inclusion membranes contain polymeric support (i.e. CTA), plasticizer and ion carrier. The ion carrier is generally a complexing agent or an ion exchanger, which chemically interacts with the species from aqueous solutions and retains it on membrane (Pospiech and Walkowiak, 2010). Plasticizer improves membrane flexibility, retention and transport properties. It penetrates between the polymer chains and increases the distance between them, such that the plasticizing process reduces the intermolecular forces (hydrogen bonds or van der Waals forces) between the polymer chains (Gherasim et al., 2011). Polymer plays a crucial role in providing the mechanical resistance of the membranes. Despite of a great variety of solid polymers, which are used in many industrial application, only cellulose triacetate (CTA) or poly(vinyl chloride) (PVC) are used as the polymer support in PIMs (Gherasim et al., 2011; De San Miguel et al., 2011). This type of liquid membranes shows higher chemical stability and mechanical resistance comparing to the most commonly used liquid membranes, i.e. bulk liquid membranes (BLMs), emulsion liquid membranes (ELMs) and supported liquid membranes (SLMs). As an example Pospiech (2012a; 2013) showed neither loss of ion carriers (Cyanex 471X and Cyanex 301) nor any significant loss of performance of PIMs after repetitive cycles during the transport of Ag(I) and Co(II). In other work (Gardner et al., 2004) authors studied the resistance to hydrolysis of various PIMs under acidic and alkaline conditions. They prepared membranes using few cellulose derivatives and showed that durability increased when acetyl substituent on the cellulose polymer was replaced by propionyl or butyryl group. It was observed that transport of metal ions across PIM decreased as the alkyl chain lengths increased. Gherasim et al. (2011) reported the preparation of PIM containing only PVC polymer and bis(2-ethylhexyl) phosphoric acid (D2EHPA) as ion carrier. Their investigation revealed that the carrier is dispersed in the polymer matrix and confirmed its plasticizing role towards the PVC polymer matrix. These PIMs containing only PVC polymer and D2EHPA showed also higher chemical stability and mechanical resistance than other types of liquid membranes.

Natural resources of platinum group metals (PGMs) are limited. On the other hand, the demand for these metals increases due to their wide application (Fornalczyk and Saternus, 2013). Recycling of spent materials is appropriate for many important reasons, i.e. it is often beneficial to recover valuable materials, especially if their supply is limited (Chagnes and Pospiech, 2013). Spent catalysts contain a number of noble metals, such as platinum (Pt), palladium (Pd), rhodium (Rh) and are the potential source of these important metals (Saternus and Fornalczyk, 2013; Pospiech, 2012b). Palladium is used extensively in the electrical and electronics industry and as a catalyst in the chemical industry. Since this metal has a very high value, its efficient recovery from mainly acidic aqueous solutions is of considerable importance (Kolev et al., 2000).

The hydrometallurgical recovery of platinum group metals (PGMs) is based on the solvent extraction processes because the noble metal ions are easily extractable into the organic phase with various reagents (Cieszynska and Wisniewski, 2011).

Palladium(II) ions were extracted from different solutions with commercial extractants, i.e. Cyanex 471X (Ahmed et al., 2011), LIX 84I and Alamine 336 (Reddy et al., 2010), 2-ethylhexyl phosphonic acid mono-2-ethylhexyl ester (PC-88A) (Bandeekar and Dhadke, 1998) and ionic liquids Cyphos 101 and Cyphos 104 (Cieszynska and Wisniewski, 2011).

Literature survey revealed that the transport process of Pd(II) ions through liquid membranes have been reported extensively by many researchers, employing ion carriers, such as tricaprilmethylammonium chloride (Aliquat 336) in PIMs (Kolev et al., 2000), Cyanex 471X in SLMs (Fontas et al., 2003), di(2-ethylhexyl)phosphoric acid (D2EHPA) and tri-*n*-octylamine (TOA) in SLMs (Sadyrbaeva, 2013) and calixarenes in PIMs (Fontas et al., 2007).

Cyanex 471X have not been used yet as an ion carrier of Pd(II) ions in transport process through polymer inclusion membranes. The results of the solvent extraction of Pd(II) with Cyanex 471X in kerosene were reported by Ahmed et al. (2011). The stripping of the loaded organic phase was performed using thiosulphate solution. The method was developed for the recovery of Pd(II) from a synthetic chloride solution similar in composition to that expected from the leaching of spent automotive catalyst and the recovery of Pd(II) was found to be 75%. This study confirms that Cyanex 471X can be used as the ion carrier of Pd(II) from chloride aqueous solutions. Therefore, the main aim of present work is to study the transport process of Pd(II) ions from hydrochloric solutions using PIMs based on cellulose triacetate with a commercial carrier (Cyanex 471 X). The effect of ion carrier concentration in the membrane, hydrochloric acid concentration in the source phase and the stripping agent concentration in the receiving phase was studied in order to determine the optimal conditions of transport process, maximum initial flux and recovery factor of Pd(II) ions from hydrochloric acid solutions across PIM.

Experimental

Inorganic chemicals, i.e. palladium(II) chloride (PdCl_2), potassium thiocyanate (KSCN), hydrochloric acid (HCl), were of analytical grade and were purchased from POCh (Gliwice, Poland). Aqueous solutions were prepared with deionized water (conductivity of $0.1 \mu\text{S}/\text{cm}$ at 25°C). The initial concentration of Pd(II) in the source phase was 0.001M .

Organic reagents, i.e. triisobutylphosphine sulphide (Cyanex 471X), cellulose triacetate (CTA), *o*-nitrophenyl octyl ether (ONPOE), dichloromethane were of analytical reagent grade (Fluka) and were used without further purification. The density of plasticizer ONPOE was 1.041 gcm^{-3} .

Synthesis of polymer inclusion membrane

A solutions of cellulose triacetate (CTA), the ion carrier (Cyanex 471X), and the plasticizer (ONPOE) in dichloromethane were prepared. A portion of this solution was

poured on a flat-bottom glass Petri dish which was kept on a leveled surface. The organic solvent was allowed to evaporate over a 12 h period. The resultant membrane was peeled off from the Petri dish and this membrane was washed with water and equilibrated in distilled water before use. The thickness of the PIM samples was measured 10 times using a digital micrometer and was shown as average value of these measurements.

Transport experiments

To transport of Pd(II) ions across PIM, a membrane module was used, to which both aqueous phases were pumped with a peristaltic pump (PP1B-05A type, Zalimp, Poland) working at a speed of $100 \text{ cm}^3 \text{ min}^{-1}$ from tanks containing source and receiving phases, respectively. The volume of source and receiving phases was 100 cm^3 . The effective membrane area, which was exposed to both phases was 12.56 cm^2 . Figure 1 shows the schematic diagram of the experimental setup of PIM system. Both, the source and receiving aqueous phases were stirred by a magnetic stirrer. The permeation of metal ions was monitored by sampling of the source phase and the receiving phase. The concentration of metal ions in aqueous phases was analyzed by an atomic absorption spectrophotometer (Solaar 939, Unicam). The source phase pH was controlled by pH meter (pH meter CX-731, Elmetron with combine pH electrode (Hydromet, Poland)). The changes of the solution acidity were negligible. It can be explained by the mechanism of the transport and chemical character of the ion carrier, which belong to solvating reagents. The PIM transport experiments were conducted at room temperature ($23\text{-}25^\circ\text{C}$).

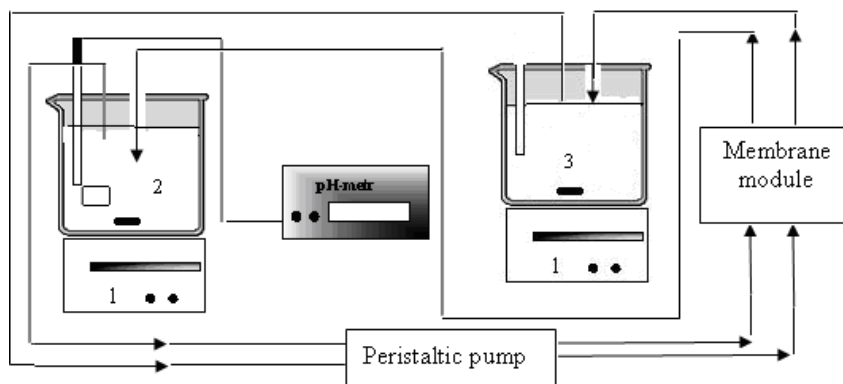


Fig. 1. Diagram of the transport experiments through PIM:
1 – magnetic stirrer, 2 – source phase, 3 – receiving phase

The kinetics of PIM transport process was described by a first-order reaction in metal ion concentration (Danesi, 1984):

$$\ln\left(\frac{c}{c_i}\right) = -kt, \quad (1)$$

where c is the metal ion concentration (M) in the source phase at some given time, c_i is the initial metal ion concentration in the source phase, k is the rate constant (s^{-1}), and t is the time of transport (s).

To calculate the k value, a plot of $\ln(c/c_i)$ versus time was generated. The obtained linear dependence of $\ln(c/c_i)$ versus time allowed to calculate permeability coefficient P ($\mu\text{m}\cdot\text{s}^{-1}$) as:

$$P = \frac{V}{A} k, \quad (2)$$

where V is volume of the aqueous source phase (m^3), and A is an effective area of membrane (m^2). The initial flux J_i ($\mu\text{mol}\cdot\text{m}^{-2}\cdot\text{s}^{-1}$) was determined as:

$$J_i = P \cdot c_i. \quad (3)$$

The recovery factor RF (%) of metal ions from the source phase into receiving phase was calculated as:

$$\ln RF = \frac{c_i - c}{c_i} \cdot 100\%. \quad (4)$$

Results and discussion

Effect of membrane composition on the transport of Pd(II)

The carrier concentration in the membrane phase plays a significant role during the permeation of metal ions in transport processes across PIM. In this stage the effect of Cyanex 471X concentration in the range from $0.5 \text{ mol}\cdot\text{dm}^{-3}$ to $3 \text{ mol}\cdot\text{dm}^{-3}$ (on volume of plasticizer), on the permeation of Pd(II) ions was investigated. The plasticizer concentration was $2.7 \text{ cm}^3/1.0 \text{ g CTA}$. The initial flux of Pd(II) was only $4.7 \mu\text{mol}\cdot\text{m}^{-2}\cdot\text{s}^{-1}$ at $0.5 \text{ mol}\cdot\text{dm}^{-3}$ concentration of the ion carrier in membrane. The permeability coefficient P increases with increasing carrier concentration up to $2.0 \text{ mol}\cdot\text{dm}^{-3}$, and then decreases for higher Cyanex 471X concentration (Fig. 2.). This concentration of Cyanex 471X represents probably a critical value above which the permeability of PIM decreases. The highest efficiency and the initial flux of Pd(II) transport was obtained by using the membrane containing 0.094 g of Cyanex 471X ($2.0 \text{ mol}\cdot\text{dm}^{-3}$ on volume of plasticizer). The highest permeability coefficient P of Pd(II) was $5.38 \mu\text{m}^{-1}$.

The resulting membrane contained 19.9 wt.% CTA and 24.9 wt.% Cyanex 471X and 55.2 wt.% ONPOE. Further increase of carrier concentration in membrane phase caused decrease of metal ion flux, probably due to limited solubility of carrier in ONPOE. This effect can be also attributed to the membrane saturation by the metal – ion carrier complex. The increase of the carrier ion concentration in membrane phase resulted also in increased thickness of the membrane, which affected the transport rates. The resulting membranes had different thickness, i.e. 61, 64, 68, 71, 73 and 78 μm , respectively. The permeability coefficient P of Pd(II) ions transport was the highest for 68 μm thick membrane. Similar results were obtained by Kolev et al. (2000), who investigated palladium(II) ions transport from hydrochloric acid solutions through PIMs for three different concentrations of Aliquat 336, i.e. 30%, 40% and 50%. They found that permeability coefficient P increases with carrier concentration increase until the critical value above which the permeability of PIM decreases.

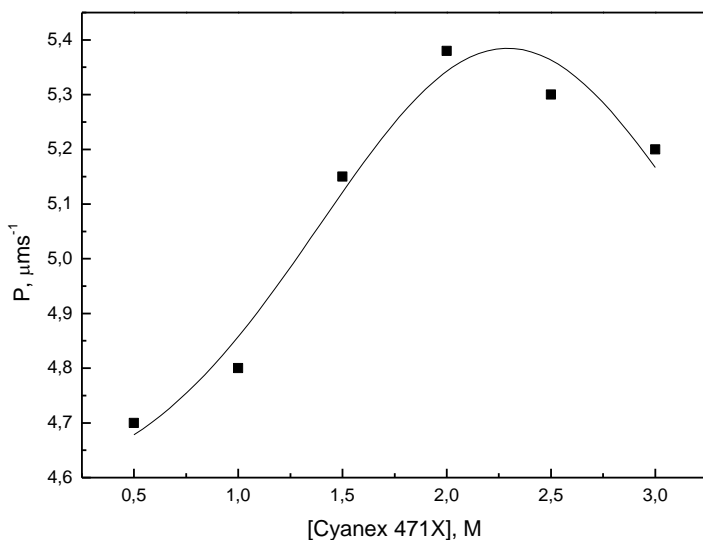


Fig. 2. Effect of Cyanex 471X concentration in PIM on the permeability of Pd(II); PIM: 0.075 g CTA, 2.7 cm^3 ONPOE/1 g CTA; the source phase: 0.001 M Pd(II) in 0.1 M HCl, the receiving phase: 0.5 M KSCN

Effect of hydrochloric acid concentration in the source phase

In next experiments the effect of hydrochloric acid concentration in the source phase on the transport of Pd(II) was studied. The concentration of hydrochloric acid varied in the range 0.1-1.0 M. In this stage the composition of polymer inclusion membranes

was selected based on previous results (19.9 wt.% CTA, 24.9 wt.% Cyanex 471X and 55.2 wt.% ONPOE). The kinetics of Pd(II) transport from the source phase containing different concentration of hydrochloric acid solutions through PIMs was studied. 0.5 M KSCN was used as the stripping phase. Figure 3 shows the dependence of $\ln(c/c_i)$ versus time for the transport processes at different hydrochloric acid concentration in the source phase. The highest rate constant of the transport process was obtained when 0.1 M HCl was used as the source phase. Figure 4 shows the variation of the initial flux of Pd(II) versus the hydrochloric acid concentration in the source phase. Table 1 shows the variation of the rate constants, the permeability coefficients of Pd(II) and recovery factors RF after 8 hours versus hydrochloric acid concentration in the source phase. Recovery factor of Pd(II) was the highest (above 87%) at 0.1 M hydrochloric acid concentration in the source phase. As it can be seen (Fig. 4, Table 1), the initial flux and permeability coefficient depend on the concentration of the acid in the source phase and decreases slightly with HCl concentration increase from 0.1 to 2.0 M. This behavior can be explained by co-transport of hydrochloric acid or the formation of non-extractable palladium(II) anionic species at high chloride concentrations or due to the combination of both factors. Transport in hydrochloric acid medium proceeds according to a coordination solvation mechanism. The equilibrium extraction reaction at the source phase-membrane interface may be represented by:



The observed high efficiency in removal of Pd(II) from acidic aqueous solutions across PIM with Cyanex 471X is due to the fact that triisobutylphosphine sulphide is a soft Lewis base and forms strong complexes with this metal, which is soft acid (Pospiech, 2012a). Pan et al. (2013) also observed that Pd(II) transferring from hydrochloric acid solutions depend on HCl concentration in the aqueous phase.

Table 1. Effect of hydrochloric acid concentration in the source phase on the kinetic parameters of palladium(II) transport. PIM: 0.075 g CTA, 2.7 cm³ ONPOE/1 g CTA, 2 M Cyanex 471 X; the source phase: 0.001 M Pd(II) in HCl, the receiving phase: 0.5 M KSCN

| Concentration of HCl, M | Rate constant, k, h^{-1} | R^2 | Permeability coefficient, $P, \mu\text{ms}^{-1}$ | Recovery factor after 8 h $RF, \%$ |
|-------------------------|--------------------------------------|-------|--|--|
| 0.05 | 0.178 | 98.44 | 3.83 | 75.3 |
| 0.1 | 0.243 | 98.89 | 5.38 | 87.2 |
| 0.3 | 0.227 | 98.71 | 5.03 | 84.4 |
| 0.5 | 0.219 | 98.34 | 4.85 | 83.5 |
| 1.0 | 0.201 | 98.03 | 4.44 | 81.7 |
| 2.0 | 0.192 | 98.51 | 4.12 | 78.0 |

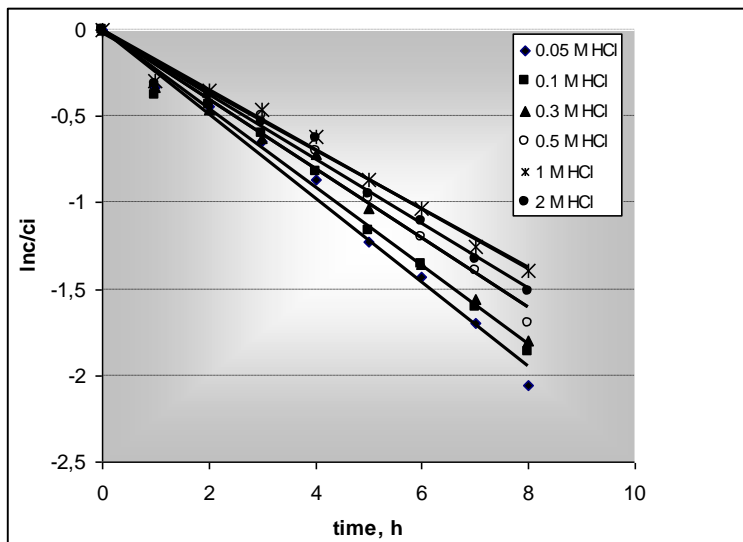


Fig. 3. Relationship of $\ln(c/c_i)$ vs. time for Pd(II) transport across PIM; PIM: 0.075 g CTA, 2.7 cm³ ONPOE/1 g CTA, 2 M Cyanex 471 X; the source phase: 0.001 M Pd(II) in HCl, the receiving phase: 0.5 M KSCN

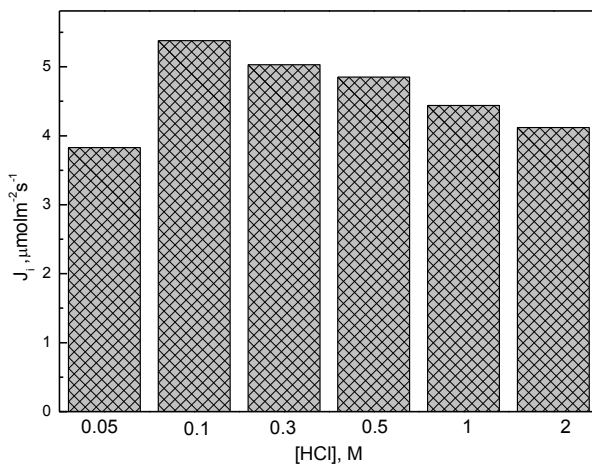


Fig. 4. Effect of HCl concentration in the source phase on the initial flux J_i of Pd(II); PIM: 0.075 g CTA, 2.7 cm³ ONPOE/1 g CTA, 2 M Cyanex 471 X; the source phase: 0.001 M Pd(II) in HCl, the receiving phase: 0.5 M KSCN

Effect of the potassium thiocyanate concentration in the receiving phase

In the next series of the experiments the influence of potassium thiocyanate concentration in the receiving phase on the transport and recovery factor of palladium(II) was studied. The stripping reaction at the membrane/strip interface plays a key role in the transport of metal ions. The transport of Pd(II) can be enhanced by the presence of thiocyanate, owing to formation of mixed-ligand Pd(II)-Cl⁻SCN⁻ Cyanex 471X complexes. In order to analyze the effect of KSCN concentration on the transport of Pd(II), the aqueous solutions of KSCN with concentration ranged from 0.05 to 0.5 M were prepared and used as receiving phase. The polymer inclusion membranes contained Cyanex 471X (2.0 mol/dm³ on the volume of plasticizer) and 2.7 cm³ ONPOE/1 g CTA. Kinetic parameters of the transport of Pd(II) and the recovery factor after 8h are shown in Table 2. All parameters increases with increase of KSCN concentration in the receiving phase. The recovery factor of Pd(II) reaches maximum for 0.5 M KSCN in the receiving phase. As it can be observed, this process depends on thiocyanate concentration in the receiving phase due to the formation of different Pd-SCN-Cl⁻ species which are transported in different extent with Cyanex 471X. Hidalgo et al. (1991) reported that analysis of the metal distribution suggests the formation of PdCl(SCN) Cyanex 471X, PdCl(SCN)₂Cyanex 471X and Pd(SCN)₂Cyanex 471X in the organic phase. The ultraviolet absorption spectra of the organic phase support the hypothesis of formation of mixed-ligand complexes.

Table 2. Effect of KSCN concentration in the receiving phase on the kinetic parameters of Pd(II) transport and the recovery factor. PIM: 0.075 g CTA, 2.7 cm³ ONPOE/1 g CTA, 2 M Cyanex 471 X; the source phase: 0.001 M Pd(II) in 0.1 M HCl

| Concentration of KSCN, M | Rate constant, k, h^{-1} | Initial flux, $J_i, \mu\text{molm}^{-2}\text{s}^{-1}$ | Recovery factor $RF, \%$ |
|--------------------------|-----------------------------------|---|--------------------------|
| 0.05 | 0.138 | 3.06 | 65.2 |
| 0.1 | 0.155 | 3.43 | 69.8 |
| 0.3 | 0.180 | 3.97 | 74.3 |
| 0.5 | 0.243 | 5.38 | 87.2 |

Conclusions

The obtained results allow to conclude that transport process across polymer inclusion membranes with Cyanex 471X as the ion carrier can be used as the method for the recovery of palladium(II) from hydrochloric acid solutions in the studied conditions. The results show that the initial fluxes and recovery factors depend on the ion carrier concentration, as well as concentration of hydrochloric acid in the source phase and potassium thiocyanate concentration in the receiving phase. The obtained results show that transport process through PIM containing 19.9 wt.% CTA and 24.9 wt.% Cyanex 471X and 55.2 wt.% ONPOE enables extraction above 87% of Pd(II) from 0.1 M HCl

into 0.5 M KSCN after 8 h. Finally, the separation system developed can be successfully applied to the recovery of palladium(II) ions from chloride aqueous solutions in the studied conditions.

References

- AHMED, I.M., NAYL, A.A., DAOUD J.A., 2011, *Extraction of palladium from nitrate solution by Cyanex 471X*, Internat. J. Miner. Process. 101, 89-93.
- AROUS, O., KERDJOUJ, H., SETA, P., 2004, *Comparison of carrier-facilitated silver(I) and copper(II) ions transport mechanisms in a supported liquid membrane and in a plasticized cellulose triacetate membrane*, J. Membr. Sci., 241 (2), 177-186.
- BANDEKAR, S.V., DHADKE, P.M., 1998, *Solvent extraction separation of platinum(IV) and palladium(II) by 2-ethylhexyl phosphonic acid mono-2-ethylhexyl ester*, Sep. Purif. Technol., 13, 129-135.
- CHAGNES, A., POSPIECH, B., 2013, *A brief review on hydrometallurgical technologies for recycling spent lithium-ion batteries*, J. Chem. Technol. Biotechnol. 88 (7), 1191-1199.
- CIESZYNSKA, A., WISNIEWSKI, M., 2011, *Selective extraction of palladium(II) from hydrochloric acid solutions with phosphonium extractants*, Sep. Purif. Technol. 80, 385-389.
- DANESI, P.R., 1984, *Separation of metal species by supported liquid membranes*, Sep. Sci. Technol. 19, 857-879.
- DE AGREDA, D., GARCIA-DIAZ, I., LOPEZ, F.A., ALGUACIL, F.J., 2011, *Supported liquid membranes technologies in metals removal from liquid effluents*, Rev. Metal., 47, 146-168.
- DE SAN MIGUEL, E., MONROY-BARETTO, R., AGUILAR, J.C., OCAMPO, A., DE GYVES J., 2011, *Structural effects on metal ion migration across polymer inclusion membranes: Dependence of membrane properties and transport profiles on the weight and volume fractions of the components*, J. Membr. Sci. 379, 416-425.
- FONTAS, C., ANTICOL, E., VOCANSON, F., LAMARTINE, R., SETA, P., 2007, *Efficient thiocalix[4]arenes for the extraction and separation of Au(III), Pd(II) and Pt(IV) metal ions from acidic media incorporated in membranes and solid phases*, Sep. Purif. Technol., 54, 322-328.
- FONTAS, C., SALVADO, V., HIDALGO, M., 2003, *Selective enrichment of palladium from spent automotive catalysts by using a liquid membrane system*, J. Membr. Sci., 223, 39-48.
- FORNALCZYK, A., SATERNUS, M., 2013, *Platinum recovery from used auto catalytic converters in electrorefining process*, METABK 52(2) 219-222.
- GARDNER, J., WALKER, J., LAMB, J., 2004, *Permeability and durability effects of cellulose polymer variation in polymer inclusion membranes*, J. Membr. Sci. 229, 87-93.
- GHERASIM, C.V., CRISTEA, M., 2011, *New polymer inclusion membrane. Preparation and characterisation*, Dig. J. Nanomater. Biostructur. 6, 1499-1508.
- HIDALGO, M., MASANA, A., SALVADO, V., MUÑOZ, M., VALIENTE, M., 1991, *Extraction of palladium with tri-isobutylphosphine sulphide (Cyanex 471) in toluene from chloride solutions containing thiocyanate*, Talanta 38, 483-488.
- KOLEV, S.D., SAKAI, Y., CATTRALL, R.W., PAIMIN, R., POTTER, I.D., 2000, *Theoretical and experimental study of palladium(II) extraction from hydrochloric acid solutions into Aliquat 336/PVC membranes*, Anal. Chim. Acta, 413, 241-246.
- O'ROURKE, M., DUFFY, N., De MARCO, R., POTTER, I., 2011, *Electrochemical impedance spectroscopy – a simple method for the characterization of polymer inclusion membranes containing Aliquat 336*, Membranes, 1, 132-148.

- PAN, L., BAO, X., GU, G., 2013, *Solvent extraction of palladium(II) and effective separation of palladium(II) and platinum(IV) with synthetic sulfoxide MSO*, J. Min. Metall. Sec. B-Metall. 49 (1) B (2013) 57-63.
- POSPIECH, B., 2012(a), *Separation of silver(I) and copper(II) from aqueous solutions by transport through polymer inclusion membranes with Cyanex 471X*, Sep. Sci. Technol. 47, 1413-1419.
- POSPIECH, B., 2012(b), *Studies on platinum recovery from solutions after leaching of spent catalysts by solvent extraction*, Physicochem. Probl. Miner. Process. 48, 239-246.
- POSPIECH, B., WALKOWIAK, W., 2010, *Studies on iron(III) removal from chloride aqueous solutions by solvent extraction and transport through polymer inclusion membranes with D2EHPA*, Physicochem. Probl. Miner. Process., 44, 195-204.
- POSPIECH, B., 2013, *Hydrometallurgical recovery of cobalt(II) from acidic chloride solutions by transport through polymer inclusion membranes*, Physicochem. Probl. Miner. Process., 49(2), 641-649.
- REDDY, B.R., RAJU, B., LEE, J.Y., PARK, H.K., 2010, *Process for the separation and recovery of palladium and platinum from spent automobile catalyst leach liquor using LIX 84I and Alamine 336*, J. Hazard. Mater., 180, 253-258.
- SADYRBAEVA, T., 2006, *Separation of copper(II) from palladium(II) and platinum(IV) by di(2-ethylhexyl)phosphoric acid-based liquid membranes during electrodialysis*, J. Membr. Sci., 275, 195-201.
- SATERNUS, M, FORMALCZYK, A, 2013, *Possible ways of refining precious group metals (PGM) obtained from recycling of the used auto catalytic converters*, METABK 52(2), 267-270.

Received June 13, 2014; reviewed; accepted August 8, 2014

ALKALINE LEACHING OF ZINC FROM STAINLESS STEEL ELECTRIC ARC FURNACE DUSTS

Anna STEFANOVA, Jari AROMAA, Olof FORSEN

Aalto University, Department of Materials Science and Engineering, PO Box 16200, FI-00076, Aalto, Finland,
anna.stefanova@aalto.fi

Abstract: Stainless steel production generates dust and sludge that are considered as a harmful waste. These dusts contain also valuable metals but extraction and recovery of valuables is difficult due their complex composition. Zinc is the most troublesome element in the dust and it hinders direct recycling of dust back into furnaces. In this paper two different stainless steel electric arc furnace dusts (EAF1 and EAF2) from Outokumpu Stainless (Tornio, Finland), were leached using NaOH solutions. The purpose was to selectively leach out zinc from the dusts and to find factors that affected most dissolution of zinc. From all leaching factors temperature, agitation speed and NaOH concentration were found to be statistically strongly significant, whereas a liquid-to-solid ratio and bubbling gas were only somehow significant. Two experiments from the test series gave clearly higher zinc extraction, that is around 60% for EAF1 and 30% for EAF2. For those experiments, a strong 8 M NaOH solution with the high temperature and agitation speed was used but bubbling gas and liquid-to-solid ratio changed. Zinc was leached selectively and practically no iron, chromium and nickel dissolved.

Keywords: *electric arc furnace dust, EAF, stainless steel, zinc, leaching, sodium hydroxide*

Introduction

Stainless steel production generates large quantities of various solid wastes in form of dust and sludge. During production of stainless steel, between 30 and 70 kg of dust and fine waste is generated per mega gram of steel produced (Denton, 2005). Their disposal or possible re-use has been a serious concern for an industry as in most industrial countries stainless steel dusts are considered as a harmful waste. On the other hand, the stainless steel dusts contain valuable metals such as alloying elements like chromium, nickel and molybdenum, and zinc from recycling of galvanized scrap. From economic and environmental point of view, it is desirable to recover the valuables and utilize these wastes (Majuste, 2009). Direct recycling of dust back to stainless steel production is however hindered, mainly because of zinc content of the

dust. Zinc vaporizes easily and condenses into steel production fumes ending up in the flue dust or sludge usually as oxide or ferrite. Zinc content in the stainless steel dusts is found to vary from 1.0 to 16.4 wt% (Nyirenda, 1992; Atkinson, 2001; Leclerc, 2002; Laforest, 2006).

A number of pyrometallurgical, hydrometallurgical and combined processes have been developed to allow better utilization of steel making dusts in primary operations (Xia, 1999; Youcai, 2000; Jha, 2000; Orhan, 2005; Havlik, 2006; Rao, 2006b) but only few of them have reached commercialization. Today, the dust treatment processes are predominantly pyrometallurgical and dusts are recycled in separate treatment plants. However, the drawbacks with pyrometallurgical processes are: high energy consumption, production of a raw zinc oxide with low commercial value, and need of relatively large tonnage of dust to be economically competitive (Nakamura, 2005; Oustadakis, 2010; Rao, 2006b). Hydrometallurgical processes are considered to be suitable for on-site treatment as they can fit on small scale and thus offer interesting alternative (Nakamura, 2008).

Principally, two most studied leaching methods for treating carbon steel dusts are sulfuric acid (H_2SO_4) and caustic soda (NaOH) leaching. The benefit with acid solutions is that they are very accessible and cheap, but the drawbacks are that also iron contained in the dust dissolves and high alkalinity of many dusts consumes a lot of acid for pH adjustment (Palencia, 1999). The major advantage of alkaline leaching is selective solubility of zinc compared to iron compounds, and thus a relatively clean and iron-free solution is obtained, and the complicated iron removal process is avoided. So far, the major obstruction in hydrometallurgical extraction of zinc has been the presence of zinc ferrite (ZnFe_2O_4) in the dust, which is insoluble in many solutions (Havlik, 2006). Usually 30–70% of zinc is in a ferrite form (Leclerc, 2002), but to enhance the zinc recovery, a low temperature roasting step prior to alkaline leaching can be used to convert zinc ferrite into soluble zinc oxide (Xia, 1999).

Dusts from stainless steel production contain many elements making metal extraction very complex and difficult. The stainless steel dust consists mainly of oxide phases that are rich in Fe, Cr, Ca, Zn, Mg, Mn and Ni, with minor amounts of phases that contain alkaline metals (K, Na), halogens (Cl, F), Si, Mo, Pb and S (Ma, 2006). However, chemical compositions and crystalline phases present in the dusts vary considerably depending on the steel grade produced, raw materials used, and operation conditions and procedures (Rao, 2006a). The composition of stainless steel dusts differs substantially from unalloyed steel dusts and typically the stainless steel flue dusts are richer in alloying elements such as chromium, nickel and manganese, but lower in zinc and lead. The previous studies on the hydrometallurgical methods have concentrated on leaching of carbon steel dusts, and for this purpose both acid and alkaline leaching-based laboratory and pilot set-ups have been constructed. Only few studies of acidic leaching of dusts from stainless steel production are found (Majuste, 2009; Kekki, 2012).

In this paper two different stainless steel electric arc furnace dusts (EAF1 and EAF2) from Outokumpu Stainless (Tornio, Finland) were leached using NaOH solutions. The purpose was to selectively leach out zinc from the dusts and to find factors that affected most on dissolution of zinc. Also possible interactions of the studied leaching factors were observed. Alkaline leaching was chosen because of its selectiveness in leaching of zinc when compared to iron compounds.

Materials and methods

Electric arc furnace dust samples (EAF1 and EAF2) from stainless steel production were received from Outokumpu Tornio Works for the leaching experiments. The EAF1 represents dust from line 1 and the EAF2 from line 2. Line 1 uses molten ferrochrome, whereas in line 2 ferrochrome is melted with scrap in EAF. The dusts are a mixture of different production batches, thus represent an average dust composition.

The chemical and mineralogical analyses of dust samples were executed with thw optical microscopy, scanning electron microscopy (SEM), electron probe micro-analyzer (EPMA), X-ray diffraction (XRD), atomic absorption spectroscopy (AAS), and inductively coupled plasma atomic emission spectroscopy (ICP-AES) with molten sodium peroxide or nitro-hydrochloride acid leaching pre-treatment. The dust samples were also subjected in a particle size analysis by a scanning-foto-sedimentograf. The results from the chemical and mineralogical analyses are given in Tables 1 and 2. The

Table 1. The chemical composition of the dust samples

| | Fe | Cr | Zn | Ca | Mn | Ni | Pb | Mg ^a | K ^a | Si ^b |
|---|--|---------------|---------------|----------------|---------------|---------------|---------------|-----------------|----------------|-----------------|
| EAF1 | 19.75 ±1.64 | 8.07 ±3.03 | 7.27 ±0.54 | 10.35 ±0.46 | 2.47 ±0.45 | 1.28 ±0.14 | 0.54 ±0.05 | 2.59 ±0.15 | 1.32 ±0.04 | 4.25 |
| EAF2 | 16.39 ±1.84 | 8.10 ±2.95 | 5.20 ±0.58 | 13.48 ±0.72 | 2.14 ±0.40 | 2.14 ±0.23 | 0.97 ±0.05 | 1.24 ±0.17 | 1.35 ±0.01 | 4.11 |
| Minor amounts 0 - < 1 % in both dusts | Al, B, Ba, C, Cd, Co, Cu, F, Mo, Na, P, S, Sr, V | | | | | | | | | |

^a calculation is based on three analyses, ^b found only in one analysis

Table 2. The main phases identified in dust samples from XRD analysis (Kukurugya, 2013)

| EAF1 | EAF2 |
|--|----------------------------------|
| FeCr ₂ O ₄ | FeCr ₂ O ₄ |
| ZnFe ₂ O ₄ | ZnFe ₂ O ₄ |
| Ni _{0.25} Fe _{0.75} Fe ₂ O ₄ | NiFe ₂ O ₄ |
| ZnO | CaO |
| CaO | CaCO ₃ |
| | MnO ₂ |

main components in the dusts are iron, zinc, chromium and calcium. Zinc was found to be present as zincite (ZnO) and as franklinite (ZnFe_2O_4) in both dusts. The microstructure of dusts consists of larger particles and grains surrounded by finer fraction. The particle size for both dusts was around 1–50 μm . Larger particles often consist of several phases and some phases were encapsulated inside of particles. A part of zinc was found in a concentrate into a fine fraction.

The leaching tests were performed using a 2^{5-2} fractional factorial design with two replicates, where the high and low levels of factor were used (Montgomery, 2009). In this method several factors are changed simultaneously in order to find out the most important factors and the possible interactions of the factors. The studied factors were temperature, NaOH concentration, liquid-solid ratio (cm^3/g), stirring rate and oxygen or nitrogen gas bubbling. The extreme values of factors range were chosen to be certain that the factors will have clear effect. The used temperatures were 25 and 95 $^\circ\text{C}$, and concentrations of NaOH solutions were 2 and 8M. The chosen liquid-to-solid ratios (cm^3/g) were 5 and 30. A stirring rate was adjusted to 100 or 400 rpm, and more oxidative or less oxidative conditions were adjusted using oxygen or nitrogen gas bubbling.

Table 3. Factorial (2^{5-2}) test series used in the leaching experiments

| N ^o | NaOH,M | L/S ratio | Temp., $^\circ\text{C}$ | Bubbling with | Agitation, rpm |
|----------------|--------|-----------|-------------------------|----------------|----------------|
| 1 | 2 | 5 | 25 | O ₂ | 400 |
| 2 | 8 | 5 | 25 | N ₂ | 100 |
| 3 | 2 | 30 | 25 | N ₂ | 400 |
| 4 | 8 | 30 | 25 | O ₂ | 100 |
| 5 | 2 | 5 | 95 | O ₂ | 100 |
| 6 | 8 | 5 | 95 | N ₂ | 400 |
| 7 | 2 | 30 | 95 | N ₂ | 100 |
| 8 | 8 | 30 | 95 | O ₂ | 400 |

The experimental setup for the leaching test consisted of a thermobath (Lauda AquaLine AL25), glass reactor and motor driver stirrer (VWR VOS16). The cover of the glass reactor provided through holes for a mercury thermometer, gas bubbling, stirrer and sampling/feeding. A water-cooled condenser was added to the structure at higher temperatures. The NaOH solutions were prepared from technical grade grains and distilled water, and a volume of 800 cm^3 was set into reactor. Oxygen or nitrogen gas was fed into the reactor for 1 hour and after that 26.67 g or 160 g of dust was charged and the stirring rate was adjusted. A liquid sample was taken off and filtered in the chosen time intervals of 5, 10, 15, 20, 25, 30, 60 and 120 minutes for EAF1 dust, and 5, 15, 30, 60 and 120 minutes for EAF2 dust. The stirring was stopped 30 seconds before each sampling. After filtering the leach samples were analysed for the

amount of leached Zn with a Perkin Elmer 372 AAS device. A part of the samples after 120 min of leaching was analyzed more precisely with a multi-element ICP-AES analysis in order to investigate which other elements leached with zinc.

Results and discussion

The main response under investigation was the percentage of zinc extraction from EAF1 and EAF2 dusts in the leach liquor. The leaching curves of zinc from the 2^{5-2} fractional factorial experiments are shown in Figs. 2 and 3. From the shape of the leaching curves it can be observed that dissolution of zinc is fast, occurring in a few minutes, and then increased only slightly. The maximum amount of leachable zinc in one experiment was usually achieved at the end of the test, which was 120 min of leaching. In a few experiments the plateau was achieved earlier, and then amount of leached zinc decreased that may indicate that part of zinc was precipitated back.

Under the present experimental conditions, zinc extraction varied from 14 to 61% for EAF1 dust. Generally, extraction was lower for EAF2 dust and varied from 8 to 33%. The difference in zinc extraction was arisen most likely from the mineralogical differences of dusts. In addition to zinc oxide, zinc ferrite was also identified in both dusts. Zinc ferrite is difficult to dissolve in alkaline solutions and zinc extraction is dependent on the amount of zinc in ferrite from.

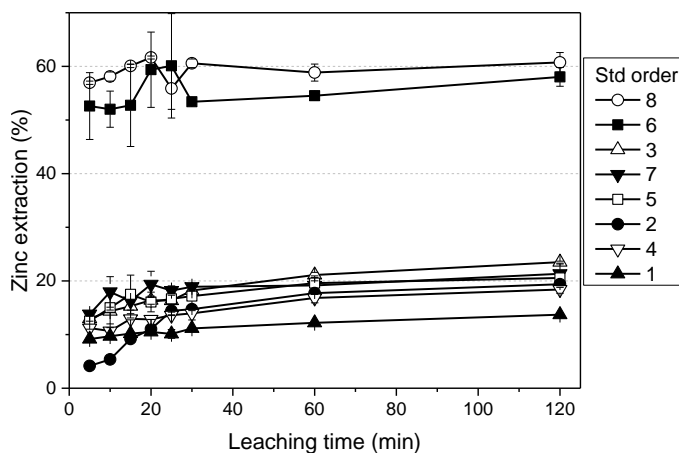


Fig. 1. Leaching curves of zinc dissolution from EAF1 dust according to results from 2^{5-2} fractional factorial design

As can be clearly seen from Figs. 1 and 2 that zinc extraction is higher under two leaching conditions. In both, strong 8 M NaOH solution with high temperature and stirring rate was used, but bubbling gas and liquid-to-solid ratio changed. Almost equivalent zinc extraction was achieved under these two leaching conditions. From

EAF1 dust around 60% of zinc and from EAF2 dust slightly over 30% of zinc was dissolved.

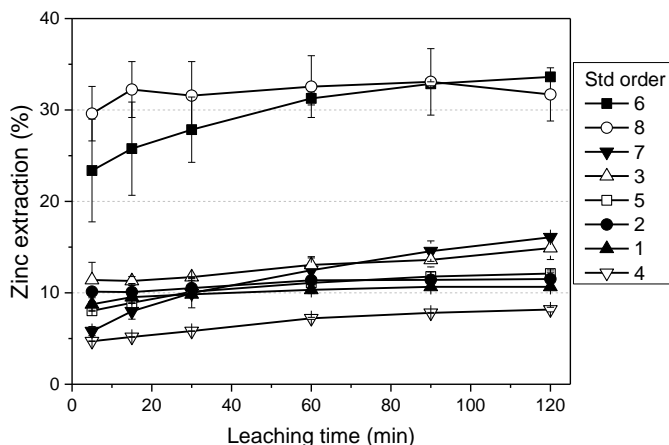


Fig. 2. Leaching curves of zinc dissolution from EAF2 dust according to results from 2⁵⁻² fractional factorial design

To study the effect and possible interaction of the leaching factors on zinc dissolution, the results were analyzed using the Minitab 16 software. Figure 3 shows the pareto charts of the standardized effects of the studied factors after 120 min leaching. Mainly, the same trends can be observed for both dusts. Temperature, NaOH concentration and agitation speed were statistically strongly significant factors of zinc dissolution in both dusts. The liquid-to-solid ratio (L/S) and bubbling gas were only somewhat significant for the EAF1 dust and for the EAF2 dust the L/S ratio was even insignificant. The response was positive for all of the studied quantitative factors and

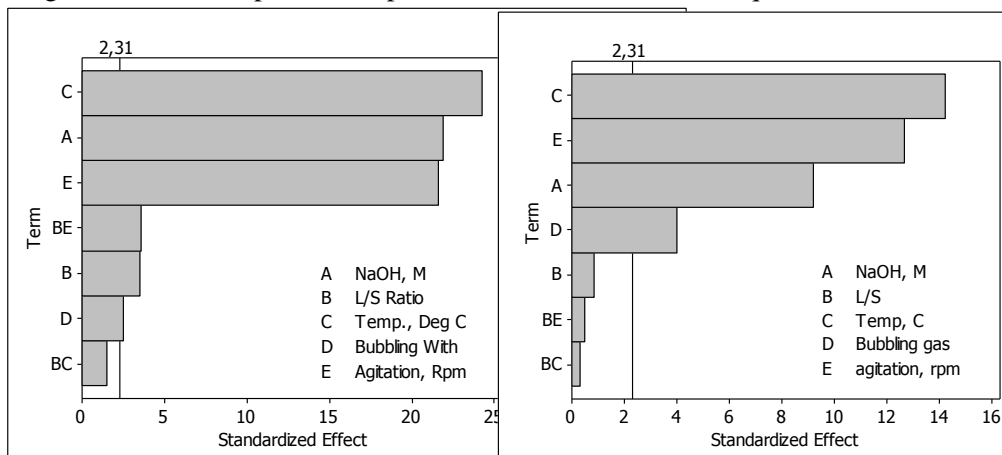


Fig. 3. Pareto chart of standardized effects of studied factors (response is Zn extraction %, alpha = 0.05) for EAF1 (left) and EAF2 (right) dusts

dissolution of zinc was enhanced with increasing level of the factors. Gas bubbling was a qualitative factor and oxygen gas bubbling had a negative response versus dissolution of zinc was enhanced with nitrogen gas bubbling.

Figures 4 and 5 show the interaction charts of the studied leaching factors (determined from extractions after 120 min leaching). The interaction between the factors occurs when the effect that one factor has on the output is dependent on the level of another factor, and the response is different at the low level of the second factor than at the high level of the second factor. For both EAF1 and EAF2 dusts two-factor interactions were found between NaOH concentration and temperature, NaOH concentration and agitation, liquid-to-solid ratio and bubbling gas, and between temperature and agitation. Three of these four interactions were between the factors that stood out with stronger effect on zinc dissolution. The interactions with NaOH

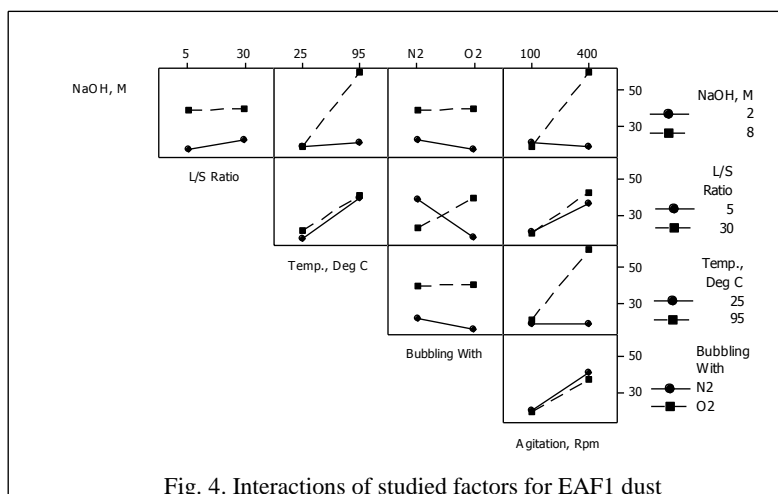


Fig. 4. Interactions of studied factors for EAF1 dust

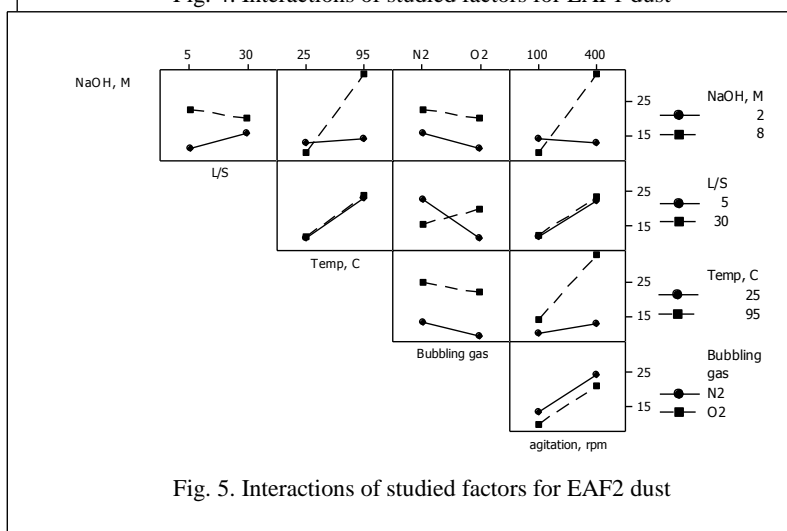


Fig. 5. Interactions of studied factors for EAF2 dust

concentration, stirring rate and temperature are explained by high viscosity of strong NaOH solution. Strong agitation and high temperature enhanced the extraction/dissolution of zinc in strong viscous NaOH solution. The reason for interaction between liquid-to-ratio and bubbling gas is unclear. Bubbling with oxygen reduced zinc extraction with high amount of solid but enhanced it when the amount of solid was low. In the EAF2 dust, the interaction between NaOH concentration and liquid-to-solid ratio was also found. Zinc extraction was slightly increased in low NaOH concentrations but slightly decreased in strong NaOH solution, when small amount of solid was used, but this interaction was not so obvious.

It should be noted that the 2^{5-2} fractional factorial design used in this leaching experiments is a resolution III design, when the main effects are confounded with two-factor interactions. The resolution describes the ability to separate the main effects and interactions from one to another. To increase the resolution and eliminate the confounding between the main effects and two-factor interactions a full fold-over design, in which the signs of all the factors are reversed, can be run and combine to the design used in this study. This would provide clearer basis for optimization of leaching conditions.

The results from the ICP-AES analyses are presented in Table 4. The results showed that zinc was leached selectively. Practically no iron (usually $<1.5 \text{ mg/dm}^3$) and nickel ($< 0.1\text{--}0.21 \text{ mg/dm}^3$) was dissolved. The leaching conditions had only minor effect on dissolution of chromium and less than 3% of chromium was leached from both dusts. In some samples from the EAF2 dust the amount of lead and cadmium was a bit higher, however only 9% of lead and 1% of cadmium was leached. Also the leaching recovery of molybdenum was higher for the EAF2 dust (40 – 60%). As iron and of the valuable alloying elements chromium and nickel remained in the leach residue, for recovering the valuables, the residue could be recycled back into furnaces if the amount of zinc can be lowered to a sufficient level.

Table 4. Amount of certain elements in leachate after 120 min leaching

| | Amount in leachate (mg/dm^3) | | | | | | | |
|------|---|-------------|----------|-------------|------------|-----------|------------|--------------|
| | Zn | Fe | Cr | Ni | Mo | Ca | Pb | Cd |
| EAF1 | 169 - 8690 | < 1.5 | 43- 277 | <0.1 - 0.21 | 4 - 32 | < 5 - 7 | 3 - 62 | < 0.25 |
| EAF2 | 145 - 3234 | <1.5 - 15.5 | 47 - 446 | ≤ 0.11 | 18.3 - 263 | <5 - 14.6 | <2.5 - 188 | <0.25 - 6.51 |

Conclusions

Dusts formed in stainless steel production are considered as a harmful waste in most industrial countries. At the same time these dusts are also a source of valuable metals but their extraction and recovery is difficult due to their complex composition. The most troublesome element in the dust is zinc, which vaporizes easily and condenses into steel production fumes ending up in the flue dust or sludge, usually as oxide or ferrite. In this study two electric arc dusts (EAF1 and EAF2) from stainless steel

production were leached in NaOH solutions aiming to selectively leach out zinc from the dusts, and to find the effect of various leaching factors on dissolution of zinc/find factors that affected most on zinc dissolution.

The results from (2^{5-2}) fractional factorial tests showed that all studied factors (NaOH concentration, temperature, agitation, solid-to-liquid ratio, and oxygen/nitrogen gas bubbling) had statistically significant effect on zinc dissolution, except the solid-to-liquid ratio for the EAF2 dust. However, an increase in the NaOH concentration, temperature and agitation improved zinc extraction preferentially. Two-factor interactions were found between those three factors and also between liquid-to-solid and bubbling gas.

From all the experiments performed in this work, two of them gave higher zinc extraction. In both, strong 8 M NaOH solution with high temperature and stirring rate was used, but bubbling gas and liquid-to-solid ratio changed. Almost equivalent zinc extraction achieved under these two leaching conditions was around 60% for the EAF1 dust and over 30% for the EAF2 dust. The difference in zinc extraction between the dusts arose from the mineralogical differences and is dependent on the amount of zinc in ferrite form.

This study showed that alkaline leaching of zinc from stainless steel EAF dusts using NaOH solutions is selective and practically no iron, chromium and nickel were dissolved. However, the dissolution of zinc is limited due to the presence of zinc ferrites that remains the main problem to be solved. When considering the possibility to recycle dust back to the process, the amount of zinc should be low to effectively recycle dust back to the process. The leaching process can be used in zinc removal if zinc ferrites are decomposed prior to leaching, for example by roasting.

Acknowledgements

This work has been done in the METDUST project of the ELEMET research program funded by FIMECC Oy. The financial support of TEKES, Outokumpu Stainless Oyj and Outotec Oyj is gratefully acknowledged. The analytical work in characterizing the dusts done by the group of Professor Tomas Havlik in Technical University of Kosice and M.Sc. Hannu Makkonen from Oulu University is gratefully acknowledged. The authors are grateful to Mr. Terry Russell for the valuable guidance in data analysis.

References

- ATKINSON, M., KOLARIK, R., 2001, *Chapter 4: Environmental Leadership. Steel Technology Roadmap*, pp, 83 - 120.
- DENTON, G.M., BARCZA, N.A., SCOTT, P.D., FULTON, T., 2005, *EAF Stainless Steel Dust Processing. In: M. Nilmani, Rankin, W.J. (Ed.), Sustainable developments in metals processing, Melbourne, Australia*, pp. 273-283.
- HAVLIK, T., SOUZA, B.V., BERNARDES, A.M., SCHNEIDER, I.A.H., MISKUFOVA, A., 2006, *Hydrometallurgical processing of carbon steel EAF dust. Journal of Hazardous Materials*, B135, 311-318.
- JHA, M.K., KUMAR, V., SINGH, R.J., 2000, *Review of hydrometallurgical recovery of zinc from industrial wastes. Resources Conservation & Recycling*, 33(2001), 1-22.

- KEKKI, A., AROMAA, J., FORSEN, F., 2012, *Leaching characteristics of EAF and AOD stainless steel production dusts*, *Physicochemical Problems of Mineral Processing*, 48, 599-606.
- KUKURUGYA, F., HAVLIK, T., KEKKI, A., FORSEN, O., 2013, *Characterization of dusts from three types of stainless steel production equipment*, *Metall-Forschung*, 67, 154-159.
- LAFOREST, G., DUCHESNE, J., 2006, *Characterization and leachability of electric arc furnace dust made from remelting of stainless steel*, *Journal of Hazardous Materials*, B135, 156-164.
- LECLERC, N., MEUX, E., LECUIRE, J-M., 2002, *Hydrometallurgical recovery of zinc and lead from electric arc furnace dust using monitrolotriacetate anion and hexahydrated ferric chloride*, *Journal of Hazardous Material*, B91, 257-270.
- MA, G., GARBERS-CRAIG, A.M., 2006, *A review on the characteristics, formation mechanism and treatment processes of Cr (VI)-containing pyrometallurgical wastes*, *The Journal of Southern African Institute of Mining and Metallurgy*, 106: 753-763.
- MAJUSTE, D., MANSUR, M.B., 2009, *Leaching of the fraction of the argon oxygen decarburization with lance (AOD-L) sludge for the potential removal of iron*, *Journal of Hazardous Material*, 153(1-2): 89-95.
- MONTGOMERY, D.C., 2009, *Design and Analysis of Experiment*, John Wiley & Sons Inc.
- NAKAMURA, T., 2005, *Zinc recycling technology now and in the future*, In: T. Fujisawa (Ed.), *Lead & Zinc '05. MMIJ*, Kyoto, Japan.
- NAKAMURA, T., SHILBATA, E., TAKASU, T., ITOU, H., 2008, *Basic consideration on EAF dust treatment using hydrometallurgical processes*, *Resources Processing*, 55, 144-148.
- NYIRENDA, R.L., 1992, *The reduction of zinc-rich ferrites and its implication for a caron-type process for carbon steelmaking dust*, *Dissertation Thesis*, Delft University of Technology.
- ORHAN, G., 2005, *Leaching and cementation of heavy metals from electric arc furnace dust in alkaline medium*, *Hydrometallurgy*, 78, 236-245.
- OUSTADAKIS, P., TSAKIRIDIS, P.E., KATSIAPI, A., AGATZINI-LEONARDOU, S., 2010, *Hydrometallurgical process for zinc recovery from electric arc furnace dust (EAFD), Part I: Characterization and leaching by diluted sulphuric acid*, *Journal of Hazardous Material*, 179, 1-7.
- PALENCIA, I., ROMERO, R., IGLESIAS, N., CARRANZA, F., 1999, *Recycling EAF dust leaching residue to the furnace: A simulation study*, *JOM*, 28-32.
- RAO, S.R., 2006A, *Chapter 8: Metallurgical slags, dust and fumes*, *Waste Management Series: Resource Recovery and Recycling from Metallurgical Wastes*, pp. 269-327.
- RAO, S.R. (ED.), 2006B, *Metallurgical slags, dust and fumes*, *Waste Management Series: Resource Recovery and Recycling from Metallurgical Wastes*, pp. 269-327.
- XIA, D.K., PICKLES, C.A., 1999, *Caustic roasting and leaching of electric arc furnace dust*. *Canadian Metallurgical Quarterly*, 38(3), 175-186.
- YOUCAI, Z., STANFORTH, R., 2000, *Integrated hydrometallurgical process for production of zinc from electric arc furnace dust in alkaline medium*, *Journal of Hazardous Material*, B80, 223-240.

Received January 20, 2014; reviewed; accepted March 24, 2014

INVESTIGATION OF SEPARATION PERFORMANCE OF DENSE MEDIUM CYCLONE USING COMPUTER SIMULATION

Yakup UMUCU

Department of Mining Engineering, Division of Mineral Processing, Suleyman Demirel University, Isparta,
TURKEY, yakupumucu@sdu.edu.tr

Abstract: Dense medium coal processing technology has been widely used in coal preparation industries in the world since it is the most accurate and efficient coal preparation process to obtain clean coal with a highest possible yield. Separation of coal and impurities using this technology is based on density differences. In literature, a number of mathematical models exist for dense medium cyclones. One of the most widely used model in the coal industry was developed by Mineral Technologies, Inc. This model consists of the equation which predicts the operating performance of a well maintained dense medium separator for a given cyclone geometry (including cyclone diameter) and separation density. In this study, MODSIM© (education/demo version) dense medium cyclone model was applied to coal preparation plant owned by Soma Uyar Mining Co. As a result, the float-sink test results at separation density of the dense medium cyclone were predicted.

Keywords: coal, dense medium cyclone, washability, float-sink test

Introduction

Coal has a very important place in the world's energy production compared to other fossil fuel sources such as oil and natural gas which are consumed rapidly. In the future, coal reserves will play an important role in energy production; therefore there is a need to have the most effective utilization and evaluation methods to obtain fine-grained high quality coal products (Das et al. 2013).

There are several common coal slurry beneficiation methods, namely centrifugal separation (hydrocyclone classifier-separator and centrifugal separator), wet gravity separation (Reichert spiral separator), and physicochemical method (flotation) (Lutyński et al. 2014).

Computer usage in all areas of industry has been increasing quickly during the last 30 years. Therefore, mining activities also need certain developments in computer software to assist coal processing operations.

There are two simulation packages developed only for the use by coal preparation. The first one, COPREP (Gottfried et al. 1982), was developed by the U.S. Department of Energy and the University of Pennsylvania. The second software, SHSP (Carmola et al. 1983), was prepared by Exxon Research and Engineering Company. SHSP consisted of modules in earlier version while in later version consisted of coal preparation plant units. While COPREP was firstly designed for mainframe computers, SHSP was directly designed for computer control of plants.

The simulation packages such as MODSIM©, Utah MODSIM©, SimPlant, JKS-imHet, GSIM, SPOC, CAMP, MINDRES, and USIM-PAC are generally prepared for mineral processing operations. The features of these packages are given in several studies (Sastry et al. 1985, Napier-Munn et al. 1992).

The float-sink test is a routine exercise, especially, in coal preparation and mineral processing plants to evaluate and cross-check the washability characteristics of coal and minerals. Data obtained from the float-sink tests are used to form a set of washability curves which are then used to assess the degree of difficulty of gravity separation of the feed and to provide qualitative or quantitative data for the products of the separation at a selected relative density (Burt 1984; Osborne 1988).

Katti et al. (1997) showed that gravity separation processes have been used in the mineral industry to separate particles under the action of hydrodynamic and gravitational forces. Although these equipments are extensively used for tonnage processing in coal industry, their uses have been now extended to waste treatment such as separation of valuable metallic matter from slag. However, these processes never run at their best due to lack of understanding of the process and the underlying principles of separation. Even though trial runs and pilot tests are conducted for efficient operation, these tests are often time consuming and expensive. Against this background, Katti et al. (1997) indicated that the capabilities of numerical simulation can give a better understanding of the process with a view to improve its performance. Data from different coal washeries are collected to simulate the behavior of the plants. A result of simulation utilizing jigging for coal washing was found to be in good agreement with the plant data. The same coal is also treated in other gravity separation processes in order to decide upon a particular washing circuit.

In this perspective, the aim of this study is to obtain the amount of clean coal and the percentage of ash beneficiated at different separation densities in dense medium cyclone at Soma Uyar Coal Co. and to simulate the results using MODSIM© software (education/demo version). For this purpose, first, the float-sink tests for the samples obtained from dense medium cyclone unit of Soma Uyar Coal Co. (Manisa, Turkey) were performed. The samples were taken from a separation device (Dense Medium Cyclone) at different time intervals. Then, the Tromp distribution curves were plotted for the dense medium cyclone from the float-sink test data of the products (clean coal and waste), and the feed and amount of clean coal and percentage of ash were determined at each separation density. Finally, the results obtained from these studies were simulated using MODSIM© (education/demo version) data.

Materials and experimental

Materials

The proximate analysis of the coal samples used for the experiments and simulation is presented in Table 1.

Table 1. Proximate analysis values of coal samples used

| Coal | Total Moisture (%) | Ash (%) | Volatile Matter (%) | Fixed Carbon (%) | Net Calorific Value (kJ/kg) |
|------|--------------------|---------|---------------------|------------------|-----------------------------|
| Unit | 15.60 | 29.95 | 35.74 | 18.71 | 13565.23 |

Experimental

Float-sink tests

A series of the float-sink tests was performed for the samples maintaining a ratio of densities of about 1.3–1.8 g/cm³. The samples were first separately subjected to size analysis to ensure the accuracy of the float-sink tests. A small head sample was collected from each size fraction for determining the ash values of the samples to cross-check the accuracy of subsequent float-sink tests. Zinc chloride was used as the heavy medium. Each size-density fraction was then subjected to ash content determination. In addition, the average density was determined for the final sink product of the coal samples using density buckets. The ash percentage for each coal samples was determined by using the ISO 1171 procedure.

MODSIM

MODSIM[®] is a simulator that calculates detailed mass balance for any ore and coal processing plant. Other special particle properties that are specific to particular systems can also be considered such as calorific value, volatile matter, pyritic sulfur, organic sulfur and ash content for coal. Additionally, sometimes very subtle particle properties such as shape and surface characteristics have important influences on the behavior of some of the unit operations of mineral processing. MODSIM[®] can accommodate all of these particulate properties.

The main unit operations of ore dressing include size-reduction (crushing and grinding), classification on the basis of size of particles, concentration operations that separate particles according to their mineralogical composition, and solid-liquid separations. MODSIM[®] provides a close perspective among the standard models for these operations (King 2001).

The use of the partition curve is the most widely used method to describe the operation of any gravity separation unit and the generalized partition function was described in connection with dense media separators. It is always possible to describe the operation of any gravity separator by means of a partition function even if the partition

function itself depends on the nature of the feed material as is always the case for gravity separators. In fact, the partition curve determined on an operating unit can be used to diagnose the operation. Ideally, partition functions should produce steep symmetric curves that show no short circuiting, and hence asymptote to the limits 1.0 and 0.0 at $\rho = 0$ and $\rho = 1$, respectively. Deviating from the ideal can be attributed to various design and operational inadequacies. Leonard and co-investigators (1979) provided a convenient tabulation of causes for poor partition functions in a variety for coal washing units. Although the partition curve is an excellent diagnostic tool, it is not entirely satisfactory for simulation because of the difficulty of predicting the partition curve for any particular item of equipment (Leonard IV et al. 1983).

The procedure of Gottfried and Jacobsen (1977) attempted to address this problem. The generalized partition curve is estimated in terms of a target density of separation for the proposed unit. The target density is the ρ_{50} point on the partition curve plotted for the sample. This point is in fact fixed by the density behavior of the material in the separator and by the density of feed. In any gravity separation operation, the partition function on a density basis varied in a systematic manner through the variations in ρ_{50} and the imperfection for each density fraction.

The relative density is the ratio of density to average density in the feed and the cut point for any density at the relative cut point for the feed material. Once the target density and the average density in the feed are known, the cut point and imperfection for each density can be obtained from the Tromp distribution curve. These can be used with any appropriate generalized partition function such as the exponential sum and logistic functions. An appropriate amount of short-circuiting to either floats or sinks can also be preferred if it is anticipated that this kind of inefficiency will be present in the equipment. MODSIM[®] provides the generalized Gottfried and Jacobsen (1977) method as an alternative model for most gravity separators.

Osborne (1988) recommends that the variation of the *écart probable moyen* (EPM, also known as the separation efficiency) with density, equipment size, and separation density should be computed using a series of factors based on Eq. 1.

$$EPM = f_1 \cdot f_2 \cdot f_3 \cdot E_s \quad (1)$$

where f_1 is a factor accounting for the variation of *EPM* with density, f_2 is a factor accounting for variation of *EPM* with equipment size, and f_3 is a manufacturer's guarantee factor usually in the range 1.1 to 1.2. E_s is a standard function representing the variation of *EPM* with separation density for each type of equipment. E_s for various types of coal washing equipment are calculated using the following equations:

$$\text{Dense-medium cyclone:} \quad E_s = 0.027\rho_{50} - 0.01 \quad (2)$$

$$\text{Dynawhirlpool:} \quad E_s = 0.15\rho_{50} - 0.16 \quad (3)$$

$$\text{Dense-medium bath:} \quad E_s = 0.047\rho_{50} - 0.05 \quad (4)$$

$$\text{Baum jig: } E_s = 0.78(\rho_{50} - 1) 0.01 \quad (5)$$

$$\text{Water-only cyclone: } E_s = 0.33 \rho_{50} - 0.31 \quad (6)$$

$$\text{Shaking table and spiral concentrator: } E_s = \rho_{50} - 1 \quad (7)$$

For dense-medium cyclones f_1 varies from 2 to 0.75 as particle size varies from 0.5 mm to 10 mm. For dense-medium vessels f_1 varies from 0.5 for coarse coal to 1.4 for fine coal.

The clean coal quantity and ash content were investigated in a unit of the plant by estimating, at the same separation density which was determined at different times, the Tromp distribution curves using the MODSIM[®] simulator (Fig. 1). The Tromp distribution curve was plotted to determine the washability performance of the dense medium cyclone that is operated by Soma Uyar Coal Co.

Firstly, the washability data were obtained from the coal sample to be beneficiated in the dense medium cyclone. After this, float-sink test data, which allow identification of the coal sample, were entered into MODSIM[®], and finally the selection of model and parameters was performed. The selection of models for the separation densities defined from the drawn Tromp distribution curve allow to predict the amount of clean coal and ash content in MODSIM[®].

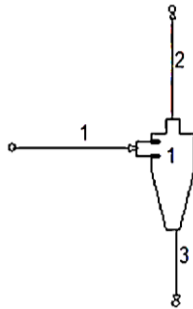


Fig. 1. Dense Medium Separator instrumentation diagram in MODSIM[®] (MODSIMTM 3.6.22-education/demo version)

Results and Discussion

Float-sink tests

A washability curve was used to determine the response of an ore to gravity separation. These curves allow prediction of the mass and assay of float and sink including the anticipated recovery at any predetermined density of separation and the ease or difficulty of the separation proposed. Alternatively, the curves can be used to determine the density of separation required to achieve a desired weight split, product assay, recovery etc. (Burt 1984). In this context, the float-sink tests were carried out for the samples and the results are seen in Fig 2.

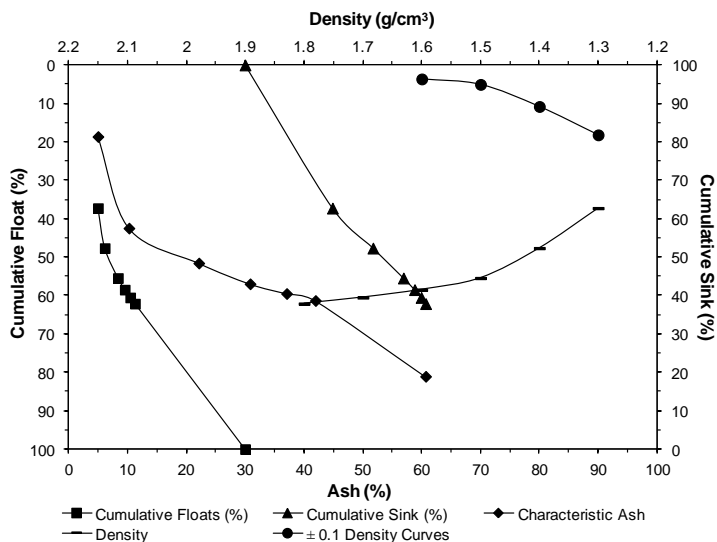


Fig. 2. Float-sink curves for $-18+0.5$ mm size fraction

The explanations for lines seen in Fig. 2 are as follows.

Cumulative float-sink curves

The cumulative percent assay for floats or sink products is plotted against the cumulative percent weight of floats (or sink) for each density of separation. These curves indicate both the assay of floats (or sink) which is the result at a particular density of the separation. They are used in conjunction with the density curve to predict the percent weights and assay of two products of separation at any particular density. Alternatively, the reverse procedure can be used to determine the required density of separation for any desired assay in the concentrate or tailings (Burt 1984).

Characteristic ash curve

Plotting the actual determined assays for each fraction against the average cumulative % weight sinks or floats for each density gives a curve which indicates the position of the values, and hence the general character of the material in relation to separation. The curve is actually drawn by plotting the determined assay of each density fraction against the cumulative percent weight of the previous fraction plus one half of the percent weight of the fraction in question. This is done because the assay refers to the whole of the weighing between the two densities. The curve, therefore, should coincide with the cumulative percent assay of floats curve (lowest assay) at zero percent cumulative weight floats. Similarly, it should coincide with the cumulative percent assay sinks curve (highest assay) at zero percent cumulative weight sink (Burt 1984).

±0.1 density curves

While the characteristic assay curve gives a qualitative indication of the ease or difficulty of separation, this is not sufficient for the prediction of the performance of gravity process (Burt 1984). As a result of amount of the mid product ratio, the ash characteristic and ±0.1 density curve (Fig. 2) was obtained from the float-sink tests performed at the particle size fraction of -18+0.5 mm. According to these results, the coal has difficult washing feature. The average value of coal ash, which is around 30%, was obtained from the cumulative float and sink curves. According to the characteristic ash curve, it was determined that the quantity of middling is more than the amount of clean coal. The most suitable washing density was appeared as 1.6 g/cm³ from ±0.1 density curve. From these results, it is understood that this coal has to be processed in heavy-media separation.

Performance of dense medium cyclone

When material has been treated in a gravity process, sequential heavy liquid tests are carried out on each of the two products (concentrate and tail) separately. From the knowledge of the weight composition of the two products and the data from float-sink tests, it is then possible to reconstruct the theoretical results of float-sink tests on the head sample of material. It is essential that both products are treated at the same densities and over the same range as each other to avoid complicated and inaccurate interpolations. From the results of these tests, there are various performance criteria that can be derived to assess separation performance. With help of distribution factors, which has been taken from performance known washing unit, it might be possible to guess washing results of minerals (Leonard 1979; Burt 1984; Osborne 1988).

The amount of clean coal and shale after the operation was determined. The operating performance was calculated in a dense medium cyclone of the Uyar Coal Co. The Tromp distribution curves drawn from float-sink data of the obtained products are shown in Fig. 3.

Determination of clean coal property with Tromp distribution curves

The separation performance of a coal washing device depends on its structure, operating conditions, separation medium, feed amount, ash of coal, and coal particle size. The Tromp distribution curve shape depends rather on the feeding material properties than the separation sensitivity of the used device. The Tromp distribution curve was plotted using the samples taken at different time periods for the same washing device, and the results are shown in Fig. 4. The results showed that the separation density for the same sample varies for different washing conditions applied in the same washing device. The dense medium cyclone of Soma Uyar Coal Co. was used in the investigations. As can be seen from the Fig. 4, the changes of the amount of clean coal and ash are time-dependent in the applied dense medium cyclone.

In the time-dependent measurements, the performance of the dense medium cyclone (as seen in Fig. 4.) was changing. These changes in the device were not caused by mechanical problems. In this plant, the performance of the dense medium cyclone was adversely affected by changes in the shift hours, lunchtime and meal breaks. Additionally, the separation densities of the dense medium in the separator also changed.

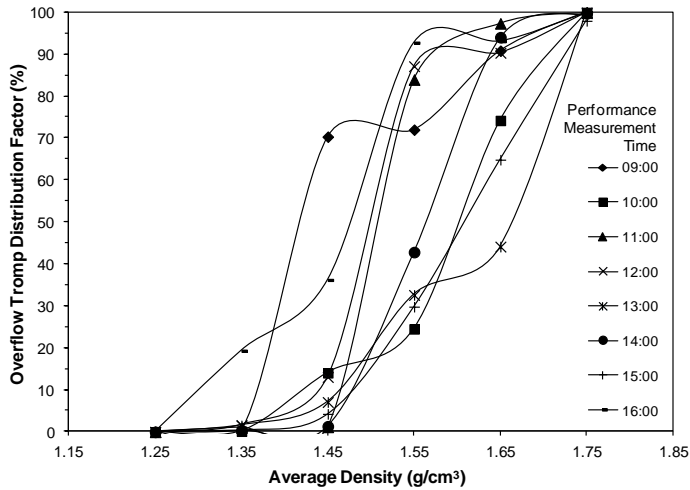


Fig. 3. Tromp distribution curves for separation at different time

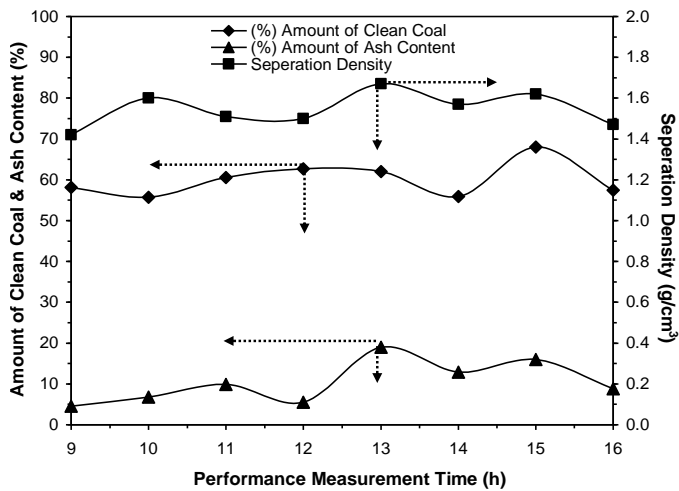


Fig. 4. Ash content and amount of clean coal depending on separation density of the dense medium in Soma Uyar Coal Co. cyclone as a function of time

MODSIM[©]

A comparison of the simulation results to that of the industrial scale of the dense medium cyclone for the samples is seen in Figs. 5 and 6. As seen in Figs. 5 and 6, real-time and artificial approach made by MODSIM[©] compared with at relatively low densities showed similar trends, but showed different results at relatively high separation densities. This can be attributed to the batch tests used in the flotation unit where there was a lot of interaction with the fluid. In the complex material with heavy liquid, the effect of water showed considerable difference. Hence, the results were different at relatively high densities. Mean while, the ash content of the samples obtained from industrial coal plant and MODSIM[©] showed similar patterns because the coal fed to dense medium cyclone showed no big change. On the other hand, the amount of clean coal was different as seen in Fig. 6. The reason for this is to move of clean coal into waste due to higher washing density.

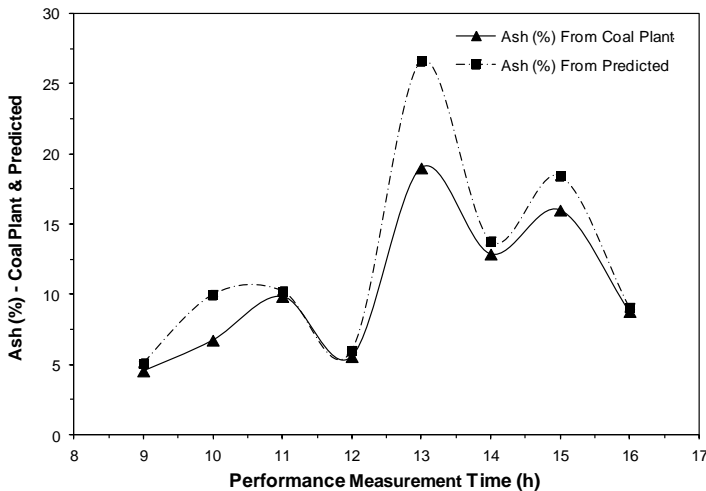


Fig. 5. Comparison of ash values obtained from MODSIM[©] and coal plant

In this study, the simulation results with MODSIM[©] appears to coincide with the real plant data. Although previous simulation results using MODSIM[©] (Katti et al. 1997) showed good results, the simulation results obtained from this study is not satisfactory because of some factors. For example, sedimentation behavior of coarse coal particles in heavy medium is different respect to fine coal particles. Additionally, in coal beneficiation plants, because the fed coal and the separation density change too much within a short time, predictions can be emerged badly.

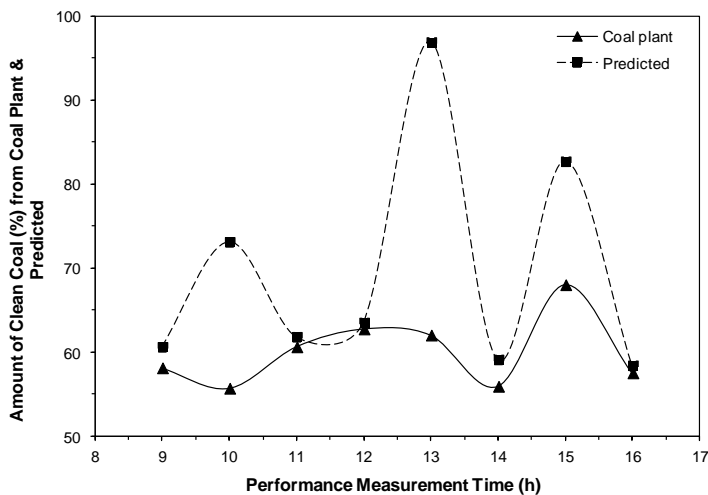


Fig. 6. Comparison of amount of clean coal obtained from MODSIM© and coal plant

MODSIM© has been not developed and used so far to quantify the flow and particle fields in the industrial dense medium cyclone at different medium properties in order to understand the effect of medium properties such as the medium density, magnetite type, and non-magnetic content on DMC's performance. The findings are summarized as follows:

1. As the density of feed medium increases, the operational head and the medium split remain constant. The off-set increases but the Ep is relatively insensitive to density of medium feed. The pressures drop significantly increases with the increasing in feed medium density, resulting in a high inward pressure gradient force on particles and reduced separating efficiencies.

2. The operating head and the medium split decrease, and the density change increases as the magnetite particles become coarser (from ultrafine to medium grade). The off-set increases and Ep increases slightly for coarse particles and remains almost constant for fine particles as the magnetite particles become coarser. The separation performance in the cylindrical section is insensitive to magnetite particle size. However, since the magnetite segregates near the spigot, the local pressure gradient, medium density and viscosity all increase, which leads to a higher density change. The difference between the pressures gradient force and the centrifugal force becomes large in this area and the particles there have more opportunities to move into the upward bulk flow, resulting in a higher off-set and Ep .

Conclusions

In dense medium cyclone clay minerals of coal often change the separation density of the device. Therefore, magnetite has to be added to the cyclone to maintain certain

separation density. However, this results in continuous variation of separation density due to the addition of indefinite amount of magnetite over a long period of time. As a result, the device performance is affected negatively in terms of operating cost and product quality. Problems associated with dense medium cyclones are attributed to manual control of the device since the observed variation in the separation density occurs during the breaks between shifts. Therefore, computerized control of the device should be performed in order to maintain a stable separation density.

In this study, it was found that there are differences between clean coal and ash content values obtained from the plant and the predicted values. The model used in MODSIM© software package showed differences between the data obtained from industrial plants and laboratory studies. The adaptation to the automation system is easy and reliable with the help of the software program packages such as MODSIM©.

By analyzing the performance of the existing dense media separation plant, it was found that improvements could be made with better process control. The models developed in this work could be used for controlling dense medium beneficiation plant in future.

Acknowledgments

Author thanks Mineral Technology Inc. to provide MODSIM© (demo /training version) for this study (<http://www.mineraltech.com/MODSIM/>). In addition we are also thankful to Soma Uyar Co. for their support during sampling campaign.

References

- BURT R. O., 1984, *Gravity Concentration Technology*, Amsterdam, Elsevier.
- CARMOLA R.E., HOOVER M.R., KIM J.M. and KLODA S.J., 1983, *Computer Simulation of Synthetic Fuels Feed Preparation Circuits*, Proceedings of the First Conference on use of Computers in the Coal Industry, AIME, New York, 177-186.
- CHAVES M.M. and SOTTFRIED B.S., 1983, *Microcomputer Simulation of Coal Preparation Plants*, Proceedings of the First Conference on Use of Computers in the Coal Industry, AIME, New York, 173-176.
- DAS T. B., PAL S. K., GOURICHARAN T., SHARMAK. K. and CHOUDHURY A., 2013, *Evaluation of Reduction Potential of Selected Heavy Metals from an Indian Coal by Conventional Coal Cleaning*. International Journal of Coal Preparation and Utilization, 33, 300-312.
- GOTTFRIED B. S.& JACOBSEN P. S., 1977, *Generalized distribution curve for characterizing the performance of coal-cleaning equipment* (No. BM-RI-8238), Bureau of Mines, Washington, DC, USA.
- GOTTFRIED B.S., LUCKIE P.T. and TIERNY J.W., 1982, *Computer Simulation of Coal Preparation Plants*, U.S. DOE, 208 Report No. DOE/PC/30144 - T7, 285.
- GOVINDARAJAN B. and RAOT. C., 1994, *A simple equation for float sink data*, Mineral Eng., 7, 1441-1446.
- ISO METHOD 1171, *International Standard specifies a method for the determination of the ash of all solid Mineral Fuels-Determination of ash*.

- KATTI A. MISHRA, B. K. and MEHROTRAS. P., 1997, *Simulation of industrial gravity separation processes using a general purpose simulator*, Proceedings of National Seminar on Processing of Fines, NML Jamshedpur, January 9-10, 229-239.
- KING R.P. 2001, *Modeling and Simulation of Mineral Processing System*, Department of Metallurgical Engineering University of Utah, USA.
- LEONARD J.W., 1979, *Coal Preparation*, AIME, 4th Edition, New York.
- LEONARD IV J.W. and LEONARD J.W., 1983, *Using Tromp Curves to Diagnose Performance Problems in Coal Cleaning in Basic Mathematics and Computer Techniques for Coal Preparation and Mining*, Ed. K.K. Humphreys and J.W. Leonard Marcel Dekker Inc., 71-79.
- LUTYNSKI A.& LUTYNSKI M., 2014, *Assessment of coal slurry deposits energetic potential and possible utilization paths*, Physicochem. Probl. Miner. Process., 50(1), 159-168.
- NAPIER-MUNN T.J. and LYNCH A.J., 1992, *The Modeling and Computer Simulation of Mineral Treatment Processes Current Status and Future Trends*, Minerals Engineering, 5(2), 143-167.
- OSBORNE D.G., 1988, *Coal Preparation Technology Vol. 1*, Graham and Trotman Ltd., Chapter 8, London.
- SASTRY K.V.S. and ADEL S.T., 1985, *A Survey of Computer Simulation Software for Mineral Processing Systems*, Control 84 Mineral/Metallurgical Processing, J.A. Herbst (Editor), AIME, New York, 121-130.

Received August 29, 2013; reviewed; accepted August 17, 2014

WETTABILITY OF SHALE ROCK AS AN INDICATOR OF FRACTURING FLUID COMPOSITION

Katarzyna KSIEZNIAK, Andrzej ROGALA, Jan HUPKA

Chemical Technology Department, Chemical Faculty, Gdansk University of Technology, Gdansk, Poland,
katarzyna.ksiezniak@gmail.com

Abstract: Shales have become one of the main unconventional gas resources in the world. However, physicochemical properties of rocks are still at the center of research. There have been conducted major researches in wettability of shales by fluids and advances in understanding and control of shale rock wettability. Also influence of interfacial phenomena on a production capacity of reservoirs have been made. The aim of this study is to find a relationship between type of fracturing fluid used during shale gas recovery and shale rock wettability. The study is the first step to evaluate conditions, under which wetting occurs most intensely, how it can be controlled by changing a composition of fracturing fluid and how this composition effects the wetting mechanism. We present a characterization of porous materials by a capillary rise method to study shale wettability by water, oil and other fluids. This work describes the experimental contributions to understand the shale rock/fluid interactions through inquire of fluid role in wettability of shale rock.

Keywords: *shale rock, wettability, porous materials, hydraulic fracturing, contact angle*

Introduction

This paper investigates interaction of shale rocks and liquids that may be used as a base of fracturing fluid. So far, such studies have not been conducted using Polish shales due to lack of shale gas recovery in Poland. Recently, exploration boreholes, which allow acquiring of this type of samples, have been drilled. Their analysis is required before conducting applied research. Shale rocks wetting by fracturing fluids should be fully described, what would help to avoid application of unsuitable technologies resulting in decrease of shale gas recovery. Nowadays, the relevance of wettability parameter is more explicitly recognized. Most national laboratories do not pay much attention to wettability of shale rocks. However, it should be noted that wettability plays the major role in gas recovery. This parameter can be considered relevant due to the fact that a large surface area per unit volume of shale rock is exposed to the

fluids (Raza et al., 1968). Therefore, this paper focuses on influence of selected experimental fluids on reservoir to understand wettability of the Polish shale rock.

Many factors have the influence on the shale rock/liquid interactions during fracturing. Considering the intricacy of reservoir, each reservoir system should be taken as an individual case, since intelligibility of these interactions leaves many doubts (Cuiec, 1984). The leading property of rocks is wettability, which affect the choice of an appropriate method for fracturing and amount of hydrocarbon recovery. Hydraulic fracturing (HF) is a method widely used for fracturing rocks in the production of natural gas (Howard et al., 1970). It is based on pumping to a drillhole the fracturing fluid under high-pressure containing a proppant as well as other additives. The first stage of gas recovery from a reservoir is drilling of wells into a gas-bearing rock. This is achieved by rotary drilling using the drilling fluid (Jones et al., 1996) that must fulfil functions such as cooling the drill, having the correct rheology and right physicochemical characteristics and environmental requirements. The use of water-based drilling muds is preferred (Maitland, 2000). The fracturing fluid consists mainly of water and proppant (99.5%) and chemical additives (0.5%). The most general fracturing fluids use natural polymers, such as guar (Gittings et al., 2000). These fluids are injected under high pressure to the rock generating the fractures. The proppants like sand, ceramic materials or resin coated sand are introduced to keep the induced hydraulic fractures open (Mader et al., 1989).

Hydraulic fracturing is an advanced technology, commonly used for many decades with lot of successes. However, the method is subjected to numerous disadvantages that should be eliminated. They include the liquid waste management, investment and environmental costs, risk of contamination of surface water and groundwater, methane emission and wide social misunderstanding over any activities related to extraction of shale gas (Piszc et al., 2014). However, some of them generate the economic, environmental and social problems. The main technological problem of extracting gas from the Polish shales is a fracturing fluid compatibility with the shale reservoir (Rogala et al., 2013). This applies both to stimulation of reservoir to the gas flow and prevention of the flow blocking. Due to fracturing fluid/shale rock compatibility issues, the estimations of amount of gas contained in the fractures and available to extraction are not precise. Brown (1956) was one of the first, who found out that differences in shale gas recovery from various reservoirs may, in part, be a result of narrow differences in wettability.

Wettability

In this study, wettability is primarily discussed in the context of shale gas recovery using hydraulic fracturing. Hydraulic fracturing has been widely used for over sixty years and accounted the most of world gas production (Morrow, 1990). Wettability of reservoir is not easily defined property. Classification of shale reservoirs as either water-wet or oil-wet is an appreciable oversimplification. Borysenko et al. (2009) demonstrated that the shales become oil-wet due to the presence of organic matter or

subjection to polar compounds in the water reservoir. Consequently, there is a risk that one would be unable to choose the proper fracturing fluid, and gas production could be lower than expected. There are many factors which have significant impact on wettability, such as the surface roughness, contaminations, fluid composition, etc. The differences in wettability may result from differences in the part of the surface that has preferentially oil-wet and water-wet (Brown, 1956). Many reservoir engineers consider in practice that most reservoirs are strongly wet by water (Morrow, 1990). The scientific substantiation for the Morrow (1990) work was that water preferentially filled the reservoir trap. Also, adsorption of polar compounds from the fluids largely effects on the wetting properties of reservoir surfaces. The capillary forces keep water in the fractures (Morrow, 1990), and the films on the porous surface indicated that wetting property of solids is prevailed by the outermost layer of particles. The further research discovered some rocks, which had flow properties indicating that they were oil-wet (Brown, 1956). The certain reservoirs have multiphase flow properties, which signify that they characterize intermediate wettability. Borysenko et al. (2009) examined that many shales differ in terms of wettability. Also the differences in mineralogy and texture of shale rock influence variant affinity for water and oil, ranging from hydrophilic to hydrophobic. Dixit et al. (1997) studied the influence of the heterogeneity on wettability in the reservoir on two phase oil–water flow. They elaborated a three-dimensional network model which entertains wettability changes as a phase trapping, film flow and variations in the advancing and receding contact angles. They discovered, that applying various combinations of fluid displacement mechanisms with properties of the porous material allowed them to reproduce the extensive variety of the oil–water system. This indicates, that the progress relates to the interfacial phenomena, surface chemistry and flow nature for oil–water systems in the porous media.

Contact angle - capillary rise method

Wetting and adhesion phenomena play an important role in nature and technological processes, such as beneficiation of materials. In all these processes, the free surface and interfacial energies, that result from the non-compensated phase interactions at the surface interface, play the fundamental role. Many physical and chemical processes occur either at the interfaces or surfaces. The wettability of surface depends on the surface tension of liquid, surface free energy of solid and solid-liquid interface. Contact angles formed by gas, liquid and solid phases play an important role in many fields of science and technology as well as in nature (Kowalczyk and Drzymala, 2011).

Wetting of a solid surface is described by the Young equation, which determines the equilibrium relationship between the contact angle (θ) and three interfacial surface tensions (σ_{lg} , σ_{sl} , σ_{sg} of the liquid-gas, solid-liquid and solid-gas, respectively) (Adamson, 1990):

$$\cos \theta = \frac{\sigma_{gs} - \sigma_{sl}}{\sigma_{lg}} \quad (1)$$

When the liquid easily spreads the solid surface it means that the contact angle is zero and the solid is hydrophilic. On the other hand, when the liquid runs off the solid surface, the contact angle is greater than 0° and the solid surface is hydrophobic (Adamson and Gast, 1997; Drzymala, 2007).

The Young equation is applicable only on homogenous and flat surfaces. If we want to use the Young equation for a solid surfaces with mechanical roughness and chemical heterogeneity, then we have to add an aforementioned corrections factors into this equation.

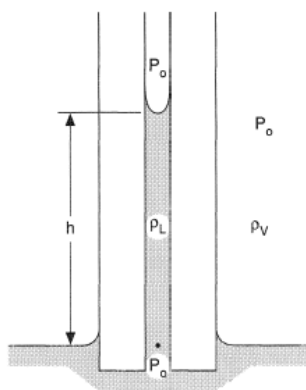


Fig. 2. Capillary rise method

There are many methods of contact angle measurements including sessile drop, drop shape on the solid surface, captive bubble, capillary rise, capillary pressure, force of detachment of air bubble from solids in liquid and many others (Drzymala, 2007; Chau, 2009). This paper is focused on a capillary rise method (Fig. 2) called the Washburn method (1921). The method depends on water saturation measurements and related capillary pressures and provides that fluid movement in the capillary occurs under the capillary pressure. The Washburn method is based on the relationship between time of penetration and wettability of solid. The wettability test method proposed in this paper is based on the macroscopic observation of affinity of liquid to the shale rock. The surface properties of solids are defined by using the contact angle of liquid or critical surface tension. For the same material, the value of contact angle depends on the pore diameter and roughness. For contact angle determination the modified Washburn equation was used (Holownia-Kedzia, 2012):

$$\cos \theta = K \cdot \frac{t_0}{t_1} \quad (2)$$

where

$$K = \frac{\gamma_0 \cdot \eta_1}{\gamma_1 \cdot \eta_0}, \quad (3)$$

and t is time of penetration, γ surface tension, η viscosity of reference (0) and investigated (1) liquids. To have the accurate determination of a contact angle it is necessary to select a suitable reference liquid. The reference liquid is the one with known value of contact angle (Chander et al., 2007; Kowalczyk and Drzymala, 2012).

Material and method

This work is based on shale rock samples originated from Baltic Basin, Pomerania, Poland, derived from the Ordovician period. Shales are source rocks for unconventional hydrocarbons. Shales are characterized by dark color (Fig. 3) and relatively high fragility that usually indicates a high content of natural gas.



Fig. 3. Shale sample from the Baltic Basin, Pomerania, Poland

The contact angle experiments by the capillary rise method were carried out by an apparatus shown in Fig. 4. All the experiments were conducted at temperature 273 K. All shale rock samples (with the fraction less than 0.425 mm) were inserted into capillary tubes with an inside diameter of 4 mm. The samples in the glass capillaries were accurately weighed (each capillary tube was filled by the same portion of porous material), and then was packed with a shaking machine until to obtain the same height in all capillaries. The capillary tubes were placed in a stand and the measurement was started. The measurements were recorded by a computer software (SNC Program Standard Radwag). The results are presented in numbers as square of mass gain in capillaries as a function of wetting time. The contact angles were calculated using Eq. 2.

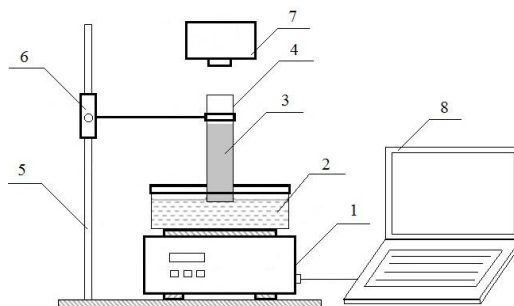


Fig. 4. Laboratory set-up used for measurements of contact angle by capillary rise method
 1 – electronic balance, a covered container with wetting liquid, 3 – shale particle bed, 4 – column,
 5 – stand, 6 – micrometric screw, 7 – camera, 8 – computer (Dang-Vu et al., 2005)

Results

Most petroleum engineers accepted hypothesis, that all reservoirs are water-wet. Problems with shale gas extraction led to the focus on the properties of rocks. Many attempts were made to determine whether reservoirs are strongly water-wet. The wettability of porous materials proved that wettability of the porous matrix medium depends on the distribution of liquid in the pores. This process has influence on the conditions, in which gas is extracted.

Table 1. Contact angles determined by sessile drop method to choose reference liquids

| Fluid | Contact angle, deg |
|-----------------|--------------------|
| Cyclohexane | 4 |
| Water | 82 |
| Diesel oil | 45 |
| Methanol | 32 |
| Aniline | 49 |
| Benzyl alkohol | 40 |
| Ethanolamine | 52 |
| Ethylene glycol | 63 |
| Hexanol | 20 |

The success of the capillary rise method relies on the correct choice of the reference liquid. Therefore, the first step was to determine the reference liquid essential for the Washburn technique. The measurements were achieved by simply sessile drop method. In this experiment, the shale sample was mechanically compressed to obtain the pastille. Then, the contact angles formed by sessile liquid drops on the smooth homogeneous solid surface were determined. Table 1 shows the contact angle of shale in the presence of different liquids. Among all the examined liquids, cyclohexane with a low surface tension of 25.3 mN/m has the lowest contact angle and wets the shale

rock best. In the literature, it is reported that cyclohexane is the most commonly used reference liquid (Yuan and Lee, 2013). Cyclohexane was chosen among the examined liquids as the reference liquid to find out if tested shale rock is oil-wet or water-wet.

It is important to notice that the wetting velocity depends on the liquid density, viscosity and surface tension. There are two steps of shale rocks wetting. The first step is when liquid fills the pores vertically and the second when it moves horizontally filling all volume of shale particle bed until the mass is constant (Fig. 5). Table 2 presents physicochemical properties and contact angles of tested fluids.

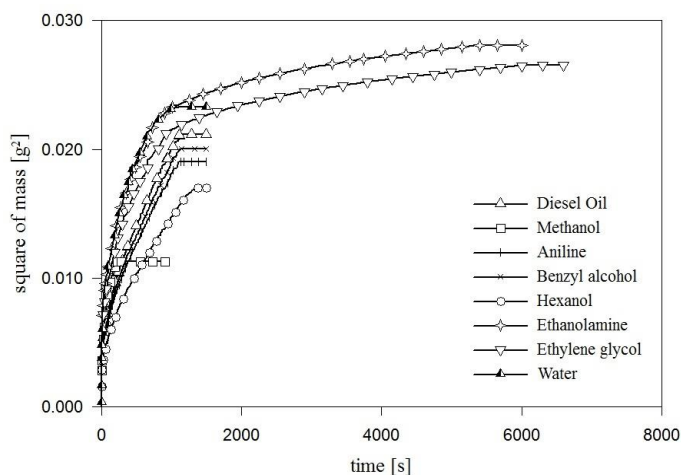


Fig. 5. Square of mass as a function of wetting time for all tested in this work liquids

Table 2. Physicochemical properties and calculated contact angles of shale in the present of different tested liquids for cyclohexane as reference liquid

| Tested liquid | Viscosity, η , mPa·s | Surface tension, γ , mN/m | Penetration time, t , s | K (Eq. 3) | $\cos\theta$ | Calculated contact angle, θ , deg (Eq. 2) |
|-----------------|------------------------------|--|------------------------------|----------------|--------------|--|
| Cyclohexane | 0.980 | 25.3 | 257 | reference | 1 | 0 |
| Water | 1.005 | 72.6 | 1102 | 0.36 | 0.083 | 85 |
| Diesel oil | 3.450 | 28.4 | 1120 | 3.14 | 0.720 | 44 |
| Methanol | 0.614 | 22.6 | 220 | 0.70 | 0.819 | 35 |
| Aniline | 4.40 | 42.90 | 1103 | 2.65 | 0.617 | 52 |
| Benzyl alcohol | 5.04 | 39.00 | 1120 | 3.34 | 0.766 | 40 |
| Ethanolamine | 24.10 | 48.89 | 5313 | 12.73 | 0.616 | 52 |
| Ethylene glycol | 21.00 | 47.00 | 6115 | 11.53 | 0.485 | 61 |
| Hexanol | 4.59 | 24.00 | 1343 | 4.94 | 0.945 | 19 |

Contrary to expectations, investigated shale rock is oil-wet. This observation was explained by the differences in oil-water wetting properties of solid surface. The contact angle for diesel oil is almost two-fold smaller (44°) than that for water (85°). Taking into account only wettability, the best choice would be fracturing fluid based on

the diesel fuel. However, during shale gas extraction it is avoided to use of hydrocarbons as a base fracturing fluid. The lowest contact angle is observed for methanol (35°). Also, for hexanol and benzyl alcohol, the values of the contact angles were low against the background of the tested liquids. It is better to use an aqueous fracturing fluid containing e.g. methanol (which has smaller angle than the diesel oil) and/or surfactants.

Conclusions

In this work wettability of Polish shale rocks using the capillary rise method was presented. The results showed that the investigated shale rock is oil-wet. This observation was explained by the differences in oil/water wetting properties of solid surface. The contact angle for diesel oil was almost two-fold smaller (44°) than that for water (85°). The lowest contact angle was observed for methanol (35°). It is better to use an aqueous fracturing fluid containing e.g. methanol (which has smaller angle than the diesel oil) and/or surfactants. This work can help to determine the direction of future research to find a way to get the most effectively control of reservoir wettability as well as whether the substances, which are currently used during hydraulic fracturing, are suitable for Polish shale and their components have beneficial effect on wettability behavior.

References

- ADAMSON, A.W., 1990, *Physical Chemistry of Surfaces*, 5th edition, John Wiley & Sons, New York.
- ADAMSON, A.W., GAST A.P., 1997, *Physical chemistry of surfaces*, 6th edition John Wiley & Sons, New York.
- BORYSENKO, A., CLENNELL, B., SEDEV, R., BURGAR, I., RALSTON, J., RAVEN, M., DEWHURST, D., LIU, K., 2009, *Experimental investigations of the wettability of clays and shales*, Journal of Geophysical Research, Volume 114, pp. 5-11.
- BROWN, J. S., California Research Corp., 1956, *Measurements Of Fractional Wettability Of Oil Fields' Rocks By The Nuclear Magnetic Relaxation Method*, Fall Meeting of the Petroleum Branch of AIME, Los Angeles, California.
- CHANDER, S., HOGG, R., FUERSTENAU, D.W., 2007, *Characterization of wetting and dewetting behaviors of powders*, KONA, 25, pp. 56–75.
- CHAU, T. T., 2009, *A Review of Techniques for Measurement of Contact Angles and Their Applicability on Mineral Surfaces*, Miner. Eng., 22, pp. 213–219.
- CUIEC, L., 1984, *Rock/Crude-Oil Interactions and Wettability: An Attempt To Understand Their Interrelation*, SPE Annual Technical Conference and Exhibition, Houston, Texas.
- DANG-VU, T., HUPKA, J., 2005, *Characterization of Porous Materials by Capillary Rise Method*. Physicochemical Problems of Mineral Processing, 39, pp. 47-65.
- DIXIT, A. B., McDOUGALL, S. R., SORBIE, K. S., 1997, *A pore-level investigation of relative permeability hysteresis in water-wet systems*, Proc SPE Intl Symp Oilfield Chemistry (SPE), 37233, pp. 2229–2240.
- DRZYMALA, J., 2007, *Mineral Processing: Foundations of Theory and Practice of Minerallurgy*; Ofic. Wyd. PWr.: Wrocław, Poland.

- GITTINGS, M. R., CIPELLETTI, L., TRAPPE, V., WEITZ, D. A., MARQUES, M. IN, C., 2000, *Structure of guar in solutions of H_2O and D_2O : an ultra-small-angle light scattering study*, J Phys Chem B, 104, pp. 4381–4386.
- HOŁOWNIA-KĘDZIA, D., 2012, *Wykorzystanie metody wzniesienia kapilarnego do pomiarów zwilżalności układów rzeczywistych*, Rozprawa Doktorska, Katedra Technologii Chemicznej, Wydział Chemiczny, Politechnika Gdańska (in Polish).
- HOWARD, G. C., FAST C. R., 1970, *Hydraulic Fracturing*, SPE of AIME, pp. 210.
- JONES, T. G., HUGHES, T. L., 1996, *Drilling fluid suspensions*, Fundamentals and applications in the petroleum industry, ACS Advances in Chemistry Series, 251, pp. 463–564.
- KOWALCZUK, P. B., DRZYMALA, J., 2011, *Contact angle of bubble with an immersed-in-water particle of different materials*, Ind. Eng. Chem. Res., 50, pp. 4207–4211.
- KOWALCZUK, P. B., DRZYMALA, J., 2012, *Surface flotation of particles on liquid. Principles and applications*, Colloids and Surfaces A: Physicochem. Eng. Aspects, 393, pp. 81–85.
- MAITLAND, G. C., 2000, *Oil and gas production*, Schlumberger Cambridge Research, High Cross, Madingley Road, Cambridge CB3 0EL, UK Elsevier, Colloid & Interface Science Volume 5, Issues 5–6, pp. 301–311.
- MADER, D. et al., 1989, *Hydraulic proppant fracturing and gravel packing*, Elsevier Science Publishers B. V., Vol. 26, 0-444-41625-0 (series).
- MORROW, N. R., 1990, *Wettability and Its Effect on Oil Recovery*, Society of Petroleum Engineers, Vol. 42, No. 12, pp. 1476–1484.
- PISZCZ, K., ŁUCZAK, J., HUPKA, J., 2014, *Mobility of shale drill cuttings constituents*, Physicochemical Problems of Mineral Processing, Vol. 50, No. 2, pp. 795–810.
- RAZA, S. H., TREIBER, L. E., ARCHER, D. L., 1968, *Wettability of reservoir rocks and its evaluation*, journal Name: Prod. Mon.; (United States); Journal Vol.: 32:4, pp. 2–4, 6–7.
- ROGALA, A., KRZYSIEK, J., BERNACIAK, M., HUPKA, J., 2013, *Non-aqueous fracturing technologies for shale gas recovery*, Physicochemical Problems of Mineral Processing, Vol. 49, No. 1, pp. 313 – 322.
- YUAN, Y., LEE, T. R., 2013, *Contact Angle and Wetting Properties*, Chapter 1, Volume 51, Surface Science Techniques, Springer Series in Surface Sciences.
- WASHBURN, E.W., 1921, *The dynamics of capillary flow*, Phys. Rev., 17 (1921), 273–283.

Received May 15, 2014; reviewed; accepted August 21, 2014

A METHOD OF PROPPANT PACK PERMEABILITY ASSESSMENT

Marcin A. LUTYNSKI

Faculty of Mining and Geology, Silesian University of Technology, Gliwice, Poland, marcin.lutynski@polsl.pl

Abstract: Hydraulic fracturing methods used for low permeability reservoirs such as shale gas or tight gas require the use of proppants. The current standard used for proppant assessment does not take into account its interaction with the rock and the embedment effect. In this paper a new method of proppant pack permeability assessment is proposed where proppant is placed into a rock sample with induced fracture. Three types of proppant were assessed to verify the method i.e. offshore sand, onshore sand and ceramic proppant. The rock sample was a Tumlin sandstone. As the flowing medium supercritical carbon dioxide was used. Tests were performed with 300-500 μm size proppants at flowing pressure of 3 MPa and confining pressure of 5 MPa. Additional test was conducted with 1–2 mm sand proppant at two confining pressure, i.e. 5 MPa and 16 MPa. Proppant were characterized in accordance with the Krumbein/Sloss diagram. Similar values of permeability for the proppant concentration of 0.5 kg/m² were obtained ranging from 2.3 to 3.3 D although the highest permeability was achieved with Baltic sand proppant and ceramic proppant. For the larger size of proppant (1 – 2 mm) the initial permeability with confining pressure of 5 MPa was initially larger but when the confining pressure was increased it declined by 37%. This proves that in the proposed method we can observe changes in the permeability of the fracture with change in confining pressure apply subjected to the sample.

Keywords: *copper nitrate, electrorefining, high purity copper, hydrometallurgy*

Introduction

Hydraulic fracturing methods are commonly used to enhance production of low permeable reservoirs such as shale gas or tight gas formations. The main goal of hydraulic fracturing treatment is to create a highly conductive system of fractures interconnecting the pores and allow gas flow to the well. There are numerous kinds of hydraulic fluids used for the treatment and these are i.a. gelled fluids, including linear or cross-linked gels, water with friction reducers (slickwater), foamed gels and others. Fracturing fluids are not only used to create/expand fractures but also to transport proppant into fractures. Proppants are sand or other granular substances injected into the formation to hold or “prop” open reservoir formation fractures created by

hydraulic fracturing. In general we can divide proppants into three types (see Table 1), i.e. natural, ceramic and other.

Table 1. Types of proppant

| Natural | Ceramic | Other |
|--------------------|--|-----------------------|
| Sands | LWC – Lightweight Ceramics | Light weight polymers |
| Resin-coated sands | IDC – Intermediate Density Ceramics HDC – High Density Ceramics Resin-coated Ceramic Proppants | High density bauxite |

A perfect proppant should provide a high conductivity of the fracture within long period of time. As the conductivity it is meant permeability multiplied by the width of the fracture. High conductivity of the fracture is provided when the size of the proppant is maximally uniform i.e. the 90% of the proppant falls between designated particle size range (typically in mesh size). Outlook on the typical proppant sizes is given in Table 2.

Table 2. Typical proppant sizes

| Tyler Mesh Size | Particle Size Range (μm) |
|-----------------|---------------------------------------|
| 10/14 | 1400–2000 |
| 12/18 | 1000–1700 |
| 16/20 | 850–1180 |
| 16/30 | 600–1180 |
| 20/40 | 420–850 |
| 30/50 | 300–600 |
| 40/70 | 212–420 |
| 70/140 | 212–106 |

The proppant shape has a an impact on the conductivity of the fracture (or permeability of the proppant bed). Therefore, a wide range of particle sizes and shapes results in a tight packing arrangement, reducing permeability/conductivity. A narrow range of sizes and a spherical shape will lead to greater conductivity.

An important feature of the proppant is its strength. The greater the depth the higher the pressure and proppant is more prone to crushing. Crushing the proppant results in shattering and releasing the fines which in turn may decrease the permeability of the proppant bed. There are other properties of the proppant which may affect its performance in the reservoir and these are: acid solubility and turbidity. Proppant testing methods are described in the EN:ISO standard 13503-2:2006 “Petroleum and natural gas industries - Completion fluids and materials – Part: 2

Measurement of properties of proppants used in hydraulic fracturing and gravel-packing operations”.

The problem with the abovementioned standard is the fact that it does describe proppant properties as a material but it does not give information on the performance of the proppant in contact with the reservoir rock. The main problem is the so called “embedment” effect which is often observed in some of the formations. Proppant grains are pushed into the rock due to formation pressure and reduce the conductivity of the fracture. In this case the proppant retains its properties (it is not crushed nor dissolved) but its size or shape causes it to embed into the rock, thus reducing the gas flow. In this article a new method of proppant testing is proposed which allows to assess the behavior of proppant in contact with reservoir rock by measuring the changes in permeability of the fracture. As the flow medium carbon dioxide was used due to the fact that a few studies show CO₂ fracturing technology as an alternative to hydraulic fracturing technologies (Almond and Harris, 1984; Rogala et al., 2013; Rogala et al., 2014).

Materials

For the purpose of the study three proppants were selected. Two natural ones, that is marine sand from Baltic coast (BS), onshore sand from Ostrowiec Swietokrzyski (OS) and one ceramic proppant (CP). The sphericity and roundness of proppants was examined in accordance with the EN:ISO 13503-2:2006 standard (EN:ISO 13503-2:2006). The sphericity and roundness is assessed by selecting under microscope 20 random grains and grade each grain visually on roundness and sphericity by comparing to the Krumbein/Sloss diagram (Fig. 1).

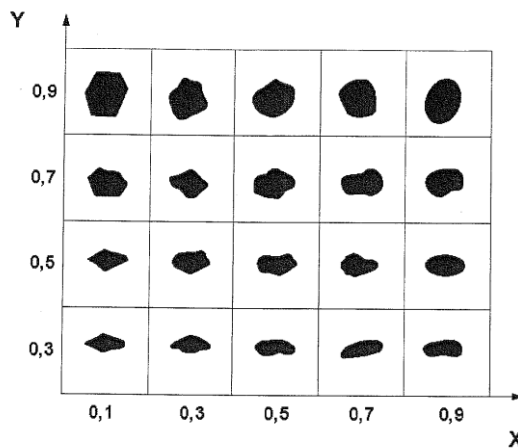


Fig. 1. Krumbein/Sloss diagram for visual assessment of sphericity and roundness (EN:ISO 13503-2:2006)

The arithmetic mean gives the grade of sphericity and roundness of the proppant. In the study the scanning electron microscope (SEM) and stereoscope microscope was used for this purpose (Ardelli, 2014). In general, the proppant for the tests was in one size: 300 – 500 μm which corresponds to commonly used mesh size of 30/50. Additionally, one test was performed for large size proppant with uncommon size of 1000 – 2000 μm (OS 1-2) for the reasons explained in the latter part of the article. Sample photos from SEM and stereoscopic microscope of BS and CP sample are presented in Figures 2 and 3 respectively.

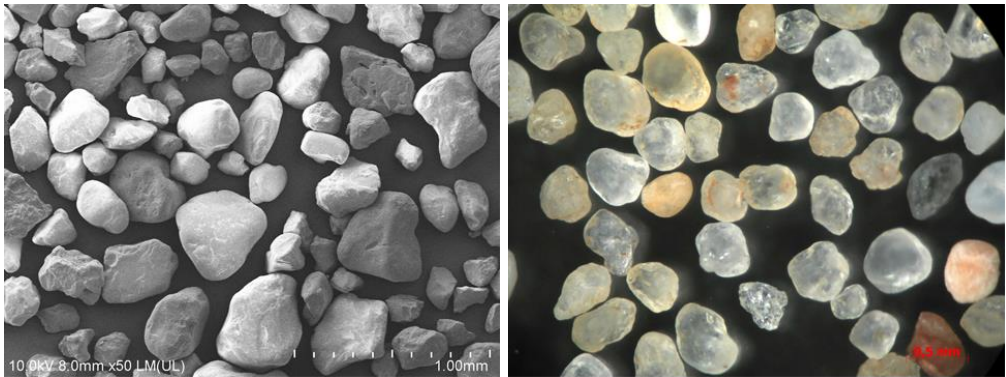


Fig. 2. SEM photo of BS sample (300–500 μm) under 50 \times magnification and stereoscopic microscope photo at 50x magnification of OS sample (300–500 μm) (b)

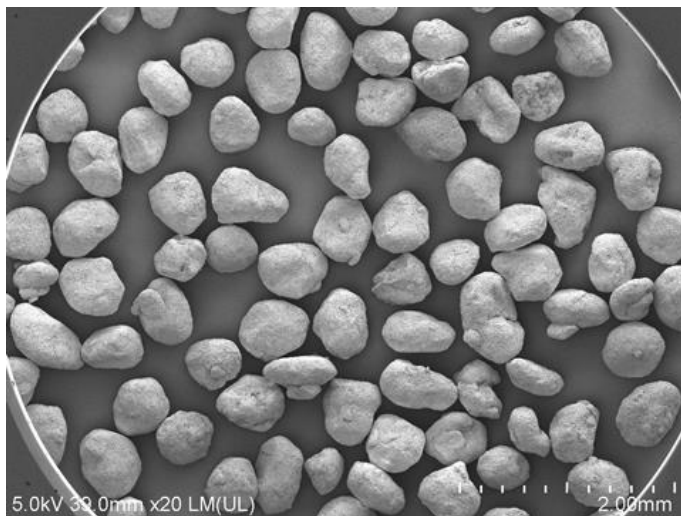


Fig. 3. Photos of CP sample (300–500 μm) under SEM

Results of sphericity and roundness examination are presented in Table 3.

Table 3. Sphericity and roundness of proppants used for permeability tests

| Proppant | Size, μm | Sphericity, - | Roundness, - |
|----------------------------|---------------------|---------------|--------------|
| Ostrowiec S. sand (OS 1-2) | 1000–2000 | 0.7 | 0.4 |
| Baltic marine sand (BS) | 300–500 | 0.4 | 0.2 |
| Ostrowiec S. sand (OS) | 300–500 | 0.8 | 0.5 |
| Ceramic proppant (CP) | 300–500 | 0.9 | 0.7 |

Surprisingly two natural proppants, BS and OS, significantly differ in shapes and onshore sand (OS) has better sphericity and roundness. As it was expected ceramic proppant was graded as the one with the highest sphericity and roundness.

Rock selected for the permeability tests with proppant was a Tumlin fine-grained sandstone (Holy Cross Mountains in Central Poland). The Tumlin sandstone has a porosity of approximately 10.5%, compressive strength of 80 MPa and permeability of approximately 50 mD. The samples were cored from large blocks to the size of 2.54 cm in diameter and length of 4 cm. In order to simulate reservoir conditions an artificial fracture along the sample had to be induced. For that purpose a load was applied along the external cylinder surface of the core (see Fig. 4) until the moment the sample cracked. This procedure allowed to obtain a split sample with a fracture along the whole length that could be filled with proppant and simulate reservoir conditions.

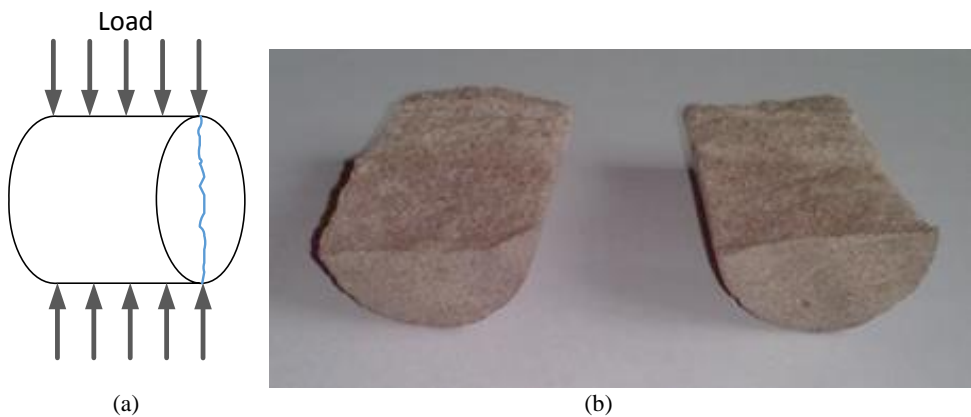


Fig. 4. Direction of the load applied to the sandstone core sample (a) and photo of the sample after the split (b)

The reason for choosing the Tumlin sandstone was its isotropy and known properties. These features allowed to obtain similar sample for each permeability test as the test was usually destructive to the sample. Typically, the sample was either cracked after the test due to the relaxation forces when confining pressure was released or due to the oil intrusion if the test failed.

Methods

In order to measure the permeability of the core sample filled with proppant a custom made permeability setup was constructed (Fig. 5). To calculate the permeability of the specimen a steady-state flow method was applied. In this method a constant stream of gas is supplied to the sample from the cylinder of known volume. The sample is subjected to a pressure gradient to facilitate the gas flow through the sample. In order to maintain a constant flow a needle valve was installed behind the core cell and the reducing valve to maintain the constant pressure. Pressure in the gas cylinder is monitored by the pressure transducer therefore the flow rate can be calculated by knowing the drop in pressure within the certain period of time.

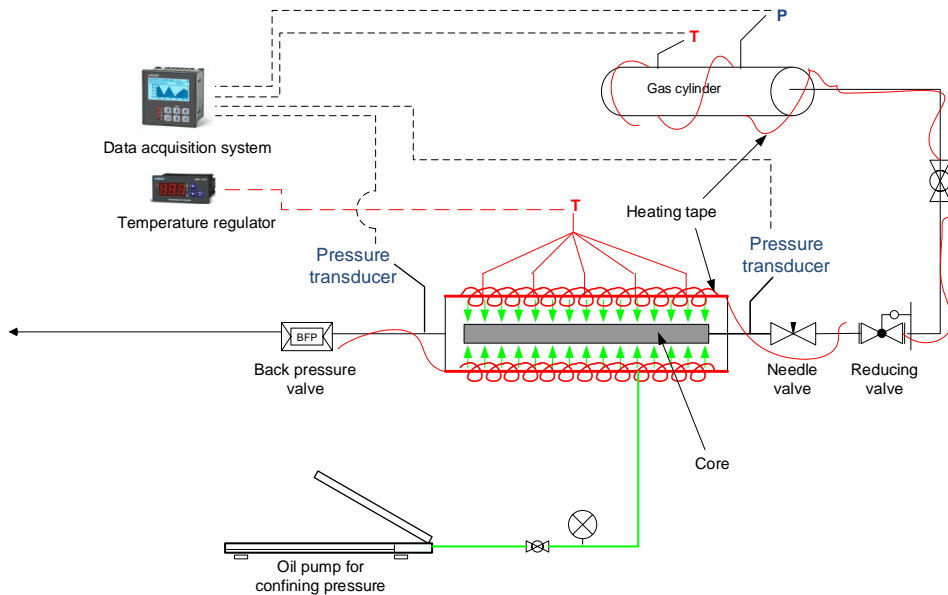


Fig. 5. Scheme of the laboratory setup used for permeability experiments

The core sample filled with proppant was placed in silicone sleeve and inserted into the high pressure cell where it was subjected to confining pressure exerted by hydraulic oil. This step is crucial in order to obtain a proper permeability measurement as the gas can flow on the sides of the sample when the confining pressure is too low. In this study we applied confining pressure which was at least 50% higher than the average gas flowing pressure. The permeability of the sample was calculated with the use of the following formula based on the modified Darcy equation (1):

$$k = \frac{2qP_oL\mu}{A(P_i^2P_o^2)}, \quad (1)$$

where k is the permeability, q is the gas flow rate, L and A is the length and cross-sectional area of the sample respectively, μ is the viscosity of gas, P_i and P_o is the inlet and outlet pressure respectively. As it was mentioned, the flow of gas could be calculated by measuring the drop in pressure of the gas in a cylinder of known volume and known temperature of the gas. As the experiments were conducted with supercritical CO_2 to calculate precisely the CO_2 density a highly accurate equation of state by Span and Wagner (1996) was used).

Experiments were conducted with the proppant concentration of 0.5 kg/m^2 and the confining pressure of approximately 5 MPa and 16 MPa. In Fig. 6 sandstone sample filled with proppant before placing in the permeability setup is shown.



Fig. 6. Photo of the sandstone core filled with CP sample before placement in the permeability setup

Results and discussion

Sandstone cores were filled consequently with three types of proppant i.e. Baltic sand (BS), Ostrowiec Swietokrzyski sand (OS) and Ceramic proppant (CP) in size of 300–500 μm . In one of the experiments it was decided to fill the sandstone sample with coarse fraction of proppant (1–2 mm) in order to verify to what extent it may affect the permeability of fracture. Such large size of proppant was selected to “prop” the sandstone which porosity was rather large and in previous experiments proppant embedment was noticed. Moreover, it was decided to increase the confining pressure in the last experiment with OS 1–2 sample to 16 MPa in order to observe the effect of fracture closure. Results of experiments are presented in Fig.7.

Tests conducted with four types of proppant of 300–500 μm in size revealed that the highest permeability of fracture was obtained with the Baltic sand (BS) and ceramic proppant (CP) sample. A slightly lower permeability was obtained for the OS sand sample. Although, the OS sand has a better grade of sphericity and roundness than BS sand - the permeability is somewhat lower. In all cases however the range of permeability in a sand pack with the same proppant concentration and confining pressure is similar. Only in the case of sample OS 1–2 with the grain size of 1000–

2000 μm the permeability was significantly higher. This is due to the fact that larger grains do not embed as much as the fines and have larger pores when compacted. Yet, when the confining pressure was increased the proppant was crushed and fracture closure was observed (see Fig. 8). In this case the permeability declined by 37%.

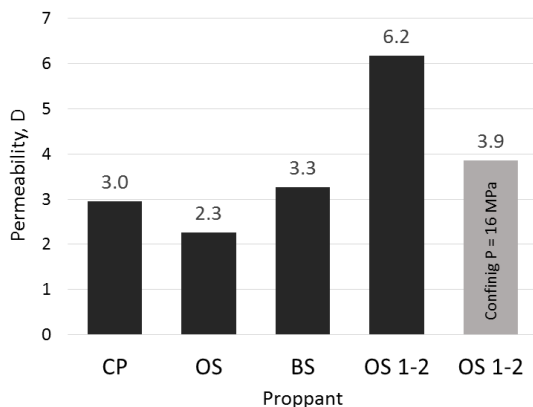


Fig. 7. Results of fracture permeability tests with different proppants at confining pressure of 5 MPa (for the sample OS 1-2 the test was also conducted for the confining pressure of 16 MPa) at the temperature of 45°C



Fig. 8. Photo of the crushed sample OS 1-2 after the pressure was increased to 16 MPa. The red circle indicates the most destroyed zone

Presented results are the initial assessment of the proposed method of proppant pack permeability testing. Due to the fact that the number of publications in this field is scarce the results were compared with data from the publication of (Wen et al., 2007). In their case the FCES-100 test unit based on the API standard was used. The range of obtained permeability for the 30/60 mesh proppant was two to three times higher. It is difficult to compare directly the results as the proppant concentration was larger – 10 kg/m² and the confining pressure (referred as closure pressure) was much

higher 10-90 MPa. Nevertheless, the proposed method is convenient and relatively easy method of proppant testing in samples where the surface of fracture is naturally rough unlike the other methods where the surface is cut and polished. Another advantage is the fact that in this method we can test small samples that can be cut from well cores.

Conclusions

A new method of proppant pack permeability testing was proposed. In this method the proppant is placed in a rock sample with induced fracture of rough surface. To verify the method tests were conducted with three types of proppants – two natural ones (sands) and one ceramic proppant. In all cases with the same flow pressure and confining pressure similar results were obtained although the highest permeability was achieved with Baltic sand proppant and ceramic proppant. For the larger size of proppant (1 – 2 mm) the initial permeability with confining pressure of 5 MPa was initially larger but when the confining pressure was increased it declined by 37%. This proves that in the proposed method we can observe changes in the permeability of the fracture with change in confining pressure subjected to the sample.

The main advantage of this method is the fact that we deal with rough surface of the rock which is the case in reservoir conditions – taking into account effects such as cracking of the rock on the surface of fracture. Current methods of proppant testing focus mainly on properties of the proppant as the material and as it was observed in the conducted test – the sphericity and roundness does not always reflects the permeability of the proppant pack.

At this stage of development, the method has some disadvantages and the main one is the relatively low flow pressure and confining pressure which can be applied to the sample. The construction of sample cell has to be improved in order to withstand higher pressure without unnecessary oil intrusions that destroy the sample as it often happened during the course of this study. This makes the method more time consuming and somehow complex in terms of sample preparation. Yet, the initial results are encouraging and will be developed in further studies.

Acknowledgments

The author of this article would like to thank Dr. Grzegorz Smolnik for the access and preparation of the sandstone samples, Aleksandra Ardelli and Miguel Angel Gonzalez Gonzalez for their involvement in conducting the tests.

References

- ALMOND, S. W., HARRIS, P. C. (1984), *Fracturing method for stimulation of wells utilizing carbon dioxide based fluids*. US Patent 4519455.
- ARDELLI, A. (2014), *Wpływ rodzaju proppantu na przepuszczalność dwutlenku węgla*. MSc THESIS, Politechnika Śląska, Gliwice.

- EN:ISO13503-2:2006 (2006), *Petroleum and natural gas industries - Completion fluids and materials – Part: 2 Measurement of properties of proppants used in hydraulic fracturing and gravel-packing operations*. European Committee for Standardization.
- ROGALA, A., KRZYSIEK, J., BERNACIAK, M., HUPKA, J. (2013), *Non-aqueous fracturing technologies for shale gas recovery*. *Physicochemical Problems of Mineral Processing*, 49(1), 313–321.
- ROGALA, A., KSIEZNIAK, K., KRZYSIEK, J., HUPKA, J. (2014), *Carbon dioxide sequestration during shale gas recovery*. *Physicochem. Probl. Miner. Process*, 50(2), 681–692.
- SPAN, R., WAGNER, W. (1996), *A new equation of state for carbon dioxide covering the fluid region from the triple-point temperature to 1100 K at pressures up to 800 MPa*. *Journal of physical and chemical reference data*, 25, 1509–1596.
- WEN, Q., ZHANG, S., WANG, L., LIU, Y., LI, X. (2007), *The effect of proppant embedment upon the long-term conductivity of fractures*. *Journal of Petroleum Science and Engineering*, 55(3–4), 221–227.

Received May 15, 2014; reviewed; accepted August 25, 2014

DEVELOPMENT OF A HYDROMETALLURGICAL TECHNOLOGY FOR PRODUCTION OF METALS FROM KGHM POLSKA MIEDZ S.A. CONCENTRATES

Tomasz CHMIELEWSKI

Wroclaw University of Technology, Faculty of Chemistry, Division of Chemical Metallurgy, Wybrzeże Wyspińskiego 27, 50-370 Wroclaw, Poland, tomasz.chmielewski@pwr.edu.pl

Abstract: Rapidly declining quality of copper concentrates produced by Lubin Concentrator of KGHM Polska Miedz SA, having very low content of Cu, high content of Pb, As and organic carbon as well as significant contents of Ag, Co, Ni, Zn, Re, V and Mo, makes the concentrates difficult-to-process by flash smelting. Currently hydrometallurgy, using sulfuric acid in the presence of iron(III) and oxygen as a leaching medium for base metals and chloride leaching for silver and lead, seems to be an alternative for pyrometallurgy. The goal of the work is to discuss main aspects of the necessity of application a new hydrometallurgical technology, based on different unit operations, including non-oxidative atmospheric, chloride and pressure leaching, recovery of Pb and Ag, separation of Cu and accompanying metals from PLS and arsenic neutralization. The unique lithological, mineralogical and chemical properties of the process feed were discussed in details. The results of laboratory investigations performed at the Wroclaw University of Technology and assumptions of the process scale-up for acquisition of data for full scale technology were summarized. Planned investigations on the pilot plant scale will provide technical and economic data for a pre-feasibility study of the future hydrometallurgical plant.

Keywords: *hydrometallurgy, copper concentrates, leaching*

Introduction

The declining quality of Polish copper ores reflects general unfavorable trends observed in the World copper metallurgy. These negative trends are perceived in particular at the Lubin plant of KGHM, where the most complex and hardest-to-treat ores are mined and beneficiated. There, for years, deteriorating properties include a decreasing copper and silver content in the feed (Figs 1 and 2) and growing amount of shale fraction (Table 1) as well as increasing impurities such as Pb, As and organic carbon. These properties essentially affect the decreasing copper and silver content in flotation concentrates (Fig. 3), considerably reducing recovery of the produced metals

(Fig. 3) and become the main reason for growing technological concerns both in flotation and flash smelting, creating high costs of copper production.

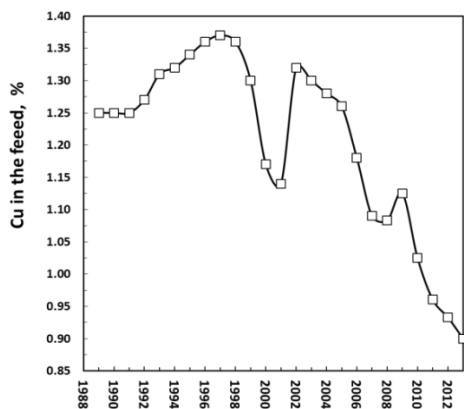


Fig. 1. Decreasing content of Cu in the feed of Lubin Concentrator (after Kukuc and Bazan, 2013)

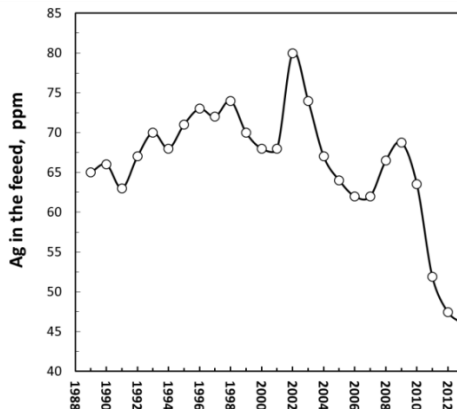


Fig. 2. Decreasing content of Ag in the feed of Lubin Concentrator (after Kukuc and Bazan, 2013)

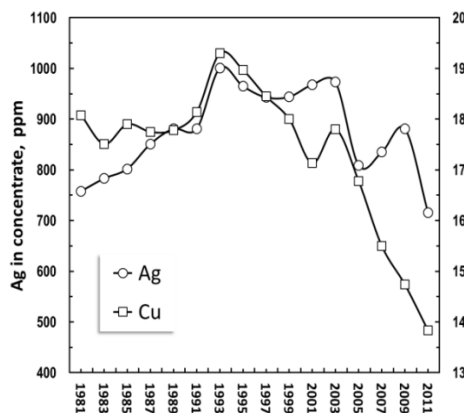


Fig. 3. Lubin concentrate grade from 1981 to 2012 (after Kukuc and Bazan, 2013)

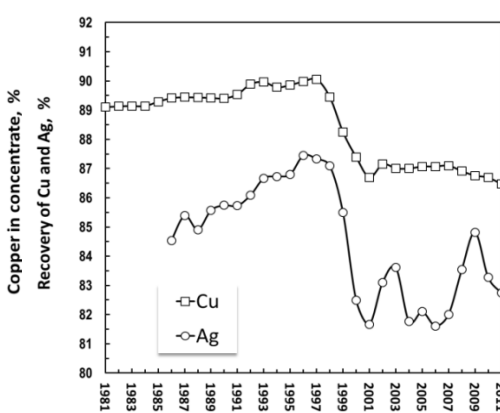


Fig. 4. Decrease of Cu and Ag recovery in Lubin concentrate from 1981 to 2012 (after Kukuc and Bazan, 2013)

The application of modern either hydro- or biometallurgy, well recognized and already approved in the world for copper recovering, becomes an urgent necessity for the Polish copper industry in order to reverse the mentioned unfavorable trends. The application of atmospheric and pressure leaching methods for copper concentrate processing have been recently investigated at the Wroclaw University of Technology as a complimentary process for treating copper concentrates and by-products from ZWR Lubin, which are difficult-to-beneficiate using the existing technologies. The

idea of application of hydrometallurgy at KGHM was previously considered by different authors and extensively investigated within the period from 2004 to 2007 in the BIOSHALE project financed by the European Commission in the VI Framework Project. The BIOSHALE project was carried out by 16 European universities and leading research institutions, including the Wroclaw University of Technology and KGHM Cuprum. The concept of application of either hydro- or biometallurgy for Lubin shale middlings was based on separation of the troublesome shale-enriched material (middlings) from the flotation circuits for a separate hydrometallurgical processing.

The role of hydrometallurgy as an alternative for production of copper and other accompanying metals has been growing for years. Nearly 25% of the world copper production is due to hydrometallurgy using sulphate, sulphate/chloride and chloride solutions. Significant progress have been recently made in advancing the use of hydrometallurgy for copper ore and concentrate treatment. Currently, at least five separate sulphate-based commercial plants have started or are under construction for copper recovery. These include the Mt. Gordon Copper Process (Richmont 2004, Richmont and Dreisinger 2002, Dreisinger et al. 2002), Phelps Dodge Total Pressure Oxidation (King et al., 1993, King and Dresinger 1995), Alliance Copper BIOCOP Process (Batty and Rorke 2005), the Oxiana Sepon Copper Process (Baxter et al., 2003) and InMet Las Cruces Copper Process (Smalley and Davis 2000). The Activox (Evans 1999), CESL (Jones 1999, CESL web page 2011), Dynatec (Barta 1999) and Xtrata Albion processes have been known for some time and are well represented in the literature.

The hydrometallurgical methods based on sulphate or mixed sulphate/chloride solutions and stirred tank leaching are currently at different development stage (Table 1). The optimum for parameters of leaching depends on feed mineralogy, metals dissemination, and concentration of accompanying metals. There is no versatile hydrometallurgical technology for copper concentrates, which can be applied for each leaching feed. It requires comprehensive investigations on laboratory and pilot scales combined with supplementing analyses and advanced measurements for products characterization. This article will focus on more recent sulphate process developed for very specific Polish sedimentary copper ores and concentrates which contain carbonate gangue.

Even though numerous hydrometallurgical processes are currently at different stages of development (Table 1), none of them can be considered as directly applicable for the KGHM flotation sulphide concentrates having a unique mineralogical and chemical composition. A high content of the carbonate gangue, very complex multimineral and multimetallic composition, dissemination of metals in sulphide and carbonate matter, high content of lead and silver, elevated organic carbon concentration and the presence of arsenic require a very specific and individual approach. An important criterion for selection of leaching environment for the KGHM

concentrates is an easy access to sulphuric acid, selected as the leaching medium, which is being produced in the KGHM-owned smelters (~ 650 gigagrams per year).

Table 1. Sulphate-based copper hydrometallurgical processes (stirred tank leaching) for sulphide ores and concentrates at different status of development

| Process | Status | Temp. °C | Pressure atm | Regrind d_{80} , μm | Special conditions |
|----------------------------------|-------------|---|---------------|----------------------------------|---|
| AA-UBS Process | Pilot plant | 150 | 10–12 | 10-15 | Reground chalcopyrite pressure leaching with addition of surfactant |
| CESL Copper Process | Demo plant | 140–150 | 10–12 | 37 | Chloride assisted pressure sulphate leaching of chalcopyrite |
| Dynatec Process | Pilot plant | 150 | 10–12 | 37 | Pressure leaching of chalcopyrite using low grade coal as additive |
| Mt. Gordon Process | Commercial | 90 | 8 | 100 | Pressure leaching of chalcocite/pyrite ore in Fe(III) solution |
| Platsol Process | Pilot plant | 220–230 | 30–40 | 15 | Total pressure oxidation in the presence of 10–20 g/dm ³ NaCl. Precious metals leached in one step |
| Sepon Copper Process | Commercial | 80 °C – Cu 230 °C – FeS ₂ | 1 at 30-40 | 100 50 | Atmospheric leach for copper from Cu ₂ S. Pressure leaching of FeS ₂ to produce H ₂ SO ₄ and Fe ³⁺ for copper leaching |
| Total Pressure Oxidation Process | Commercial | 200-230 | 30–40 | 37 | Extreme conditions of <i>T</i> and <i>p</i> designed to rapidly destroy chalcopyrite and other sulphides |
| Las Cruces Copper Process | Commercial | 90 | 1 | 100 | Atmospheric leach of copper from sulphide ore using oxygenated and acidified Fe(III) |

Current state of copper production at KGHM

An analysis of flotation indices at all KGHM concentrators reveals a descending trend for both metals recovery and concentrate grade. This tendency is particularly visible at the Lubin Concentrator (ZWR Lubin), where copper recovery currently only slightly exceeds 86% and the copper content in the concentrate is only about 14%. This concentrate is now almost not acceptable for processing by flash smelting, and has to be subjected to more effective and alternative processing methods. A similarly unfavorable trend has been also observed for silver in the form of decreasing grade

(about 700 g/Mg) and recovery (83 %) (Kukuc and Bazan, 2013). Despite an appreciable content of other accompanying metals (Pb, Zn, Ni, Co, Re, Mo, V), some of them are either recovered only partially (Pb, Ni) or not at all (Zn, Co, V, Mo). Currently, the used technology at ZWR Lubin reached a limit of its efficiency and it is a major reason of growing metals losses and increasing production costs.

Unique properties of Polish copper ores and concentrates

Polish LGOM copper deposits exhibit unique, sedimentary and complex nature. It results in the presence of three lithological ore fractions: dolomitic, sandstone, and shale (Table 2). Among the three ore fractions, the shale component reveals two exceptional and contradictory properties. Although the shale exhibits the highest concentrations of copper and accompanying metals (Ag, Ni, Co, Zn, Pb, Re, V, Mo) it is simultaneously the most troublesome in terms of flotation upgradeability. Fine dissemination of metal sulfides in the carbonate matter and black shale - clay rocks, that form the majority of the gangue, is observed. Such a fine dissemination of copper sulfides in the carbonate-organic matrix considerably reduces the susceptibility of the ore to both effective sulphides liberation and to froth flotation.

Table 2. Composition of lithological ore layers and content of copper, silver, and organic carbon in feed of KGHM copper concentrators in nineties (Luszczkiewicz, 2000) and in 2004 (Luszczkiewicz, 2004)

| Ore component | Rudna | | Polkowice –Sierszowice | | Lubin | |
|-----------------------------|-------|------|------------------------|------|-------|------|
| | '90s | 2004 | '90s | 2004 | '90s | 2004 |
| Carbonate ore % | 51.0 | 33.0 | 84.0 | 75.0 | 38.0 | 25.0 |
| Shale ore, % | 5.0 | 11.0 | 6.0 | 17.0 | 8.0 | 15.0 |
| Sandstone ore, % | 44.0 | 56.0 | 10.0 | 8.0 | 54.0 | 60.0 |
| Cu content, % | 2.05 | 2.23 | 1.81 | 2.0 | 1.36 | 1.28 |
| Ag content, g/Mg | 47.0 | 53.0 | 34.0 | 40.0 | 68.0 | 67.0 |
| C _{org} content, % | 0.64 | 1.49 | 1.14 | 1.66 | 1.76 | 1.62 |

A relative increase of concentration of shale-clay and carbonate fractions in the flotation feeds, which are known as hard-to-treat in flotation circuits, is currently observed. According to the latest data, the content of the shale fraction in the Lubin deposit is about 15% and occasionally can reach 25% (Kubacz and Skorupska, 2007). It was found that separation of the shale middlings from the Lubin flotation circuit for alternative, either by bio- or hydrometallurgical treatment (Fig. 5), could be considered as one of the ideas of intensification of metals recovery at KGHM (Chmielewski and Charewicz, 2006; Chmielewski et al., 2007). The results of comprehensive laboratory investigations indicated, that the main reason for the observed metal losses in flotation was fine dissemination of sulphides in the shale-carbonate fraction (Fig. 4 and Table 2).

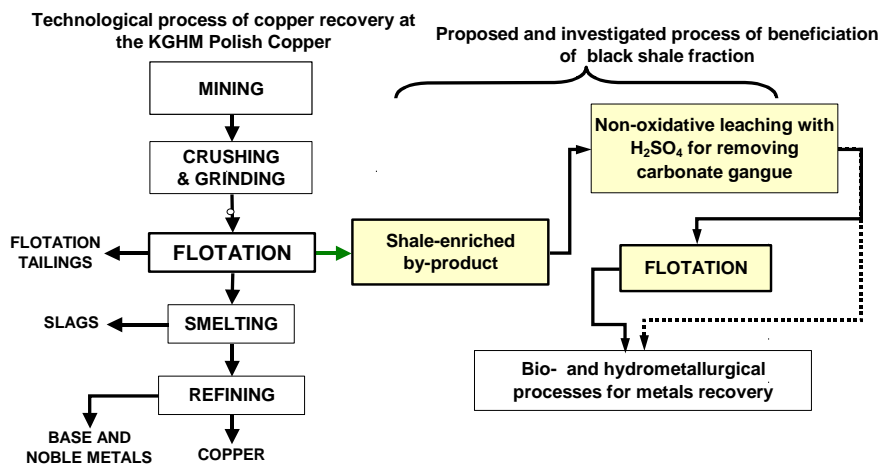


Fig. 5. General BIOSHALE concept of separate processing of black shale ore fraction from Polish copper deposits

The application of non-oxidative leaching for carbonate decomposition (Luszczkiewicz and Chmielewski, 2008; Chmielewski, 2007; Chmielewski et al., 2008; Chmielewski et al., 2007; Konopacka et al., 2007), followed by either atmospheric or pressure leaching and metals separation from PLS using solvent extraction (Chmielewski and Charewicz, 2006; Chmielewski, 2007; Wodka et al., 2007; Chmielewski and Wodka, 2010; Rotuska and Chmielewski, 2007), were considered as a complimentary way for processing of shale flotation by-product at ZWR Lubin, which is exceptionally difficult to beneficiate using existing techniques. This approach, presented by the author within the research program of BIOSHALE (Chmielewski and Charewicz, 2006; d'Hugues et al., 2007; d'Hugues et al., 2008) primarily involved the separation of the most troublesome ore fraction (shale containing middlings) from the flotation circuit and introduction of hydrometallurgical methods for their alternative, effective processing. All development concepts for processing of the Lubin-Glogow complex sedimentary copper ores were summarised by Chmielewski et al. (2014).

Table 3. Mineralogy of flotation feeds at KGHM Lubin Concentrators (2007-2008) (Luszczkiewicz, 2009)

| Bornite % | Chalcocite digenite % | Chalcopyrite % | Pyrite marcasite % | Covellite % | Sphalerite % | Tennantite % | Galena % |
|--------------|-----------------------------|-------------------|--------------------------|----------------|-----------------|-----------------|-------------|
| 33.1 | 14.5 | 26.1 | 17.4 | 3.5 | 1.8 | 2.0 | 1.9 |

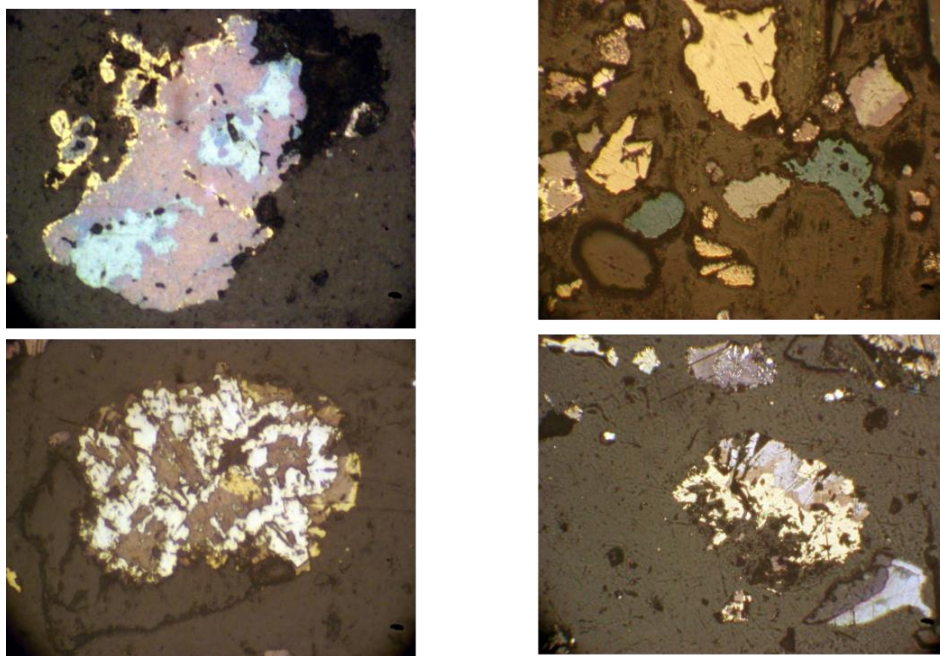


Fig. 6. Mineralogical images of polymineral Lubin concentrate (fraction $> 71 \mu\text{m}$) indicating possible and beneficial, for hydrometallurgy, galvanic interactions between minerals during leaching

The unique properties of Polish copper ores and concentrates make them very suitable for hydrometallurgy. Sedimentary copper ores from all three LGOM deposits (Polkowice, Rudna, Lubin) exhibit specific polymetallic and polymineral composition (Table 3). Bornite and chalcocite are generally dominating copper-bearing sulphides, with chalcopyrite and covellite as minor components. This is a very advantageous element for hydrometallurgical treatment, since chalcocite and bornite are the easiest leachable copper sulphides, in contrary to chalcopyrite, being the most refractory in leaching. Additionally, the Polish copper ores contain pyrite and marcasite, minerals which are well known as galvanic activators in leaching of sulphides.

Electrochemical nature of sulfides flotation (Chanturija and Vigdergauz, 2009) and leaching along with electrocatalytic properties of pyrite has already been described (Majima and Peters, 1968; Nowak et al., 1984; Holmes and Crundwell, 1995) and used for leaching of copper sulphidic concentrates in the Galvanox Process (Dixon and Mayne, 2007), where finely ground FeS_2 is added to the leaching slurry to intensify the process in a galvanic manner, by facilitating the charge transfer from the oxidant to dissolved sulfide. The presence of numerous sulphidic copper, iron, zinc and lead minerals in the feed to leaching coming from the Lubin Concentrator (Fig. 6) can advantageously result in mutual electrochemical interactions caused by different potentials attained by sulfides in leaching conditions. These interactions have already been examined for conditions of non-oxidative leaching of the Lubin shale middlings

(Kowalczyk and Chmielewski, 2010) and for atmospheric leaching conditions (Chmielewski and Kaleta, 2011) and are expected to create significant acceleration of copper leaching by forming a vast number of intergrowths and inter-mineral galvanic cells, which remarkably elevate the leaching rate.

Recently, hydrometallurgy has been investigated at the Wrocław University of Technology for improving Cu and accompanying metals recovery from Lubin flotation concentrates (Project HYDRO supported by NCBiR – National Centre for Research and Development, Poland). Advantageous for hydrometallurgy composition of these concentrates (Table 3, Figs 6 and 7) and rapidly declining Cu and Ag grade within the years of 2009-2013 (Table 4) indicate a necessity of essential technological changes and applications of hydrometallurgy for concentrate alternative treatment.

Table 4. Metals content in Lubin flotation concentrate within the years of 2009-2013

| Year | Cu % | Zn % | Ni g/Mg | Co g/Mg | Ag g/Mg | Pb % | As % | V g/Mg | Mo g/Mg |
|------|---------|---------|------------|------------|------------|---------|---------|-----------|------------|
| 2009 | 15.85 | 0.947 | 415 | 1040 | na | 2.67 | 0.290 | - | - |
| 2010 | 15.26 | 0.928 | 488 | 1206 | 938 | na | 0.343 | 569 | 265 |
| 2011 | 14.56 | 0.570 | 483 | 1250 | 755 | na | 0.258 | 672 | 221 |
| 2012 | 13.98 | 0.712 | 461 | 1325 | 736 | 4.48 | 0.313 | 670 | 257 |
| 2013 | 12.87 | 0.740 | 494 | 1482 | 455 | 5.42 | 0.266 | 657 | 272 |

Table 5. Metals content and quantity of metals in Lubin “high-in-recovery” flotation concentrate

| Metal content in concentrate | | | | | | | | | | |
|--|----------|------------|------------|----------|----------|------------|----------|-----------|------------|---|
| Cu, % | Zn, % | Ni, g/t | Co, g/t | Fe, % | Pb, % | Ag, g/t | As, % | V, g/t | Mo, g/t | Z _{max} ^{H2SO4} (kg/t) |
| 7,42 | 0,436 | 498 | 1251 | 5,09 | 4,94 | 429 | 0,161 | 942 | 292 | 235 |
| Metal quantity in concentrate, Mg/year | | | | | | | | | | |
| 66 800 | 3 930 | 449 | 1129 | 45 810 | 44 593 | 387 | 1 450 | 850 | 263 | - |

As a result of comprehensive laboratory studies and detailed analysis of possible leaching feed, both the final concentrate and the Lubin “high-in-recovery” concentrate, with lower Cu content (about 7%) and significantly elevated metal recovery (from 88 to 95%), were selected as the leaching feed (Tables 4 and 5). However, the suitability of the “high-in-recovery” concentrate was not confirmed by economical evaluation of the project, and the final concentrate currently produced at the Lubin Plant was indicated as more encouraging as a feed for hydrometallurgy, on the basis of laboratory investigations.

The mineralogical composition of the “high-in-recovery” Lubin concentrate (Fig. 7) is very beneficial for hydrometallurgy. Copper is in the form of two dominating minerals: bornite and chalcocite/digenite. Moreover, the content of

accompanying metals (Pb, Zn, Co, Ni, Re, V, Mo) in the concentrate is also very high and comparable with final flotation concentrate (Table 4). Zn, Co, Mo and V are still underestimated components and are not recovered by the current technologies.

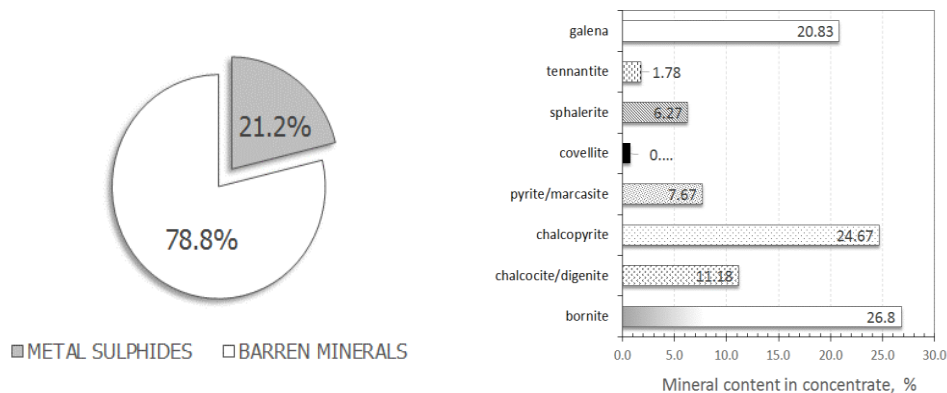


Fig. 7. Mineralogy of "high-in-recovery" Lubin concentrate used for hydrometallurgical investigations

A systematic control of mineralogical parameters of the feed, by-product and solid residues is a principal issue for every unit operation and at every stage of the process. Optical microscopy analyses, SEM examinations as well as MLA analysis are necessary for mineralogical assessment. The content of carbonate matter and acid-consuming components should be determined as a so-called Z_{\max} parameter, which is the amount (mass in kg) of H_2SO_4 required for total decomposition of these compounds per one megagram of concentrate. The procedures for such determinations were elaborated in our laboratory.

Hydrometallurgical processing

A commercial final flotation concentrate, containing about 14% of Cu, from the Lubin Concentrator and a "high-in-recovery" concentrate, being a low grade material (about 7.5% of Cu), were used for the hydrometallurgical processing to get general information about copper ores beneficiation properties. Basing on the obtained data a flowsheet was created (Fig.8). According to the flowsheet the non-oxidative leaching, a controlled decomposition of acid-consuming compounds (mainly Ca and Mg carbonates) with sulphuric acid, will be the initial chemical unit operation followed by separation of precipitated gypsum by flotation and separation of magnesium in soluble form of $MgSO_4$. The magnesium sulphate solutions will be a possible source of magnesium for manufacturing of MgO for either refractory ceramic or magnesium metal production by silicothermal reduction. The first step of Mg recovery includes purification of the solution by hydrolytic precipitation and/or cementation, followed by $MgSO_4$ crystallization. Finally, thermal conversion of $MgSO_4$ to MgO will be carried out.

The principal leaching operation to dissolve Cu, Zn, Co, Ni, Re, V and Mo will be conducted in sulphuric acid solutions containing iron(III) sulphate as necessary oxidant and gaseous oxygen for regeneration of Fe(II) to Fe(III) during leaching (Chmielewski et al., 2011; Gibas et al., 2014). The leaching process will be performed in stirred tanks under atmospheric conditions at temperature 90-95 °C, selected solid/liquid ratios (from 1:10 to 1:4), and controlled stirring and oxygen flow rates. The polymineral composition of examined concentrate and presence of pyrite appeared to be beneficial for leaching due to the formation of galvanic contacts facilitating both leaching rate and metals recovery.

As an alternative to atmospheric leaching, pressure leaching in sulphuric acid solutions, under elevated oxygen pressure (from 2 to 20 atm) and temperature (from 120 to 180° C), will be recommended as a method of process intensification. This intensive pressure leaching, performed in stirred pressure reactors (autoclaves), was found to be very effective during laboratory examinations in terms of high metals recovery and short leaching time. Neither Ag nor Pb will be leached in sulphate environment and will require an additional unit operation for recovering.

The suspension after leaching operations will be subjected to CCD decantation and filtration for phase separation. The PLS will be subsequently subjected for purification and metals separation by means of SX (Solvent Extraction) and IX (Ion Exchange), whereas a solid residue will be a feed for further leaching of Ag and Pb in chloride solutions (concentrated NaCl). The solution after stripping will be used in the EW process to produce metallic cathodic copper of high quality.

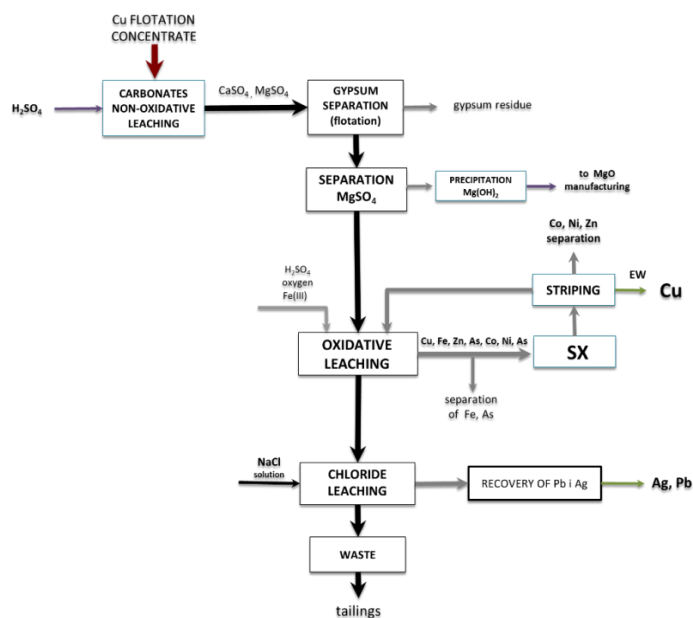


Fig. 8. General flowsheet of hydrometallurgical processing of Lubin flotation concentrate

Solvent extraction (SX) is a separation process typically used to isolate the solutes from solutions, as well as their separation and concentration. During the HYDRO research project, different flotation concentrates were leached (Chmielewski et al., 2011, Gibas et al., 2014), resulting in solutions of varying composition, particularly with regard to copper(II). Initially, the metal concentration in PLS reached 30 g/dm^3 , while in the final stage low-grade material was selected for leaching, which resulted in solutions containing up to 10 g/dm^3 of Cu. In the initial stages of the HYDRO project, three commercial hydroxyoxime reagents were tested as copper(II) extractants: LIX 984N, LIX 612 and N-LV Acorga M5640. The effect of diluent on extraction efficiency was also considered. In this case two commercial reagents differing in the content of aromatic compounds were compared: Escaid 100 (20%) and Escaid 110 (<0.5%) (Ochromowicz and Chmielewski, 2013). Due to the high acidity of PLS, neutralization of the excess acid was suggested using raw concentrate (containing carbonate), or alkali, such as CaCO_3 , in order to increase Cu(II) extraction efficiency.

The obtained results exhibited that the best extraction system was 30% (v/v) + Acorga M5640 Escaid 110. The preliminary flowsheet concept developed assumes the need of partial copper extraction from 30 g Cu/dm^3 to 10 g Cu/dm^3 and recycling the raffinate to the leaching operation. We have also assumed that it will be feasible to produce electrolyte containing at least 40 g Cu/dm^3 in the stripping section, which will be used in the copper electrolysis. In the later stages of the research the Cu/Fe extraction selectivity was also investigated. It was shown that transfer of iron between ongoing operations can be effectively controlled and thus washing operation between extraction and stripping operations was suggested. Few simulations of countercurrent extraction process were performed in order to compare two models: with wash stage (2-1-2) and without washing (2-0-2). Significant reduction in the concentration of iron in strip solutions in 2-1-2 model was noticed when compared to the 2-0-2 model.

In further stages of HYDRO project, the extraction of zinc(II) from solutions simulating CuSX raffinates, assuming complete elimination of Fe was studied. Two commercial organophosphorus acids: D2EHPA and Cyanex 272 were chosen as Zn(II) extractants. These studies have shown that Zn(II) extraction efficiency is significantly improved at elevated temperatures, and that much better results were obtained for D2EHPA system. It was also proved that it is possible to effectively strip loaded organic phase using H_2SO_4 solutions.

In the closing phase of the project, a final choice of material for leaching was made. Therefore the composition of pregnant leach solution has drastically changed, especially with respect to copper(II). Despite this change Acorga M5640 in Escaid 110 was still proposed as the best extraction system for Cu(II).

While maintaining the previously proposed extractant concentration in the organic phase Cu, extraction efficiency can reach from 72 to 96%, depending on whether the PLS is subjected to neutralization prior to the first extraction step. Solutions directed to electrolysis contain about 50 g/dm^3 of Cu.

Separation of Ag from chloride leach solution can be accomplished by cementation on metallic lead. Pb will be precipitated from chloride solutions in the form of lead carbonate (using soda or CO_2). Precipitate can be then used for production of Pb bullion in existing plant at the Glogow smelter.

The solid residue after the oxidative leaching contains considerable amount of elemental sulfur and organic carbon. It is necessary to develop a method of carbon and sulphur elimination from the sludge and management of the gaseous phase from the process. The proposed process will involve a roasting operation. It allows to reduce the flow of material streamed to the extraction of lead and silver with simultaneously enrichment in these components. The management of the gaseous phase allow to utilize SO_2 and simultaneous heat recuperation, which is produced during combustion of carbon and sulfur. It is expected that as the result of such process, the material with more favorable chemical properties will be obtained. It will increase the lead and silver extraction efficiency and make the final residue sustainable management possible.

Investigations of Zn, Ni, Co, Re, V and Mo recovery processes will be possible only after performing continuous operation using laboratory and pilot installations. It is necessary to achieve solutions with the appropriate concentration of these metals (recirculation). Combinations of different hydrometallurgical techniques like oxyhydrolysis, precipitation, cementation, SX, IX and crystallization will be used in the tests of the metals recovery in form of saleable chemical compounds like either $\text{ZnCO}_3/\text{ZnSO}_4$, NiSO_4 , CoSO_4 , NH_4ReO_4 , V_2O_5 , MoO_3 or metals concentrates.

In the process, it is necessary to control the iron concentration in the leach solutions by its precipitation as goethite, jarosite and hematite. The application of hydrothermal hydrolysis at elevated temperatures is also considered. The process can also control the concentration of As in the leaching – SX circuits by hydrothermal or atmospheric precipitation of scorodite: $\text{FeAsO}_4 \cdot 2\text{H}_2\text{O}$, the safest form of arsenic for storage.

Unit operations of the new technology

The proposed hydrometallurgical processing of the Lubin copper concentrate is a sum of a great number of single unit operations. They include various mineral processing, hydrometallurgical and thermal techniques, comprising:

- non-oxidizing leaching of magnesium and calcium (controlled decomposition of barren rock dolomites with the solution of sulfuric acid),
- decantation and filtration of magnesium sulphate for further treatment and application,
- froth flotation: at the stage of feed preparation and initial treatment of the concentrate for testing and its purification after the non-oxidizing leaching operation (gypsum removal by flotation),
- oxidative leaching of the concentrate valuable and barren components, including acidic oxidizing leaching of the key sulfide valuable components (Cu, Zn, Ni, Co,

V, Re, Mo) with the oxygenated solution of sulfuric acid in the presence of Fe(III) at elevated temperatures (atmospheric and pressure processes),

- chloride leaching of silver and lead,
- various techniques of phase separation (sedimentation-decantation, pressure filtration),
- solvent extraction (SX) - for PLS purification and metals separation: copper, zinc, cobalt and nickel, in systems operating in counter-current mode,
- ion-exchange (IX) separation of metals from recirculation solution in leaching – SX circuit; ion-exchange columns for recovering associated metals (e.g. Re, V, Mo),
- electrodeposition of copper (EW) from strip solutions or directly from pressure leaching PLS,
- precipitation and cementation for recovery of silver and lead from brine solutions, as a method for production of concentrates of the metals,
- crystallization for recuperation of magnesium salt,
- thermal processes to valorise the final process wastes or the sludge between the acid and chloride leaching,
- technology for purification of the process effluents.

Acknowledgements

In part (non-oxidative, atmospheric and chloride leaching) this work was carried out in the frame of HYDRO project (Polish NCBiR project contract ZBP/56/66309/IT2/10). Authors acknowledges the financial support given to this project by the NCBiR (National Center for Research and Development) under the IniTech Enterprise. The work was also co-financed by statutory activity subsidy from the Polish Ministry of Science and Higher Education for the Faculty of Chemistry of Wrocław University of Technology.

References

- BARTA L., et al., 1999, *Pressure leaching of chalcopyrite concentrates by Dynatec*. Proceedings of Copper 99 Conference, vol. IV, pp. 167-180.
- BATTY J.D. AND RORKE G.V., 2005, *Development and commercial demonstration of the BioCOP™ thermophile process*, 16th International Biohydrometallurgy, Harrison S.T.L., Rawlings D.E. and Petersen J. (Eds.), Cape Town, S. Africa, Sept. 2005, 153-161.
- BAXTER K., DREISINGER D.B., PRATT G., 2003, *The Sepon Copper Project: Development and Flow Sheet*, Hydrometallurgy 2003, (Young C. et al. Eds.) The Mineral, Metals and Materials Society Warrendale PA USA 2003, 1487-1502.
- CESL Copper Process Description, <http://www.cesl.com/>, 2014.
- CHANTURIJA V.A., VIGDERGAUZ V.E. 2009, *Electrochemistry of Sulfides, Theory and Practice of Flotation*, Ore and Metals, Moscow 2009.
- CHMIELEWSKI T., 2007, *Atmospheric leaching of shale by-product from Lubin concentrator*, Physicochemical Problems of Mineral Processing, 41 (2007) 337-348.

- CHMIELEWSKI T., 2007, *Non-oxidative leaching of black shale copper ore from Lubin Mine*, Physicochemical Problems of Mineral Processing, 41 (2007) 323-335.
- CHMIELEWSKI T., BOROWSKI K., GIBAS K., OCHROMOWICZ K., WOŹNIAK B., 2011, *Atmospheric leaching of copper flotation concentrate with oxygenated sulphuric acid solutions*, Physicochemical Problems of Mineral Processing, 47, 193-206.
- CHMIELEWSKI T., CHAREWICZ W., 2006, *Hydrometallurgical processing of shale by-products from beneficiation circuits of Lubin Concentrator*, In: Perspectives for applying bioleaching Technology to process shale-bearing copper ores, BIOPROCOP'06, Lubin 2006, KGHM Cuprum, Wrocław 2006, 125-145.
- CHMIELEWSKI T., KALETA R., 2011, *Galvanic interactions of sulphide minerals in leaching of flotation concentrate from Lubin Concentrator*, Physicochemical Problems of Mineral Processing, 46, 21-34.
- CHMIELEWSKI T., LUSZCZKIEWICZ A., KONOPACKA Z., 2008, *Acidic pretreatment of hard-to-tread copper ore flotation middlings to facilitate flotation efficiency*, Proc. XXIV International Mineral Processing Congress, Beijing – China, Sept. 24-28 2008, vol.1, (Wan Dianzuo et al., Eds.), Science Press Beijing 2008, 1189-1200.
- CHMIELEWSKI T., LUSZCZKIEWICZ A., KONIECZNY A., KOWALSKA M., 2007, *Non-oxidative acidic treatment of copper sulfide concentrates in the flotation circuit*, Proceedings of the 6th International Copper-Cobre Conference, Toronto, Canada 27-29 August 2007, Vol. II (del Villar R., Nessel J.E., Gomez C.O., and Stradling A.W. – Eds.), Can. Inst. Min. Metal. Petrol., 2007, 53-62.
- CHMIELEWSKI T., LUSZCZKIEWICZ A., KONOPACKA Z., 2007, *Separation and concept of processing of black shale copper ore from Lubin Mine*, 7th International Conference on Non-ferrous Ore Processing, May 21-23, Wojcieszycze, Poland, KGHM Cuprum, Wrocław 2007, 171-184.
- CHMIELEWSKI T., WODKA J., 2010, *Pressure leaching of shale middlings from Lubin concentrator in oxygenated sulphuric acid*. In: Copper 2010, June 6-10, 2010, Hamburg, Germany: proceedings. Vol. 7. Clausthal-Zellerfeld: GDMB, 2010. pp. 2673-2691.
- CHMIELEWSKI T., KONIECZNY A., DRZYMALA J., KALETA R., LUSZCZKIEWICZ A., 2014, *Development concepts for processing of Lubin-Glogow complex sedimentary copper ores*, Proceedings XXVII Int. Min. Process. Congress, Santiago, Chile, 20-24 October, 2014 (accepted for publication).
- d'HUGUES P., NORRIS P.R., HALLBERG K.B., SANCHEZ F., LANGWALDT J., GROTOWSKI A., CHMIELEWSKI T., GROUDEV S., 2008, *Bioshale consortium, Bioshale FP6 European project: Exploiting black shale ores using biotechnologies?*, Minerals Engineering 21, 111–120.
- d'HUGUES P., NORRIS P.R., JOHNSON B., GROTOWSKI A., CHMIELEWSKI T., ŁUSZCZKIEWICZ A., SADOWSKI Z., SKŁODOWSKA A., FARBISZEWSKA T., *Presentation of the FP6 European Project Bioshale. Exploitation of black shale ores using biotechnologies - Polish case studies*, Physicochemical Problems of Mineral Processing, 41 (2007) 373-386.
- DIXON D.G., MAYNE D.D., 2007: *Galvanox – a novel galvanically assisted atmospheric leaching technology for copper concentrates*, Proc. Copper/Cobre 2007 Conference, Toronto (Canada), Riveros P., et al., eds., Vol. IV (1), CIM Montreal, Canada: 191.
- DREISINGER, D.B., RICHMOND, G., HESS, F. AND LANCASTER, T., 2002, *The Competitive Position of the Mt. Gordon Copper Process in the Copper Industry*, ALTA Copper Hydrometallurgy Forum, Perth, Australia, ALTA Metallurgical Services Australia.
- EVANS H., 1999, *The Activox Copper Process*, TMS Copper Hydrometallurgy Short Course (Copper 99), October 1999.

- GIBAS K., BOROWSKI K., CHMIELEWSKI T., WEJMAN K., 2015, *Recovery of cobalt and nickel in atmospheric leaching of flotation sulfide concentrate from Lubin concentrator*, Physicochemical Problems of Mineral Processing, 51, in press.
- HOLMES P.R., CRUNDWELL F.K., 1995: *Kinetic aspects of galvanic interactions between minerals during dissolution*, Hydrometallurgy 39: 353-375.
- JONES D., 1999, *The CESL Copper Process. TMS Copper Hydrometallurgy Short Course (Copper 99)*, October 1999.
- KING J., DREISINGER D. AND KNIGHT 1993, *The total pressure oxidation of copper concentrates*, The Paul E. Queneau Int. Symp. Extract. Metall. of Copper Nickel and Cobalt, vol. I. (Reddy R.G. and Weizenbach R.N., Eds.) Denver, Colorado 735-756
- KONOPACKA Z., LUSZCZKIEWICZ A., CHMIELEWSKI T., 2007. *Effect of non-oxidative leaching on flotation efficiency of Lubin Concentrator middlings*. Physicochemical Problems of Mineral Processing, 41, 275-289.
- KOWALCZUK P. B. and CHMIELEWSKI T. 2010. *Changes of electrode potential in the non-oxidative leaching*, Physicochem. Probl. Miner. Process., 44 (2010): 115-126.
- KUBACZ N., SKORUPSKA B. 2007. *Estimation of influence of organic carbon on concentration and smelting processes*. Conf. Proc. VIII International Conference On Non-ferrous Ore Processing, ICNOP'07, 21-23 May, Wojcieszycze, Poland, KGHM, IMN, 157-166 (in Polish).
- LUSZCZKIEWICZ A. 2004, *Evaluation of upgradeability of the ore with elevated content of black shale Report of Investigation*, Archive of Laboratory of Mineral Processing, Wrocław University of Technology, Wrocław, (in Polish).
- LUSZCZKIEWICZ A., 2000, *Utilisation of black copper shale ores from Lubin-Glogow region*. in: Recent problems on copper ores processing in Poland, November 16, 2000., Conference Proceedings, Mining Committee of Polish Academy of Sciences and KGHM "Polish Copper", 137-156 (in Polish).
- LUSZCZKIEWICZ A., 2009, *Physicochemical Problems of Minerals Processing Seminar*, Niepolomice, Poland, 16-18 Sept, 2009, plenary lecture.
- LUSZCZKIEWICZ A., CHMIELEWSKI T., 2008, *Acid treatment of copper sulfide middlings and rougher concentrates in the flotation circuit of carbonate ores*, Int. J. Min. Process 88, 45-52.
- MAJIMA H. AND PETERS E. 1968: *Electrochemistry of sulphide dissolution in hydrometallurgical systems*, Proc. Int. Mn. Proc. Congress, Leningrad: 13.
- MEHTA, A.P., MURR, L.E., 1983. *Fundamental studies of the contribution of galvanic interaction to acid-bacterial leaching of mixed metal sulfides*. Hydrometallurgy, 9: 235-256.
- NOWAK P., KRAUSS E., POMIANOWSKI A. 1984: *The electrochemical characteristics of the galvanic corrosion of sulfide minerals in short-circuited model galvanic cell*, Hydrometallurgy, 12, 95-110.
- OCHROMOWICZ K., APOSTOLUK W., CHMIELEWSKI T., WOZNIAK B., 2011, *Solvent extraction of copper and accompanying metals from sulfate leach liquors*, Separation science - theory and practice 2011: proceedings of the 1st International Conference on Methods and Materials for Separation Processes, 85-88.
- OCHROMOWICZ K., CHMIELEWSKI T., 2008, *Growing role of solvent extraction in copper ores processing*, Physicochemical Problems of Mineral Processing, 42, 29-36.
- OCHROMOWICZ K., CHMIELEWSKI T., 2011, *Solvent extraction in hydrometallurgical processing of Polish copper concentrates*, Physicochemical Problems of Mineral Processing. 46, 207-218.
- OCHROMOWICZ K., CHMIELEWSKI T., 2013, *Solvent extraction of copper(II) from concentrated leach liquors*, Physicochemical Problems of Mineral Processing. 49(1), 357-367.

- RICHMOND, G.D., AND DREISINGER, D.B. 2002, *Processing of Copper Sulfide Ores by Autoclave Leaching Followed by Extraction and Electrowinning*, Australian Patent 749257, (2002).
- RICHMONT G., *The Mount Gordon Process*, Hydro-Sulfides 2004, International Colloquium on Hydrometallurgical Processing of Copper Sulfides, Santiago, Chile, April 2004, 75-88.
- ROTUSKA K., CHMIELEWSKI T., 2007, *Solvent extraction of valuable metals from pregnant leach solutions of cupriferous shale*, Physicochemical Problems of Mineral Processing, 41, 365-372.
- SMALLEY N. AND G. DAVIS G, 2000, *Operation of the Las Cruces ferric sulphate leach pilot plant*, Minerals Engineering, 13(6) 599-608.
- WODKA J., CHMIELEWSKI T., ZIOŁKOWSKI B., 2007, *Pressure leaching of shale ore in oxygenated sulphuric acid*, Physicochemical Problems of Mineral Processing, 41, 349-3.

Received March 16, 2014; reviewed; accepted August 25, 2014

DEWATERING OF BARITE CLAY WASTEWATER BY INORGANIC COAGULANTS AND CO-POLYMER FLOCCULANTS

Vedat DENIZ

Department of Polymer Engineering, Hitit University, Corum, Turkey, vedatdeniz@hitit.edu.tr

Abstract: This work is focused on dewatering of barite-containing clay waste from a barite beneficiation plant by coagulation and flocculation to enhance the dewatering rate and recycling of process water. A flocculation performance of co-polymers (Superfloc A-130 and A-100) was compared with coagulants ($\text{Al}_2\text{SO}_4 \cdot 18\text{H}_2\text{O}$, CaCl_2 and $\text{FeCl}_3 \cdot 6\text{H}_2\text{O}$). The best results were obtained with an anionic co-polymer, i.e. Superfloc A-130. The settling rate increased 635-fold in the case of using anionic co-polymer Superfloc A-130 in comparison with the natural settling rate of the same wastewater. In laboratory tests, an optimum thickener design was developed for the barite clay wastewater. In this paper, sedimentation studies on the barite clay wastes are presented for the first time, both as the laboratory studies and industrial applications.

Keywords: *dewatering, sedimentation, inorganic coagulant, co-polymer flocculants, wastewater, barite*

Introduction

Clarifications of municipal and industrial wastewaters by solid-liquid separation techniques as well as removal of suspended particles are challenging problems for plants and people because of growing environmental consciousness. On the other hand, there are very limited number of studies reporting in the literature on flocculation and settling properties of mineral industry wastewaters containing high specific gravity mineral such as manganese and chromite. Solid-liquid separation or dewatering processes generally involve unique set of challenges because of the presence of colloidal particles with different sizes, shapes, and specific gravities as well as solution chemistry of their environments. Currently, the most common method for solid-liquid separation is the use of thickeners, in which the particulates settle out to form a bed, leaving a clear supernatant, which can be recycled back to the plant. The settling rate during solid-liquid separation within the thickener is important, so

that this influences the size of the required thickener and the rate at which water can be recycled back to the plant (Kominek and Lash, 1979; Nasser and James, 2006; Cengiz, et al., 2009; Deniz, 2013).

In the mineral industry, many of these wastes contain minerals such as clay, which due to the small particle sizes and charge properties are difficult in order to settling and consolidation. The conventional method used to colloidal particles (e.g. kaolinite) involves inorganic salts-aided coagulation or high molecular weight polymer-aided flocculation and subsequent sedimentation in thickeners (Naser and James, 2006).

The addition of coagulants is used to reduce the overall negative surface charge that surrounds each particle. The coagulants enable the weak van der Waals forces to dominate, which results in attraction between particles causing the colloidal clay-rich suspension to settle out. This is a result of the coagulants neutralizing the surface charge of clay. Two different coagulation mechanisms are used in order to efficiently settle out slimes: inorganic salts and poly-electrolyte coagulation. The most common electrolyte coagulants are aluminum, ferric and calcium salts (Fowler and Morkel, 2010).

Whereas inorganic salts promote coagulation by charge neutralization and double-layer compression, the organic polymers promote solid-liquid separation by the bridging mechanism, sometimes in combination with charge patch effects. Flocculation of fine particles may occur by polymer bridging, charge neutralization, polymer-particle surface complex formation and depletion flocculation, or by a combination of these mechanisms (Gregory, 1985; Ersoy, 2011).

Nowadays, the flocculants used for the flocculation process are non-ionic, anionic and cationic polymers. The non-ionic and anionic polymers cause to form big, fast sedimentation and fairly compact flocs. However, it is preferable to use higher molecular weight anionic or non-ionic polymers over cationic flocculants for the sedimentation process. It is known that the non-ionic polymers are usually used in acidic slurries and the high molecular weight anionic polymers are used in alkali slurries (Sabah and Yeşilkaya, 2000).

The several studies have shown that high molecular weight anionic polymers (e.g. polyacrylamide) are commonly used in settling of negatively charged particulate clay (Scheiner and Wilmen, 1987; Richardson and Connely, 1988; Singh et al., 1999; Hogg, 2000; Abd-Wl Rahman, 2000; Patience et al., 2003; Ozkan, 2003; Tao et al., 2010; Kursun, 2010; Sabah and Aciksoz, 2012; Kurama and Karaguzel, 2012). In that case, the polymer bridging mechanism is of primary importance, whereas charge neutralization will be of secondary or little importance (Patience et al., 2003). The use of high molecular weight anionic polyacrylamide in flocculating negatively charged particles have the advantage of being more effective than cationic polymers by increasing the settling rate and producing a distinct sediment structure, and in addition, re-stabilization of clay particles by excessive polymer adsorption driven by strong electrostatic attraction may be avoided. The electrostatic repulsion between the clay particles and the anionic polyacrylamide allows only limited polymer adsorption. On

the other hand, the polymer molecule expansion arising from the charge repulsion produces loops and tails, which lead to formation of large open structure flocs. This effect has been seen to be effective in the flocculating negatively charged clay dispersions (Somasundaran and Moudgil, 1988).

A barite beneficiation plant belonging to Baser Mining Co. (Sarkikaragac/Isparta) in Turkey has a capacity of 40 Mg/h. The barite slime is concentrated with multi gravity separator (MGS) and shaking tables to increase its quality. Six settling ponds (Fig. 1) are used in the beneficiation plant to separate the slime from water by natural sedimentation (Deniz, 2000). The barite-containing clay wastewater in the ponds does not contain appreciable amount of chemical pollutant and the amount of clean water, which is needed by the plant. However, it cannot be cleaned due to very slow settling rate of solid ingredients in the settling ponds.

In this study, dewatering of barite clay wastewaters belonging to Baser Mining Co. from Isparta (Turkey) was investigated using the sedimentation technique. This technique was found to be a suitable solution for fresh water for barite beneficiation plant.

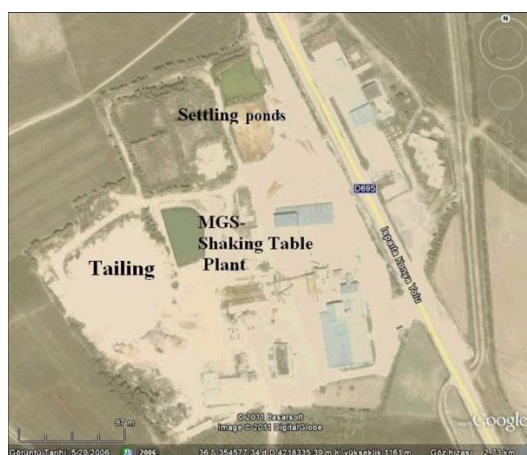


Fig. 1. View of settling ponds sand tailing area in the Başer barite beneficiation plant

Material and methods

Material

During beneficiation of Isparta (Turkey) barite ores, a fine particle fraction ($-106\ \mu\text{m}$) is separated by cyclones as a dilute (7% solids by weight) aqueous slurry. The solids are a mixture of clay minerals, barite and other fine divided minerals, such as: orthoclase, calcite and quartz. This slurry is pumped into large impoundment areas for the natural settling. Due to the colloidal nature and slow consolidation characteristics of such clays, a large storage area is required. In order to place these clays, together

with the sand tailings (from a jigging process), back into the original mine cut without building aboveground dams, the clays would have to be dewatered to over 50% solids by weight. Unfortunately, decades are needed for clays to dewater to such high solid level in the conventional settling areas. Thus, a huge volume of water and large areas of land are tied-up by impounding these clays for a long period.

Methods

The chemical composition of particulate tailings was analyzed by an X-ray fluorescence, and a particle size distribution was determined using Malvern Mastersizer Particle Size Analyzer (Mastersizer 2000). The mineral composition was determined by an X-ray diffraction (XRD). Electrokinetic (zeta potential) measurements were obtained using a Zeta-Meter 3.0 device. The pH was measured with a lab pH-meter.

The flocculation and coagulation experiments were carried out using a mechanical mixer with a speed control. The tests were conducted on original barite clay wastewater samples. For each test, a 500 cm³ of original slime wastewater containing 7% wt./wt. solids was placed in a 600 cm³ glass measuring cylinder and stirred for 2 minutes at a rotational speed of 500 rpm to ensure homogeneous dispersion. The required amount of coagulant and polymer solution was added continuously into the suspension during the stirring, which was stopped after the optimum mixing time.

A base case natural settling test on the samples was performed in order to highlight the problem areas of material type and depths. The coagulants were Fe³⁺, Ca²⁺ and Al³⁺ salts. The inorganic coagulants solution, distilled water and 10 g of dry sample were mixed together and then stirred at 500 rpm for 30 min. The anionic polyacrylamide flocculants, Superfloc A-100 and A-130, an acrylamide– acrylic acid random copolymer were obtained courtesy of Cytec Industries, USA. Superfloc A-100 and A-130 have a molecular weight of 12·10⁶ g/mol and the content of acrylic acid monomer of approximately 30% and 35%, respectively. The addition of 0.5% by weight polymer solution was made up by adding a dry polymer powder to the vortex of a stirred solution followed by high speed mixing for 1 h. The solution was mixed for 12 h. The solution was then rested for a further 12 h prior to use. The suspensions were diluted in tap water.

After addition of the coagulant and flocculant, the suspension was mixed for 20 sec, and then the prepared clay suspensions were transferred to the 600 cm³ measuring cylinders (60 mm in diameter). The height of the slurry and water interface was recorded as a function of time and used to calculate the settling rates of coagulated and flocculated suspension.

Results and Discussion

Chemical and mineralogical analysis

The chemical compositions of the associated minerals in the barite tailing were determined by an XRF method as shown in Table 1. As expected, the tailing is mainly composed of SiO_2 , Al_2O_3 and CaO .

Table 1. Chemical compositions of barite tailing

| Components | SiO_2 | Al_2O_3 | CaO | Fe_2O_3 | MgO | SO_3 | Na_2O | K_2O | BaSO_4 | LOI* |
|------------|----------------|-------------------------|--------------|-------------------------|--------------|---------------|-----------------------|----------------------|-----------------|------|
| Amount, % | 60.17 | 12.84 | 6.66 | 3.85 | 1.06 | 9.79 | 1.44 | 3.41 | 5.05 | 0.78 |

*LOI: Loss-on-ignition

The XRD analysis of the barite tailings indicated that the main minerals are chlorite, serisite, barite, orthoclase, calcite and quartz (Fig. 2). According to the chemical analysis data and the XRD results, the original tailings, theoretically, contain approximately 45% clay minerals (serisite, chlorite), 14% calcite, 5% orthoclase and 6% quartz, with the percentage of barite being about 5%.

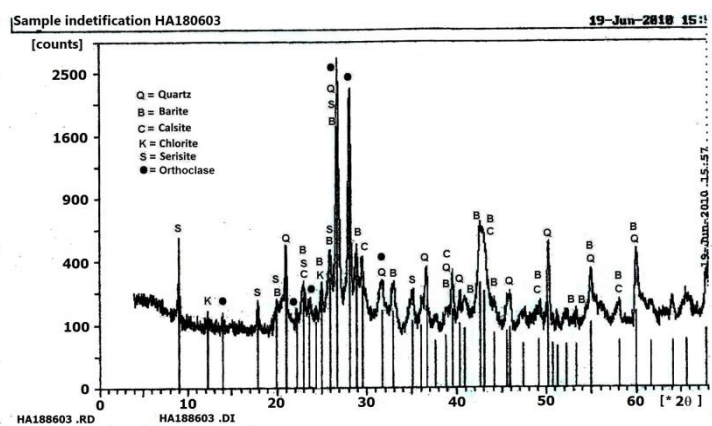


Fig. 2. XRD patterns of barite tailing elements

Particle size distribution

The average particle size determined from the Gaudin-Schuhman type of plot was $9.47 \mu\text{m}$, and the percentage of slime size ($<20 \mu\text{m}$) constituted 74% of the overall material, which indicates the presence of very high specific surfaces area. Based on classification of Wentworth (1922), although the percent of particles in clay size accounts for 25% ($<4 \mu\text{m}$), the percentage of particles in the silt size is 72% ($4\text{--}95 \mu\text{m}$). Those particles in the sand size were 3% ($>95 \mu\text{m}$).

Zeta potential tests

Because of the high ionic strength (or high conductivity) of barite tailing, the zeta potential of particles from the wastewater was not measured directly. Instead of this, the original tailing was dried at first, and then the test solution was prepared with distilled water and the solid particles of 106 μm in size. The zeta potential of this solution was measured at different pH values. Figure 3 presents the effect of pH on the zeta potential of barite tailings. As apparent, the tailings exhibit negative charge at all practical pH values with no apparent zero point of charge. The highest zeta potential (28.4 mV) measured in the neutral pH (8) indicates that the suspension is quite stable. The pH of solution was adjusted by adding HCl and NaOH. The relatively moderate zeta potential values obtained particularly at high pH are in a good agreement with the presented data by Tunçan (1995) for different types of clay minerals. It indicates that there is a higher percentage of chlorite and sericite than kaolinite and illite in the barite plant tailings.

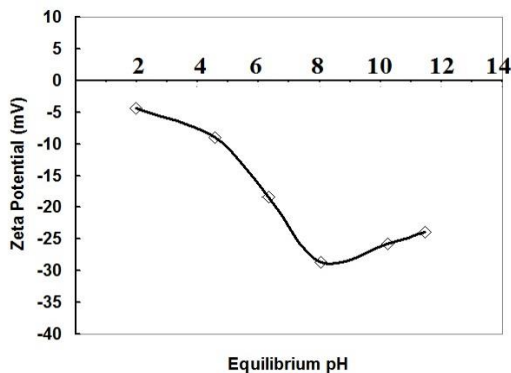


Fig. 3. Zeta potential-pH profile for the particles from barite tailing

Sedimentation tests

The coagulant tests were performed in the presence of three types of inorganic coagulants at different dosages (Figs. 4-6). It is found that aluminium sulphate ($\text{Al}_2\text{SO}_4 \cdot 18\text{H}_2\text{O}$), calcium chloride (CaCl_2) and iron(III) chloride ($\text{FeCl}_3 \cdot 6\text{H}_2\text{O}$), alone, are not effective for the sedimentation processes. As it can be seen from Fig. 7, the settling rate increased with increasing coagulant dosage for three coagulant types. For coagulants, settling rate reached a maximum at around 2400 ($\text{Al}_2\text{SO}_4 \cdot 18\text{H}_2\text{O}$), 4800 (CaCl_2) and 1800 ($\text{FeCl}_3 \cdot 6\text{H}_2\text{O}$) g/Mg dosage, and then began to decrease with increasing coagulant dosage. Unfortunately, as it was expected, sedimentation depending on electrostatic and van der Waals attraction forces did not occur by expectation that adding cations such as Al^{3+} , Ca^{2+} and Fe^{3+} to negatively charged solution would decrease the zeta potential of particles. The reason for this is that the Al^{3+} , Ca^{2+} and Fe^{3+} cations alone are not effective coagulants and they form a series of

hydrolysis reactions in the colloidal systems, where the solids concentration and alkalinity are low. Since these cations are amphoteric, they behave as acid in alkali medium and vice versa. The reactions dependent upon this property show repetitive hydrolysis of cations.

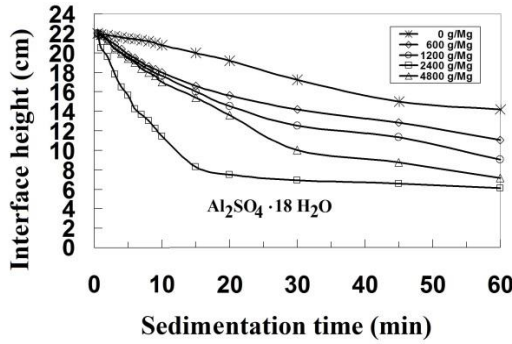


Fig. 4. Sedimentation curves of barite tailing elements for different doses of aluminum sulphate

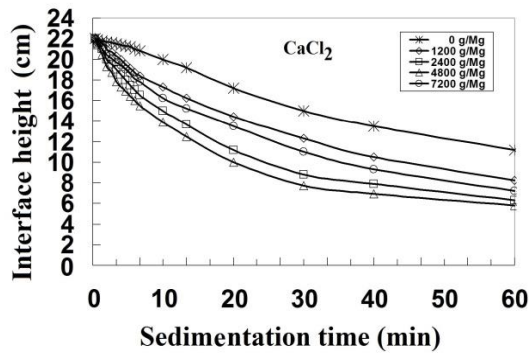


Fig. 5. Sedimentation curves of barite tailing elements for different doses of calcium chloride

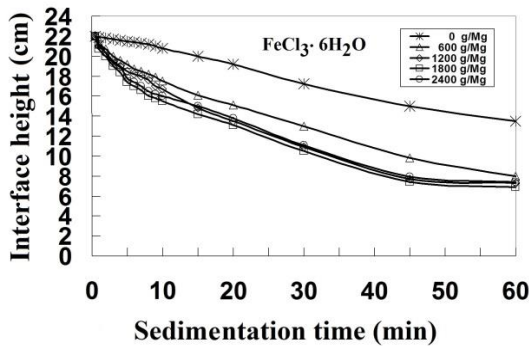


Fig. 6. Sedimentation curves of barite tailing elements for different doses of ferric chloride

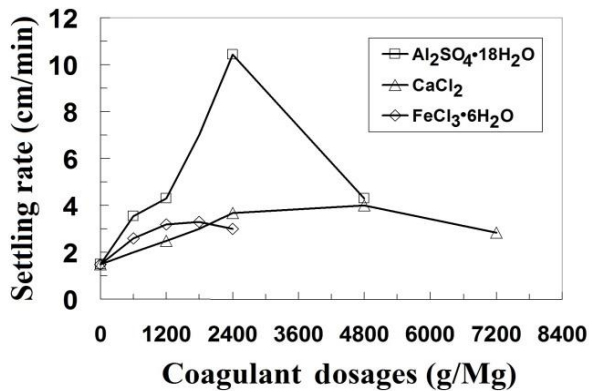


Fig. 7. Effect of flocculant dosages on settling rate for different coagulants

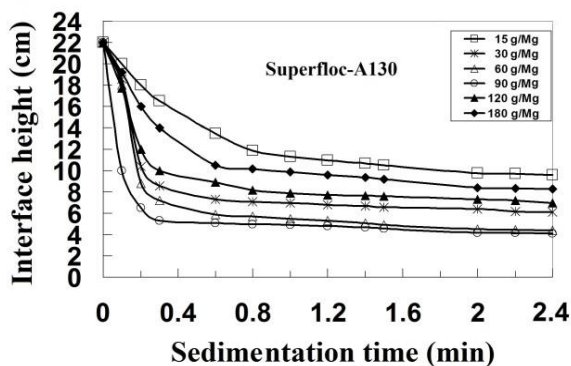


Fig. 8. Sedimentation curves of barite tailing elements for different doses of Superfloc A-130

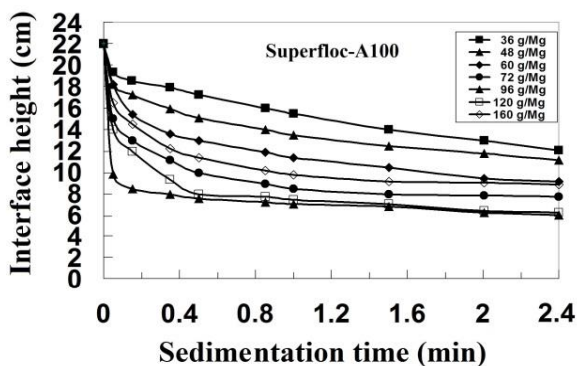


Fig. 9. Sedimentation curves of barite tailing elements for different doses of Superfloc A-100

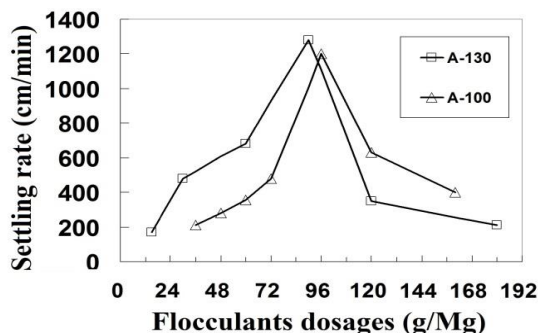


Fig. 10. Effect of flocculant dosages on settling rate for different flocculant types

The flocculation tests were performed in the presence of two types of polymer flocculants (Figs. 8 and 9) at different dosages. Figures 8 and 9 show the effect of polymer type and its dosage on the settling rate of particulate clays, while Figure 10 the relationship between settling rate and flocculant dosage. For Superfloc A-130 and Superfloc A-100, the settling rate reached the maximum for 90 and 96 g/Mg polymer dosage, respectively, and then began to decrease with increasing in the polymer dosage. At low dosages, the floc size is expected to be very small because of insufficient amount of polymer adsorption on the particles. The increase in the amount of adsorbed polymer results in incorporation of more suspended particles in the floc and in turn enlargement of the floc size, leading to the enhanced settling rate. Figure 10 clearly shows that the Superfloc A-130 settling rates are higher than for Superfloc A-100 flocculant in the most polymer dosages. In other words, for the same polymer dosages (90-96 g/Mg) Superfloc A-130 produces larger flocs. In addition, Superfloc A-130 shows much better performance than inorganic coagulants. For instance, whereas the highest settling rate of Superfloc A-130 has 1275 cm/min and A-100 has 1200 cm/min, on the other hand, $\text{Al}_2\text{SO}_4 \cdot 18\text{H}_2\text{O}$ has 10.5 cm/min, CaCl_2 4 cm/min and $\text{Fe}_2\text{Cl}_3 \cdot 6\text{H}_2\text{O}$ 3.2 cm/min settling rates.

Figure 11 provides the photographic description of settling behaviour of coagulant and flocculant dosed in the 600 cm³ measuring cylinder sets. The natural settling behaviour of barite clay wastewater is shown in Fig. 11(a). Under this condition, there is no clear distinct interface between the accumulated sediment bed and overlying water, thereby the volume fraction at the top of the accumulated sediment cannot be considered as the gel point (see Fig. 11(a)). When the particles are coagulated, the van der Waals and other colloidal forces are dominant and the coagulated particles settle together forming the interface between the coagulated sediment network and supernatant (see Figs. 11(b-d)). It can be seen from Figs. 11(e) and 11(f), that there is a very rapid settlement, leading to the formation of a coarsely structured matrix of deposited solids, with using flocculant. The settlement properties of this solids column appear to be largely insensitive to dose. Through time this layer slowly reduces in height as water is gradually released due to compressive settlement of the solids

matrix. Because of low particle charges, an effective flocculation of tailings, which contain high amounts of serisite and chlorite with anionic Superfloc A-100 and A-130 can be explained by the presence of electrostatic attraction forces and /or bonds of particles with the polymer bridges and van der Waals forces. Although polymers and particles have the same charges, better flocs obtained with Superfloc A-130 rather than Superfloc A-100 indicate that the particles are coated with the polymer bridges. Again, with the use of anionic polymer, a very high amount of anions adsorbed onto cations sites such as calcium, magnesium with the resultant electrostatic attraction forces and thus strong flocs are obtained.

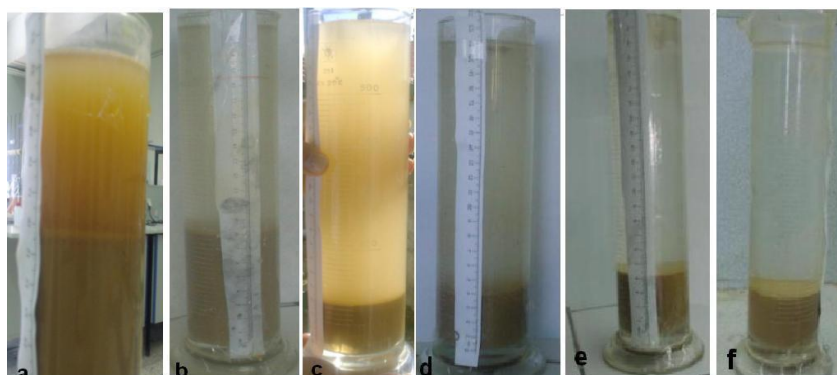


Fig. 11. Settling test after 30 min for various samples studied: (a) natural settling, (b) iron chloride, (c) calcium chloride, (d) aluminum sulphate, (e) Superfloc A-100 and (f) Superfloc A-130

Calculations of thickener area

The thickener design was used by Talmage and Fitch (1958) to determine the limiting flux, and thus to predict the unit area for specific thickening applications. The value of the area (A) was developed by the following equation (Talmage and Fitch, 1958):

$$A = \frac{Q \cdot t_u}{C_0 \cdot H_0}, \quad (1)$$

where A is the thickener area, m^2 , Q feed solid rate (9.49 Mg/h), t_u maximum time for underflow concentration (h), H_0 initial height (0.22 m), C_0 initial concentration (73 kg/m^3).

From the definition point of view, the thickener capacity was defined as the amount of the clear solution overflowing of slime slurry. In this work, the thickener area was calculated for each coagulant and flocculant type (Table 2). Table 2 summarized the data of the above factors, affecting flocculation behaviour of slime.

Table 2. Effect of coagulant and flocculant dose on the thickener area

| Name | Dose g/Mg | Sediment rate mm/min | Thickener Area (m ²) |
|--|--------------|-------------------------|-------------------------------------|
| None | 0.0 | 20.4 | 963 |
| Al ₂ SO ₄ ·6H ₂ O | 600 | 36 | 723 |
| | 1200 | 41 | 410 |
| | 2400 | 105 | 141 |
| | 4800 | 44 | 336 |
| | 1200 | 25 | 591 |
| CaCl ₂ | 2400 | 36 | 410 |
| | 4800 | 40 | 369 |
| | 7200 | 28 | 528 |
| | 600 | 26 | 568 |
| FeCl ₃ ·6H ₂ O | 1200 | 30 | 492 |
| | 1800 | 32 | 462 |
| | 2400 | 30 | 492 |
| Superfloc A-130 | 15 | 1700 | 8.69 |
| | 30 | 4800 | 3.08 |
| | 60 | 6850 | 2.16 |
| | 90 | 12750 | 1.15 |
| | 120 | 3500 | 4.22 |
| | 180 | 2200 | 6.71 |
| Superfloc A-100 | 36 | 2150 | 6.87 |
| | 48 | 2650 | 5.57 |
| | 60 | 3500 | 4.22 |
| | 72 | 5000 | 2.95 |
| | 96 | 12000 | 1.23 |
| | 120 | 6250 | 2.36 |
| | 156 | 4100 | 3.60 |

According to the above calculations, a thickener was designed (Fig. 12). The thickener was realized for 130 m³/h wastewater treatment with the installed motor power of 40 kW. The flocculant consumption (Superfloc A-130) and transmittance of the reclaimed water were in a good agreement with the laboratory studies. The operating cost of the facility excluding labor is less than two cents (penny) per m³ of reclaimed water. For a comparison, one can take the cost of fresh municipal water from a municipality which is around ten cents per m³. The facility is able to reclaim approximately 86% of the wastewater and it has been run without any problems.



Fig. 12. Wastewater treatment plant belonging to the Baser barite beneficiation plant

Conclusions

Based on this study, the following conclusions can be made:

- X-ray and XRD analysis showed that the material used in this work is composed of serisite and chlorite,
- the measured electrical surface charges on the barite tailing are evaluated. It is observed that natural sedimentation of mineral particles in pulps is difficult,
- the electrical surface charges of clay minerals are negative (-), so, the change of OH^- and H^+ ion concentration of the pulp does not affect the sedimentation process,
- natural settling of suspended solids was found to be very slow and it took approximately 6 h of settling. The present study showed that the supernatant after 6 h of settling was not free from suspended particulate clays. The average settling rate was estimated to be 20.4 mm/min,
- the cations (Al^{3+} , Ca^{2+} and Fe^{3+}) can be used to improve the settling rate of barite tailings. However, the cations had a poor effect on sedimentation. The cation Al^{3+} proved to be the most effective coagulant in this test work,
- the flocculant settling tests work produced the highest settling rate. Also polyacrylamides are bound to the surface of particles with electrostatic attraction forces along with polymer bridges,
- the flocculation of clays (the net negative charge) by anionic polyacrylamides was explained in the light of interaction of the carboxylate group ($-\text{COOH}$) with positive site edges of clay minerals,
- the Superfloc A-130 flocculant had the best results in settling the slimes. The dosage of 90 g/Mg of polyacrylamide flocculant showed the best settling rate.
- clarification of barite tailing by polyacrylamide flocculants was achieved within 1-2 min against the natural settling time of 6-8 h.

The results showed that a simple solid-liquid separation system may reclaim the water input very efficiently. The simultaneous recovery of clay particulates from the

barite beneficiation plant effluent is essential from the economic point of view, as well as for the water pollution control.

References

- ABD-EL RAHMAN M.K., 2000, *Dewatering of phosphatic clay waste by flocculation*, Chemical Engineering Technology, 23(5): 457–461.
- CENGIZ I., SABAH E., OZGEN S., AKYILDIZ H., 2009, *Flocculation of fine particles in ceramic wastewater using new types of polymeric flocculants*, Journal of Applied Polymer Science, 112: 1258–1264.
- DENIZ V., 2000, *Recovery of barite from BASER Co. barite processing plant slimes by using MGS*, GEOSOUND Science Technology Bulletin Earth Science, 36: 207–212.
- DENIZ, V., 2013, *Use of co-polymer flocculants for eliminate of the environmental effects of wastewater of a coal washer and design of a thickener for supplies of fresh water*, Energy Sources (Part A): Recovery, Utilization, and Environmental Effects, 35 (22): 2132–2140.
- ERSOY B., 2011, *Influence of pH and chloride-based metal salts on coagulation/dispersion behavior of talc suspension*, Separation Science & Technology, 46: 1519–1527.
- FOWLER M., MORTEL J., 2010, *The effect of cation and organic addition on the settling and compaction behaviour of clay-rich slimes*, Journal of South Africa Intuition Mining & Metallurgy, 110: 99–106.
- GREGORY J., 1985, *The use of polymeric flocculants*, Proceedings of the Engineering Foundation Conferences on Flocculation, Sedimentation and Consolidation, Georgia, USA, American Institute of Chemical Engineer, New York, USA, 253–263.
- HOGG R., 2000, *Flocculation and dewatering*, International Journal of Mineral Processing, 58: 223–236.
- KOMINEK E.G., LASH L.D., 1979, *Sedimentation, Handbook of Separation Techniques for Chemical Engineers* (ed. by Schweitzer, P.A), McGraw-Hill, New York.
- KURUN I., 2010, *Determination of flocculation and adsorption-desorption characteristic of a Na-feldspar concentrate in the presence of different polymers*, Physicochemical Problems of Mineral Processing, 44(1), 127–142.
- KURAMA H., KARAGUZEL C., 2012, *The effect of zeta potential on the sedimentation behavior of natural stone processing effluent*, Physicochemical Problems of Mineral Processing, 49(2), 575–586.
- NASSER M.S., JAMES A.E., 2006, *The effect of polyacrylamide charge density and molecular weight on the flocculation and sedimentation behaviour of kaolinite suspensions*, Separation Purification Technology, 52: 241–252.
- OZKAN A., 2003, *Coagulation and flocculation characteristics of talc by different flocculants in the presence of cations*, Minerals Engineering, 16: 59–61.
- PATIENCE M., ADDAI-MENASH J., RALSTON J., 2003, *Investigation of the effect of polymer type on flocculation, rheology and dewatering behaviour of kaolinite dispersions*, International Journal of Mineral Processing, 71: 247–268.
- RICHARDSON P.F., CONNELLY L.J., 1988, *Industrial coagulant and flocculants, Reagents in mineral technology* (Eds. by Somasundaran P. & Modugil B.M), Surfactant Science Series, 27: 519–528.
- SABAH E., ACIKSOZ C., 2012, *Flocculation performance of fine particles in travertine slime suspension*, Physicochemical Problems of Mineral Processing, 48(2), 555–566.
- SABAH E., YESILKAYA L., 2000, *Evaluation of the settling behavior of Kirka borax concentrator tailings using different type of polymers*, Journal of Ore Dressing, 2: 1–12.
- SCHEINER B.J., WILEMON G.M., 1987, *Applied flocculation efficiency: a comparison of polyethylene oxide and polyacrylamides*, Flocculation in Biotechnology & Separation Systems. 4: 175–185.

- SINGH B.P., BESRA L., PRASAD A.R., 1999, *Coagulation and flocculation study of iron ore fines*, Separation Science & Technology, 34(5): 743–753.
- SOMASUNDARAN P., MOUDGIL B.M., 1988, *Reagents in Mineral Technology*, 27, Marcel–Dekker, New York.
- TAO D., PAREKH B.K., ZHAO Y., ZHANG P., 2010, *Pilot-scale demonstration of Deep ConeTM paste thickening process for phosphatic clay/sand disposal*, Separation Science & Technology, 45: 1418–1425.
- TALMAGE W.B., FITCH E.B., 1958, *Determining thickener unit areas*, Industrial Engineering Chemical, 47: 38–41.
- TUNCAN A. 1995, *Determination of physico-chemical properties of some clay minerals in laboratory*, Seventh National Clay Symposium, Ankara/Turkey, 187–199 (in Turkish).
- WENTWORTH C.K., 1922, *A scale of grade and class terms for clastic sediments*, Journal of Geology, 30: 377–392.